



'New Insights on the Selective Oxidation of Methanol to Formaldehyde on FeMo Based Catalysts'

Catherine Brookes

School of Chemistry
Cardiff University

Thesis for the degree of Doctor of Philosophy

This thesis was submitted for examination in August 2015.

Abstract

The selective oxidation of methanol has been studied in detail, with particular focus on gaining insights into the surface active sites responsible for directing the selectivity to formaldehyde. Various Fe and Mo containing oxides have been investigated for their reactivity with methanol, to gain an understanding of the different roles of these components in the industrial catalyst employed, which is a mixed phase comprised of MoO_3 and $\text{Fe}_2(\text{MoO}_4)_3$. Catalysts have primarily been tested through using TPD (temperature programmed desorption) and TPPFR (temperature programmed pulsed flow reaction). The reactivity of Fe_2O_3 is dominated by combustion products, with CO_2 and H_2 produced via a formate intermediate adsorbing at the catalyst surface. For MoO_3 however, the surface is populated by methoxy intermediates, so that the selectivity is almost 100 % directed to formaldehyde. When a mixture of isolated Fe and Mo sites co-exist, the surface methoxy becomes stabilised, resulting in a dehydrogenation reaction to CO and H_2 . CO and CO_2 can also be observed on Mo rich surfaces, however here a consequence of the further oxidation of formaldehyde, through a linear pathway. TPD and DRIFTS identify these intermediates and products forming.

Since the structure of the industrial catalyst is relatively complex, in that it contains both MoO_3 and $\text{Fe}_2(\text{MoO}_4)_3$, it is difficult to identify the active site for the reaction with methanol. A novel approach to understanding this further, has involved the synthesis of a series of MoO_x modified Fe_2O_3 catalysts in an attempt to make core-shell oxidic materials of the type $\text{MoO}_x/\text{Fe}_2\text{O}_3$. Various monolayer loadings are investigated. It is conclusively shown that for all coverages the Mo stays in the surface region, even after annealing to high temperatures, only reacting with the iron oxide surface when the material is annealed above 400°C . From drying at 120°C to calcining at 500°C , the Mo converts from a MoO_3 -like octahedral layer to $\text{Fe}_2(\text{MoO}_4)_3$, with Mo in a tetrahedral structure. Although changes in the Mo phase are clearly evident, it is shown that for all catalysts a one monolayer equivalent of amorphous octahedral MoO_x also remains at the surface, regardless of the calcination temperature employed. It is this layer which is deemed as the surface active layer, since all catalysts at varying monolayer overages and anneal temperatures show a similar reaction with methanol. This overlayer is unique, and is suggested to be comparable to the surface terminating layer in bulk catalysts such as $\text{Fe}_2(\text{MoO}_4)_3$. Successive work involved studying the reactivity of this upper layer, with suggestions of a two site Mo-Mo surface species forming on adsorption of methanol.

Concluding work involves an investigation into the redox properties of $\text{Fe}_2(\text{MoO}_4)_3$, to address the significance of this mixed oxide in commercial materials. $\text{Fe}_2(\text{MoO}_4)_3$ forms the

majority of the industrial catalyst, and although it shows a superior performance in terms of its activity, it cannot compete with the near 100 % selectivity of MoO_3 to formaldehyde. Other supports have been trialled for their performance under reaction with methanol. It is shown that $\text{Fe}_2(\text{MoO}_4)_3$ has increased bulk lattice oxygen mobility. Under normal reaction conditions, the reaction is carried out aerobically. However if oxygen supplies are restricted, $\text{Fe}_2(\text{MoO}_4)_3$ is able to demonstrate a satisfactory performance above 300°C , as lattice oxygen is able to replace lost surface oxygen. This can continue for some time, until reduced phases containing Mo(IV) form. At this point formaldehyde selectivity drops, matched by a rise in CO production. High oxidation states are crucial to catalyst performance, with the reaction continuously cycling between Mo(VI) and Mo(VI), with a very short lifetime for the Mo(IV) species.

Acknowledgements

Firstly, I would like to express my sincere gratitude to my supervisor, Professor Mike Bowker, for his continual support and guidance throughout the course of my PhD. Whether it was a chat about ongoing work, a reassurance that I was on track, or a general catch up at the onsite Costa, I thank him for his patience, immense knowledge and his ability to calculate any sum without a calculator! I could not have imagined having a better supervisor.

In addition to Mike I would like to thank the following people who have provided me with significant help and support which I have greatly appreciated. My sincere thanks must go to Dr Peter Wells.

My journey to obtaining this thesis has been one of a unique kind, entering as the first student in to the UK Catalysis Hub based at Harwell. It was a rocky start...with just three of us based permanently in the office, and a number of empty labs! Although there were initial doubts, Peter was there to ensure me that things would work out for the best. They did, of course, and I am now proud to be working at the fully developed catalysis institution here today. Thank you Peter for putting up with me, and for the continual encouragement. I finally got 'that' paper finished, even if it did come after a lacrosse match or two! In all seriousness, thank you for all the support, all the time you have put aside, and for your positive attitude towards the work of others.

I should also here mention Dr Nikolaos Dimitratos, who was one of the three who began on the journey with us at Harwell. I still miss our daily coffees as the original 'dreamteam' which must include the infamous Ricardo!

I acknowledge the contributions of David Morgan, David Mora Fonz, Emma Gibson, and Diego Gianolio, and also thank the support staff at both institutions. I thank Diamond Light Source and the EPSRC for their funding of this PhD.

I thank my fellow labmates for the stimulating discussions and office banter, and for the fun we have had over the last few years. This includes both those at Harwell and Cardiff University. In particular I'd like to thank Wilm Jones and Scott Rogers for their valuable input.

Of course I would like to thank Macey for his support during the stressful process of writing up. I'm so glad I could look forward to weekends away cycling with you, visiting friends. I'm not sure I would have been able to get through the PhD if it hadn't been for some of our amazing trips abroad, and your ability to always put a smile on my face!

Last but not least I would like to thank my parents. My mum and best friend Eve Rees- thank you for always being there for me, no matter what, even when I acted like the 'PhD zilla'. Your support extends to every aspect of my life, and I really would not have been able to get where I am today without you. And finally, my father John Brookes. From you I have inherited my academic drive and discipline. I hope you would be proud.

Glossary

MeOH	Methanol
AHM	Ammonium Heptamolybdate
ATR	Attenuated Total Reflectance
B.E	Binding Energy
B.N	Boron Nitride
C.N	Co-ordination Number
CH₃OH	Methanol
CH₄	Methane
CO	Carbon Monoxide
CO₂	Carbon Dioxide
DME	Dimethyl Ether
DRIFTS	Diffuse Reflectance Infrared Fourier Transform Spectroscopy
EDX	Energy Dispersive X-Ray
EM	Electron Microscopy
EXAFS	Extended X-Ray Absorption Fine Structure
Fe₂(MoO₄)₃	Iron Molybdate
Fe₂O₃	Iron Oxide
FT	Fourier Transform
FTIR	Fourier Transform Infrared Spectroscopy
FWHM	Full Width Half Maximum
GC	Gas Chromatography
GPE	Gibb's Potential Energy
H₂	Hydrogen
H₂CO	Formaldehyde
HC	Hydrocarbon
HNO₃	Nitric Acid
HTF	Heat Transfer Fluid
HTF	High Temperature Furnace
IPFR	Isothermal Pulse Flow Reaction
IR	Infrared
K.E	Kinetic Energy
LCF	Linear Combination Fitting
LEIS	Low Energy Ion Scattering

MFC	Mass Flow Controller
MFP	Mean Free Path
ML	Monolayer
MoO₃	Molybdena
MPW	Multi Pole Wiggler
MS	Mass Spectrometry
MVK	Mars-Van Krevelen
O.D	Outer Diameter
O_h	Octahedral
QMS	Quadrupole Mass Spectrometer
RDS	Rate Determining Step
RF	Radio Frequency
RPM	Revs Per Minute
SEM	Scanning Electron Microscopy
SR	Synchrotron Radiation
STEM	Scanning Transmission Electron Spectroscopy
TCD	Thermal Conductivity Detector
T_d	Tetrahedral
TEM	Transmission Electron Microscopy
TOF	Turn Over Frequency
TPD	Temperature Programmed Desorption
TPO	Temperature Programmed Oxidation
TPPFR	Temperature Programmed Pulsed Flow Reaction
TPR	Temperature Programmed Reduction
VOC's	Volatile Organic Compounds
w/t	Weight
XAFS	X-ray Absorption Fine Spectroscopy
XANES	X-ray Absorption Near Edge Spectroscopy
XPS	X-ray Photoelectron Spectroscopy
XRD	X-ray Diffraction

Contents

Chapter 1: Introduction	1
Chapter 2: Experimental	50
Chapter 3: ..Bulk Metal Oxides for Methanol Oxidation.....	117
Chapter 4: Core-Shell Structures of the Type MoO _x /Fe ₂ O ₃ , Probing the Nature of the Structural Motifs Responsible for Methanol Oxidation Catalysis.....	189
Chapter 5: <i>In situ</i> studies for Understanding Surface Structural Changes.....	241
Chapter 6: Investigating the Redox Nature of FeMo Based Catalysts.....	276
Chapter 7: Investigating the Redox Nature of FeMo Based Catalysts.....	318

A breakdown of each Chapter is detailed at the start of each section

Chapter 1: Introduction

Contents

1. Catalysis	2
1.1. General	2
1.2. Catalytic Mechanisms and Energetics	3
1.3. Heterogeneous vs. Homogeneous Catalysis	4
2. Background	5
2.1. Selective Oxidation	5
2.2. The History of Formaldehyde Production	5
2.3. The Current Active Catalyst: Iron Molybdate ($\text{Fe}_2(\text{MoO}_4)_3$) with Excess Molybdena (MoO_3)	7
3. Basic materials	13
3.1. Methanol	13
3.2. Iron	14
3.2.1. Iron (III) Oxide.....	15
3.2.2. $\text{Fe}_2(\text{MoO}_4)_3$	16
3.2.3. FeMoO_4	17
3.3. Molybdenum	18
3.3.1. Molybdenum Oxide (Molybdena)	18
3.3.2. MoO_2	20
4. Preparation Methods	21
5. Reactivity	24
5.1. Fe_2O_3	24
5.2. MoO_3	26
6. Kinetics and the Mars-van Krevelen Mechanism	29
7. Thermodynamics.....	33
8. Supported Catalysts.....	35
9. Deactivation of $\text{Fe}_2(\text{MoO}_4)_3$ Based Catalysts	39
10. Research Objectives	42

1. Catalysis

1.1. General

The term ‘catalysis’ was first defined in 1836 by Berzelius [1], to identify a new entity proficient in promoting a chemical reaction by a ‘catalytic contact’. However, catalysis can also be traced back to ancient times, with the fermentation process as a significant example. Essentially, a catalyst is a material which increases the rate of a chemical reaction, enabling the reaction to proceed with less energy input to initiate it. It does this by lowering the activation energy of the reaction, providing an alternate reaction pathway to avoid the rate determining step of the un-catalysed reaction. The catalyst may participate in multiple chemical transformations, but are usually specific to a certain reaction, and often take the form of a transition metal, transition metal oxide or enzyme (in living cells). Since the catalyst is not consumed during the process, and does not take part as a reactant, it can be recycled for repeated use. For this reason, only small amounts are required to increase the rate of reaction.

Figure 1 demonstrates the effect of catalyst use on reaction rate. With catalyst, the reaction can reach completion at a faster rate, as highlighted by the line in red. It is important to note that a catalyst does not affect the final equilibrium composition of a system, since the effect is present in both the forward and reverse reaction (second law of thermodynamics). The equilibrium yield will remain constant, but with the addition of a catalyst, the achievement of the chemical equilibrium between reactants and products will be accelerated.

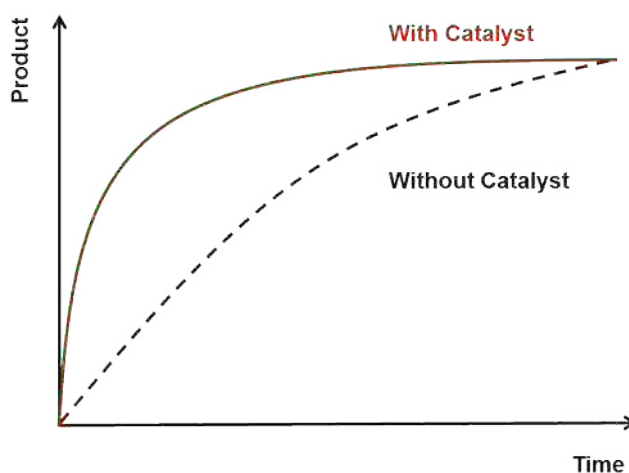


Figure 1. Effect of catalyst on reaction rate.

Catalytic activity is not a kind of reaction rate, but a property of the catalyst under certain conditions. To express the rate of the reaction, a measurement is taken in mols^{-1} .

1.2. Catalytic Mechanisms and Energetics

In general, catalysts react with one or more reactants to form an intermediate, which proceeds to form the product (Equations 1-4). They provide a means for the reactant molecules to break bonds, and then form temporary bonds with the catalyst. Firstly, the reactants (R_1 and R_2) adsorb at the catalyst surface. The adsorbed reactants are free to migrate over the catalyst surface. In doing so, they meet at the active site and subsequently react, whilst still being bound to the surface (Equation 3). Finally, the products from the reaction are desorbed from the catalyst surface, freeing up the catalyst surface for a repeat of the process.



Where C= Catalyst, R_1 = Reactant 1, R_2 = Reactant 2, and P = Product.

As mentioned, the catalyst works by lowering the activation energy, so that with catalyst present, there is less free energy required to reach the transition state. Figure 2 represents this in terms of a potential energy (GPE) diagram. A potential energy diagram plots the change in potential energy that occurs during a chemical reaction.

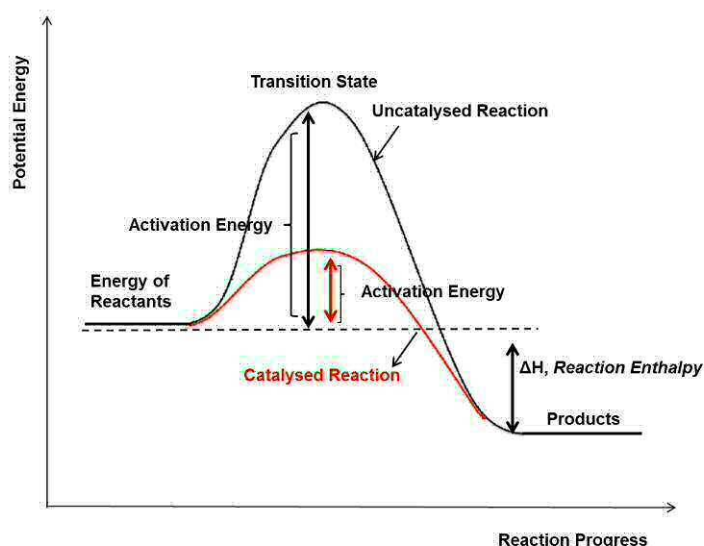


Figure 2. GPE diagram for reaction with and without catalyst present. With catalyst present, it can be seen that an alternate reaction pathway with a lower activation energy is available.

The reaction enthalpy can be related to Gibb's Free Energy, and is a measure of the net energy given off or absorbed during the reaction (depending on its exothermic or endothermic nature). With catalyst present, more molecular collisions are occurring with the required energy for the reaction to proceed. It is important to note that the total free energy from reactants to products is unchanged, and that the overall thermodynamics remain the same.

1.3. Heterogeneous vs. Homogeneous Catalysis

Catalysts can be divided broadly into two major types: heterogeneous and homogeneous. The main major distinction between these catalyst types is in comparing the catalyst nature in relation to the reactants. Heterogeneous catalysis occurs when the catalyst and the reagents are in different phases. Most commonly, this will be a solid catalyst with gaseous reactants. Most large scale, industrially catalysed processes use heterogeneous catalysis, with example catalysts including oxides and supported metal nanoparticles. For homogeneous catalysis, the reactants and catalyst are in the same phase. Typically everything will be present as a gas, or contained within a single liquid phase. There are a number of different homogeneous catalysts widely used, including Brønsted and Lewis acids, biocatalysts and many organometallic complexes.

Heterogeneous catalysis holds a major advantage over homogeneous catalysis, due to the ease of product separation after reaction. Catalyst recovery is easy and cheap, and catalysts

generally have a good thermal stability resulting in longer term use. However, due to a lower contact area, they are intrinsically less active and selective than homogeneous catalysts.

2. Background

2.1. Selective Oxidation

Oxidation is a key reaction in synthetic chemistry. Traditionally, stoichiometric inorganic (or organic) oxidants have been employed, such as chromium (VI) reagents [2]. However, the use of such reagents brings multiple problems, primarily due to their low selectivity and high toxicity. With a requirement for catalytic alternatives employing clean oxidants such as oxygen, the use of heterogeneous catalysis is at the forefront of creating greener alternatives. There is an increasing demand on the chemical industry to produce more environmentally benign synthetic routes, with the twelve principles of Green Chemistry advocating the use of solvent free, one step reactions, that reduce the amount of by-product released in the process. Catalytic oxidation remains as a key foundation for synthetic chemistry.

2.2. The History of Formaldehyde Production

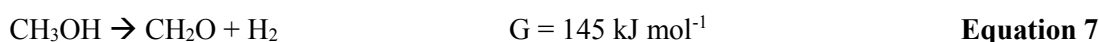
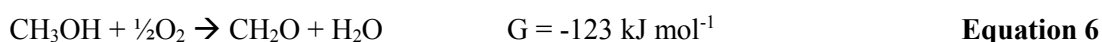
Aldehydes are of particular interest within the chemical industry, due to their diverse range of applications. Of these, formaldehyde is the simplest aldehyde, with a chemical formula of H_2CO . Although first synthesised in 1859 by Aleksandr Butlerov [3], it was only officially identified in 1868 by August Wilhelm Von Hofmann, when he passed methanol vapours and air over a heated platinum spiral. Formaldehyde, as the most profitable aldehyde in the chemical industry, is now used worldwide for a range of different purposes. It rarely exists as a monomer, but instead is more commonly found in forms of aqueous solutions and solid polymers. Formaldehyde has been used commercially for over 100 years, with its initial application as a disinfectant and embalming agent. In 1909 Leo Baekeland discovered the use of formaldehyde for the resin industry, which formed bakelite from the reaction of formaldehyde and phenol under heat and pressure. This was the start of a high commercial demand for this essential product, with it now serving as a key platform chemical in the manufacture of innumerable compounds, including:

- As a disinfectant.
- As a preservative.
- In textile finishing.
- In the production of resins to act as binders for woods, including plywood, chipboard, and MDF. Formaldehyde is used extensively in the woodworking and

cabinet-making industries. The resins and plastics industry constitutes 80 % of the total formaldehyde consumption [4].

- Formaldehyde is a common building block for the synthesis of more complex compounds and materials, particularly within the chemical industry for the production of traditional and high growth products such as acetals.
- As a prerequisite for many important pharmaceuticals.

The industrial production of formaldehyde from methanol can be carried out using two different types of catalyst. Commercial production of this heavy chemical initially started in 1910 [5] under a silver catalysed process, which thereafter remained the sole catalyst in use for approximately 40 years. The process exploits the use of these catalysts under a high methanol:air mixture, adopting high reaction temperatures of 600 °C [6]. Two processes can occur with methanol at the surface of the silver catalyst to ultimately produce formaldehyde: partial oxidation (Equation 5), or dehydrogenation (Equation 6). The process which occurs is heavily dependent on the reaction conditions employed, including the temperature, water content of the feed, and the ratio of methanol to oxidant.



Any vapours produced have to be quenched immediately using superheated steam, as otherwise the produced formaldehyde is shown to decompose. The reactor bed comprises a thin layer of unsupported electrolytic silver enclosed between silver gauze. The catalyst must be activated under oxygen prior to use [7]. Silver catalysts have also been used in the form of a bulk metal or dispersed supported silver. Of these, silica and alumina supported catalysts have shown promise, exhibiting high catalytic activity, even with low loadings of silver. Electrolytic and pumice supported catalysts have also been trialled. Unfortunately, as a result of the high temperatures required for the desired selectivity, this induces particle agglomeration and sintering, evoking a detrimental effect on formaldehyde yields. The catalyst also becomes more susceptible to deactivation. For this reason alternative preparation routes have been investigated.

In 1931, Adkin and co-workers discovered a new method for formaldehyde production, carrying out direct oxidation of methanol using mixed FeMo based catalysts [8]. This did not scale up for industrial use until 1950. Under this process, a low methanol:air mixture is required, with temperatures lower than 350 °C to prevent further oxidation of the formaldehyde product [9]. Under the oxygen-rich conditions, methanol vapour is exposed to

the mixed oxide catalyst, carried out in the packed-bed reactor. Yields were appreciably higher, at >90 % as opposed to the 86 % reported for the silver process. The catalyst was also discovered to be much more resilient to poisoning, bringing with it increased catalyst lifetimes of 6-12 months. In industry, the production was also considered safer due to lower fire and explosion hazards as a consequence of the lowered methanol concentration used.

2.3. The Current Active Catalyst: Iron Molybdate ($\text{Fe}_2(\text{MoO}_4)_3$) with Excess Molybdena (MoO_3)

There are two stoichiometric iron molybdates in existence: ferrous molybdate, FeMoO_4 , and ferric molybdate, $\text{Fe}_2(\text{MoO}_4)_3$. Only the latter is active and exploited for selective methanol oxidation [10]. The current industrial catalyst contains iron molybdate, $\text{Fe}_2(\text{MoO}_4)_3$, with an excess of MoO_3 to give a Mo:Fe ratio of 2.2:1. It is thought that the excess MoO_3 primarily acts to replace any molybdenum lost through sublimation at reactor hot spots, which is associated with the formation of the unselective Fe_2O_3 phase. However, with these two phases present, the active site of these catalysts has been a huge topic of debate in the literature, with some authors assigning MoO_3 as the sole active phase, others in dispute arguing $\text{Fe}_2(\text{MoO}_4)_3$, whilst some even state a synergistic relationship between the two. A further debate concerns whether $\text{Fe}_2(\text{MoO}_4)_3$ acts as a benign support for segregated MoO_3 , or if there is an intrinsic property of the surface structure which facilitates its high catalytic efficacy.

$\text{Fe}_2(\text{MoO}_4)_3$, MoO_3 and catalysts with a mixture of the two phases have been tested for their effectiveness in the selective oxidation of methanol. All demonstrate a good selectivity towards formaldehyde, with varying levels of activity [11]. This makes the identification of the active phase somewhat complicated. Soares *et al.* [12], have carried out work to rationalize this. Two catalysts, one stoichiometric (Mo:Fe 1.5:1), and another with a Mo excess (Mo:Fe 3:1), have been prepared and tested for their ability in the oxidative reaction. The authors argue that $\text{Fe}_2(\text{MoO}_4)_3$ is the active phase, since although an increase in the amount of Mo may improve selectivity, the fundamental activity per unit surface demonstrates no change. Further to this, temperature programmed desorption (TPD) of methanol on stoichiometric bulk $\text{Fe}_2(\text{MoO}_4)_3$ is 2–4 times more active than bulk MoO_3 [13]. The increased activity was suggested to be primarily due to the increased number of exposed catalytic active sites for isotropic $\text{Fe}_2(\text{MoO}_4)_3$, than for anisotropic MoO_3 . Only the edge sites of crystalline MoO_3 are available for catalytic activity [14]. The lowered activity of MoO_3 is also attributed to its significantly low surface area, of approximately $1 \text{ m}^2\text{g}^{-1}$, hence bulk MoO_3 is not considered for industrial use.

Where bulk $\text{Fe}_2(\text{MoO}_4)_3$ has been identified as the active component, excess molybdena has been labelled a spectator phase given that the slower redox mechanism operating in MoO_3 cannot improve specific activity [9, 15, 16]. Alessandrini *et al.* [16] agree with this, and ascribe MoO_3 to improved catalyst homogeneity and texture. Catalyst characterisation showed that the Mo in excess is embedded within the bulk crystalline network, without substitution of Fe(III) ions by Mo(VI). This however is disagreed by Fagherazzi and Pernicone [17], who employ XRD to identify active $\text{Fe}_2(\text{MoO}_4)_3$ as Fe defective, due to Fe(III) substitution by Mo(VI) in octahedral co-ordination. Additional oxygen is also required for overall charge balance, which can result in lattice expansion. However Massarotti *et al.* [18] obtain comparable lattice-constant values for the stoichiometric $\text{Fe}_2(\text{MoO}_4)_3$ catalyst and that with excess MoO_3 , therefore disagreeing with this theory.

Although the activity has been ascribed to $\text{Fe}_2(\text{MoO}_4)_3$ by many, there is a counter argument that MoO_3 is not simply there to replenish any lost molybdena, but is also required for complete selectivity to formaldehyde [11, 19]. MoO_3 is highly regarded for its ability to improve the selectivity of this reaction, with Bowker *et al.* [11] carrying out studies to show a 100 % selectivity towards formaldehyde under TPD of MeOH/He. A recent study by Söderhjelm *et al.* [20] enforces this idea that MoO_3 is not simply there to replace lost Mo. Here they propose a synergistic effect between MoO_3 and $\text{Fe}_2(\text{MoO}_4)_3$, implying that the active phase may be Mo-rich, existing as an amorphous layer in octahedral co-ordination at the surface. Each oxide plays its own specific role. Specifically, MoO_3 is believed to undergo dissociation of molecular O_2 to atomic oxygen, whilst $\text{Fe}_2(\text{MoO}_4)_3$ utilises this atomic oxygen to oxidise methanol to formaldehyde. The idea postulated arises from initial studies involving $\text{MoS}_2/\text{Co}_9\text{S}_8$. Here it was suggested that the promotion of one phase occurs at the junction of the two phases, modifying the electronic density of the catalytic active phase. This is in line with the remote control theory [21], which is applied to catalysts with two oxide phases. One acts as an acceptor phase (in this instance $\text{Fe}_2(\text{MoO}_4)_3$), whilst the other is the donor (MoO_3). $\text{Fe}_2(\text{MoO}_4)_3$ enables HC activation, acting independently with limited activity. MoO_3 as the donor phase has a role in providing oxygen activation at a high rate, to spill over and accelerate the overall catalytic cycle.

House *et al.* [19] examined the activity and selectivity of bulk $\text{Fe}_2(\text{MoO}_4)_3$ catalysts for methanol oxidation as a function of Mo:Fe ratios from 0.02 to 4. It was found that a Mo:Fe ratio greater than 1.5 is required for both high catalytic activity and selectivity for formaldehyde. It is thought that the increase in Mo consequently leads to a larger oxygen availability at the catalyst surface, and induces changes in catalyst acidity. DME is well known to form over acidic sites. Any reduction in the DME signal for catalysts with excess

MoO₃, infers a decrease in the number of acidic surface sites, and complimentary increase in the redox active centres. Due to the increased oxygen availability, Mo rich catalysts will therefore have a higher capacity to intensify surface re-oxidability. There is compelling evidence to endorse excess molybdate as a principal component in the reaction [22, 23]. A comprehensive study by Trifiro *et al.* [24] discusses the requirement for excess Mo, concluding that it is required for the following purposes:

- To increase the mechanical properties of the catalyst.
- To obtain a catalyst with a Mo:Fe ratio of greater than 1.5:1, for both an active and selective catalyst.
- To assist in the re-oxidation of β -FeMoO₄ to Fe₂(MoO₄)₃, allowing for repeated catalyst performance. Grasselli *et al.* [25] have studied ammoxidation, demonstrating that even with a small excess of molybdenum, the catalytic performance could be optimised. The excess MoO₃ was considered to be a spectator phase which provides mobile MoO₃ or MoO(OH)₂ to the reduced phase.

Regardless of the active phase, it has been well documented that the surface of the catalyst is terminated in molybdenum. Work by Bowker *et al.* [26] has used aberration corrected scanning transmission electron microscopy (acSTEM), to verify this surface concentration of Mo. On studying Fe₂(MoO₄)₃ particles, it was discovered using the EELS facility, that the surface was enriched in Mo, to the detriment of the Fe signal. Results were conclusive across a range of particles.

A study by Routray *et al.* has investigated the nature of catalytic active sites in bulk Fe₂(MoO₄)₃ based catalysts [9], including MoO₃, Fe₂O₃, Fe₂(MoO₄)₃, MoO₃/Fe₂(MoO₄)₃ and model supported MoO₃/Fe₂O₃ catalysts. The addition of excess MoO₃ to Fe₂(MoO₄)₃ significantly increased the overall steady-state catalytic performance towards formaldehyde production. Low-energy ion scattering (LEIS) analysis was performed, and it was discovered that the outermost surface layer was comprised of a MoO_x species. Investigations by Sun-Kuo *et al.* strengthened these findings, discovering that suprapstoichiometric oxide possess a Mo-enriched surface of amorphous, low-dimensional crystalline molybdena (MoO_x) [27]. It has been proposed that this MoO_x surface is responsible for improved catalytic performance [28, 29].

2.4. Industrial Process (The Formox Process)

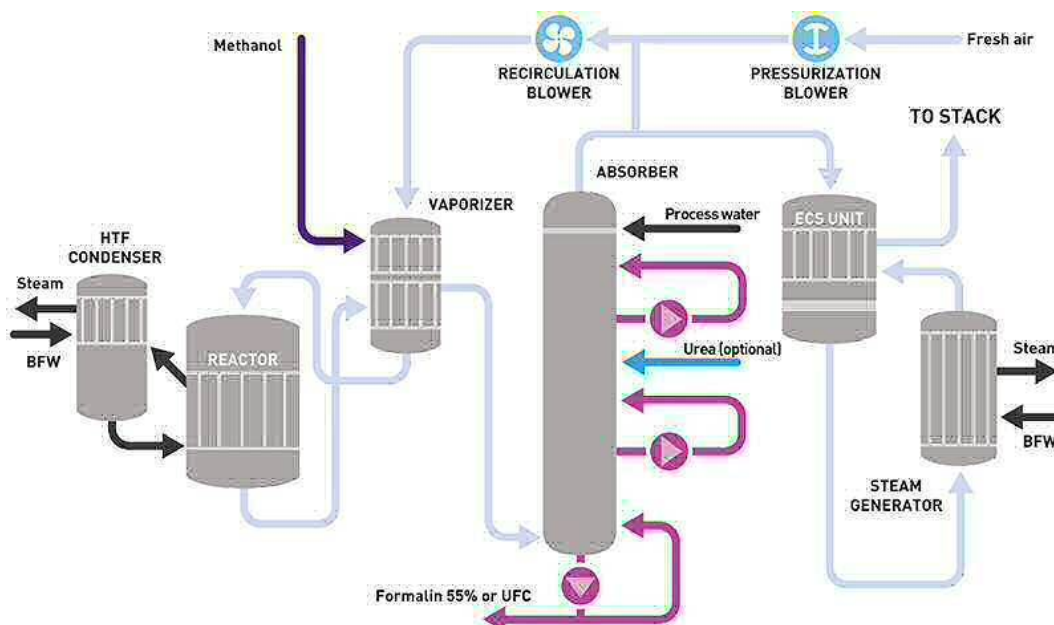


Figure 3. Schematic of the formaldehyde production plant [30].

Figure 3 is a schematic for the formaldehyde production plant. The initial process begins with blowers drawing air into the system, mixing it with recycled process gas to give a gas feed with 11 mol % O_2 . Following this, the mixture enters the vaporiser, where methanol is sprayed in for vapourisation [31]. The combined methanol/gas mixture subsequently passes through to the reactor at a pressure of 1.4 bar. The reactor tube is comprised of 8000-16000 reactor tubes with varying lengths. This maintains a uniform heat profile across the reactor. Figure 4 details the composition of these tubes.

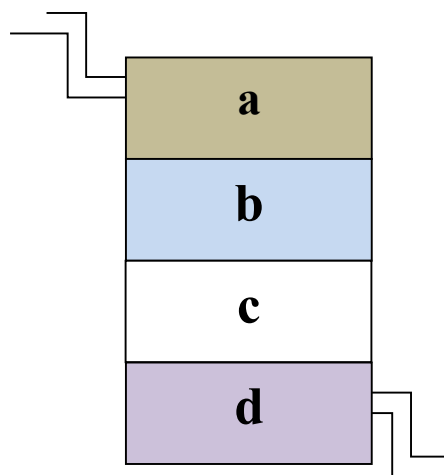


Figure 4. Reactor tube schematic. Each tube contains **(a)** a layer of inert ceramic rings which keep the gas heated. The inert ceramic rings spread the catalyst out, so heat generated during the reaction is not too concentrated: **(b)** a layer of inert and catalyst, used to avoid hot spot temperatures within this region and hence deactivation: **(c)** a pure layer of catalyst further along the bed. Here, methanol content has decreased, so that there is reduced conversion of methanol and therefore less heat generated and **(d)** a final layer of inert to allow cooling of the product before leaving the reactor.

The reactor temperature is controlled by a heat transfer fluid (HTF), which acts to cool areas of concentrated heat where the reaction is occurring. The HTF temperature is raised throughout the course of catalyst operation from 250 °C to 320 °C, keeping the yield high with decreasing catalyst activity. Vapours created from the HFT are taken away to the condenser, where the heat can be recovered through steam generation for electricity/heating. The condensed fluid can then be returned to the reactor, making the process more economically viable.

Once it has travelled through the reactor, the process gas passes through the outside of the vaporiser, where excess energy is used to evaporate the incoming methanol. Formaldehyde absorbs into process water (at the absorbers), with the flow adjusted accordingly to meet the requirements for the concentration of formalin solution desired. The process water contains trace amounts of NaOH, which promotes formaldehyde absorption. Production is typically quoted at 37 w/t % formaldehyde in water. Process water is not recycled back into the system as the aforementioned Na is a poison, detrimental to catalyst performance. Cooling water is used to remove the heat of absorption, prompting further absorption and maximising the efficiency of the process. Some process gas is recycled, with the rest sent to the emission control system which contains a heat exchanger and Pt catalyst. Here, all VOC's are oxidised to CO₂ and H₂O.

The overall formaldehyde yield is 93 %: with CO, unconverted methanol, dimethyl ether and trace amounts of CO₂ contributing to the remaining 7 %.

At the Formox base plant in Sweden, the steam generator was adapted for a remote heat programme, providing heat to the surrounding villages.

The advantages of the process detailed are as follows:

- Sound understanding of the process, plant and catalyst.
- High yields.
- High formaldehyde concentration, with low MeOH content in the product.
- High steam production, which can be used for further processes.
- Safe and environmentally friendly.
- Low operating costs.

Perstop were the major producers of formaldehyde, until they recently announced the sale of their formaldehyde technology to Johnson Matthey in March 2013. This iron molybdate based production process constitutes approximately 50% of formaldehyde production, the rest synthesised by the Ag process, as mentioned previously.

Demand for formaldehyde will continue to grow with the developing manufacture sector, in line with increasing demands for disinfectants, cosmetics, and pharmaceuticals. The future demand has been forecasted as in Figure 5. Demand is influenced by population growth, urbanisation, income rise, and expansion of health services.

There is fundamental requirement to understand the process and the catalyst in more detail, in order to maximise productivity further, and make the process even more economically and environmentally viable [31].

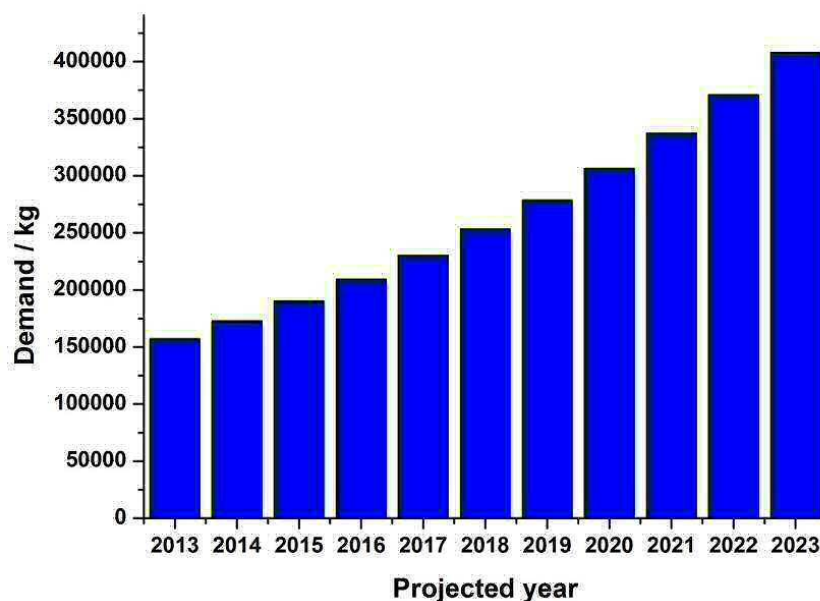
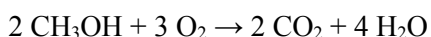


Figure 5. Predicted future demands for formaldehyde.

3. Basic materials

3.1. Methanol

Methanol, chemical formula CH_3OH , is a volatile, colourless, flammable liquid, also referred to as methyl alcohol, wood alcohol or wood naptha/spirits. Its first discovery was in 1661 by Robert Boyle [32] when he distilled boxwood, with Jean-Baptiste Dumas and Eugene Peliot determining the elemental composition in 1834. Some of the properties of this naturally occurring substance include the following: it has a density of 0.7914g cm^{-3} , boiling point of 65.0°C and a melting point of -93.9°C . Care should be taken in handling the alcohol: it is a toxin which must not be ingested, since consequences of this action can result in blindness or damage to the central nervous system. One of the primary hazards with using methanol in the lab is its flammable nature. It forms explosive mixtures with air, burning with a non-luminous flame (Equation 5).



Equation 5

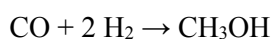
Due to its many applications, its global demand reaches around 60 million tonnes per year, ranking it as the 4th most globally used chemical. Methanol is a building block to a number of compounds in the chemical industry. The production of formaldehyde constitutes the majority of its use, contributing 40 %. Further products derived from methanol include adhesive resins for construction materials, polyester fibres and packaging, plastics, paints,

foams, silicones, coatings and fuel additives. In the early 1970s, a methanol to gasoline process was developed by Mobil for producing gasoline ready for use in vehicles. Methanol has been suggested as a renewable alternative to petroleum based hydrocarbons, since it can be produced from wood and organic materials. However, current petrol engines would require modification before they were able to run on pure bio alcohol. At the forefront of current scientific research, methanol is also widely considered to be a potential hydrogen carrier for many future fuel cell applications.

Methanol is produced naturally in the anaerobic metabolism of bacteria, and also occurs naturally in small amounts in the atmosphere. However, referring to Equation 5 above, over time, atmospheric methanol is oxidized under sunlight to carbon dioxide and water.

Industrial production was first initiated by Matthias Pier in 1923 [33], working with BASF. The process involved making methanol from synthetic gas, using a zinc chromate catalyst under pressures of 300-1000 atm and a temperature of approximately 400 °C.

Current industrial production occurs from syngas [34, 35], reacting carbon monoxide and hydrogen over a mixed copper, zinc oxide and alumina catalyst at 5–10 MPa, and 250 °C (Equation 6).



Equation 6

The reaction proceeds with >99.8 % selectivity to methanol. Two moles of hydrogen gas are consumed per mole of carbon monoxide.

A second, less dominant production route to methanol, involves the direct conversion of methane using Cu-Zeolites. A direct generation from CO₂ is also achievable using sunlight and in solution using copper oxide (CuO) nanorods coated by cuprous oxide (Cu₂O). Although not yet scaled up to industrial scale, the process has thus far shown great promise, demonstrating a 95 % electrochemical efficiency.

3.2. Iron

Iron, chemical symbol Fe, has an atomic number of 26. It is a transition metal in the first row of the transition series block, neighbour to manganese and cobalt. It is known to occur naturally in meteorites, and combined in igneous rocks. The concentration of iron in the various layers of the Earth range from highly concentrated at the inner core, to approximately 5 % in the outer crust. Iron is the most used metal worldwide, existing as a malleable, ductile magnetic element that readily rusts in moist air. The appearance of the

metal is silver-grey, and is known to exist in four crystalline forms. Iron is chemically active and forms two major types of chemical compounds: bivalent Fe(II) (ferrous), and trivalent Fe(III) (ferric).

Iron is the most abundant metal on earth (34.6 % by mass), with its properties making it a relevant choice for many applications. Worldwide production of new iron is over 500 million tonnes a year, and recycled iron 800 million tonnes. With its low cost and high strength, it is an ideal choice in the production of steel for use in making cars, cargo ships, and structural components in buildings. Some other forms of iron include: pig iron, cast iron, carbon steel, wrought iron, alloy steels, and iron oxides. Reserves of iron ores exceed 100 billion tonnes with the main mining areas being China, Brazil, Australia, Russia and Ukraine. Industrially, iron is extracted from its ores, primarily hematite (Fe_2O_3) and magnetite (Fe_3O_4), by reduction with carbon in a blast furnace at very high temperatures of over 2000 °C. Iron ore prices have recently risen considerably, from US \$ 23.87 ton^{-1} in 2001, to an estimated US \$ 44.00 ton^{-1} in 2005.

3.2.1. Iron (III) Oxide

Iron oxide is a distinctive dark red solid (otherwise known as rust), with the chemical formula Fe_2O_3 . The most common occurring structure is $\alpha\text{-Fe}_2\text{O}_3$ (hematite), however γ and β polymorphs also exist. Fe_2O_3 is a functional material which can be applied in various fields [36, 37]. Conventional synthesis for the $\alpha\text{-Fe}_2\text{O}_3$ form, involves acid hydrolysis of FeCl_3 at low temperature. There are many advantages associated with this preparation, including its precise control on particle size, morphology, and size distribution [38].

For the main polymorphs, (the α and γ -forms), the geometry of these oxides adopts octahedral co-ordination, with each Fe centre bound to 6 oxygen ligands. Each oxygen atom shares four iron atoms [39]. $\alpha\text{-Fe}_2\text{O}_3$ exhibits a rhombohedral, corundum structure, with antiferromagnetic properties. Oxygen atoms are hexagonally close packed, and the cations occupy 2/3 of the octahedral voids. Figure 6, below, illustrates this structure. The hexagonal crystal structure has the space group $R\bar{3}c$ and demonstrates lattice parameters of $a = 5.038 \text{ \AA}$ and $c = 13.772 \text{ \AA}$. $\gamma\text{-Fe}_2\text{O}_3$ displays a cubic structure, easily formed from the α -phase at high temperatures. This polymorph is ferromagnetic, occurring naturally from the mineral magnetite. The β -polymorph demonstrates the cubic body centred phase, with space group $Im\bar{3}m$. This polymorph is also metastable, converting to $\alpha\text{-Fe}_2\text{O}_3$ above 500 °C.

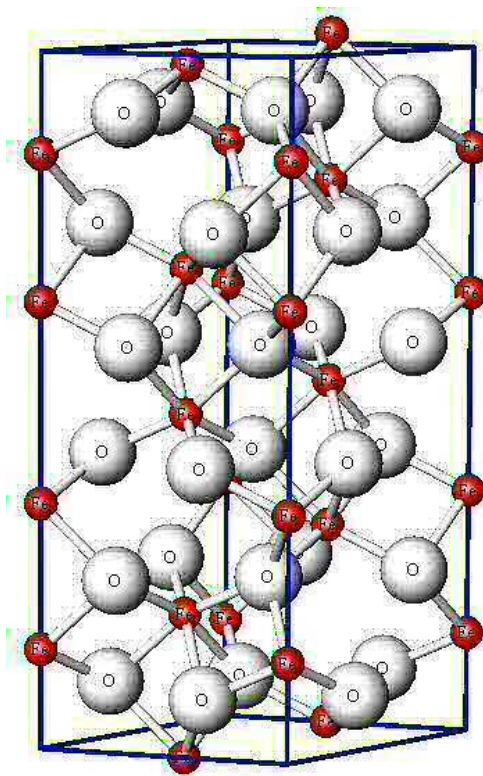


Figure 6. α -Fe₂O₃ (Hematite) with corundum crystal structure.

3.2.2. Fe₂(MoO₄)₃

The details of Fe₂(MoO₄)₃, including preparation and industrial application are discussed throughout the chapter, therefore are not discussed in detail here.

Fe₂(MoO₄)₃ demonstrates a monoclinic structure [40], with the space group P2₁ and lattice parameters $a = 15.693 \text{ \AA}$, $b = 9.235 \text{ \AA}$, $c = 18.218 \text{ \AA}$ and $\beta = 125.21^\circ$. The eight Fe atoms are in octahedral co-ordination with six oxygen atoms, and demonstrate an average Fe-O distance at 1.992 \AA [41]. The twelve oxygen atoms hold a distorted tetrahedral structure, with an average Mo-O distance of 1.756 \AA . The structure contains isolated MoO₄ tetrahedra and FeO₆ octahedra, which share corners through oxygen atoms. Each oxygen is 2-coordinated, being shared between two polyhedra. This leads to an open, flexible structure, with the nearest Fe-Fe distance at 5.03 \AA . Figure 7 shows details of this structure.

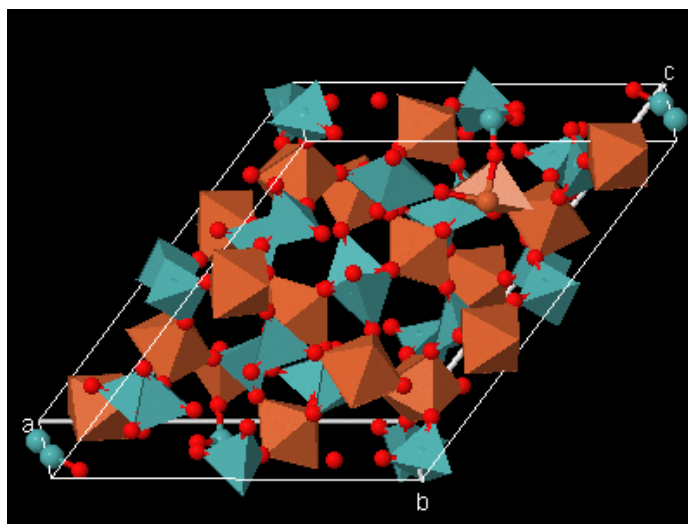


Figure 7. Crystal structure of $\text{Fe}_2(\text{MoO}_4)_3$ [42].

3.2.3. FeMoO_4

Iron molybdates with molecular formulas of FeMoO_4 and $\text{Fe}_2(\text{MoO}_4)_3$ are well known for their use in the partial oxidation of alcohols and hydrocarbons. FeMoO_4 is the reduced form of $\text{Fe}_2(\text{MoO}_4)_3$. Generally, FeMoO_4 exists in two different polymorphs including (i) the low temperature α -phase which is isotopic with $\alpha\text{-CoMoO}_4$ and stable at room temperature, and (ii) the high temperature β -phase which is isotopic with $\alpha\text{-MnMoO}_4$. $\alpha\text{-FeMoO}_4$ possesses a monoclinic unit cell, with the space group C and lattice parameters $a = 9.807 \text{ \AA}$, $b = 8.950 \text{ \AA}$, $c = 7.659 \text{ \AA}$ and $\beta = 114.02^\circ$. $\beta\text{-FeMoO}_4$ is stable at higher temperatures, between $25\text{--}800^\circ\text{C}$, also with the space group C . The unit cell is a primitive unit cell, with lattice parameters $a = 10.301 \text{ \AA}$, $b = 9.402 \text{ \AA}$, $c = 7.053 \text{ \AA}$, and $\beta = 106.28^\circ$ (Figure 8). The significant differences between the two phases are (i) the unit cell of the β -phase is more than 6 % larger than the α -phase, and (ii) Both phases have octahedrally co-ordinated iron located in two crystallographically distinct sites, however the α -phase has two distinct tetrahedrally co-ordinated Mo sites, whilst the β -phase has two distinct octahedrally co-ordinated Mo sites.

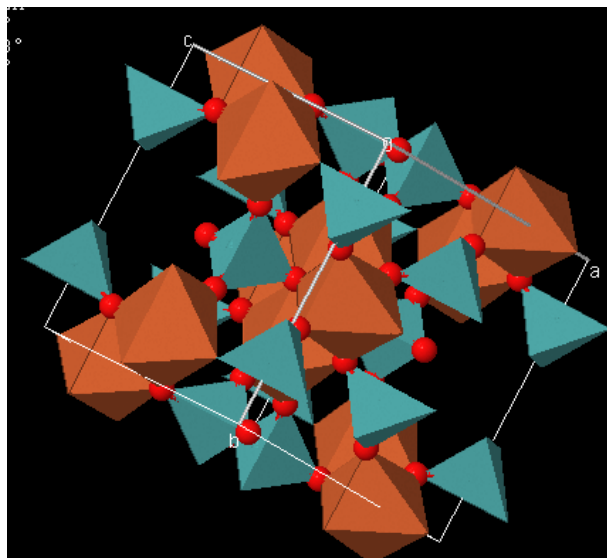


Figure 8. Structure of β -FeMoO₄ [43].

3.3. Molybdenum

Molybdenum is a second row transition metal with atomic number 42 and electron configuration [Kr] 4d⁵ 5s¹. The metal was first isolated in 1781 by Peter Jacob Hjelm, after the initial discovery in 1778 by Carl Wilhelm [44]. Molybdenum does not occur naturally as a free metal, but instead occurs in minerals due to its variable oxidation states. These include wulfenite (PbMoO₄), powellite (CaMoO₄), and molybdenite (MoS₂), the principle ore from which Mo is mined. Once extracted, the metal has a silvery appearance, with one of the highest melting points known in the periodic table, at 2623 °C.

Molybdenum can readily form hard, stable carbides, which gives rise to its use in making high strength steel alloys. The production of steel constitutes 80 % of the world production of this element, and with the increasing demand for steel, molybdenum demand is subsequently on the rise. As a direct result of this, there has been a tenfold price increase in the last 5 years. Industrially, approximately 14 % of the world production of molybdenum compounds are used in high-pressure and high-temperature applications, as pigments, and as catalysts. A further important use of Mo is as a catalyst in the petroleum industry, used for removing organic sulphurs.

3.3.1. Molybdenum Oxide (Molybdena)

Molybdenum trioxide, MoO₃, is the most commonly acknowledged Mo compound, being widely used as an oxidation catalyst. The structure of β -MoO₃ was first described by Kihlberg in 1963 [45], with the space group Pbnm, and lattice parameters of $a = 3.962 \text{ \AA}$, $b =$

13.858 Å and $c = 3.607$ Å [46]. The structure itself is somewhat complicated. It is shown, (Figure 9), that there are three oxygen atoms double bonded to a central Mo atom. In the commercially available solid state, layers of distorted MoO_6 octahedra make up the orthorhombic crystal. Distorted-octahedral MoO_6 units are connected through corner- and edge-sharing in the bc plane, with cohesion between double-layers of MoO_6 maintained by inter planar van der Waals forces. The layers are parallel to the (010) crystal plane, making the (010) plane the most exposed and thermodynamically stable, with only O ions exposed to the surface. Many studies have been carried out to investigate this oxide structure in depth [47, 48], however there is limited information regarding the number of surface lattice oxygens acting as the active site. With such an irregular structure, only select faces are able to facilitate the partial oxidation of methanol.

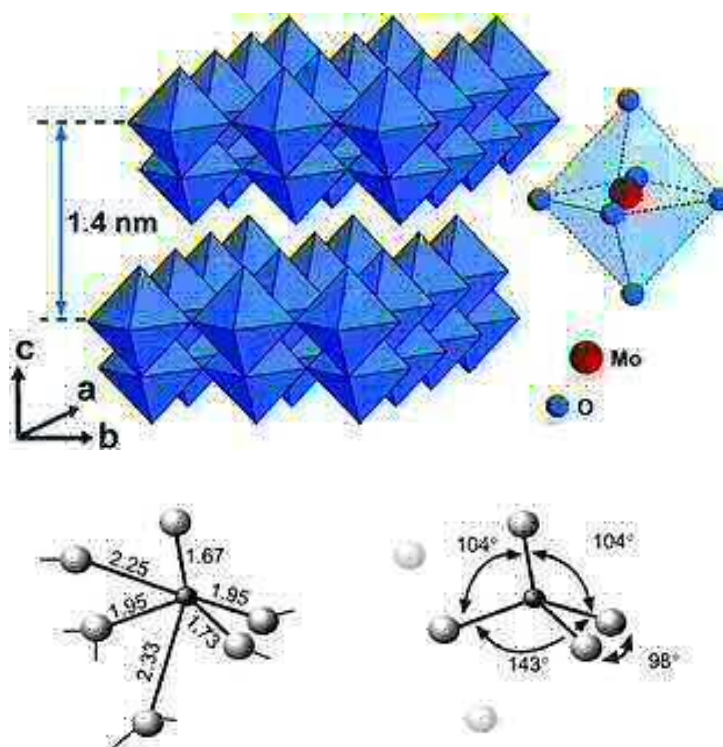
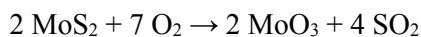


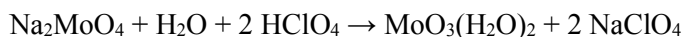
Figure 9. - MoO_3 solid state structure. The layer structure is built up of distorted MoO_6 octahedra at two levels connected along one direction by common corners, and in another direction by common corners and edges [49, 50].

Also known is the structure of $\beta\text{-MoO}_3$, a monoclinic form of MoO_3 with the space group $P2_1/c$ and lattice parameters of $a = 7.122$ Å, $b = 5.374$ Å and $c = 5.565$ Å. The structure is isostructural with ReO_3 .

To produce MoO_3 industrially, large quantities of the molybdenum disulphide ore are roasted under the following process:

**Equation 7**

To produce MoO_3 on a smaller lab-based scale, a few methods can be employed. The most common is the acidification of aqueous solutions of sodium molybdate with perchloric acid, as detailed in Equation 8. The dihydrate produced can then be dehydrated relatively easily, to leave the monohydrate, which is a distinctive bright yellow colour.

**Equation 8**

Molybdenum trioxide plays a significant role in a number of applications. First and foremost, it can act as a source of Mo, which as mentioned previously can be used for steel production. For this, MoO_3 is reacted with H_2 to yield Mo and H_2O . Another principle use of MoO_3 is as a component in the catalyst used for acrylonitrile production, through the oxidation of propene and ammonia. The layered properties and ease of Mo(VI)-Mo(VI) coupling make it a popular catalyst choice in electrochemical devices and displays.

3.3.2. MoO_2

Molybdenum dioxide (Figure 10), molar mass $127.94 \text{ g mol}^{-1}$, exists in a monoclinic structure with the space group P21/n. The lattice parameters for the unit cell are $a = 5.607 \text{ \AA}$, $b = 4.860 \text{ \AA}$, $c = 5.537 \text{ \AA}$, and $\beta = 119.37^\circ$ [51]. The compound is grey/violet in colour, and demonstrates the properties of a metallic conductor. The crystal structure is akin to that for distorted rutile [52]. In TiO_2 the oxide anions are close packed and titanium atoms occupy half of the octahedral holes. The difference in MoO_2 is that the octahedra are distorted, with the Mo atoms off-centre. This leads to alternating short and long distances of Mo-Mo. The Mo-Mo bond distance found is 2.51 \AA , which is less than that typically seen for bulk metal at 2.72 \AA .

Preparation of MoO_2 can occur in several ways. One of the most obvious, is through the reduction of MoO_3 . The catalyst either undergoes an extensive reduction treatment with Mo for 70 hours at 800°C (Equation 9), or by reducing MoO_3 with H_2 or NH_3 below 470°C [53].

**Equation 9**

Some of the uses of MoO_2 include its role in catalysing the dehydrogenation of alcohols, and also in the reforming of hydrocarbons. Since the compound upholds a very high thermal stability, this makes it suitable for processes in which the temperature is ramped above 1000°C .

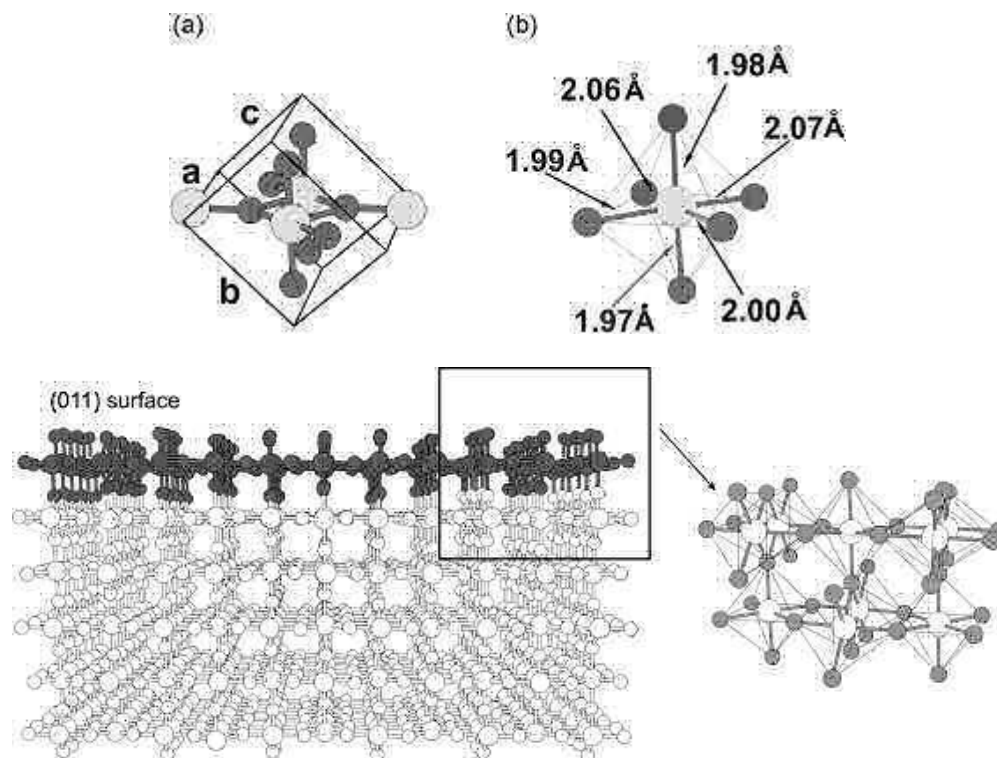


Figure 10. Structure of MoO_2 [54].

4. Preparation Methods

The most commonly described method for $\text{Fe}_2(\text{MoO}_4)_3$ synthesis is through co-precipitation. Iron molybdate catalysts are industrially manufactured from the co-precipitation of aqueous solutions of FeCl_3 and ammonium heptamolybdate (AHM) [55]. Both of these reagents are expensive, and problems arise due to the significant amounts of water used in the commercial manufacture. Additionally, during the calcination procedure, large amounts of nitrous oxides (NO_x), ammonia (NH_3) and hydrochloric acid (HCl) pollutants are formed. The catalysts also suffer from a lack of homogeneity, since the composition of the precipitate varies in formation, and part of the molybdenum remains in the mother liquor, being absorbed reversibly on the precipitate. As a consequence, catalysts used industrially may present a Mo:Fe atomic ratio of anything between 1.7:1 and 4.5:1. Furthermore, slight deviations from the synthesis procedure can have adverse effects on the final catalyst composition.

In light of this, there is a requirement for new synthesis procedures to create $\text{Fe}_2(\text{MoO}_4)_3$ catalysts with a more homogeneous consistency. In particular, methods are required which involve more common reagents, require less water, and reduce pollutant levels.

Work of Soares *et al.* reports a method of $\text{Fe}_2(\text{MoO}_4)_3$ production involving a sol-gel preparation [12, 56]. Iron and molybdenum precursor solutions were prepared in organic acid medium. The iron solution was slowly added to the Mo solution without precipitation. Following this, the solvent was evaporated and the formed gel removed. For comparison, stoichiometric $\text{Fe}_2(\text{MoO}_4)_3$ and Mo rich catalysts were also prepared via conventional co-precipitation. It was found that the preparation method employed dictated the catalyst activity and stability. The sol-gel like technique led to a better dispersion of the MoO_3 excess in the $\text{Fe}_2(\text{MoO}_4)_3$ lattice, therefore hindering the loss of MoO_3 from reactor hot spots, resulting in a more stable catalyst. These catalysts were also believed to be capable of operating at lower temperatures than the current industrial catalyst, whilst also reducing the amount of formaldehyde further oxidised to unselective CO. After catalytic testing of both materials, the co-precipitated sample however proved more active than the sol-gel one, since the surface of the sol-gel like catalyst was more reduced. This irreversible surface reduction occurs during calcination, due to the combustion of the carbon organic used in the preparation. To counteract this eventuality, the temperature of calcination should remain below 400 °C to avoid re-crystallisation of ferric molybdate, and to prevent loss of mechanical resistance.

Beale *et al.* have demonstrated an alternate preparation route to Fe-O-Mo based catalysts, adopting a one-step, low-temperature hydrothermal method, employing Mo:Fe ratios ranging between 1.5:1 to 3:1 [57]. Catalysts produced with a Mo:Fe ratio of 3:1, resulted in a mixed crystalline Mo_5O_{14} /amorphous FeMo oxide phase, which was unstable above 300 °C, forming mixed $\text{Fe}_2(\text{MoO}_4)_3/\text{MoO}_3$. Low-temperature hydrothermal methods were trialled in the preparation of $\text{Fe}_2(\text{MoO}_4)_3$, as well as a mixed Mo_5O_{14} /non-crystalline FeMo oxide material. The potential of such a synthetic approach was recognised as a way to improve current catalyst properties, and create novel new materials with varied catalytic properties. The original mixed phase material showed a low thermal stability, however in using it as a precursor through the medium of calcination temperature, the catalytic behaviour was able to be controlled. Hydrothermal techniques can therefore be considered in the preparation of both precursors and the final catalyst.

Iron molybdates were prepared by Demidov *et al.* [58] using an amorphous precursor technique. An aqueous solution of ferric nitrate was prepared in the presence of a large excess of citric acid. This prevented co-precipitation during the addition of aqueous ammonium heptamolybdate. All water was evaporated to leave an amorphous precursor, after which a thermal treatment was carried out at 400 °C for over 6 hours. The authors fail

to compare the catalysts prepared by this technique with those synthesised by conventional co-precipitation.

Other preparation techniques in addition to those mentioned are less investigated in the literature. Nano-structured $\text{Fe}_2(\text{MoO}_4)_3$ materials have been formed from $\text{Fe}_2(\text{MoO}_4)_3$ nanoparticles anchored onto MoO_3 nano-rods via incipient wetness [59]. It was discovered that the optimum calcination conditions were 450–500 °C for 2 h. Any lower, the temperature was too low for the solid-state reaction between the MoO_3 nano-rod and the Fe to form $\text{Fe}_2(\text{MoO}_4)_3$. At higher temperatures, the nano-rod morphology becomes irregular, and particles of $\text{Fe}_2(\text{MoO}_4)_3$ agglomerate causing a loss of catalyst activity.

Popov *et al.* [60] prepared Mo rich catalysts by centrifugal milling of a paste formed from iron oxalate and molybdic acid. Without the milling, a temperature of 200 °C or higher is required to form the $\text{Fe}_2(\text{MoO}_4)_3$ phase. Catalysts were also prepared by co-precipitation, however the paper lacks information regarding the advantages of each technique.

It has however been discovered that *in situ* formation of metal-molybdate catalysts can occur through a physical mixture of a source of catalytically active metal oxide such as Fe_2O_3 , and a source of molybdenum oxide such as MoO_3 [61]. $\text{Fe}_2(\text{MoO}_4)_3$ formation occurs readily, and without the presence of water Hassan *et al.* have also investigated the effectiveness of this novel method involving mechanical mixing of molybdenum and iron oxides. Solid phase MoO_3 and Fe_2O_3 were mixed together and ground. A calcination was performed at 600–700 °C for 10–70 hours, followed by further grinding. Although an easy and straightforward method, the catalysts were found to have a low surface area, so hence poor activity in the selective oxidation of methanol to formaldehyde [62].

Li *et al.* have investigated the preparation by dry and wet mixing of iron molybdates from solid salts of Fe and Mo, with the latter method demonstrating the best catalytic performance [63]. It is their view that a wet technique is required, as this increases the incorporation of Mo species into the $\text{Fe}_2(\text{MoO}_4)_3$ lattice, thus bringing an increase to the number of active sites. Unfortunately the structure they suggested demonstrating Mo in connection with Fe through an oxygen bridge, could not be proved (Figure 11). It was also found that wet mixing method was more reproducible than the dry mixing method, but with both showing phases of $\text{Fe}_2(\text{MoO}_4)_3$ and MoO_3 after calcination.

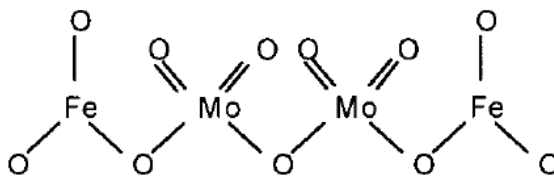


Figure 11. Structure presented by Li *et al.* formed through wet mixing of iron molybdates from solid salts of Fe and Mo.

5. Reactivity

The reaction of methanol on various oxides has been studied by several authors in the literature [11, 23, 64-67]. Catalytic testing has been crucial in assessing the nature of the absorbed intermediate [19, 23], whilst other techniques such as DRIFTS can be influential in identifying these adsorbates [68, 69]. One of the important steps in understanding and improving an oxidation catalyst, is a detailed knowledge of the interaction and conversion of reactants on the active sites at the surface.

5.1. Fe₂O₃

Fe₂O₃ is known to be highly selective towards combustion products, making it unfavourable for the reaction to formaldehyde [11]. The interactions between methanol and formic acid on iron oxide have been studied using XPS and Fourier Transform Infrared (FTIR). Results indicate the adsorption of methanol to be either dissociative, producing hydroxy and methoxy adsorbates: or molecular, in which the methanol interacts with the Lewis acid and base sites at the surface. Upon chemisorption of methanol, reduction of the Fe₂O₃ surface occurs, with the O:Fe ratio showing a definite decrease from 1.5 to 1.3. Ramping the temperature above 120 °C, surface formates are detected, due to the direct combination of methoxy groups with lattice oxygen. It is thought to be the lattice oxygen involved, since the formate can form in both aerobic and anaerobic conditions. On elevating the temperature further to over 220 °C, the surface formate decomposes to CO, CO₂, H₂ and H₂O. A similar study was performed using Fe₂O₃ dosed on Co₃O₄. XPS revealed the Fe 2p peak does not change upon exposure to methanol at RT, whereas in the Co 2p region the increment of the shake-up peaks occurs, therefore suggesting surface reduction of the Co₃O₄ support to CoO [70]. This result confirms that the formation of formate from methanol proceeds through the inclusion of lattice oxygen, as also hypothesised from the DRIFTS data. Glisenti *et al.* [71] discuss the reactivity of simple alcohols on Fe₂O₃ powders, also using XPS and FTIR as an analysis tool. They agree that when methanol is chemisorbed, a formate intermediate forms upon heating. Referring to the data obtained through FTIR, between 400-420 K, three new bands centred at 1583, 1379 and 1358 cm⁻¹

appear and grow with temperature. These bands are indicative of formate species formation on the Fe_2O_3 surface [72]. Partial oxidation of methanol over Fe_2O_3 -supported aerogels was investigated between 225 and 300 °C. Formate was dominant, and formaldehyde was only favoured if the support was changed to molybdenum oxide (20 % iron oxide). FTIR probe molecule characterization studies revealed that methanol adsorbs as methoxy as the first step in all reaction processes. This initial finding enabled a further study into the mechanisms behind the oxidation of methanol over iron oxide based materials. With very low loadings of Mo, CO production is observed at 210 °C in the TPD. This is not seen for Fe_2O_3 or catalysts with a Mo:Fe ratio <1. It is believed that this CO still comes from methoxy.

A study by Bowker *et al.* [11], uses TPD and pulse flow studies to assess the reactivity on various component oxides. The desorption profile for Fe_2O_3 demonstrated zero selectivity to formaldehyde, with the spectra dominated by CO_2 at 300 °C. H_2 shows two desorption peaks, one at 200 °C and another coincident with CO_2 at 290 °C. The only other products to be detected are methanol, which desorbs at 90 °C, and also water which shows a broad desorption peak across the temperature range. Under pulsed flow studies, methanol conversion does not occur until approximately 250 °C. The formate is presumed to be bidentate and very stable, therefore blocking any reaction with methanol until above 250 °C. Formaldehyde production does not occur, and again CO_2 , H_2O and H_2 are the main products to evolve. With little evidence of CO production, this leads to the assumption that combustion occurs through the formate intermediate. Since no formaldehyde is produced, it is suggested that the decomposition of the formate becomes the rate limiting step, again a result of its stability on the surface. This agrees with the work of Glisenti *et al.*, who show formate to be the most stable intermediate, more stable than methoxy.

Further work by the group of Bowker *et al.* attempted to understand what determines high selectivity in mixed metal oxide systems of FeMo. Layers of Mo were doped onto Fe_2O_3 by incipient wetness, to analyse the effect this had in TPD. With no Mo dosed, Fe_2O_3 showed a lack of selectivity to formaldehyde, with combustion products dominating the mass spectrum. However, even with very low loadings of Mo deposited (0.25 monolayers) at the surface, the selectivity to formaldehyde and CO shows a dramatic rise, with CO_2 production decreasing. The change in selectivity is reflective of the changing adsorbing intermediate. In haematite and Mo-deficient iron molybdate, a high concentration of surface cations compels close proximity of iron centres. This allows the formation of the bridging formate precursor to occur [19, 23].

5.2. MoO₃

In stark contrast to the performance on Fe₂O₃, the reaction of methanol on MoO₃ is highly selective towards formaldehyde in both TPD and pulsed flow studies [19, 23]. Two types of adsorbed methanol exist, one as a chemisorbed bound methoxy, the other as undissociated weakly chemisorbed methanol. There is no evidence for a bidentate formate, as seen for Fe₂O₃, since combustion products are not shown to form. MoO₃ is a high yield material, with a selectivity to formaldehyde of up to 90 % under reaction with MeOH/O₂.

Higher order by-products may also be observed under α -MoO₃ catalysis, particularly at low temperatures and under restricted oxygen supply, that promote condensation of methoxy intermediates [73]. However, acidic oxides such as α -MoO₃ experience a high energetic barrier to higher oxidation, benefiting formaldehyde selectivity [19, 74].

The partial oxidation activity of α -MoO₃ has been well studied in the literature. Analysis of α -MoO₃ has revealed that the three most exposed faces are the (010), (100) and (001 +101), with the relative proportions of these dependent on the preparation method employed [48]. The different faces can react with methanol via either the Mars-van Krevelen mechanism, or the Eley-Rideal mechanism to produce formaldehyde. The reactive site on MoO₃ has been a topic of debate. It has been proposed that methanol adsorption on α -MoO₃ occurs largely at edge facets and defect sites, since the saturation uptake of methanol correlates well with the number of active centres exposed on non-basal planes [75]. Interestingly, it was discovered that approximately 10 % of the surfaces of powdered MoO₃ demonstrate the (010) face, which matches well with experimental data, denoting 12 % of surface MoO₃ sites to be catalytically active. This supports the (010) face to be the active site for dehydrogenation to formaldehyde. The (010) basal surface is the plane of lowest free energy [75, 76]. *Ab initio* quantum mechanical studies of Allison *et al.* [77] and TPD have suggested that methanol adsorbs at dual-dioxo sites available at the (010) face of MoO₃. However, there is a discrepancy in this theory, with others revealing that the (010) plane exhibits too low a saturation coverage. Where methanol adsorption did occur at this face, it was associative and did not lead to formaldehyde production [75]. It has since been suggested that the (010) face is not involved in the chemisorption, instead occurring on other crystal faces and defects, where the C.N of Mo < 6, and the saturation uptakes correlates well with the number of active centres exposed. This is demonstrated through AFM studies [78], in which a study of the (010) face of MoO₃ showed anaerobic methanol reaction at under co-ordinated molybdenum sites. These edge planes are formed by bond cleavage perpendicular to the MoO₃ double-layers, exposing co-ordinatively unsaturated molybdenum [76]. Specifically, non (010) faces possess dual acid-base sites [76], consisting of an unsaturated

metal cation (O-Mo-O) and adjacent terminal oxygen (Mo=O). Where methanol adsorbs at a bi-functional site, dissociative chemisorption occurs. The O-Mo-O site acts as a Lewis acid and binds the methoxy fragment, whilst the basic M=O oxygen abstracts a proton to yield a hydroxyl intermediate. Different reactive steps are found to occur at different crystal faces, therefore the ratio of the various faces is responsible for overall catalyst selectivity.

O'Brien *et al.* [79] have investigated the active site in bulk MoO₃ during anaerobic dehydrogenation of methanol *in situ*, combining ultraviolet–visible (UV–Vis), Raman, wide-angle X-ray scattering (WAXS), and online mass spectroscopy (MS) techniques. Comparing data, it was revealed that methanol initially chemisorbs onto the surface at defect sites. The reaction then proceeds producing formaldehyde, DME and water. At low temperatures, CO and MoO₂ are too produced, as the re-oxidation of the active sites is too inefficient to occur and avoid this reduction. After 125 minutes of reaction, bulk MoO₂ is observed and WAXS data indicates that one of the three oxygen environments becomes more active than the others (O1). The work identified this oxygen as the most likely to be that transferred through the bulk of the oxide during the Mars–Van Krevelen oxygen transfer. However, a comparison to previous work of the same group and the MS/UV data also shown, indicated no relationship between the bonding in the bulk oxide and its surface reactivity. In other words, although O1 is abstracted and transferred through the bulk, it may be replacing other oxygen atoms (O2/ O3) at the surface. An understanding of both the bulk and surface sites is required in order to fully understand the oxide and its reactivity. What can be concluded from this study however, is that bulk oxygen is provided to the surface via a MVK mechanism to regenerate the active sites for initial formaldehyde production. Pulsed flow reaction studies under anaerobic conditions revealed that at low temperatures, formaldehyde selectivity can be sustained for some time [80]. The result supported the Mars-van Krevelen (MVK) redox mechanism theory [80, 81].

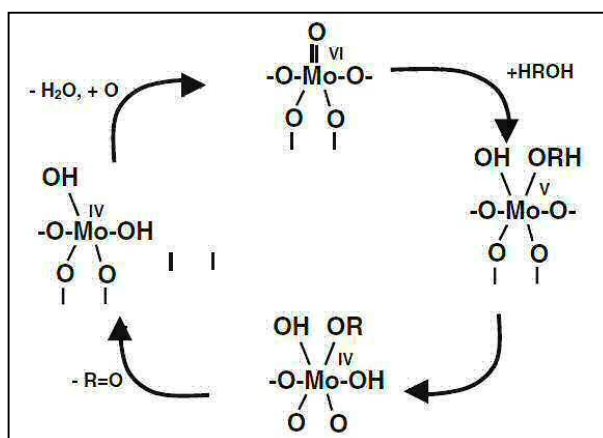


Figure 12. Suggested mechanism of formaldehyde production on Mo rich surfaces. The redox nature of the Mo should be noted.

House *et al.* study in depth the role of Mo in the selective oxidation of methanol (Figure 12) [23]. Mo was found to segregate to the surface, as proven by STEM, XPS and reaction data. It is believed that Mo dominates the chemistry due to this surface presence. During reaction, the active Mo(VI) reduces to Mo(IV), which can readily use lattice oxygen to re-oxidise back to Mo(VI). Confirmation of this derives from experiments carried out to determine the activity profile of the other main oxidation state of Mo, which is Mo(IV). From experimental observations the following scheme was proposed:

1. An acid-base type reaction with the terminal oxygen of the Mo site results in methoxy and OH formation (g= gas phase, a= adsorbed species). The covalent nature of the terminal oxygen is stronger than either of the two bridging oxygens. This makes it the most stable site for hydrogen adsorption. It has been claimed that the bulk M=O bond [76, 82] length and strength is a significant factor in the selectivity of these oxide materials. Too strong, and the catalyst is unreactive, too weak, and over-oxidation occurs making the catalyst less selective. However this is not agreed by all. More recently, a comparison between the activity and bond distance of a number of catalyst materials revealed no support for such a relationship at surface and in the bulk.



2. Attack of the bridging oxygen (O_b) on methoxy occurs. This occurs at a much higher temperature and is deemed as the rate determining step in formaldehyde formation. It is presumed that the step involves bridging oxygen, since when Fe is present at the surface, high selectivity to CO occurs due to the altered binding energy of the Mo-O-Fe bridging oxygen, which dehydrogenates the methoxy intermediate.



3. OH recombination occurs to yield H_2O from the catalyst [83]. The anion vacancy is re-oxidised from the bulk (anaerobic) or gas phase (aerobic) oxygen.



Once formed, formaldehyde can be further oxidised to CO or CO_2 . However, the high selectivity of $\alpha\text{-MoO}_3$ is derived from the presence of undissociated methanol and water blocking the adsorption sites, therefore preventing the further oxidation of formaldehyde. A

study of methane oxidation on MoO_3 performed by Smith *et al.* [84], has highlighted that the O_t sites are responsible for the production of formaldehyde and subsequent oxidation to CO , with the O_b sites responsible for the direct production of CO and CO_2 . Due to the lower stability of the bridging oxygen sites, TPR data has shown these sites to be more readily reduced. Work of Farneth *et al.* is in close agreement with this proposed mechanism [85]. Popov *et al.* [86] also observed that an increase in the methanol concentration of the reactor feed from 6.5 % to 13 %, results in a decrease of formaldehyde selectivity between 6 % to 8 %. These authors suggested that higher methanol content in reactor feed causes a greater reduction of the catalyst surface, which leads to an overall increase of CO selectivity.

Trifiro and Pasquon [87] have investigated the oxidation of methanol over a series of bulk oxides and found that MoO_3 was active for the oxidation of methanol to CO_2 . IR analysis revealed that only certain bulk oxides (including MoO_3) possessed a $\text{Mo}=\text{O}$ bond, so based on this qualitative observation, it was suggested that the $\text{Mo}=\text{O}$ bond plays a significant role in the selective oxidation of methanol, abstracting a H atom from the adsorbed hydrocarbon and coordinating it with $\text{Mo}=\text{O}$. This leaves a free valence on the Mo site, which can bond with the dehydrogenated molecule.

6. Kinetics and the Mars-van Krevelen Mechanism

The mechanism of methanol adsorption and reaction on the surface of FeMo based catalysts has been extensively researched, with the majority of authors accepting the Mars-van Krevelen mechanism. Under this mechanism, methanol oxidation employs surface lattice oxygen [88]. The incoming organic reactant becomes oxidized by lattice oxide ions at the catalyst surface. Methanol reacts with the weakly bound topmost oxygen of the catalyst to form the product, therefore leaving an oxygen vacancy at the surface. Gas-phase oxygen functions to replace the reduced sites by adsorption, ending the catalytic cycle [89].

Although justified, the Mars-van Krevelen mechanism only considers surface oxygen, and does not take into account the possibility of bulk oxygen migration to the surface. Bowker *et al.* [90] describe a modified mechanism, discovered on reacting methanol with $\text{Fe}_2(\text{MoO}_4)_3$ under anaerobic conditions. Catalysts were able to maintain their activity over a wide temperature range on reaction in MeOH/He , however selectivity diminished significantly at greater temperatures. It was revealed that a considerable amount of bulk lattice oxygen was mobile enough to migrate to the surface, capable of reacting with methanol in a selective reaction to formaldehyde. The authors ascribe the adapted mechanism to oxidative reactions on oxides in anaerobic or low oxygen ratio conditions, with modified kinetics. The

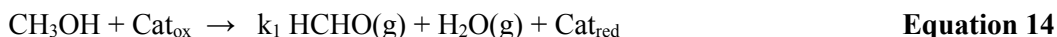
mechanism is referred to as the Extended Mars-van Krevelen mechanism [23]. Under this mechanism, the surface concentration of CH_3OH^* is relatively low. The rate of methanol oxidation to formaldehyde is detailed as follows:

$$r = k_{\text{rds}} K_{\text{ads}} P_{\text{CH}_3\text{OH}} N_s \quad \text{Equation 13}$$

Where k_{rds} = First-order rate constant / s^{-1} , K_{ads} = MeOH adsorption equilibrium constant / atm^{-1} , P = Partial pressure of methanol / atm and N_s = Surface density of redox sites / $\mu\text{mol}/\text{m}^2$.

Since the surface oxygen for the reaction is supplied through bulk lattice oxygen for the molybdate catalysts, the methanol oxidation reaction rate is therefore independent of molecular O_2 partial pressure, demonstrating zero-order dependence.

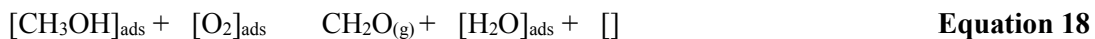
The first recorded studies of the reaction kinetics in selective methanol oxidation were noted by Jiru *et al.* [91], obtained in integral reactor conditions. The following mechanisms were proposed, with the rate limiting step identified as the re-oxidation of the catalyst:



Where Cat_{ox} = Oxidised catalyst, and Cat_{red} = Reduced catalyst.

A Langmuir Hinshelwood mechanism did not fit the recorded kinetic data accordingly. However, a recent kinetic study concluded that the reaction could be well described with Langmuir–Hinshelwood kinetics, assuming two different metal oxide sites. These two sites exist as adsorbed oxygenates and the other lattice oxygen. The rate of CO production was revealed to be first order with respect to formaldehyde. It has been shown from previous work that the production of CO at high temperature was from the further oxidation of formaldehyde. The reaction is still dehydrogenation, however no H_2 is evolved, and instead water is seen as a pre-sequel to formaldehyde production.

Evemenenko and Gorokhovatski [92] investigated the kinetics of methanol oxidation over $\text{Fe}_2(\text{MoO}_4)_3$ catalysts in the presence of CO_2 and water. Only H_2O demonstrated a profound effect in inhibiting the reaction. As a result of this finding, the following mechanism was proposed with the adsorption of methanol and oxygen at different active sites on the catalyst:



Where $[]$ = an active site on the catalysts surface.

The overall rate of the reaction can provide crucial information regarding the catalyst surface, since it depends on the concentration of active sites. The ability to break the C-H bond will depend on the basic or nucleophilic character of the oxygen species close to the methoxy group. If the acid sites are too strong, the formaldehyde resides for too long, enabling the formation of dioxymethylene species. This reaction will only occur at lower temperatures, since at higher temperatures the desorption rate of formaldehyde is too high. If the acid and basic sites are very strong, the dioxymethylene species are oxidized into formate species which can react with methanol to form methyl formate, or further oxidise to carbon oxides. If strong acid sites and very weak basic centres are present, only dimethyl ether is proven to form [93].

To provide further information on the kinetics involved, reactor studies are essential. Lafaytis *et al.* [94] investigate methanol oxidation over Cr doped Mo-Fe-O catalysts. The results from the pulsed catalytic testing combined with MS analysis infer that the reaction follows the Mars-van Krevelen mechanism, agreeing with the majority of authors. The rate determining step was determined to be H abstraction from the adsorbed methoxy. Infact, the rate determining step for formaldehyde formation has been determined by many to be the C-H bond breaking from an adsorbed methoxy group [95, 96]. Kinetic isotope studies by Machiels and Sleight [97], in particular expose hydrogen abstraction from the methoxy group to be rate limiting.

House *et al.* [19] exploit the use of reactor testing (TPD and pulsed flow studies), combined with XRD and Raman to investigate the adsorption and reaction of methanol with iron molybdate catalysts of varying Mo:Fe ratios. Higher Fe content leads to CO production, and possible CO₂ with Fe₂O₃ surface exposure. Mo dominated surfaces lead to formaldehyde production, with the following reaction steps believing to occur (Equations 20-22):





Step 1: Molecular methanol adsorption.

Step 2: Dissociative dehydrogenation of adsorbed methanol.

Step 3: Methoxy dehydrogenation to yield formaldehyde in the gas phase.

The same authors believe that molecular formaldehyde is weakly held on the surface, so its evolution is dependent on the decomposition kinetics of the methoxy intermediate, the rds. This is supported by the fact that this state begins to decompose in the TPD at 150 °C, which is well matched to the temperature at which conversion begins in the reactor data. Water is produced coincident with formaldehyde production, due to recombination of hydroxyl species.

It is important to note that an increase in the conversion will support consecutive reactions, leading to the formation of carbon oxides, which are also more thermodynamically favoured (See Section 7). Cheng [98] stated that the formaldehyde selectivity for methanol oxidation depends on methanol conversion. Data shows that the formaldehyde selectivity increases with conversion, except for high conversions where formaldehyde oxidation begins. Although $\text{Fe}_2(\text{MoO}_4)_3$ catalysts show high selectivity to formaldehyde, other side products are known to exist, such as CO, CO_2 and DME, MF and DMM. CO dominates as the major by-product. The selectivity towards formaldehyde increases with methanol conversion except for high levels of conversion where the formation of CO starts to be important.

The rate determining step is also thought to change under varying reaction conditions. According to Soares *et al.* [99], depending on the reaction conditions employed, the desorption of formaldehyde can also be the rate limiting step. Pernicone *et al.* [100] also agree that formaldehyde desorption is rate limiting, but in addition recognise that re-oxidation of the catalyst is also a slow process. Liberti *et al.* [101] highlight the formaldehyde desorption as the rate limiting step based on pulsing data, thus disagreeing with the original findings of Jiru *et al.* who identify re-oxidation as the rds (Equation 14-15).

7. Thermodynamics

The mild catalytic oxidation of aliphatic alcohols over simple metal oxides is known to lead to the formation of carbonyl compounds. Primary alcohols such as methanol are selectively oxidized to aldehydes such as formaldehydes.

Although iron molybdates present high selectivity to formaldehyde, other products are also possible, depending on the catalyst composition and reaction conditions employed. The main reactions to be considered when methanol is oxidised to formaldehyde are shown in Figure 13. Thermodynamics for the various reactions at 250 °C (the typical temperature for the reaction carried out), are presented in Table 1. The reactions from methanol can be divided into two main types: oxidative reactions requiring oxygen, and dehydration reactions which do not. Referring to the thermodynamic data, it is evident that combustion to CO₂ and H₂O is more favourable than the oxidative dehydrogenation reaction to H₂CO. This is evidenced through the larger exothermic nature of the reaction, giving out heat and leading to a products with lower energy. This therefore inhibits the oxidative dehydrogenation path. The catalyst must be tailored to follow the oxidative dehydrogenation pathway to prevent unwanted side products, which include DME, MF, and carbon oxides. With oxygen present, H₂ is not detected, and instead water forms. In a recent review of Soares *et al.* [102], it was found that the mechanism of reaction on Fe₂(MoO₄)₃ is highly dependent on reaction conditions, with focus on reaction temperature. For reaction temperatures below 170 °C, all by-products except CO and CO₂ are formed. They ascribe the formation of by-products at low temperatures due to the longer retention time of reaction intermediates on the active surface. Above 210 °C, formaldehyde and CO are observed. Soares *et al.* believe this CO comes from formaldehyde oxidation or direct methanol oxidation.

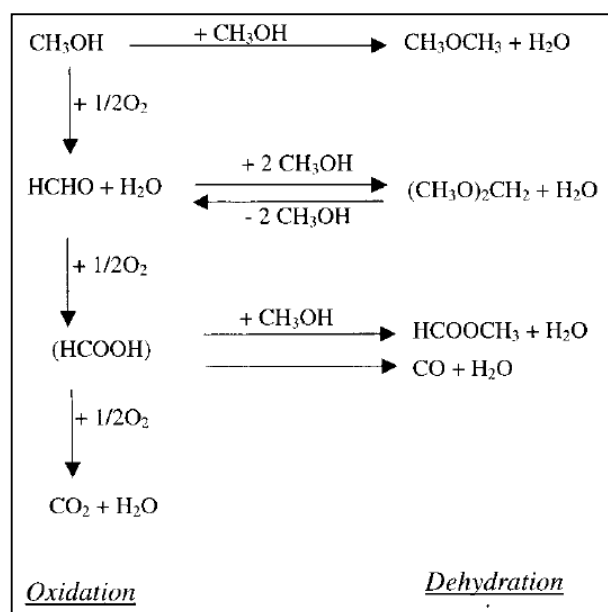


Figure 13. Various reactions for the oxidation and dehydration of methanol [96]. Referring to the scheme (excluding dimethyl ether, obtained directly through a bimolecular dehydration of methanol), the formation of all products requires one oxidation step.

Thermodynamic data can be seen in Equations 23-29.

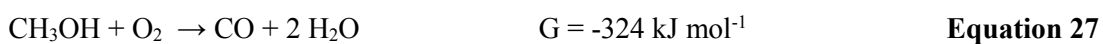
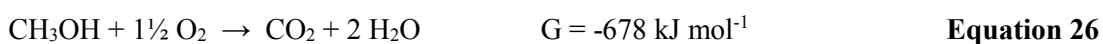
Dehydrogenation Reactions:



Oxidative Dehydrogenation Reaction:



Combustion Reactions:



Other Side Reactions:

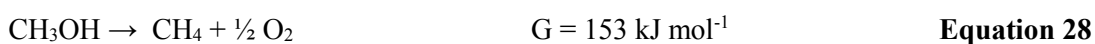


Table 1. Thermodynamic data for various reactions involved with methanol oxidation.

Equation	H / kJmol ⁻¹	S / JK ⁻¹ mol ⁻¹	G / kJmol ⁻¹
28	80	-122	145
29	88	-245	216
30	-164	-72	-123
31	-707	-55	-678
32	-400	-145	-324
33	124	-53	153
34	-27	15	-34

8. Supported Catalysts

The industrial reactor employed commonly uses a fixed bed reactor. However, it has since been proposed that a fluidised bed reactor might be more appropriate for the reaction since it would reduce the possibility of reactor hot spots occurring. Since methanol and air can also be fed into the reactor separately, it would decrease the possible explosion risk, and allow for increased methanol flow rates to be used, thus resulting in increased productivity. Although fluidised bed reactors show many advantages, they cannot be considered for bulk catalysts such as Fe₂(MoO₄)₃, since they are unable to withstand the mechanical abrasion impacted on them. For this reason, focus has turned to supported molybdates [103], which demonstrate higher mechanical resistance. As well as their increased resilience to mechanical abrasion, focus has also been on utilising these supported catalysts as an opportunity for high surface area catalysts, specifically through dosing molybdena or Fe₂(MoO₄)₃ on various high surface area supports [66, 104, 105]. The choice of support for supported catalysts however is crucial to catalyst performance, with the interaction between the support and the active phase changing the nature of the catalyst.

The design and control of the surface is extremely important for the development of heterogeneous catalysts, because the surface plays a key role in catalytic performance. It is of great interest to exclusively analyse the surface and how it reacts with methanol. Mo has been shown to segregate to the surface of iron molybdate [26], and thus implied to be the active site for the reaction to formaldehyde. It would therefore be beneficial to create catalysts in which Mo is dosed at the surface of supports with varying properties, to monitor the effect this has on catalytic activity. By dosing the Mo entirely at the surface, it enables scientists to exclusively probe how the Mo reacts with surface intermediates.

Typically, supported catalysts are synthesised through the incipient wetness technique using a solution ammonium heptamolybdate tetrahydrate impregnated onto the chosen support [106]. It has been discovered that due to the limited solubility of the precursor, the preparation method had to be adapted to involve multiple impregnations with the same solution, in order to achieve the desired loading.

The most commonly researched materials in this area are those formed from molybdena doped on Fe_2O_3 [103]. Bamroomgwongdee *et al.* [107] fabricate complex model oxide catalysts, primarily Mo oxide on Fe_3O_4 (111). Previous studies demonstrated a surface enrichment of Mo, and work here developed model systems using hot filament metal oxide deposition technique, to investigate the surface structure-reactivity relationship. The principal techniques involved in investigating the surface structure included LEED, XPS and STM. Mo was discovered to form in its active Mo(VI) state, with a high stability. However above 573 K, Mo drives into the Fe support to form $\text{Fe}_2(\text{MoO}_4)_3$. Reactivity was highly dependent on Mo coverage.

Work of Routray *et al.* [106] has carried out an extensive study on various FeMo based catalysts. Low-energy ion scattering (LEIS) analysis of the outermost surface layer in bulk $\text{Fe}_2(\text{MoO}_4)_3$ demonstrated a monolayer of amorphous surface MoO_x species. The addition of excess MoO_3 to $\text{Fe}_2(\text{MoO}_4)_3$ significantly increased the steady-state catalytic performance towards formaldehyde production. This was ascribed to the formation of this surface MoO_x monolayer. Focus was then turned to $\text{MoO}_3/\text{Fe}_2\text{O}_3$ to justify this finding. Catalysts in this instance were prepared through impregnation of the ammonium heptamolybdate precursor onto the Fe_2O_3 support, to yield supported 2.3 and 3 w/t % $\text{MoO}_3/\text{Fe}_2\text{O}_3$. 3D LEIS sputtering series plots of the supported 2.3 w/t % $\text{MoO}_3/\text{Fe}_2\text{O}_3$ revealed that the outermost surface layer was Mo dominated. The Fe signal only grew with increasing number of sputtering scans, due to removal of Mo from the surface. Results confirmed a complete monolayer was achieved for supported 2.3 w/t % $\text{MoO}_3/\text{Fe}_2\text{O}_3$ catalyst with only surface MoO_x species present in its outermost layer.

The MoO_x overlayer on the Fe_2O_3 support also demonstrated that the acidic surface sites of Fe_2O_3 are titrated by the redox surface MoO_x species. This makes the catalyst redox in nature, manufacturing it effective for the selective oxidation reaction to formaldehyde. The selectivity of these catalysts was found to be higher than that of the bulk $\text{Fe}_2(\text{MoO}_4)_3$, implying the surface MoO_x species to be the active site in mixed metal oxide catalysts. Catalytic activity was indistinguishable with or without excess MoO_3 .

Dosing onto Fe_2O_3 brings multiple benefits. It is believed that the Fe_2O_3 not only yields catalysts with a higher surface area, but it may also play an active role [23] in aiding the surface morphology of Mo. In addition, it is likely that the mobility of oxygen anions within the lattice can aid re-oxidation of the catalyst upon reduction.

With the discovery of surface MoO_x , focus has turned to dosing molybdenum on further supports to see if a similar effect is achieved. There is ample debate in the literature regarding the effects of support surface area and activity. Some argue that supports with a lower surface area present better performances. However, others will dispute that supported iron molybdates using high surface area supports such as silica present improved catalyst performance [108]. The choice of the support is a decisive factor in assessing how the catalyst will perform. Firstly, it can be crucial in dictating catalyst selectivity, especially if the support is not fully covered by the molybdenum precursor. Secondly, the choice of support can severely affect the molybdenum structure formed. By example, whether the supported molybdena exists with tetrahedral Mo sites, a mixture of dioxo ($\text{Mo}=\text{O}$) tetrahedral sites, or distorted octahedral sites. By example, on Al_2O_3 the sites are thought to be adsorbed MoO_4 units [109], whilst on TiO_2 distorted octahedral sites exist.

New Mo-Fe-O silica supported catalysts have been investigated by Soares *et al.* [110], in an attempt to improve the activity or spread of Mo further. Approximately 2.2 monolayers of Mo were loaded. Several Fe precursors were available for use, including nitrate, phosphate, chloride and pyrophosphate. Problems arose in that some elements remained in the catalyst. For example, samples prepared from phosphate and pyrophosphate had phosphorus in their compositions. All catalysts showed a high activity and selectivity towards formaldehyde, even at low and high methanol conversion. The catalyst prepared from iron pyrophosphate was the most active, which can be explained due to either the presence of heteropolymolybdates, or an Mo rich surface which is known to show almost 100 % selectivity to formaldehyde. Catalysts prepared from iron pyrophosphate showed huge catalytic potential for use in fluidized bed reactors, even showing greater yields than bulk industrial catalysts for one sample. However Mo loss during reaction was a problem, with SEM for post reaction samples displaying MoO_3 needle like structures, implying MoO_3 segregation and loss of Mo spread. This would hinder selectivity on subsequent catalytic runs. The mechanism of methanol oxidation over highly dispersed 1 w/t % $\text{MoO}_3/\text{SiO}_2$ was studied using steady state and transient kinetic measurements [111], coupled with *in situ* Fourier transform infrared (FTIR). Methoxy dominated as the surface intermediate, as in the case for bulk $\text{Fe}_2(\text{MoO}_4)_3$. It would infer the surfaces to be similar, with both demonstrating Mo enrichment. Deuterium substitution experiments showed that these species decomposed

through a rate-determining C-H bond-breaking step, to produce formaldehyde. However, although the oxidation occurred on the Mo centres for the selective reaction, the methoxide species were found to migrate to the silica support, displacing silica OH groups. Quantitative FTIR measurements demonstrated that the number of methoxide species on the silica support was about six times that of the Mo centres dosed. This implied that the silica surface held a substantial number of the reactive intermediates, but due to its inert nature there is no change to the catalyst selectivity.

Al_2O_3 has also been postulated as a support for molybdenum species [104]. Al_2O_3 benefits from a high surface area, so if prepared efficiently with a full monolayer coverage of Mo, it could bring catalysts demonstrating high activity. However, due to its high surface area, to produce one monolayer coverage requires a far greater weight percentage of molybdena. It has been discovered that Al_2O_3 does not become sufficiently covered until over 10 w/t % of molybdena is dosed onto the oxide surface. With such an increased loading of Mo, this will bring a substantial decrease in catalyst surface area, and therefore reduction in activity. On the surface of Al_2O_3 , it is also thought that Mo(V) forms as opposed to Mo(VI), which is required for selective catalysis. Mo(V) is responsible for the formation of non-selective by-products such as DME. It was discovered that the methanol oxidation activity of $\text{MoO}_3/\text{Al}_2\text{O}_3$ was sensitive to the preparation parameters examined [109], including volume of impregnation solution, pH, and calcination conditions. XPS demonstrated a migration of Mo to the surface taking place during the calcination. The effects of the volume and pH of the impregnation solution and of the calcination conditions were examined on the catalytic properties of a 13 w/t % $\text{MoO}_3/\text{Al}_2\text{O}_3$ catalyst. The dispersion of the Mo oxide improved as the volume of the impregnation solution increased, whilst an increase in pH of the impregnation was found to reduce the dispersion of Mo oxide species. The parameters must be fine-tuned in order to produce an efficient catalyst for the reaction. For Mo-Fe-O mixed oxides deposited on alumina, Carbucicchio [112] found that, supported on $\gamma\text{-Al}_2\text{O}_3$, significant activity was not observed at temperatures higher than 280°C , with formaldehyde selectivity around 90 %. This is comparable to that for bulk unsupported iron molybdates. Mo-Fe-O mixed oxides supported on $\gamma\text{-Al}_2\text{O}_3$ with $5\text{ m}^2\text{g}^{-1}$ of surface area demonstrated a formaldehyde selectivity of 80 %. Supported on $\gamma\text{-Al}_2\text{O}_3$ with $120\text{ m}^2\text{g}^{-1}$ surface area, zero formaldehyde was observed and DME resulted as the major reaction product.

Vanadia-molybdena catalysts supported on $\gamma\text{-Al}_2\text{O}_3$ have been reported by Chary *et al.* [113]. The influence of molybdenum oxide on the dispersion of vanadium oxide supported on alumina was investigated, created through dosing MoO_3 loadings ranging from 1-5 w/t % by wet impregnation of the ammonium molybdate precursor onto the already prepared 10

w/t % $\text{V}_2\text{O}_5/\text{Al}_2\text{O}_3$. Dispersion of vanadia was determined by oxygen chemisorption at 195 K, and was found to decrease with the increase of molybdena loading. However, with this, the selectivity of formaldehyde was also found to increase with molybdena loading. It was concluded that the additional MoO_3 provides further sites for the oxidation reaction to formaldehyde, and decreases the exposed acidic Al_2O_3 which leads to DME production.

TiO_2 has been less investigated in the literature as a support for molybdena. One study conducted by Kin *et al* [114], used DFT to examine the oxidation of methanol to formaldehyde by MO_3 clusters supported on rutile, where $\text{M}=\text{V}$, Mo and Cr . Thermodynamic analysis showcased that in the presence of oxygen, the metal atom takes three oxygen atoms from the gas phase, and this MO_3 species is the oxidant in the catalyst. They discuss the structures forming for each metal, and found that in terms of the catalyst performance, Vanadium outperformed the others. In 2007, the support effect on the structure and activity of MoO_3 was further investigated by Tsilomelekis *et al.* [118]. Supports included were ZrO_2 , Al_2O_3 , TiO_2 and SiO_2 . The nature of the oxide support material and of the Mo-O-support bond has a great influence on catalytic behaviour. The dependence of reactivity proceeded in the following order: $\text{ZrO}_2 > \text{Al}_2\text{O}_3 > \text{TiO}_2 > \text{SiO}_2$. The oxygen site involved in the anchoring Mo-O-support was determined to be an influential factor. On TiO_2 supported MoO_3 , dispersed molybdenum oxide is thought to be more easily reduced than crystalline MoO_3 on the surface, which in turn is more reducible than bulk MoO_3 . The dispersed Mo species bond to the Ti cations through a bridging oxygen bond. Surface species observed with adsorbed methanol are similar for dispersed and crystalline MoO_3 on TiO_2 . Formate groups form above 200°C , as in the case for MoO_3 supported on Fe_2O_3 , which is detrimental to catalyst selectivity. High levels of methyl formate are also observed. The catalyst was therefore deemed unsuitable for this specific reaction.

9. Deactivation of $\text{Fe}_2(\text{MoO}_4)_3$ Based Catalysts

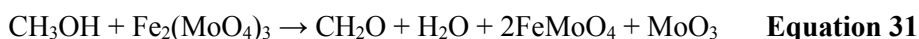
An understanding of the reaction and deactivation processes of catalytic systems is essential for the development and improvement of many industrial processes. Although the description of a catalyst states that the catalyst should undergo no net chemical change, realistically over long periods of time catalyst activity will drop as the catalyst begins to deactivate. Iron molybdates demonstrate a typical lifetime of 6-12 months, with the deactivation mechanism of these catalysts a keen topic of interest to authors. Krasimir *et al.* [115] have investigated catalyst deactivation using a pseudo-isothermal reactor, mimicking the conditions of those used industrially. The results demonstrated that deactivation can occur below 300°C . This was due to the change in surface layer composition, as a

consequence of the sublimation of part of MoO₃. Catalyst surface areas were also shown to decrease.

Under prolonged reactions, MoO₃ is shown to condense on the surface as a separate phase further along the catalyst bed [56]. The volatilised molybdenum species are seen in the form of needle like crystals under SEM observation. The loss of MoO₃ leaves an unselective Fe rich, FeMoO₄ phase. A slightly reddish brown catalyst also remains in the upper part of the spent catalyst, confirming a small proportion of Fe₂O₃ formation from the re-oxidation of FeMoO₄ (Equation 30).



A similar study by Andersson *et al.* [116] reports ageing and deactivation on catalysts from the Perstop Formox plant. A sample of catalyst was taken from the reactor after half the expected lifetime of the catalyst, and also after reaction completion. A layer was taken from both the front of the catalyst bed, and the middle to end of the bed. Characterisation was performed by BET, FT-IR, XRD, and AAS. Characterisation showed that there was migration of Mo species from the upper part of the reactor towards the outlet, deposited as MoO₃ like needles. The activity measurements also demonstrated significant deactivation of the catalyst. Loss of Mo resulted in the decrease of the MoO₃/Fe₂(MoO₄)₃ mole ratio in the catalyst, which in turn leads to rapid deactivation of the active Fe₂(MoO₄)₃ phase. It was concluded that to maintain the active phase, an excess of MoO₃ is needed according to the redox process as follows: Main reaction:



With this MoO₃ excess, the re-oxidation process will occur as follows:



However, under a MoO₃ deficient environment, the following route occurs to form unselective Fe₂O₃ and subsequent CO₂ production:



It is important to obtain the correct Mo:Fe ratio in order to achieve both an active and stable catalyst. It claimed that a Mo:Fe ratio of 1.7:1 is optimum. If too large a Mo excess is used, part of Mo cannot participate in that process since its loss rate is too large. This has been reported by Sun-Kuo and co-workers [117].

While a remarkable catalyst, there is still a surprisingly low knowledge about the catalyst surface layer and how it reacts with the adsorbent and so quickly regenerates. Beale *et al.* [118] recently published a study involving a combined multi-technique *in situ* approach to probe the stability of $\text{Fe}_2(\text{MoO}_4)_3$ catalysts during redox cycling. Information attainable from multiple techniques allows scientists to more accurately identify the nature of catalytic materials. Combining techniques *in situ* offers a quick and accurate observation of catalyst deactivation routes. The use of synchrotron light affords a way to examine catalysts under more realistic conditions. According to these authors, the $\text{Fe}_2(\text{MoO}_4)_3$ phase is generally considered to be the primary active phase, agreeing that during standard reaction, a partial reduction of this phase occurs to produce formaldehyde, inactive $\beta\text{-FeMoO}_4$ and MoO_3 . The FeMoO_4 phase is short lived, and is rapidly re-oxidised back to $\text{Fe}_2(\text{MoO}_4)_3$ by gas phase oxygen. To study this mechanism in more detail, the stoichiometric $\text{Fe}_2(\text{MoO}_4)_3$ catalyst has been studied in harsher anaerobic conditions, to accelerate the changes occurring. The catalyst was first reduced under MeOH/He , yielding formaldehyde. Post anaerobic treatment the catalyst was re-oxidised in air to monitor the ability of the catalyst to regenerate. *In situ* combined wide-angle X-ray scattering, X-ray absorption near edge spectroscopy and ultraviolet–visible spectroscopy with online mass spectrometry (MS) were combined to study the structure–activity relationships under redox cycling. Under redox cycling, it is shown that the initial $\text{Fe}_2(\text{MoO}_4)_3$ is partially regenerated, however with subsequent re-oxidation, after the anaerobic treatment little regeneration occurs, and can only do so after a long period of time.

Soares *et al.* [56] investigate different factors and their effect on $\text{Fe}_2(\text{MoO}_4)_3$ deactivation. Two methods of preparation were involved in the study, including co-precipitation and a sol-gel method of both $\text{Fe}_2(\text{MoO}_4)_3$ with and without Mo excess. For both techniques, the catalytic stability was tested in the presence and absence of water in the reactor feed. The stoichiometric catalysts deactivated significantly, with water shown to accelerate this process, and also impede the re-oxidation process. The sol–gel like technique provides a better dispersion of the MoO_3 excess in the $\text{Fe}_2(\text{MoO}_4)_3$ lattice, which hinders its volatilisation. Characterisation demonstrated the deactivation mechanism to involve an increase of surface reduction (Fe (II)/(III)) to the detriment of surface Mo loss. This was a direct effect of MoO_3 sublimation, and formation of Mo-methanol and Mo-water volatile compounds. The loss of Mo as these volatile compounds is proportional to the methanol concentration and reaction temperature used.

Recently, Dazhuang and co-workers studied the kinetics of Mo loss from Mo-Fe/SiO_2 catalysts under nitrogen [119]. They reported that for Mo rich catalysts, the MoO_3 phase is lost at the beginning. Wachs *et al.* [120] have shown the ability to regenerate the spent

catalyst, by moving the MoO_3 formed around with methanol in a nitrogen gas flow in the opposite direction to that of the proceeding reaction.

The reduction process of various FeMo based catalysts has been discussed. Methanol itself essentially acts as a reductant, removing oxygen from the surface to bring a multitude of phases which are detailed. It is important to consider not only the reaction conditions, but also the preparation methods employed, and the effect they have on catalyst lifetime. Further work is required in identifying the reduction mechanisms occurring, and attempts must be made to increase catalyst longevity for prolonged industrial catalyst use.

10. Research Objectives

One of the fundamental challenges of this work is in identifying the active site for the selective oxidation of methanol to formaldehyde. With the ongoing literature debate regarding the roles of various oxides, primarily $\text{Fe}_2(\text{MoO}_4)_3$ and MoO_3 , there is a requirement to ultimately decipher the active site, and to determine whether there is a common adsorption site between catalysts.

In Chapter 3, the preparation of FeMo based catalysts will be discussed in detail, including factors such as pH, whether filtering is applied, and calcination time and temperature. All of these are thought to have a profound effect on the resulting catalyst composition, ultimately with direct effects on catalyst activity, selectivity and longevity.

During preparation, the addition of excess Mo to the catalyst is believed necessary, as any Mo lost through sublimation has the potential to leave vacant, unselective Fe sites [90]. The excess Mo is present to counter this eventuality [121]. However, this approach is shown to leave a system containing multiple distinct phases including, both MoO_3 and $\text{Fe}_2(\text{MoO}_4)_3$, with MoO_3 shown to segregate to the surface [19]. There is little knowledge of the involvement of each of these phases during the reaction. Unravelling the nature of the active site, has thus been limited due to the presence of both these phases.

Disregarding the different phases present, conventional *in situ* X-ray diffraction (XRD) or X-ray absorption fine structure (XAFS) studies of bulk $\text{Fe}_2(\text{MoO}_4)_3$ catalysts are unable to identify how the surface layer changes during important catalytic processes e.g. catalyst preparation, catalytic testing and catalytic deactivation. The surface layer makes up a very small proportion of the overall catalyst, so bulk characterisation cannot realistically characterise the active and important species.

To investigate the surface activity, core-shell catalysts of the type $\text{MoO}_x/\text{Fe}_2\text{O}_3$ will be exploited, exclusively dosing Mo at the surface of the catalyst, with its surface existence proven by techniques such as TEM EDX (Chapter 4). This enables bulk techniques, particularly XAFS, to become surface sensitive when probing the Mo structure. XAFS studies are element specific and provide a per atom average of the environments probed. However, when Mo is exclusively at the surface, XAFS is able to provide surface-sensitive information.

A key focus of the work has involved *in situ* characterisation. This will be detailed in Chapter 5. The work demonstrates how model $\text{MoO}_x/\text{Fe}_2\text{O}_3$ catalysts with precise structural surface motifs, can be studied *in situ* in both their preparation, reaction and deactivation, in order to relate this to the same processes occurring in the conventional $\text{Fe}_2(\text{MoO}_4)_3$ catalyst. The constant development of synchrotrons has enabled studies involving a combination of techniques used simultaneously to examine how catalysts change under realistic conditions. Explicitly for this work, Raman has been used in conjunction with XAFS, showing complementary results. It is the ultimate aim to be able to address how reaction with methanol occurs at the surface, and how the catalyst is able to regenerate for further reaction with maintained selectivity. It is hoped that with further knowledge of the catalyst, materials can be optimised to bring maximised product yield.

Due to its many benefits already mentioned, $\text{Fe}_2(\text{MoO}_4)_3$ currently stands as the world leading catalyst in methanol oxidation to formaldehyde, and has done since first reported by Adkin and co-workers in 1931 [8]. Reasons for this include its ability to react under relatively mild oxidative conditions, and also its ability in retaining catalyst activity for repeated use. However, it is not specified why Fe is such a key contender in the catalyst composition. It is important to address whether the bulk $\text{Fe}_2(\text{MoO}_4)_3$ merely acts as a support for MoO_3 , or whether it has its own inherent activity. It has been suggested that $\text{Fe}_2(\text{MoO}_4)_3$ has superior properties including its bulk lattice oxygen mobility. This allows the catalyst to always ensure oxygen regeneration to the surface during reaction, maintaining catalyst selectivity. The final chapter of this project explores the reasons why Fe works so well in these systems, and whether other supports such as SiO_2 or Al_2O_3 could show similar if not superior performances.

In the final concluding chapter, the data discussed will be summarised and related to the original aims of the project. Future work will also be suggested.

11. References

1. Chorkendorff, I. and J.W. Niemantsverdriet, *Concepts of modern catalysis and kinetics* 2006: John Wiley & Sons.
2. Davis, S.E., M.S. Ide, and R.J. Davis, *Selective oxidation of alcohols and aldehydes over supported metal nanoparticles*. Green Chemistry, 2013. **15**(1): p. 17-45.
3. Butlerow, A., *Ueber einige Derivate des Jodmethylen*. Justus Liebigs Annalen der Chemie, 1859. **111**(2): p. 242-252.
4. Walker, J.F., *Formaldehyde* 1944: Reinhold publishing corporation.
5. Nagy, A. and G. Mestl, *High temperature partial oxidation reactions over silver catalysts*. Applied Catalysis A: General, 1999. **188**(1-2): p. 337-353.
6. Maldonado, C., et al., *Conversion of methanol to formaldehyde on TiO₂ Supported Ag nanoparticles*. Journal of the Chilean Chemical Society, 2010. **55**: p. 506-510.
7. Lloyd, L., *Handbook of Industrial Catalysts* 2011: Springer.
8. Adkins, H. and W.R. Peterson, *The oxidation of methanol with air over iron, molybdenum, and iron-molybdenum oxides*. Journal of the American Chemical Society, 1931. **53**(4): p. 1512-1520.
9. Routray, K., et al., *Origin of the synergistic interaction between MoO₃ and iron molybdate for the selective oxidation of methanol to formaldehyde*. Journal of Catalysis, 2010. **275**(1): p. 84-98.
10. Soares, A.P.V., M.F. Portela, and A. Kiennemann, *Methanol selective oxidation to formaldehyde over iron-molybdate catalysts*. Catalysis Reviews, 2005. **47**(1): p. 125-174.
11. Bowker, M., et al., *The selective oxidation of methanol to formaldehyde on iron molybdate catalysts and on component oxides*. Catalysis Letters, 2002. **83**(3-4): p. 165-176.
12. Vieira Soares, A.P., M. Farinha Portela, and A. Kiennemann, *A comparison of iron molybdate catalysts for methanol oxidation prepared by coprecipitation and new sol-gel method*, in *Studies in Surface Science and Catalysis*, S.T.O.A.M.G. R.K. Grasselli and J.E. Lyons, Editors. 1997, Elsevier. p. 807-816.
13. Chowdhry, U., et al., *Mechanism and surface structural effects in methanol oxidation over molybdates*. Applied Surface Science, 1984. **19**(1-4): p. 360-372.
14. Farneth, W.E., et al., *Mechanism of partial oxidation of methanol over MoO₃ as studied by temperature-programmed desorption*. Journal of Physical Chemistry, 1985. **89**(12): p. 2493-2497.
15. Soares, A.P.V., et al., *Iron molybdate catalysts for methanol to formaldehyde oxidation: effects of Mo excess on catalytic behaviour*. Applied Catalysis A: General, 2001. **206**(2): p. 221-229.
16. Alessandrini, G., et al., *Chemical, structural and catalytic modifications of pure and doped iron(III) molybdate*. Journal of the Less Common Metals, 1977. **54**(2): p. 373-386.
17. Fagherazzi, G. and N. Pernicone, *Structural study of a methanol oxidation catalyst*. Journal of Catalysis, 1970. **16**(3): p. 321-325.
18. Massarotti, V., G. Flor, and A. Marini, *Crystal data for ferric molybdate: Fe₂(MoO₄)₃*. Journal of Applied Crystallography, 1981. **14**(1): p. 64-65.
19. House, M.P., et al., *Effect of varying the cation ratio within iron molybdate catalysts for the selective oxidation of methanol*. The Journal of Physical Chemistry C, 2008. **112**(11): p. 4333-4341.
20. Söderhjelm, E., et al., *On the Synergy Effect in MoO₃-Fe₂(MoO₄)₃ Catalysts for Methanol Oxidation to Formaldehyde*. Topics in Catalysis, 2008. **50**(1-4): p. 145-155.
21. Routray, K., *Catalysis Science of Bulk Mixed Metal Oxides* 2009: ProQuest.

22. Bowker, M., et al., *Evolution of active catalysts for the selective oxidative dehydrogenation of methanol on Fe₂O₃ surface doped with Mo oxide*. Physical Chemistry Chemical Physics, 2013. **15**(29): p. 12056-12067.
23. Bowker, M., et al., *The selective oxidation of methanol on iron molybdate catalysts*. Topics in Catalysis, 2008. **48**(1-4): p. 158-165.
24. Walzel, I., *Untersuchungen an FeMoO-Katalysatoren zur Formaldehydproduktion*, 2009, Universitätsbibliothek.
25. Grasselli, R.K. and J.D. Burchington, *Selective oxidation and ammoxidation of propylene by heterogeneous catalysis*. Advances in Catalysis, 1981. **30**: p. 133-163.
26. House, M.P., M.D. Shannon, and M. Bowker, *Surface segregation in iron molybdate catalysts*. Catalysis Letters, 2008. **122**(3-4): p. 210-213.
27. Sun-Kou, M.R., et al., *Influence of the preparation method on the behaviour of Fe-Mo catalysts for the oxidation of methanol*. Journal of Materials Science, 1995. **30**(2): p. 496-503.
28. Söderhjelm, E., et al., *On the synergy effect in MoO₃-Fe₂(MoO₄)₃ catalysts for methanol oxidation to formaldehyde*. Topics in Catalysis, 2008. **50**(1-4): p. 145-155.
29. Brookes, C., et al., *Molybdenum oxide on Fe₂O₃ core-shell catalysts: probing the nature of the structural motifs responsible for methanol oxidation catalysis*. ACS Catalysis, 2013. **4**(1): p. 243-250.
30. <http://www.formox.com/formox-process>.
31. Weissermel, K. and H.-J. Arpe, *Industrial organic chemistry* 2008: John Wiley & Sons.
32. Boyle, R., *The Sceptical Chymist: The Classic 1661 Text* 1911: Courier Corporation.
33. Mittasch, A. and M. Pier, *Synthetic manufacture of methanol*, 1926, Google Patents.
34. Bart, J. and R. Sneed, *Copper-zinc oxide-alumina methanol catalysts revisited*. Catalysis Today, 1987. **2**(1): p. 1-124.
35. Bowker, M., et al., *The mechanism of methanol synthesis on copper/zinc oxide/alumina catalysts*. Journal of Catalysis, 1988. **109**(2): p. 263-273.
36. Wang, W.W., Y.J. Zhu, and M.L. Ruan, *Microwave-assisted synthesis and magnetic property of magnetite and hematite nanoparticles*. Journal of Nanoparticle Research, 2007. **9**(3): p. 419-426.
37. Wan, J., et al., *Monodisperse water-soluble magnetite nanoparticles prepared by polyol process for high-performance magnetic resonance imaging*. Chemical Communications, 2007(47): p. 5004-5006.
38. He, Y.T., J. Wan, and T. Tokunaga, *Kinetic stability of hematite nanoparticles: The effect of particle sizes*. Journal of Nanoparticle Research, 2008. **10**(2): p. 321-332.
39. *Oxides and oxyhydrides*. Physics and Chemistry of the Earth, 1992. **18**, Part 2(0): p. 67-86.
40. Rapposch, M.H., J.B. Anderson, and E. Kostiner, *Crystal structure of ferric molybdate, Fe₂(MoO₄)₃*. Inorganic Chemistry, 1980. **19**(11): p. 3531-3539.
41. Chen, H.-y., *The crystal structure and twinning behavior of ferric molybdate, Fe₂(MoO₄)₃*. Materials Research Bulletin, 1979. **14**(12): p. 1583-1590.
42. Chen, H.-y., *The crystal structure and twinning behavior of ferric molybdate, Fe₂(MoO₄)₃*. Materials Research Bulletin, 1979. **14**(12): p. 1583-1590.
43. Sleight, A., B.t. Chamberland, and J. Weiher, *Magnetic, Moessbauer, and structural studies on three modifications of FeMoO₄*. Inorganic Chemistry, 1968. **7**(6): p. 1093-1098.
44. Weeks, M.E., *The discovery of the elements. Chronology*. Journal of Chemical Education, 1933. **10**(4): p. 223.
45. Kihlberg, L., *Studies on molybdenum oxides*. Acta Chem. Scand, 1959. **13**(0): p. 5.
46. Cora, F., et al., *An ab initio Hartree-Fock study of α-MoO₃*. Journal of Materials Chemistry, 1997. **7**(6): p. 959-967.
47. Chernova, N.A., et al., *Layered vanadium and molybdenum oxides: batteries and electrochromics*. Journal of Materials Chemistry, 2009. **19**(17): p. 2526-2552.

48. Tatibouët, J.M. and J.E. Germain, *A structure-sensitive oxidation reaction: Methanol on molybdenum trioxide catalysts*. Journal of Catalysis, 1981. **72**(2): p. 375-378.
49. Balendhran, S., et al., *Enhanced charge carrier mobility in two dimensional high dielectric molybdenum oxide*. Advanced Materials, 2013. **25**(1): p. 109-114.
50. Dieterle, M., G. Weinberg, and G. Mestl, *Raman spectroscopy of molybdenum oxides Part I. Structural characterization of oxygen defects in MoO_{3-x} by DR UV/VIS, Raman spectroscopy and X-ray diffraction*. Physical Chemistry Chemical Physics, 2002. **4**(5): p. 812-821.
51. Scanlon, D.O., et al., *Theoretical and Experimental Study of the Electronic Structures of MoO₃ and MoO₂*. The Journal of Physical Chemistry C, 2010. **114**(10): p. 4636-4645.
52. Eyert, V., et al., *Embedded Peierls instability and the electronic structure of MoO₂*. Journal of Physics: Condensed Matter, 2000. **12**(23): p. 4923.
53. Cotton, F.A., et al., *Advanced inorganic chemistry*. Vol. 5. 1999: Wiley New York.
54. Tokarz-Sobieraj, R., R. Gryboś, and M. Witko, *Electronic structure of MoO₂. DFT periodic and cluster model studies*. Applied Catalysis A: General, 2011. **391**(1–2): p. 137-143.
55. Pernicone, N., *MoO₃–Fe₂(MoO₄)₃ catalysts for methanol oxidation*. Journal of the Less Common Metals, 1974. **36**(1): p. 289-297.
56. Soares, A.P.V., et al., *Mechanism of deactivation of iron-molybdate catalysts prepared by coprecipitation and sol–gel techniques in methanol to formaldehyde oxidation*. Chemical Engineering Science, 2003. **58**(7): p. 1315-1322.
57. Beale, A.M., et al., *An iron molybdate catalyst for methanol to formaldehyde conversion prepared by a hydrothermal method and its characterization*. Applied Catalysis A: General, 2009. **363**(1–2): p. 143-152.
58. Demidov, A., et al., *Effect of anions on the catalytic properties of ferric molybdate in the selective oxidation of methanol*. Kinetics and catalysis, 1992. **33**(5-6): p. 910-914.
59. Chen, Y., et al., *In situ diffusion growth of Fe₂(MoO₄)₃ nanocrystals on the surface of α-MoO₃ nanorods with significantly enhanced ethanol sensing properties*. Journal of Materials Chemistry, 2012. **22**(25): p. 12900-12906.
60. Popov, B., A. Pashis, and L. Shkuratova, *Effect of calcination temperature on the surface composition of Mo–Fe catalysts for methanol oxidation*. Reaction Kinetics and Catalysis Letters, 1986. **30**(1): p. 129-135.
61. Burcham, L.J., L.E. Briand, and I.E. Wachs, *Quantification of active sites for the determination of methanol oxidation turn-over frequencies using methanol chemisorption and in situ infrared techniques. 2. Bulk metal oxide catalysts*. Langmuir, 2001. **17**(20): p. 6175-6184.
62. Hassan, K.H. and P.C.H. Mitchell, *Evaluation of different methods to prepare the Fe₂O₃/MoO₃ catalyst used for selective oxidation of methanol to formaldehyde*, in *Studies in Surface Science and Catalysis*, M.D.S.H.P.A.J.J.A.M. E.M. Gaigneaux and P. Ruiz, Editors. 2010, Elsevier. p. 475-478.
63. Li, J.-L., et al., *Improvement in reactivity, reproducibility and stability of Fe–Mo catalysts by wet mixing*. Catalysis today, 1999. **51**(1): p. 195-199.
64. Taylor, S.H., et al., *Methanol Oxidation Over Oxide Catalysts*, in *Methane and Alkane Conversion Chemistry* 1995, Springer. p. 339-345.
65. Deo, G. and I.E. Wachs, *Reactivity of supported vanadium oxide catalysts: the partial oxidation of methanol*. Journal of Catalysis, 1994. **146**(2): p. 323-334.
66. Hu, H. and I.E. Wachs, *Catalytic properties of supported molybdenum oxide catalysts: in situ Raman and methanol oxidation studies*. The Journal of Physical Chemistry, 1995. **99**(27): p. 10911-10922.
67. Jin, G., et al., *Fe₂(MoO₄)₃/MoO₃ nano-structured catalysts for the oxidation of methanol to formaldehyde*. Journal of Catalysis, 2012. **296**(0): p. 55-64.

68. Centi, G., S. Perathoner, and S. Tonini, *In situ DRIFT study of the reactivity and reaction mechanism of catalysts based on iron–molybdenum oxides encapsulated in Boralite for the selective oxidation of alkylaromatics*. Catalysis Today, 2000. **61**(1): p. 211-221.
69. Burcham, L.J., L.E. Briand, and I.E. Wachs, *Quantification of active sites for the determination of methanol oxidation turn-over frequencies using methanol chemisorption and in situ infrared techniques. 1. Supported metal oxide catalysts*. Langmuir, 2001. **17**(20): p. 6164-6174.
70. Natile, M.M. and A. Glisenti, *New NiO/Co₃O₄ and Fe₂O₃/Co₃O₄ nanocomposite catalysts: synthesis and characterization*. Chemistry of materials, 2003. **15**(13): p. 2502-2510.
71. Glisenti, A., G. Favero, and G. Granozzi, *Reactivity of simple alcohols on Fe₂O₃ powders An XPS and FTIR study*. Journal of the Chemical Society, Faraday Transactions, 1998. **94**(1): p. 173-182.
72. Glisenti, A., G. Favero, and G. Granozzi, *Reactivity of simple alcohols on Fe₂O₃ powders - An XPS and FTIR study*. Journal of the Chemical Society-Faraday Transactions, 1998. **94**(1): p. 173-182.
73. Holstein, W.L. and C.J. Machiels, *Inhibition of methanol oxidation by water vapor—effect on measured kinetics and relevance to the mechanism*. Journal of Catalysis, 1996. **162**(1): p. 118-124.
74. Groff, R.P., *An infrared study of methanol and ammonia adsorption on molybdenum trioxide*. Journal of Catalysis, 1984. **86**(1): p. 215-218.
75. Chowdhry, U., et al., *Mechanism and surface structural effects in methanol oxidation over molybdates*. Applications of Surface Science, 1984. **19**(1–4): p. 360-372.
76. Tatibouet, J.M., *Methanol oxidation as a catalytic surface probe*. Applied Catalysis A: General, 1997. **148**(2): p. 213-252.
77. Allison, J.N. and W.A. Goddard Iii, *Oxidative dehydrogenation of methanol to formaldehyde*. Journal of Catalysis, 1985. **92**(1): p. 127-135.
78. Smith, R.L. and G.S. Rohrer, *An atomic force microscopy study of the morphological evolution of the MoO₃ (010) surface during reduction reactions*. Journal of Catalysis, 1996. **163**(1): p. 12-17.
79. O'Brien, M.G., et al., *On the active oxygen in bulk MoO₃ during the anaerobic dehydrogenation of methanol*. The Journal of Physical Chemistry C, 2009. **113**(12): p. 4890-4897.
80. Bowker, M., A.F. Carley, and M. House, *Contrasting the Behaviour of MoO₃ and MoO₂ for the Oxidation of Methanol*. Catalysis Letters, 2008. **120**(1-2): p. 34-39.
81. Farneth, W.E., et al., *Mechanism of partial oxidation of methanol over molybdenum(VI) oxide as studied by temperature-programmed desorption*. The Journal of Physical Chemistry, 1985. **89**(12): p. 2493-2497.
82. Routray, K., L.E. Briand, and I.E. Wachs, *Is there a relationship between the M O bond length (strength) of bulk mixed metal oxides and their catalytic activity?* Journal of Catalysis, 2008. **256**(1): p. 145-153.
83. Chung, J.S., R. Miranda, and C.O. Bennett, *Mechanism of partial oxidation of methanol over MoO₃*. Journal of Catalysis, 1988. **114**(2): p. 398-410.
84. Smith, M. and U. Ozkan, *The partial oxidation of methane to formaldehyde: Role of different crystal planes of MoO₃*. Journal of Catalysis, 1993. **141**(1): p. 124-139.
85. Farneth, W.E., et al., *Mechanism of partial oxidation of methanol over molybdenum (VI) oxide as studied by temperature-programmed desorption*. The Journal of Physical Chemistry, 1985. **89**(12): p. 2493-2497.
86. Popov, B., L. Shkuratova, and L. Orlova, *Effect of excess molybdenum trioxide on the activity and selectivity of some molybdates in methanol oxidation*. Reaction Kinetics and Catalysis Letters, 1976. **4**(3): p. 323-328.
87. Trifirò, F. and I. Pasquon, *Classification of oxidation catalysts according to the type of metal-oxygen bond*. Journal of Catalysis, 1968. **12**(4): p. 412-416.

88. Doornkamp, C. and V. Ponc, *The universal character of the Mars and Van Krevelen mechanism*. Journal of Molecular Catalysis A: Chemical, 2000. **162**(1–2): p. 19-32.
89. Lewandowski, M., et al., *Scanning tunneling microscopy evidence for the Mars-van Krevelen type mechanism of low temperature CO oxidation on an FeO (111) film on Pt (111)*. Catalysis Today, 2012. **181**(1): p. 52-55.
90. House, M.P., A.F. Carley, and M. Bowker, *Selective oxidation of methanol on iron molybdate catalysts and the effects of surface reduction*. Journal of Catalysis, 2007. **252**(1): p. 88-96.
91. Jiru, P., B. Wichterlova, and J. Tichy, *Mechanism of Oxidation of Methyl Alcohol to Formaldehyde on Oxide Catalysts*. Proc. 3rd Int. Congr. Catal., Amsterdam, 1965.
92. Evmenenko, N. and Y.B. Gorokhovatskii, *Kinetics of methanol oxidation at a ferromolybdenum catalyst*. Kinetics and Catalysis, 1969. **10**(6): p. 1071-1075.
93. Carrizosa, I., G. Munuera, and S. Castanar, *Study of the interaction of aliphatic alcohols with TiO₂: III. Formation of alkyl-titanium species during methanol decomposition*. Journal of Catalysis, 1977. **49**(3): p. 265-277.
94. Lafyatis, D.S., G. Creten, and G.F. Froment, *TAP reactor study of the partial oxidation of methanol to formaldehyde using an industrial Fe-Cr-Mo oxide catalyst*. Applied Catalysis A: General, 1994. **120**(1): p. 85-103.
95. Hair, L.M., et al., *Modeling of catalytic coupling of methane*. Prepr. Pap.-J. Am. Chem. Soc., Div. Fuel Chem, 1991. **36**: p. 370-376.
96. Tatibouet, J., *Methanol oxidation as a catalytic surface probe*. Applied Catalysis A: General, 1997. **148**(2): p. 213-252.
97. Machiels, C. and A. Sleight, *Kinetic isotope effect in the selective oxidation of methanol to formaldehyde over some molybdate catalysts*. Journal of Catalysis, 1982. **76**(1): p. 238-239.
98. Cheng, W.-H., *Methanol and formaldehyde oxidation study over molybdenum oxide*. Journal of Catalysis, 1996. **158**(2): p. 477-485.
99. Soares, A.V., M.F. Portela, and A. Kiennemann, *Kinetics of the Main and Side Reactions of the Methanol Oxidation Over Iron Molybdates*. Studies in Surface Science and Catalysis, 2001. **133**: p. 489-494.
100. Pernicone, N., *Deactivation of Fe-Mo oxide catalyst in industrial plant and simulation tests on laboratory scale*. Catalysis Today, 1991. **11**(1): p. 85-91.
101. Liberti, G., N. Pernicone, and S. Soattini, *Pulse microreactor study of methanol oxidation over MoO₃/Fe₂O₃ catalyst*. Journal of Catalysis, 1972. **27**(1): p. 52-55.
102. Soares, A.P.V., M.F. Portela, and A. Kiennemann, *Methanol Selective Oxidation to Formaldehyde over Iron Molybdate Catalysts*. Catalysis Reviews, 2005. **47**(1): p. 125-174.
103. Shi, G.J., et al., *Thin-film beta-MoO₃ Supported on alpha-Fe₂O₃ as a Shell-Core Catalyst for the Selective Oxidation of Methanol to Formaldehyde*. Chemcatchem, 2012. **4**(6): p. 760-765.
104. Matsuoka, Y., M. Niwa, and Y. Murakami, *Morphology of molybdena supported on various oxides and its activity for methanol oxidation*. Journal of Physical Chemistry, 1990. **94**(4): p. 1477-1482.
105. Amiridis, M.D., et al., *Simulation of methane partial oxidation over silica supported MoO₃ and V₂O₅*. AIChE journal, 1991. **37**(1): p. 87-97.
106. Routray, K., et al., *Origin of the synergistic interaction between MoO₃ and iron molybdate for the selective oxidation of methanol to formaldehyde*. Journal of Catalysis, 2010. **275**(1): p. 84-98.
107. Bamroongwongdee, C., et al., *Fabrication of complex model oxide catalysts: Mo oxide supported on Fe₃O₄ (111)*. Faraday discussions, 2013. **162**: p. 201-212.
108. Carbucicchio, M. and F. Trifiro, *Redox processes at the surfaces of Fe₂O₃/MoO₃/SiO₂ catalysts*. Journal of Catalysis, 1980. **62**(1): p. 13-18.

109. Heracleous, E., et al., *Surface properties and reactivity of Al₂O₃-supported MoO₃ catalysts in ethane oxidative dehydrogenation*. Catalysis letters, 2003. **88**(1-2): p. 47-53.
110. Dias, A.P.S., et al., *New Mo-Fe-O silica supported catalysts for methanol to formaldehyde oxidation*. Applied Catalysis a-General, 2008. **345**(2): p. 185-194.
111. Seman, M., et al., *Reactive and inert surface species observed during methanol oxidation over silica-supported molybdenum oxide*. Journal of Physical Chemistry B, 2002. **106**(50): p. 12965-12977.
112. Carbucicchio, M., *Mössbauer analysis of Fe₂O₃-MoO₃ supported on SiO₂ and Al₂O₃*. The Journal of Chemical Physics, 1979. **70**(2): p. 784-787.
113. Chary, K.V.R., et al., *Characterization and reactivity of vanadia-molybdena catalysts supported on gamma-Al₂O₃*. Applied Catalysis a-General, 2000. **202**(1): p. 133-139.
114. Kim, H.Y., et al., *Oxidative Dehydrogenation of Methanol to Formaldehyde by Isolated Vanadium, Molybdenum, and Chromium Oxide Clusters Supported on Rutile TiO₂(110)*. Journal of Physical Chemistry C, 2009. **113**(36): p. 16083-16093.
115. Ivanov, K.I. and D.Y. Dimitrov, *Deactivation of an industrial iron-molybdate catalyst for methanol oxidation*. Catalysis Today, 2010. **154**(3-4): p. 250-255.
116. Andersson, A., M. Hernelind, and O. Augustsson, *A study of the ageing and deactivation phenomena occurring during operation of an iron molybdate catalyst in formaldehyde production*. Catalysis Today, 2006. **112**(1-4): p. 40-44.
117. Sun-Kou, M., et al., *Influence of the preparation method on the behaviour of Fe-Mo catalysts for the oxidation of methanol*. Journal of materials science, 1995. **30**(2): p. 496-503.
118. O'Brien, M.G., et al., *A combined multi-technique in situ approach used to probe the stability of iron molybdate catalysts during redox cycling*. Topics in Catalysis, 2009. **52**(10): p. 1400-1409.
119. Dazhuang, L., et al., *Kinetics of molybdenum loss from iron molybdate catalysts under nitrogen atmosphere*. Reaction Kinetics and Catalysis Letters, 1997. **62**(2): p. 347-352.
120. Wachs, I.E. and L.E. Briand, *In situ regeneration of metal-molybdate catalysts for methanol oxidation to formaldehyde*, 2000, Google Patents.
121. Routray, K. and I.E. Wachs, *Role of excess MoO₃ in iron-molybdate methanol oxidation catalysts*. Abstracts of Papers of the American Chemical Society, 2007. **233**.

Chapter 2: Experimental

Contents

1. Introduction.....	53
2. Catalyst Preparation	53
2.1. Fe_2O_3 and MoO_3	53
2.2. Iron Molybdates	55
2.3. Production of Core-Shell $\text{MoO}_x/\text{Fe}_2\text{O}_3$	56
2.4. Varying the Support of Molybdenum Based Catalysts.....	56
2.5. Reduction and Oxidation Process of Mixed Metal Catalysts.....	56
3. Catalytic Testing	57
3.1. Reactor Setup	57
3.2. Modes of operation	58
3.2.1. Temperature Programmed Desorption (TPD).....	58
3.2.2. Temperature Programmed Pulsed Flow Reaction (TPPFR)	60
3.2.3. Isothermal Pulsed Flow Reaction (IPFR)	63
3.3. Cracking Patterns	64
3.4. Methanol Uptake.....	66
3.5. Quadrupole Mass Spectrometry.....	67
3.5.1. Vacuum Pumps	68
3.5.2. Turbo Molecular Pumps.....	68
3.5.3. Gauges.....	70
3.6. Detectors	71
3.7. Quantification and Reproducibility.....	72
3.7.1. Blank Tube Reactivity	72
3.7.2. Reproducibility	73
4. Catalyst Characterisation	74
4.1. Raman Spectroscopy.....	74
4.1.1. Theory	74

4.1.2. Experimental	76
4.2. FTIR and DRIFTS	77
4.2.1. FTIR Theory	77
4.2.2. FTIR Experimental	78
4.2.4. DRIFTS Experimental	80
4.3. Powder X- Ray Diffraction (PXRD).....	80
4.3.1. Theory	80
4.3.2 Experimental	83
4.4. X-Ray Photoelectron Spectroscopy (XPS)	83
4.4.1. Theory	83
4.4.2. Experimental	85
4.5. BET Analysis	86
4.5.1. Theory	86
4.5.2. Experimental	88
4.6. Scanning Electron Microscopy (SEM)	88
4.6.1. Theory	88
4.6.2. Experimental	90
4.7. Transmission Electron Microscopy (TEM)	90
4.7.1. Theory	90
4.7.2 .Experimental	92
4.8. Energy Dispersive X-Ray Spectroscopy (EDX)	92
4.8.1. Theory	92
4.9. Synchrotron techniques.....	93
4.9.1. Theory	93
4.9.2. How is Synchrotron Light Generated?.....	94
4.9.3. Insertion Devices.....	95
4.9.4. At the Beamline	96
4.9.5. B18.....	97
4.9.5.1. Ion Chambers	99
4.9.6. XAFS: X-Ray Absorption Fine Structure	100
4.9.6.1. X-Ray Absorption process	100
4.9.6.2. Understanding EXAFS	104
4.9.6.3. XANES	108
4.9.7. Data Reduction.....	111
4.9.7.1. Fourier Transforms (FT)	111
4.9.8. IFEFIT	112

4.9.9. Preparing Your Sample (Solids)	112
4.9.10. Experimental	114
5. References	114

1. Introduction

The chapter herein details the preparation methods employed in catalyst synthesis, the processes used in testing for their activity and selectivity, and the characterisation techniques applied to provide phase identification and information on catalyst morphology. Detailed information regarding the theoretical and practical aspects will also be addressed. Table 1 outlines the solid materials purchased commercially from external suppliers. All materials were characterised prior to their use, to ensure they were fit for purpose.

Table 1. List of standard chemicals used and their suppliers.

Chemical	Supplier
MoO₃	BDH
(NH₄)₆Mo₇O₂₄.4H₂O	Sigma Aldrich
Fe₂O₃	Sigma Aldrich
Fe(NO₃)₃.9H₂O	Sigma Aldrich
γ -Al₂O₃	Alfa Aesar
SiC	Sigma Aldrich
Cellulose	Sigma Aldrich
Boron Nitride	Sigma Aldrich

2. Catalyst Preparation

A variety of synthesis techniques have been employed in catalyst preparation. Most commonly, bulk catalysts were prepared through co-precipitation, whilst core-shell catalysts were synthesised through incipient wetness. Other methods have also been trialled and tested, and will be detailed throughout the chapter.

2.1. Fe₂O₃ and MoO₃

Commercially available haematite (Fe₂O₃, Aldrich=99%) and molybdena (MoO₃, BDH= 99.5 %) were purchased as reference standards. Both catalysts have also been produced in-house in an attempt to create materials with improved catalytic properties. For Fe₂O₃, the synthesis procedures trialled were as follows:

(i) Fe₂O₃ was prepared through the drop wise addition of 50 ml Fe(NO₃)₃.9H₂O (Sigma Aldrich= 98%) to 100 ml of HNO₃ solution at pH 2, with stirring, at 60 °C. Water was evaporated from the orange solution under heating at 90 °C. The resultant dark orange/brown slurry was dried for 24 hours in the muffle furnace at 120 °C overnight, after

which it was calcined at 500 °C for 24 hours. Characterisation confirmed the material to be α -Fe₂O₃.

(ii) Fe₂O₃ was also produced through synthesis of a mixed metal FeMo oxide catalyst, in which the Fe amount dominated. A catalyst with a Mo:Fe ratio of 0.02:1 was produced through co-precipitation of molybdenum and iron precursors. 6.83 g of Fe(NO₃)₃·9H₂O was dissolved in 50 ml of water, and added drop wise to an acidified solution of (NH₄)₆Mo₇O₂₄·4H₂O (AHM) made from 0.06 g of AHM dissolved in 100 ml of acidified deionised water. The combined solution was heated to 90 °C to evaporate off any excess water, after which the catalyst was dried at 120 °C for 24 hours, followed by a calcination at 500 °C for 24 hours.

(iii) A final method was employed through collaboration with UCL. Fe₂O₃ nanoparticles possessing a high surface area of 75.76 m² g⁻¹ were synthesised by continuous hydrothermal flow synthesis (CHFS). For this, Fe(NO₃)₃·9H₂O (40 °C) was exposed under pressure to supercritical water (335 °C), inducing rapid precipitation and crystallisation of α -Fe₂O₃. Quenching inhibits nanoparticle growth following initial nucleation [1]. Unfortunately it was found that for this method, the surface area was shown to decrease to that of the commercial standard after calcination (See Table 2)

Table 2. Various catalysts and their surface areas, obtained through BET.

Catalyst	Surface Area / m ² g ⁻¹
Fe ₂ O ₃ commercial	21
Fe ₂ O ₃ method i)	8
Fe ₂ O ₃ method ii)	45
Fe ₂ O ₃ method iii)	21

MoO₃ synthesis has also been considered. MoO₃ inherently suffers from a low surface area [2], and there has been a great amount of interest in improving this in order to create a substantially more active catalyst. Several preparation routes [3-5] have been investigated in the literature, and some of the preparations attempted within the lab are detailed below.

(i) **Oxidation of MoO₂:** 0.5 g of MoO₂ was added to a small ceramic boat, to fit within the tube furnace (see setup Figure 1). The catalyst was heated at 500 °C for 4 hours under a continuous flow of compressed air.

(ii) **Acidification of AHM:** The required amount of AHM was added to 200 ml of deionised water under stirring. A 1:10 HNO₃:H₂O mix was added drop wise to the stirring solution to induce precipitation of MoO₃, which was seen to crash out as a white needle-like solid. This was left to dry on an evaporating dish overnight in air, after which it was dried at 120 °C for 24 hours, and calcined at 500 °C for a further 24 hours.

(iii) **Heating of AHM:** 1 g of AHM was added to a small ceramic boat, fitted within the tube furnace. The catalyst was heated to a range of calcination temperatures (100, 150, 200, 300, 400, 500 and 600 °C), each for 4 hours under a gentle flow of compressed air (See setup Figure 1).

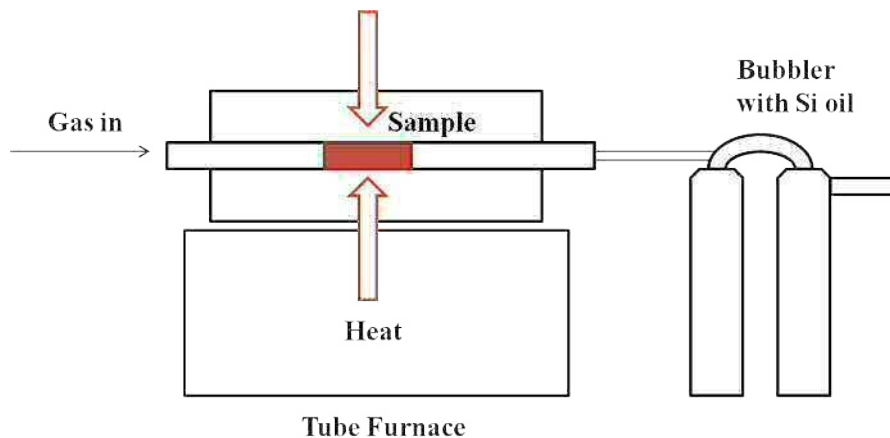


Figure 1. Tube furnace setup for the calcination procedures described. Gas enters at one end of the quartz sample tube. Gases can be passed over the sample bed which is held in place with quartz wool. A bubbler is in place after the bed, to ensure a flow of gas is maintained.

2.2. Iron Molybdates

Typically, bulk iron molybdates are synthesised via co-precipitation [6-8]. This includes the stoichiometric single phase $\text{Fe}_2(\text{MoO}_4)_3$, and those with an excess of molybdenum, yielding $\text{Fe}_2(\text{MoO}_4)_{3-x}\text{MoO}_3$. Initially Mo:Fe ratios of 1:1, 1.5:1, 1.7:1 and 2.2:1 were prepared. The co-precipitation procedure of these catalysts is as follows:

1. The required mass (Appendix A1) of $\text{Fe}(\text{NO}_3)_3 \cdot 9\text{H}_2\text{O}$ for the ratio of Mo:Fe required, was dissolved in 50 ml distilled H_2O in a 200 ml beaker. An orange solution formed.
2. The required amount of AHM, $(\text{NH}_4)_6\text{Mo}_7\text{O}_{24} \cdot 4\text{H}_2\text{O}$, was dissolved in 100 ml of distilled H_2O in a 60 ml beaker. A colourless solution formed.
3. A dilute solution of nitric acid (1:3 $\text{HNO}_3:\text{H}_2\text{O}$) was added drop wise to the molybdate solution until pH 2 was achieved.
4. The iron nitrate solution was added dropwise at room temperature into the acidified molybdate solution. Once dropping commenced, the temperature on the thermocouple was set to 60 °C. A canary yellow solution formed.
5. Once all the iron nitrate solution was added, the temperature was increased to 90 °C to evaporate off excess water to almost near dryness. The remaining yellow slurry was left to air dry on an evaporating dish overnight. A green solid formed.
6. The catalyst was dried at 120 °C in the muffle furnace for 24 hours.

7. After drying, a calcination was performed at 500 °C for 48 hours in both the muffle and tube furnaces. Calcinations have been performed in each of the furnaces, to compare the effects of the different calcination treatments on catalyst homogeneity. Heating gradients have been assessed in each case, to ensure that the thermocouples were accurately calibrated (Appendix A2)

There have been several modifications to this co-precipitation method. Details can be referred to in the experimental section of Chapter 3.

2.3. Production of Core-Shell MoO_x/Fe₂O₃

Core-shell structures of the type MoO_x/Fe₂O₃ were synthesised using incipient wetness impregnation. Commercial Fe₂O₃ (Sigma Aldrich, <50 nm) was first calcined at 500 °C for 3 hours, before adding the desired amount of AHM for 1, 3 or 6 MLs (monolayers) MoO_x/Fe₂O₃, dropwise under constant mixing. The samples were dried at 120 °C for 24 hours, after which they were calcined at 500 °C for 2 or 24 hours.

2.4. Varying the Support of Molybdenum Based Catalysts

Different supports have been trialled and tested for their ability in the selective oxidation of methanol to formaldehyde. Supports investigated included SiC (Sigma Aldrich) and Al₂O₃ (Alfa Aesar). Prior to doping with AHM, the point of incipient wetness was found for each material. This ensures an accurate calculation of the amount of molybdenum precursor to dose. The support was pre-treated for 3 hours in the muffle furnace, after which the desired amount of aqueous AHM for 1, 3 or 6 monolayers MoO_x was added drop wise to the support. The samples were dried at 120 °C for 24 hours, before being calcined at 500 °C for 24 hours.

2.5. Reduction and Oxidation Process of Mixed Metal Catalysts

Catalysts have been reduced under MeOH/He, using the small tube furnace described in Figure 1, fitted with a methanol bubbler prior to the sample bed. Approximately 1 g of catalyst was packed between two layers of quartz wool in the sample tube. A steady and continuous flow of He was passed through the methanol bubbler and subsequently over the catalyst bed. The furnace was ramped to 350 °C at a ramp rate of 10 °Cmin⁻¹, and the temperature held isothermally for 4 hours. Catalysts demonstrated a clear colour change to black upon reduction.

Catalyst re-oxidation was carried out in one of two ways. Firstly, catalysts were re-oxidised in the muffle furnace at 500 °C for 24 hours. Secondly, 0.5 g of catalyst was placed in the CATLAB microreactor (Figure 2), and held isothermally at 400 °C for 1 hour, under a flow of 10% O₂/He.

3. Catalytic Testing

All catalytic testing has been performed using the Hiden CATLAB, a catalyst characterisation and microreactor system. The reactor itself is able to mimic industrial processes on a smaller scale, in a rapid and simple way. Ultimately it provides information regarding catalyst activity, including conversion rates and selectivity under temperature programmed techniques.

Typical CATLAB experiments include TPD (temperature programmed desorption) and TPO/R (temperature programmed reduction/oxidation). The benefits of running these experiments using the CATLAB include the following:

- (i) Detection limits of the mass spectrometer (MS) show high sensitivity; within 0.1 to 1 ppm. The system is optimised for maximum mass spectrometer sensitivity.
- (ii) The MS is coupled to allow for synchronized measurement of temperature from the furnace, with detection of desorbing gases in the MS.
- (iii) An unlimited number of gases can be measured simultaneously.
- (iv) Data acquisition is fast.
- (v) Sample temperatures can be raised up to 1000 °C, with ramp rates between 1-20 °C.
- (vi) Accurate mass flow controllers allow for precise gas flow regulation.

3.1. Reactor Setup

Figure 2 demonstrates a simple schematic for the various components of the integrated Hiden system. The QGA mass spectrometer (RHS) is a compact bench top analysis system, enabled for continuous analysis of gases. The system includes a Hiden QIC inlet: a fast response inert sampling capillary which can provide less than 500 ms response times for most common gases and vapour. The unit is controlled directly from the PC controlled CATLAB software.

In addition to the mass spectrometer, the CATLAB system includes a standard gas manifold with four streams. Gas/vapour delivery options include an eight stream inlet. The eight flow channel interface allows for enhanced composition control for realistic simulation of process mixtures. The flow range is between 2-100 mlmin⁻¹, with a minimum supply pressure of 3 bar.

The CATLAB also comprises the microreactor (Figure 2 and Appendix A3) and the electronics cabinet. The electronics cabinet contains the temperature control unit to control

the furnace, and the gas control unit with the 4 way flow channel interface. The sample is contained within a quartz tube, approximately 0.5 cm in width. There is a hole at the bottom of the tube for gas flow, so the catalyst must be loaded onto a bed of quartz wool to prevent it falling through. This quartz tube is then inserted into the microreactor unit, in which it sits in a second quartz tube. The quartz microreactor is with low thermal mass, air cooled radiant furnace and close-couple QIC sampling. An in-bed thermocouple allows for temperature measurement, with a linear ramp control enabling set point regulation to 1000 °C for atmospheric pressure. The gases can be fed either over the catalyst bed, or can be shut off by switching to the by-pass configuration using the switching valve. Switching to the by-pass is particularly useful for establishing flow regimes and feed compositions, without exposure to the catalyst sample.

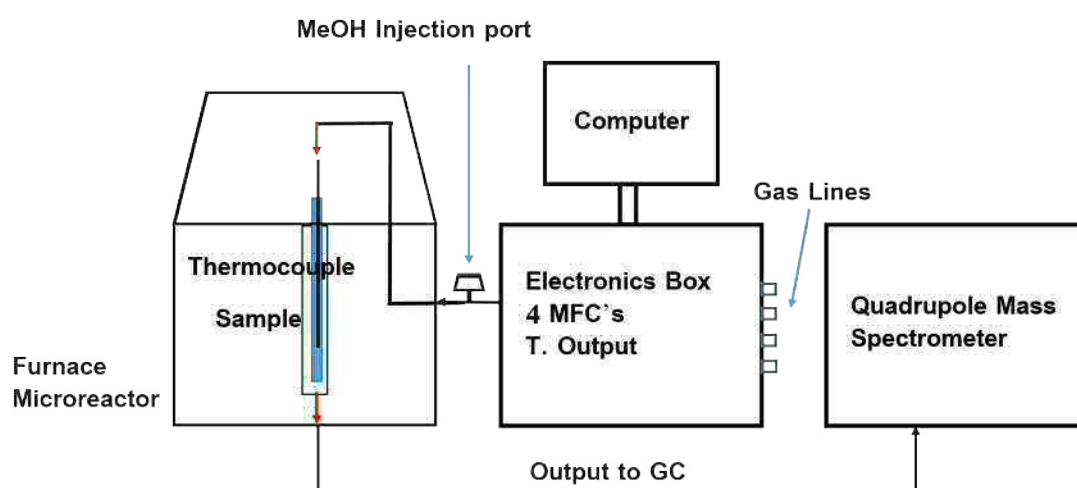


Figure 2. Schematic for the Hidden CATLAB microreactor. The reactor comprises of the furnace with sample loaded (left), MFC unit (middle), and the mass spectrometer (right).

See Appendix A3 for further details.

3.2. Modes of operation

Once prepared, all catalysts were subjected to catalytic testing, to analyse their selectivity and activity in the selective oxidation of methanol to formaldehyde. For the purpose of this work, two main operation modes were used: TPD (temperature programmed desorption) and TPPFR (temperature programmed pulsed flow reaction).

3.2.1. Temperature Programmed Desorption (TPD)

TPD is an extremely useful catalytic tool, used to probe the surface by identifying the strength, number and type of active sites on a catalyst [9, 10]. Other information obtainable

includes quantitative coverage and surface area, heats of adsorption, adsorption probabilities (dissociative versus non-dissociative), and the kinetics of adsorption/desorption mechanisms. The method itself is versatile and simple to operate, being able to analyse a range of materials.

For the purpose of this work, 1 μl injections of MeOH were dosed onto the catalyst, under ambient temperature in a flow of 30 ml min^{-1} of He. This was followed by ramping the temperature to 400 $^{\circ}\text{C}$ at a rate of 8 $^{\circ}\text{C min}^{-1}$, whilst monitoring the products formed by mass spectrometry. Desorption occurs when the adsorbate contains sufficient energy to overcome the activation energy of desorption from the surface. This allows the user to probe information between the active sites and the adsorbing gas, hence revealing crucial information regarding the kinetics of the desorption process.

Typical TPD spectra for MeOH desorption are plotted as in Figures 3-4:

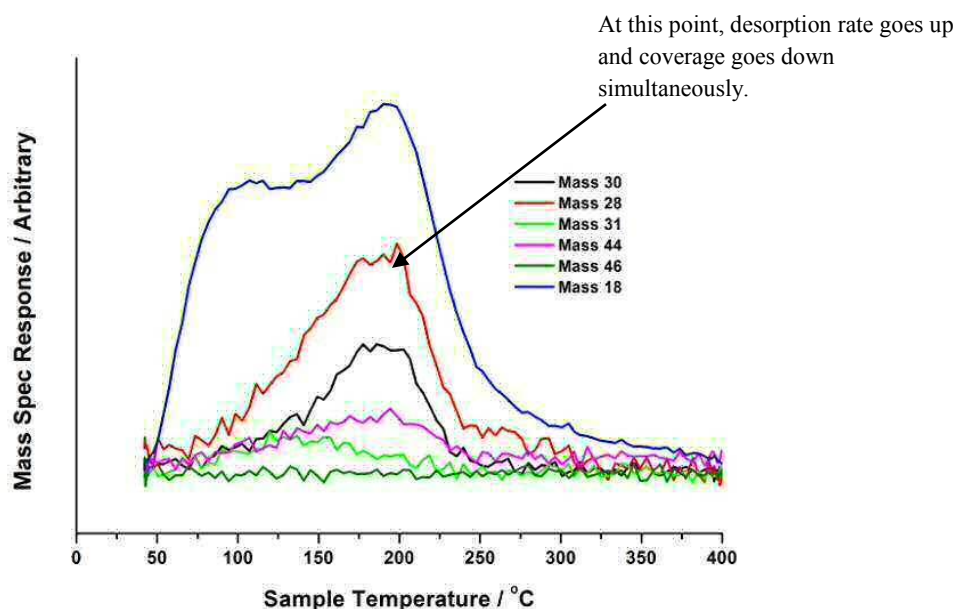


Figure 3. A typical TPD spectrum (raw data) after TPD in MeOH/He of $\text{Fe}_2(\text{MoO}_4)_3$ (Mo:Fe 1.5:1). Masses explained in Section 3.3.

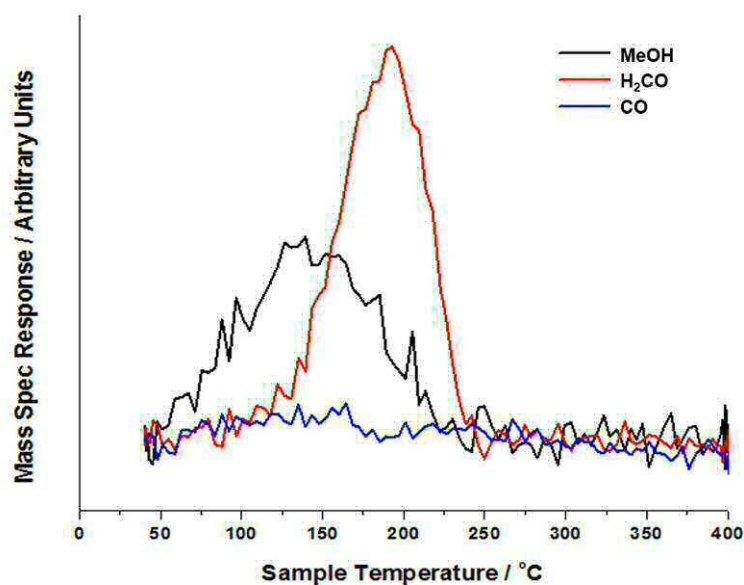


Figure 4. TPD of MeOH/He once processed (accounting for the mass subtraction of various cracking fragmentations and mass spectrometer sensitivity), for $\text{Fe}_2(\text{MoO}_4)_3$ (Mo:Fe 1.5:1).

3.2.2. Temperature Programmed Pulsed Flow Reaction (TPPFR)

TPPFR is a useful catalyst tool for identifying the light off point of a reaction, providing information on conversion, as well as selectivity. For the catalytic reaction, 1 μl of liquid MeOH was injected every 2 minutes into a flow of 10 % O_2/He , at a flow rate of 30 ml min^{-1} . During this time, the temperature of the catalyst bed was ramped linearly ($8\text{ }^\circ\text{C min}^{-1}$) to 400 $^\circ\text{C}$, whilst monitoring the products evolving at the mass spectrometer. Figure 5 demonstrates the raw data typically obtained from a TPPFR reaction. Data has been stacked for presentation purposes.

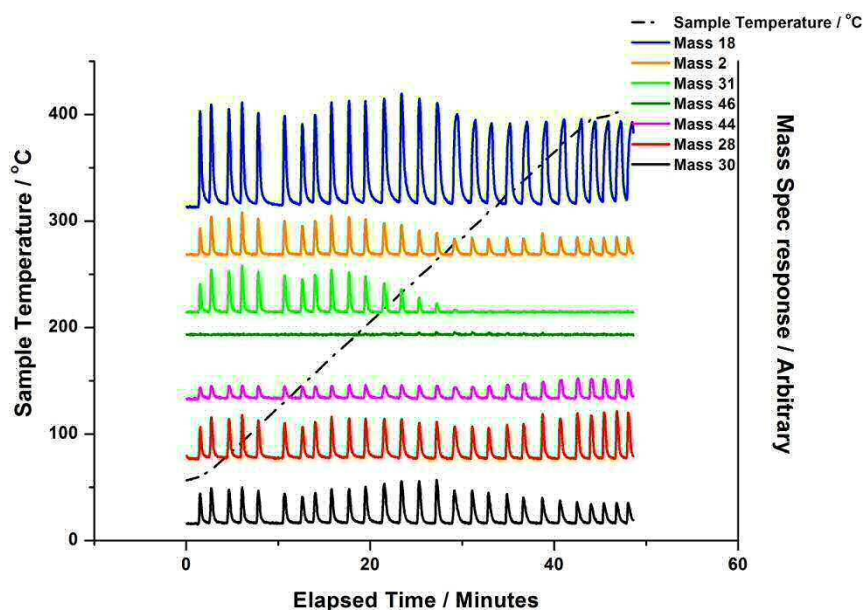


Figure 5. A typical TPPFR plot for 0.05 g of $\text{Fe}_2(\text{MoO}_4)_3$ (Mo:Fe 1.5:1) catalyst (raw data). 1 μL injections of MeOH were passed over the catalyst bed every 2 minutes whilst ramping the temperature of the catalyst bed to 400 °C. Masses are explained in Section 3.3.

Prior to running the reaction, several pulses of MeOH were applied at room temperature in the by-pass, to gage the degree of sensitivity of the reactor. This stage is run separately to the main reaction, as switching from by-pass to over the catalyst bed was found to create a disturbance in the gas flow when monitoring Mass 32 for oxygen. An important discovery of this by-pass stage, and also on referring to the TPD above (Figure 3), is that methanol oxidation is continually occurring on the tungsten oxide filament of the mass spectrometer. Mass 44 is not considered a fragmentation of MeOH (Section 3.3), however is shown to be present across the temperature range as a result of this oxidation on the filament.

Across the series of injections, certain trends and patterns occur, depending on the relative amounts of Mo and Fe in the catalyst. Common to all testing carried out, the first injection applied is always lower in intensity than subsequent injections. This is a consequence of methanol initially adsorbing over the catalyst surface. The temperature of the furnace was ramped with continual pulsing of methanol, whilst the masses required for analysis were detected through the mass spectrometry. Referring to Figure 6 for the 1.5:1 Mo:Fe catalyst, it is only after ~18 minutes, and having reached 210 °C, that methanol conversion begins. With a decrease in the methanol signal generated, a simultaneous increase in the formaldehyde signal, Mass 30, is observed. Measurement of the area under each peak allows for a

calculation of methanol conversion, with 50 % conversion reached within 23 minutes at 240 °C (Figure 6).

To calculate conversion, the following is applied:

- 1- The Mass 31 peaks are integrated, to provide the peak area.
- 2- Integrals are normalised.
- 3- The following is applied:

$$\text{Conversion} = (1 - (\text{normalised Mass 31}) * 100 \%)$$

Equation 1

A plot of conversion (from Equation 1) versus sample temperature can then be drawn (Figure 6).

To obtain information regarding the selectivity, the raw peak integrals for each mass must initially be attained, with integration carried out using the Origin 9.0 software installed with a peak analyser function. From the raw integrals, it is possible to gain an indication of the reaction process and the products forming.

To obtain the final selectivity plot (Figure 6) from the raw integrals, the contributions from various components to each mass must be removed. Masses to be removed are taken from the fragmentation patterns (See Table 2). For instance, in the case of CO, contributions from methanol and formaldehyde must be removed. Once all the integrals have been subtracted they are further adjusted to account for the sensitivity of the mass spectrometer.

The selectivity of the catalyst to each component can be calculated using the following:

$$\text{Selectivity}_{[\text{Mass } x]} = (S_{[\text{Mass } x]} / S_{\text{Products}}) * 100$$

Equation 2

Where $S_{[\text{Mass } x]}$ = Selectivity to Mass x, and S_{Products} = Selectivity to all other products.

With selectivity and conversion for each mass calculated at each of the injection points, the final plot can be obtained, as demonstrated in Figure. With a knowledge of both selectivity and conversion, % yield is achieved using the following equation (Equation 3):

$$\text{Yield} / \% = (\text{Conversion} (\%) \times \text{Selectivity} (\%)) / 100$$

Equation 3

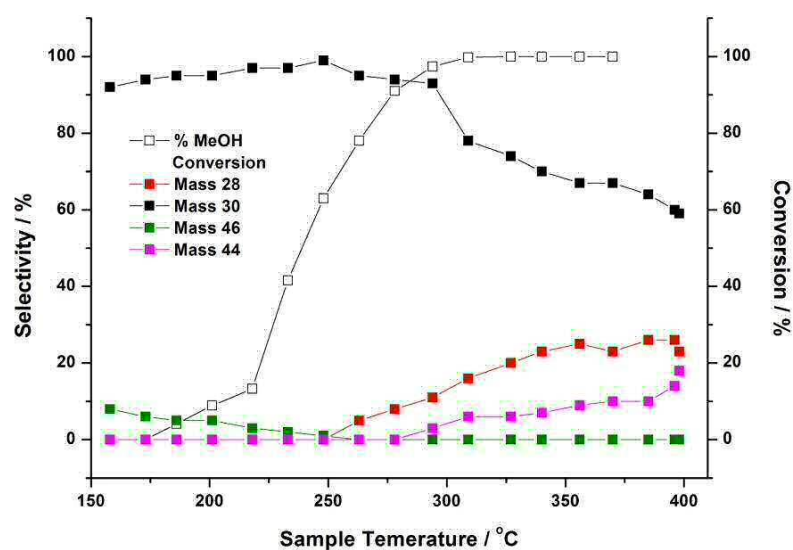


Figure 6. Plot of selectivity and conversion calculated for $\text{Fe}_2(\text{MoO}_4)_3$ (Mo:Fe 1.5:1). MeOH was pulsed over the catalyst in 10 % O_2/He , whilst monitoring the mass spectrometer response with an increase in temperature to 400 °C. Peak areas for each mass were integrated. Mass subtraction of various cracking fragmentations and mass spectrometer sensitivity were then accounted for to derive the final plot.

3.2.3. Isothermal Pulsed Flow Reaction (IPFR)

A final analysis mode to obtain information regarding catalyst reactivity, is the isothermal pulsed flow reaction (IPFR). This mode works similarly to TPPFR, except in this instance the catalyst bed is held isothermally at a specific temperature whilst dosing MeOH over the catalyst surface in 10 % O_2/He . An example is shown below in Figure 7.

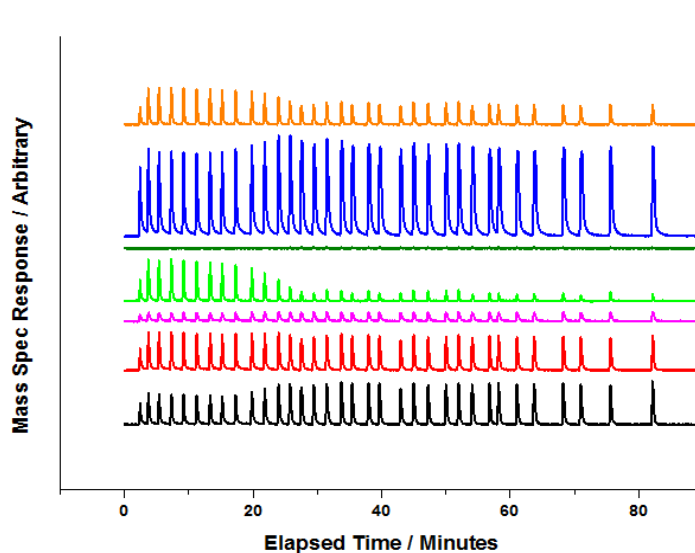


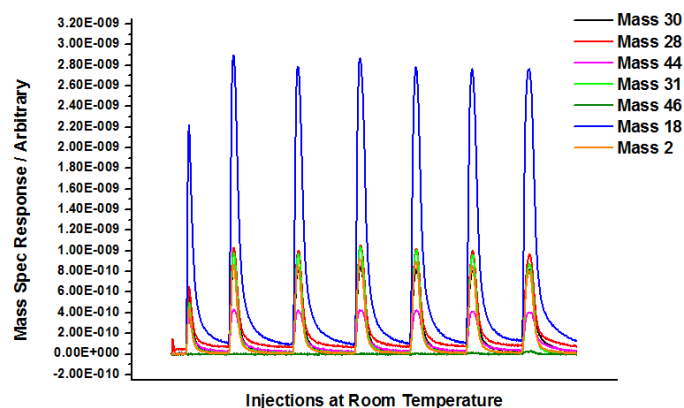
Figure 7. Pulse flow data for $\text{Fe}_2(\text{MoO}_4)_3$ Mo:Fe 1.7:1, in MeOH/ O_2 /He held isothermally at 350 °C. Fragmentation patterns: Orange= Mass 2 for H_2 , Blue= Mass 18 for Water, Dark Green= Mass 46 for DME, Pale Green= Mass 31 for MeOH, Pink= Mass 44 for CO_2 , Red= Mass 28 for CO, Black= Mass 30 for H_2CO .

3.3. Cracking Patterns

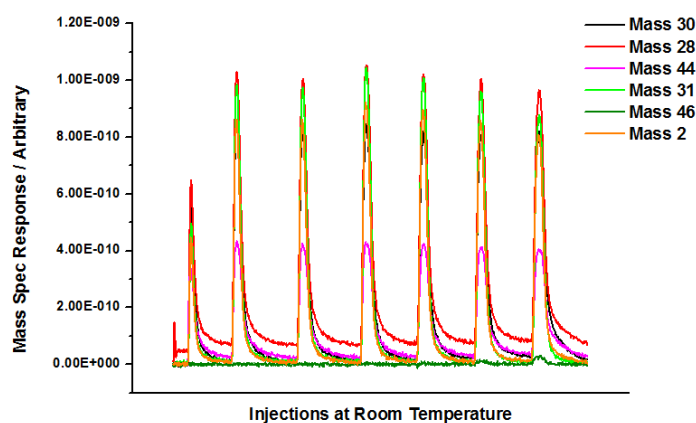
Table 2. Cracking fragmentation patterns for various molecules [11-13]. The cracking fragmentation pattern for MeOH can be referred to in Figures 8 (a-b), with injections taken at room temperature where no reaction is occurring.

Molecule	Cracking Fragments
Hydrogen	2, 1
Water	18, 17, 16, 19, 20
Dimethyl ether	45, 29, 15, 31, 43, 30, 28, 44, 42, 27
Methanol	31, 32, 29, 28, 30, 33, 27
Carbon dioxide	44, 16, 28, 12
Carbon monoxide	28, 12, 16, 29, 14, 30, 13
Formaldehyde	29, 30, 28, 31, 15, 27
Oxygen	32, 16

(a)



(b)



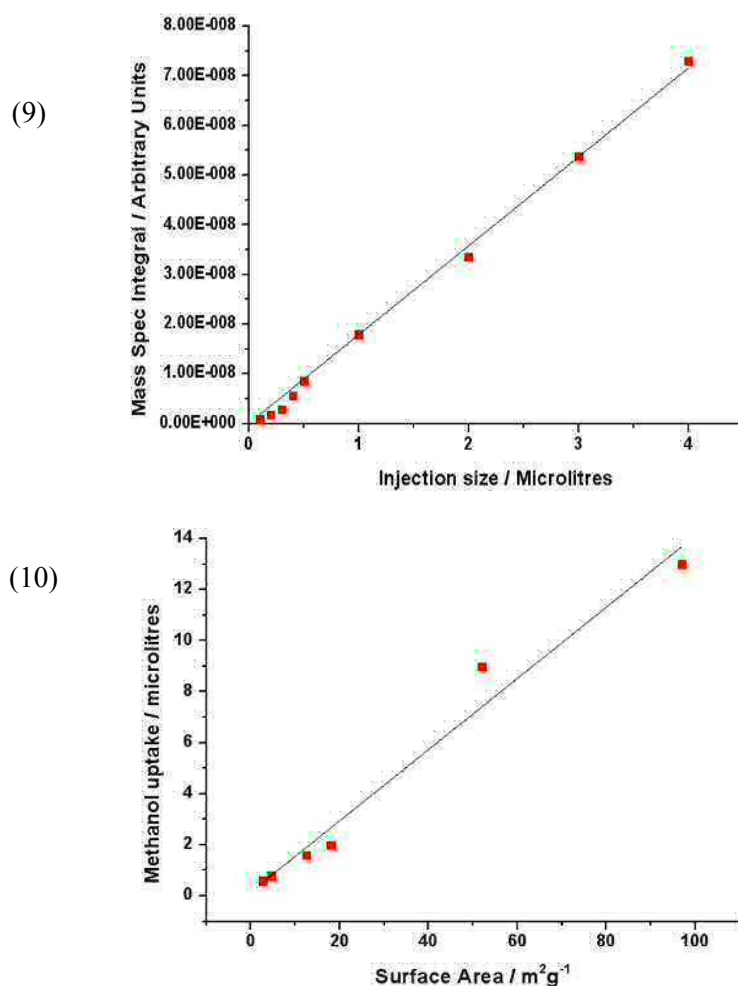
Figures 8(a-b). The cracking fragmentation pattern for MeOH, with injections taken at room temperature where no reaction is occurring.

Table 2 details the cracking fragmentation patterns for the molecules referred to throughout this work. It should be noted that these values are recorded using a magnetic sector mass spectrometer, which may vary slightly from the quadrupole mass spectrometer in our lab. Differences may occur, as a consequence of the change in filament used between the two spectrometers. The tungsten oxide filament adopted in the quadrupole mass spectrometer can essentially acts as a catalyst, delivering further oxidation products such as CO_2 from formaldehyde. In order to achieve a superior guide on the masses expected, calibrations were carried out regularly (six monthly), which also enables a gain in knowledge of the sensitivity of the mass spectrometer. The main masses monitored during methanol oxidation are given in Table 3.

Table 3. General masses plotted for TPD/TPPFR, with their corresponding assignments.

Mass Number / gmol^{-1}	Molecule
2	Hydrogen
16	Methane
18	Water
28	Carbon monoxide
30	Formaldehyde
44	Carbon dioxide
46	Dimethyl ether
31	Methanol

3.4. Methanol Uptake



Figures 9-10. Peak integral plotted against methanol injection size in a 30 mlmin^{-1} He flow (top), and methanol uptake against various catalysts of differing surface areas (bottom).

Methanol was injected with varying pulse sizes from $0.1\text{-}5 \mu\text{L}$ in a flow of 30 mlmin^{-1} of He. The area of the peaks obtained were integrated, and the average plotted against the

injection size. A linear plot was fitted, which passes through the origin (Figure 9). It is important to investigate injection size, to ensure that the injections made during the reaction are below the saturation point of the multiplier detector. If the injection size is too large, the straight line plot would begin to plateau. A further graph of surface area (taken from testing a range of different catalysts) against methanol uptake has been plotted, also showing linear character (Figure 10). The plot can be used to give an approximation of an unknown catalyst surface area, based upon the number of injections required for surface saturation of the catalyst with MeOH.

3.5. Quadrupole Mass Spectrometry

Mass spectrometry is a common analytical tool, used for identifying the amount and type of chemicals present in an unknown sample.

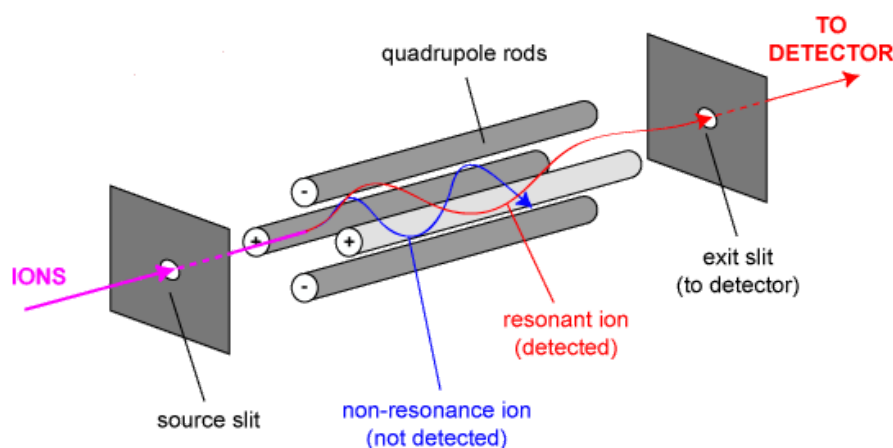


Figure 11. Schematic of a quadrupole mass spectrometer [14].

A quadrupole mass spectrometer is a mass analyser, which exploits the fact that ions can be separated according to their mass charge ratio. The basic principles of operation are as follows:

- (i) The analysed gas atoms are ionised to positive ions.
- (ii) The positive ions are accelerated so that they all reach the same K.E.
- (iii) Ions are deflected under a strong magnetic field according to their mass. Lighter ions characteristically deflect more, with the degree of deflection also dependant on the number of positive charges on the ion.
- (iv) The ions are detected.

Figure 11 represents a schematic for a quadrupole mass spectrometer. The spectrometer consists of four parallel metal cylindrical rods, fitted with a quadrupole, responsible for

filtering the sample ions by their mass/charge ratio [15]. Opposing metal rods are connected together electrically, and an RF voltage applied across each pair of rods to create an electric field. Positive ions created by the ion source are channelled through the quadrupole field, by use of focusing electrodes. The electric field is then alternated in order to produce the required potential for specific mass detection. Only ions of a certain mass:charge ratio will reach the detector for a given ratio of voltages, since their trajectory is stable enough to do so. Any other ions will collide with the rods in their trajectory. In this way, the quadrupole acts as a filter. High mass ions are more difficult to separate, since the oscillation amplitude of the applied field is greatest for these masses. As a result, the ions are more likely to collide with one of the metal rods causing their rejection.

The capabilities of the Hiden quadrupole mass spectrometer include the following:

- It has a 200 amu mass range, dual Faraday/Electron Multiplier detector, with a detection range from 100 % to 0.1 ppm.
- Scan speeds are achievable up to 100 amu/sec.
- Low dead volume.
- There is a heated inlet for fast response to vapours.

Quadrupole mass spectrometers (QMS) hold many advantages over GC (gas chromatography) or TCD (thermal conductivity detection). QMS is able to run continuous detection of components simultaneously, with uninterrupted quantification. Any leaks are easily detected. However, disadvantages include that the masses to be analysed must be submitted into the MID scan setup before running the experiment. The equipment itself is also very costly.

3.5.1. Vacuum Pumps

All mass spectrometers must be fitted with a good vacuum system, to ensure its proper function. This is to allow any ions produced in the ionisation chamber to have free path through without any collisions with air molecules. The pumping system in the vacuum is one of the key components, used to drive the vacuum down to $<10^{-7}$ mbar.

3.5.2. Turbo Molecular Pumps

A turbo molecular pump is a kinetic pump used to create ultra-high vacuums. The pump itself consists of a stack of rotors with blades or slots (Figures 12-13). Between the rotor

discs are fixed discs called stators, containing the same blades or slots as the rotors, but facing in the opposite direction. The blades rotate at 20000 rpm.

On colliding with the surface of these very high speed blades, gas molecules gain a significant amount of energy, enabling them to move towards the pump outlet after a certain length of time. They are able to move upwards due to the orientation of the blades. Once entering the outlet, the gas molecules are collected by the backing pump and exhausted to atmosphere (or lab vent line).

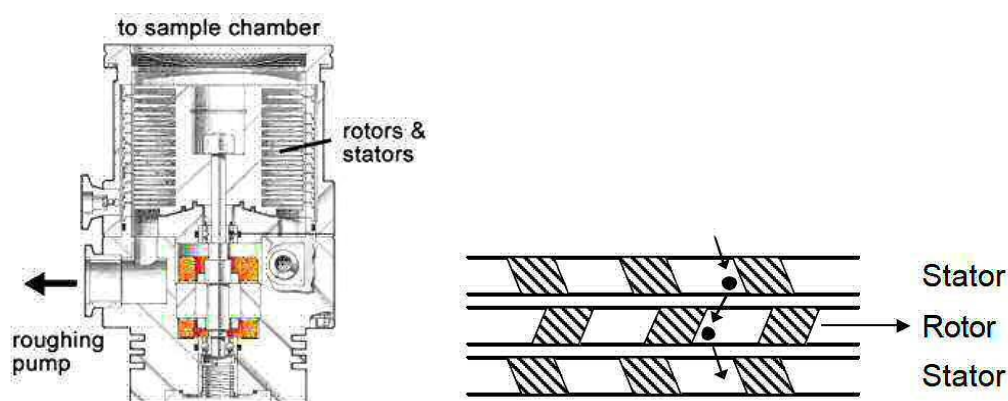


Figure 12-13. Turbo pump design (left) and path of gas molecules within a turbo pump (right) [16].

3.5.3 Rotary Pumps

Rotary pumps are responsible for ensuring a good vacuum for the turbo molecular pump, preventing it from being open to air. The rotary pumps consists of vanes mounted to a rotor, which rotates inside the main cavity being driven by an electric motor. The vanes maintain contact with the sides of the cavity walls as the pump rotates. This creates vane chambers which do the pumping work. Gas is drawn in, compressed, and then expelled through the exhaust valve. Figure 14 demonstrates a schematic for the inside of these pumps.

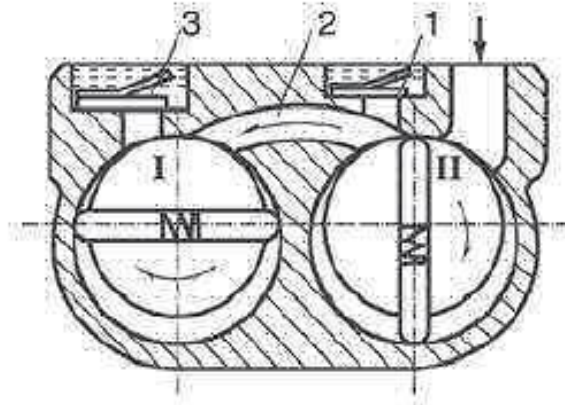


Figure 14. Schematic of a two stage rotary vane pump. 1= Senior exhaust valve, 2= Passage, 3= Low-level exhaust pipe [17].

The pumps used for the Hiden CATLAB work off a two stage design, with the exhaust from the first stage connected to the inlet of the second. With this design, the pumps can work together to improve the overall pressure of the pump, reducing any potential for back leakage where the rotor and stator fluid are sealed.

3.5.3. Gauges

There are two types of gauges used within the reactor system: the pirani gauge, and the ionisation gauge.

Pirani Gauges:

The pirani gauge is a thermal conductivity gauge, used for measuring the pressure under low vacuum range. The gauge consists of a metal filament connected to the vacuum system. From this filament, an electric circuit is able to take the pressure reading, measuring the resistance of the heated wire. Under atmospheric pressure, gas molecules collide with the filament, taking heat from the wire and removing it. On lowering the gas pressure in forming a vacuum, the number of gas molecules present will fall proportionally, inducing a slower heat loss from the filament wire. With an increased temperature of the wire, the resistance will increase. This heat loss is an indirect measurement of pressure, since the difference in resistance can be detected by the circuit, and a correlation to pressure made.

Ionisation Gauges:

The ionisation gauge is used to measure pressures below that recorded by the pirani gauge, achieving as low as 10^{-11} bar. The gauge itself consists of 3 major components: the filament, the grid, and the detector. Electrons are produced at the filament, which are attracted to the grid with its positive charge. The electrons circulate the grid, colliding with gas molecules to cause their ionisation. A negative ion collector attracts the positively charged gas molecules, which are also repelled from the positively charged grid (See Figure 15 for schematic). The number of ions colliding with the collector is directly proportional to the molecular density of the gas in the vacuum system. Therefore a measure of the ion current gives a reading of pressure.

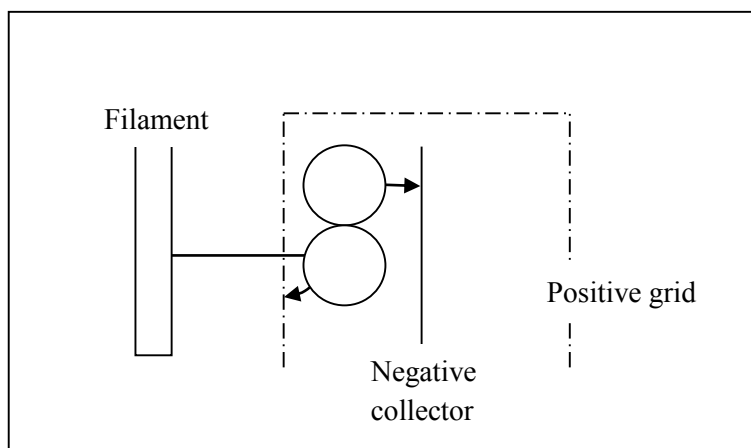


Figure 15. Schematic of an Ionisation gauge.

3.6. Detectors

Once separated by their mass to charge ratio, ions can be detected by one of two detectors which can be chosen in the file setup of the CATLAB software. These are the Faraday cup, and the secondary electron multiplier (SEM).

The Faraday cup was named after its inventor, Michael Faraday, post 1830 [18, 19]. The detector essentially acts as an ion collector and works as follows:

- (i) A metal conductive cup under vacuum is in place to catch charged particles deflected from the mass spectrometer. The ions transfer their charge to the cup.
- (ii) The resulting current is measured and used to determine the number of ions/electrons hitting the cup.

However, since the ions entering the cup often have an energy significantly higher than the threshold of the cup, this results in the production of secondary electrons, which can leave the cup. For this reason, for high mass or high charge/energy ions, a secondary

electron multiplier detector may be a more suitable choice for improved sensitivity and detection range.

An SEM detector is a vacuum contained structure, which multiplies incident charges through secondary electron emission. When ions hit a surface, it causes the electrons in the uppermost atom to be released. These are secondary electrons. The number released is dependent on many factors such as particle type, angle at which the ions hit the surface and energy of the surface. The process occurs as follows:

- (i) At the dynode (metal plate), incoming ions generate electrons on bombardment with the secondary emissive material. Typically 1 to 3 electrons are generated.
- (ii) On applying an electric potential, electrons accelerate through the electric field to the next dynode, where they release further electrons again by secondary emission, the number released dependent on the energy difference between dynodes.
- (iii) This can be repeated a number of times, as electrons deflect back and forth across the channel (made of semi-conductive glass). The process repeats until enough electrons have been emitted for a measurable current.
- (iv) A dead time is then allowed, to enable the tube walls to recover.

3.7. Quantification and Reproducibility

Regular calibration of scientific equipment is essential, in order to provide knowledge and evidence of how the instrument measures, and to provide meaningful and reliable results. Calibration allows for quantification of results. Also required is a reproducibility check at various time periods, to ensure that data is consistent, and to verify the accuracy of the equipment.

3.7.1. Blank Tube Reactivity

Under the CATLAB setup, samples are loaded into quartz capillaries, with a layer of wool at the bottom of the tube to prevent any loss of sample. To ensure that the capillaries and wool have no effect on the reaction itself, an experiment was conducted to check the reactivity of a blank tube loaded with the same amount of quartz wool used in measurements. Both TPD and pulse flow studies were performed. It was evidenced that the quartz tube showed zero reactivity towards methanol in either TPD or pulse flow studies, even to elevated temperatures of 400 °C. 0 % conversion of methanol is seen throughout (Appendix A4). The only products detected were from the reaction of methanol on the stainless steel tube and oxide filament of the mass spectrometer, being CO₂ and H₂O.

3.7.2. Reproducibility

At certain time intervals across the course of the PhD, the same catalyst has been tested in the CATLAB reactor by TPD and pulse flow studies, to ensure reproducibility and reliability. The time periods included: the initial reactor setup day, 6 months, 12 months, 18 months and 30 months. The catalyst tested was a bulk catalyst with a Mo:Fe ratio of 2.2:1. Comparing across the time period, specifically at 6 and 30 months, it can be seen that MeOH conversion is consistent throughout, except one slight anomaly at approximately 250 °C for 30 months (Figure 16). Both time periods demonstrate 50 % conversion of methanol at approximately 225 °C in pulse flow studies. At low conversions, the error between the selectivities are negligible, whilst at high conversion is accurate to +/-5 % at a given temperature (Also Figure 16). It would be expected that selectivity accuracy would improve with increasing conversion, since there will be more product to detect, meaning the data is further from the detection limits of the reactor. TPD profiles are well replicated, all revealing a 100 % selectivity to formaldehyde (Figures 17-18) at approximately 190 °C (the signal for CO₂, Mass 44, is a consequence of methanol oxidation on the mass spectrometer filament as discussed Section 3.2.2).

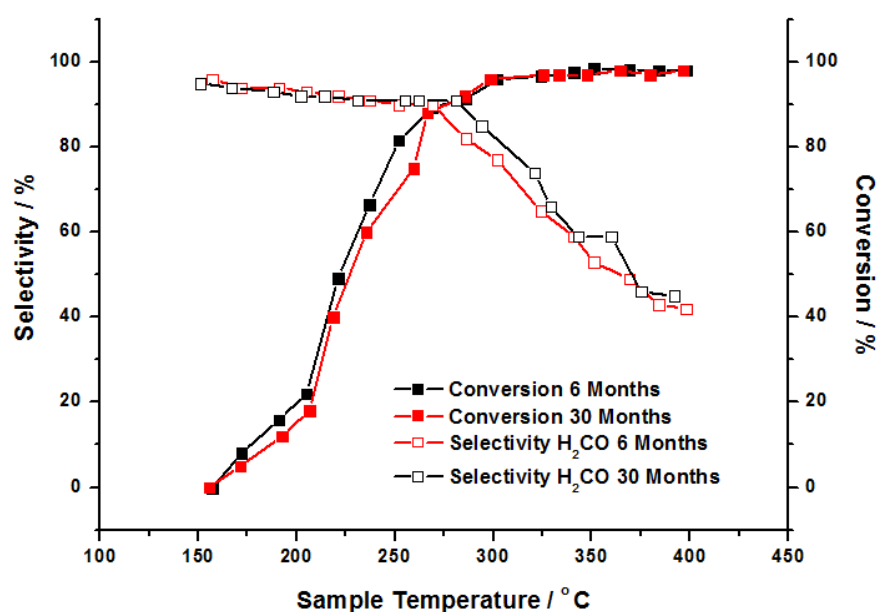
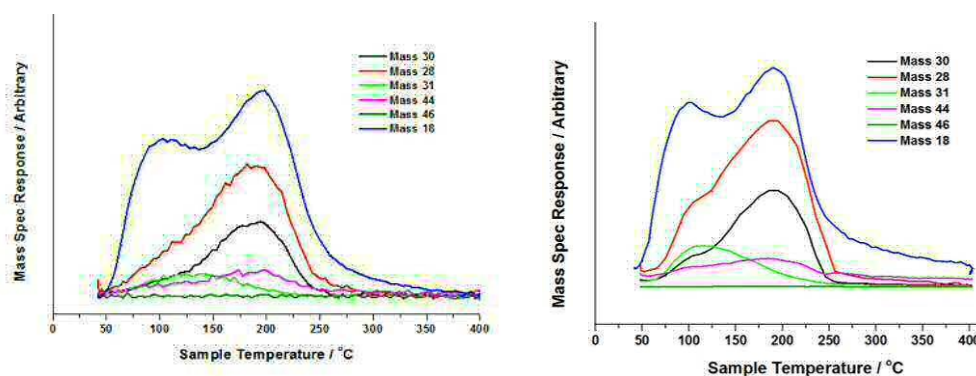


Figure 16. Comparison of selectivity and conversion data for 6 and 30 months for Fe₂(MoO₄)₃ (Mo:Fe ratio 2.2:1), achieved through TPPFR. The catalysts were subjected to MeOH pulsing in 10 % O₂/He, whilst ramping the temperature of the sample bed to 400 °C.



Figures 17-18. TPD of MeOH/He (raw data) for bulk $\text{Fe}_2(\text{MoO}_4)_3$ (Mo:Fe 2.2:1) after 6 months (left), and 30 months (right).

4. Catalyst Characterisation

Catalyst morphology and composition have been examined through a number of techniques. The theory and operation of these are detailed below.

4.1. Raman Spectroscopy

4.1.1. Theory

Raman spectroscopy is a vibrational spectroscopy, used for probing molecular motions. Based on inelastic scattering of monochromatic light, this means that the frequency of the incoming photons from a light source will change upon interaction with that molecule. The outgoing frequency of the re-emitted photons dictates the type of Raman effect observed, depending on whether we see an increase or decrease in the energy of these photons. The principles of Raman spectroscopy are highlighted in Figure 19.

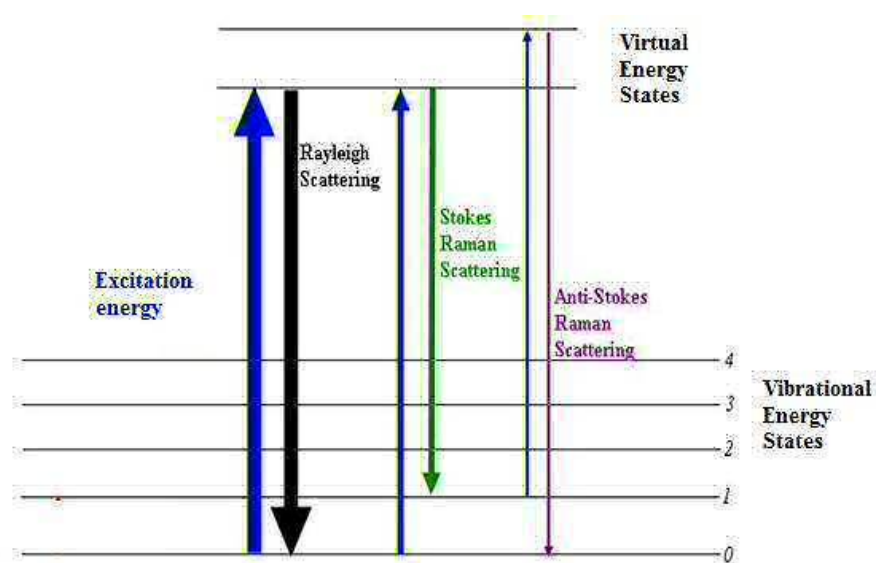


Figure 19. Energy level diagram showing the states involved in Raman signal.

In the majority of cases, the light scattered from a molecule is elastically scattered, resulting in zero net energy exchange between the photons and the molecule. This is referred to as Rayleigh scattering. However, when energy exchange does occur, one of the following is the outcome:

- (i) The molecule absorbs energy from the incoming photons, giving rise to Stokes radiation. The resulting photons are lower in energy. This generates a Stokes line, as shown in green (Figure 19).
- (ii) The molecule loses energy to the incoming photons, giving rise to anti-Stokes radiation. The resulting photons are higher in energy than the original frequency. An anti-Stokes line is generated, as shown in red (Figure 19).

Selection rules:

In order to be Raman active, a molecular vibration or rotation must cause a change in the polarizability component of that molecule.

For vibrational Raman, the gross selection rule states that there must be a change in the polarizability during the vibration. The selection rule (Equation 4) is written as:

$$\nu = \pm 1$$

Equation 4

Where ν = Vibrational Quantum Number.

For rotational Raman, as a molecule rotates, the polarizability presented to the E field changes. Even non-polar molecules such as O₂ or N₂ exhibit rotational Raman Spectra. The specific selection rule (Equation 5) is written as:

$$J = 0, \pm 2$$

Equation 5

Where J is the rotational quantum number. 0 = Rayleigh, -2 = anti-Stokes, +2 = Stokes

The main advantage of Raman is that a multitude of samples can be measured including solids, liquids and some gases. Further to this, different compounds in a mixture can be analysed. Peak intensities are able to provide quantitative information. Running the technique itself is relatively simple and quick, and since the technique is non-destructive under low laser power, samples may be reclaimed after measurement.

The disadvantages associated with this technique are that Raman cannot be used to analyse pure metals and their alloys, since here the Raman effect is negligible. Samples very dark in colour, or with low concentration, are also difficult to analyse. Finally, one of the fundamental problems of Raman, is its interference from fluorescence.

A Raman system itself consist of four major components (Figure 20):

1. A laser source
2. Sample illumination system
3. Wavelength filter- monochromator
4. Detector

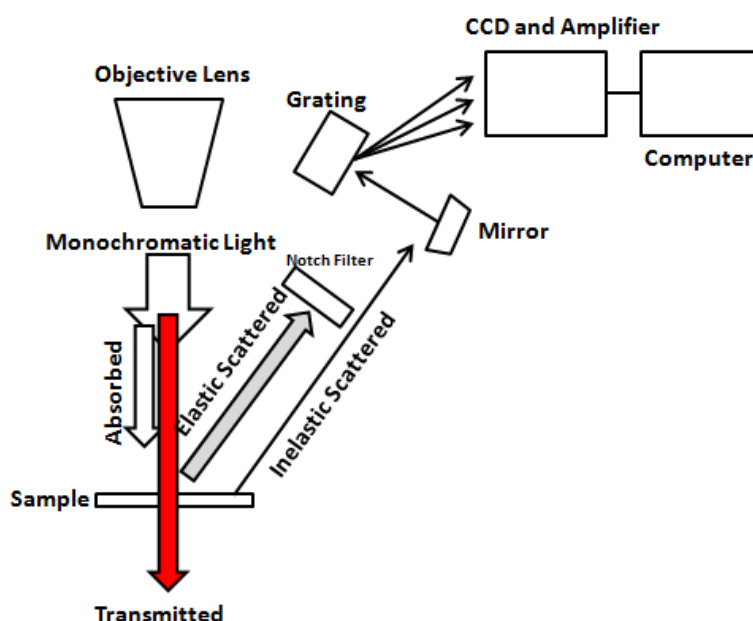


Figure 20. Schematic of the Raman Microscope setup. The sample is illuminated with a highly collimated monochromatic laser beam in the ultraviolet (UV), visible (Vis) or near infrared (NIR) range. The majority of the light undergoes Rayleigh scattering. However, approximately 1 in 10^{11} photons will undergo inelastic scattering. The oscillating electromagnetic field of the incoming photon creates a dipole moment in the targeted molecule's bond. Scattered light is collected with a lens and sent through an interference filter or spectrophotometer, to obtain a Raman spectrum of a sample.

4.1.2. Experimental

Data was recorded using a Renishaw inVia Ramanscope. The basic procedure of operation involved the following;

- (i) Approximately 0.1 g of sample was mounted onto the sample stage.

- (ii) A laser was focussed onto the sample using a camera linked to the software on the computer.
- (iii) Spectra were recorded using the 830 nm wavelength laser. Typically, a laser power of 0.1 % was used, taking 4 accumulations at each selected point. Maps could also be created to examine a collection of points over a set area.
- (iv) For each sample, spectra were recorded in different areas of the sample, to ensure results were representative of the whole sample.

Before each use, the Raman spectrometer was checked using a silicon standard, with a static run centred at 520 cm^{-1} .

4.2. FTIR and DRIFTS

4.2.1. FTIR Theory

The infrared region of the electromagnetic spectrum is that between the visible and microwave range. IR spectroscopy is a commonly used lab based technique, enabling identification of functional groups within compounds, both organic and inorganic. The energy from IR radiation is unable to cause electron excitation as it would with UV, but may induce rotational changes or vibrational excitation of covalently bonded atoms and groups. The success of the technique derives from the fact that compounds absorb at a certain frequency, characteristic of their structure. The frequency of the absorbed radiation will be equal to that of the transition energy of the bond or group under vibration/rotation. As a result, IR spectroscopy is successful in determining the functional groups within a sample. On obtaining IR data, the spectrum can be compared to a library database in order to identify the structure. Each molecule will have its own unique fingerprint.

In order to be IR active, selection rules state that vibrations or rotations within a molecule must cause a net change in the dipole moment of the molecule [20]. Incoming radiation with an alternating electric field will interact with the fluctuating dipole moment of the concerned molecule. Radiation absorption occurs when the frequency of the incoming radiation matches that of the vibrational frequency of the molecule, causing a change in the amplitude of the molecular vibration [21].

There are two types of molecular vibrations: stretching and bending. Molecules can vibrate by several different vibrational states. For molecules containing N atoms, linear molecules will achieve $3N-5$ degrees of vibrational modes. Non-linear molecules will

demonstrate 3N-6 degrees of vibrational degrees of freedom. This accounts for the multiple peaks observed for each molecule.

IR spectroscopy holds many advantages. Firstly, the experiment itself is quick and simple to execute, with data analysis relatively straight forward. It works for a wide variety of different samples, and detects strongly in cases where for example, Raman may not be applicable. The experiments undergo with high scan speeds, high sensitivity, and high resolution. However there are a number of disadvantages associated with the technique, such that many compounds are not IR active, meaning they are undetectable. Also if the sample contains a large proportion of water, this makes analysis a problem, since the hydroxyl radicals interfere with the measurement.

A range of IR spectroscopies are available, with the most commonly used being transmission mode. Here, incoming infrared radiation is passed through a sample, whilst the frequency of resonant absorption of IR-active modes is detected. The sample must be transparent to IR radiation above 1000 cm^{-1} , so not to obscure diagnostic absorption bands. In addition to this, the sample must be used in pellet form, which can induce distortions within the sample. When transmission IR is not applicable, reflectance IR spectroscopy is often adopted. Attenuated total reflectance (ATR) IR spectroscopy is used to obtain the IR spectrum for samples which are too strongly absorbing. The angle of incidence of the incoming IR radiation onto the surface is required to exceed the critical angle in order for total internal reflectance to occur [22]. When the sample begins to absorb radiation, the change in intensity of the reflected light gives rise to an absorption spectrum.

4.2.2. FTIR Experimental

IR data were recorded using a Spectrometer fitted with an ATR accessory, recording in the range of $500\text{--}2500\text{ cm}^{-1}$. Prior to analysis, a background was run. Approximately 0.1 g of sample was placed on the sample stage crystal, and the ATR accessory wound down in order to touch the top of the sample. The spectra was obtained, to provide a plot against either % absorption or transmittance.

4.2.3 DRIFTS (Diffuse Reflectance Infrared Fourier Transform Spectroscopy)

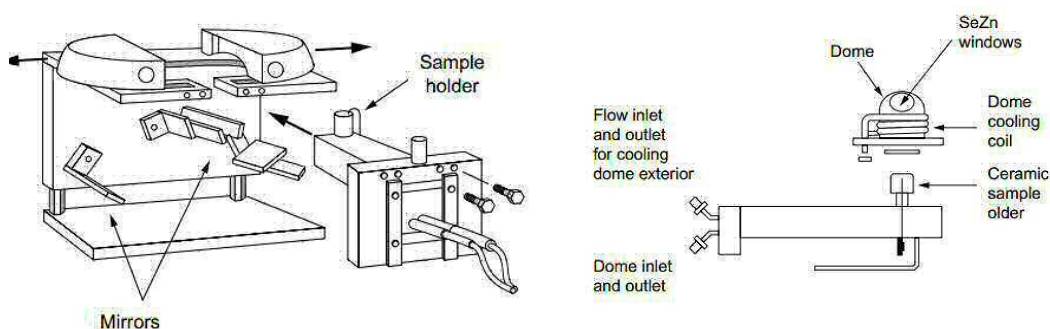
Theory

DRIFTS is a surface localized FTIR spectroscopy. It is an invaluable analysis tool, used for investigating the chemical and physical structures of materials. It is particularly useful for *in situ* analysis, and for the study of non-transparent materials [23, 24]. The main

difference between DRIFTS and traditional transmission IR, is the way in which the IR radiation is monitored. In transmission IR, the absorbance of IR radiation passing *through* the sample is monitored, whilst in DRIFTS the radiation is *incident*, at a fixed low angle, relative to the surface.

In general, when radiation is impacted onto a surface, many processes can occur: including absorption, specular reflection, internal reflection or diffusion in many directions. DRIFTS exploits the radiation which is diffused in all directions; the part of the beam that is scattered within a sample and returned to the surface. When incident light strikes a surface, the light that penetrates is reflected in all directions. The back reflected, diffusely scattered light is collected by the accessory and directed to the detector optics. As the light that leaves the surface has passed through a thin layer of the reflecting material, its wavelength content becomes modified, due to the optical properties of the matrix. As a result, the wavelength and the intensity distribution of the reflected light will contain structural information on the substrate. The specular reflectance component in diffuse reflectance spectra causes changes in band shapes, their relative intensity, and can also cause complete band inversion.

DRIFTS is much more sensitive to the surface species than a traditional transmission experiment would be. Due to grazing angle of the incoming radiation, the relative contribution of the surface to the overall spectrum is far greater than in FTIR [23]. Since the surface is generally considered the most crucial component contributing towards catalyst activity, the use of DRIFTS can be fundamental in learning more about the catalyst.



Figures 21-22. DRIFTS setup (left) and dome and sample holder (right) [25].

Figures 21-22 display the apparatus for the aforementioned DRIFTS technique. The infrared beam is focused onto the surface, using a series of mirrors. Diffuse radiation from the sample is then directed to the detector through use of further mirrors.

With the setup as mentioned, the DRIFTS system can be fitted with a high temperature and pressure cell for acquiring *in situ* measurements. This sample holder is comprised of a ceramic crucible, containing a resistor and a thermocouple. The holder is then placed inside the dome (Figure 22). In order to withstand the high temperatures applied, the windows of this dome are comprised from Se_2Zn , a highly thermally stable material which can withstand temperatures of up to 200 °C, whilst also not causing any interference to the beam. To remove heat, the dome is fitted with a coil system through which cooled nitrogen gas flows. Inlets and outlets are able to send gas to and from the sample, with the flow of gases from bottom to top, which allows for thermostatic control of the gases.

Using DRIFTS offers a range of advantages. Firstly, samples require little preparation, being performed on solid powders, to maximise radiation scattering. In addition to this, samples with no transparency and irregular surfaces can be analysed. Furthermore, DRIFTS can be coupled with other spectroscopic techniques such as XAS, to reveal additional information during catalyst preparation and reaction [26].

4.2.4. DRIFTS Experimental

The spectrometer used was a Carey 680 FTIR Spectrometer, with praying mantis optics and a Harrick high temperature DRIFTS cell, fitted with ZnSe FTIR windows. Spectra were collected with a DTGS detector every 90 s, as the temperature was increased to a maximum of 600 °C at a ramp of 10 °Cmin⁻¹. Spectra were collected at a resolution of 4 cm⁻¹, taking 64 scans per spectrum.

4.3. Powder X- Ray Diffraction (PXRD)

4.3.1. Theory

Powder X-ray diffraction is a non-destructive analytical technique, providing crucial information regarding a samples crystallographic structure. This includes the atomic spacing of the material, the crystal structure, size, shape and internal stress within small crystalline regions. Approximately 95 % of materials are crystalline in nature, so upon interaction with X-rays, a diffraction pattern can be obtained. The technique involves taking a powder and illuminating it with X-rays of a specific wavelength, which will be relative to the repeat structure within the material. A goniometer is in place to measure the intensity of the reflected radiation.

The Principles:

In XRD, the atomic planes of a crystal cause an incident beam of X-rays to interfere with one another upon leaving the crystal. The diffracted radiation is very intense, occurring in certain directions. These directions correspond to constructive interference (in phase coherent scattering) from waves reflected from the layers of the crystal.

The Bragg Equation:

Bragg's Law gives the conditions required for constructive interference to occur (Equation 6).

$$n\lambda = 2d_{hkl}\sin\theta$$

Equation 6

Where n = An integer, λ = Incident wavelength, d_{hkl} = Atomic plane spacing of the planes (hkl), θ = Angle between the incident radiation and the scattering planes.

The law relates the wavelength of electromagnetic radiation, to the diffraction angle and the lattice spacing in a crystalline sample (Figure 23). Diffraction occurs when Bragg's Law is satisfied, and the centers in a periodic array scatter radiation coherently to give constructive interference at specific angles. Using Figure 23, the beam diffracted from the lower surface travels further than that from the upper surface. When the path difference is equal to some integral multiple of the wavelength, constructive interference ensues.

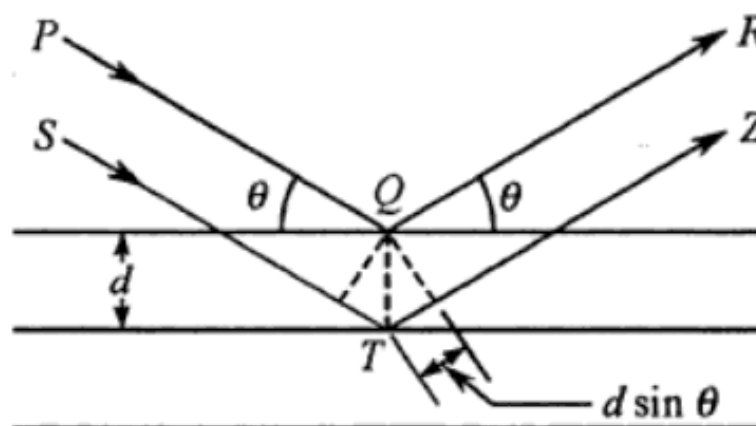


Figure 23. Principles of XRD, Bragg's Reflections [27].

In order to create X-Rays for the technique, electrons sourced from a hot tungsten filament are bombarded at a metal target such as Cu, Al, Mo or Mg through applying a voltage. When electrons have sufficient energy to eject the inner shell electrons of the target metal, X-rays are produced. Once generated, the X-rays are collimated and directed towards the sample (Figure 24). As the sample and detector are rotated, the intensity of the reflected X-rays are recorded. When the geometry of the incident X-rays colliding with the sample satisfies the Bragg Equation, constructive interference occurs and a peak is detected. The sample will be scanned through a range of 2θ angles, to determine all possible diffraction directions of the sample. Diffracted X-rays will be detected using a photographic film, and subsequently processed and counted. The diffraction peaks are converted to d- spacings to enable identification of the sample. The positions of these reflections tell the user information regarding the inter-layer spacings of atoms in the crystal structure, through use of Bragg's Law. Peak intensities provide information about how much X-ray scattering is contributing to that reflection, which ultimately gives an indication of how much of a particular phase is present within a sample.

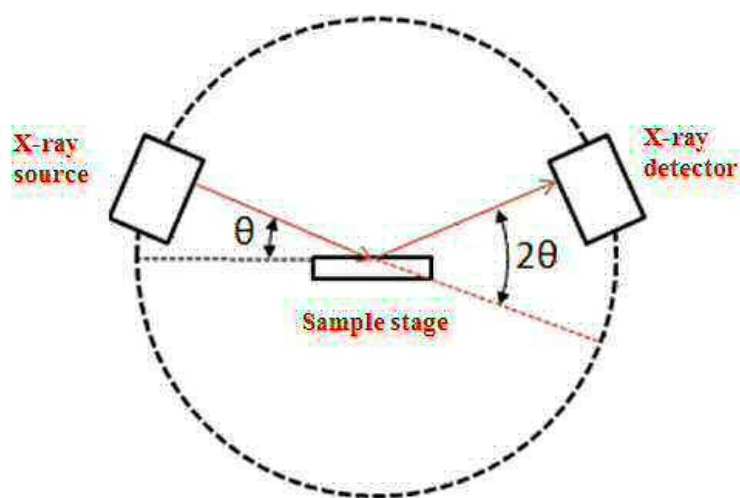


Figure 24. XRD instrumentation schematic.

XRD has been used for several applications. The primary uses include:

- (i) Determining the orientation of a single crystal or grain.
- (ii) Finding the crystal structure of an unknown material.
- (iii) Measuring the size and shape of small crystalline area. The diffraction lines broaden on decreasing particle size. This broadening can be used to give an estimate of the particle size, by measuring the FWHM value of the peak after a background has been subtracted and a

Gaussian peak fitted. Using the FWHM value, the average particle size can be estimated using the Scherrer equation.

(iv) Measuring the thickness of thin films.

(v) To determine atomic arrangement. The technique is able to detect to a limit of 3 % in a two phase mixture under a lab based setup. Quantitative phase analysis is possible, in addition to phase composition identification.

Advantages of XRD include that it is powerful and rapid, requiring minimal sample preparation. The interpretation of the outputted data is relatively simple, with XRD units widely available. However to exploit the technique, a standard reference must be accessible. In addition, for samples with more than one phase, the detection limit is approximately 2 w/t % of the sample, and problems can occur with peak overlaying. It is best if the sample is homogeneous.

4.3.2 Experimental

XRD was performed using a Rigaku SmartLab X-Ray Diffractometer fitted with a hemispherical analyser. The conditions employed were Cu K α radiation with a voltage of 40 kV, and a current of 30 mA. The diffractometer incorporates a 9 kW rotating anode for high intensity X-Ray generation. XRD was applied after preparation, reduction, and oxidation of various catalysts. The spectra obtained were compared to a reference library, to identify the phases formed after these processes. To ensure accurate and reliable results, the spectrometer was calibrated periodically using silicon.

The XRD equipment mentioned contains an autosampler, which allows for 6 samples per run. Catalysts were loaded into the aluminium sample holders. Approximately 0.5 g of sample was poured into the holder, and the sample flattened using a glass slide to give a flat and uniform surface. The holders were placed onto the sample rack, and fastened through a magnetic catch. The door to the XRD was closed and the measurement file setup, including the sample ID, scan speed, step size and scan range. Typically, scans were in the range of 0-80° 2 θ .

4.4. X-Ray Photoelectron Spectroscopy (XPS)

4.4.1. Theory

XPS is a semi-quantitative, highly sensitive surface technique, which uses X-rays to eject electrons from inner-shell orbitals. It typically uses soft X-rays with a photon energy of 200-2000 eV, to examine core-levels electrons. The technique is based on the photoelectric effect (Figure 25) discovered by Einstein in 1905 [28]. Here, electrons are emitted from the

surface of a material as a consequence of the adsorption of energy from electromagnetic radiation such as visible or UV light. The ejected electrons are referred to as photoelectrons. For XPS, Al Alpha or Mg Alpha are commonly the photon energies of choice. Due to the short range of photoelectrons excited from the surface, XPS is considered a highly surface specific technique. Once the photoelectrons leave the sample, their energy is calculated using a concentric hemispherical analyser. The kinetic energy, E_k , of the photoelectrons is determined by the energy of the X-ray radiation, $h\nu$, and the electron binding energy, E_B (Equation 7).

$$E_k = h\nu - E_B - \Phi_s$$

Equation 7

E_B = Binding energy of the atomic orbital from which the electron originates,
 $h\nu$ = Characteristic energy of the X-ray photon (Al or Mg). E_k = Binding energy of ejected photoelectron and Φ_s = Spectrometer work function, specific to each instrument.

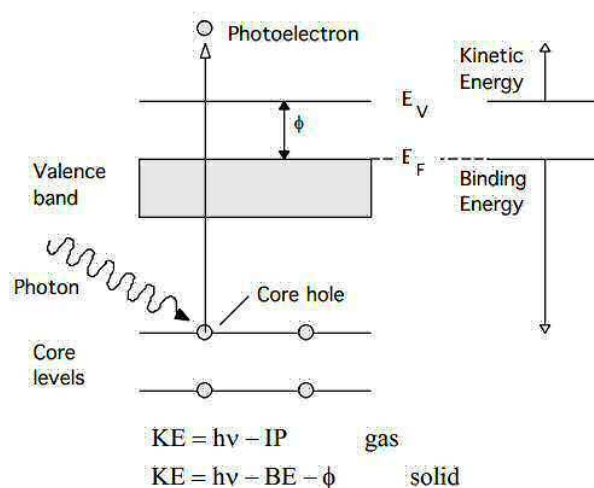


Figure 25. Schematic of the photoelectric effect, as discovered by Einstein.

On determining the energy of the photoelectrons, a spectrum of photoelectron peaks are produced. The binding energies of the peaks are used to characterise the elements present within the sample, whilst the peak areas provide information regarding the composition of the materials surface. Binding energy (B.E) represents the strength of interaction between the electron (n, l, m, s) and the nuclear charge, with each elements orbital unique and dependent on its bonding environment. Therefore, the B.E can act as ‘fingerprint’ for identifying elements and chemical compounds.

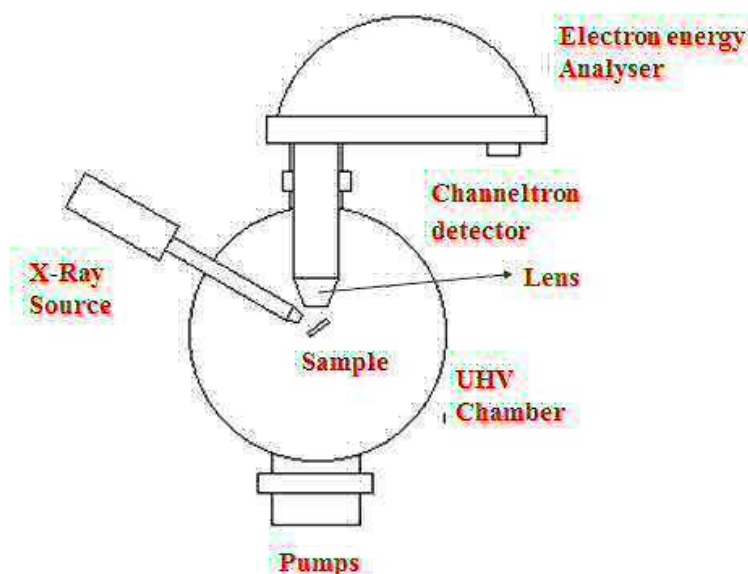


Figure 26. Schematic of an XPS analyser. Typically an XPS will consist of a source of X-rays, an ultra-high vacuum, an electron collection lens, an electron energy analyser, an electron detector system, a sample mount, a sample stage and a set of stage manipulators.

During XPS analysis the following occurs (Refer to Figure 26):

- (i) Low energy X-rays (10 keV) are produced by firing electrons from the electron gun at an aluminium target. The target is aimed at a quartz crystal which creates a monochromatic beam focused to a fine point on the samples surface.
- (ii) Upon hitting the sample surface, the sample electrons become excited. With enough energy (i.e. the B.E < X-ray energy), the electrons will leave the atom. The majority of electrons will be re-absorbed by the sample, however those nearer the surface (typically 10-100 Å), are able to leave.
- (iii) Electrons are detected by the electron detector. By placing a negative charge on the outside to repel the electrons, and a positive charge on the inner plate to attract the electrons, the potential difference between these two plates will only allow photoelectrons of a specific voltage to reach the hemispherical analyser. Electrons with insufficient energy will collide with the inner plate, with only electrons of a known voltage producing a signal at the detector. The energy range can be changed systematically, and the XPS spectrum produced with a plot against the binding energy of the photoelectrons.

4.4.2. Experimental

XPS spectra were obtained with thanks to David Morgan at Cardiff University, using an ESCALAB 220 spectrometer equipped with AlK α and MgK α sources, and fitted with a fast

entry lock for easy sample loading. AlK α (1486.6 eV) irradiation was used, to prevent Fe Auger peaks overlapping with the Fe 2p $_{1/2}$ and Fe 2p $_{3/2}$ peaks.

4.5. BET Analysis

4.5.1. Theory

Adsorption is defined as the adhesion of atoms or molecules of gas to a surface. The amount of gas adsorbed depends on the exposed surface area, but furthermore on the temperature, gas pressure and strength of interaction between the gas and solid.

The surface area of a catalyst is an important factor in determining the activity of the catalyst. BET refers to the Brauner, Emmett and Teller technique used to measure the specific surface area of a material, based on adsorption of gas on a surface [29]. The amount of gas adsorbed at a given pressure allows scientists to determine the surface area, with larger surfaces providing more space for reagents to adsorb and hence react. Units are expressed in m²g⁻¹.

The BET concept is an extension of the Langmuir theory, which is the theory for monolayer molecular adsorption. Langmuir discovered a dependence between the surface coverage of an adsorbed gas, and the pressure of the gas above the surface (at constant temperature). This would only satisfy monolayer adsorption, so work of Brauner, Emmett and Teller [30] extended from this to allow for multilayer adsorption. In this way, the isotherm will no longer plateau at higher coverages, and will rise indefinitely as pressure is increased. There is no limit on the amount of material that may adsorb when multilayer adsorption can occur. Therefore multilayer adsorption differs from monolayer quite significantly.

The BET equation can be expressed as Equation 8:

$$\frac{v}{v_m} \frac{P}{P_0 - P} = \frac{c}{1 + c} + \frac{c - 1}{1 + c} \left(\frac{P}{P_0} \right)^2 \quad \text{Equation 8}$$

Where, P and P₀ are the equilibrium and the saturation pressure of adsorbates at the temperature of adsorption, v = The adsorbed gas quantity, v_m = The quantity of the monolayer adsorbed gas, and c = BET constant.

Where, $c = \exp \frac{E_1 - E_2}{RT}$

Equation 9

E_1 = Heat of adsorption for the first monolayer, and E_2 = heat of adsorption for the second and subsequent layers.

The BET equation shown above is an adsorption isotherm, giving a straight line BET plot as shown below (Figure 27):

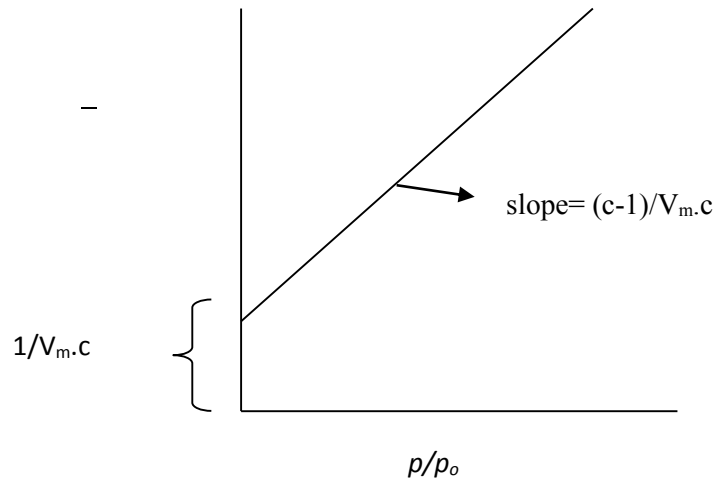


Figure 27. BET plot

The slope (A) and intercept (I), are used to calculate the monolayer adsorbed gas quantity, and c, the BET constant (Equations 10-11).

$$V_m = \frac{1}{A+1} \quad c = 1 + \frac{A}{I}$$

Equations 10 - 11

The following assumptions are applied for the BET theory:

- (i) The surface is homogeneous.
- (ii) There are no lateral interactions between layers.
- (iii) The uppermost layer is in equilibrium with the vapour phase.
- (iv) The Langmuir theory can be applied to each layer.

Adsorption isotherms can take many forms, and typically there are 5 types dictated by the porosity of the material [31]. Figure 28 provides three examples of these.

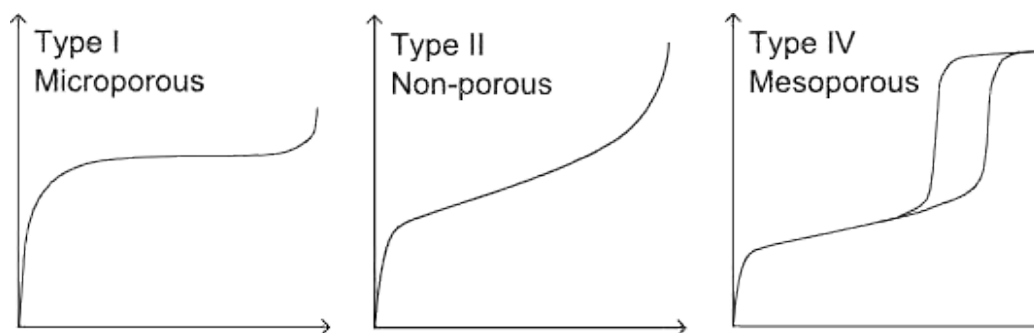


Figure 28. Adsorption isotherm examples. Type 1 depicts monolayer adsorption, which can be explained using the Langmuir Adsorption Isotherm. When $P/P_o \ll 1$, and $c \gg 1$ this leads to monolayer formation and a Type 1 isotherm. Type II shows a large deviation from the Langmuir model of adsorption. The intermediate flat region corresponds to monolayer formation and the value of C is \gg than 1. Type IV shows the formation of a monolayer followed by multilayer adsorption. Saturation is reached at a pressure below the saturation vapour pressure. It is possible that gases condense in the tiny capillary pores of the adsorbent at a pressure below the saturation pressure of the gas.

BET holds several advantages. The technique itself is cheap, fast and reliable. It is very well understood, and has been applied to many fields. The major applications are in pharmaceuticals, catalysts, projectile propellants, medical implants, filters and cements. However, it must be noted that it is not applicable to all types of isotherms.

4.5.2. Experimental

BET surface areas were measured three times for each sample under nitrogen physisorption at 77 K using a Micromeritics Gemini surface area analyser. The following was carried out:

- (i) The sample was degassed to remove any surface contaminants at 120°C in N_2 .
- (ii) Liquid N_2 was introduced in known aliquots to saturation pressure.
- (iii) A vacuum was applied and the gas removed.
- (iv) The relative pressure and quantity of gas adsorbed was measured. An adsorption isotherm could then be obtained.
- (v) The surface area of the sample was calculated using the BET equation.

4.6. Scanning Electron Microscopy (SEM)

4.6.1. Theory

The SEM microscope is an electron microscope, which images the sample through rastering the surface with a high energy beam of electrons. An SEM can magnify an object

up to 30,000 times, allowing sub-micron scale features and therefore revealing much more detail than the typical light microscope. Using SEM holds many advantages. Firstly rapid and high resolution is achievable at high magnification. The best resolution possible in a light microscope is about 200 nm, whereas a typical SEM has a resolution of better than 10 nm. Secondly, the depth of field is much greater for the SEM, enabling greater topographical information. Finally, microanalysis is available for SEM analysis, including information on chemical composition, magnetic and electrical characteristics.

Bombardment of the sample with a high energy beam of electrons leads to electron sample-interactions, and consequently generates signals at the solid surface. These signals include secondary electrons, backscattered electrons, diffracted back scattered electrons, photons, visible light and heat. These reveal information about the sample, including morphology, chemical composition, and crystal structure. Secondary electrons are routinely used to provide topography and morphology information on samples, whereas back scattered electrons are valuable for providing information on composition.

The essential components of an SEM include an electron source, electron lenses, sample stage, detectors, data output devices, a power supply, vacuum system and cooling system.

The following process occurs:

- (i) A beam of electrons is initially generated in the electron gun towards the top of the column. The filament often used to create these electrons is a tungsten hairpin, which acts as a cathode.
- (ii) On applying a voltage to this filament, it heats up, and the electrons formed are accelerated towards the positively charged anode.
- (iii) The beam is then accelerated through the anode, and is condensed by two condenser lenses, finally being focussed by the objective lenses to a very fine point on the sample.

In order to enable rastering across the sample surface, the beam passes through a pair of scanning coils. Upon being energised, the scanning coils create a magnetic field which deflects the beam horizontally and vertically, so that the beam scans across the sample. Interaction with the sample causes the electrons to lose their energy. The size of interaction volume depends on a number of factors, including the electrons landing energy and the sample atomic number and density. The exchange of energy between the electron beam and the sample gives rise to the emission of electrons and EM. These are detected in order to form an image.

SEM can also be coupled with EDX (Energy Dispersive X-Ray Analyser), to provide elemental identification and quantitative compositional information (see Section 4.8 for details). Although the SEM holds many advantages including its high resolution and depth of field, there are however a few disadvantages. Firstly, the SEM must be operated under a vacuum, meaning that the sample must be stable under these conditions. Secondly, the sample being analysed must be conductive. If this is not the case, a very thin layer of metal or carbon must be applied to the surface of the sample, in order to dissipate the charge from the electrically charged electrons. Finally, EDX detectors on SEM's cannot detect very light elements such as H, He, and Li.

4.6.2. Experimental

SEM images were obtained using a JEOL JSM- 6610LV microscope. Samples were initially pressed onto carbon film stubs, and then loaded into the aluminium holder. The holder was fastened into the SEM chamber, the door closed, and the system evacuated. An image was taken of the sample holder to allow for navigation between samples. Choosing a point on the sample, the image was focused and the brightness and contrast corrected to give a high quality image. Images of varying magnification were acquired across different areas on the sample.

4.7. Transmission Electron Microscopy (TEM)

4.7.1. Theory

A TEM uses high energy electrons to provide morphological, compositional and crystallographic information. It is successful in providing direct images of catalyst microstructure, and in turn gives information about particle size distributions, structure, shape, and texture. A TEM is able to gain much higher resolution than a light microscope, due to the smaller de Broglie wavelength of the electrons. Objects can be seen in the order of a few angstroms, making the TEM the most powerful microscope available.

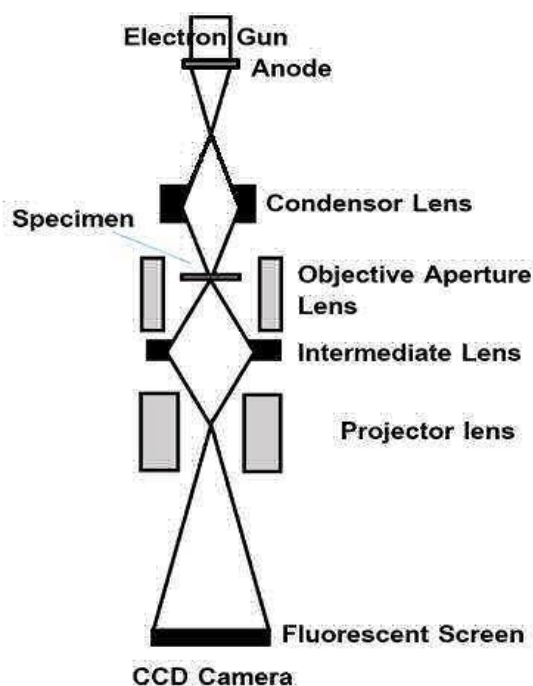


Figure 29. Schematic setup of the TEM with various components.

The TEM works as follows:

- (i) An electron gun at the top of the microscope emits a source of monochromatic electrons, which travel under vacuum through the column.
- (ii) Electromagnetic lenses (condenser lenses 1 and 2), are used to focus the electrons into a very thin beam. The beam is restricted by the condenser aperture which eliminates high angle electrons.
- (iii) The beam travels through the sample specimen. The specimen has to be a very thin, typically less than 2000 Å. Depending on the density of the material being sampled, some of the electrons are scattered. Non-scattered electrons hit a fluorescent screen at the bottom of the microscope, where electrons are converted to light to create an image of the specimen. Different darkness's correspond to change in density, with the lighter areas corresponding to a greater passage of electrons through the sample. The image can be adjusted through varying the voltage of the gun, which alters the speed of the electrons and hence EM wavelength (the shorter the wavelength, the faster the electrons move, and therefore the clearer the image). The setup of a typical TEM is shown in Figure 29. In addition to viewing the sample on the florescent screen, the microscope is also fitted with a camera which must work in the vacuum within the microscope, typically 1×10^{-5} mbar.

TEM use hosts both advantages and disadvantages. This impressive piece of kit offers the most powerful magnification available, to give high quality and detailed images. They have

been used for multiple applications, yielding information on element and compound structure. After the required initial training, the operation is relatively straight forward.

On the other hand, TEMs are known for their high costs, in both initial purchase and maintenance, including maintaining them under a constant voltage, and constant cooling with water. They are large, therefore requiring significant lab space. The samples used must be electron transparent, and also must be stable under the vacuum conditions required for the electron beam. Non-conductive samples must also be sputter coated, as for SEM.

4.7.2 .Experimental

TEM was performed using a JEM-2100 microscope, which features a very stable goniometer stage, tuned for high tilt tomographic applications, and the ability to use a range of illumination conditions. Most recently it has been coupled with an EDX analyser, which functions similarly to that of the SEM, providing elemental identification and quantitative compositional information. The sample was dissolved in ethanol with sonication. A small amount of sample was dropped onto a copper grid with carbon film, to be loaded onto the sample holder. The holder was placed into the TEM and a vacuum applied. For high resolution images, a full alignment must be applied to focus the beam. The sample can then be viewed and images acquired.

4.8. Energy Dispersive X-Ray Spectroscopy (EDX)

4.8.1. Theory

Both SEM and TEM can benefit from being coupled with EDX analysis. EDX is an analytical technique used by scientists for elemental and localised chemical analysis. The technique exploits the X-ray spectrum emitted by the sample on bombardment by a high energy electron beam (such as in TEM/SEM), and is capable of detecting all elements from atomic mass 4 to 92. Each element has its own unique atomic structure, which also means that each element has its own unique set of peaks on its X-ray spectrum. As an electron beam interacts with the sample, it will cause ejection of an electron from an inner shell of that atom. This creates an electron hole, which is subsequently filled by an electron which drops down from an outer shell. The energy difference between the outer and inner shell dictates the X-ray intensity. EDX measures the number, wavelength and energy of these emitted X-rays using a spectrometer, the energy difference corresponding to the specific element being analysed. Since lower atomic elements have fewer filled shells, they therefore have fewer X-ray peaks, since there are fewer shells from which an electron drops down from to fill the hole.

The use of EDX analysis holds both advantages and disadvantages. In general the technique is considered both quick and inexpensive. However its limitations include that it is element specific, it gives a lack of chemical bonding information, and can be time consuming.

4.9. Synchrotron techniques

4.9.1. Theory

Synchrotron light is the electromagnetic radiation emitted when electrons moving at a speed close to that of light, undertake a forced change to their direction due to an applied magnetic field. The electromagnetic radiation is emitted in a narrow cone in the forward direction, at a tangent to the electron's orbit.

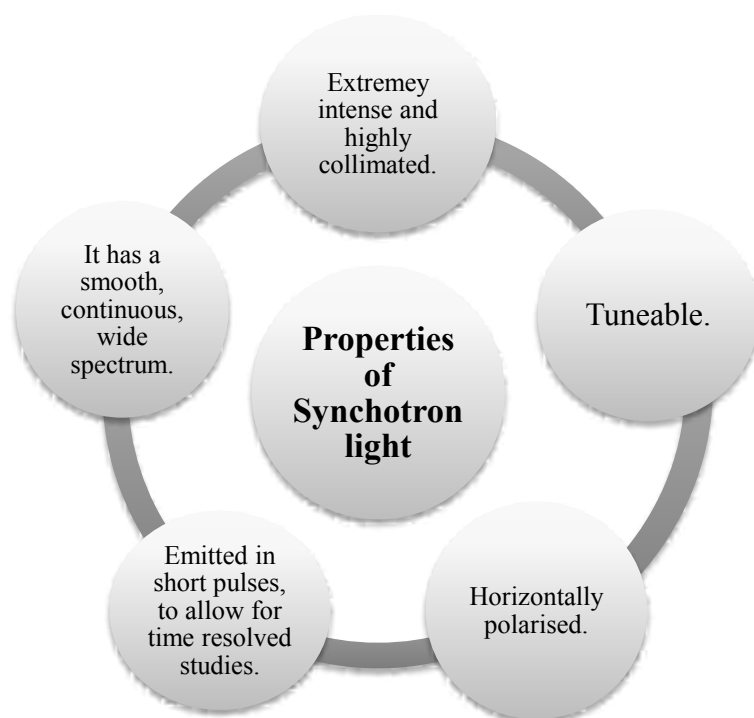


Figure 30. Properties of Synchrotron Light.

Synchrotron radiation is allowing for huge advancements in research and development, due to its many unique properties (Figure 30). Synchrotron radiation sources have revolutionised experimental X-ray studies. It has many applications including medical research, environmental sciences, mineral exploration, forensics, engineering, advanced materials and biosciences.

4.9.2. How is Synchrotron Light Generated?

Synchrotron radiation is created at a synchrotron, which can be defined as a cyclic particle accelerator. There are 5 main sections of the synchrotron involved in creating the high intensity radiation (Figure 31).

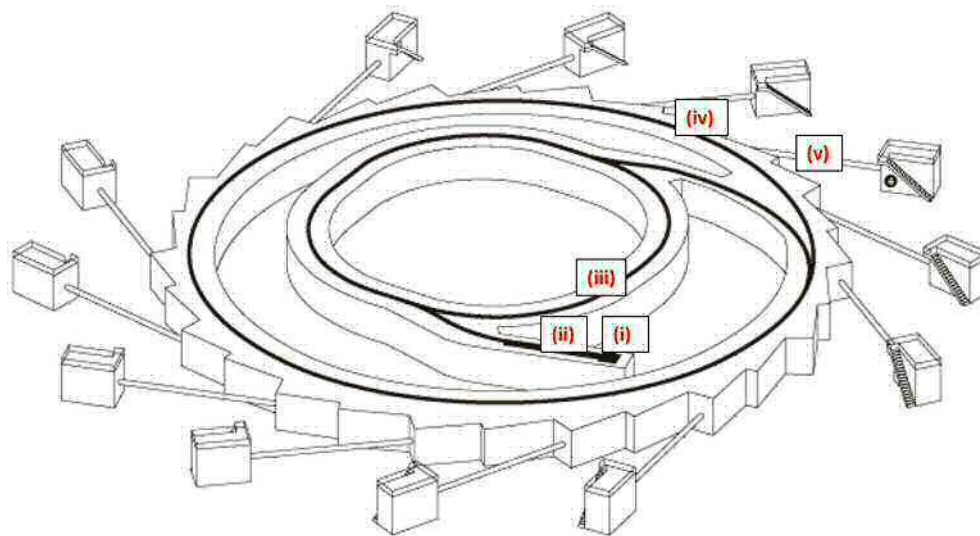


Figure 31. Synchrotron Schematic.

- (i) **The electron gun:** Here the electrons are generated. A transformer feeds electricity through a cathode (typically a tungsten oxide), which causes the ejection of electrons from the surface.
- (ii) **LINAC:** In the linear accelerator, the electrons are accelerated to 99.9997% of the speed of light. After the electrons are fed from the electron gun, microwave radio frequency fields give the electrons the correct energy to accomplish these speeds. The LINAC produces electron pulses up to 132 nanoseconds in duration. The electrons travel within a vacuum, with a pressure lower than 10^{-11} torr.
- (iii) **Booster ring:** The booster ring forms the second part of the particle accelerator. From the linac, electrons enter the booster synchrotron, where they gain in energy up to 6 GeV. The electrons follow a trajectory with two straight sections joined with semi-circular curves. Dipole bending magnets are applied to curve the electrons around the trajectory, and an RF voltage source accelerates the electrons along the straight sections.
- (iv) **Storage ring:** When the electrons have enough energy to produce light, they enter the storage ring at a rate of once per second, where they will circulate for four to twelve hours. The storage ring is a polygon comprised of straight sections angled together with bending/dipole magnets, which direct the electrons around the ring. As the electrons pass through each magnet, the direction of their flow is altered, causing them to give up their energy in the form of light. This light is then channelled to the beamlines. The intensity of

the light can be further enhanced through the use of insertion devices in the straight sections of the ring. There are two different types available: a multiple wiggler and an undulator.

(v) **Beamline:** The beamline is where the sample is placed in the X-ray beam. Each beamline has three sections, the optics hutch, the experimental hutch, and the control cabin, with each beamline optimised for the experiment to be carried out (Figure 32).

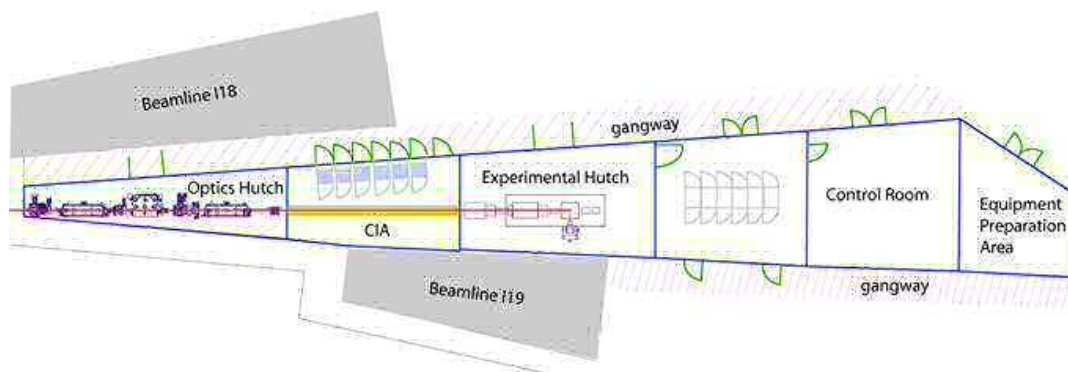


Figure 32. General beamline setup [32].

4.9.3. Insertion Devices

As mentioned, electrons are able to create electromagnetic radiation as a result of their deflection through the magnetic field created by the magnets. The intensity of this light produced can be further enhanced by the means of insertion devices in the straight sections of the polygon ring. This enables scientists to specifically tailor the radiation produced to the requirements of the experiment. The insertion devices can be classified into two types: undulators and wigglers, and their basic principle is illustrated in Figure 33. They are both high-field, linear magnet arrays, causing an oscillatory movement of the electron beam.

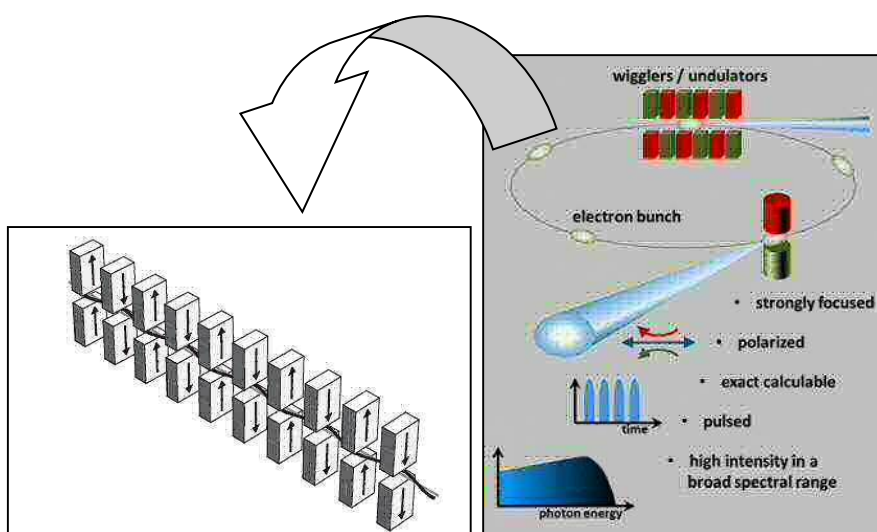


Figure 33. Undulators and wigglers schematic, demonstrating the alternating magnetic poles.

A wiggler is a three pole magnet. In a multipole wiggler (MPW), a cone of light is emitted at each bend in the 'wiggle'. The beams of light produced reinforce each other, producing a broad beam of incoherent SR in the horizontal plane. The emissions from different poles are uncorrelated, producing an emission far greater than that for a bending magnet spectra, in a chicane type path. This reduces the radius of curvature, and shifts the characteristic wavelength to lower values (higher energy).

The second type of device is an undulator. The principles here are very similar to those of a wiggler, however the deflection of the electron beam is significantly less with many more periods, due to the less powerful magnets used. An undulator uses an array of permanent magnets above and below the path of the electron beam, and as the beam passes through the magnets, its path oscillates in the horizontal plane. Emissions from each period in the undulator are in-phase, resulting in a narrow beam of coherent SR. Variation in the distances between the magnets and the electron beam allow the user to optimise the radiation for the experiment.

The use of insertion devices brings a whole new depth to scientific studies using synchrotrons. Focusing on the size and positioning of the straight sections, allow scientists to optimise the intensity of the radiation produced. It is therefore possible to enhance the brightness, extend/narrow the radiation spectrum, and also adjust the coherence of the beam. In general, undulators are used for soft X-ray experiments, whereas wigglers are used for hard X-ray experiments.

4.9.4. At the Beamline

On reaching the beamline, the experiment can be carried out. Each beamline is optimised for its specific use, however there are several common features to all. First, the light is passed through the *optics hutch*, where it is modified for use. Specialised mirrors and crystal optics are in place to focus the beam, and to select the energy required for the experiment. Slits define the beam size and remove scatter, whilst mirrors focus the beam and remove higher energy.

Subsequent to the optics hutch, is the *experimental hutch*, where the sample is placed in the X-ray path. There are many different sample environments available, including open to air, heated, cooled by liquid nitrogen, under pressure, and in liquid cells. This makes the XAFS technique very adaptable to most sample types. The sample can also be analysed under *in situ* analysis combining XAFS with other techniques such as XRD, Raman and DRIFTS. The sample workspace may include motors that position the sample very precisely

with respect to the beam. To collect data for analysis, detectors are in place around the sample for either transmission or fluorescence modes.

Finally, there is a *control cabin*, where users can control their experiments separate to where the X-rays are contained. Figure 32 demonstrates this setup. The sample can be positioned and the experiment set to run.

4.9.5. B18

B18 is a general purpose XAFS beamline in Zone 1 of Diamond Light Source. It has been built on a bending magnet, and is able to access energies in the range of 2-35 keV. The optical configuration has been designed to maximise the efficiency and reliability of the beam, whilst still maintaining the flux. Three main optical elements are in place: a collimating mirror, a double crystal monochromator and a double toroidal focusing mirror. Harmonic rejection mirrors may also be exploited for the lower energy range. Figure 34 details the various components within the hutches.

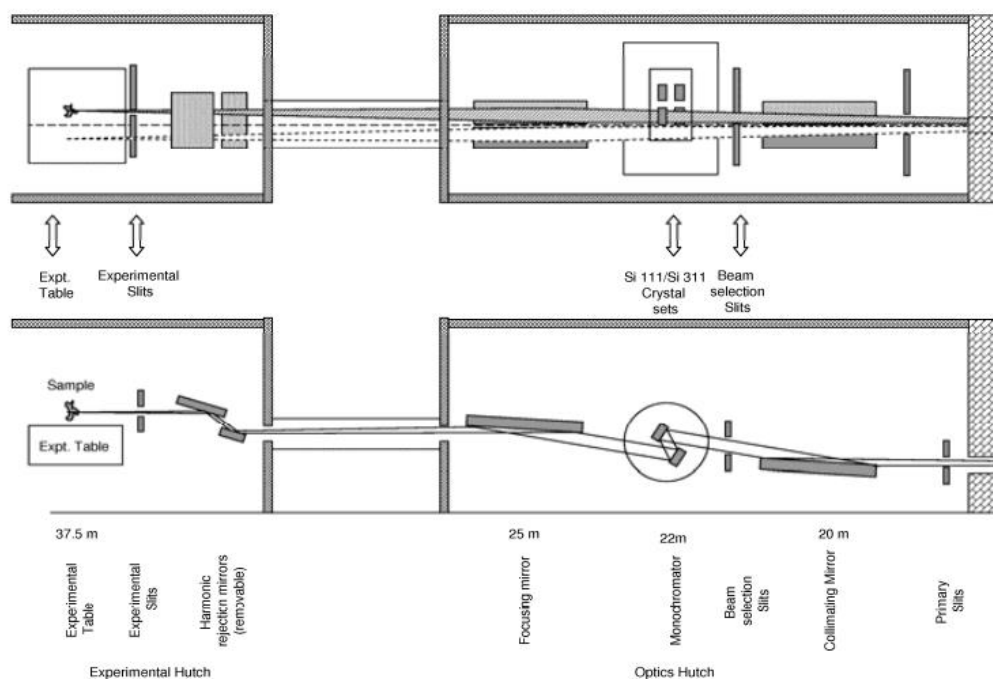


Figure 34. Schematic of the optic and experimental hutches on B18 [33].

On entrance to the optics hutch, the white beam is first filtered. If not required, high-pass filters remove low-energy photons, to lower heat load onto the downstream optics. Next the beam enters the collimating mirror positioned at a fixed incident angle. The mirror is coated in 2 stripes, Pt and Cr, one for each beamline branch. Mirrors can be used as low-pass filters,

to filter out any unnecessary high energy photons. The filtering depends on the mirror material and the grazing angle applied [34].

Beam branch selection occurs at the secondary slits, just before the monochromator. To maximise the available energy range, two crystal monochromators are available on B18. The Si (111) gives a range of 2.1-20.2 keV, whilst the Si (311) gives an energy range of 4-35 keV, which is primarily used for high energy, but also at low energy for improved edge resolution. These crystals are both water-cooled and under vacuum. The X-rays diffract from the crystals lattice planes, which are aligned at an angle with respect to the incoming beam. Only specific X-ray wavelengths can satisfy the Bragg equation for constructive interference from the crystals lattice planes. In changing the orientation of the two crystals, a different energy can therefore be selected. The monochromator will operate in both step-scan and continuous (QEXAFS) scan modes. Post monochromator, a double bent cylinder focusing mirror is in place, again the cylinders are coated in Cr and Pt.

A pair of harmonic rejection mirrors with Ni and Pt coatings are located in the experimental hutch. These are for use when operating under 15 keV. Also found here are the final monochromatic beam slits and the diagnostics unit to measure either X-ray fluorescence from the reference foils in the high energy range, or total electron yield for the low energy range. The monochromatic beam passes through an ion chamber that monitors the beam intensity, I_0 , by absorbing part of it (Figure 35). The beam then passes through the sample, and the transmitted X-ray intensity, I , is monitored by the second ionisation chamber. For an ideal sample, between 50 and 90 percent of the X-ray beam intensity is absorbed. Taking the log of the ratio of I/I_0 yields the total absorption. If measuring in fluorescence mode, the intensity of the X-ray fluorescence can also be measured by a second ionisation chamber at approximately 45° to the sample. Finally, the beam passes through the reference foil. Reference data is essential in correcting for uncertainties in the beams energy, whilst also enabling alignment between data sets.

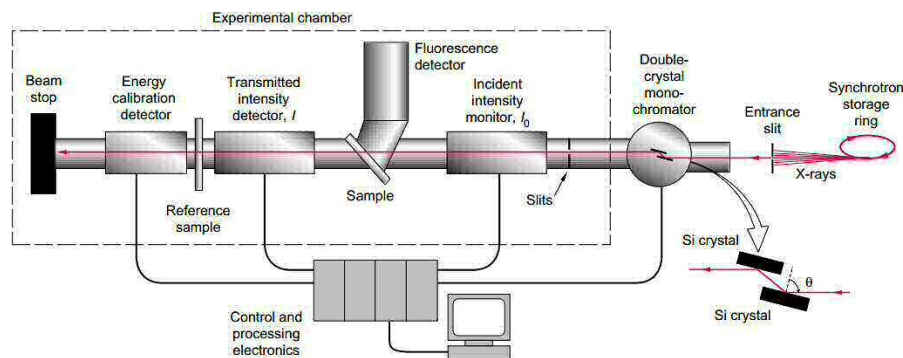


Figure 35. Typical XAFS setup [35], as seen on B18. Use of the double crystal geometry of the monochromators enables selection of a single, well-defined energy from the X-ray source. The Bragg relation (Equation 6) relates reflections from a crystal plane as a function of the incident angle, which can be used to select the photon energy required.

4.9.5.1. Ion Chambers

An ionisation chamber is a gas filled radiation detector, used to measure the X-rays both pre and post sample. The basic principle of the ionisation chamber is that it measures the charge created through the direct ionisation of a gas from the X-rays [36]. The chamber consists of a gas-filled unit, with two electrodes (cathode and anode). A voltage is applied across the electrodes to stimulate an electric field in the fill gas. Gas between the electrodes becomes ionised by the incoming radiation, creating ion pairs. Positive ions will quickly diffuse to the cathode, whilst the electrons produced will attract to the anode under the influence of the electric field. This results in an ionisation current, measured by an electrometer. Each ion pair created deposits or removes a small electric charge to or from the electrode. The accumulated charge is proportional to the number of ion pairs created in the process. This will therefore indicate the X-ray dose.

I_t measures the X-rays intensity after passing through the sample, and I_r measures the intensity of X-rays after passing through the sample and a reference foil. I_0 is set to absorb 20 %, and I_r and I_t are set to absorb 80 % of the flux.

4.9.6. XAFS: X-Ray Absorption Fine Structure

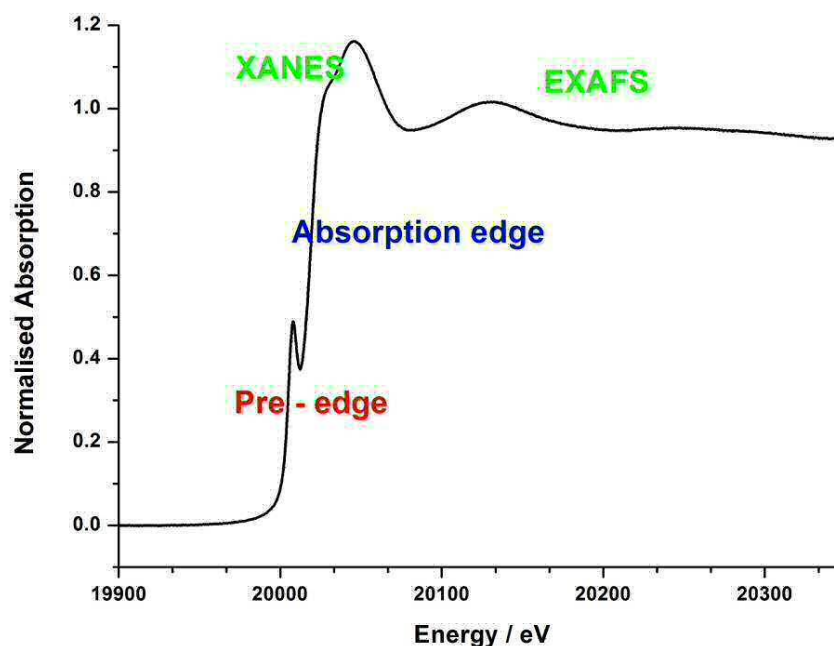


Figure 36. Typical XAFS plot. A XAFS Spectrum consists of two major regions: XANES and EXAFS, with descriptions to follow.

X-ray absorption fine structure (XAFS) is an invaluable technique for analysing how X-rays are absorbed by an atom, at energies near and above the core-level binding energies of that specific atom/element. Depending on the chemical or physical state of that atom, the absorption profile can change significantly, and XAFS can be used to probe these changes, providing information on local geometric and electronic structure. This includes detecting changes in oxidation state, co-ordination geometry, and bond lengths. Figure 36 details a typical XAFS absorption spectrum.

There are two main regions to consider [37]:

- (i) **XANES:** X-ray Absorption Near-Edge Spectroscopy and,
- (ii) **EXAFS:** Extended X-ray Absorption Fine-Structure

Both are related, but provide different information on the elements local environment/chemical state.

4.9.6.1. X-Ray Absorption process

As X-rays pass through a material, there is a reduction in their intensity as they are absorbed by matter under the photo-electric effect. XAFS data are obtained by tuning the

photon energy using a crystalline monochromator, to a range where core electrons within the atom can be excited. Above the B.E, photons are absorbed through deep core excitation, and as a result electrons are kicked out from the core shell [38]. The name of the edge is directly related to the shell from which the core electron is ejected from. For instance, if a 1s electron is excited, this corresponds to the K-edge.

The atom is left in an excited state, presenting an empty core hole. In order to return to the ground state, a higher level core electron drops into the core hole, with one of two processes occurring (Figure 37):

- (i) Filling of the core hole by an electron in another level, accompanied by fluorescence. An X-ray with energy equal to the difference in the core-levels is emitted.
- (ii) Filling of the core hole by an electron in another level, followed by emission of an Auger electron. An electron is promoted to the continuum from another core-level.

Both these processes occur at energies which are specific to the absorbing atom, therefore providing an element specific technique.

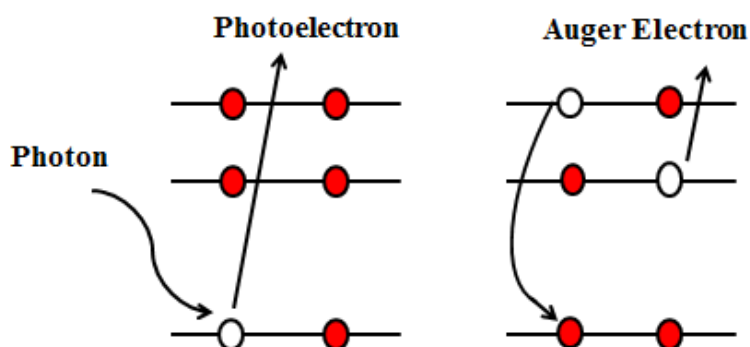


Figure 37. Relaxation processes for fluorescence (left) and Auger emission (right).

The absorption of X-rays and the X-ray Absorption Co-efficient:

This loss in X-ray intensity of the incoming X-ray is proportional to the incident intensity of the X-rays, (I_0), and the path length, (x), (See Equation 12).

$$dI = -\mu I dx$$

Equation 12

Where I = the intensity of the X-rays, μ = the linear absorption coefficient, a function of the photon energy, E . I

In integrating over the path length, x , the result is the Beer Lambert Law (Equation 13):

$$I = I_o e^{-\mu(E)x} \quad \text{Equation 13}$$

The absorption of X-rays by the material will decrease with increasing photon energy. The focal point of the XANES region is the absorption edge, occurring at the threshold frequency for photoelectron emission. This is shown as a sharp rise in the absorption spectrum (Figure 36), occurring when the critical energy is reached. The X-ray absorption coefficient, $\mu(E)$, dictates the intensity of the absorption edge and is proportional to the probability of the absorption of a photon. $\mu(E)$ depends significantly on the X-ray energy (E), the atomic number (A), atomic mass (Z), and density (ρ).

The equation is derived as:

$$\mu(E) \sim \rho Z^4 / AE^3 \quad \text{Equation 14}$$

The absorption edge energy corresponds to the characteristic core-level energies of the atom. All elements with $Z > 18$ have either a K-, or L-edge between 3 and 35 keV. Table 5 details the transitions responsible for the various edges. Dipole selection rules apply:

$$\Delta = \pm 1, \Delta = \pm 1, \Delta = 0$$

Where Δ = total orbital angular momentum, j = total angular momentum, s = total spin

Table 5. Absorption edges and their associated transitions.

K edge	1s			
L edge	2s	2p		
M edge	3s	3p	3d	
N edge	4s	4p	4d	4f

XAS measures the energy dependence of the X-ray absorption coefficient, $\mu(E)$, at and above the absorption edge of a selected element. Several measurement modes can be used.

1) Transmission:

The simplest type of XAS measurement is transmission XAS, commonly used for measuring concentrated samples. It is essential that the sample is homogeneous. Transmission measures the X-ray flux transmitted through a sample (Figure 38). The intensity of the X-ray beam is measured before and after the sample, and the absorbance (μt) calculated using the Beer Lambert Law (Equation 15). The intensity of the X-ray beam is typically measured using ionisation detectors.

$$I = I_0 e^{-\mu t}$$

Equation 15

Where I_0 = Initial X-ray energy and I = Transmitted X-ray energy, t = Sample thickness.

The element must be concentrated enough in order to give an edge step of >0.1 absorption lengths. Reasonably concentrated elements would be $>3-5$ w/t %. Measuring in transmission mode provides a better quality of data at further out energy values. However, the types of samples suitable to run in this mode are limited. A further consideration is the thickness of the sample. The thickness must be adjusted so that the total absorption is <2.5 absorption lengths, ideally giving an edge step of approximately 1. If the absorption of the sample is too high this could induce self-absorption, resulting in errors in the determination of co-ordination numbers in EXAFS analysis.

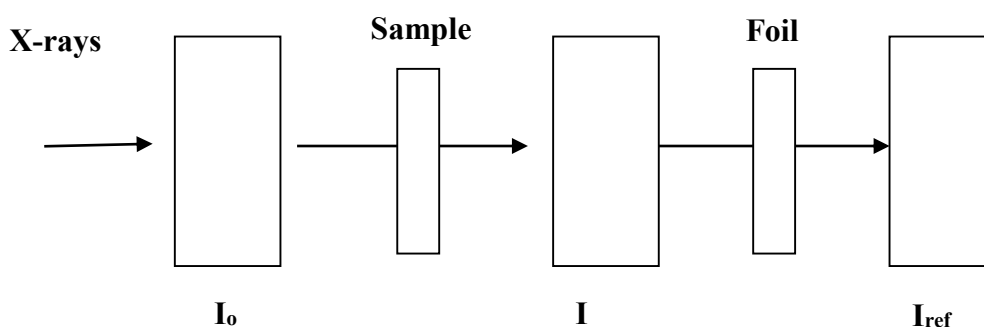


Figure 38. Schematic for a transmission measurement setup.

2) Fluorescence

Fluorescence mode is more appropriate for dilute (down to ppm levels) or thick samples. Fluorescence experiments are much more sensitive than transmission experiments. The absorbance of the sample is measured by monitoring the intensity of the X-ray fluorescence produced, when higher-shell electrons relax and refill the deep core hole left by the photoelectron. The energy difference between the outer shell and the inner shell is emitted as fluorescent radiation characteristic of the target element. The detector is placed at 45° to the sample (Figure 39).

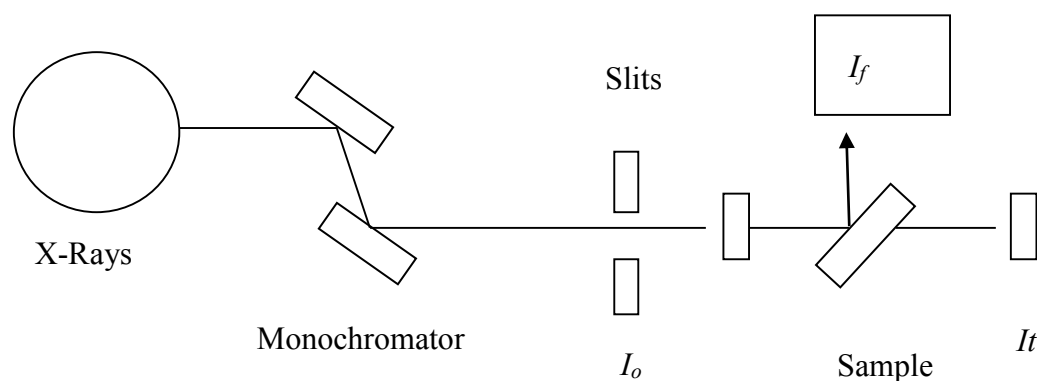


Figure 39. Schematic for a fluorescent measurement setup.

Although fluorescence benefits in that most samples can be analysed, it suffers from poorer data quality compared to that obtained in transmission mode.

3) Electron Yield

A final measurement technique is through electron yield, which collects the emitted Auger electrons. This proves useful when the fluorescence yield is low, or when fluorescence self-absorption effects occur. Electron yield measurements require a conducting sample. The measurement is normally achieved by biasing the sample, and collecting the drain current. However it can also be done with a collector plate above a floating sample.

4.9.6.2. Understanding EXAFS

It has been discussed that the X-ray absorption co-efficient for an atom is directly proportional to the probability of absorption of a photon. Absorption edges are observed when the incident energy equals that of the binding energy of an electron in a core shell of the atom. This induces the ejection of a photoelectron from the atom. Edge energies are therefore element specific. If an atom were to exist in complete isolation, the absorption co-efficient would decrease monotonously with energy, as the photoelectron propagates as an unperturbed isotropic wave. However, more realistically, in most situations the absorber atom will exist surrounded by others, with the result shown as oscillations in the spectrum which starts approximately 50 eV after the edge.

The propagating electron will have the characteristics of a particle and a wave (Figure 40). The extended fine structure fundamentally derives from this wave nature. The outgoing photoelectron can be described as a spherical wave function (Equation 14) with wave vector, k :

$$k = \frac{\sqrt{8\pi^2 m_e}}{h} \sqrt{h\nu - E_0} \quad \text{Equation 16}$$

Where m_e = Electron mass, E_0 = Zero point energy, ν = Frequency, and h = Planck's constant.

As the photoelectron wave leaves the atom, it will become back scattered by the surrounding atoms, with its final state described by the sum of the outgoing and back-scattered waves (Equation 17).

$$\Phi_f = \Phi_{\text{outgoing}} + \Phi_{\text{backscattered}} \quad \text{Equation 17}$$

The effect of constructive and destructive interference will cause an increase or decrease in the absorption co-efficient respectively, giving rise to the oscillations in the spectrum.

Figure 48 represents the process contributing to the EXAFS region.

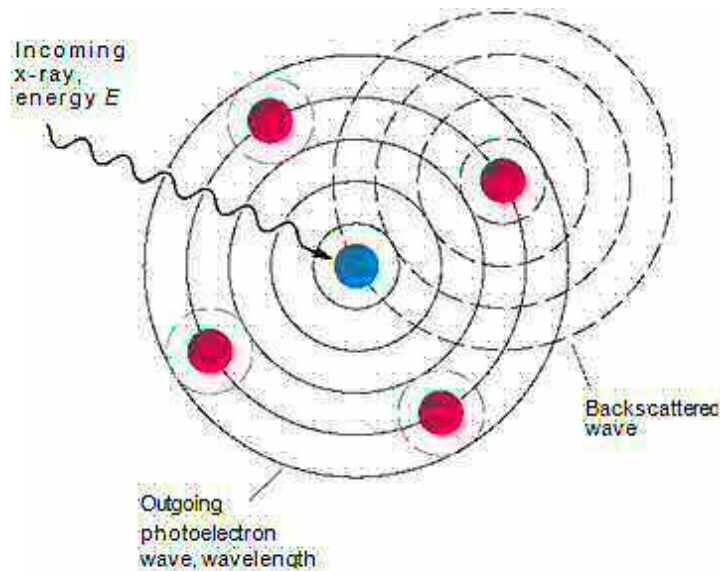


Figure 40. Process contributing to EXAFS. The photoelectron propagates outwards as a spherical wave from the central absorber (blue). The wave is back-scattered from nearby atoms (red), causing interference. The result of constructive interference (as shown) will increase the amplitude of the final wave state function, producing a maximum in the oscillatory region of EXAFS. For destructive interference, the waves are out of phase, resulting in a decrease in the amplitude of the final wave state function, and a subsequent trough in the oscillatory region of the spectrum.

The electron scattering process is influenced by several factors, including the following:

- (i) The atomic number of the scatterer. Heavier atoms will inherently scatter more than lighter ones.
- (ii) The distance between the absorber and the scatterer. This will have a pronounced effect on the phase of the scattered electron and frequency of the oscillations.
- (iii) Thermal effects and the Debye Waller factor. Temperature dampens the oscillations in the EXAFS region.
- (iv) The energy of the scattered electron. Scattering is a function of electron energy.

In summary, extended X-ray absorption fine structure (EXAFS) is an oscillatory modulation in the X-ray absorption coefficient, occurring at higher energies of the absorption edge. Analysis yields information on the number and types of atoms in the immediate environment of the absorbing atom, as well as accurate absorber-neighbour distances [39]. EXAFS is not dependent on long-range structure.

The EXAFS equation:

The EXAFS signal, $\chi(k)$, can be defined as a function of the wave vector, k [40] (Equation 18). EXAFS is commonly described in terms of the wave behaviour of the propagating photo-electron, created during absorption. It is therefore more common to convert the X-Ray energy to k , the wavenumber of the photo-electron, with the dimensions of $1/d$.

It is mathematically defined as:

$$\chi(k) =$$

Equation 18

Where μ = The observed absorption co-efficient, and μ_0 = The absorption observed in the absence of EXAFS effects, i.e. a smooth background function representing the absorption of an isolated atom.

The subtracted μ_0 represents removal of the background, and the division by μ_0 represents the normalization of the function, to represent the average structure surrounding the central absorber atom. Since μ_0 cannot be directly measured, it is approximated, by fitting a smooth spline function through the data.

To extract quantitative information from the EXAFS experimental spectra, a simple analytical expression that relates the EXAFS signal to the structural parameters is used. Several simplifying assumptions allowed Stern, Sayers, and Lytle [41] to derive the

following expression, the EXAFS equation (Equation 19). The theory assumes that the distance to the neighbouring atom is much larger than the atomic radius of the central atom. For this reason, the spherical wave can be approximated as a plane wave, to simplify the analysis. This plane wave approximation also assumes that single scattering effects dominate, i.e. the photoelectron is only scattered once before returning to the central atom. Of course, multiple scattering can also occur for many systems, which greatly affects the EXAFS.

The EXAFS function can be represented as a summation of the sine waves produced by the outgoing photoelectron wave function, together with the backscattered wave function from each coordination shell.

$$\chi = \sum_{shells} \frac{n_X \cdot S_0^2 \cdot f_X(k) \cdot e^{-2k^2\sigma^2}}{k \cdot r^2} \sin(2kr + \alpha_{MX}(k))$$

Equation 19

Where n_X = The number of X atoms in the shell, S_0^2 = Amplitude reduction factor, $f_X(k)$ = Amplitude function, $e^{-2k^2\sigma^2}$ = Debye-Waller term, r = Average MX distance from central absorber to scatterer, $\alpha_{MX}(k)$ = Phase function, σ^2 = Mean-square-displacement in the bond distance MX (absorber to scatterer).

Breaking down the equation:

In the equation, $f_X(k)$ and $\alpha_{MX}(k)$ represent the amplitude and the phase shift. Both these terms can be calculated for a certain k value, and are directly affected by the atomic number, Z . This leave r , n and σ^2 as unknowns to be calculated, providing information regarding radius, co-ordination number and the disorder within the structure. S_0^2 provides information regarding the probability of the scattering, and depends on the element, distance and the energy being used.

S_0 , the amplitude reduction factor, describes the multi-electron processes and central atom shake up and shake off as a result of relaxation after photo-ionisation. The value for this is typically between 0.7-1.1. It takes into account the fraction of the voltage measured that is lost e.g. inelastic losses.

The Debye Waller factor represents the decay of the signal with increasing thermal or static disorder. The effect of thermal or static disorder causes fluctuations in the positions of

the atoms from their equilibrium atomic positions. As we go further out from the central absorber, the effects will become greater, hence a dampening of the EXAFS signal further out in k . This is a result of the mean squared disorder term.

$e^{\frac{-2R_j}{\lambda(k)}}$ accounts for the finite lifetime of the excited state. λ = mfp of the photoelectron.

The sine function represents the origin of the sinusoid shape. A larger phase shift will bring an increase in oscillations. The phase shift factor is a crucial component, reflecting the effects that interatomic distances and energy have on the oscillations. It will be affected by

both the type of element, and the distance between the absorber and the scatterer (Equation 20):

$$\sin q_k = \sin [2kR_j + \phi_j(k)] \quad \text{Equation 20}$$

Where R_j = Interatomic distance between the absorber and the backscatterer, and $\phi_j(k)$ = Back scattering phase shift, which can be represented as:

$$\phi_j(k) = \frac{2\pi}{\lambda(k)} R_j \quad \text{Equation 21}$$

Referring to Equation 21, it is shown that the absorber contributes twice the amount of phase factor as the backscatterer does, since the photoelectron receives potential created by the absorber twice. The phase shift can be extracted from reference compounds, and can also be calculated theoretically.

The EXAFS equation is a significant discovery, used to extract structural parameters from the experimental data. This includes bond distances from absorber to neighbouring atoms, co-ordination numbers to different atom types, and a calculation of the Debye Waller factor.

4.9.6.3. XANES

XANES is the region of the X-ray absorption spectrum within ~50 eV of the absorption edge, arising mainly due to electronic transitions from the core level to higher unfilled or partially filled orbitals, e.g. $s \rightarrow p$, or $p \rightarrow d$. It strongly depends on local geometry (co-ordination number and ligand symmetry), with the absorption edge position and shape providing information on the oxidation of the absorber [42]. XANES can be separated into three main features:

(i) The absorption edge, E_0 : The absorption edge is the most prominent feature in the XANES spectrum, and defines the onset of continuum states. The energy of the edge is specific to the element analysed, and the energy position and shape can also define the oxidation state of the absorber. E_0 is a function of the absorber oxidation state and binding geometry. It may also increase by several eV per oxidation unit.

(ii) The pre-edge: The pre-edge occurs at a lower energy than the rising edge, and is a result of electronic transitions to empty bound states near the Fermi energy. This differs from the absorption edge, which is dictated by transitions to continuum states. The final state is usually not atomic-like, and may have hybridization with other orbitals. Pre-edges provide information about absorber local geometry and electronic state around the absorber. They are often associated with tetrahedral structures, as the lack of symmetry allows for orbital overlap within the molecule, giving rise to the required empty orbitals for electron transition. However, they can also be seen, albeit weaker, for distorted octahedral complexes. Some absorption edges have a very large initial peak after the absorption edge. This peak is termed the ‘white line’ as it appeared as a bright white line in early XAS experiments involving photographic plates. This feature is associated with electronic transitions to orbitals with a high density of states.

(iii) Post-edge: The post edge is reliant on multiple scattering features. The analysis of the post-edge provides information regarding the local atomic structure and geometry.

In summary, as an element specific technique, XANES directly probes the angular momentum of the unoccupied electronic states, which may be one of the following: bound or unbound, discrete or broad, atomic or molecular. The advantages of XANES analysis are outlined below in Figure 41.

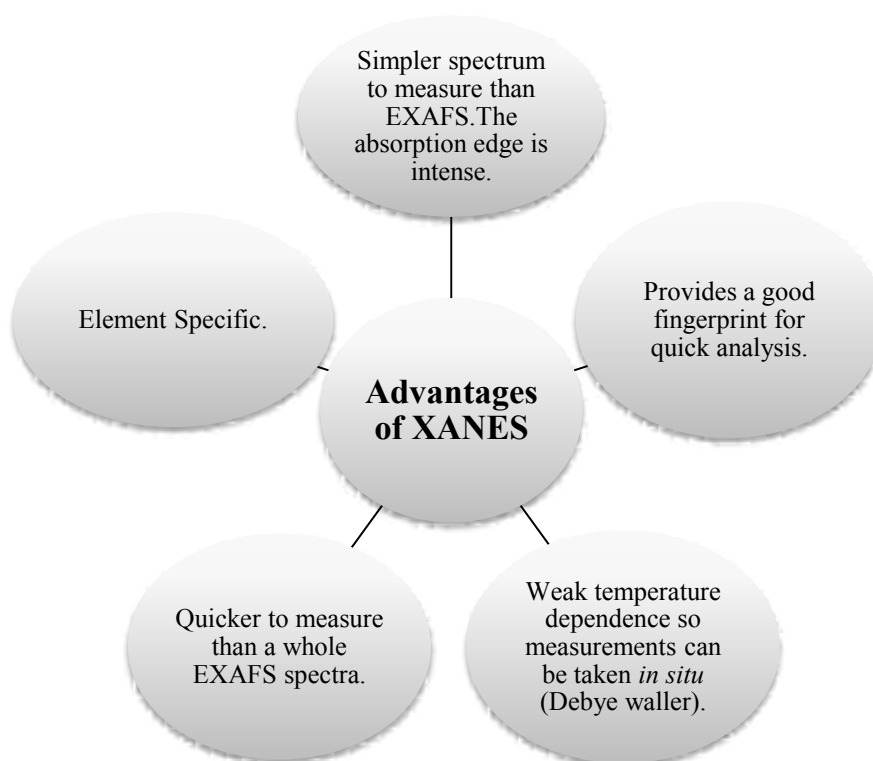


Figure 41. Summary of the advantages of XANES analysis.

Although XANES benefits from the above advantages, it can be very complicated to analyse, since features are dominated by multiple scattering resonances of the photoelectrons ejected at low kinetic energy. This gives rise to a large scattering cross section. The EXAFS equation breaks down at low k , due to the $1/k^3$ term and the increase in the mfp at very low k . This complicates the XANES interpretation significantly, and as a consequence, the majority of XANES analysis is limited to a semi-quantitative interpretation.

For the majority of analysis, the approach used is therefore through linear combination fittings (LCF's). Here, linear combinations of known spectra from reference compounds are able to quantify ratios of valence states and phases within unknown compounds. Most users refer to the ATHENA software to carry out this analysis. The fits can be done using normalized $\mu(E)$ spectra or $\chi(k)$ spectra. A specific example of LCF use is in determining reaction kinetics across a series of spectra in an oxidation or reduction reaction. Intermediate spectrums can be fitted with LCF's using the start and end compound, and the rate determined.

4.9.7. Data Reduction

Regardless of the acquisition mode applied, data reduction is essential for analysis, to manipulate the data into a standardized form. The following steps are performed:

- (i) Measured intensities are converted to absorption $\mu(E)$, to derive a plot of $\mu(E)$ against energy/eV.
- (ii) A smooth pre-edge function is subtracted from $\mu(E)$, to remove the baseline from the EXAFS. This accounts for any instrumental background, and absorption from other edges.
- (iii) A post-edge function is subtracted. Post-edge background subtraction involves drawing a smooth background through the oscillatory part of the XAFS and extracting $\chi(k)$.
- (iv) E_0 is defined. This is usually performed taking the maximum of the first or second derivative of $\mu(E)$.
- (v) The data is normalised between 0 and 1, i.e. so that the edge jump is equal to 1. This allows the user to compare between data sets, as well as the comparison of data with theory.
- (vi) A conversion is performed from $\chi(E)$ to $\chi(k)$, i.e. isolation of the XAFS $\chi(k)$.
- (vii) k -weighting of the XAFS is performed (weighting between k^{-1} - k^3). This can then be Fourier transformed to give a radial distribution plot in R-Space.

4.9.7.1. Fourier Transforms (FT)

Fourier transforms are an essential part of XAFS. The use of Fourier transforms (FT) in XAFS was discovered in the early 1970s, after Dale Sayer, Edward Stern, and Farrel Lytle demonstrated that a Fourier transform could be used to analyze the absorption spectra [43]. In short, an FT is a mathematical transform which converts one mathematical function into another. In XAFS, the FT essentially acts as a frequency filter transforming into frequency space, which results in a radial distribution function where peaks correspond to the most likely distances of the nearest-neighbours. The FT of an infinite sine wave is a delta function. For $\sin(2k)$, this is a peak at $R=1$. The FT can therefore take a signal which is delocalised in k -space, and transform it so that it is localised in R space (See Figure 42). In other words, FT's can break down a k -space signal into its different constituent frequencies. The IFFEFIT package enables the user to perform FT's quickly and easily, with the ability to do both forward FT's and reverse.

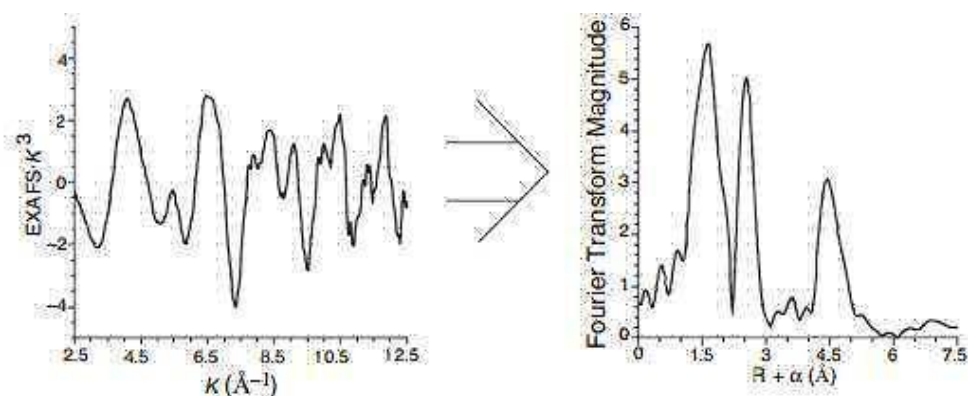


Figure 42. FT delocalise in k - space to localised in R space [44].

4.9.8. IFFEFIT

IFEFFIT is a combination of programs for XAFS analysis, including Hephaestus, Athena and Artemis [43]. Athena is the software specifically designed for the XANES part of the analysis, whilst Artemis is the software primarily used for EXAFS investigations. The software enables the user to do a multitude of tasks including the following:

- Read/Write ASCII data files.
- Data manipulation.
- Data plotting.
- XAFS pre and post edge removal, normalisation and E_0 determination.
- XAFS Fourier Transform (Hanning, Kaiser-Bessel, and Sine Window Functions).
- Simultaneous refinement of multiple data sets.
- Apply constraints and restraints to the fit.

The software package was constructed primarily by Matt Newville, and the web page is hosted at CARS.

4.9.9. Preparing Your Sample (Solids)

There are many challenges associated with the preparing of samples for beamtime. Not only must they be both uniform and homogeneous, as with any experiment, the use of pure and well characterised materials is also necessary. The amount of sample used in the experiment is a key factor, influenced by both the experimental mode used (being transmission or fluorescence), and the edge chosen.

Figure 43 indicates how the edge may be chosen. Edges used should not have an energy greater than 40 keV. For smaller atomic numbers, the energy to excite the core electron is

less, so it may be possible to use the K-edge. For greater atomic numbers, an increase in the binding energy occurs, so a greater edge such as the L- or M-edge may be required.

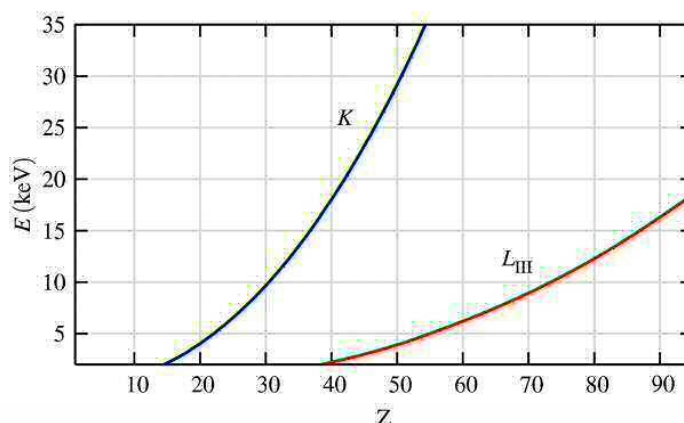


Figure 43. Plot of the Atomic number, Z , versus Energy/eV.

Hard X-ray region: 4-40 keV Soft X-ray region: 0.2-4 keV [45].

With a knowledge of the edge energy, the amount of sample to be used can be considered (Equation 22). This can be done by calculating the total absorption of the sample. To do this the absorption coefficient, μ , is calculated using the following equation:

$$\mu = \sigma \rho$$

Equation 22

Where, σ = Cross section, ρ = Density.

The cross section can be obtained online from various XAFS related sites. The absorption co-efficient is calculated for each of the elements in the sample, and the total absorption interpreted. For transmission, the absorber should be between 0.1-1.5 absorption lengths, with the total absorption < 2.5 (See Appendix A5 for worked example).

For the work involved herein, the molybdenum has been loaded onto an Fe_2O_3 support. The energy of the Mo K-edge is very high (approximately 19900 eV), therefore a transmission experiment is possible. However the absorption properties of Fe must also be considered (see Appendix A5).

Problems with an Absorbing matrix:

Care must be taken for samples in which an element is supported on an absorbing support, e.g. TiO_2 , CeO_2 , Fe_2O_3 . To solve for this, dilute samples must be considered, or the experiment run in fluorescence mode acquisition. Typical diluting agents include cellulose

or boron nitride. It is important to note never to use powders with particle sizes larger than the absorption length.

With the amount of sample to use calculated, and the acquisition mode chosen, the sample can be pelletized (either with or without the diluting agent), using the Press and DIE located within the support labs at Diamond.

4.9.10. Experimental

The required amount of $\text{MoO}_x/\text{Fe}_2\text{O}_3$ (See table 6), was mixed with 0.1 g of cellulose, and ground to give a uniform coloured powder. This was then added to the DIE and pressed to 0.5 tonnes. The pellet was loaded onto the designated sample rack. Mo k-edge XAFS studies were carried out on the B18 beamline at the Diamond Light Source, Didcot, UK. Measurements were performed using a QEXAFS setup with a fast-scanning Si (111) double crystal monochromator. The time resolution of the spectra reported herein was 5 min/spectrum ($k_{\text{max}} = 18$), on average three scans were acquired to improve the signal to noise level of the data. All transmission XAFS spectra were acquired concurrently with a Mo foil placed between I_t and I_{ref} .

Table 6. Masses used for the various loadings of Mo on Fe_2O_3 . A small edge step of 0.1 was achievable for the monolayer samples, since any higher and the absorption properties of Fe would be too high.

Sample	Mass of sample to use / g	Mass of cellulose to add / g	Edge jump
1ML $\text{MoO}_x/\text{Fe}_2\text{O}_3$	0.35	0.1	~0.1
3ML $\text{MoO}_x/\text{Fe}_2\text{O}_3$	0.1	0.1	~0.1
6ML $\text{MoO}_x/\text{Fe}_2\text{O}_3$	0.05	0.1	~0.1
Bulk $\text{Fe}_2(\text{MoO}_4)_3$	0.04	0.1	~1
MoO_3	0.025	0.1	~1

5. References

1. Lubke, M., *Continuous hydrothermal flow synthesis of haematite nanoparticles*, 2014, University College London.
2. Bowker, M., et al., *The selective oxidation of methanol to formaldehyde on iron molybdate catalysts and on component oxides*. Catalysis Letters, 2002. **83**(3-4): p. 165-176.
3. Song, L.X., et al., *Formation, structure and physical properties of a series of alpha- MoO_3 nanocrystals: from 3D to 1D and 2D*. Crystengcomm, 2012. **14**(8): p. 2675-2682.
4. Andersson, A., M. Hernelind, and A. Augustsson, *A study of the ageing and deactivation phenomena occurring during operation of an iron molybdate catalyst in formaldehyde production*. Catalysis Today, 2006. **112**(1-4): p. 40-44.

5. Ramachandra, B., et al., *Partial oxidation of methanol to formaldehyde on molybdenum based mixed oxide catalyst*. Catalysis Letters, 2005. **105**(1-2): p. 23-27.
6. House, M.P., et al., *Effect of varying the cation ratio within iron molybdate catalysts for the selective oxidation of methanol*. Journal of Physical Chemistry C, 2008. **112**(11): p. 4333-4341.
7. Soares, A.P.V. and M.F. Portela, *Methanol selective oxidation to formaldehyde over iron-molybdate catalysts*. Catalysis Reviews-Science and Engineering, 2005. **47**(1): p. 125-174.
8. Sunkou, M.R., et al., *INFLUENCE OF THE PREPARATION METHOD ON THE BEHAVIOR OF FE-MO CATALYSTS FOR THE OXIDATION OF METHANOL*. Journal of Materials Science, 1995. **30**(2): p. 496-503.
9. Davies, P.R. and G.G. Mariotti, *Oxidation of methanol at Cu (110) surfaces: New TPD studies*. The Journal of Physical Chemistry, 1996. **100**(51): p. 19975-19980.
10. Gorte, R., *Temperature-programmed desorption for the characterization of oxide catalysts*. Catalysis Today, 1996. **28**(4): p. 405-414.
11. Mullins, D.R., M.D. Robbins, and J. Zhou, *Adsorption and reaction of methanol on thin-film cerium oxide*. Surface Science, 2006. **600**(7): p. 1547-1558.
12. Christmann, K. and J. Demuth, *The adsorption and reaction of methanol on Pd (100). I. Chemisorption and condensation*. The Journal of Chemical Physics, 1982. **76**(12): p. 6308-6317.
13. Poulston, S., et al., *Temperature-programmed desorption studies of methanol and formic acid decomposition on copper oxide surfaces*. Catalysis Letters, 1998. **52**(1-2): p. 63-67.
14. <http://www.bris.ac.uk/nerclsmf/techniques/gcms.html>.
15. http://instructor.physics.lsa.umich.edu/adv-labs/Mass_Spectrometer/MassSpecQMS.pdf.
16. <http://www4.nau.edu/microanalysis/microprobe-sem/instrumentation.html>.
17. <http://www.pacificpumpgroup.com/product/sliding-rotary-vane-vacuum-pumps-o4.html>.
18. Scoles, G., et al., *Atomic and molecular beam methods*. Vol. 1. 1988: Oxford University Press New York.
19. Faraday, M., *Experimental researches in electricity* 1951: Magikeria.
20. Larkin, P., *Infrared and Raman Spectroscopy; Principles and Spectral Interpretation* 2011: Elsevier Science.
21. Ryczkowski, J., *IR spectroscopy in catalysis*. Catalysis Today, 2001. **68**(4): p. 263-381.
22. Hollas, J.M., *Modern Spectroscopy* 2004: Wiley.
23. Smith, B.C., *Fundamentals of Fourier Transform Infrared Spectroscopy*. 2 ed 2011: Taylor & Francis.
24. Armaroli, T., T. Bécue, and S. Gautier, *Spectroscopie infrarouge en réflexion diffuse (DRIFTS) : application à l'analyse in situ de catalyseurs*. Oil & Gas Science and Technology - Rev. IFP, 2004. **59**(2): p. 215-237.
25. Armaroli, T., T. Becue, and S. Gautier, *Diffuse reflection infrared spectroscopy (DRIFTS): Application to the in situ analysis of catalysts*. Oil & Gas Science and Technology-Revue D Ifp Energies Nouvelles, 2004. **59**(2): p. 215-237.
26. Marinkovic, N.S., Q. Wang, and A.I. Frenkel, *In situ diffuse reflectance IR spectroscopy and X-ray absorption spectroscopy for fast catalytic processes*. Journal of Synchrotron Radiation, 2011. **18**(3): p. 447-455.
27. P.V. Naik, P.o.p., *Quantum Theory*, Page. 279.
28. Einstein, A., *The photoelectric effect*. Ann. Phys, 1905. **17**: p. 132.
29. Brunauer, S., P.H. Emmett, and E. Teller, *Adsorption of gases in multimolecular layers*. Journal of the American Chemical Society, 1938. **60**: p. 309-319.
30. McMillan, W. and E. Teller, *The assumptions of the BET theory*. The Journal of Physical Chemistry, 1951. **55**(1): p. 17-20.
31. <http://www.chemistrylearning.com/adsorption-isotherm/>.

-
32. <http://www.diamond.ac.uk/Beamlines/Spectroscopy/B18/Specification.html>.
 33. Dent, A.J., et al., *Performance of B18, the Core EXAFS Bending Magnet beamline at Diamond*. 15th International Conference on X-Ray Absorption Fine Structure (Xafs15), 2013. **430**.
 34. Dent, A.J., et al., *B18: A core XAS spectroscopy beamline for Diamond*. 14th International Conference on X-Ray Absorption Fine Structure (Xafs14), Proceedings, 2009. **190**.
 35. Mino, L., et al., *Low-dimensional systems investigated by x-ray absorption spectroscopy: a selection of 2D, 1D and 0D cases*. Journal of Physics D-Applied Physics, 2013. **46**(42).
 36. Pettifer, R., M. Borowski, and P. Loeffen, *The physics of ionization chambers—or how to improve your signal-to-noise ratio for transmission EXAFS measurements*. Journal of synchrotron radiation, 1999. **6**(3): p. 217-219.
 37. Smart, L.E. and E.A. Moore, *Solid State Chemistry: An Introduction*. 4 ed 2012: Taylor & Francis.
 38. Koningsberger, D., et al., *XAFS spectroscopy; fundamental principles and data analysis*. Topics in Catalysis, 2000. **10**(3-4): p. 143-155.
 39. Kelly, S., D. Hesterberg, and B. Ravel, *Analysis of soils and minerals using X-ray absorption spectroscopy*. Methods of soil analysis. Part, 2008. **5**: p. 387-464.
 40. Vlaic, G. and L. Olivi, *EXAFS spectroscopy: a brief introduction*. Croatica Chemica Acta, 2004. **77**(3): p. 427-433.
 41. Lytle, F., D. Sayers, and E. Stern, *Extended X-ray-absorption fine-structure technique. II. Experimental practice and selected results*. Physical Review B, 1975. **11**(12): p. 4825.
 42. Rehr, J. and A. Ankudinov, *Progress in the theory and interpretation of XANES*. Coordination Chemistry Reviews, 2005. **249**(1): p. 131-140.
 43. Newville, M., *IFEFFIT: interactive XAFS analysis and FEFF fitting*. Journal of synchrotron radiation, 2001. **8**(2): p. 322-324.
 44. J. E. Penner-Hahn, X.-r.A.S., The University of Michigan, Ann Arbor, MI, USA.
 45. Matthew Newville, F.o.X., Chapter 2. X-ray Absorption and Fluorescence, Page 6, Consortium for Advanced Radiation Sources University of Chicago, Chicago, IL.

Chapter 3: Bulk Metal Oxides for Methanol Oxidation

Contents

1. Introduction	119
2. Experimental	122
2.1. Isothermal Pulsed Reaction	122
2.2. Continuous flow studies	122
2.3. Production of Iron molybdate with various Mo:Fe ratios	122
3. Results and Discussion	124
3.1. The Fundamental Oxides: MoO_3 and Fe_2O_3 and $\text{Fe}_2(\text{MoO}_4)_3$	124
3.1.1. BET	124
3.1.2. Raman	126
3.1.3. FT- IR	127
3.1.4. XRD	128
3.1.5. Reactivity Data	129
3.1.6. DRIFTS	135
3.1.7. Thermal Plots	139
3.2. Varying the Mo:Fe Ratio	139
3.2.1. BET	140
3.2.2. Raman	140
3.2.3. XRD	143
3.2.5. Reactivity Data	147
3.3. Varying the Preparation Method	160
3.3.1 Co-Precipitation with Adaptations	160
3.3.2. Effects of Calcination Temperature	163

3.3.3. Solid State Mixing	167
3.3.4. Preparation of High Surface Area Molybdena.....	172
3.4. Variables in CATLAB operation	179
3.4.1. Ramped Pulse versus Isothermal pulse.....	179
3.4.2. Mass Size Variation.....	180
4. Conclusions.....	184
5. References.....	185

1. Introduction

The chapter herein investigates a range of FeMo containing catalysts for their reactivity in the selective oxidation of methanol to formaldehyde. Single oxides of MoO_3 and Fe_2O_3 , and mixed phase stoichiometric $\text{Fe}_2(\text{MoO}_4)_3$ will initially be characterised and probed for their reactivity via temperature programmed studies. With a sound understanding of these fundamental phases, this aids an understanding of novel catalysts synthesised for the same catalytic reaction. The most conclusive characterisation techniques applied for these bulk materials include Raman, XRD, XPS and IR.

Various preparation routes will be studied and examined for their effect on catalyst structure and performance. $\text{Fe}_2(\text{MoO}_4)_3$ synthesis prepared via co-precipitation has been at the forefront of catalyst preparation since it was first reported in 1931 by Adkins and co-workers [1]. Since then, variables within the preparation method have been extensively investigated, to create catalysts with optimum performance and efficiency [2, 3]. A comprehensive review by Trifiro *et al.* [4] highlights some central considerations during iron molybdate preparation, specifically: the molybdenum ion species within the aqueous solution, the formation of heteropolyanions, and the transition from amorphous to crystalline structure. The influence of pH, ageing time and temperature of the co-precipitated solution, and the ratio of Mo:Fe in the precursor solution are just a few of the many variables to be considered for their effect on the morphology and microstructures of iron molybdate. A review by Soares *et al.* [2] summarises the efforts of several researchers in investigating the optimum preparation method to give catalysts of high homogeneity with enhanced activity. Work by Wachs *et al.* has highlighted the effect of catalyst composition on the activity and selectivity of these materials [5]. Others [6] detail the effect of various parameters including metal loading, calcination temperatures and catalyst surface area, all showing a resounding effect on catalyst performance.

Although co-precipitation has been valued for its use in the preparation of $\text{Fe}_2(\text{MoO}_4)_3$, other preparation routes have been considered, exploiting the fact that catalytic characteristics are highly dependent on the catalyst preparation method employed. The extent of dispersion and interaction between Mo and Fe, the surface area of the catalyst, and the crystal structure are all traits which can be modified through altering the catalyst preparation. One of the simplest methods has involved dry and wet mixing of iron molybdates from solid salts of the two metals [7]. It is thought that the wet mixing gives a more homogeneous spread of Mo, with higher incorporation of the Mo species into the $\text{Fe}_2(\text{MoO}_4)_3$ lattice. More research is required including catalyst testing and

characterisation, if catalysts were to become viable for industrial use. Wachs and Briand [8] have prepared catalysts *in situ* in a fixed bed reactor through simple mixing of MoO_3 and Fe_2O_3 in the absence of water. Remarkably the catalysts showed reactivity data akin to that seen for the industrial catalysts. Iron molybdate was found to be present from the simple mixing and heating of these two solid precursors. The formation of iron molybdate appears to occur readily, with the preparation temperatures employed industrially at approximately 250–400 °C. Beale *et al.* [9] demonstrate the use of a one step-low temperature hydrothermal method to prepare iron molybdates with varying Mo:Fe ratios. Stoichiometric $\text{Fe}_2(\text{MoO}_4)_3$ is found to form as low as 100 °C in a short time period. With the relative ease of its formation, this shows the potential for discovering novel preparation routes for such iron molybdate based catalysts.

Regardless of the preparation procedure employed, it is unanimously agreed that the Mo:Fe ratio plays a crucial role in the catalyst behaviour. A study by Bowker *et al.* [10] explores this in detail. A marked difference was exposed between the behaviour of pure Fe_2O_3 , and catalysts with just a small amount of Mo in the composition. Fe_2O_3 is a poor catalyst, a clear combustor of methanol, with the predominant product as CO_2 . With just small amounts of Mo in the preparation, the sample begins to show selectivity to formaldehyde. Catalytic investigations have uncovered a strong correlation between product distribution and Fe:Mo ratio in nonstoichiometric iron molybdates. The optimum catalysts are believed to be those with a Mo:Fe ratio of 1.5:1 or greater [11].

The catalytic activity of iron molybdate surpasses that of $\alpha\text{-MoO}_3$ significantly [12]. Increased performance is attributed to the catalytically-isotropic ferric molybdate structure [13], where all surface Mo atoms are co-ordinatively unsaturated, and therefore able to act as potential active sites [14]. The activity with Fe mole ratio has been shown to follow a volcano curve plot (Figure 1), as evidenced by Hummadi *et al.* [15]. Beyond a Fe mole fraction of 0.4, the activity rises to a maximum as Fe is added to MoO_3 . The activity then drops off with further loading, as Fe_2O_3 begins to dominate, and the preference alters from formaldehyde for MoO_3 , to combustion products for Fe_2O_3 . This demonstrates the necessity of MoO_3 within the catalyst composition.

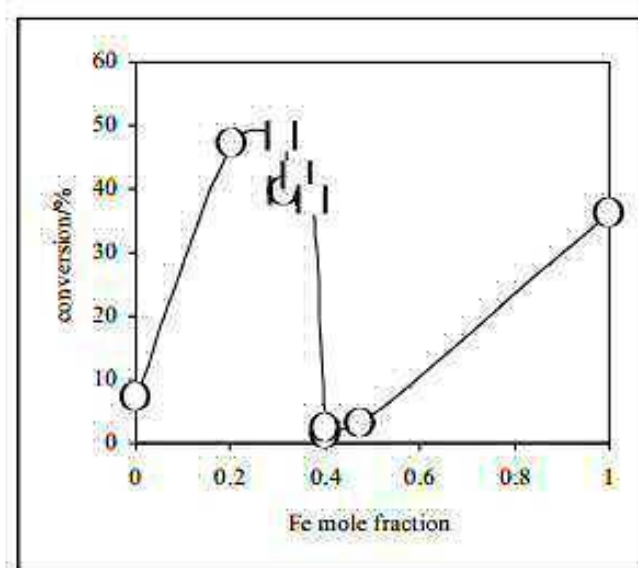


Figure 1. Conversion of methanol vs. mole fraction of Fe, for $\text{Fe}_2(\text{MoO}_4)_3$, Iron Molybdate [15].

A number of explanations for improved catalytic activity with surplus molybdena have been proposed, however there is no substantial proof in the literature as to why this might be. It has been shown that maximum catalytic performance is achieved for bulk iron molybdate with a Mo:Fe atomic ratio of 1.7 [16], showing both a good activity and improvements in formaldehyde selectivity [17, 18]. The balance between the Mo and Fe present within the catalyst is a significant factor, and the catalyst must be tailored to create a compromise between the two. One of the crucial discoveries was that Fe (III) must be well dispersed amongst MoO_3 , to avoid formation of Fe aggregates materializing. For Fe_2O_3 and catalysts where the Mo is in deficit, the Fe cations become close enough in proximity to allow for bridging bidentate formation, subsequently resulting in CO_2 production. Soares *et al.* [11] propose the excess MoO_3 is required as a reservoir for lost MoO_3 through volatilisation at reactor hot spots, with the activity attributed to $\text{Fe}_2(\text{MoO}_4)_3$. Alessandri *et al.* consider MoO_3 to have an indirect influence on the catalytic activity, acting to enhance the overall homogeneity and texture of the active phase [19]. Others have commented on improvements in catalyst mechanical stability with excess MoO_3 .

Although the active phase is neither well understood or agreed amongst authors, there is a vast amount of evidence indicating the surface to be Mo enriched and therefore acting as the active site for the reaction. This high surface concentration of Mo has been revealed by STEM [20] and XPS [21, 22]. Sun-Kuo *et al.* [3] discovered that catalysts

with a Mo:Fe ratio above that for stoichiometric iron molybdate, possessed a Mo-enriched surface of amorphous or low-dimensional crystalline molybdena (MoO_x). This is also agreed by Routray *et al.* [23], who define this MoO_x overlayer as the active site for the reaction. With Mo at the surface, there is a requirement to concentrate on this transition metal oxide and exploit its use further. MoO_3 is shown to be 100 % selective to formaldehyde in TPD [24] measurements, but the performance of the catalyst is hindered by its low surface area. It would be beneficial to improve this surface area, through investigation of molybdena preparation.

This preliminary chapter provides the groundwork for subsequent chapters. Single oxides of MoO_3 and Fe_2O_3 will be investigated and compared to bulk iron molybdate with various Mo:Fe ratios. Preparation modifications and catalytic testing modes will also be addressed.

2. Experimental

2.1. Isothermal Pulsed Reaction

Pulsed flow studies of MeOH/O_2 have been implemented under isothermal conditions, to ensure that product distribution is stable at a given temperature. 1 μl injections of methanol were passed over the catalyst bed every two minutes at an allocated temperature for a set time period.

2.2. Continuous flow studies

Continuous flow studies have been performed under isothermal conditions to investigate whether the pulse flow mode was accurate in representing catalyst performance. Methanol was introduced under gas flow via a methanol bubbler at a flow rate of 30 mlmin^{-1} . Conditions were matched where possible to those used industrially. Therefore the methanol was introduced so that it made up 10 % of the total flow. Once production stabilised, activity and selectivity were measured.

2.3. Production of Iron molybdate with various Mo:Fe ratios

The details of the standard iron molybdate preparation via co-precipitation can be referred to in Chapter 2, Section 2.2. Iron molybdate catalysts have been produced via co-precipitation with a variety of Mo:Fe ratios, including 2.2:1, 1.7:1, 1.5:1, 1:1, 0.5:1 and 0.02:1. The 1.5:1 ratio represents the stoichiometric catalyst, in which there is just one single phase of $\text{Fe}_2(\text{MoO}_4)_3$ in the chemical composition. For Mo ratios in excess of this, MoO_3 also exists. With Mo ratios lower than the stoichiometric value, the catalyst becomes iron rich, which can result in the formation of Fe_2O_3 . Catalysts have been

prepared in various ratios to investigate the effects different possible oxide phases present can have on catalytic performance.

Several adaptation of the co-precipitation method have been performed. Firstly, the effects of calcination method, time and temperature have been investigated for their influence on catalyst homogeneity. Secondly, the effect of filtering the catalyst prior to calcination was explored. The co-precipitation method described in Chapter 2.2 was repeated with the following modifications:

Method 1:

After drying, a calcination was performed in one of two ways. A calcination was performed at 500 °C for 8 hours in the muffle furnace. Secondly, a calcination was performed at 500 °C for 8 hours in a tube furnace, under a steady flow of (i) compressed air and (ii) nitrogen.

Method 2:

After drying, a calcination was performed at the following temperatures 120, 220, 320, 380, 400, 450 and 500 °C for 8 hours in the tube furnace (Figure 1, Chapter 2), under a steady flow of compressed air.

Method 3:

Once all the iron nitrate precursor was added during co-precipitation, the temperature was increased to 90 °C to evaporate off the majority of the liquid. The resulting yellow solution was allowed to filter overnight using a whatman filter paper and a funnel, after which it was dried and calcined at 500 °C.

Method 4:

Once all the iron nitrate solution was added during co-precipitation, the temperature was increased to 90 °C to evaporate off the majority of the liquid. The resulting yellow solution was allowed to filter overnight using a whatman filter paper and a funnel. A green solid remained on the filter paper, which was washed with water acidified to pH 2 (approx. 400 ml). The catalyst was dried and calcined at 500 °C.

Alternative preparations:

An alternative approach has been employed in an attempt produce bulk iron molybdate. $\text{Fe}(\text{NO}_3)_3 \cdot 9\text{H}_2\text{O}$ and $(\text{NH}_4)_6\text{Mo}_7\text{O}_{24} \cdot 4\text{H}_2\text{O}$ were added to a crucible in the required Mo:Fe ratio. The precursors were ground using a pestle and mortar to give a uniform

consistency. Once mixed, the solid was dried at 120 °C / 24 hours, followed by calcination at 500 °C / 24 hours. The homogeneity obtained through this method was examined through Raman mapping.

A variant on this method involved adding a few drops of dilute HNO₃ to the mix, to mimic the acidic conditions employed in the co-precipitation method.

3. Results and Discussion

3.1. The Fundamental Oxides: MoO₃ and Fe₂O₃ and Fe₂(MoO₄)₃

3.1.1. BET

The BET surface areas of bulk MoO₃, Fe₂O₃ and stoichiometric Fe₂(MoO₄)₃ (Mo:Fe 1.5:1) are detailed in Table 1. It is important to address the surface area of catalysts prior to testing their catalytic performance, to make surface area-activity correlations. For example, if two catalysts have identical conversions at the same temperature, but the surface area of one is appreciably lower than the other; this will ultimately have the highest activity per unit area, and therefore be the more efficient catalyst. Fundamentally, smaller particles expose a greater surface area of catalyst for substrate interaction, which can improve the specific activity.

However, other considerations must also be addressed. If particle morphology is modified by decreasing particle size, or particle curvature affected: this could alter the exposed active planes, therefore reducing the adsorption site availability for reaction. A further consideration is whether the catalytic performance is independent of the bulk phase or not. It has already been mentioned that Mo plays a key role in the activity of these catalysts. Therefore the specific surface area of Mo could be a crucial factor in tailoring such materials.

Table 1. BET surface areas for standard catalysts.

Catalyst	Surface Area / m ² g ⁻¹
MoO ₃	1
Commercial Fe ₂ O ₃ (<50 nm)	21
Commercial Fe ₂ O ₃ (<50 nm) after calcination at 500 °C / 3 hours	20
Fe ₂ O ₃ in-house production	7-8
CHFS produced Fe ₂ O ₃	76
CHFS Fe ₂ O ₃ after calcination at 500 °C / 3 hours	25
Fe ₂ (MoO ₄) ₃	6

The acquired data shows that MoO_3 demonstrates a particularly poor surface area, and cannot compete with the superior areas shown for the iron containing oxides. It is expected that the activity will be 2-4 times lower than the industrially-favoured iron molybdate catalyst. This is a result of the irregular structure exhibited in this bulk oxide.

Data also shows that the Fe_2O_3 produced in-house could not match that of the commercial standard. A further technique has involved a collaboration with UCL, in which Fe_2O_3 nanoparticles are produced via Continuous Hydrothermal Flow Synthesis. This allows for rapid precipitation of crystalline materials. Surface areas were appreciably higher, at $75 \text{ m}^2\text{g}^{-1}$, which could potentially enable a greater surface area of catalyst for substrate interaction, therefore improving the catalyst activity. However, problems arose on exposing the CHFS haematite to typical calcination conditions, as shown by the significant loss in surface area (by approximately 60 %) after a calcination at 500°C for 3 hours. A loss of surface area in nanoparticulate systems can be explained in terms of the surface free energy. Smaller particles possess a higher surface free energy, which will encourage the agglomeration and growth of particles to reduce this unfavourable situation [25]. Sintering also becomes a problem at high temperature.

BET revealed that the commercial haematite was stable under the same calcination conditions, with a negligible decline in surface area. The surface area adopted by this catalyst is significantly higher than bulk $\text{Fe}_2(\text{MoO}_4)_3$, and could lead to the possibility of more active catalysts with Mo doping.

3.1.2. Raman

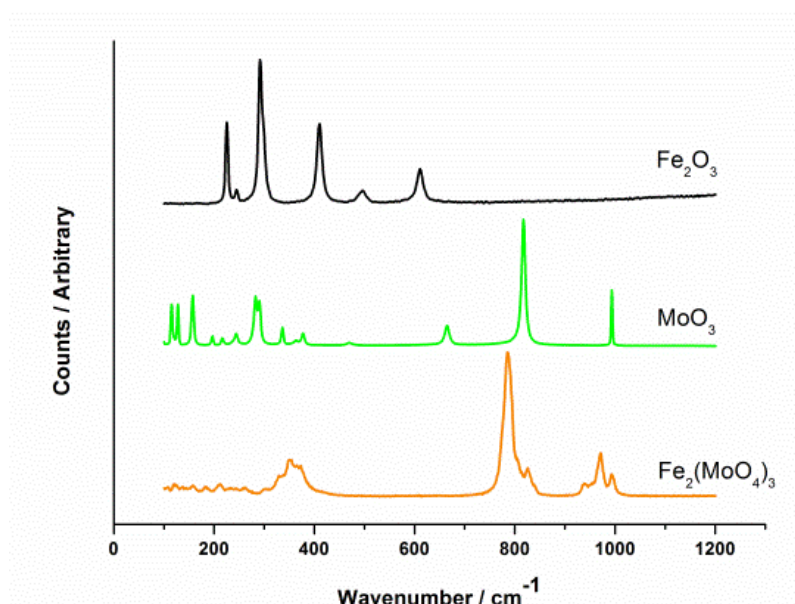


Figure 2. Raman data for the bulk standards of Fe_2O_3 , MoO_3 and $\text{Fe}_2(\text{MoO}_4)_3$. These data can be used for phase identification in future catalysts.

Raman spectroscopy is one of the most widely used techniques for identifying iron molybdates and their component oxides. Raman spectra have been recorded prior to catalyst use (Figure 2). The spectra are dominated by M-O-M and M=O stretches. The key bands to identify are presented in Table 2, with associated assignments.

Table 2. Raman bands and assignments MoO_3 and $\text{Fe}_2(\text{MoO}_4)_3$ systems.

Wavenumber / cm^{-1}	Band Assignment
667	Mo-O-Mo symmetric stretch in MoO_3 [14, 26]
700-850	Antisymmetric Mo-O-Mo stretching vibrations in MoO_3 [26]
	T_d Mo species in $\text{Fe}_2(\text{MoO}_4)_3$ [27]
780	Mo-O-Mo asymmetric vibrations in $\text{Fe}_2(\text{MoO}_4)_3$ [28]
821	Mo-O-Mo asymmetric stretch in MoO_3 [26] Mo=O asymmetric stretch in $\text{Fe}_2(\text{MoO}_4)_3$
966	<i>Debate in assignments:</i> Mo=O symmetric stretch of the three distinct isolated sites in $\text{Fe}_2(\text{MoO}_4)_3$ [26] Fe-O-Mo asymmetric stretch in $\text{Fe}_2(\text{MoO}_4)_3$
992	Terminal Mo=O symmetric stretch in MoO_3 [14, 26, 29] Symmetric Mo=O stretch in $\text{Fe}_2(\text{MoO}_4)_3$

The Raman spectra for bulk MoO_3 exhibits characteristically sharp crystalline bands at 990, 820, 660 and 280 cm^{-1} . For Fe_2O_3 , the bands to recognise are located at 600, 410, 290 and 220 cm^{-1} . The Raman bands at 965, 930, 780 and 350 cm^{-1} are key indicators of the mixed oxide phase $\text{Fe}_2(\text{MoO}_4)_3$. It should be noted that the bands at 821 and 990 cm^{-1} are much weaker in $\text{Fe}_2(\text{MoO}_4)_3$, and are not related to those seen for MoO_3 . It is clear to differentiate between these phases due to the additional vibrations unique to MoO_3 at 660 and 284 cm^{-1} .

For stoichiometric $\text{Fe}_2(\text{MoO}_4)_3$, there is no evidence for Fe_2O_3 , implying that there was no excess Fe present during the co-precipitation synthesis. However, Fe_2O_3 is notoriously known for its dark red colour, which may cause problems in its identification when present in trace amounts. The Raman bands shown in Figure 2 are in good agreement with the literature, and can now be used to assign for these phases in future novel catalysts.

3.1.3. FT- IR

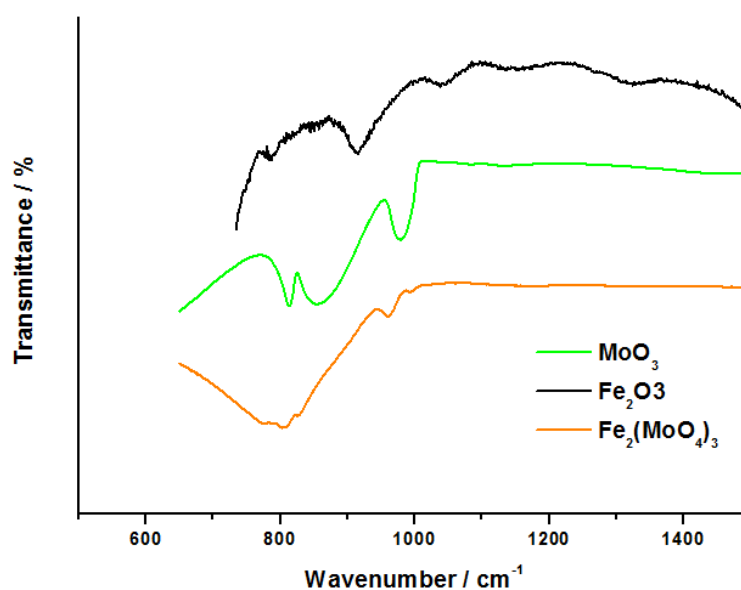


Figure 3. FT- IR data for the bulk standards of Fe_2O_3 , MoO_3 and $\text{Fe}_2(\text{MoO}_4)_3$.

Infrared spectroscopy is a complementary vibrational spectroscopy technique, used to investigate catalyst composition. IR was run in ATR mode (attenuated total reflectance), which is typically applied to strongly absorbing samples. If the angle of the incident IR radiation bombarding the surface exceeds the critical angle, total internal reflectance

occurs. As the sample begins to absorb IR radiation, the change in intensity of the reflected light gives rise to an absorption spectrum.

Figure 3 shows the IR spectra obtained for Fe_2O_3 , MoO_3 and $\text{Fe}_2(\text{MoO}_4)_3$, with similar trends observed to those seen in the Raman. The most prominent band for MoO_3 is seen at 990 cm^{-1} [27, 30, 31], representative of the $\text{Mo}=\text{O}$ stretching mode. For $\text{Fe}_2(\text{MoO}_4)_3$, there is a shift of this major peak at 990 cm^{-1} , to 970 cm^{-1} . Other IR-active modes of $\text{Fe}_2(\text{MoO}_4)_3$ include the $\text{M}=\text{O}$ stretch at 828 cm^{-1} (broad) [32] and tetrahedral MoO_4 at 886 cm^{-1} [18]. For hematite, the most characteristic bands occur at 786 , 915 (broad) and 1050 cm^{-1} . [33]

3.1.4. XRD

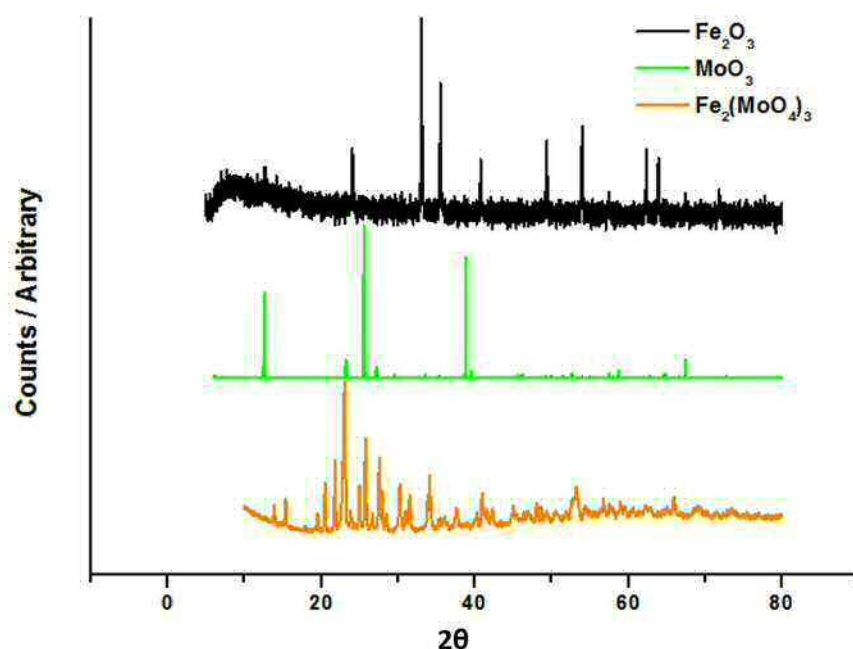


Figure 4. XRD data for bulk standards of Fe_2O_3 , MoO_3 and $\text{Fe}_2(\text{MoO}_4)_3$.

Diffraction patterns for Fe_2O_3 , $\text{Fe}_2(\text{MoO}_4)_3$ and MoO_3 are displayed in Figure 4. All demonstrate a high degree of long range order, making their identification relatively straightforward. The results presented correspond well with the patterns seen in the literature [2, 34]. For $\alpha\text{-MoO}_3$, the most significant band to identify appears at $12^\circ 2\theta$, relating to the (020) reflection. In addition to this, the peaks at 25.7 , 27.3 and $39.2^\circ 2\theta$ can be indexed to MoO_3 , attributed to the planes at (040), (021) and (060) respectively. The Bragg peaks are particularly sharp for this oxide, demonstrating its highly crystalline

nature. $\text{Fe}_2(\text{MoO}_4)_3$ can be identified through the reflections at 19.5, 20.5, 21.8 and 23.1 ° 2 θ , which correspond to the (204), (313), (214) and (114) planes respectively. $\alpha\text{-Fe}_2\text{O}_3$ shows bands at 24.16, 33.20, 35.66, 40.90, 49.52, 54.12, 61.74 and 64.62 ° 2 θ , identified as the (012), (104), (110), (113), (024), (116), (213) and (300) planes respectively.

3.1.5. Reactivity Data

The following section assesses the reactivity data achieved through TPD and TPPFR of methanol for the single oxides and stoichiometric $\text{Fe}_2(\text{MoO}_4)_3$. Experimental procedures can be referred to in Chapter 2, Section 3.

The reactivity profile of Fe_2O_3 is shown in Figures 5-6. Whilst considerably more active than MoO_3 (as shown by the lower conversion temperature), Fe_2O_3 demonstrates 0 % selectivity to formaldehyde, acting as a combustor of methanol. On initial inspection of the TPD data, it is obvious that the catalyst performs poorly in the discussed reaction, as evidenced through the CO_2 and H_2 production at higher temperatures. The presence of these two species is the result of a bound formate intermediate, which has been confirmed through IR spectroscopy [17, 35]. Methanol adsorbs dissociatively on Fe_2O_3 to yield methoxy and hydroxy intermediates. XPS studies have revealed a decrease in the O:Fe surface ratio after chemisorption of methanol at room temperature, as a partial reduction of the surface occurs to facilitate the partial oxidation of the adsorbate [36]. Subsequently, oxygen insertion from the lattice oxygen into the methoxy intermediate results in the formate intermediate. This process is highly favourable, with the absence of any CO confirming the loss of methoxy. Strong Fe-O interactions stabilise this bidentate formate over monodentate methoxy. The low surface enthalpy also promotes combustion to CO_2 [34, 37].

Referring to the TPPFR data (Figure 6), it is shown that 50 % conversion is reached by 260 °C, attaining 100 % by 340 °C. The selectivity of the catalyst is mainly towards CO_2 at higher temperatures, with the signal for CO depreciating considerably after 250 °C. The results here differ to those reported by House *et al.* [24], which demonstrates only a small amount of CO formation (<10 % selectivity) being produced at low conversions (<10 %). The Fe_2O_3 reactivity data presented is for the aforementioned commercial Sigma Aldrich <50 nm particle size powder. The activity is greater than the values reported in the literature, due to the substantial increase in surface area (Table 1), allowing for increased methanol conversion.

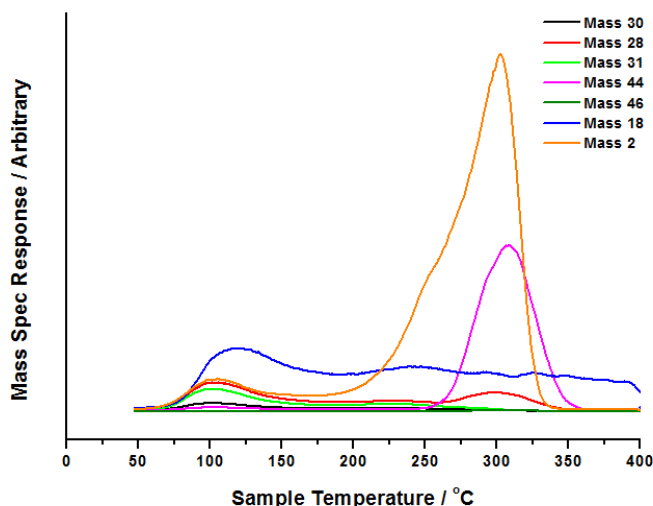


Figure 5. TPD data for commercial Fe_2O_3 . For these experiments, MeOH was dosed over the catalyst surface under He flow to saturation. The temperature was then ramped to 400°C whilst monitoring the mass spectrometer response. Fragmentation patterns: Mass 30 corresponds to H_2CO , Mass 28 to CO , Mass 31 to MeOH , Mass 44 to CO_2 , Mass 46 to DME, Mass 18 to H_2O and Mass 2 to H_2 . Data presented is the raw data, plotted in real time as seen on the mass spectrometer.

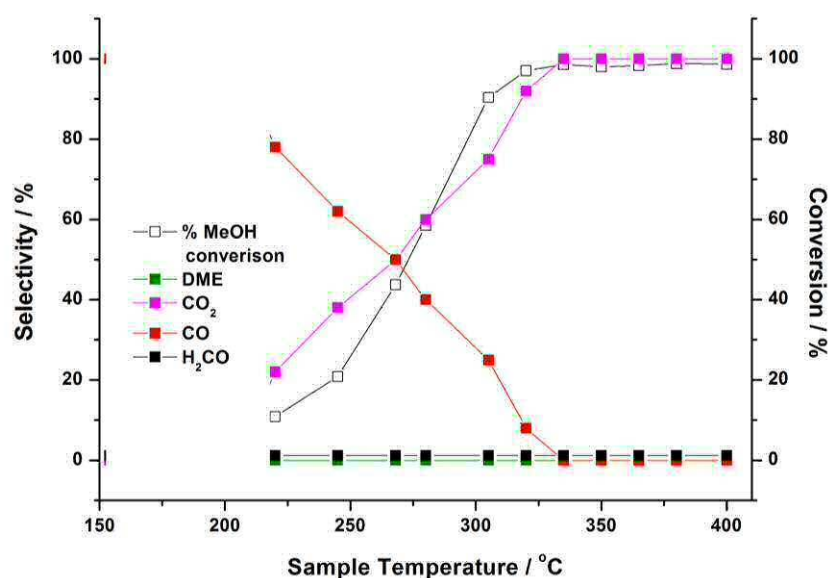
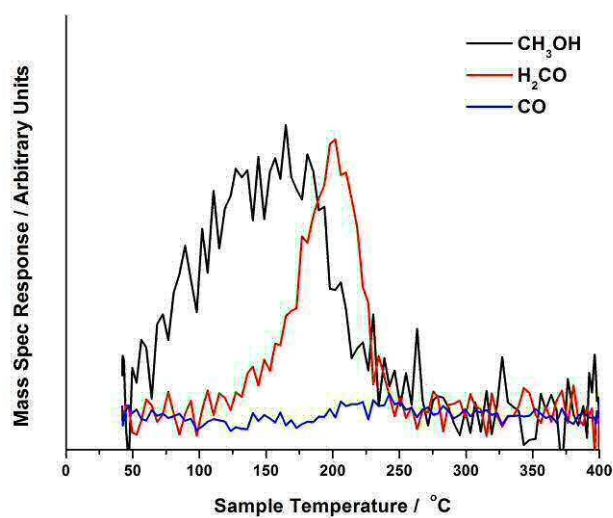
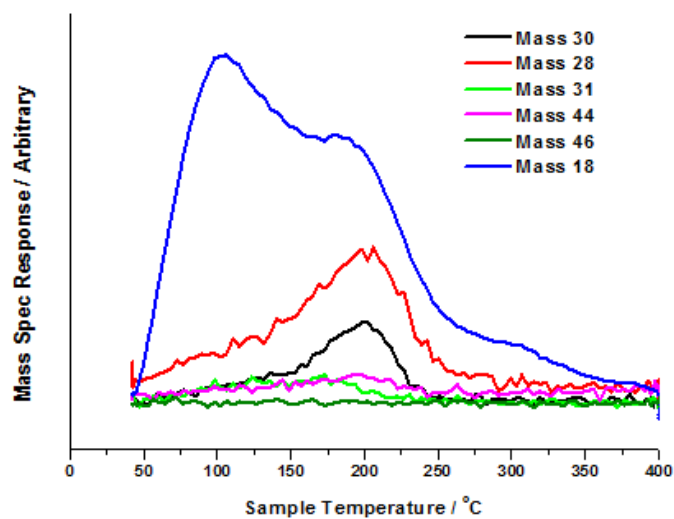


Figure 6. TPPFR data for Fe_2O_3 . For these experiments, MeOH was injected over the catalyst at regular time intervals, whilst ramping to 400°C in 10 % O_2/He . Subtractions have been made for the various cracking fragmentation of each product (Chapter 1, Section 3.3), to give a plot of selectivity and conversion.

In contrast, the reactivity profiles for MoO_3 , show a far superior performance towards formaldehyde selectivity. Referring to Figures 7-8, the TPD demonstrate a 100 % selectivity to formaldehyde. This is a consequence of an adsorbed methoxy intermediate at the surface, as opposed to formate seen for Fe_2O_3 . However, the overall performance of the catalyst is limited in terms of its activity, with the $T_{\text{H}_2\text{CO}}$ at approximately 210°C . The activity can be between 2-4 times lower than the industrially-favoured iron molybdate catalyst [13]. This is primarily a consequence of the low surface area of this catalyst, at just $1\text{m}^2\text{g}^{-1}$, however is also partly attributed to the crystal structure. The structure of $\alpha\text{-MoO}_3$ exists as an orthorhombic double-layered structure, with distorted O_h MoO_6 units [38]. These connect through corner and edge sharing in the bc plane. Van der Waal forces exists between the double layers of MoO_6 . The overall structure is irregular (Figure 18) , with only select faces able to perform the selective oxidation of methanol [39, 40].

The low activity is also exposed in the TPPFR profile (Figure 9). 50 % conversion is not reached until 275°C , only able to obtain 91 % conversion by 360°C . Here, the selectivity to formaldehyde is very high, however begins to decline gradually from 350°C , as a small amount ($<20\%$) of CO_2 becomes evident. Since there is no evidence of other further oxidation products such as CO , this would imply that the CO_2 produced is a result of formate formation at increased temperature as opposed to formaldehyde oxidation. Oxygen mobility is known to be high in MoO_3 , therefore would easily facilitate the insertion of bulk lattice into the adsorbed methoxy to yield formate at the surface.



Figures 7- 8. TPD of MeOH/He for commercial MoO₃, raw (top) and fragmentation subtracted (bottom). Method as Figure 5.

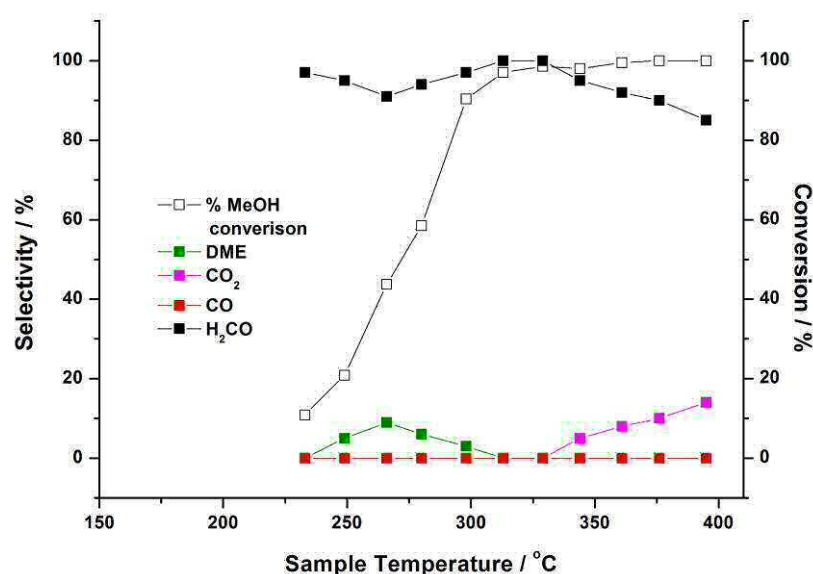
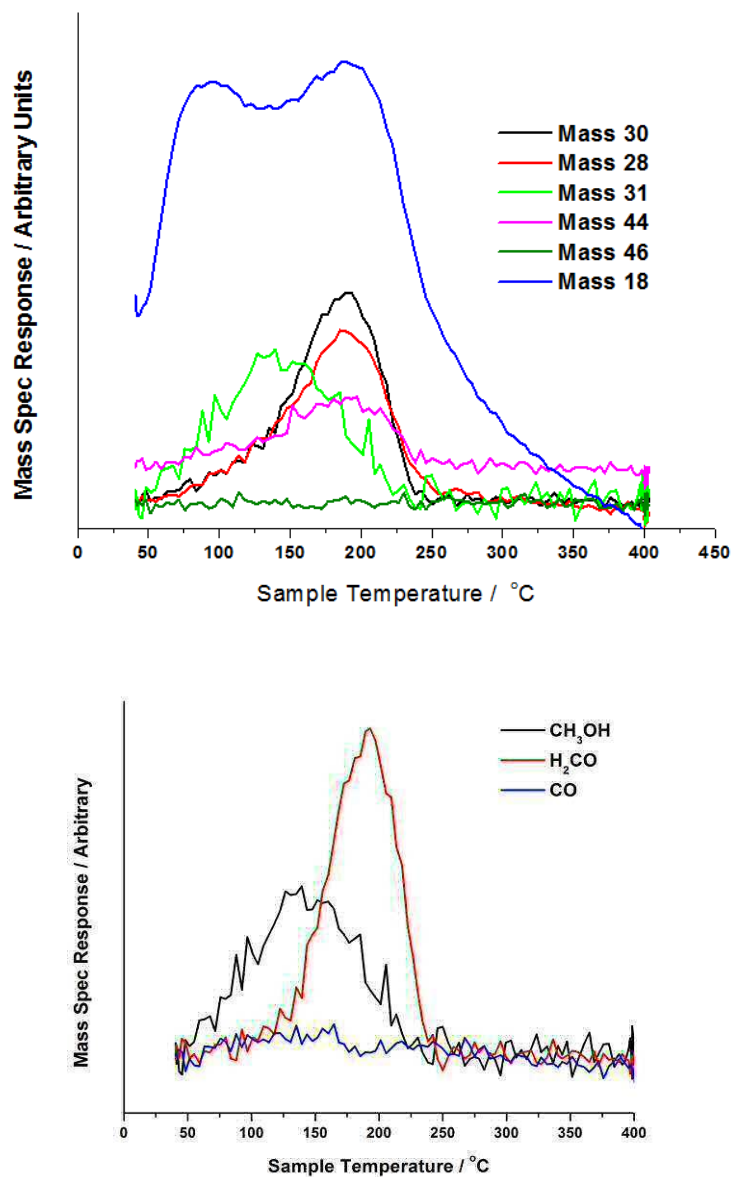


Figure 9. TPPFR for commercial MoO₃. MeOH was injected over the catalyst at regular time intervals, whilst ramping to 400 °C in 10 % O₂/He. Subtractions have been made for the various cracking fragmentation of each product (Chapter 1, Section 3.3), to give a plot for selectivity and conversion.

The stoichiometric catalyst (Mo:Fe 1.5:1), demonstrates a good balance between activity and selectivity. The selectivity to formaldehyde is shown to be 100 % in the TPD profile (Figures 10-11), echoing the results seen for commercial MoO₃. Methoxy dominates as the adsorbed surface intermediate, to yield formaldehyde (H₂CO). However, the amount of H₂CO produced is approximately three times greater than MoO₃, due to the increased surface area of the mixed phase catalyst (Table 1). The increased performance is also attributed to the isotropic ferric molybdate structure [13], which establishes a surface where all surface Mo atoms are co-ordinatively unsaturated and therefore able to act as potential active sites [14].

The TPPFR (Figure 12) reveals 50 % conversion at 240 °C, reaching 100 % conversion by 310 °C (50 °C lower in temperature than bulk MoO₃). The selectivity of the catalyst is virtuous at low temperature, peaking at over 90 % towards formaldehyde. However, this drops to 60 % by 400 °C. At this point further products are detected including CO, rising to approximately 25 % towards the end of the run, and CO₂ rising from 290 °C, to 20 %. Both are considered further oxidation products of formaldehyde.



Figures 10-11. TPD of MeOH/He for stoichiometric $\text{Fe}_2(\text{MoO}_4)_3$, raw (top) and fragmentation subtracted (bottom). Method as Figure 5.

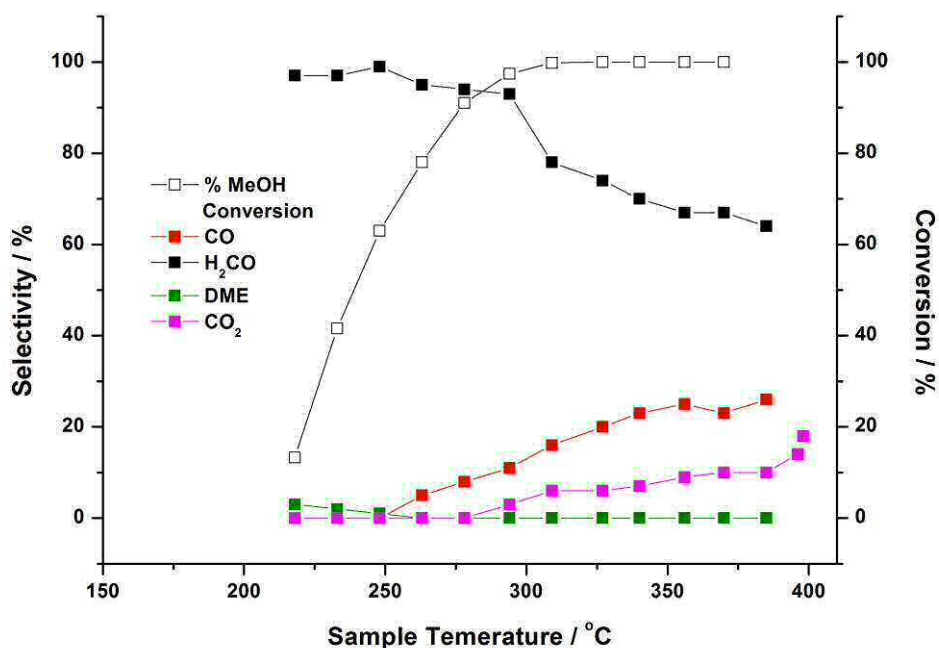


Figure 12. TPPFR for bulk $\text{Fe}_2(\text{MoO}_4)_3$. MeOH was injected over the catalyst at regular time intervals, whilst ramping to 400 °C in 10 % O_2/He . Subtractions have been made for the various cracking fragmentation of each product (Chapter 1, Section 3.3), to give a plot for selectivity and conversion.

3.1.6. DRIFTS

In situ diffuse reflectance infrared Fourier transform spectroscopy (DRIFTS) can be used to monitor surface bound intermediates simultaneously to TPD analysis with methanol. Methanol serves as both the reactant and an excellent probe molecule, allowing the identification of catalyst behaviour under reaction conditions.

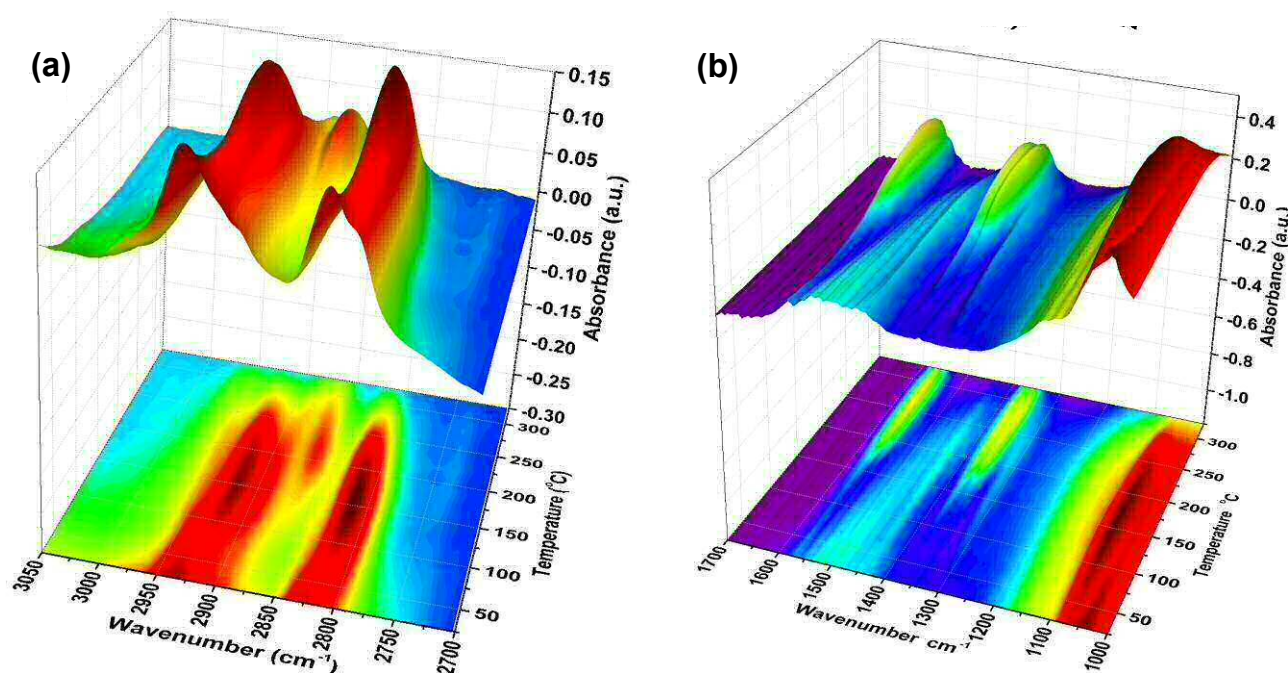


Figure 13 (a-b). *In situ* DRIFTS spectra for Fe_2O_3 under TPD of MeOH/He (differing spectral ranges). The catalyst surface was saturated with MeOH pulses under He at room temperature. The temperature was then raised to 400°C , monitoring the reaction products through TPD with simultaneous DRIFTS analysis of the surface species.

Referring to TPD of MeOH on Fe_2O_3 (Figure 5), it has been shown that weakly adsorbed methanol desorbs at low temperatures, with a maximum at 100°C . Subsequently, a major desorption occurs at approximately 310°C , identified as simultaneous CO_2 and H_2 desorption. The appearance of these products is indicative of a formate species on the surface. DRIFTS has been used to formerly identify this intermediate. Figure 13 (a-b) presents the TPDRIFT (temperature-programmed diffuse reflectance infra-red Fourier transform) spectra after TPD of methanol on Fe_2O_3 . Upon adsorption of methanol at room temperature, a variety of bands appear, due to a mixture of methanol and methoxy present at the surface. However, after heating to $\sim 100^\circ\text{C}$, solely methoxy bands exist, appearing at 1070 , 2827 and 2937 cm^{-1} (Table 3). Heating above 175°C , however, a change of surface species occurs, with the formation of formate bands at 1569 , 1377 , 1358 and 2866 cm^{-1} (Table 3), to the detriment of the bands present for the methoxy intermediate. Methoxy is slowly lost, leaving mainly formate by 330°C . It would appear methoxy is lost as a prerequisite to formate formation.

Table 3. Assignments for the bands observed in the DRIFTS experiments on Fe₂O₃ (Figure 13) [41]. ^b Bands observed above 175 °C.

Assignment	Methoxy (cm ⁻¹)	Methanol (cm ⁻¹)	Formate (cm ⁻¹)	This work, above 100 °C, (cm ⁻¹)
				TPD
$\nu_{as}(\text{COO})+\delta(\text{CH})$			2960	2960 ^b
$\nu_s(\text{CH})$	2898	2925	2880	2922, 2895, 2866 ^b
$2\delta(\text{CH}_3)$	2805	2824		2816,
$\nu_s(\text{COO})+\delta(\text{CH})$			2730	2734 ^b
$\nu_{as}(\text{COO})$			1565	1569 ^b
$\delta(\text{CH})$	$\delta_{as}(\text{CH})$ 1460, $\delta_s(\text{CH})$ 1439		1379	1377
$\nu_s(\text{COO})$			1358	1358 ^b
$\nu(\text{CO})$ ¹¹	1070	1036		1073

Formate exists prior to CO₂ desorption, however is not present upon adsorption, therefore implying it is formed during the heating process. In the case of H₂ however, desorption occurs from the methoxy decomposition, maximised at ~ 250 °C, with its full desorption by 300 °C (Figure 13). It appears that the low temperature shoulder on the hydrogen curve during TPD is associated with the methoxy decomposition.

DRIFTS studies on 6ML (monolayers) MoO_x/Fe₂O₃ calcined at 600 °C, have also been executed. At this temperature, the molybdenum dosed at the surface reacts with Fe₂O₃ to form Fe₂(MoO₄)₃ segregated at the surface (Chapter 4). Therefore reaction on the mixed phase oxide can be probed. Studying on model catalysts produced in this way, creates catalysts with higher surface areas for maximised infrared signal.

Referring to Figure 14, upon dosing MeOH at room temperature, the formation of methanol is clearly dominant, the recorded spectra revealing two methanolic surface species, insinuating a dual adsorption pathway. The first species exists as a non-dissociatively adsorbed O-H group of methanol, appearing at 3100-3500 cm⁻¹ (not shown in the range for Figure 14). A second species is seen through the pair of bands at ~2955 and 2847 cm⁻¹ which can be indexed to the stretch and the first overtone of the symmetric bend of methanol CH₃, respectively [42]. The C-H region is especially useful in IR analysis for methanol adsorption. In addition to functional group assignments, DRIFTS can reveal surface acid-base character. Under adsorption of methanol, the binding mechanism occurs via a lone pair of electrons on the methoxyl group, acting as a Lewis base attacking a surface metal cation. If the metal oxide has the correct basic character, surface oxygen or adsorbed hydroxyl may abstract the proton of the alcohol. By 100 °C, the DRIFTS spectrum (Figure 14) can also distinguish the bands of methoxy on

moderately Lewis-acidic oxides (2933 & 2835 cm^{-1}), differentiating them from the C-H vibrations of undissociated methanol on acidic surfaces at this temperature ($2959/2854$ cm^{-1}). It should be noted, whilst molecular methanol remains the dominant surface species at low temperature, methoxy dominates at higher temperatures, shown through the maintained intensity of methoxy compared to the loss of related MeOH bands. This would reflect the stronger surface interactions of the methoxy.

All associated bands diminish by 200°C . At this point, the species have reacted to form the products of the reaction, identified as H_2CO and CO through TPD.

Table 4. Assignments for the bands observed in the DRIFTS experiments [41].

Assignment	MeOH / cm^{-1}	Methoxy / cm^{-1}
$\nu_s(\text{CH}_3)$	2958 (Lewis bound surface MeOH)	2934
$2\delta_s(\text{CH}_3)$	2852 (Lewis bound surface MeOH)	2835

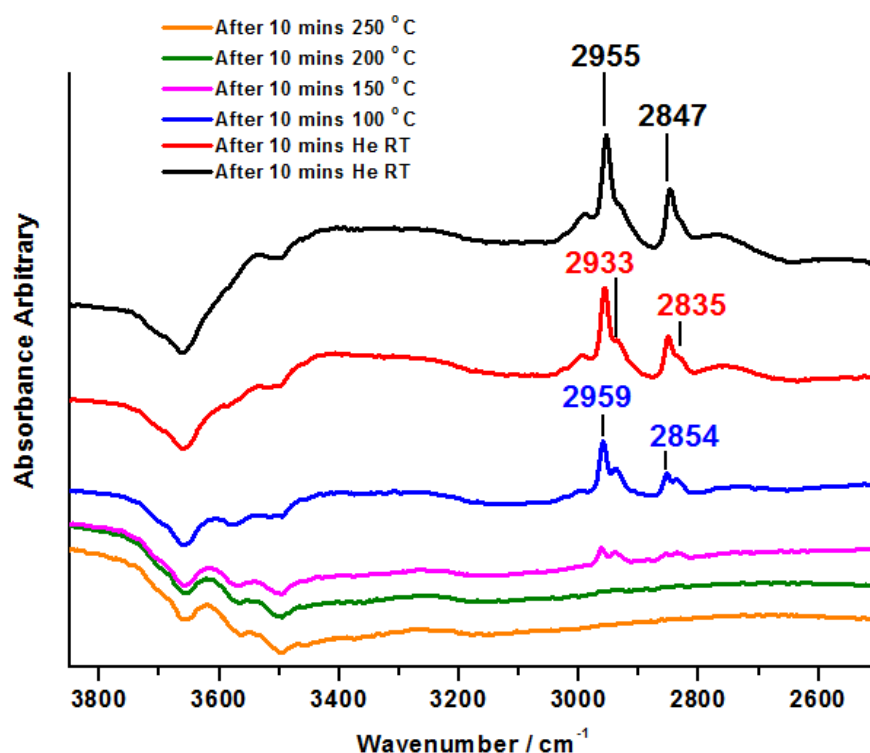


Figure 14. *In situ* DRIFTS spectra for 6ML $\text{Fe}_2(\text{MoO}_4)_3/\text{Fe}_2\text{O}_3$ under TPD of MeOH/He. The catalyst surface was saturated with MeOH pulses under He at room temperature. The temperature was then raised to 400°C , monitoring the reaction products through TPD with simultaneous DRIFTS analysis of the surface species.

In studying by DRIFTS analysis, it has been possible to identify the key reaction intermediates during reaction with methanol on both Fe_2O_3 and $\text{Fe}_2(\text{MoO}_4)_3$ type materials (since Mo dosed on the surface of Fe_2O_3 forms $\text{Fe}_2(\text{MoO}_4)_3$ at elevated temperatures). In studying through DRIFTS, it is now proven that formate is unique to Fe_2O_3 , with also the presence of methoxy: whilst on $\text{Fe}_2(\text{MoO}_4)_3$ methoxy and methanol co-exist. The assignments complement the reaction products already seen through TPD analysis. In recognition of these surface intermediates, this will assist in future studies (Chapter 5) of catalytic mechanisms.

3.1.7. Thermal Plots

Under reaction with methanol, the temperature profile has been monitored carefully, enabling further assessment of the nature of the reaction. Figure 15 reveals the findings for MoO_3 and Fe_2O_3 . The dominance of combustion products on Fe_2O_3 is clearly evident at higher temperatures, the sharp spikes in the thermal profile indicative of the highly exothermic reaction (Equation 1). Fe_2O_3 is a combustor of methanol and this, as mentioned, leads to the exclusive production of unselective CO_2 , coinciding with H_2O .

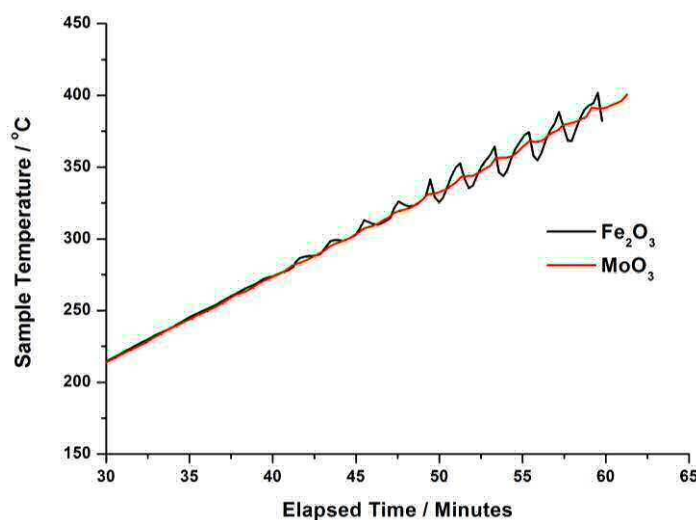


Figure 15. Thermal profiles for MoO_3 and Fe_2O_3 , during TPPFR. Fluctuations in the temperature profile are clearly evident with injections at higher temperatures, especially for Fe_2O_3 .

3.2. Varying the Mo:Fe Ratio

It has been discussed previously, and highlighted heavily in the literature, that the Mo:Fe ratio is one of the most influential factors in controlling catalyst reactivity. It has

been suggested that a Mo:Fe ratio equal to 1.7:1 gives optimal activity, however there is lack of agreement amongst authors. A range of catalysts with varying Mo:Fe ratios have been synthesised in an attempt to investigate this further.

3.2.1. BET

BET has been performed on each of the varying Mo:Fe ratios (Table 5). The BET surface area values of the metal oxide catalysts employed are of modest values, especially in comparison to Fe_2O_3 which demonstrates a surface area of $21 \text{ m}^2\text{g}^{-1}$. The addition of Mo into the synthesis procedure initially has a marked effect on surface area, bringing a loss of area from 12.52 to 4.64 for the 1:1 to 1.5:1 Mo:Fe ratios respectively. Stoichiometric iron molybdate, $\text{Fe}_2(\text{MoO}_4)_3$, demonstrates a Mo:Fe ratio of 1.5:1. For the catalyst in which the Mo:Fe ratio is 1:1, Fe dominates in the form of Fe_2O_3 throughout the bulk structure. Fe_2O_3 is already shown (Table 1) to have a high surface at $21 \text{ m}^2\text{g}^{-1}$, therefore enhancing the overall surface area of the mixed phase catalyst. With additions of Mo above the stoichiometric ratio, there does not appear to be any substantial change in the surface areas measured. This disagrees with the work of Soares *et al.*[43].

The disproportionality large contribution of Mo to the catalyst composition has been attributed to surface segregation in iron molybdate, as shown through various electron microscopy studies [20]. With this surface enhancement of Mo, the effect on the bulk surface area of the catalyst is diminished.

Any discrepancies reported between the surface areas here and those in the literature, could be accounted for due to factors such as differences in thermal treatments or preparation method employed.

Table 5. BET surface area measurements for catalysts with varying Mo:Fe compositions.

Catalyst	Surface Area / m^2g^{-1}
Mo:Fe 1:1	12.52
Mo:Fe 1.5:1	4.64
Mo:Fe 1.7:1	2.94
Mo:Fe 2.2:1	2.73
Mo:Fe 0.5:1	32.56
Mo:Fe 0.02:1	35.51

3.2.2. Raman

Vibrational spectroscopy is widely used to characterise iron molybdate catalysts, and is particularly useful in identifying the phases forming with varying Mo:Fe ratios. Raman spectroscopy has been recorded for each of the Mo:Fe ratios discussed above, and are in excellent agreement with the literature (Figure 16) [9, 23, 44]. Using the assignments in

Table 6, it is shown that for the 1:1 Mo:Fe ratio, the catalyst is comprised of Fe containing phases, in the form of Fe_2O_3 and $\text{Fe}_2(\text{MoO}_4)_3$. Evidence for Fe_2O_3 is seen through the bands at 299 and 412 cm^{-1} , which can be indexed to the bands shown for commercial Fe_2O_3 also in Figure 16. The overall spectrum however is dominated by $\text{Fe}_2(\text{MoO}_4)_3$, with the bands at 780 and 970 cm^{-1} for Mo-O-Mo asymmetric stretch and M=O symmetric stretch respectively. The low Raman scattering from the dark Fe_2O_3 limits its detection, so it would not be feasible to comment on the relative amounts of each Fe phase within the catalyst composition. Note that the weak bands at approximately 990 and 937 cm^{-1} and a shoulder at 821 cm^{-1} , are associated with $\text{Fe}_2(\text{MoO}_4)_3$, and are not related to bulk MoO_3 . The difference between these two bulk phases is clarified by the additional vibrations unique to bulk MoO_3 seen at 997, 666 and 284 cm^{-1} .

At the stoichiometric ratio, the catalyst composition is monophasic, with only $\text{Fe}_2(\text{MoO}_4)_3$ identified. Above this ratio, Mo in octahedral co-ordination also becomes obvious, demonstrated by the bands at 660, 820 and 990 cm^{-1} , for Mo-O-Mo symmetric stretch, Mo-O-Mo asymmetric stretch and terminal Mo=O stretching respectively. This is most likely to be in the form of MoO_3 , as shown through literature studies [2, 13]. The band at 666 cm^{-1} derives from the symmetric Mo-O-Mo stretch between neighbouring monolayers of MoO_3 . Therefore it is not present for stoichiometric iron molybdate, where it is possible that existing is just one monolayer of terminating MoO_3 so no neighbouring Mo layers to bond to. No evidence for excess crystalline Fe_2O_3 is obvious, suggesting no excess iron present during the catalyst preparation.

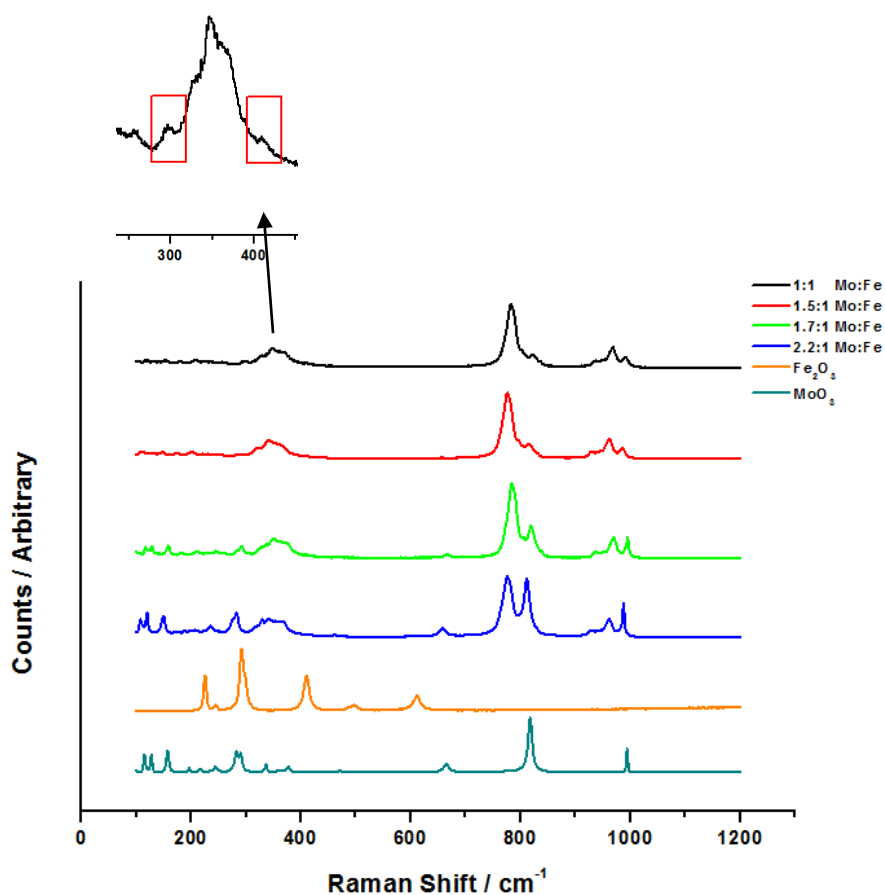


Figure 16. Raman spectroscopy data for various Mo:Fe ratios in bulk $\text{Fe}_2(\text{MoO}_4)_3$, with reference standards for comparison.

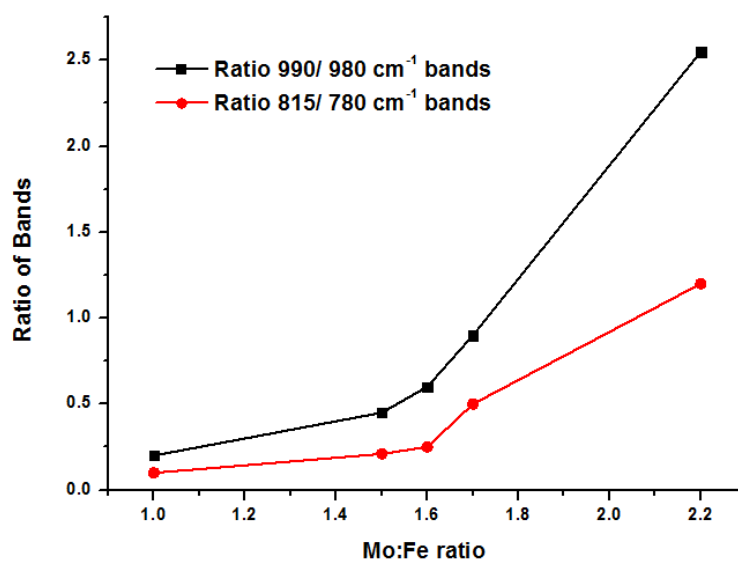


Figure 17. Ratio of Mo:Fe plotted against ratio of 990:980 cm^{-1} (Black) and ratio of 815/780 cm^{-1} (red) Raman bands.

The structure of MoO_3 has previously been discussed in Chapter 1, and is again emphasised in Figure 18.

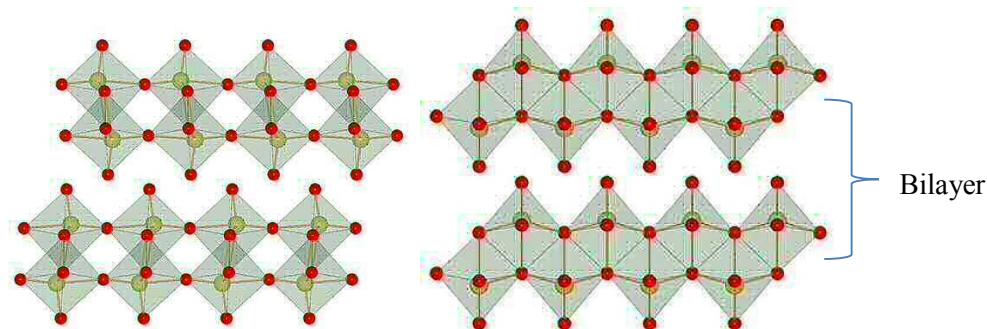


Figure 18. Crystal structure of MoO_3 a) corner connected, and b) edge sharing octahedral viewed along the ab and bc planes [45].

The orthorhombic crystal structure of molybdena is formed from three oxygen atoms, bonded to a central Mo atom. Distorted MoO_6 octahedra corner and edge share in the bc plane to form chains which are cross linked by oxygen atoms [9]. The overall structure forms layers of octahedral bilayers, as highlighted in Figure 18. Van der Waal forces maintain the cohesion between the bilayers.

Figure 17 is able to provide information on the possible surface termination in bulk iron molybdates. It is shown that the ratio of the stretching vibrations in MoO_3 (990 and 820 cm^{-1}) to stretching bands in $\text{Fe}_2(\text{MoO}_4)_3$ (970 and 780 cm^{-1}) falls with dropping Mo:Fe ratio. However it does not reach zero, implying that there is still some terminal $\text{Mo}=\text{O}$ present even for the catalyst rich in iron with a Mo:Fe ratio of 1:1.

In comparison, the Raman band at 660 cm^{-1} , representing O-Mo-O symmetric stretch formed between the layers within the bilayer structure, is seen to disappear for the stoichiometric ratio and Mo:Fe ratios below this. In detail, the bond is associated with the symmetrical bridging oxygen connecting the layers of atoms within the sheet-like MoO_3 structure. The conclusion is that it could be possible that one of the terminating $\text{Mo}=\text{O}$ layers within the bilayer structure is still present at the catalyst surface. It is this layer which is responsible for forcing the reaction towards selective products.

3.2.3. XRD

XRD data for the single oxides have already been discussed. XRD analysis for the varying Mo:Fe ratios (Figure 19) reinforces Raman spectroscopy, demonstrating the presence of both MoO_3 and $\text{Fe}_2(\text{MoO}_4)_3$ for catalysts with a molybdenum content above that for stoichiometric catalyst. The sample with a Mo:Fe ratio of 2.2:1 most clearly evidences this, with the most prominent signal for MoO_3 demonstrated through the peak

at $12^\circ 2\theta$, corresponding to the (020) lattice plane. The presence of MoO_3 can also be seen however, through the Bragg peaks at 25.7 , 27.3 , and $29.3^\circ 2\theta$, representing the (040), (021), (060) planes respectively [2, 46]. $\text{Fe}_2(\text{MoO}_4)_3$ can be identified most evidently by the series of peaks at 19.5 , 20.5 , 21.8 and $23.0^\circ 2\theta$, Bragg peaks which correspond to the (204), (313), (214) and (114) lattice planes of the monoclinic system [46, 47].

The stoichiometric catalyst shows a monophasic structure, consisting of pure $\text{Fe}_2(\text{MoO}_4)_3$.

For the 1:1 Mo:Fe catalyst, $\text{Fe}_2(\text{MoO}_4)_3$ can clearly be indexed from the pattern. However the Fe_2O_3 phase shown to exist through Raman spectroscopy is not so clear to identify. This may be due to the dominance of $\text{Fe}_2(\text{MoO}_4)_3$, which exists as the majority phase. The Fe_2O_3 may also be present in an amorphous state, making its detection through XRD impossible. Amorphous materials do not possess periodicity as atoms are randomly distributed in 3D space. X-rays from amorphous materials will therefore be scattered in many directions, leading to a large bump distributed in a wide range instead of high intensity narrower peaks. Fe_2O_3 also has a weak relative intensity compared to Mo containing phases in XRD, so traces of the Fe_2O_3 phase at concentrations below the limit of detection will not be distinguished.

For the 1.7:1 sample, it is not clear where the additional Mo in the synthesis resides, with the detection of the main MoO_3 Bragg peak less easy to identify; the Bragg peak at $12^\circ 2\theta$ is just visible. Deltcheff *et al.* [48] have shown that MoO_3 is only detected by XRD when its content is higher than 7 w/t % of the catalyst composition. For the 1.7:1 sample, theoretical evaluation of the composition of phases present (through High XPert Analysis software) have shown that MoO_3 is present at 10 w/t %, so in theory according to Deltcheff *et al.*, it should be identifiable. Peak broadening is consistent across the Mo:Fe range, suggesting that the intrinsic crystallite sizes are similar for all ratios. It has been

suggested excess Mo retards the crystallisation of $\text{Fe}_2(\text{MoO}_4)_3$ [11], however this is not apparent here.

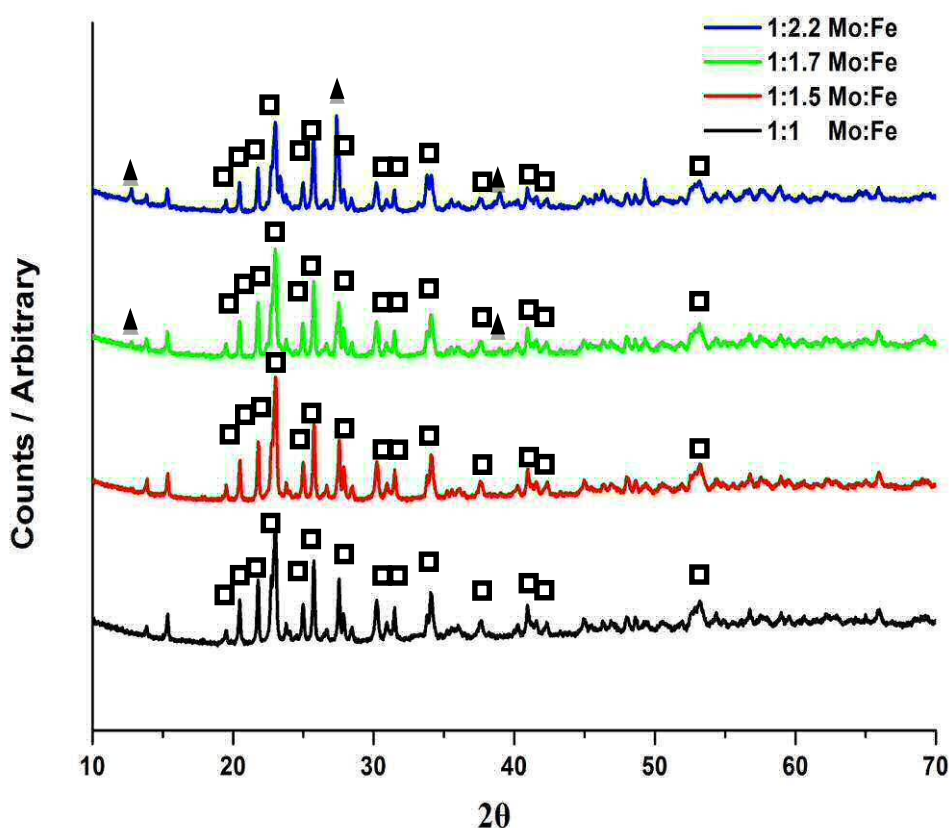


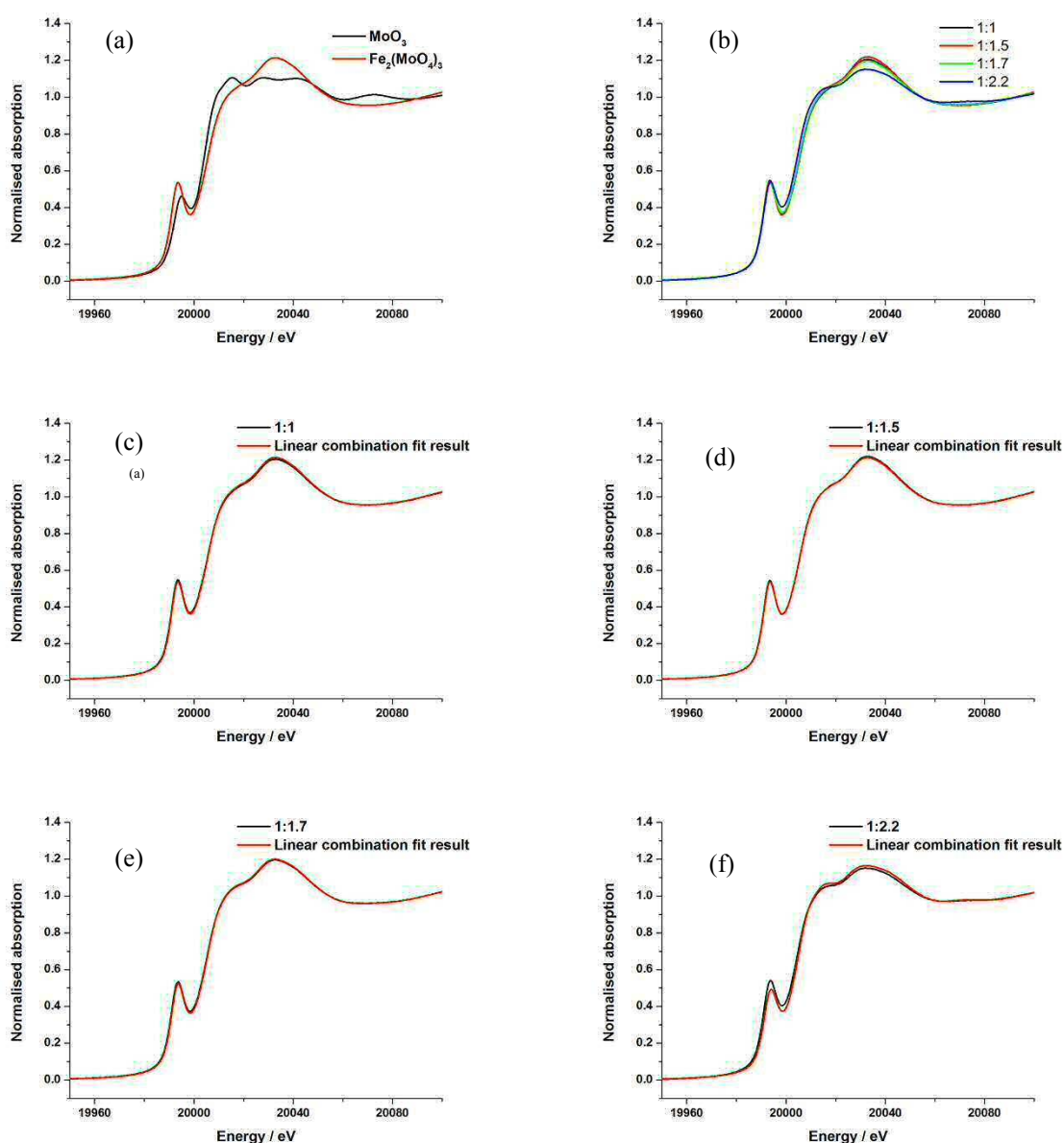
Figure 19. XRD data for various Mo:Fe ratios. Black triangles= MoO_3 formation, White squares= $\text{Fe}_2(\text{MoO}_4)_3$ formation.

3.2.4. XAFS Study of Iron Molybdate Catalysts

Conventionally prepared iron molybdate samples were produced with Fe:Mo ratios of 1:1, 1:1.5, 1:1.7 and 1:2.2. Previous XRD studies have shown that samples prepared with excess Mo produce a mixture of MoO_3 and $\text{Fe}_2(\text{MoO}_4)_3$ phases. Assuming this is the case, this can be quantified by performing a linear combination fit of the XANES reference spectra i.e. as XAFS is an averaging technique, the XANES area is also a combination of the relative contribution from each phase. The XANES spectra with associated linear combination fits using MoO_3 and $\text{Fe}_2(\text{MoO}_4)_3$ references are detailed in Figure 20 with the associated parameters detailed in Table 6.

Table 6. Phase composition of bulk iron molybdate samples

Fe:Mo ratio	MoO ₃ %	Theoretical MoO ₃ %	Fe ₂ (MoO ₃) ₄ %	Theoretical Fe ₂ (MoO ₃) ₄ %
1:1	1.6	0	100	98.4
1:1.5	0	0	100	100
1:1.7	10.5	11.8	89.5	88.2
1:2.2	41	31.8	59	68.2

**Figure 20(a)-(f).** Normalised XANES data and linear combination fit (LCF) results of MoO₃ and Fe₂(MoO₄)₃ phases (top left) and for different Fe:Mo stoichiometric ratios of iron molybdate.

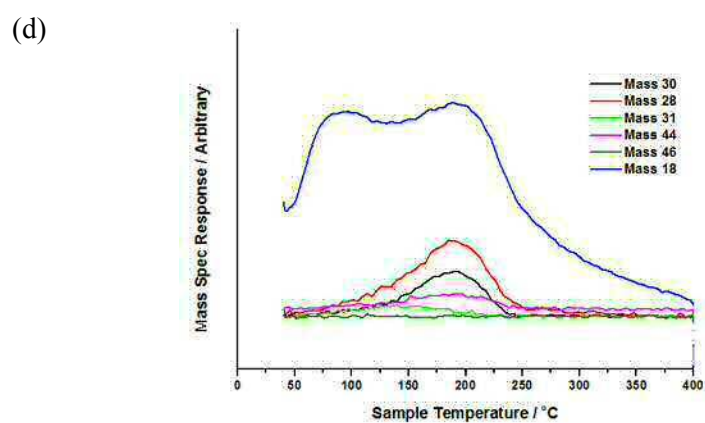
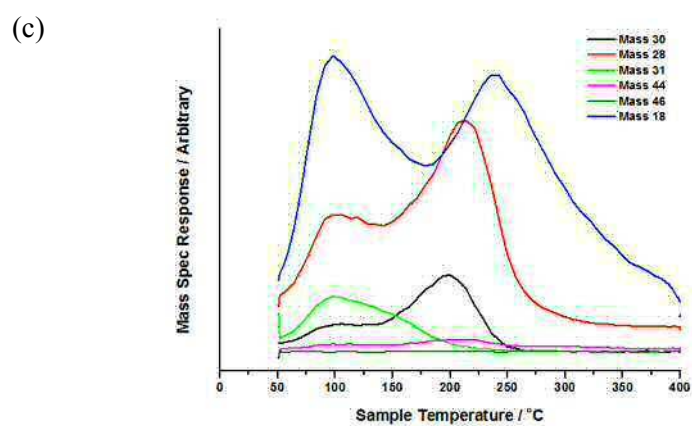
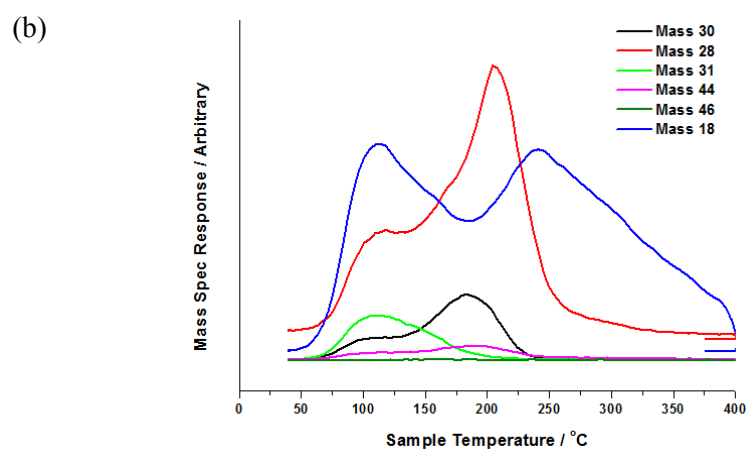
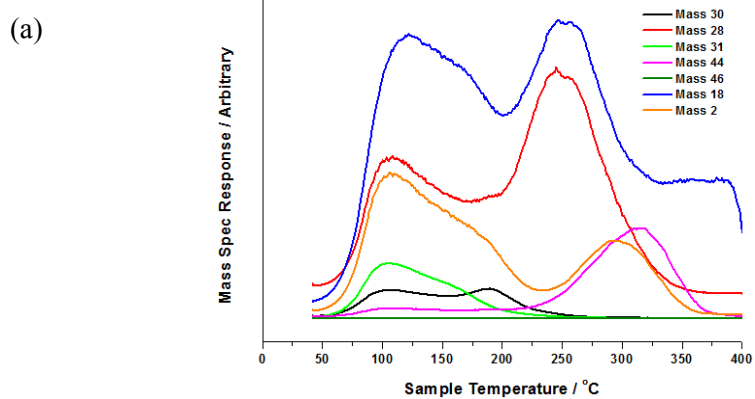
MoO_3 and $\text{Fe}_2(\text{MoO}_4)_3$ have different XANES spectra as a result of their different associated geometries and oxidation states. Providing that iron molybdate samples of different Fe:Mo ratio are comprised entirely of these two phases, a linear combination fit of the references should be able to provide a model of the XANES spectrum. For samples with Fe:Mo ratio of 1:1, 1:1.5 and 1:1.7 the calculated composition is very close to what is expected theoretically, with good agreement with the XANES spectra and linear combination fit. However, the sample with Fe:Mo ratio of 1:2.2 is not in good agreement with that calculated theoretically, and there is neither a worthy agreement with the linear combination fit and the XANES spectrum. This suggests that the sample is not comprised of MoO_3 / $\text{Fe}_2(\text{MoO}_4)_3$ alone and that other Mo oxide phases are present. This will be re-addressed in Chapter 4.

3.2.5. Reactivity Data

It has been shown in Section 3.1.5 that catalysts containing molybdenum are able to produce formaldehyde, with MoO_3 demonstrating an excellent performance in terms of its selectivity. On the contrary, Fe rich catalysts such as Fe_2O_3 produce vast amounts of CO_2 , performing as combustors of methanol. In haematite, a high concentration of surface cations induces close proximity of Fe centres, and neighbouring iron pairs allow for a bridging formate precursor to bind.

Unfortunately, the performance of MoO_3 is limited due to the poor surface area and therefore activity of this catalyst, hence making it unsuitable for industrial use. For this reason the addition of iron has been adopted, to bring an increase in the surface area of the catalyst. The increased performance is also attributed to the isotropic ferric molybdate structure [13], which establishes a surface where all surface Mo atoms are co-ordinatively unsaturated, and able to act as potential active sites. With more Fe in the chemical makeup however, it is possible that this could evoke a negative effect on the catalyst selectivity. It has been proposed that isolated Fe-Mo pairs are responsible for CO production [34].

To investigate this in more detail, catalysts have been synthesised with varying Mo:Fe ratios, and examined for their reactivity in the selective oxidation of methanol to formaldehyde. Figures 21(a)-(f) show TPD data (raw data) for catalysts with Mo:Fe ratios of 0.02:1, 0.5:1, 1:1, 1.5:1, 1.7:1 and 2.2:1 respectively. TPD enables probing of the catalyst surface, enabling investigation of surface intermediates and the energy barriers required to overcome the formation of products. Methanol is adsorbed onto the surface to saturation under He, and the temperature then ramped to assess the products of desorption.



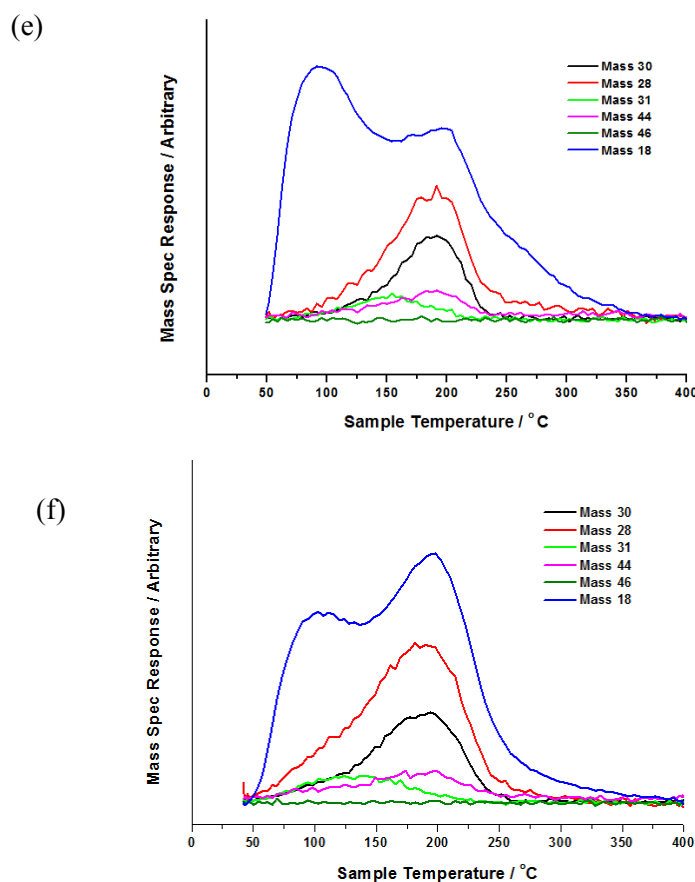


Figure 21(a)-(f). TPD of methanol in He for (a) Mo:Fe 0.02:1, (b) Mo:Fe 0.5:1, (c) Mo:Fe 1:1, (d) Mo:Fe 1.5:1, (e) Mo:Fe 1.7:1, (f) Mo:Fe 2.2:1 (raw data). Mass 30=H₂CO, Mass 28=CO, Mass 31=MeOH, Mass 44=CO₂, Mass 46=DME, Mass 18=H₂O.

The desorption profile for Mo:Fe 2.2:1 (Figure 21(f)) shows a broad and low temperature peak for methanol desorption (Mass 31) at 130 °C, closely followed by the desorption of formaldehyde (Mass 30) at 195 °C. Water (Mass 18) is clearly detected in the mass spectrometer response, with two distinct peaks for its desorption at 100 and 200 °C. Aside from this, no other by-products are shown to desorb. The catalyst performs well demonstrating a 100 % selectivity to formaldehyde. This is also explicitly seen in the literature [10].

The desorption profile for the stoichiometric catalyst has been discussed in detail (Figure 10-11), demonstrating a similar reactivity profile to that for the Mo:Fe 2.2:1 catalyst. In fact, all catalysts in the range of Mo:Fe 1.5-2.2:1 react in a similar fashion, revealing formaldehyde as the only carbon product in their TPD profile (at approximately 190 °C).

The Mo:Fe 1:1 catalyst shows a similar $\text{T}_{\text{H}_2\text{CO}}$ desorption at 195°C . However, CO production (Mass 28) becomes apparent, as evidenced through the increased mass spectrometer response for this carbon by-product, and a shift in temperature of its formation to 220°C . Water is once again shown to desorb as two peaks at 90 and 245°C .

A TPD was also taken for the higher Fe containing catalyst, being Mo:Fe 0.02:1. Although slightly more active ($\text{T}_{\text{H}_2\text{CO}}$ desorption at 185°C (Mass 30)), it suffers significantly in terms of its selectivity. The profile shows a broad methanol desorption peak centred at 110°C , tailing to zero by 210°C . CO dominates the desorption spectra, with a large peak centered at 255°C . In addition to this, H_2 and CO_2 desorb near coincidentally at 300 and 320°C (Mass 2 and Mass 44 respectively). The detection of CO_2 within this temperature range is a key indicator of formate adsorption, a detrimental intermediate for this reaction. The TPD shown shows a strong resemblance to that seen for commercial Fe_2O_3 (Figure 5), thus suggesting Fe_2O_3 to be present at the catalyst surface.

In summary, there are several key differences to note between the various TPD data discussed. For high Mo:Fe ratios, where the mole ratio of Mo forms the majority, the principal products to desorb are formaldehyde and water, as in the case for commercial MoO_3 . This is a key indicator that the surfaces of these catalysts show some similarity, signifying it to be Mo rich for the higher Mo:Fe catalysts. This has been evidenced by Bowker and co-workers [10]. For very low Mo:Fe ratios (Mo:Fe $<0.05:1$), H_2 and CO_2 are clearly evident at elevated temperatures. For the intermediate Mo:Fe ratios ($0.5\text{--}1:1$ Mo:Fe), CO is the major product. The source of these differences are the altering reaction intermediates which are seen to form at the surface (DRIFTS Figures 13-14) of the catalyst [36]. Dissociative methanol adsorption on Fe_2O_3 leads to formate groups, whilst on MoO_3 leads to methoxy. Methoxy intermediates can have one hydrogen abstracted to yield formaldehyde, whilst in formates complete hydrogenation leads to CO_2 production [2] (Section 3.1.5 details this further).

Table 7 summarises the temperature of CO desorption versus the Mo:Fe ratio. For the lowest Mo:Fe ratio ($0.02:1$), it is shown that the temperature of CO desorption is substantially higher than it is for higher Mo:Fe ratios. The Redhead equation (Equation 2) can be applied to approximate the activation energy (E_a) for this process using the peak desorption temperature (T_p) [49]. The equation assumes both a first order and a frequency factor (ν) of 10^{13} s^{-1} .

v

Equation 2

Table 7. Temperature of H₂CO desorption of various Mo:Fe containing catalysts.

Catalyst Mo:Fe ratio	Product Formed	Peak temperature / °C	E_a (CO) / kJ mol⁻¹	Surface Area / m²g⁻¹
0.02:1	CO	255	145	35.51
0.5:1	CO	215	130	32.56
1:1	CO	212	131	12.52

The higher activation energy of CO desorption seen for the higher surface area Mo:Fe 0.2:1, is attributed to the increase in surface free energy of smaller particles. With a smaller particle size, surface curvature is enhanced, resulting in low-coordinate surface sites. To stabilise this high surface energy, an increase in the number of surface-adsorbate interactions must occur to increase active site co-ordination. Therefore, to remove such surface intermediates, a higher energy input (higher temperature), must be applied.

There appears to be two distinct temperatures for CO desorption, occurring at approximately 215 and 250 °C. It has been suggested by Matt House (Thesis, The Selective Oxidation of Methanol Over Iron Molybdate Catalysts, 2007), that for lower Mo:Fe ratios, the high temperature CO occurs as a primary product in the oxidation of methanol. For higher Mo:Fe ratios, low temperature CO desorption is a secondary product from the further oxidation of formaldehyde. Further details of this phenomenon are described in Section 3.4.5.

In addition to TPD, reaction profiles under methanol pulsing in O₂/He with increasing temperature (TPPFR) have also been performed. Results for the stoichiometric catalyst have previously been discussed, and can be referred to in Figure 12.

Figure 22 shows the reactivity performance for the catalyst with a Mo:Fe ratio of 1:1. The catalyst demonstrates a good activity, achieving 50 % conversion by 188 °C. For this ratio, it is possible to reach 100 % conversion by 290 °C, in stark contrast to commercial MoO₃, which is only able to perform to 95 % conversion even at the most elevated temperatures. Although the conversion of this higher Fe content catalyst shows a good activity, the selectivity is comprised due to the exposure of Fe at the catalyst surface. At low temperatures, the selectivity of the catalyst towards formaldehyde is good, demonstrating almost 95 % selectivity at 160 °C. However, by 245 °C, this has dropped to 50 %, and by the end of the experiment, upon reaching 400 °C, the selectivity to formaldehyde is poor at just 10 %. At this point CO and CO₂ co-exist with equal

selectivity (45 % each). The production of CO begins to rise steadily from 160 °C, before stabilising at 45 % from 270 °C. CO₂ production activates slightly later from 200 °C, showing a steady progressive increase in selectivity to 45%. DME production is low, at less than 5 % at low temperatures (175 °C). The selectivity of this organic drops steadily, so that by 280 °C it is below 1 %.

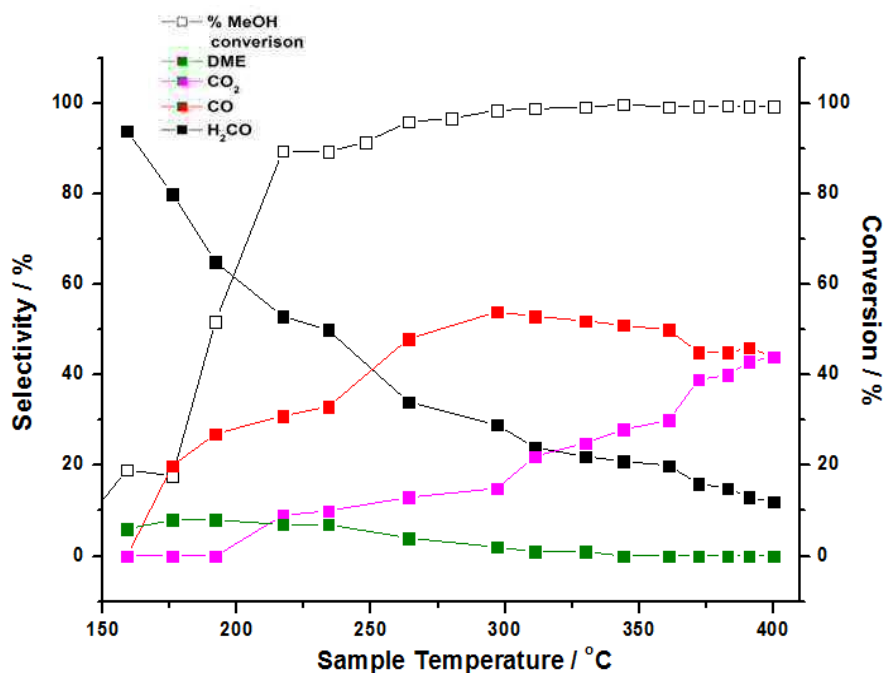


Figure 22. TPPFR for a Mo:Fe ratio of 1:1. MeOH was injected over the catalyst at regular time intervals, whilst ramping to 400 °C in 10 % O₂/He. Subtractions have been made for the various cracking fragmentation of each product (Chapter 1, Section 3.3), to give a plot for selectivity and conversion.

The reactivity profile for the 1.7:1 (Figure 23) catalyst also demonstrates good activity, however is not able to perform to the same activity of the 1:1 catalyst. 50 % conversion is reached by 225 °C, and with further temperature increase, 100 % conversion is achieved at 310 °C. The maximum selectivity to formaldehyde is shown to be 92 %, occurring as low as 150 °C, and maintained with increasing temperature until approximately 250 °C. The selectivity to formaldehyde then begins to drop at higher temperatures (to approximately 40 %), with the onset of CO and CO₂ production occurring from 200 °C and 270 °C respectively, escalating to 35 and 10 %. The production of DME tails off more quickly for this catalyst in comparison to the Mo:Fe 1:1 catalyst, falling to 0 % by 225 °C. Overall, the catalyst performs well at low temperature, demonstrating a very high selectivity to formaldehyde at low conversion.

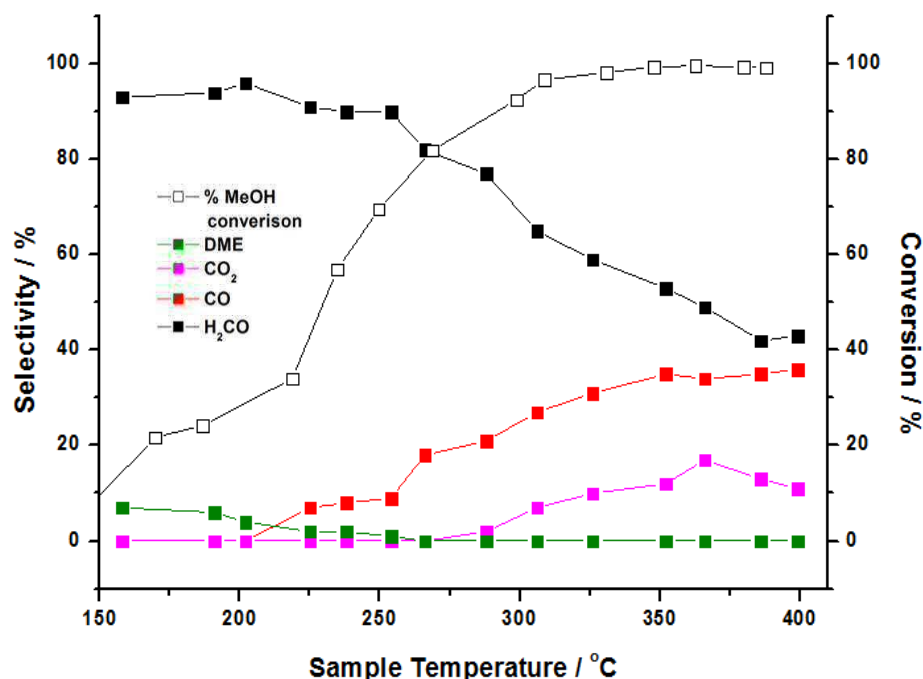


Figure 23. TPPFR for a Mo:Fe ratio of 1.7:1. MeOH was injected over the catalyst at regular time intervals, whilst ramping to 400 °C in 10 % O₂/He. Subtractions have been made for the various cracking fragmentation of each product (Chapter 1, Section 3.3), to give a plot for selectivity and conversion.

For the highest Mo:Fe ratio (2.2:1) the activity is not able to compete with the aforementioned Mo:Fe catalysts (Figure 24). 50 % conversion is not achieved until 245 °C, and 100 % until 315 °C. However, although the catalyst expresses moderate activity, the selectivity of the catalyst is able to outperform the other ratios. The selectivity to formaldehyde is maintained at over 90 % for a far greater temperature span, only dropping above 300 °C. By 400 °C the selectivity is at 60 %, which is higher than any of the other reported catalysts in this section. The production of CO and CO₂ as a result of this maintained selectivity, do not begin to rise until post 250 °C, with both present below 30 % at the highest temperature of 400 °C. It becomes obvious why industrially, a Mo:Fe catalyst with Mo excess is employed. The commercial reaction is run well below 400 °C, which when comparing data sets for this catalyst with excess Mo, shows that within this temperature range, the catalyst is able to give reasonable conversions with high selectivity.

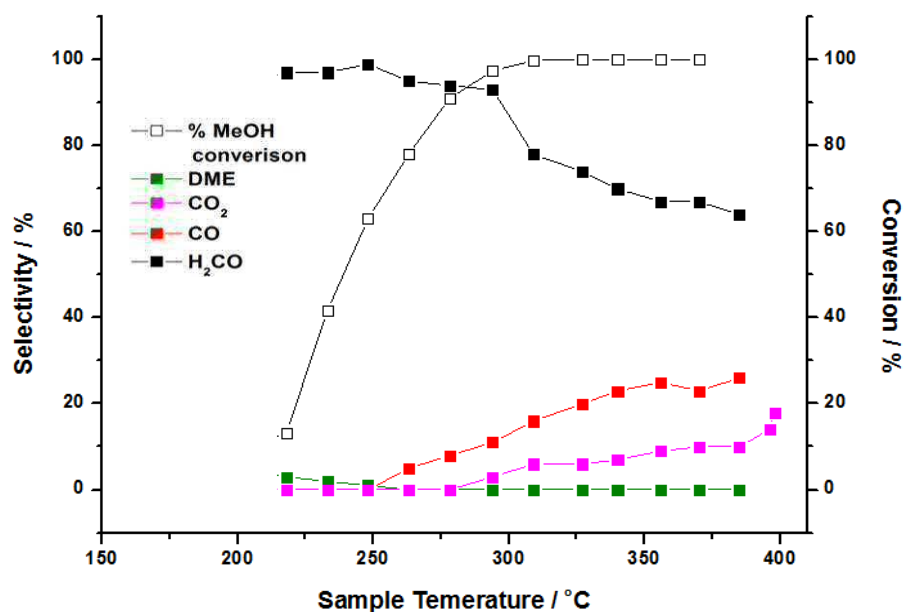
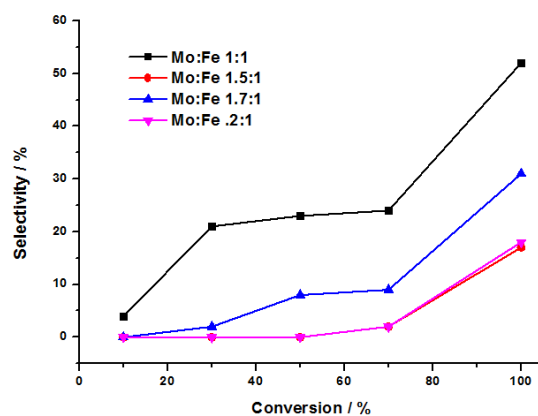


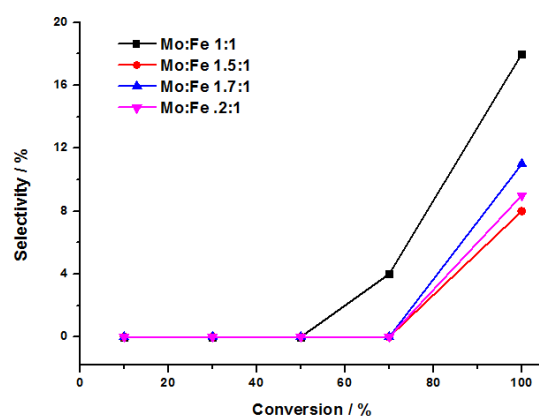
Figure 24. TPPFR for a Mo:Fe ratio of 2.2:1. MeOH was injected over the catalyst at regular time intervals, whilst ramping to 400 °C in 10 % O₂/He. Subtractions have been made for the various cracking fragmentation of each product (Chapter 1, Section 3.3), to give a plot for selectivity and conversion.

Comparing conversions for the discussed ratios of Mo:Fe, and also including those for lower Mo:Fe contents (Figure 25 (d)), there is a strong trend between the composition of Mo and Fe in the catalyst and the conversion of methanol. It is shown that the catalyst with a ratio of 0.02:1, requires the lowest temperature for 50 % conversion. The substantial improvement versus that for the 2.2:1 Mo:Fe catalyst can be justified when considering the surface area of these two catalysts (Table 5). The catalyst with a Mo:Fe ratio of 0.02:1 has a surface area over ten times greater than that for Mo:Fe 2.2:1, thereby showing a much greater conversion per unit area. Since the mass of catalyst is kept constant throughout the measurements (0.5 g), the dramatic change due to fluctuations in surface area is a reasonable consideration.

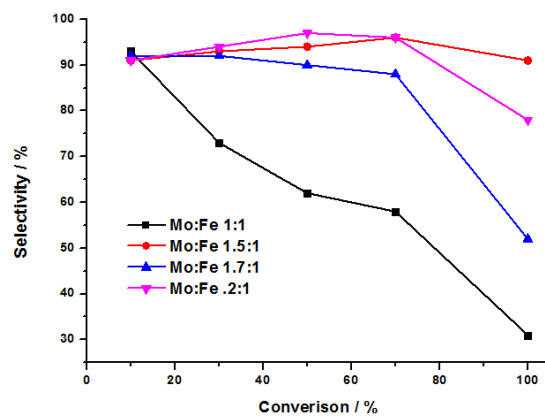
(a)



(b)



(c)



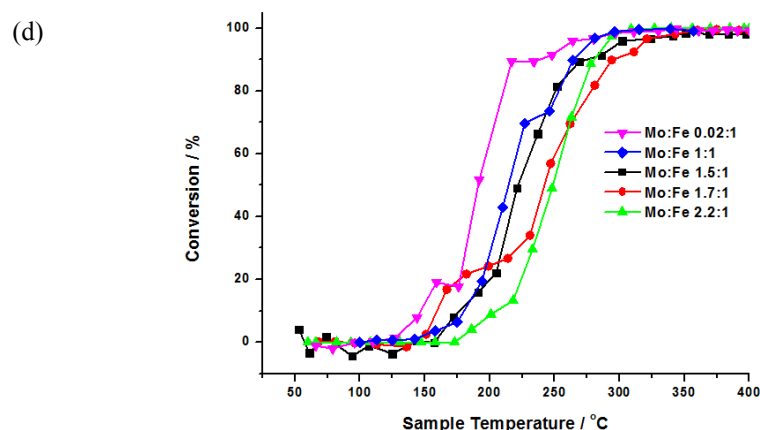


Figure 25(a)- (d). Summary of TPPFR data for various Mo:Fe ratios (a) Selectivity to CO production (b) Selectivity to CO₂ production, (c) Selectivity to H₂CO production, (d) Conversion of methanol. The production of CO dominates for Mo:Fe 1:1, whilst formaldehyde production cannot be maintained. CO₂ production does not begin until high conversion. With lowering Mo content, the conversion shifts to lower temperature (Figure (d)).

Catalytic investigations have uncovered a strong correlation between product distribution and Fe:Mo ratio in nonstoichiometric iron molybdates. When considering the various products unveiled for each of the Mo loadings in both TPD and TPPFR, it is important to identify the phases present for each of the discussed catalysts. Figure 26 is a simplified schematic representing the change in catalyst composition with increasing Mo content, as ascertained through various characterisation techniques (Raman, XRD, IR).

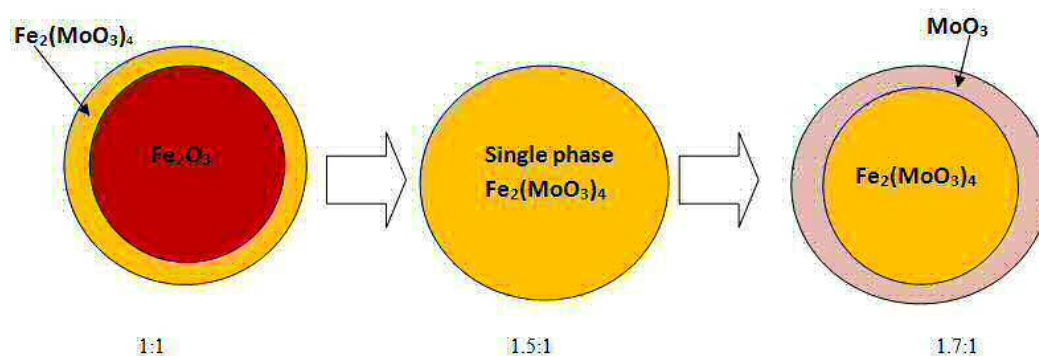
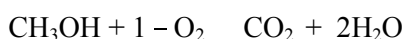


Figure 26. Variation in phase formation with increasing Mo loading in iron molybdate catalysts. From left to right, increasing the Mo:Fe ratio.

In summary, in molybdenum-deficient systems (Mo:Fe <1.5), deep oxidation of methanol succeeds. With Mo in shortage, X-ray diffraction (XRD) and Raman studies have resolved mixed phase Fe₂(MoO₄)₃ phase with Fe₂O₃. Therefore, the

nonstoichiometric mixed oxide it thought to exist as in Figure 26 comprising a molybdate-enriched surface over haematite bulk.

The presence of Fe_2O_3 is clearly noticeable for Mo:Fe with a ratio of 0.02:1, where combustion products (CO_2 and H_2) prevail at higher temperatures (Figure 21). It would infer the surface is not completely covered with the $\text{Fe}_2(\text{MoO}_4)_3$ phase. A high concentration of surface cations induces a close enough proximity of iron centres (3\AA), to allow for formate adsorption at two neighbouring sites (Figure 27). Subsequently, combustion occurs as detailed in Equation 3. Referring to the TPD for Fe_2O_3 (Figure 5), the peak shape implies a reaction with 1st order kinetics, and the lack of CO implies the combustion products are from the formate and not from the clean dehydrogenation of methanol. As with $\alpha\text{-MoO}_3$, methanol adsorbs dissociatively on $\alpha\text{-Fe}_2\text{O}_3$, initially yielding methoxy and hydroxyl surface species. Lattice oxygen insertion into the methoxy readily occurs to yield formate. Strong iron-oxygen interactions favour bidentate anchoring of formate, over monodentate methoxy. The low surface enthalpy promotes decomposition to CO_2 via the exothermic combustion pathway (Equation 3). Decomposition of this surface formate has been suggested (Bowker [10]) to be rate limiting, since it is relatively stable. Due to the increased binding of oxygen in Fe_2O_3 , the reaction pathway goes through a lower enthalpy situation, resulting in a higher barrier to formaldehyde production. Hence it is not seen.



Equation 3

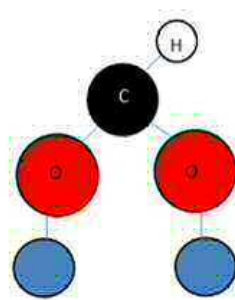


Figure 27. Bidentate formate intermediate existing at the surface of Fe_2O_3 . Blue= Surface.

With small amounts of Mo increased into the catalyst synthesis, CO_2 selectivity declines and CO dominates (Figures 25(a)-(c)). Formaldehyde also evolves. CO produced on the mixed oxide is a primary product from methanol oxidation and can be differentiated from that evolved on reduced MoO_3 by a higher desorption temperature.

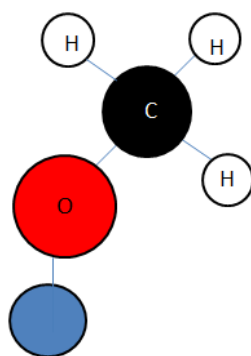
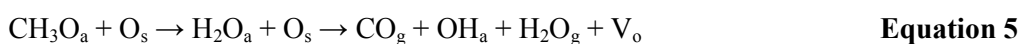


Figure 28. Monodentate methoxy intermediate existing at the surface of Mo rich species.
Blue = Surface.

When methanol adsorbs onto a Mo centre, a methoxy intermediate forms, as demonstrated in Figure 28. In order to proceed to formaldehyde production, a second methoxy should be adsorbed at a neighbouring Mo site, so that oxidative dehydrogenation can occur. If Mo is found to be isolated, the methoxy becomes stabilised. Surrounded by Fe atoms, dehydrogenation occurs (Equations 4-5) to yield CO. It is thought that on catalyst surfaces where Mo-Fe [10] sites occur, the methoxy is held in the correct orientation to facilitate this dehydrogenation.



Broken down:



Production of CO will be maximised when equal amounts of Mo and Fe exist at the surface. Stoichiometric $\text{Fe}_2(\text{MoO}_4)_3$ shows a low selectivity for CO production in TPD (Figures 10-11). This can be explained when considering the surface terminating layer. It has been proven by many [13, 20, 50], that a skin of Mo exists at the surface of the bulk $\text{Fe}_2(\text{MoO}_4)_3$ catalyst. This eliminates the opportunity for Mo-Fe to form in close proximity. When comparing between the Mo:Fe 0.02:1 and 0.5:1, the amount of CO produced is evidently less for the 0.5:1 catalyst. It can therefore be assumed that fewer Fe sites are exposed for this catalyst.

The selectivity of $\text{Fe}_2(\text{MoO}_4)_3$ and high Mo:Fe ratios is comparable to that of the pure $\alpha\text{-MoO}_3$ with all following the Mars–Van Krevelen mechanism. However, the catalytic activity of $\text{Fe}_2(\text{MoO}_4)_3$ surpasses that of $\alpha\text{-MoO}_3$, and also outperforms those with higher

Mo:Fe ratios (Figure 25(d)) [12]. Increased performance is attributed to the catalytically-isotropic ferric molybdate structure [13], where all surface Mo atoms are co-ordinatively unsaturated and thus potential active sites.

The mechanism to formaldehyde from methoxy adsorption is believed to occur as follows:



Formaldehyde and CO are the main products shown to form through methoxy adsorbate. Reduced oxygen vacancy sites in MoO_3 weaken the C-H bond, but strengthen the C-O bond in the chemisorbed methoxy. As a result, this leads to the increase in the formation of more hydrogen abstracted products. Once formed, formaldehyde can be further oxidised to CO or CO_2 .

Depending on the surface properties, the methoxy intermediate will yield various products. Figure 29 summarises the possible products to form. Formaldehyde is seen to be produced over redox sites, DME over acid sites, and CO/ CO_2 over basic sites. Hence, for bulk MoO_3 , the primary product is formaldehyde, since the surface of MoO_3 is redox site rich. In addition to formaldehyde, higher order by-products may also be observed on $\alpha\text{-MoO}_3$. This includes DME, visible at lower temperatures, produced from the dehydration of methoxy intermediates (Equation 9) [51].



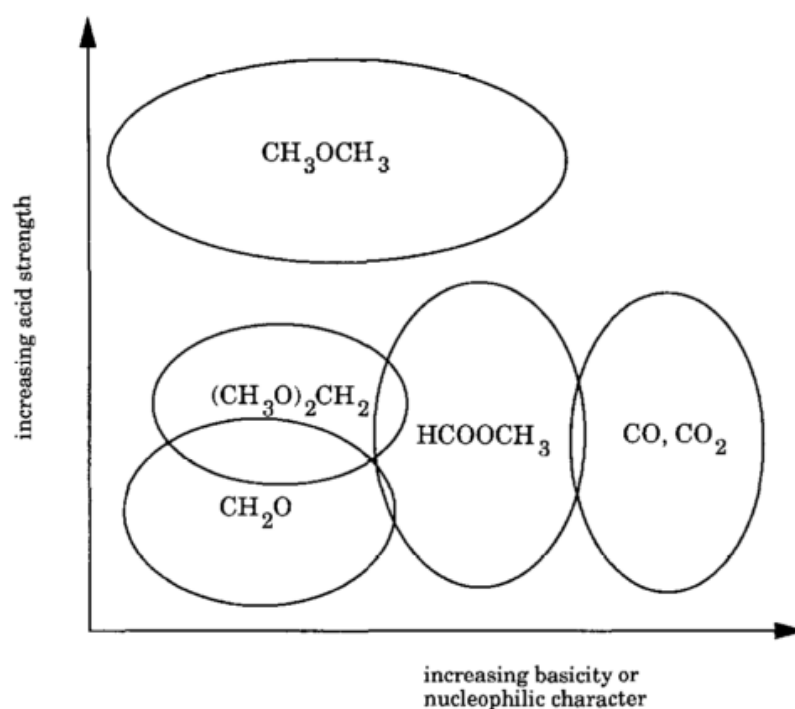


Figure 29. Schematic of the various products from methanol oxidation as a function of catalyst acid/base character [52].

3.3. Varying the Preparation Method

3.3.1 Co-Precipitation with Adaptations

The conventional catalyst preparation method involves co-precipitation, followed by evaporation and drying. The effects of filtering and washing on the stoichiometric catalyst have been investigated (Mo:Fe 1.5:1), in particular assessing the effects they have on catalyst composition. Figures 30-32 represent the relevant Raman and XRD data for these variations in preparation procedure. It is clear that filtering and washing have detrimental effects on controlling the Mo:Fe ratio within the catalyst. With filtering, both the Raman and XRD data are unanimous, demonstrating a mixed phase catalyst containing both $\text{Fe}_2(\text{MoO}_4)_3$ and MoO_3 . This is most strongly evidenced through Raman, by the increase in intensity of the band at 820 cm^{-1} (Mo-O-Mo vibrations in MoO_3), relative to the band at 780 cm^{-1} (Mo-O-Mo vibrations in $\text{Fe}_2(\text{MoO}_4)_3$). This is unexpected, since the stoichiometric catalyst is anticipated to be monophasic, comprised solely of mixed phase $\text{Fe}_2(\text{MoO}_4)_3$.

With washing, this effect is further enhanced, in particular the XRD shows a clear band at $12^\circ 2\theta$, which can be confidently assigned to MoO_3 (Figure 4). There is a far greater spectral intensity of MoO_3 than for the catalyst prior to washing, which has previously been seen by Hill and Wilson [53]. It is believed that this is due to the higher solubility of

Fe, which washes away in the filtrate. Raman of the filtrate is Fe enriched (Figure 31), with a strong resemblance to the iron nitrate precursor initially used in the synthesis. It can be assumed that since Raman and XRD are bulk techniques, the washing of Fe from the catalyst extends to the bulk and it not just limited to the surface.

SEM-EDX studies confirm the loss of Fe to the catalyst with washing, as shown in Appendix A6 by the increase in Mo signal in the final catalyst. The colour of the catalyst is also an indication of Fe loss, with the catalyst post washing showing a much greener colour indicative of the increase Mo atomic ratio. The stoichiometric catalyst usually has a far browner appearance, as seen in Figure 33.

With an increase in Mo content, it is predicted that the reactivity data will show an improved selectivity to formaldehyde. However, due to the lack of reliability in creating the desired ratio of Mo:Fe in the final catalyst, the catalysts were not considered for reactor testing.

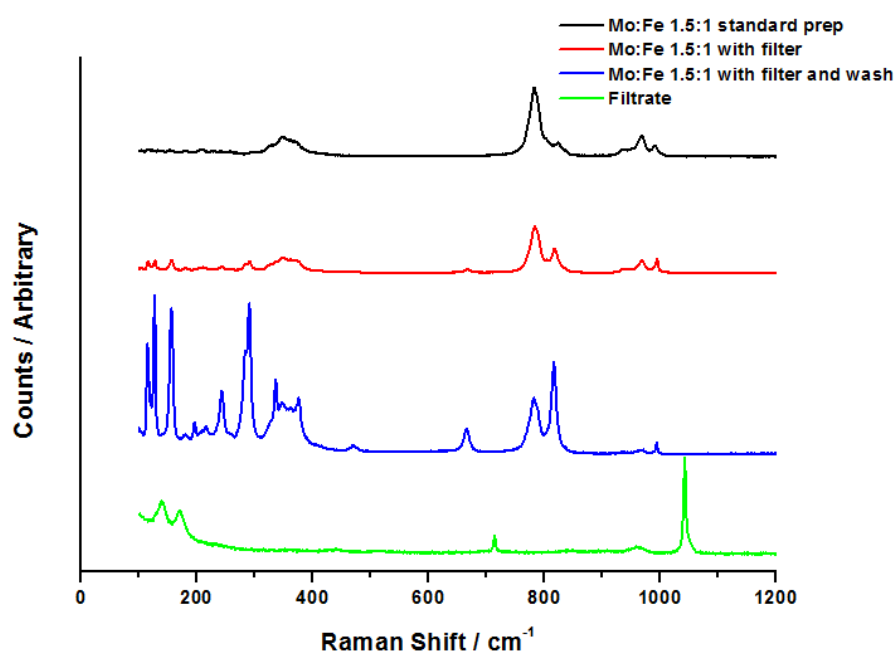


Figure 30. Raman data for stoichiometric $\text{Fe}_2(\text{MoO}_4)_3$ standard co-precipitation, after washing, and after washing and filtering, and the filtrate after drying and calcining.

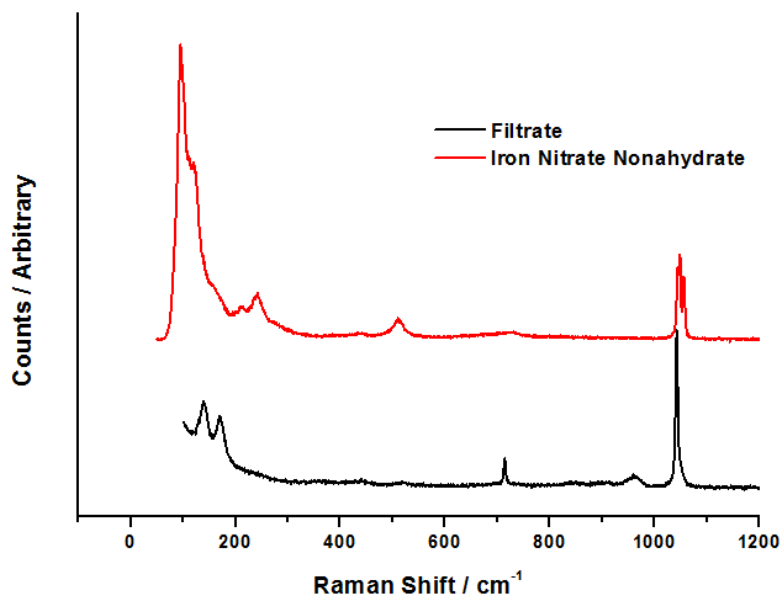


Figure 31. Raman of the filtrate after washing, compared with initial iron nitrate precursor.

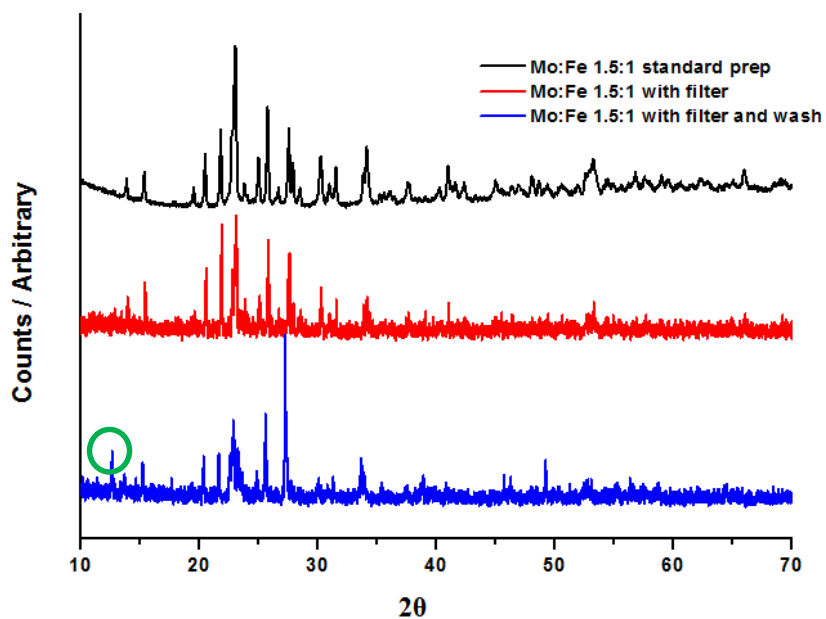


Figure 32. XRD data for stoichiometric $\text{Fe}_2(\text{MoO}_4)_3$ standard, after washing, and after washing and filtering. Green circled band is a strong indication for MoO_3 formation.

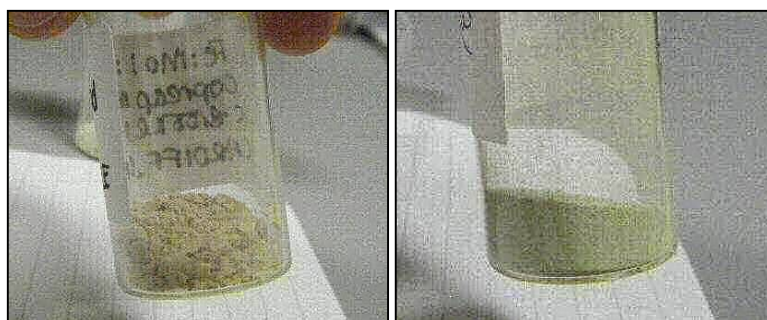


Figure 33. Colour of the stoichiometric catalyst (left, yellow/brown) vs. catalyst after washing and filtering (right, pale green).

3.3.2. Effects of Calcination Temperature

Further preparation variables have been addressed. It is of the opinion of Stiles and Koch [54], that even very slight deviations from the conventional preparation scheme can bring adverse effects on the catalytic performance. The same authors comment on how the molybdenum species is highly susceptible to changes in calcination temperature. With Mo thought to exist at the catalyst surface in the industrial catalyst, it is important to address this variable in more detail.

Table 8. BET surface areas for Mo:Fe 2.2:1 catalysts calcined to various temperatures.

Catalyst	Surface Area / m^2g^{-1}
2.2:1 Mo:Fe dried at 120 °C	1.2349
2.2:1 Mo:Fe calcined at 220 °C	4.0394
2.2:1 Mo:Fe calcined at 280 °C	4.8452
2.2:1 Mo:Fe calcined at 320 °C	3.91
2.2:1 Mo:Fe calcined at 500 °C	2.94
2.2:1 Mo:Fe calcined at 600 °C	1.05

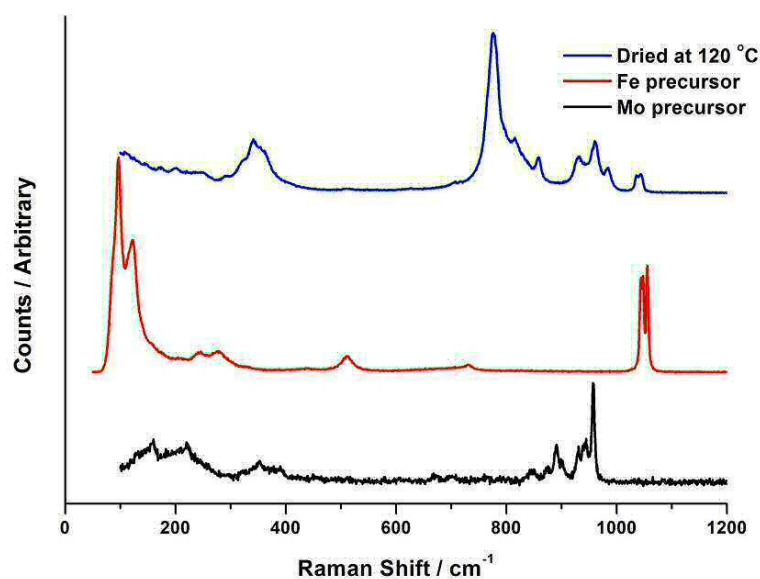


Figure 34. Raman data for Mo:Fe 2.2:1 catalyst after drying at 120 °C/ 24 hours, and Fe and Mo nitrate precursors.

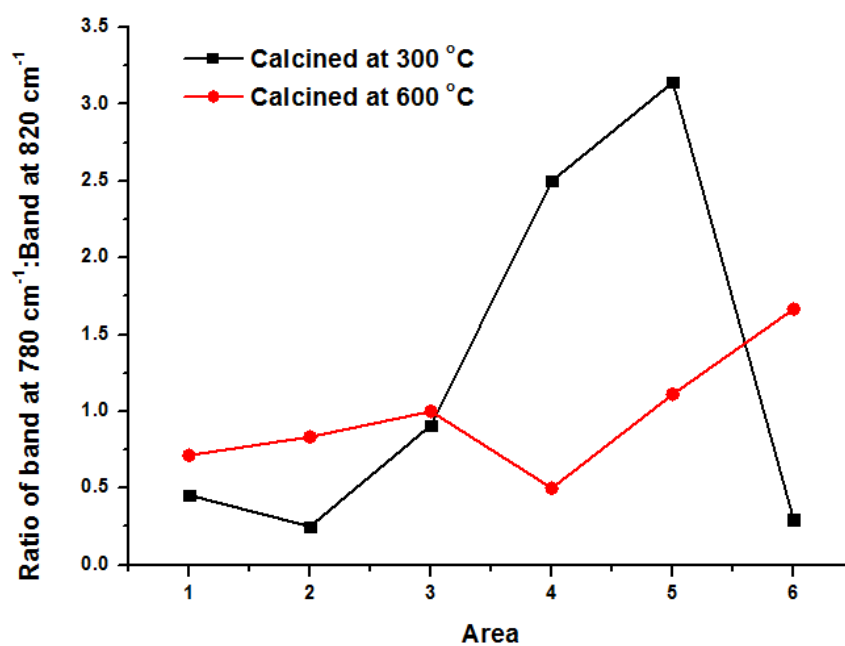


Figure 35. Raman mapping for two calcination treatments at 300 and 600 °C, for the catalyst with a Mo:Fe ratio of 2.2:1.

The calcination of co-precipitated iron molybdate (Mo:Fe 2.2:1) has been investigated under several conditions. Initial investigations involved studying the phase formed with increasing calcination temperature. Raman was used to examine this, whilst also probing the homogeneity of the samples. Spectra taken of the dried phase demonstrates that the

formation of iron molybdate has already begun, highlighted through the bands at 780 and 820 cm^{-1} , and also the bands in the region of 960-990 cm^{-1} (Figure 34). However, in addition to this, there are also further bands present at 860 cm^{-1} (indexed to the Mo nitrate precursor) and 1050 cm^{-1} (indexed to the Fe nitrate precursor). Since prepared in a Mo:Fe ratio of 2.2:1, the bands at 820 and 990 cm^{-1} are expected to be more intense, with a greater spectral intensity than those for $\text{Fe}_2(\text{MoO}_4)_3$ (Figure 16). However this is not the case, and with the presence of the precursor bands it is suggesting that not all the precursor has been combined into the synthesis procedure, and further calcination is required.

A study by Beale *et al.* prepared iron molybdates of varying ratios successfully by a hydrothermal method [9]. For Mo:Fe 1.5:1, phase-pure $\text{Fe}_2(\text{MoO}_4)_3$ resulted from syntheses performed at temperatures as low as 100 °C in under 4h. For the catalyst with a Mo:Fe ratio of 3:1, XRD, Raman and EXAFS data revealed the formation of a high surface area formed from a mixed phase material, consisting of a poorly crystalline Mo_5O_{14} , and an amorphous $\text{Fe}_2(\text{MoO}_4)_3$ type precursor. Both these phases proved thermally unstable above 300 °C, forming mixed phase $\text{Fe}_2(\text{MoO}_4)_3/\text{MoO}_3$.

Catalysts have been calcined in the range of 120- 600 °C. Results for the Mo:Fe 2.2:1 catalyst calcined at 300 °C are demonstrated in the Appendix (A7). It is shown that there is no longer evidence for the initial Mo and Fe precursors, as was seen for the dried material. The MoO_3 has now formed, with the intensity of the bands at 820 and 990 cm^{-1} clearly more intense than they were for the dried sample. However, Raman mapping (Figure 36 and also Appendix A7) across sections of the sample reveals that the catalyst lacks homogeneity, with huge differences between the relative intensities of the bands at 780/820 cm^{-1} , and 970/990 cm^{-1} for the $\text{Fe}_2(\text{MoO}_4)_3$: MoO_3 phases respectively. This was conclusive across a range of sample areas.

With an increase of calcination temperature to 600 °C, this delivers a more homogeneous catalyst. Raman mapping was once again performed across a section of the catalyst, with results exhibited in Figure 35. The fluctuations in catalyst composition are far less sporadic than those seen for the catalyst calcined at 300 °C. It would therefore infer that a higher calcination is required for catalyst homogeneity. There doesn't appear to be any loss of MoO_3 though volatilisation, with MoO_3 clearly evident (Appendix A7).

A study by Popov *et al.* [55], studies the effect of calcination temperature on the surface composition of MoFe catalysts for methanol oxidation. XPS studies revealed a decrease in the concentration of Fe atoms on the catalyst surface with increasing calcination temperature. Through cross comparison with reactivity data, the conclusions

of the study dictated that the active component of the catalyst is molybdenum oxide at the surface of ferric molybdate.

Trifiro *et al.* [56] further highlight the effects of calcination temperature on catalyst structure. They note three different transformations in the catalyst with temperature increase. The first change was viewed at 350 °C, initiated by bulk diffusion. The second transformation is observed between 450- 500 °C, originated from the total oxidation of Fe(II) to Fe(III). The final transformation occurs at 600 °C, characterised by a decrease of catalyst surface area. This is also seen here, referring to Table 8, where a decrease in surface area is seen for the 2.2:1 catalyst calcined at 600 °C. It is assumed sintering effects take place, which would bring a decrease in the catalyst activity.

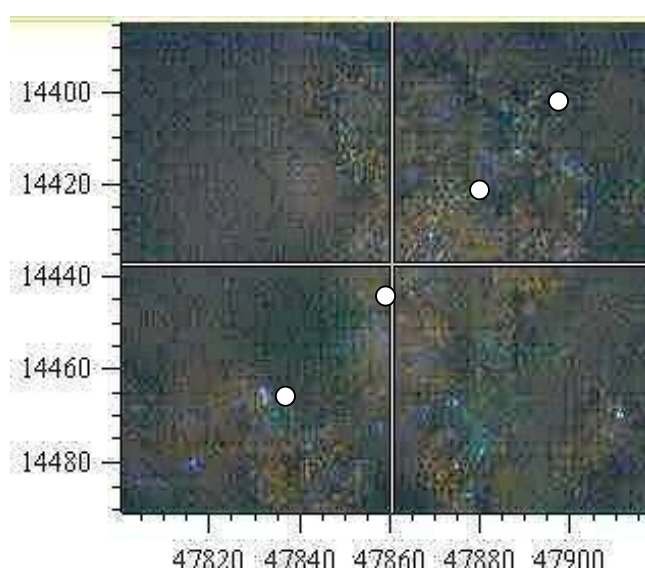


Figure 36. Microscope set up for Raman mapping.

Further effects of calcination variations have been investigated, comparing the effects of calcining in the lab muffle furnace under static air, versus the tube furnace with flowing compressed air, both at 500 °C for a Mo:Fe ratio of 2.2:1. For the sample calcined under the muffle treatment, there was a far more homogeneous consistency (Figure 37), as also proven through Raman mapping. MoO₃ was clearly present, with no indication for Fe enrichment at any point across the scan. The calcination performed in the tube furnace was executed by loading the sample in a calcination boat in the middle of the furnace bed, whilst flowing compressed air over the catalyst bed. Analysis of the Raman data showed a sample with less homogeneity, whilst also evidencing a loss of MoO₃, presumably through volatilisation. Figure 37 shows the sample calcined in the tube furnace to have a higher intensity for the Fe₂(MoO₄)₃ phase, as opposed to the expected MoO₃ phase bands at 820 and 990 cm⁻¹. A build-up of white solid was also seen to form at the end of the

tube on cooling. It is concluded that calcining under flowing air is not suitable. It brings significant problems with sample consistency.

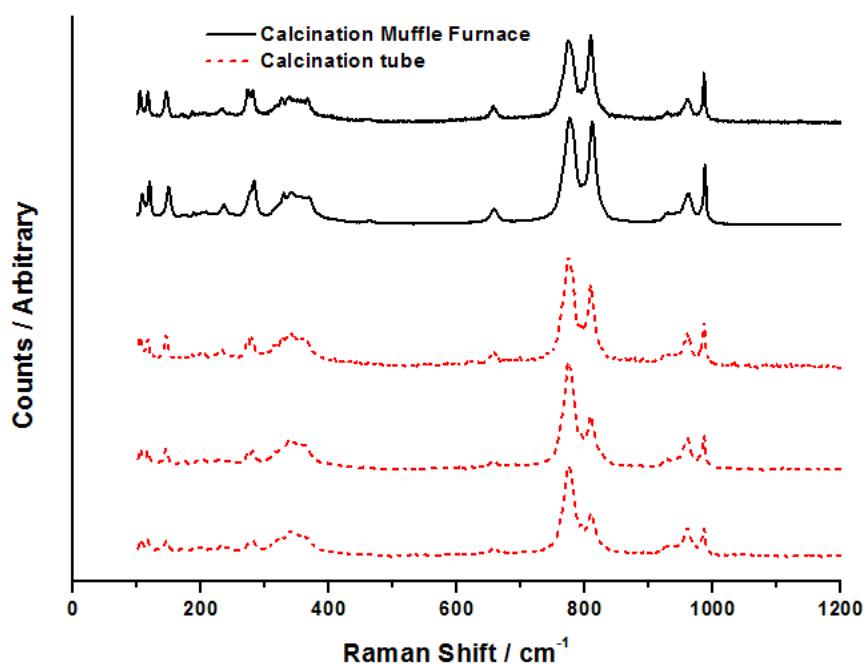


Figure 37. Raman data for Mo:Fe 2.2:1 under different heat treatments. Catalysts were calcined in the muffle furnace under static air (black) and in the tube furnace under flowing compressed air (red dashed).

3.3.3. Solid State Mixing

Table 9. BET surface area characterisation of solid state mixing method.

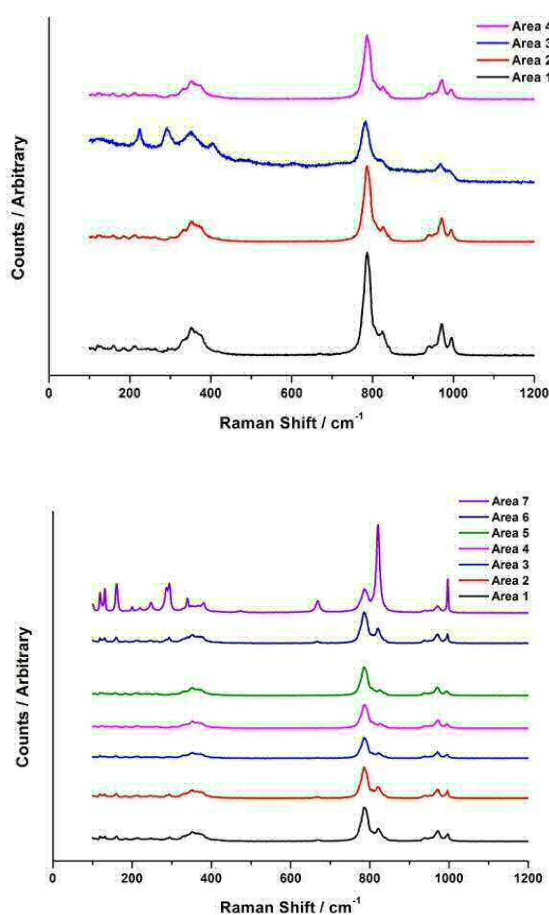
Catalyst	Surface Area / m ² g ⁻¹
Bulk Mo:Fe 1.7:1 co-precipitation	2.94
Solid state mixing Mo:Fe 1.7:1 without acid	5.23
Solid state mixing Mo:Fe 1.7:1 with acid	1.54

As well as investigating preparation variables, an alternative synthesis method has been adopted by means of physical mixing of the solid state precursors. This method benefits from being simple and quick to execute. Catalysts were produced with a Mo:Fe ratio of 1.7:1, one procedure involving the addition of nitric acid, the other without. Nitric acid is thought to be required to evoke the correct Mo (VI) species for molybdate formation.

Initial characterisation exploited Raman spectroscopy (Figure 38). Without acid present in the synthesis procedure, the catalyst appears to be homogeneous, applicable for several scans taken in different areas across the sample. However, problems arrive with the stoichiometry of the catalyst, demonstrating a catalyst with a Mo:Fe ratio of 1.5:1.

The bands at 820 and 990 cm^{-1} representative of MoO_3 formation, are less defined than expected for a 1.7:1 catalyst. There are also areas of high Fe content, with Area 3 demonstrating Fe_2O_3 formation (Refer to Figure 2 for comparison of bands). Fe_2O_3 has been shown to hinder catalyst performance in terms of selectivity.

With acid present in the preparation, this allows for a higher incorporation of the Mo species into the $\text{Fe}_2(\text{MoO}_4)_3$ lattice. Raman spectroscopy supports this, showing areas where MoO_3 is clearly dominating (Figure 39). However, these catalysts can't be produced in a reproducible way, showing a very inhomogeneous composition, when comparing between different areas on the sample. This agrees with work of Li *et al.* [7], who prepare iron molybdates through the preparation of dry and wet mixing of solid salts of the two metals. Better performances were achieved through the wet technique, due to higher Mo integration, which results in an increase in the number of active sites (Mo (VI) in connection with Fe(III) through an oxygen bridge).



Figures 38 -39. Raman mapping data for solid state mixing catalysts with a Mo:Fe ratio of 1.7:1 without (top) and with (bottom) acid during the preparation.

BET results (Table 9) show a detrimental effect on catalyst surface area when prepared through solid state mixing with acid. However, when prepared without acid, the catalyst surface area is increased by 2 fold against co-precipitation, which could improve the catalytic activity. Conversely, the increase in surface area could be a result of the inhomogeneity of the sample. Areas of high Fe content will bring a higher surface area as shown previously, with the surface area of Fe_2O_3 being significantly higher than FeMo containing catalysts (Table 1). However it would also bring a negative effect on the catalyst performance.

Reactivity data has been pinnacle in assessing the potential of these mixed state catalysts. Figure 40 shows TPD data for the Mo:Fe 1.7:1 catalyst produced under dry conditions without acid. The TPD data is comparable to that for bulk iron molybdate produced through co-precipitation (Figure 10), with the TH_2CO at 195°C . Similar selectivity was also observed.

However, on inspection of the TPPFR data, the catalyst shows an inferior performance to that for the co-precipitated sample. At higher temperatures above 300°C (Figure 41) selectivity diminishes, as CO production begins to prevail. This is an effect of the isolated surface iron sites formed from the dry mixing of the solid state precursors. It has been proposed that isolated Fe-Mo pairs are responsible for CO production [34]. More crucially, there is also the possibility of formate adsorption, inferred by the production of H_2 and CO_2 at temperatures above 350°C . This reinforces what has already been revealed from the Raman data.

For the catalyst prepared with acid, again the TPD profile (Figure 42) shows analogous results to those for the catalyst prepared through co-precipitation. Formaldehyde appears to be the only C1 product detected, with the temperature of its formation slightly higher at 210°C . The TPPFR (Figure 43) shows an improvement over the catalyst prepared without acid. Formate adsorption does not appear to have occurred, with no evidence for H_2 and CO_2 production detected in the mass spectrometer at higher at higher temperatures. The conversion is comparable to that of the co-precipitated method (Figure 44).

In conclusion, although initially attractive due to their ease of preparation, catalysts prepared through solid state mixing bring problems in terms of their homogeneity and reproducibility. It would therefore be difficult to scale the process up to use on an industrial scale. Although the catalysts are able to match the conversion of the co-precipitated sample (Figures 10-12), the selectivity data evidences that these catalysts are unable to compete with that of the conventional co-precipitated sample.

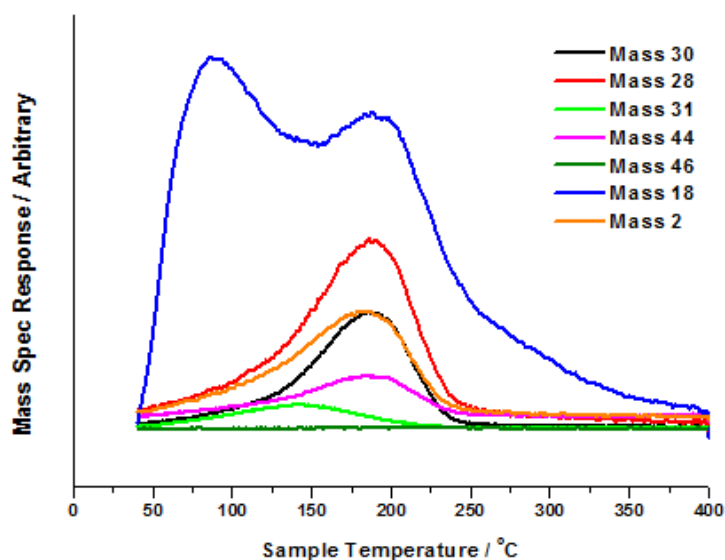


Figure 40. TPD of MeOH/He data (raw) for Mo:Fe 1.7:1 prepared through solid state mixing without acid. Mass 30= H_2CO , Mass 28= CO , Mass 31= MeOH , Mass 44= CO_2 , Mass 46= DME , Mass 18= H_2O , Mass 2= H_2 .

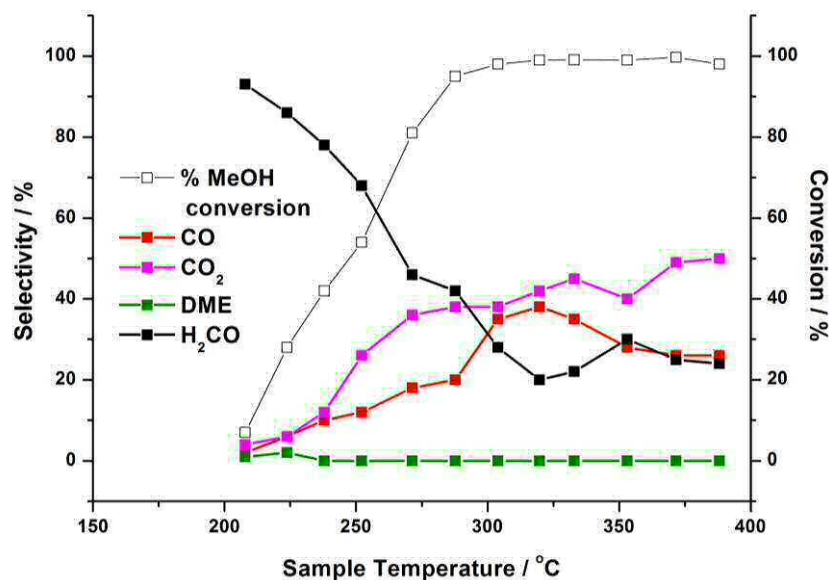


Figure 41. TPPFR under MeOH in O_2/He data for Mo:Fe 1.7:1 prepared through solid state mixing without acid. Subtractions have been made for the various cracking fragmentation of each product (Chapter 1, Section 3.3), to give a plot for selectivity and conversion.

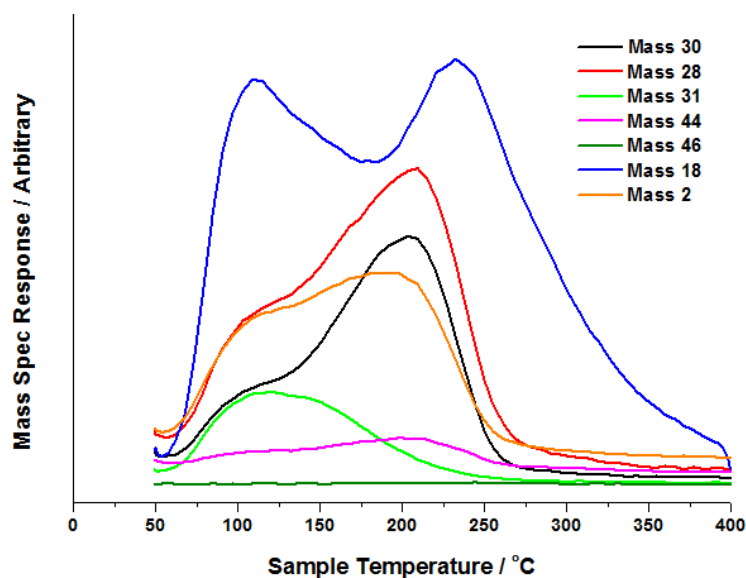


Figure 42. TPD in MeOH/He data for Mo:Fe 1.7:1 prepared through solid state mixing with acid. Mass 30= H_2CO , Mass 28= CO , Mass 31= MeOH , Mass 44= CO_2 , Mass 46= DME , Mass 18= H_2O , Mass 2 = H_2 .

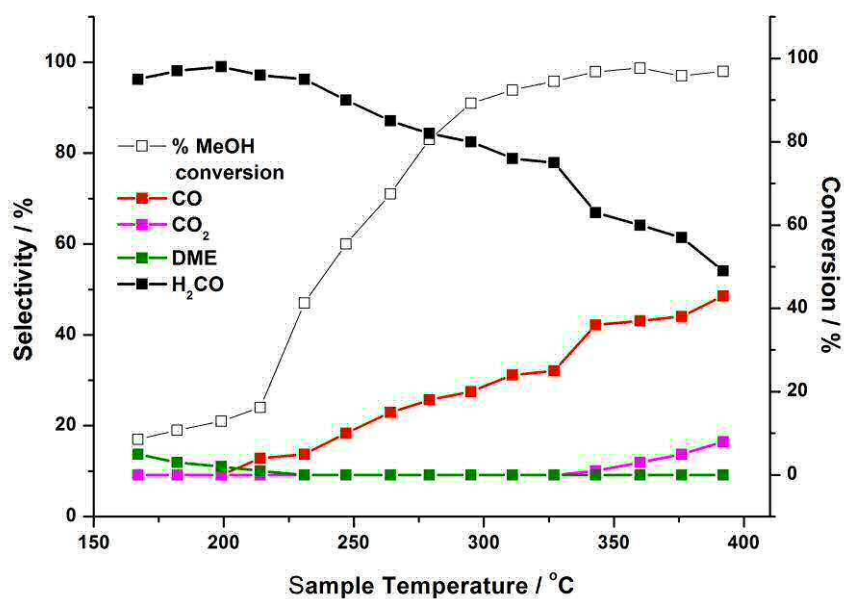


Figure 43. TPPFR under MeOH in O_2/He data for Mo:Fe 1.7:1 prepared through solid state mixing with acid. Subtractions have been made for the various cracking fragmentation of each product (Chapter 1, Section 3.3), to give a plot for selectivity and conversion.

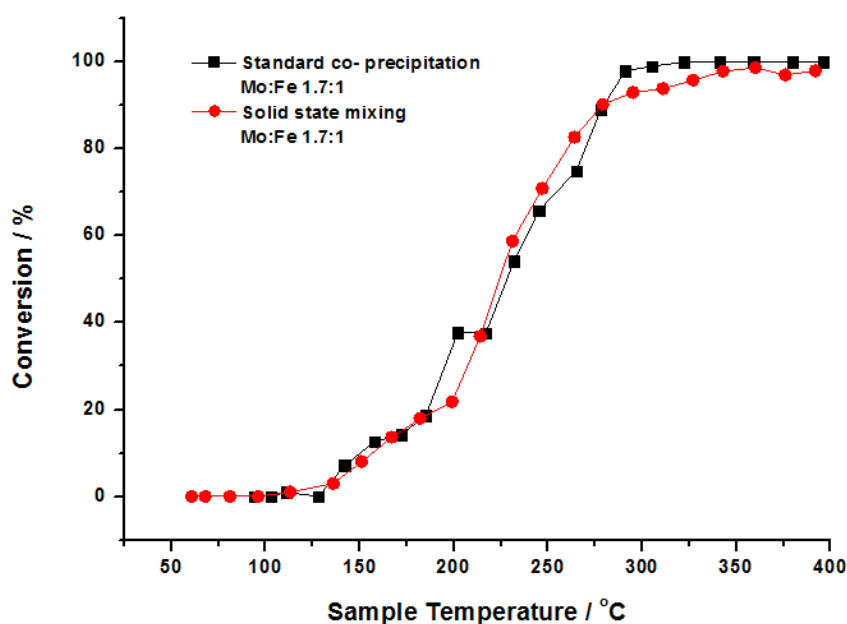


Figure 44. Comparison of conversion for conventional co-precipitated Mo:Fe 1.7:1 versus that prepared through solid state mixing (with acid).

3.3.4. Preparation of High Surface Area Molybdena

Molybdenum oxides are of great interest to scientists, acting as attractive compounds in selective oxidation catalysis. As mentioned previously, orthorhombic MoO_3 consists of a layered structure built up of two layers of chain distorted MoO_6 octahedra, which run along the c axis. Kihlberg *et al.* [57] study this structure in detail, specifically through use of XRD analysis. Five different Mo-O bond distances are recognised; two terminal Mo=O bonds at 1.67 and 1.73 Å, a Mo-O bridging oxygen distance of 1.94 Å, and two final remaining distances at 2.33 and 2.25 Å, attributed to the neighbouring oxygen distances within the chains of MoO_6 octahedra. The structure is considered distorted octahedral, since Mo-O-Mo angles differ from that for conventional values found in a symmetric octahedron (Figure 47).

It has been shown (Figures 7-9), that MoO_3 shows a good selectivity to formaldehyde. However, although superior to other MoFe based catalysts in this respect, it fails to show the conversion that bulk iron molybdate is able to demonstrate. In order to create a catalyst which adopts both maximised selectivity and conversion, it would be desirable to create MoO_3 with a higher surface area. Several methods have been employed in an attempt to accomplish this.

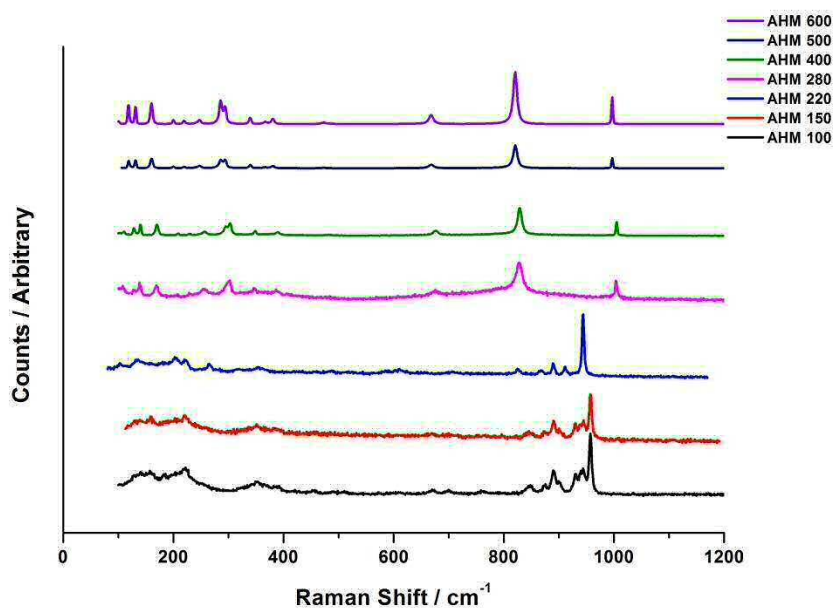


Figure 45. Increasing calcination temperature of ammonium heptamolybdate (AHM).

AHM was placed in a calcination boat in the centre of the tube furnace. A flow of compressed air was passed over the catalyst at increasing temperatures. Raman was used to assess the Mo oxide phases forming with increasing calcination temperature.

The Raman spectra in Figure 45 illustrate the effect of annealing temperature on the AHM precursor. It is shown that MoO_3 does not form until 280°C , as evidenced through the bands at 820 and 990 cm^{-1} , assignable to the stretching vibrations of the terminal $\text{Mo}=\text{O}$ bonds along the a and b axes respectively. With increasing temperature, these bands become more defined in nature, as a result of the increased crystallinity and order created within the sample.

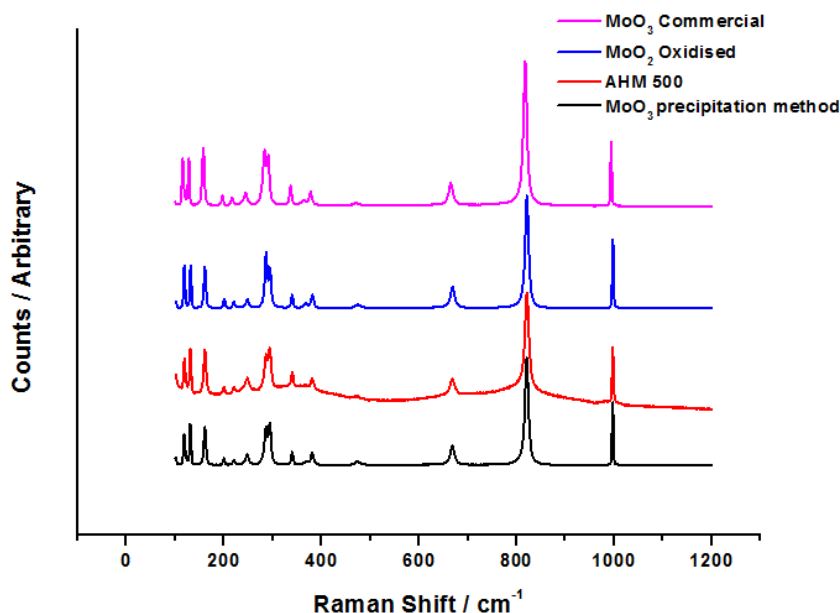


Figure 46. Raman for various prepared MoO_3 catalysts. MoO_3 was produced through oxidising MoO_2 under a flow of compressed air in the tube furnace (blue), AHM was heated to 500°C (red), and a dilute solution of AHM was added dropwise to acidified water (black). MoO_3 was seen to crash out from the dropping solution (Experimental details Chapter 2).

A number of other techniques have also been trialled for their effectiveness in the production of MoO_3 . Figure 46 shows Raman data for these catalysts. All samples show the characteristic Raman bands of MoO_3 , outlined in Table 10.

Table 10. Raman bands for MoO_3 and schematic representation Figure 47.

Raman Band / cm^{-1}	Assignment
996	Stretching vibration of terminal $\text{Mo}=\text{O}$
822	Stretching vibration of terminal $\text{Mo}=\text{O}$
667	$\text{Mo}-\text{O}-\text{Mo}$ stretch
473	$\text{O}-\text{Mo}-\text{O}$ stretch and bend
380	$\text{O}-\text{M}-\text{O}$ scissor
366	$\text{O}-\text{Mo}-\text{O}$ scissor
334	$\text{O}-\text{M}-\text{O}$ bend
293	Wagging mode terminal $\text{Mo}=\text{O}$
285	Wagging mode terminal $\text{Mo}=\text{O}$
247	$\text{O}=\text{Mo}=\text{O}$ twist
216	Rotational rigid MoO_4 mode
197	$\text{O}=\text{Mo}=\text{O}$ twist
159	Translational rigid MoO_4 chain mode
129	Translational rigid MoO_4 chain mode
116	Translational rigid MoO_4 chain mode
100	Translational rigid MoO_4 chain mode
89	Translational rigid MoO_4 chain mode

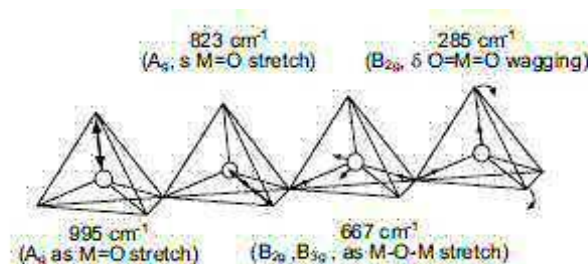


Figure 47. Schematic drawing of the atomic motions for the Raman bands at 285, 666, 820 and 990 cm^{-1} (Thesis, Martin Dieterle, Berlin, 2001).

The Raman bands at 990 and 820 cm^{-1} are here assignable to the terminal Mo=O stretching vibrations along the *a* and *b* axes respectively [58], although this is not agreed by all authors (Table 2). The bridging oxygens along the *c*-axis are the most weakly bound, therefore this brings a weakness to the structure making it more susceptible to change. With the generation of oxygen vacancies, this leads to anion vacancies along the *c*-axis. With loss of a bridging oxygen, this can cause a displacement of a Mo atom towards the terminal oxygen in the *b*- direction, ultimately weakening the terminal O bond along the *a*-axis. Changes of these types are responsible for small deviations in the Raman spectra.

Only minor variations are observed of the Raman bands for the main vibrations at 660, 820 and 990 cm^{-1} for the various produced catalysts. The AHM catalyst calcined to 500 °C shows the highest degree of peak broadening at these bands, which could infer finer particle morphology. Finer particle size material will react more effectively in chemical and catalytic processes than larger particle size material. Hence this catalyst could provide a means of improving the conversion rate of methanol.

In Figure 46, the intensity of the wagging modes of the terminal Mo=O groups at 280 and 290 cm^{-1} alter with changing catalyst preparation. These wagging modes are polarised parallel to the *c*-direction, and are a function of the oxygen to metal ratio present within the catalyst.

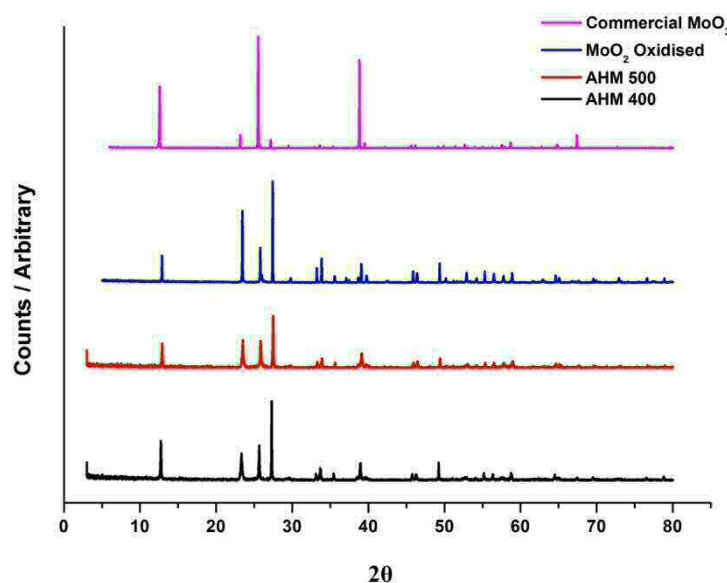


Figure 48. XRD for various prepared MoO_3 catalysts (description as Figure 46).

XRD analysis was run to complement the results obtained through Raman spectroscopy. It is shown that the samples prepared in-house show slight variations to the commercial bulk MoO_3 . Additional bands are detected further out in 2θ , as well as a change in the relative intensities of bands throughout. With a change in the preparation method employed, bonds within the structure are expected to change, as a result of changes in oxygen vacancies. Bonds will become elongated, and in addition to this, effects of stress/strain and/or particle size will further affect the structure.

With a knowledge of slight structural changes occurring with novel catalyst preparations, BET analysis was performed to assess the surface area of the generated catalysts. Figure 49 summarises the results. Of all the catalysts produced, it is shown that the catalyst produced from heating AHM to 500°C shows the most promise of having improved catalytic activity. The low surface area of MoO_3 can be attributed to the platelet like morphology of the catalyst. The catalyst synthesised from heating AHM to 500°C , demonstrates an almost ten- fold increase in surface area over that of the commercial standard. Infact, the surface area at approximately $5.5 \text{ m}^2\text{g}^{-1}$, is comparable to that for bulk iron molybdate, which demonstrates good activity (Figure 12).

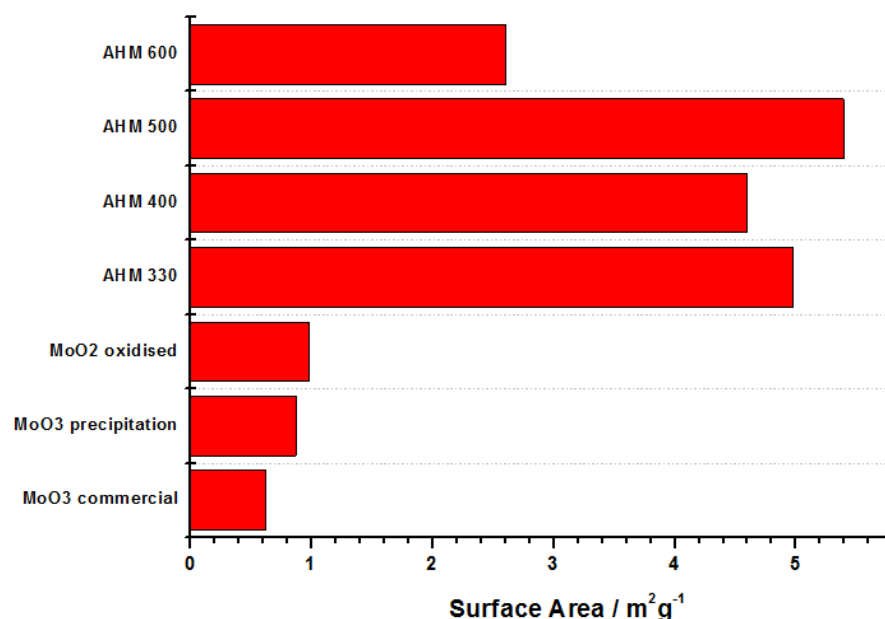


Figure 49. Measured surface areas for various prepared Mo oxide catalysts, obtained through BET.

Catalytic testing was performed, with focus on the AHM catalyst heated to 500 °C, since this catalyst shows the most potential due to its improved surface area. Comparing between datasets (AHM 500 °C with commercial MoO₃), the two perform very similarly in terms of their selectivity, with both demonstrating a 100 % selectivity to formaldehyde at low temperatures (Figures 50-51). Both produce DME and CO₂ as by-products, with the onset of CO₂ production occurring slightly earlier for the AHM catalyst, from 300 °C. This would imply that there could be a higher oxygen availability at the surface of this catalyst, aiding the additional oxidation of formaldehyde to further oxidation products. A marked difference between the two materials is the conversion rate of methanol. The commercial catalyst is well known for its undesirable activity, with 50 % conversion not reached until 275 °C. For the AHM catalyst calcined to 500 °C, there is a significant improvement, with 50 % conversion by 235 °C, in line with the conversion rates described for bulk iron molybdate (Figure 12).

Unfortunately the catalyst was not able to uphold its improved activity, with subsequent TPPFR studies showing results analogous to that of commercial MoO₃. The catalyst is assumed to be prone to sintering upon use, unable to maintain the stability required for repeated performance.

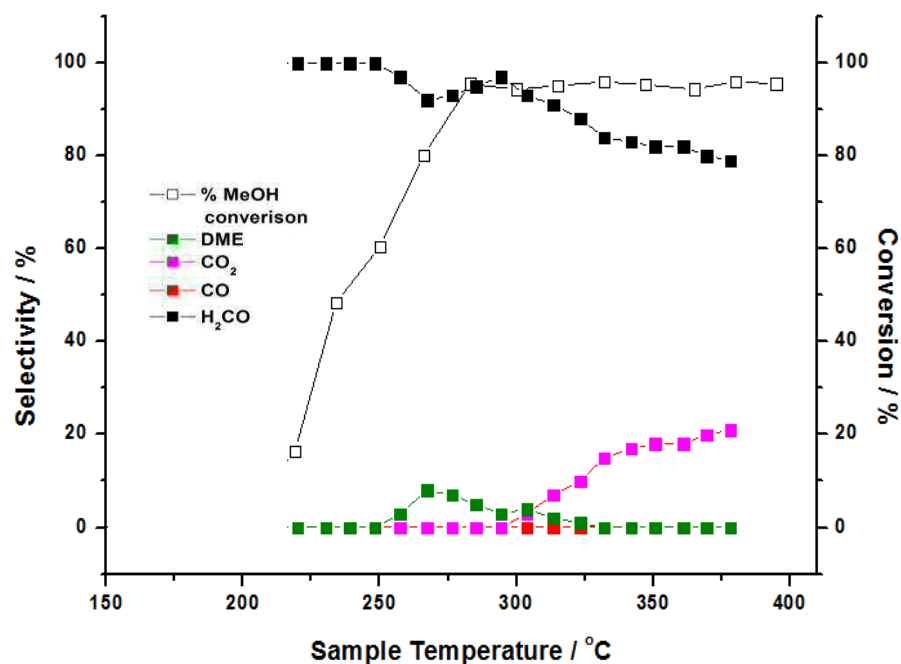


Figure 50. TPPFR under MeOH in O₂/He data for AHM 500°C. Subtractions have been made for the various cracking fragmentation of each product (Chapter 1, Section 3.3), to give a plot of selectivity and conversion.

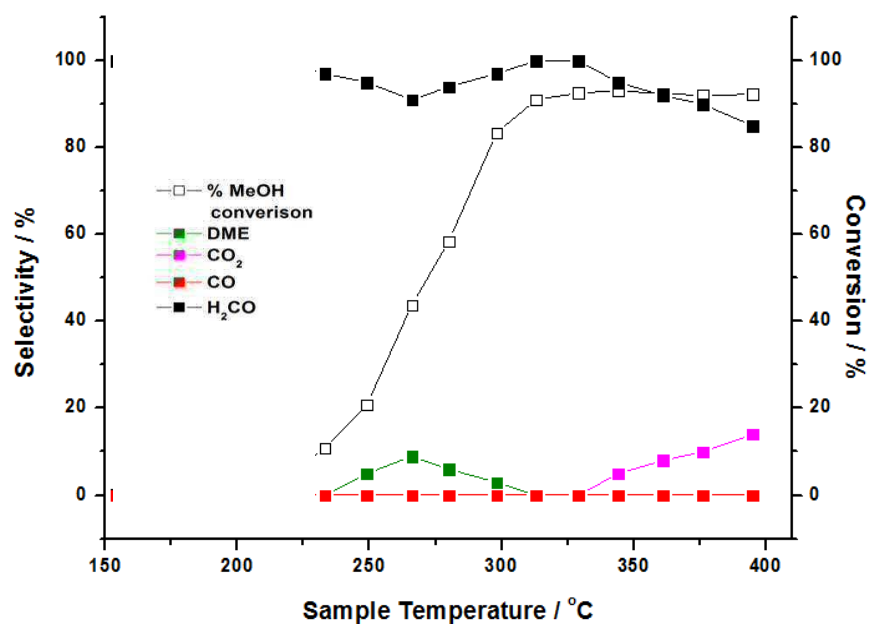


Figure 51. TPPFR under MeOH in O₂/He data for commercial MoO₃. Subtractions have been made for the various cracking fragmentation of each product (Chapter 1, Section 3.3), to give a plot of selectivity and conversion.

3.4. Variables in CATLAB operation

3.4.1. Ramped Pulse versus Isothermal pulse

Under ordinary reaction conditions (TPPFR), the catalyst is ramped in temperature, whilst MeOH is pulsed over the sample under O_2 , monitoring the reaction products obtained. To ensure that the methanol reaction is stable at any given temperature, isothermal pulsing studies were applied. For this, 1 μ l methanol pulses were passed over the catalyst bed every two minutes, at constant temperature for a set time period. Figure 52 displays the results for the Mo:Fe 1.7:1 catalyst under isothermal pulsing at 275 °C. It is shown that the reactivity profile maintains constant throughout, thus implying a stable product distribution. The conversion of MeOH remains high (83 %), which is comparable to the 81 % observed over the catalyst under pulsing conditions upon ramping and arriving at 275 °C. For the isothermal study, the selectivity to formaldehyde was observed at 85 %, whilst for the TPPFR reaction it is slightly lower at 78 %. Selectivity remained constant, varying only within the limits of error. Industrially, catalysts are used for 6-12 months, during which they are required to maintain formaldehyde selectivity throughout. The isothermal pulsing was continued for 60 minutes. In order to assess the long term stability of the catalyst, the pulsing would need to be continued for longer, under automated control. With manual injections, there is a limit to the time period over which the injections can be continued. Continuous flow testing would also be beneficial.

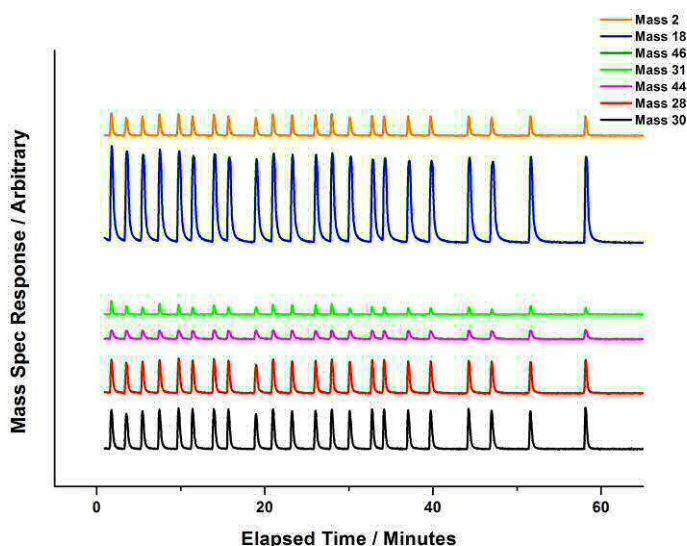
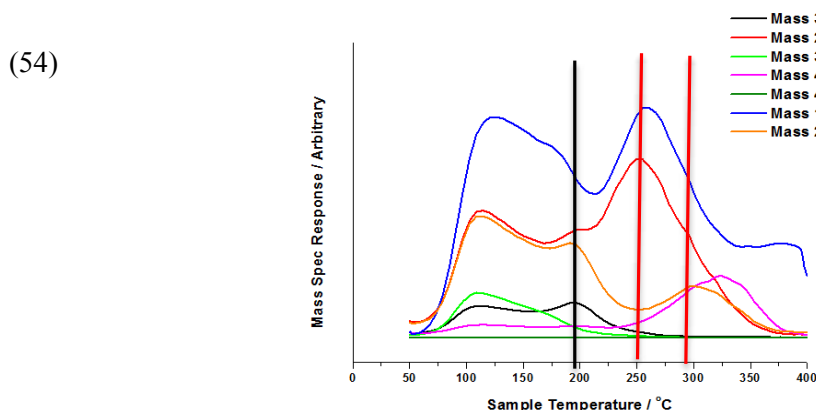
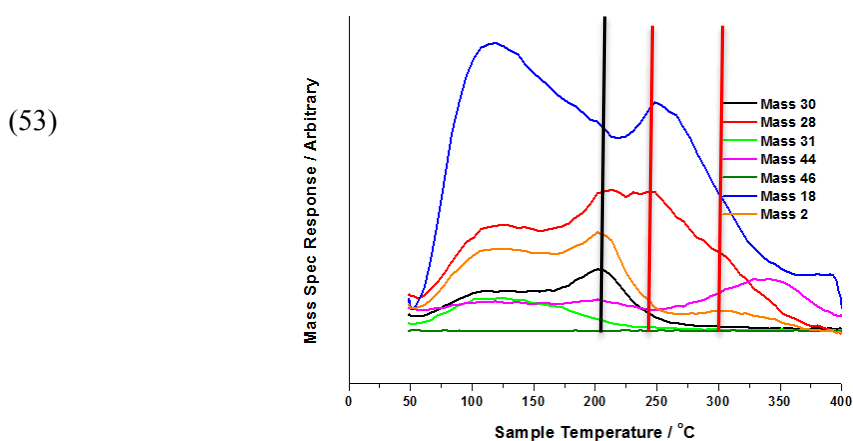


Figure 52. Isothermal pulsing data (raw data) of MeOH in 10% O_2/He , for Mo:Fe 1.7:1 held at 275 °C. MeOH was continually injected over the catalyst and the mass spectrometer response recorded. Mass 30= H_2CO , Mass 28= CO , Mass 31= $MeOH$, Mass 44= CO_2 , Mass 46= DME , Mass 18= H_2O , Mass 2 = H_2 .

3.4.2. Mass Size Variation

The mass of catalyst used in the reactor is a fundamental consideration which must be addressed and maintained, since the mass used is a major contributor to the overall selectivity observed for the reaction. This has been exposed through varying the bed length of the catalyst, with the specific example of the Mo:Fe 0.02:1 catalyst addressed. In studying different catalyst loadings, it is possible to understand the reactivity profile in each section of the catalyst bed, deducing the products produced at the start of the bed, from the end.



Figures 53-54. TPD of MeOH/He for Mo:Fe 0.02:1 for 0.05 g (top) and 0.25 g (bottom) - raw data. MeOH was dosed to saturation over the catalyst at room temperature. The furnace was then ramped in temperature and the products of formation observed by mass spectrometry. Corresponding masses are; Mass 30= H_2CO , Mass 28= CO , Mass 31= MeOH , Mass 44= CO_2 , Mass 46= DME , Mass 18= H_2O . Black line= H_2CO formation, Red line= CO formation.

TPD for the Mo:Fe 0.02:1 catalyst are presented in Figures 53- 54 for 0.05 and 0.25 g respectively. Comparing between datasets, it is apparent that both produce formaldehyde, and significant amounts of CO (Mass 28) and CO_2 (Mass 44) are produced as C1

products. However, the temperature of formation, and selectivity to each of these individual products varies considerably with catalyst loading.

It is shown that for a 0.05g loading, the H_2CO (Mass 30) occurs at 210°C . The production of CO (Mass 28) shortly follows, rising from 225°C and peaking at 245°C . A second peak of CO desorption appears at 300°C . At temperatures above this, CO_2 (Mass 44) is detected, with a peak in the desorption profile at 340°C .

For the 0.25 g loading, the H_2CO occurs at a lowered temperature of 190°C . CO production appears to desorb at approximately 255°C , but in this instance with a much higher intensity in the desorption profile. There is also a second desorption peak hidden within the large desorption tail of the Mass 28 response for CO, occurring at 300°C . CO_2 is again detected, with a T_{CO_2} at 330°C .

The lower temperature of formaldehyde (Mass 30) for the 0.25 g loading is a direct reflection of the higher activity of this loading. The relative intensities of the formaldehyde (Mass 30):CO (Mass 28) peaks however, can provide information regarding the reaction mechanisms.

The slightly higher temperature of CO evolution (Mass 28) is believed to occur as a primary product, whilst lower temperature CO evolution is a secondary product produced from further oxidation of formaldehyde.

The ratio of $\text{H}_2\text{CO}:\text{CO}$ remains at a constant value of approximately 1:1 for the primary CO, when increasing the catalyst loading from 0.05 g to 0.25 g. However in contrast, the $\text{H}_2\text{CO}:\text{CO}$ ratio for the lower temperature peak shifts from approximately 1:1 to 1:3 with increased catalyst loading.

This supports the low temperature CO to be produced through secondary reaction kinetics. With a greater loading of catalyst, there is an increase in secondary CO production, as a lengthened bed increases the opportunity for formaldehyde re-adsorption at empty sites further along the bed. Under re-adsorption it is more likely that the formaldehyde will further oxidise to carbon oxide products. As well as a rise in CO formation, there is also evidence for a rise in CO_2 (Mass 44) production for the 0.25 g loading, thus supporting this theory further.

TPPFR studies have also been executed, with results revealed in Figures 55-56. Both show a very similar reaction path with both mutually demonstrating 100 % conversion (Figure 56). The rate of conversion is significantly improved for the higher weight

loading (Figure 57), with T_{50%} conversion occurring at 185 and 260 °C for the 0.05 and 0.25 g catalysts respectively.

For the reaction loaded with 0.05 g of catalyst (Figure 55), at low temperatures, the major product formed is formaldehyde with 90 % of the overall selectivity. Formaldehyde selectivity then drops with rising temperature, so that by 285 °C it reaches 50 %. At this point, CO production constitutes the other 50 % of the total selectivity, rising steadily to 70 % by 330 °C. Formaldehyde production is maintained until 350 °C. CO₂ production does not begin until above 285 °C, upon reaching 75 % conversion. At the end of the thermal ramp, CO₂ forms the dominant product, demonstrating 60 % of the total selectivity, with the remainder as CO. No evidence for DME is detected at any point during the run. If DME was to form, it is more likely that this could proceed on the catalyst with a 0.05g loading. DME is formed through a coupling reaction of surface methoxys [58]. If sites are not saturated, the methoxy intermediates become more spread, and therefore less likely to react through dehydration. The lower the catalyst loading, the higher the possibility for surface saturation with methanol at room temperature.

The corresponding data for the reactor testing performed on 0.25 g of catalyst is also presented in Figure 55. The reactivity profile shows a strong resemblance to that for 0.05 g, however with an overall reduction in temperature for the onset of product formation. At 210 °C, formaldehyde forms 70 % of the products yielded, with CO forming the remaining 30 %. As formaldehyde production decreases with rising reaction temperature, CO production simultaneously rises. This implies CO production derives from the further oxidation of formaldehyde. The onset of CO₂ production arises earlier for this higher weight loading, forming from 250 °C. Again, CO₂ production does not occur until high conversions are reached.

In comparing the two weight loadings in TPD and TPPFR, the conversion and selectivity's at higher temperatures are able to enable insights into what happens towards the end of the catalyst bed (Figure 57). In the first 0.05 g of the catalyst bed, 100 % methanol conversion is achieved, with the drop in formaldehyde occurring later than for the higher loading. CO and CO₂ are both produced, forming 40 and 60 % respectively at the highest temperature. Towards the end of the bed, (shown from the data when 0.25 g is loaded), formaldehyde production diminishes earlier, allowing for the earlier onset temperature of CO production. CO and CO₂ production exist at 90 and 10 % respectively at the end of the reaction. CO₂ is now the dominant product. Adding more catalyst creates secondary reactions with formaldehyde being oxidised to unselective by-products in the

following way (Equation 10):



Equation 10

CO is likely to oxidise to CO_2 , occurring above 250°C , as opposed to the direction oxidation of methanol in a primary reaction. This agrees with the aforementioned TPD data.

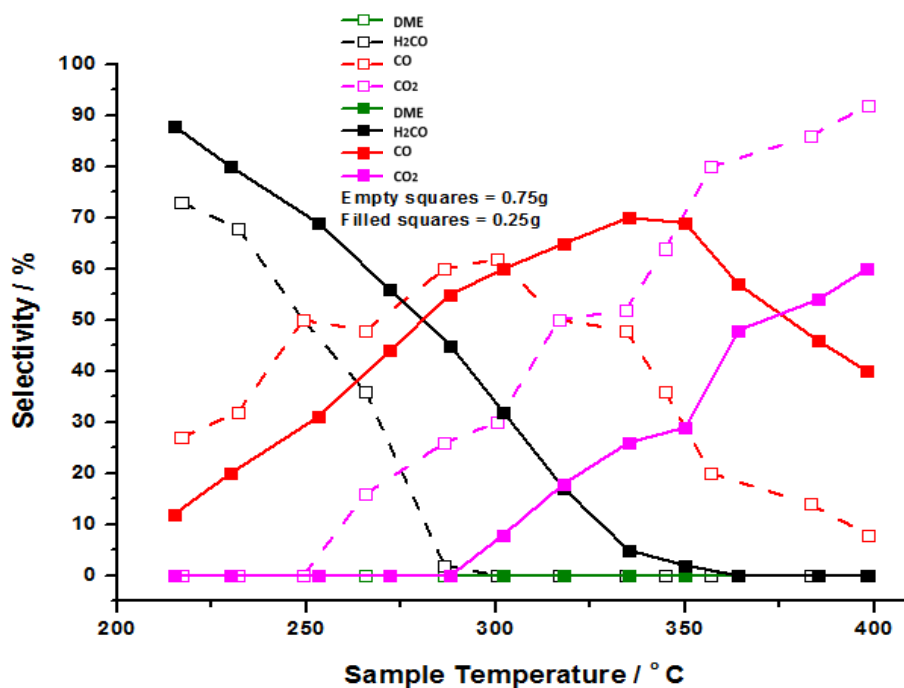


Figure 55. Comparison of selectivity data for iron molybdate with a Mo:Fe of 0.02:1 for 0.05 g and 0.25 g respectively for reaction in MeOH. MeOH was dosed continuously over the catalyst bed in 10 % O₂/He, whilst ramping the temperature of the catalyst bed to 400°C . Masses were monitored though mass spectrometry. Subtractions have been made for the various cracking fragmentation of each product (Chapter 1, Section 3.3), to give a plot of selectivity and conversion.

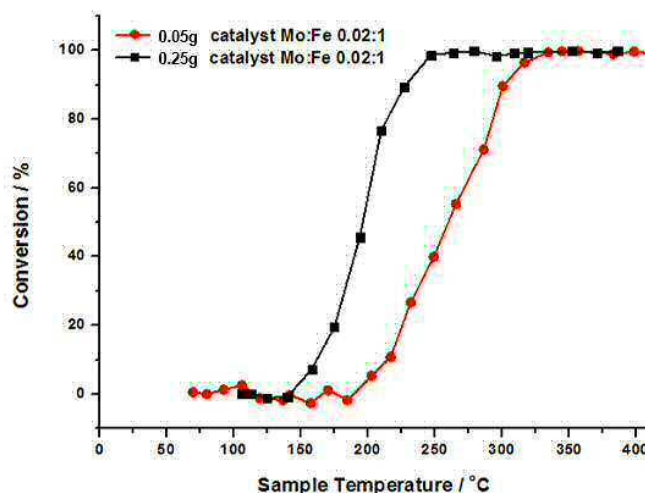


Figure 56. Comparison of MeOH conversion for Mo:Fe 0.02:1 for 0.05 g and 0.25 g respectively with increasing temperature.

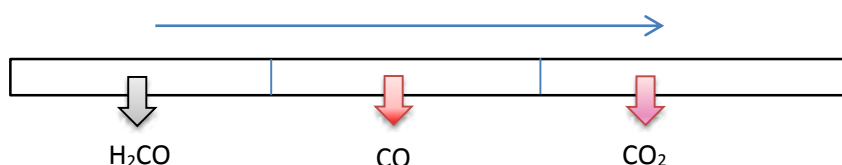


Figure 57. Products produced from different areas of the catalyst bed, from left to right represents the increasing length of catalyst bed.

4. Conclusions

Work within the chapter has summarised the importance of catalyst preparation and composition. It has been demonstrated that Fe rich catalysts are poor for the selective oxidation of methanol to formaldehyde, yielding CO_2 and H_2 as the dominant products. However the activity of these catalysts is desirable. Mo rich catalysts show a contradicting argument, favouring formaldehyde production, however are unable to show the same activity of the Fe rich catalysts.

Variations in catalyst preparation have involved solid state mixing, attempts to improve the low surface area of MoO_3 , altering catalyst calcination temperature, and the effect of filtering and washing during co-precipitation. Reactor variables have been tested and a standard protocol defined for testing catalysts. The effect of mass of catalyst used has been shown to have a significant influence on catalyst performance.

Catalysts have been characterised primarily through XRD and Raman spectroscopy, with data indexed to literature studies. It is shown that the stoichiometric catalyst with a Mo:Fe 1.5:1 ratio is formed from monophasic $\text{Fe}_2(\text{MoO}_4)_3$, with any Mo ratio above this also demonstrating MoO_3 in the catalyst composition.

TPPFR and TPD testing are essential techniques for studying the performance of catalysts, and it has been shown that this way of catalytic testing is comparable to the continuous flow mode used industrially. Since the TPD data for MoO_3 and $\text{Fe}_2(\text{MoO}_4)_3$ are so similar, this is the first inclination that the surface terminating layers in these catalysts is also comparable: being Mo rich. This will be the focus of proceeding chapters.

5. References

1. Adkins, H. and W.R. Peterson, *The oxidation of methanol with air over iron, molybdenum, and iron-molybdenum oxides*. Journal of the American Chemical Society, 1931. **53**(4): p. 1512-1520.
2. Soares, A.P.V., M.F. Portela, and A. Kiennemann, *Methanol selective oxidation to formaldehyde over iron molybdate catalysts*. Catalysis Reviews, 2005. **47**(1): p. 125-174.
3. Sun-Kou, M., et al., *Influence of the preparation method on the behaviour of Fe-Mo catalysts for the oxidation of methanol*. Journal of materials science, 1995. **30**(2): p. 496-503.
4. Cairati, L., et al., *Oxidation of Methanol in a Fluidized Bed. 1. Catalyst Attrition Resistance and Process Variable Study*. Industrial & Engineering Chemistry Process Design and Development, 1980. **19**(4): p. 561-565.
5. Wachs, I.E. and K. Routray, *Catalysis science of bulk mixed oxides*. ACS Catalysis, 2012. **2**(6): p. 1235-1246.
6. Topsøe, H., B. Clausen, and S. Mørup, *Mössbauer spectroscopy studies of catalysts: Some recent examples with emphasis on hydrodesulfurization catalysts*. Hyperfine Interactions, 1986. **27**(1-4): p. 231-248.
7. Li, J.-L., et al., *Improvement in reactivity, reproducibility and stability of Fe-Mo catalysts by wet mixing*. Catalysis today, 1999. **51**(1): p. 195-199.
8. Wachs, I.E. and L.E. Briand, *Mixing ferric oxide and molybdenum trioxide to form iron molybdate in fixed bed; catalytic oxidation of methanol to formaldehyde*, 2001, Google Patents.
9. Beale, A.M., et al., *An iron molybdate catalyst for methanol to formaldehyde conversion prepared by a hydrothermal method and its characterization*. Applied Catalysis A: General, 2009. **363**(1): p. 143-152.
10. Bowker, M., et al., *The selective oxidation of methanol on iron molybdate catalysts*. Topics in Catalysis, 2008. **48**(1-4): p. 158-165.
11. Soares, A.V., et al., *Iron molybdate catalysts for methanol to formaldehyde oxidation: effects of Mo excess on catalytic behaviour*. Applied Catalysis A: General, 2001. **206**(2): p. 221-229.
12. Chowdhry, U., et al., *Mechanism and surface structural effects in methanol oxidation over molybdates*. Applications of Surface Science, 1984. **19**(1-4): p. 360-372.

13. Routray, K., et al., *Origin of the synergistic interaction between MoO₃ and iron molybdate for the selective oxidation of methanol to formaldehyde*. Journal of Catalysis, 2010. **275**(1): p. 84-98.
14. Briand, L.E., A.M. Hirt, and I.E. Wachs, *Quantitative determination of the number of surface active sites and the turnover frequencies for methanol oxidation over metal oxide catalysts: application to bulk metal molybdates and pure metal oxide catalysts*. Journal of Catalysis, 2001. **202**(2): p. 268-278.
15. Hummadi, K.K., K.H. Hassan, and P.C. Mitchell, *Selectivity and Activity of Iron Molybdate Catalysts in Oxidation of Methanol*.
16. Soares, A.P.V., et al., *Iron molybdate catalysts for methanol to formaldehyde oxidation: effects of Mo excess on catalytic behaviour*. Applied Catalysis A: General, 2001. **206**(2): p. 221-229.
17. Burcham, L.J., L.E. Briand, and I.E. Wachs, *Quantification of active sites for the determination of methanol oxidation turn-over frequencies using methanol chemisorption and in situ infrared techniques. 1. Supported metal oxide catalysts*. Langmuir, 2001. **17**(20): p. 6164-6174.
18. Soares, A.P.V., M.F. Portela, and A. Kiennemann, *Methanol selective oxidation to formaldehyde over iron-molybdate catalysts*. Catalysis Reviews, 2005. **47**(1): p. 125-174.
19. Alessandrini, G., et al., *Chemical, structural and catalytic modifications of pure and doped iron(III) molybdate*. Journal of the Less Common Metals, 1977. **54**(2): p. 373-386.
20. House, M.P., M.D. Shannon, and M. Bowker, *Surface segregation in iron molybdate catalysts*. Catalysis Letters, 2008. **122**(3-4): p. 210-213.
21. Söderhjelm, E., et al., *On the synergy effect in MoO₃-Fe₂(MoO₄)₃ catalysts for methanol oxidation to formaldehyde*. Topics in Catalysis, 2008. **50**(1-4): p. 145-155.
22. Okamoto, Y., et al., *Role of excess of MoO₃ in Fe₂O₃-MoO₃ methanol oxidation catalysts studied by X-ray photoelectron spectroscopy*. Journal of the Chemical Society, Chemical Communications, 1981(19): p. 1018-1019.
23. Routray, K., et al., *Origin of the synergistic interaction between MoO₃ and iron molybdate for the selective oxidation of methanol to formaldehyde*. Journal of Catalysis, 2010. **275**(1): p. 84-98.
24. Bowker, M., et al., *The selective oxidation of methanol to formaldehyde on iron molybdate catalysts and on component oxides*. Catalysis letters, 2002. **83**(3-4): p. 165-176.
25. Koch, C.C., *Nanostructured Materials: Processing, Properties and Applications* 2006: Elsevier Science.
26. Routray, K., et al., *Origin of the synergistic interaction between MoO₃ and iron molybdate for the selective oxidation of methanol to formaldehyde*. Journal of Catalysis, 2010. **275**(1): p. 84-98.
27. Davies, R., et al., *The oxidation of Fe(III)*. Surface Science. **605**(17-18): p. 1754-1762.
28. Beale, A.M., et al., *An iron molybdate catalyst for methanol to formaldehyde conversion prepared by a hydrothermal method and its characterization*. Applied Catalysis a-General, 2009. **363**(1-2): p. 143-152.
29. Tian, H.J., C.A. Roberts, and I.E. Wachs, *Molecular Structural Determination of Molybdena in Different Environments: Aqueous Solutions, Bulk Mixed Oxides, and Supported MoO₃ Catalysts*. Journal of Physical Chemistry C, 2010. **114**(33): p. 14110-14120.
30. Belhekar, A.A., S. Ayyappan, and A.V. Ramaswamy, *FT-IR Studies on the Evolution of Different Phases and their Interaction in Ferric Molybdate-Molybdenum Trioxide Catalysts*. Journal of Chemical Technology and Biotechnology, 1994. **59**: p. 395.

31. Belhekar, A.A., S. Ayyappan, and A.V. Ramaswamy, *FT IR studies on the evolution of different phases and their interaction in ferric molybdate—molybdenum trioxide catalysts*. Journal of Chemical Technology and Biotechnology, 1994. **59**(4): p. 395-402.
32. Yamada, H., M. Niwa, and Y. Murakami, *Methanol oxidation on a molybdena monolayer supported on iron oxide*. Applied Catalysis A: General, 1993. **96**(2): p. 113-123.
33. Glotch, T. and M. Kraft, *Thermal transformations of akaganéite and lepidocrocite to hematite: assessment of possible precursors to Martian crystalline hematite*. Physics and Chemistry of Minerals, 2008. **35**(10): p. 569-581.
34. House, M.P., et al., *Effect of varying the cation ratio within iron molybdate catalysts for the selective oxidation of methanol*. The Journal of Physical Chemistry C, 2008. **112**(11): p. 4333-4341.
35. Natile, M.M. and A. Glisenti, *Surface reactivity of NiO/Co₃O₄ and Fe₂O₃/Co₃O₄ nanocomposite catalysts: Interaction with methanol*. Journal of Molecular Catalysis A: Chemical, 2004. **217**(1): p. 175-184.
36. Glisenti, A., G. Favero, and G. Granozzi, *Reactivity of simple alcohols on Fe₂O₃ powders An XPS and FTIR study*. Journal of the Chemical Society, Faraday Transactions, 1998. **94**(1): p. 173-182.
37. Groff, R.P., *An infrared study of methanol and ammonia adsorption on molybdenum trioxide*. Journal of Catalysis, 1984. **86**(1): p. 215-218.
38. Wooster, N., *The Crystal Structure of Molybdenum Trioxide, MoO₃*. Zeitschrift für Kristallographie-Crystalline Materials, 1931. **80**(1): p. 504-512.
39. Gai, P.L. and E.D. Boyes, *Electron Microscopy in Heterogeneous Catalysis* 2003: Taylor & Francis.
40. Ziolkowski, J., *Catalytic anisotropy of MoO₃ in oxidation reactions in the light of bond-strength model of active sites*. Journal of Catalysis, 1983. **80**(2): p. 263-273.
41. Busca, G., et al., *FT-IR study of the adsorption and transformation of formaldehyde on oxide surfaces*. Journal of the American Chemical Society, 1987. **109**(17): p. 5197-5202.
42. Burcham, L.J., L.E. Briand, and I.E. Wachs, *Quantification of active sites for the determination of methanol oxidation turn-over frequencies using methanol chemisorption and in-situ infrared techniques. I. Supported metal oxide catalysts*. Langmuir, 2001. **17**(20): p. 6164-6174.
43. Soares, A., et al., *Iron molybdate catalysts for methanol to formaldehyde oxidation: effects of Mo excess on catalytic behaviour*. Applied Catalysis A: General, 2001. **206**: p. 221-229.
44. Xu, Q., et al., *Surface phase composition of iron molybdate catalysts studied by UV Raman spectroscopy*. The Journal of Physical Chemistry C, 2008. **112**(25): p. 9387-9393.
45. Huang, P.-R., et al., *Impact of lattice distortion and electron doping on α -MoO₃ electronic structure*. Scientific reports, 2014. **4**.
46. Kim, T.H., et al., *Selective oxidation of methanol to formaldehyde using modified iron-molybdate catalysts*. Catalysis Letters, 2004. **98**(2-3): p. 161-165.
47. Soares, A.P.V., et al., *Mechanism of deactivation of iron-molybdate catalysts prepared by coprecipitation and sol-gel techniques in methanol to formaldehyde oxidation*. Chemical Engineering Science, 2003. **58**(7): p. 1315-1322.
48. Rocchiccioli-Deltcheff, C., et al., *Structure and catalytic properties of silica-supported polyoxomolybdates: II. Thermal behavior of unsupported and silica-supported 12-molybdosilicic acid catalysts from IR and catalytic reactivity studies*. Journal of Catalysis, 1990. **126**(2): p. 591-599.
49. Redhead, P.A., *Thermal desorption of gases*. Vacuum, 1962. **12**(4): p. 203-211.

50. Brookes, C., et al., *The Nature of the Molybdenum Surface in Iron Molybdate. The Active Phase in Selective Methanol Oxidation*. The Journal of Physical Chemistry C, 2014. **118**(45): p. 26155-26161.
51. Holstein, W.L. and C.J. Machiels, *Inhibition of methanol oxidation by water vapor—effect on measured kinetics and relevance to the mechanism*. Journal of Catalysis, 1996. **162**(1): p. 118-124.
52. Tatibouet, J.M., *Methanol oxidation as a catalytic surface probe*. Applied Catalysis A: General, 1997. **148**(2): p. 213-252.
53. Wilson Iii, J.H., C.G. Hill Jr, and J.A. Dumesic, *Raman spectroscopy of iron molybdate catalyst systems: Part III. IN SITU studies of supported and bulk catalysts under reaction and redox conditions*. Journal of Molecular Catalysis, 1990. **61**(3): p. 333-352.
54. C, K.C., *Nanostructured Materials: Processing, Properties and Applications*, Elsevier Science 2006.
55. Popov, B.I., A.V. Pashis, and L.N. Shkuratova, *Effect of calcination temperature on the surface composition of Mo–Fe catalysts for methanol oxidation*. Reaction Kinetics and Catalysis Letters, 1986. **30**(1): p. 129-135.
56. Alessandrini, G., et al., *Chemical, structural and catalytic modifications of pure and doped iron (III) molybdate*. Journal of the Less Common Metals, 1977. **54**(2): p. 373-386.
57. Kihlborg, L., *Studies on molybdenum oxides*. Acta Chem. Scand, 1959. **13**(0): p. 5.
58. Moreno-Castilla, C., et al., *Dehydration of methanol to dimethyl ether catalyzed by oxidized activated carbons with varying surface acidic character*. Carbon, 2001. **39**(6): p. 869-875.

Chapter 4: Core-Shell Structures of the Type $\text{MoO}_x/\text{Fe}_2\text{O}_3$, Probing the Nature of the Structural Motifs Responsible for Methanol Oxidation Catalysis.

Contents

1. Introduction.....	191
2. Experimental	194
3. Results and Discussion	196
3.1. BET Analysis	196
3.2. Catalyst Morphology.....	197
3.3. Vibrational Spectroscopy	198
3.4. XRD	204
3.5. XPS	205
3.6. TPD and TPPFR Analysis.....	207
3.6.1. Catalytic Testing for 3ML $\text{MoO}_x/\text{Fe}_2\text{O}_3$	207
3.6.2. Catalytic Testing for Other Monolayer Loadings of $\text{MoO}_x/\text{Fe}_2\text{O}_3$	211
3.6.3. Calcination Effects.....	216
3.7. XAS Study	217
3.7.1. XAS Analysis Mo K-edge 3ML $\text{MoO}_x/\text{Fe}_2\text{O}_3$	217
3.7.1.1. XANES Analysis	217
3.7.1.2. EXAFS Analysis	221
3.7.2. XAS Analysis Mo K-edge 1, 3 and 6 ML $\text{MoO}_x/\text{Fe}_2\text{O}_3$: Varying the Monolayer Coverage at the Surface of Fe_2O_3	226
3.7.2.1. XANES Analysis	226

3.7.2.2. EXAFS Analysis	232
3.8. Computer Modelling	233
4. Conclusions	236
5. References	238

1. Introduction

The catalyst typically used industrially is a bulk iron molybdate catalyst with an excess of MoO_3 . It is thought that the excess MoO_3 primarily acts to replace any molybdenum lost through sublimation at reactor hot spots [1-3], which in turn leads to unselective Fe_2O_3 formation (See Chapter 3). It is majority agreed that Fe at the surface is deemed detrimental to catalyst performance [4]. However, with a multitude of oxide phases present within the catalyst composition, it is debated in the literature as to which phase, MoO_3 or $\text{Fe}_2(\text{MoO}_4)_3$, provides the active site for these reactions [3, 5-9]. Some consider the $\text{Fe}_2(\text{MoO}_4)_3$ to be acting solely as the active phase [7], with the excess MoO_3 present playing a significant role in purely regenerating lost MoO_3 at high temperatures, and not partaking in the reaction itself. However, there is a counter argument that MoO_3 is also required for complete selectivity to formaldehyde [2, 10, 11]. MoO_3 is highly regarded for its ability to improve the selectivity of this reaction, since an increase in Mo will consequently lead to a larger oxygen availability at the catalyst surface, and changes in acidity which favour formaldehyde production. Mo rich catalysts will have a higher capacity to increase surface re-oxidisability, and have also been reported to improve the mechanical stability of the catalyst.

The surface layer is the active component within any catalyst. The majority of surface investigations have so far been limited to electron microscopy studies. Work by Bowker *et al.* has used aberration corrected scanning transmission electron microscopy (acSTEM) [5], to show that the surface of these catalysts are enriched with Mo. EDX line scans show a clear dominance of the surface region by Mo, to the detriment of Fe. This has also been agreed by the work of Routray *et al.* [12], through the use of HRTEM. Reactivity data has also been a key tool for evidencing Mo segregation [13]. Fe_2O_3 itself is a highly unselective catalyst for methanol oxidation, with a formate intermediate leading to CO_2 through complete combustion. However, with low loadings of Mo, the iron oxide exhibits significantly different selectivity, with a change in the selectivity profile to CO and H_2CO production. This suggests that Mo is having a direct effect on the reaction, and indicates that the Mo must be predominantly at the surface. TPD data of MoO_3 and $\text{Fe}_2(\text{MoO}_4)_3$ are remarkably similar (Chapter 3), albeit a slight difference in the ratio of formaldehyde production due to the difference in activity of these two materials. This would infer a similar terminating layer in these bulk materials, indicating that the surface is Mo rich. Further work of Bowker *et al.* has specified the active site for the reaction to be Mo(VI), which cycles

through Mo(IV) during the reaction [5, 14]. Several different oxygen sites have been defined and clarified in their roles during this oxidative reaction.

Although the debate regarding the active phase is still on-going, it is unanimously agreed that the topmost layer of any heterogeneous catalyst is crucial to the efficiency of that material. It is fundamental to learn as much as possible about this surface layer, and how it interacts with incoming reactants to form surface intermediates. With an understanding of this surface interaction, scientists can tailor the catalyst to improve the efficiency of the reaction. It is important not only to identify the phase present, but also how this can be related to activity and overall performance of the catalyst.

Characterisation of bulk FeMo catalysts has been possible through a number of techniques, most commonly through Raman, FT-IR, DRIFTS, XRD and XPS [5, 13, 15-18]. The structures of MoO_3 and $\text{Fe}_2(\text{MoO}_4)_3$ are reasonably well understood, however there still remains some doubt in how they react with methanol, and which phase is predominantly involved in the reaction. There is a requirement to turn to more surface sensitive techniques to probe the uppermost layers in these catalysts. The use of X-ray absorption spectroscopy (XAS) in a surface sensitive way is the focus of this chapter.

Work by Holmberg *et al.* has focused on the surface of FeMo catalysts, specifically the origin of the enhanced catalytic performance of bulk iron molybdate catalysts with excess crystalline MoO_3 [19]. Low-energy ion scattering (LEIS) analysis of the outermost surface layer revealed that the molybdate catalysts possess a monolayer of surface MoO_x species, onto which surface CH_3OH and CH_3O are seen to absorb by IR spectroscopy. The enhanced catalytic performance of bulk $\text{Fe}_2(\text{MoO}_4)_3$ catalysts in the presence of excess MoO_3 is attributed to this surface MoO_x monolayer. HRTEM imaging proved an amorphous surface structure on the edges of the crystals. A similar structure was observed by Gai and Labun [20], when focussing on bulk structures and their reduction. The EDS data showed that the amorphous structure on the fresh catalyst was rich in Mo, whereas for the post reaction sample there was a lower Mo content. The link between ageing and composition was an implication that the active material is the amorphous structure at the surface. The Mo:Fe ratio was shown to be higher on the molybdate surface than in the bulk, as proven by XPS. The structure of $\text{Fe}_2(\text{MoO}_4)_3$ with excess MoO_3 is considered a very open structure, built up of regular tetrahedral and octahedra. Therefore, it is feasible that an amorphous layer could form at the surface, to enable its stabilisation. The molybdate is thought to act as a support

for the active structure, which is an amorphous surface layer with a higher Mo:Fe ratio compared to the bulk. The Mo exists in octahedral co-ordination.

The use of XAS to probe $\text{Fe}_2(\text{MoO}_4)_3$ has been limited in the literature. Due to the significance of the surface layer, XAS as a bulk technique has not been highly considered. There are however a few examples of surface Mo studies [21]. Sarti *et al.* [22] have investigated the structural and morphological characterization of Mo coatings for high gradient accelerating structures on Al_2O_3 . XAS experiments were performed at the Mo K-edge, to determine the chemical status of the Mo atoms. Mo was discovered to exist as a slightly disordered structure at the surface. Hangchun and Wachs *et al.* [23] also study the surface structures of supported MoO_3 catalysts by Raman and Mo L-edge XANES. Supported MoO_3 catalysts on TiO_2 , Al_2O_3 , ZrO_2 , and SiO_2 , were prepared through incipient-wetness impregnation. At high surface coverages of MoO_3 , for TiO_2 , the Mo species was shown to form in octahedral co-ordination, whereas for Al_2O_3 there was a mixture of tetrahedral and octahedral co-ordinated species. On SiO_2 the Mo oxide showed an isolated structure, which resembles a co-ordination between tetrahedral and octahedral formation.

The objective of this chapter is to determine the nature of the surface layer(s) in the catalysts prepared, both in terms of reactivity and structure. A series of MoO_x modified Fe_2O_3 catalysts have been synthesized, in an attempt to make core-shell oxidic materials of the type $\text{MoO}_x/\text{Fe}_2\text{O}_3$. In dosing Mo on unselective Fe_2O_3 , any changes in catalyst activity can be related to the Mo being present at the surface having a direct involvement in the reaction. Mo surface enrichment can be proven through TEM EDX data. Dosing surface layers of Mo onto Fe_2O_3 allows exclusive analysis of surface structural changes by probing Mo structure using XAFS. XAFS is usually regarded as a bulk technique, probing a per atom average local environment. However, by tuning to the Mo K-edge, and with a knowledge of Mo surface enrichment through TEM EDX; the technique can be exploited as a surface sensitive tool. A range of other techniques including electron microscopy, powder XRD, IR and Raman spectroscopy have been used to provide insight into the composition and morphology of these new materials. Whilst also probing the nature of the catalyst surface, in varying the monolayer loading of Mo at the surface of Fe_2O_3 , these novel catalysts will be investigated for their ability in the selective oxidation of methanol to formaldehyde. The work highlights how catalyst surfaces are significantly different to bulk structures, with emphasis on the effect on catalyst performance.

2. Experimental

The majority of work in this chapter involves the study of core-shell structures of the type $\text{MoO}_x/\text{Fe}_2\text{O}_3$. A series of catalysts were prepared of $\text{MoO}_x/\text{Fe}_2\text{O}_3$ by doping either 1, 3 or 6 monolayer equivalents of Mo oxide onto the surface of commercial Fe_2O_3 (Sigma Aldrich, <50 nm particle size). The required amount of ammonium heptamolybdate was dissolved in 10 cm³ of deionised water, and sonicated to ensure thorough mixing. This was then added dropwise to the Fe_2O_3 support with constant mixing between drops. This process was continued until incipient wetness had been reached. Catalysts were then dried at 120 °C for 24 hours in a muffle furnace, after which they were calcined at varying temperatures in air, for 2 or 24 hours. A further 1ML (monolayer) $\text{MoO}_x/\text{Fe}_2\text{O}_3$ catalyst was produced through physical mixing and grinding of commercial MoO_3 and Fe_2O_3 in the appropriate quantities. The catalyst was dried at 120 °C / 24 hours, and then calcined at 500 °C / 24 hours in the muffle furnace. These monolayer catalysts are compared in terms of characterisation and catalyst performance with bulk standards of MoO_3 and $\text{Fe}_2(\text{MoO}_4)_3$. MoO_3 was bought in commercially, whilst $\text{Fe}_2(\text{MoO}_4)_3$ was produced in-house via the co-precipitation method (See Chapter 2 for experimental procedure). Table 1 summarises the relevant catalysts synthesised for the basis of this chapter.

Table 1. Synthesised catalysts for the purpose of this work.

Catalyst	Equivalent Monolayers	Precursor	Heat Treatment	Catalyst colour
$\text{MoO}_x/\text{Fe}_2\text{O}_3$	1	$(\text{NH}_4)_6\text{Mo}_7\text{O}_{24}\cdot 4\text{H}_2\text{O}$	120, 300, 400, 500, 600 °C for 2 and 24 hours.	Red
	3	$(\text{NH}_4)_6\text{Mo}_7\text{O}_{24}\cdot 4\text{H}_2\text{O}$	120, 300, 400, 500, 600 °C for 2 and 24 hours.	Red
	6	$(\text{NH}_4)_6\text{Mo}_7\text{O}_{24}\cdot 4\text{H}_2\text{O}$	120, 300, 400, 500, 600 °C for 2 and 24 hours.	Red
MoO_3	-	Commercial standard	500 °C / 24 hours	White
$\text{Fe}_2(\text{MoO}_4)_3$	-	$(\text{NH}_4)_6\text{Mo}_7\text{O}_{24}\cdot 4\text{H}_2\text{O}$ and $\text{Fe}_3(\text{NO}_3)_9\cdot 9\text{H}_2\text{O}$	500 °C / 24 hours	Yellow

Characterisation has involved a number of techniques including FT-IR, Raman, SEM, TEM-EDX, BET, XRD and XPS, all *ex situ*. The methodology for each of these techniques are detailed in Chapter 2.

Mo K-edge XAS spectra were acquired on the B18 beamline at DLS, Rutherford Appleton Laboratory. B18 uses a double crystal Si (111) monochromator [24, 25] for EXAFS in the range of 19800 to 21000 eV. For *ex situ* analysis, XAFS were collected in transmission mode. Reference XAFS of MoO₃ and Fe₂(MoO₄)₃ standards were also acquired. For these XAS measurements, all catalysts were prepared as homogeneous pellets, each sample diluted with BN.

The interpretation of features in the Mo XANES spectra involves the assignment of the pre-edge peak at ~ 19995 eV, and the peak at 20010 eV. The pre-edge peak is attributed to the dipole forbidden/quadrupole allowed $1s - 4d$ transition [26], associated primarily with tetrahedral geometry, but can also be present in structures with distorted octahedral geometry [21, 27, 28]. The peak at 20010 eV is assigned to the dipole allowed $1s - 5p$ transition, and is a characteristic feature of Mo species with octahedral/distorted octahedral geometry [21, 27, 28]. These transitions are restricted by certain selection rules: $\Delta l = \pm 1$, $\Delta J = 0, \pm 1$, where l = orbital angular momentum quantum number, and J = total orbital angular momentum.

When analysing data, there are three crucial components to consider including background removal, alignment of the sample and reference spectra, and normalisation of the data. To align the data, edge alignment is achieved through adjusting the energy scales of the spectra. Athena allows the user to align data groups interactively by visually comparing $\mu\mu(E)$, normalized $\mu\mu(E)$, or derivative $\mu\mu(E)$ spectra. The amount of the energy shift is displayed in view, and updated in the selected groups parameters. There is an auto-align option, which applies a crude algorithm to align the spectra. The algorithm works by computing the difference spectrum of the derivative spectra of the standard and the second data groups. It optimizes an E_0 shift by minimizing the difference spectrum. You can also use a reference channel to align your data. The alignment of the edges is achieved by adjusting the energy scales of the spectra so 0 eV corresponds to the inflection point of the edge. Appendix Section A8 details this.

To remove the background absorption, a linear gradient is fitted to the pre-edge slope. The gradient is then subtracted from the spectrum.

To normalise the data, if different edges are analysed, the energy scale must be adjusted. Subsequent to this, the intensity must be normalised by setting the intensity of one of the inflection points of the EXAFS oscillations to 1. The normalization procedure, in which the data are divided by the size of the edge step, compensates for the uncertainties in the concentration and sample thickness (See Appendix Section A8).

3. Results and Discussion

3.1. BET Analysis

Table 2. BET surface area measurements for the varying monolayer (ML) catalysts and commercial standards.

Sample	Surface Area / m^2g^{-1}
Commercial Fe_2O_3 (<50 nm)	21
1ML MoO_3 / Fe_2O_3 500 °C 2 Hours	20
3ML MoO_3 / Fe_2O_3 500 °C 2 Hours	15
6ML MoO_3 / Fe_2O_3 500 °C 2 Hours	12
3ML MoO_3 / Fe_2O_3 500 °C 24 Hours	14
$\text{Fe}_2(\text{MoO}_4)_3$	4.5
MoO_3	0.6
3ML MoO_3 / Fe_2O_3 Dried 120 °C	15
3ML MoO_3 / Fe_2O_3 400 °C 2 hours	15
3ML MoO_3 / Fe_2O_3 500 °C 2 hours	15
3ML MoO_3 / Fe_2O_3 600 °C 2hours	14

The surface areas of the main catalysts involved in this chapter have been probed through BET analysis. Surface area must be considered, since it will have a direct effect on the activity of the catalyst. From Table 2, it is observed that Mo content has a significant effect on the surface area of the $\text{MoO}_3/\text{Fe}_2\text{O}_3$ catalysts. It is evident that as the amount of molybdenum dosed at the surface is increased, there is a decrease in the overall surface area of the catalyst (from a 1 to 3 monolayer increase in coverage, there is an obvious decrease in surface area of approximately $4 \text{ m}^2\text{g}^{-1}$). It also important to note that these monolayer catalysts have a significantly higher surface area than bulk $\text{Fe}_2(\text{MoO}_4)_3$. For bulk catalysts (such as $\text{Fe}_2(\text{MoO}_4)_3$), a small amount of Mo has been shown to cause an increase in the total surface area [1]. This is since the Mo is thought to insert into the bulk structure to provoke an increase in the bulk lattice dimensions, rather than substituting the Fe(III) ions directly. However, in the case of the monolayer catalysts, since the Mo is dosed at the surface, an increase in its loading has a negative effect on the surface area.

Table 2 also compares the effect of calcination time and temperature on the surface area of the monolayer catalysts. Comparing the 3ML $\text{MoO}_x/\text{Fe}_2\text{O}_3$ catalyst calcined at both 2 and 24 hours, it is shown that there is no significant change in surface area for the longer calcinations. This infers no significant loss of molybdenum and/or sintering of the catalyst. There is also no change in surface area with increasing calcination temperature, implying no significant sintering effect.

The Fe_2O_3 standard used (Sigma Aldrich <50 nm particle size) has a surface area of $21 \text{ m}^2\text{g}^{-1}$. This was found to be stable under prolonged heat treatments at 500°C .

3.2. Catalyst Morphology

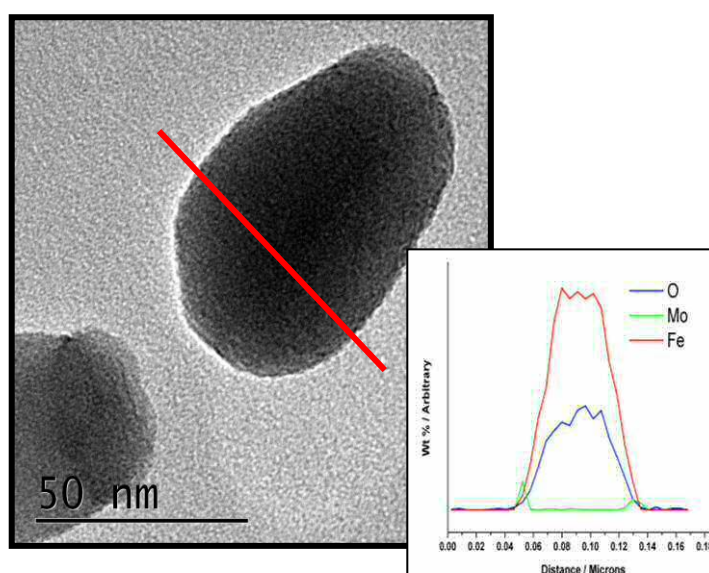


Figure 1. TEM image of a particle from 3ML $\text{MoO}_x/\text{Fe}_2\text{O}_3$ after a calcination at 500°C with accompanying EDX line scan (right).

TEM has been used to evidence molybdenum at the surface of the Fe_2O_3 support. Figure 1 shows a TEM image for a typical particle in a 3ML $\text{MoO}_x/\text{Fe}_2\text{O}_3$ catalyst calcined at 500°C . There are no obvious isolated molybdenum units at the surface, indicating a surface monolayer arrangement. Particle sizes for the catalyst are typically in the range of 30–50 nm. Images were sampled over a range of areas across the sample, and results proved consistent. Figure 1 also displays the accompanying TEM EDX profile for the particle. Data shows a surface enriched in both Mo and O, to the detriment of iron. The Mo signal appears more prominent at the edge of the particle, with no signal in the core, thus suggesting that the Mo is concentrated on the surface of the Fe_2O_3 particle. Results were conclusive across a range of particles and monolayer loadings.

3.3. Vibrational Spectroscopy

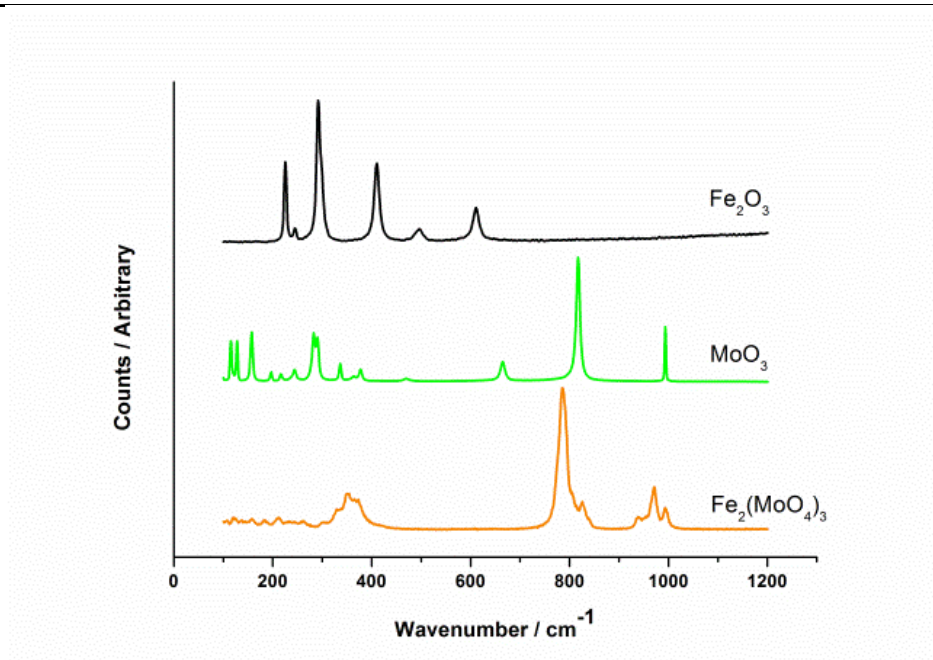
Raman has been influential in the characterisation of FeMo based catalysts. Referring to the bulk standards (Figure 2), the major bands to observe are for M-O-M and M=O stretches. In MoO_3 , the main contributing bands occur at 990, 820, 660 and 280 cm^{-1} . In Fe_2O_3 the bands to identify are at 600, 410, 290 and 220 cm^{-1} , and for $\text{Fe}_2(\text{MoO}_4)_3$ at 970, 930, 780 and 350 cm^{-1} . Table 3 assigns the stretches and vibrations responsible for each of these bands, with further details in Chapter 3 (3.1.2).

Raman spectroscopy was performed for 1, 3 and 6ML's $\text{MoO}_x/\text{Fe}_2\text{O}_3$ (Figures 3-6). The Raman spectra for the 3ML $\text{MoO}_x/\text{Fe}_2\text{O}_3$ catalyst annealed to various temperatures are detailed in Figure 3, with the spectral range centred around the fundamental Mo-related bands. There is one main band from haematite at 610 cm^{-1} , as expected since iron oxide forms the majority of the sample. However, there are also smaller bands representative of Mo in the sample, which are manifested as MoO_3 -like features up to 400°C (990 and 820 cm^{-1}), converting to $\text{Fe}_2(\text{MoO}_4)_3$ (960 and 780 cm^{-1}) on raising the temperature to 500°C . A similar situation arises for 6ML $\text{MoO}_x/\text{Fe}_2\text{O}_3$ (Figure 4), however for this monolayer loading, the onset of MoO_3 formation occurs much earlier at 300°C . $\text{Fe}_2(\text{MoO}_4)_3$ again forms by 500°C , shown by the bands at 780 and 970 cm^{-1} [8, 29, 30], for bridging and terminal stretches respectively. Raman bands are inherently most pronounced for the 6ML $\text{MoO}_x/\text{Fe}_2\text{O}_3$ sample, due to the higher weight loading of the molybdenum oxide.

For 1ML $\text{MoO}_x/\text{Fe}_2\text{O}_3$, there is very little signal for Mo, as might be expected for such a low loading of Mo (Figures 5-6). There is no evidence for extended MoO_3 or $\text{Fe}_2(\text{MoO}_4)_3$, the spectra being dominated by the bands of iron oxide (haematite), with major peaks at 280 and 390 cm^{-1} . However there is some evidence of broad Mo=O bands in the $950\text{-}1000\text{ cm}^{-1}$ region, most probably due to the monolayer form of molybdena. All spectra across the calcination range are identical, implying no change in Mo co-ordination at the surface. Molybdena concentrations of 0.4 monolayers have been observed by Raman previously, however this was due to the high surface area of the support, which was $>50\text{ m}^2\text{g}^{-1}$.

Table 3. Raman band assignments for FeMo based catalysts.

Wavenumber / cm^{-1}	Band Assignment (Raman)
667	Mo-O-Mo symmetric stretch in MoO_3 [29, 31]
700-850	Antisymmetric Mo-O-Mo stretching vibrations in MoO_3 [29]
	T_d Mo species in $\text{Fe}_2(\text{MoO}_4)_3$ [32]
780	Mo-O-Mo asymmetric vibrations in $\text{Fe}_2(\text{MoO}_4)_3$ [27]
816	Mo-O-Mo asymmetric stretch in MoO_3 [29] Mo=O asymmetric stretch in $\text{Fe}_2(\text{MoO}_4)_3$
966	<i>Debate in assignments:</i> Mo=O symmetric stretch of the three distinct isolated sites in $\text{Fe}_2(\text{MoO}_4)_3$ [29] Fe-O-Mo asymmetric stretch in $\text{Fe}_2(\text{MoO}_4)_3$
992	Terminal Mo=O symmetric stretch in MoO_3 [29, 31, 33] Symmetric Mo=O stretch in $\text{Fe}_2(\text{MoO}_4)_3$

**Figure 6.** Reference Raman spectra for Fe_2O_3 , MoO_3 and $\text{Fe}_2(\text{MoO}_4)_3$.

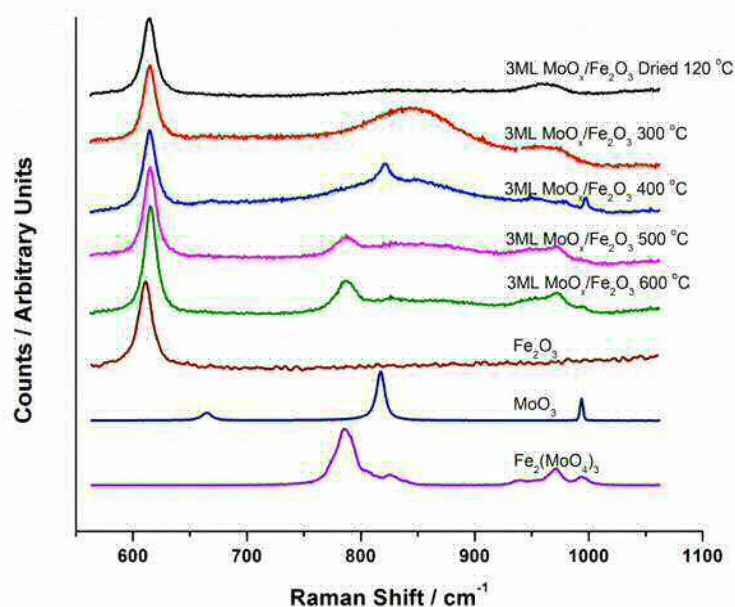


Figure 3. Raman spectroscopy for 3ML MoO_x/Fe₂O₃, dried at 120 °C, and for calcination temperatures of 300, 400, 500, 600 °C, accompanied by with reference spectra of Fe₂O₃, MoO₃ and Fe₂(MoO₄)₃.

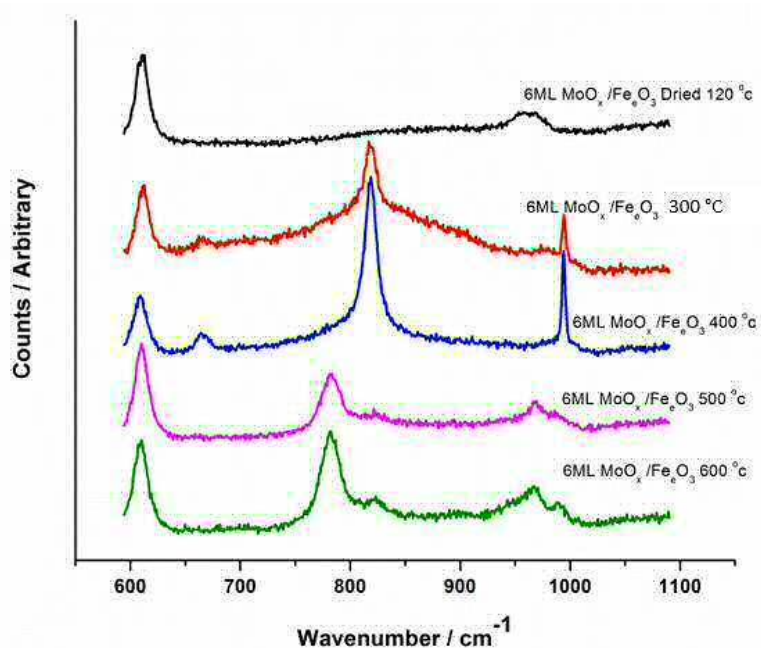


Figure 4. Raman spectroscopy for 6ML MoO_x/Fe₂O₃ dried at 120 °C, and for calcination temperatures of 300, 400, 500, 600 °C.

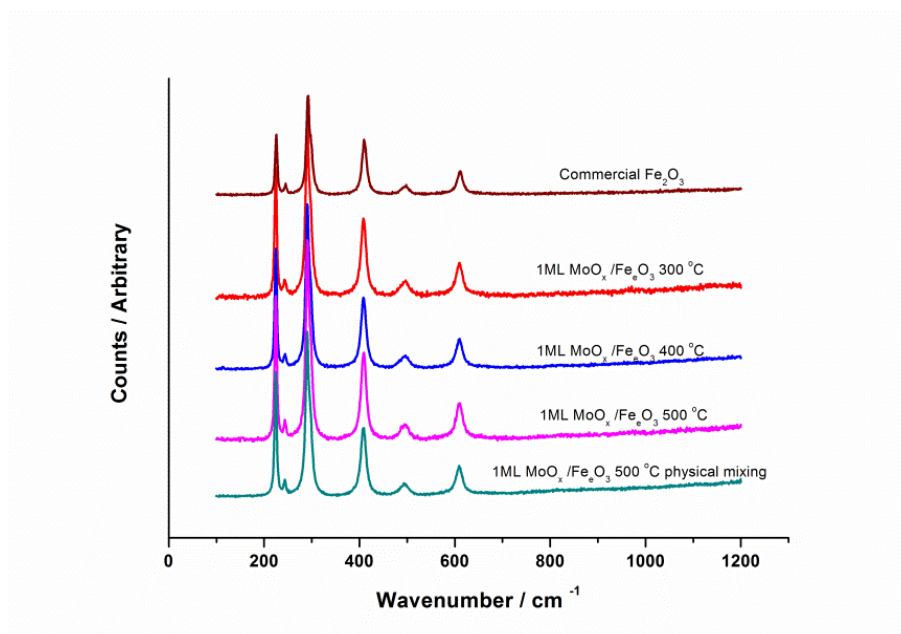


Figure 5. Raman spectroscopy for 1ML MoO_x/Fe₂O₃, dried at 120 °C, and for calcination temperatures of 300, 400, 500, 600 °C.

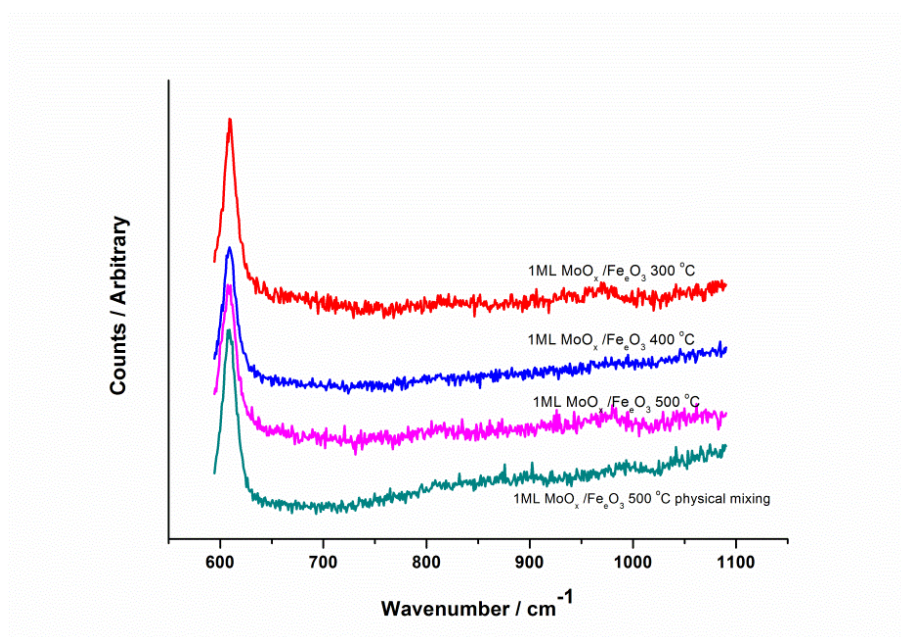


Figure 6. Raman Spectroscopy for 1ML MoO_x/Fe₂O₃, dried at 120 °C, and for calcination temperatures of 300, 400, 500, 600 °C, centred on the molybdenum related bands.

Effects of calcination time have been investigated (Figure 7). After a 24 hour calcination, the bands for Fe₂(MoO₄)₃ still remain intact at 780 and 960 cm⁻¹, indicating no loss of Mo after prolonged thermal treatment. SEM EDX mapping was performed (Appendix A9), and demonstrated a more uniform distribution of molybdenum across the 24 hour calcined catalyst when compared with that for the 2 hour calcination.

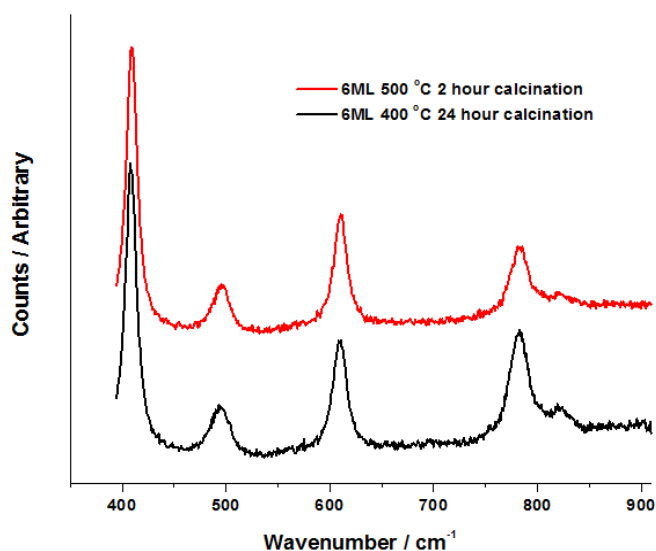


Figure 7. Comparison of Raman data for different calcination times, 2 and 24 hours, at 500 °C, for 6ML MoO_x/Fe₂O₃.

FTIR investigations have been used to support the findings under Raman spectroscopy. Figures 8-10 demonstrate the IR spectra obtained, with similar trends observed to those seen through Raman. The most prominent band for molybdena is identified at 990 cm⁻¹ [32, 34], assigned to the Mo=O stretching mode. For 3ML MoO_x/Fe₂O₃ this occurs at 400 °C (Figure 8), whereas for the 6ML MoO_x/Fe₂O₃ catalyst (Figure 9) signs appear at 300 °C. For a 1ML coverage of MoO_x/Fe₂O₃, there is no evidence for this MoO₃ phase, with indistinguishable spectra across the calcination range (Figure 10), complementing the results of the Raman.

Both the 3 and 6ML MoO_x/Fe₂O₃ catalysts show that upon calcining to 500 or 600 °C, there is a shift of the major peak at 990 cm⁻¹, to 970 cm⁻¹, which is indicative of Fe₂(MoO₄)₃ formation. A comparison to IR obtained for Fe₂(MoO₄)₃ can be made using Figure 8.

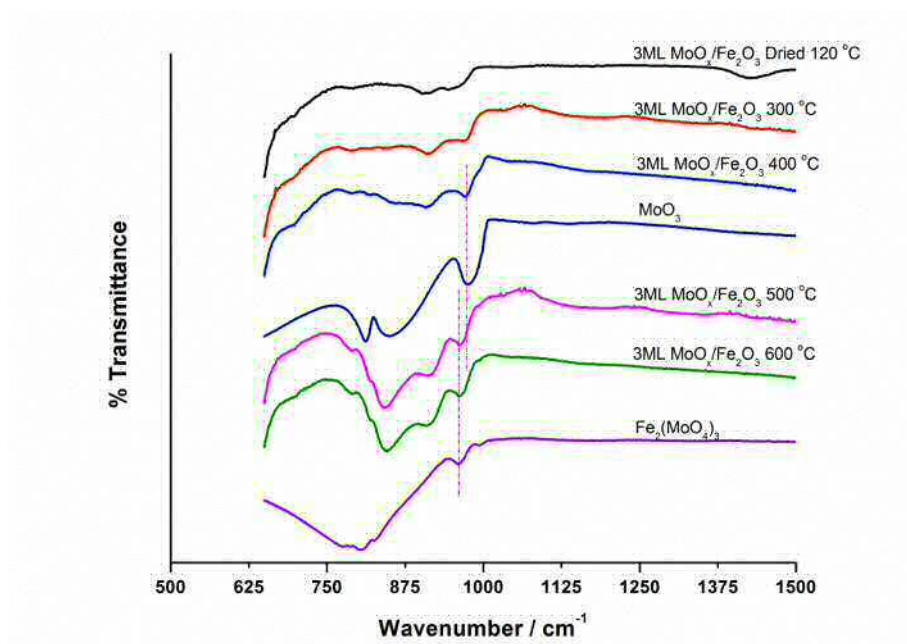


Figure 8. FTIR spectra of 3ML $\text{MoO}_x/\text{Fe}_2\text{O}_3$ dried at 120°C and after calcination at 300°C , 400°C , 500°C , and 600°C , with reference spectra of MoO_3 and $\text{Fe}_2(\text{MoO}_4)_3$.

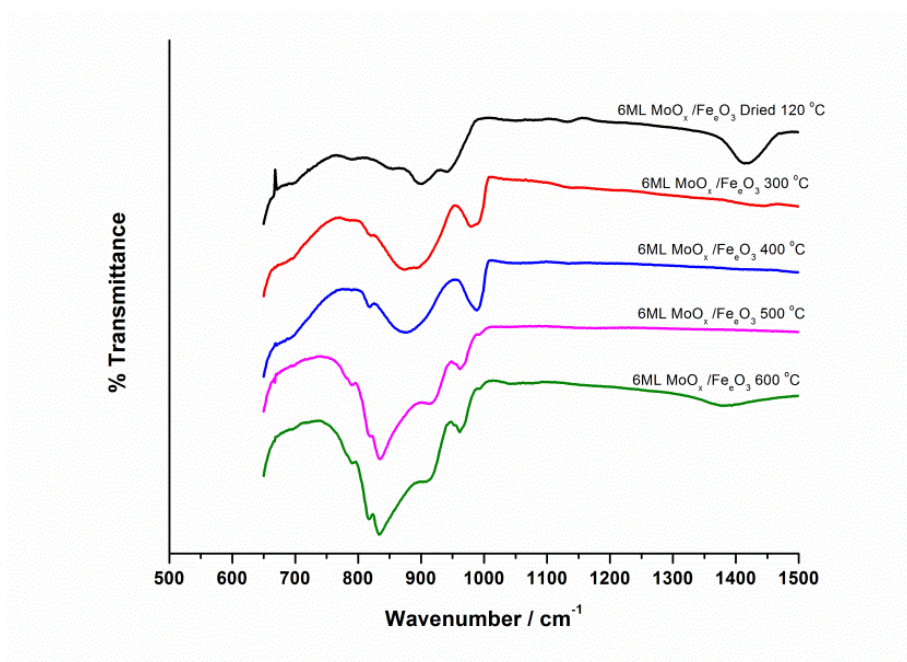


Figure 9. FTIR spectra of 6ML $\text{MoO}_x/\text{Fe}_2\text{O}_3$ dried at 120°C and after calcination at 300°C , 400°C , 500°C , and 600°C .

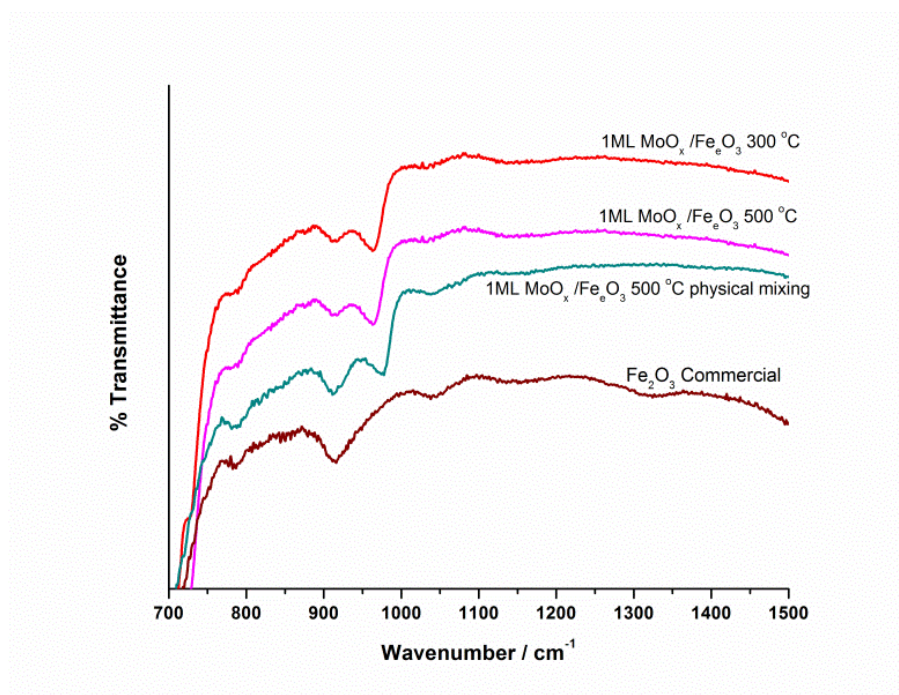


Figure 10. FTIR spectra of 1ML MoO_x/Fe₂O₃ after a calcination at 300 and 500 °C, together with commercial Fe₂O₃ and 1ML MoO_x/Fe₂O₃ prepared through physical mixing of MoO₃ with Fe₂O₃. Spectra are indistinguishable for the 1ML MoO_x/Fe₂O₃ catalysts, even after the highest anneal temperature.

3.4. XRD

XRD was initially used in an attempt to identify the molybdenum species present in the catalyst (Figure 11). For the 1ML and 3ML MoO_x/Fe₂O₃ catalysts, both demonstrate a pattern typical for pure Fe₂O₃. There are no separate phases, indicating either Mo is in an amorphous phase, or is present in ordered phases of low dimensionality. However, since XRD provides bulk analysis, the absence of Mo peaks does not totally rule out the existence of MoO₃ at the surface, as has been seen through vibrational spectroscopy. The 6ML MoO_x/Fe₂O₃ catalyst shows signs of a distinct molybdenum phase, with a band at 12° 2θ indexed to the (020) plane in MoO₃ [35] appearing for the 300 and 400 °C calcined samples. By 500 °C, this band disappears, as evidence of Fe₂(MoO₄)₃ formation appears (highlighted through the orange dots in Figure 11). Fe₂(MoO₄)₃ can be identified by the peaks at 22 and 23° 2θ, corresponding to the (214) and (114) lattice planes respectively.

Comparing across the calcination treatments (Figure 11), it is apparent that there does not appear to be any peak broadening with increasing temperature. This suggests that crystallite size is maintained, agreeing with the BET surface area data, in which there is no loss in surface area with increasing calcination temperature for prolonged periods of time.

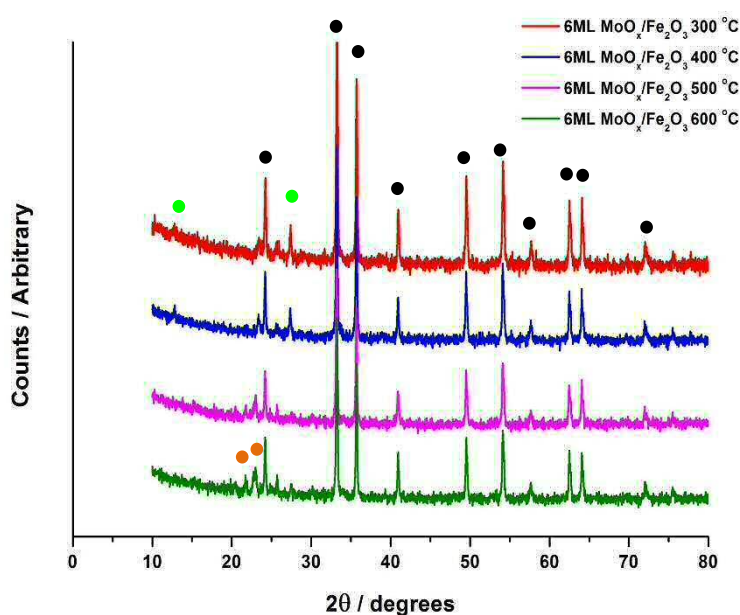


Figure 11. XRD data obtained for the 6ML MoO_x/Fe₂O₃ catalyst after a calcination at 300, 400, 500, and 600 °C. Green dots= MoO₃, Orange dots= Fe₂(MoO₄)₃, Black dots= Fe₂O₃.

3.5. XPS

XPS data supports the TEM analysis, evidencing Mo segregation at the surface of Fe₂O₃. This technique has been exploited to study the 3ML MoO_x/Fe₂O₃ catalyst calcined to a range of anneal temperatures (Figure 12-13). Wide scans were initially taken to give an overall picture of the surface composition. This was undertaken at low resolution. Fe, Mo, O and C were identified. A carbon signal was always observed in the spectrum due to the high sensitivity of the technique. This is merely just a contamination effect from air.

A narrow range scan was also taken in the region of 245-255 eV. It was discovered that Fe and Mo were always in their highest oxidation states of (III) and (VI) respectively. The Mo 3d states for the three calcination temperatures show no change in the peak position, with the binding energy indicative of Mo(VI) (Figure 12, Mo 3d ^{5/2} at 232.4 eV corresponds to Mo(VI)) [2, 36]. There may be some broadening of the lower binding energy at the higher temperatures, which could be due to environmental changes.

It was also discovered that the surface region Mo:Fe atomic ratio declined from 0.14 to 0.09 during annealing to 600 °C. This is a direct effect of molybdenum at the surface reacting with the Fe₂O₃ support to form Fe₂(MoO₄)₃ in the surface region.

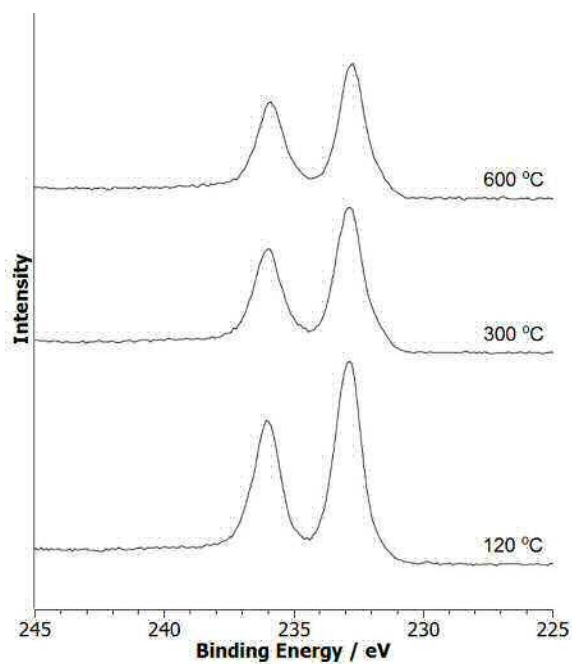


Figure 12. Mo 3d XPS spectra for 3ML MoO_x/Fe₂O₃ dried at 120 °C, and calcined at 300 and 600 °C. A narrow range scan was taken in the region of 245-255 eV.

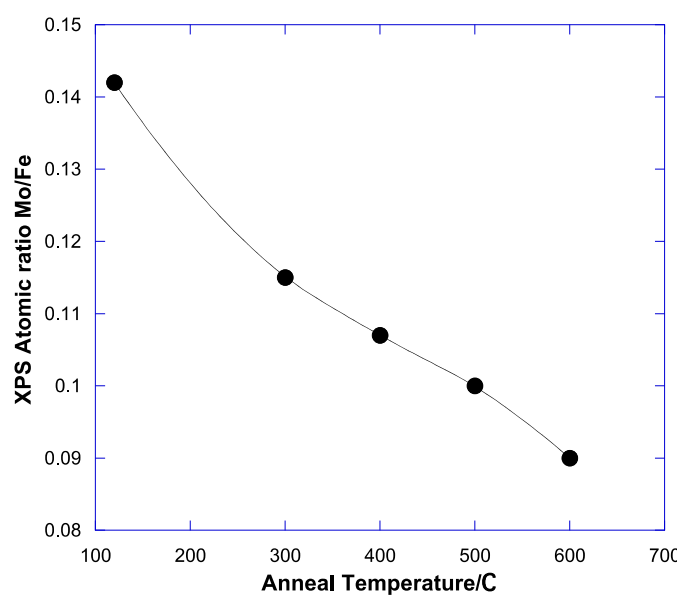


Figure 13. The change in Mo:Fe ratio for 3ML MoO_x/Fe₂O₃ with annealing from 100- 600 °C, as taken from the XPS data in Figure 12.

3.6. TPD and TPPFR Analysis

3.6.1. Catalytic Testing for 3ML MoO_x/Fe₂O₃

With a detailed understanding of the structural changes in the catalysts presented, it is important to relate these structural changes to catalytic performance, and for this purpose temperature programmed desorption (TPD) of adsorbed methanol was used.

The 3ML MoO_x/Fe₂O₃ catalyst was initially examined under MeOH TPD and compared with the reactivity of Fe₂O₃, MoO₃, and Fe₂(MoO₄)₃. Figure 14 shows the TPD for Fe₂O₃, which predominantly yields CO₂ (Mass 44), hydrogen (Mass 2), and water (Mass 18); the result of formate decomposition. The catalyst demonstrates zero selectivity to formaldehyde. MoO₃ and Fe₂(MoO₄)₃ on the other hand yield only formaldehyde (Mass 30) due to methoxy decomposition (Figures 15-16), with the TPD for these two bulk oxides very similar in nature.

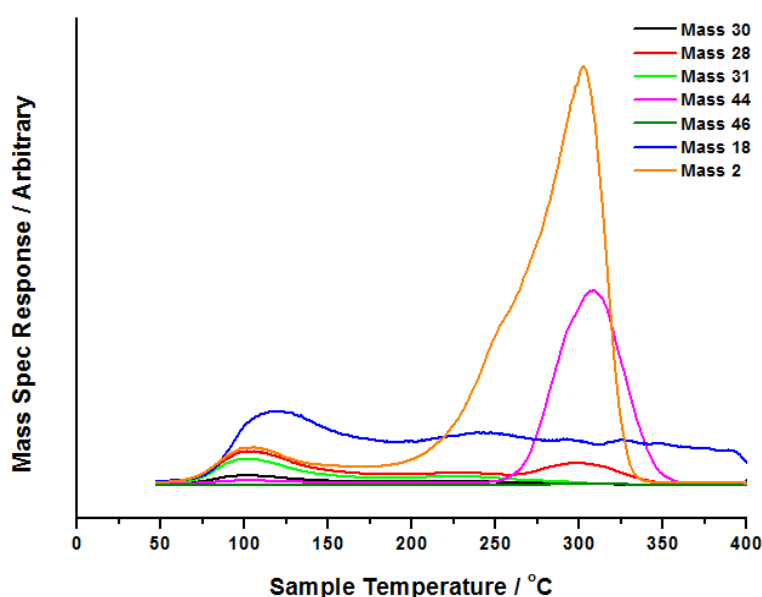


Figure 24. TPD (raw data) of MeOH/He for Fe₂O₃, demonstrating the dominant products as CO₂ (Mass 44) and H₂ (Mass 2). Methanol was dosed onto the catalyst surface under a He flow to saturation. The temperature was then ramped to 400 °C whilst monitoring the mass spectrometer response. Mass 30 corresponds to H₂CO, Mass 28 to CO, Mass 31 to MeOH, Mass 44 to CO₂, Mass 46 to DME, Mass 18 to H₂O and Mass 2 to H₂. Data presented is the raw data, as seen on the mass spectrometer.

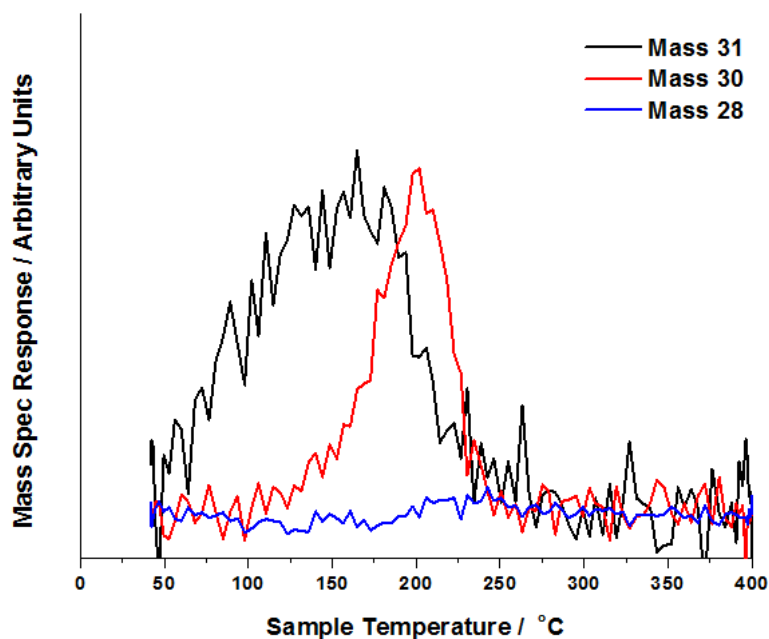


Figure 15. TPD of MeOH/He for MoO₃, demonstrating the dominant product as H₂CO. Subtractions have been made for the various cracking fragmentations of each product (Chapter 1, Section 3.3).

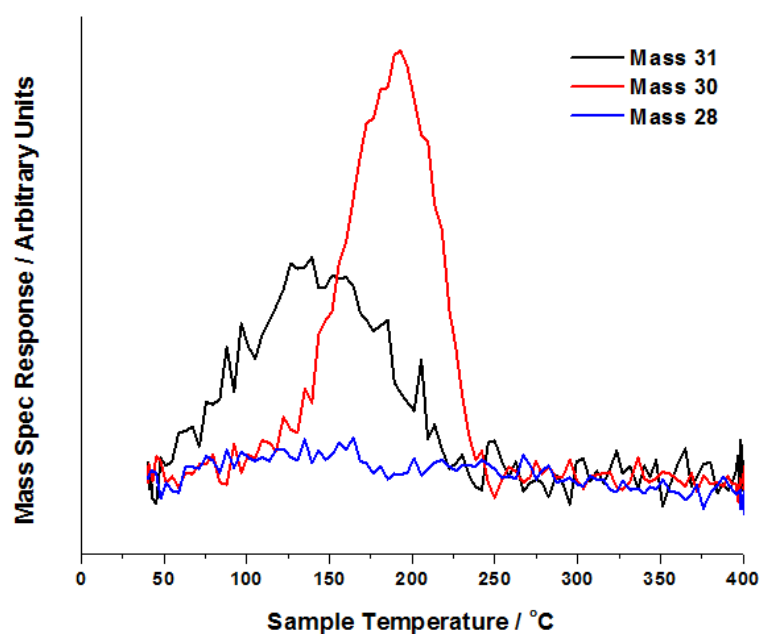


Figure 16. TPD of MeOH/He for bulk Fe₂(MoO₄)₃, demonstrating the dominant product also as H₂CO. Subtractions have been made for the various cracking fragmentations of each product (Chapter 1, Section 3.3).

Figure 17 demonstrates results for the TPD of MeOH/He for the 3ML MoO_x/Fe₂O₃ samples calcined at different anneal temperatures for 2 hours. All catalysts predominantly yield formaldehyde in the absence of any CO₂, which would be an indication for a surface consisting of iron oxide [13]. This shows that the surface has been significantly modified and is mainly Mo. There is a difference from the performance of bulk MoO₃ and Fe₂(MoO₄)₃ however, since there is a significant amount of CO also desorbed. It has been proposed that isolated Fe-Mo pairs are responsible for CO production [1]. This has been witnessed previously for catalysts where the bulk ratio of Fe and Mo has been varied [3, 13, 16]. With Fe present, it is thought that the Mo-O-Fe bridging oxygen undergoes a change in binding energy to facilitate this extra dehydrogenation to CO.

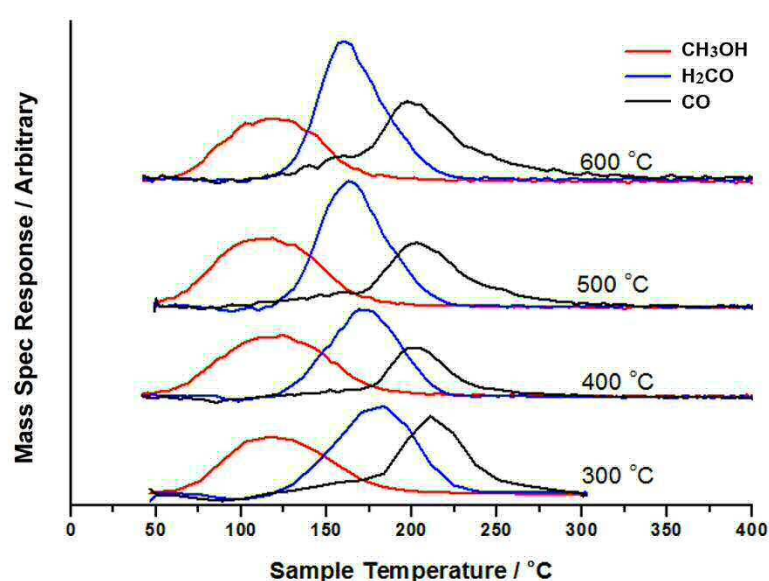


Figure 17. TPD of MeOH/He for 3ML MoO_x/Fe₂O₃ catalysts calcined to 300, 400, 500, and 600 °C. Note that the contributions to the Mass 28 signal from methanol (Mass 31, peaking at 120 °C) and formaldehyde (Mass 30, peaking at 170 °C) have been removed, leaving only that from CO itself at 200 °C.

Comparing across the calcination range, there are slight variations in the reactivity patterns with anneal temperature. Firstly, the intensity of the CO peak appears to be diminishing with a rise in calcination temperature, relative to the H₂CO. Table 4 documents the calculated selectivity to H₂CO, together with the peak desorption temperatures for CO and H₂CO. Selectivities are calculated by taking into account the different cracking patterns of formaldehyde and CO, which contribute to the total integral. Because the only products seen in TPD are formaldehyde and CO, selectivity is calculated as H₂CO/(H₂CO + CO).

Table 4. Summary of the TPD data of MeOH/He obtained for 3ML MoO_x/Fe₂O₃ after various calcination temperatures to 600 °C.

Anneal Temp / °C	Peak Temp/ °C		Selectivity to H ₂ CO / %
	H ₂ CO peak	CO peak	
300	180	210	77
400	170	200	79
500	162	200	82
600	162	197	85

Secondly, with increasing calcination temperature, it is apparent that clear shifts in the H₂CO and CO desorption temperatures occur, especially noticeable after annealing at 500 and 600 °C. The formaldehyde peak (H₂CO) appears to shift from 180 to 162 °C, whilst for CO from 210 to 200 °C, therefore becoming more clearly resolved from the formaldehyde peak. The catalysts annealed to 500 and 600 °C show a significantly improved activity in comparison to bulk standards, with the temperature of formaldehyde production at 160 °C as opposed to 180 °C for Fe₂(MoO₄)₃. This improved activity is a significant finding, and could be of potential interest in the development of future FeMo based catalysts in this selective oxidation reaction.

Pulse flow reaction studies (as outlined previously Chapters 2-3) have been used to assess the activity of the various calcined catalysts in more detail (Figure 18). Remarkably, there is little apparent difference in activity of the various calcined 3ML MoO_x/Fe₂O₃ samples, all giving 50 % conversion by 175 °C. Significant changes only occur in the overall selectivity to formaldehyde at high conversion (Table 5). The 300 °C sample has a lower selectivity to formaldehyde at high temperatures, and produces much more CO, in line with the effects in the TPD. When comparing with the previously reported data obtained for bulk loadings of Mo:Fe (Chapter 3), it is apparent that these data are between the results for bulk ratios of 1:1 and 1.5:1 Mo:Fe, which implies a mix of Fe and Mo sites at the catalyst surface. The difference in reactivity data for the 300 versus 500 °C calcined samples can be ascribed to the spread of Mo over the Fe₂O₃ surface. With a more efficient spread of Mo (as in the case of the 500/600 °C calcined samples), there is much less CO production, resulting in a higher selectivity to formaldehyde. For the 300 °C calcined sample, the MoO₃ is presumed to form as agglomerate like structures on the surface of Fe₂O₃, therefore exposing more Fe sites for the dehydrogenation of methanol to CO. Huang *et al* [37] have shown that “spreading” of the MoO₃ phase over such catalysts appears to be a relatively slow process, and requires temperatures over 400 °C for several hours.

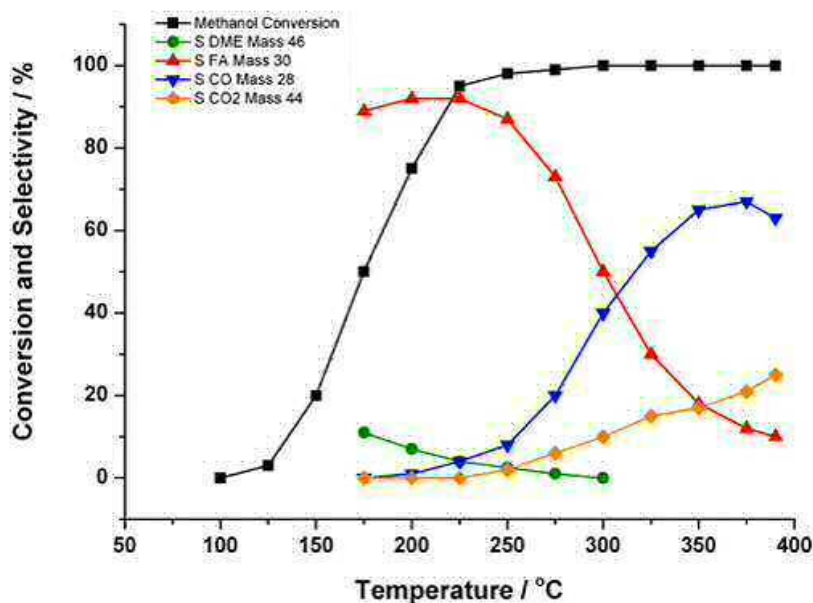


Figure 18. TPPFR MeOH oxidation reaction measurements over the 3ML $\text{MoO}_x/\text{Fe}_2\text{O}_3$ sample annealed to 500 °C, showing the conversion of methanol and the selectivity (S) to the various products observed. MeOH was injected over the catalyst at regular time intervals, whilst ramping to 400 °C in 10 % O_2/He . Subtractions have been made for the various cracking fragmentation of each product (Chapter 1, Section 3.3), to give a plot for selectivity and conversion. There was little change in this profile for different anneal temperatures between 300 and 600 °C, (see Table 5 for comparisons).

Table 5. Selectivity data achieved from pulse flow studies (as Figure 18) for the 3ML $\text{MoO}_x/\text{Fe}_2\text{O}_3$ catalysts calcined at 300 and 500 °C.

Anneal Temp / °C	Selectivity to H_2CO at		
	Conversion 50 %: T=175 °C	Conversion 90 %: T=225 °C	Conversion 100 %: T=300 °C
300	85	80	10
500	89	92	50

3.6.2. Catalytic Testing for Other Monolayer Loadings of $\text{MoO}_x/\text{Fe}_2\text{O}_3$

With a knowledge of the reactivity of 3 monolayers of Mo loaded at the surface of Fe_2O_3 , the study has been extended to other monolayer coverages to investigate whether just one monolayer is sufficient for the reaction, and whether higher monolayer coverages can further increase the selectivity to formaldehyde. Figures 19 and Table 6 show the effect of monolayer loading (1, 3 and 6ML $\text{MoO}_x/\text{Fe}_2\text{O}_3$) on the selectivity to formaldehyde, obtained through TPD of MeOH/He. It is revealed that the selectivity to formaldehyde increases with

growing monolayer coverage, however, even the 1ML MoO_x/Fe₂O₃ catalyst shows a satisfactory performance. For methanol oxidation, the 6ML MoO_x/Fe₂O₃ catalyst has a selectivity to formaldehyde of 87 %, compared to that of the bulk Fe₂(MoO₄)₃ catalyst [38] which demonstrates ~100 % selectivity in TPD. The somewhat reduced selectivity for the 1 ML MoO_x/Fe₂O₃ catalyst (81 %) is due to the increased formation of CO, proposed to derive from isolated surface Fe sites [5]. This increase in CO is obvious from the ratio of CO:H₂CO in Table 7. The presence of molybdenum dosed on the surface of the iron oxide clearly has a marked effect on the catalyst performance. For Fe₂O₃ alone, CO₂ is the dominant product, with no evidence for formaldehyde production [5]. In comparison, with just 1ML of Mo at the surface of the Fe₂O₃ support, there is no evidence for CO₂ production under a prolonged calcination.

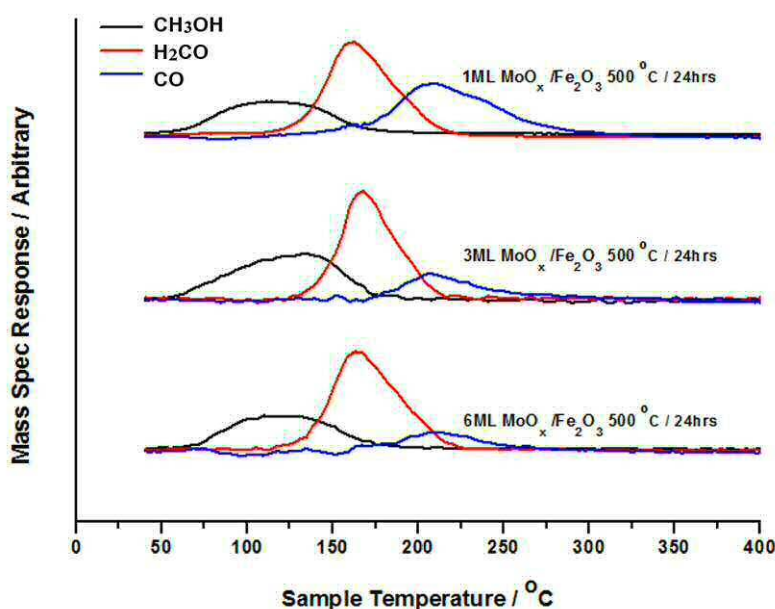


Figure 19. TPD data obtained for the 1, 3 and 6 ML MoO_x/Fe₂O₃, after calcining at 500°C for 24 hours, with noticeable reduction in CO production. Subtractions have been made for the various cracking fragmentations of each product (Chapter 1, Section 3.3).

Table 6. Summarised TPD data of MeOH/He for 1, 3 and 6ML MoO_x/Fe₂O₃ catalysts, compared with Fe₂O₃, Fe₂(MoO₄)₃ and MoO₃.

Catalyst	T _{H₂CO} / °C	T _{CO} / °C	Ratio peak areas Mass 30:Mass 28
1ML MoO_x/ Fe₂O₃	161	208	4:1
3ML MoO_x/ Fe₂O₃	165	209	5:1
6ML MoO_x/ Fe₂O₃	164	210	7:1
Fe₂O₃	-	-	-
Fe₂(MoO₄)₃	191	-	-
MoO₃	205	-	-

The effect of monolayer loading on catalyst performance has also been probed using temperature programmed pulsed flow studies. The reactor data in Figure 20 demonstrates calculated conversions for the 1, 3 and 6 monolayer coverages of Mo on Fe₂O₃. It is shown that the 1ML MoO_x/Fe₂O₃ catalyst is the most active, with its temperature for 50 % MeOH conversion shifted to lower value than the 3 and 6ML MoO_x/Fe₂O₃ equivalents. This is most likely to be an effect of the increased surface area of this loading, which demonstrates a surface area of 20 m²g⁻¹ (Table 2). The MoO_x/Fe₂O₃ series of catalysts calcined at 500 °C for 24 hours as a whole all exhibit an improved activity over that of the conventional Fe₂(MoO₄)₃ catalyst. This increase in activity is especially noticeable in the temperature for 50 % conversion (T₅₀) values; 50 % methanol conversion occurs at 190 °C for the 6ML MoO_x/Fe₂O₃, a significant improvement over that for bulk Fe₂(MoO₄)₃ which only reaches the same conversion at 212 °C. It could be that this is due to the difference in surface area of these catalysts [39-41] (Table 2). The MoO_x/Fe₂O₃ series of samples demonstrate a 3-4 fold increase in surface area compared to conventional Fe₂(MoO₄)₃ catalysts, a benefit afforded by this preparation method. If future optimisation can be made to improve the selectivity further, this increase in surface area will lead to a much more efficient catalyst.

Selectivity data is also shown for the 1, 3 and 6ML MoO_x/Fe₂O₃ coverages (Figures 21-23). A significantly greater amount of CO is produced for the 1ML MoO_x/Fe₂O₃ catalyst, presented as the dominant product from approximately 280 °C. Production of formaldehyde peaks earlier for this monolayer loading (at 160 °C), diminishing by 350 °C. A small amount of CO₂ is produced towards the end of the experiment. For the 3ML MoO_x/Fe₂O₃ catalyst, formaldehyde production peaks at approximately 200 °C. This steadily drops to 25 % of the overall selectivity by the end of the experiment at 400 °C, along with 41 % CO and 34 % CO₂. The increase in CO₂ production is a secondary oxidation product of formaldehyde, due to its increased production for this monolayer loading. The reactivity profile for the 6ML MoO_x/Fe₂O₃ catalyst is very similar to the 3ML MoO_x/Fe₂O₃ catalyst, albeit a slight rise in the T_{H₂CO} formation, a result of the lower surface area and reduced activity of this catalyst

(Table 2). The data presented through TPPFR compliments well the TPD for the various monolayers (Figure 19). Although an increase in CO formation for the one monolayer loading, in general, the three catalysts perform very similarly, implying that there is a common active phase to all catalysts.

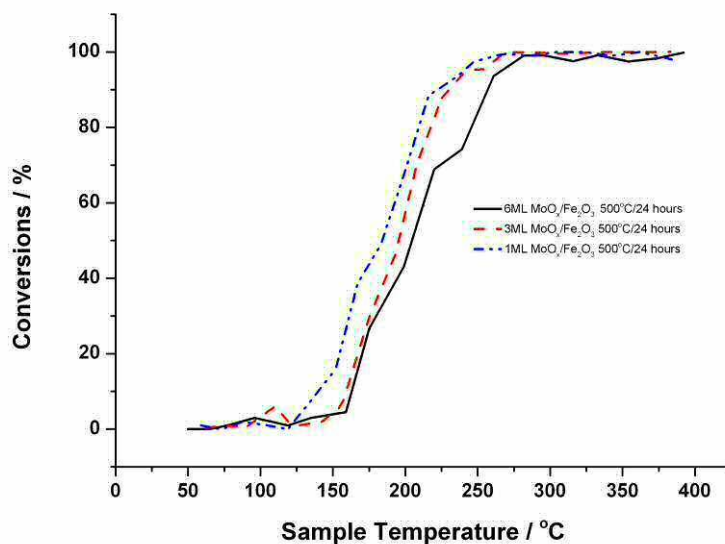


Figure 20. Comparative conversion data of MeOH under O_2/He flow for 1, 3 and 6 ML MoO_x/Fe_2O_3 calcined at 500 °C for 24 hours. MeOH was injected over the catalyst at regular time intervals, whilst ramping to 400 °C in 10 % O_2/He .

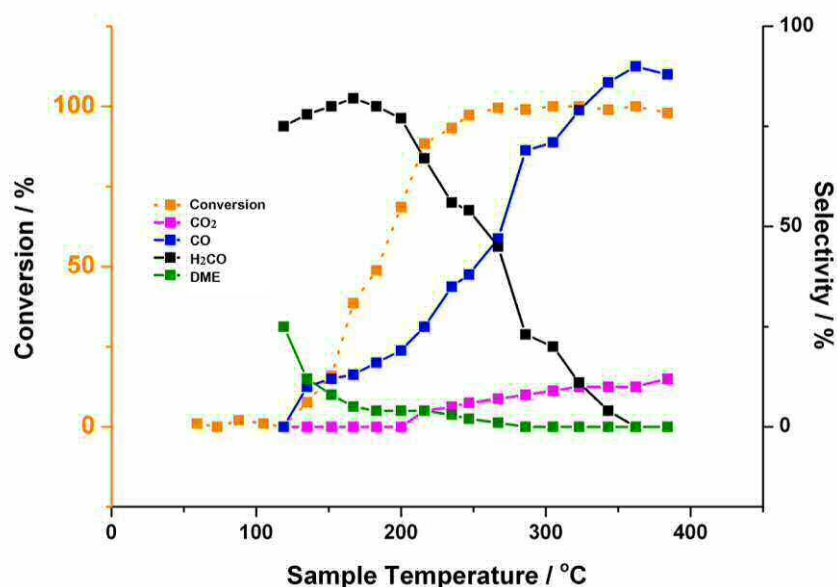


Figure 21. TPPFR for 1ML MoO_x/Fe_2O_3 calcined at 500 °C for 24 hours. MeOH was injected over the catalyst at regular time intervals, whilst ramping to 400 °C in 10 % O_2/He .

Subtractions have been made for the various cracking fragmentations of each product (Chapter 1, Section 3.3), to give a plot for selectivity and conversion.

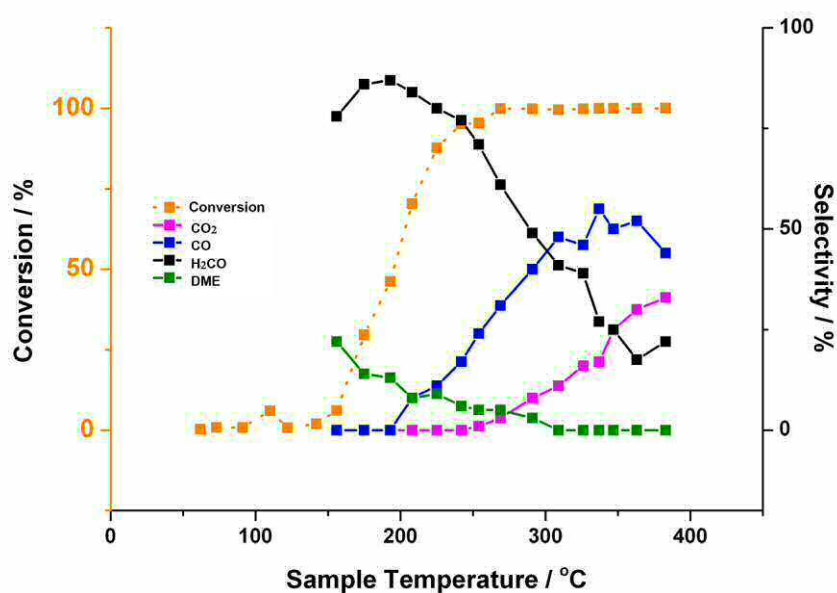


Figure 22. TPPFR for 3ML MoO_x/Fe₂O₃ calcined at 500 °C for 24 hours. MeOH was injected over the catalyst at regular time intervals, whilst ramping to 400 °C in 10 % O₂/He. Subtractions have been made for the various cracking fragmentations of each product (Chapter 1, Section 3.3), to give a plot for selectivity and conversion.

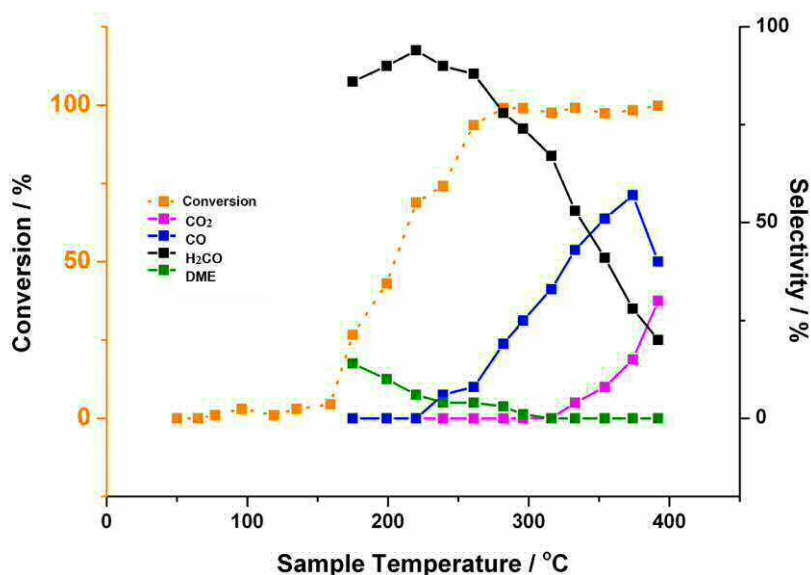


Figure 23. TPPFR for 6ML MoO_x/Fe₂O₃ calcined at 500 °C for 24 hours. MeOH was injected over the catalyst at regular time intervals, whilst ramping to 400 °C in 10 % O₂/He. Subtractions have been made for the various cracking fragmentations of each product (Chapter 1, Section 3.3), to give a plot for selectivity and conversion.

3.6.3. Calcination Effects

A further study on the effects of calcination time (2 vs 24 hours) on selectivity found a considerable decrease in the level of CO observed for the catalyst calcined for a longer period of time. This has been identified for all monolayer coverages (Figure 24 vs 19). This improved selectivity is ascribed to a greater uniformity of the Mo coverage on the Fe surface, since Raman, XANES, and IR show no significant change in the bulk phases present within the catalyst. This theory correlates well when considering the effect of calcination temperature for 3ML MoO_x/Fe₂O₃. With a higher coverage of Mo on the support, fewer Fe sites are available to react with the adsorbed methoxy intermediate, reducing the amount of CO production. The effect was most pronounced in the case of 1ML MoO_x/Fe₂O₃. For this catalyst, after just a 2 hour calcination, the reaction with MeOH yielded CO₂, H₂, CO and H₂CO. As mentioned, CO₂ production when formed co-incident with H₂ is suggestive of a formate intermediate. This would infer exposed Fe₂O₃ at the surface, providing an Fe-Fe site, onto which this bidentate can bind (See Chapter 3, 3.1.5-6). However, after an extensive heat treatment of 24 hours, the products detected are limited to just H₂CO and CO, as a result of the increased Mo spread.

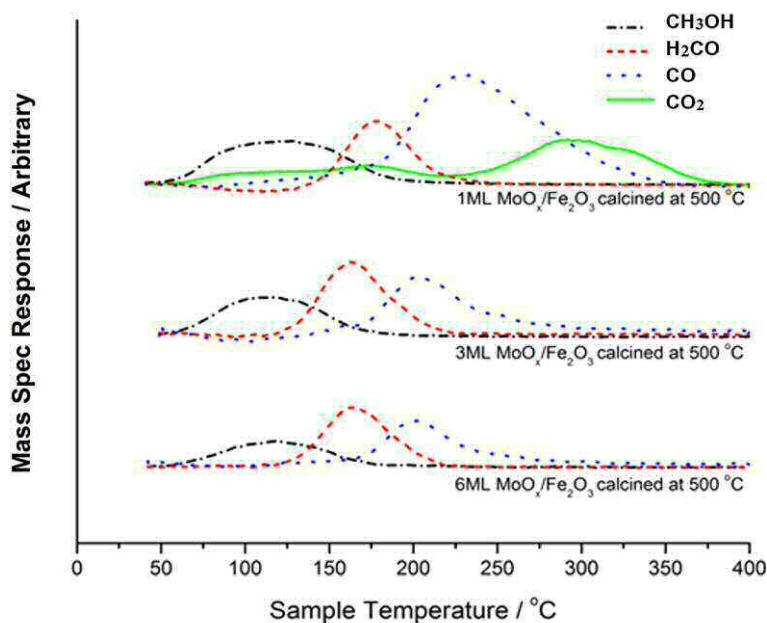


Figure 24. TPD of MeOH/He obtained for the 1, 3 and 6 ML MoO_x/Fe₂O₃ catalysts, after calcining at 500 °C for 2 hours. Methanol was dosed onto the catalyst surface under a He flow to saturation. The temperature was then ramped to 400 °C, whilst monitoring the Mass spectrometer response. Subtractions have been made for the various cracking fragmentations of each product (Chapter 1, Section 3.3).

TPPFR has also been used to probe this surface phenomenon.

Table 7. A comparison of selectivity to H₂CO between 1, 3 and 6ML MoO_x/Fe₂O₃ catalysts calcined for 2 and 24 hours at 500 °C.

Anneal Temperature / °C	Selectivity to H ₂ CO at:	
	T = 175 °C	T = 225 °C
1ML MoO_x/Fe₂O₃ 500 °C / 24 hours	82	62
3ML MoO_x/Fe₂O₃ 500 °C / 24 hours	86	83
6ML MoO_x/Fe₂O₃ 500 °C / 24 hours	86	93
1ML MoO_x/Fe₂O₃ 500 °C / 2 hours	80	74
3ML MoO_x/Fe₂O₃ 500 °C / 2 hours	74	69
6ML MoO_x/Fe₂O₃ 500 °C / 2 hours	80	76

Table 7 compares the reactivity data obtained for the varying monolayers under both a 2 and 24 hour calcination at 500 °C, as obtained through TPPFR. For the 1ML MoO_x/Fe₂O₃ catalyst there appears to be little difference between the reactivity data across the two calcination lengths. For the 3 and 6ML MoO_x/Fe₂O₃ catalysts, there is an obvious improvement in the catalyst selectivity for the 24 hour calcination. Both show an increase in selectivity to formaldehyde at both 175 °C and 225 °C, with the 6ML MoO_x/Fe₂O₃ outperforming the other catalysts and maintaining its selectivity at higher temperatures. However, although an improvement in the catalyst selectivity under an extended calcination time, activity is compromised. This is evidenced through a rise in the temperature of formaldehyde temperature for both the 3 and 6 monolayer catalysts after a 24 hour calcination.

3.7. XAS Study

3.7.1. XAS Analysis Mo K-edge 3ML MoO_x/Fe₂O₃

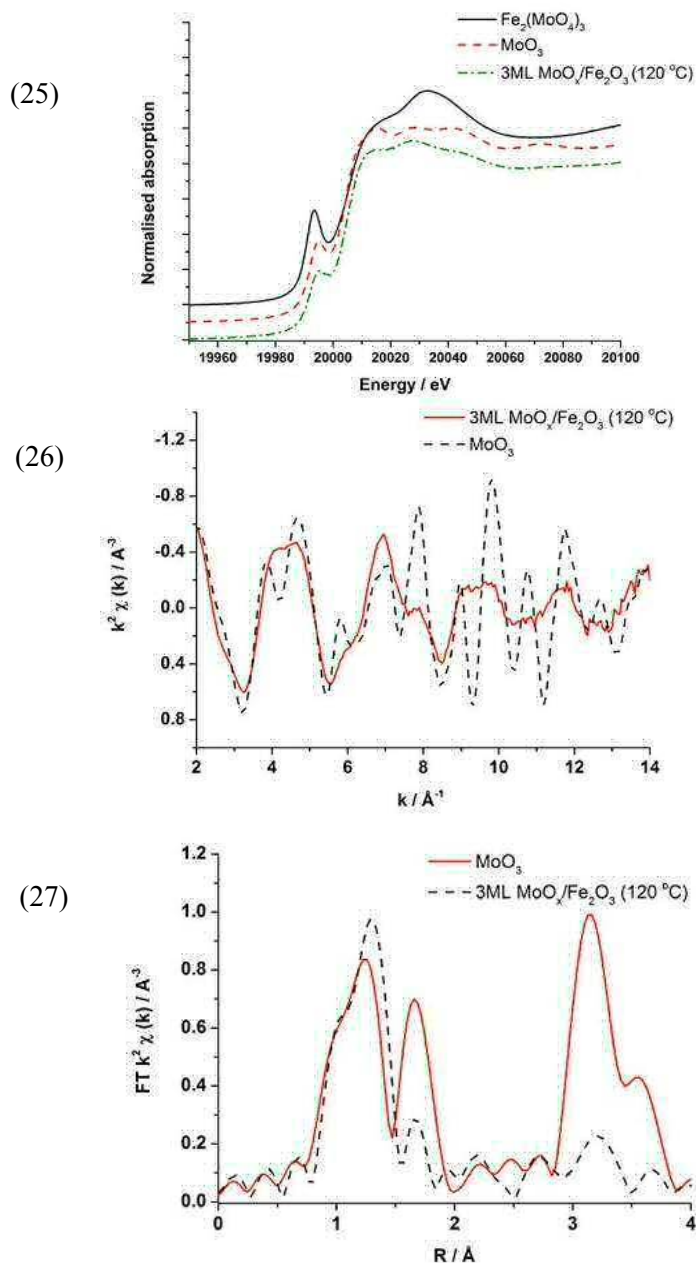
3.7.1.1. XANES Analysis

XANES analysis allows for information regarding the electronic properties and oxidation state of the Mo environment. XANES directly probes the angular momentum of the unoccupied electronic states: these states can be bound states (exitonic) or unbound states (continuum), discrete or broad, atomic or molecular.

Initially, studies focussed on the 3ML MoO_x/Fe₂O₃ catalyst, investigating the Mo structures present under increasing calcination temperature. This was carried out *ex situ*, having taken samples after different calcination procedures (120, 300, 400, 500 and 600 °C) prior to the run. A three monolayer loading was chosen since this gave a good signal for

complimentary characterisation such as Raman, FT-IR and XRD. It also meant that the XAFS could be run in transmission mode, even with such a high atomic weight of Fe within the sample, which is known to be a strong absorber.

The XANES spectrum of the dried 3ML $\text{MoO}_x/\text{Fe}_2\text{O}_3$ sample has been compared with that of MoO_3 and $\text{Fe}_2(\text{MoO}_4)_3$ standards run on the same experiment. Comparison of these XANES spectra shows that in the dried 3ML $\text{MoO}_x/\text{Fe}_2\text{O}_3$ (120°C) sample, the geometry of Mo is distorted octahedral. It is obvious that the dried sample does not show the same characteristic pre-edge feature as the tetrahedrally co-ordinated $\text{Fe}_2(\text{MoO}_4)_3$, therefore cannot show this co-ordination geometry. It is also evident that it is not purely octahedral. A comparison of the processed XAFS data of MoO_3 and the dried 3ML $\text{MoO}_x/\text{Fe}_2\text{O}_3$ (120°C) sample is detailed in Figures 25-27. The k^2 -weighted chi data shows a similar phasing and amplitude for the two samples at values of low k . However, further out in k -space, there is a discrepancy in the phasing between the two, with less long range ordering present in the Mo oxide deposited on Fe_2O_3 and less high Z neighbours. This is supported by the radial distribution function, where the data is dominated by the primary oxygen co-ordination distances. At higher values of R , there are only small contributions which are difficult to confidently assign. This is in stark contrast to the radial distribution function of MoO_3 where a large secondary shell of Mo neighbours is readily apparent. In summary, the dried sample does not show the same long range order displayed by MoO_3 , supporting its distorted octahedral nature.



Figures 25- 27. (25) Normalised XANES spectra of dried 3ML $\text{MoO}_x/\text{Fe}_2\text{O}_3$ (120 °C), MoO_3 , and $\text{Fe}_2(\text{MoO}_4)_3$, (26) k^2 - weighted data and (27) Fourier transform (non phase-corrected) for 3ML $\text{MoO}_x/\text{Fe}_2\text{O}_3$ (120 °C) and MoO_3 .

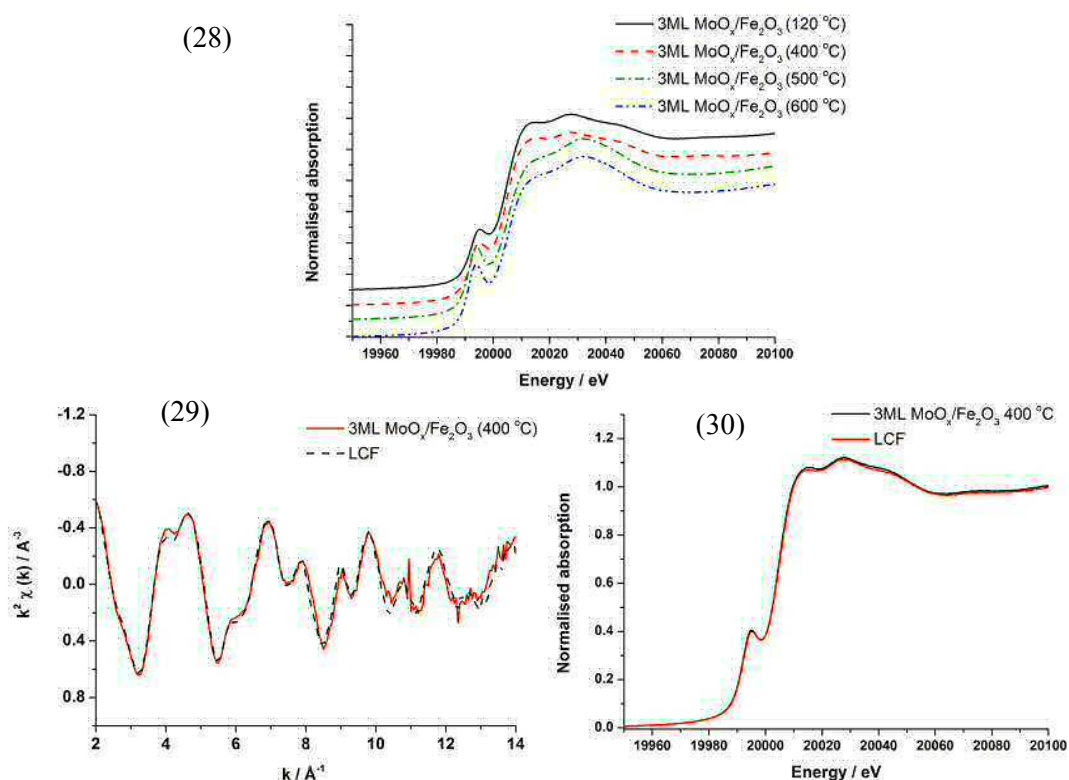
The effect of further annealing temperature on the nature of the Mo at the surface of Fe_2O_3 is demonstrated in the XANES data in Figure 28. The sample calcined at 300 °C is comparable to the sample dried at 120 °C, with an almost identical spectra. However by 400 °C initial changes in the Mo structure start to emerge, beginning to show features associated with MoO_3 formation. The k^2 - weighted chi spectrum of the 400 °C annealed sample compared to MoO_3 can be seen in Figures 29-30, which demonstrates these subtle changes. An analysis of the phase composition was assessed by performing a linear

combination fit of the XANES and chi data (Table 8) using the initial dried sample and MoO_3 as reference spectra. From the fit, it is shown that the distinct phase of MoO_3 is clearly present at this anneal temperature.

Upon annealing to 500°C , further changes are seen in the Mo geometry, with the samples annealed at 500 and 600°C both suggesting that large amounts of Mo begin to be incorporated into a tetrahedral phase likely in the form of $\text{Fe}_2(\text{MoO}_4)_3$. This is most clearly evidenced by the increase in the pre-edge feature at 19995 eV , typical for tetrahedral complexes. Linear combination fits (LCF's) were also performed for these samples, with $\text{Fe}_2(\text{MoO}_4)_3$ and the dried 3ML $\text{MoO}_x/\text{Fe}_2\text{O}_3$ (120°C) used as reference spectra, as these were found to give the most satisfactory fit. Fit analysis was able to ascertain the extent of $\text{Fe}_2(\text{MoO}_4)_3$ formation. Attempts were made to incorporate MoO_3 , however, more satisfactory fitting parameters were determined without the inclusion of this reference. Table 9 documents all these fittings. The data generated from the linear combination fits show that the spectra can be modelled to a large degree of confidence using these reference spectra. In summary, the results show that the amorphous Mo oxide initially dosed at the surface is converted to MoO_3 , prior to forming $\text{Fe}_2(\text{MoO}_4)_3$. Significant amounts of $\text{Fe}_2(\text{MoO}_4)_3$ phase is formed above 500°C , as the Mo at the surface drives into the Fe_2O_3 support to form this mixed oxide phase. However, it can also be seen through LCF analysis, that a large amount ($\sim 40\%$) of Mo oxide, similar in nature to the initial dried catalysts, remains even after annealing at 600°C , proven to be at the surface (TEM EDX).

Table 8. XANES LCF fittings for 3ML $\text{MoO}_x/\text{Fe}_2\text{O}_3$.

Sample	Reference Standards		
	MoO_3 (%)	$\text{MoO}_x/\text{Fe}_2\text{O}_3$ (%)	$\text{Fe}_2(\text{MoO}_4)_3$ (%)
3ML $\text{MoO}_x/\text{Fe}_2\text{O}_3$ (400°C) XANES fit	14	86	-
3ML $\text{MoO}_x/\text{Fe}_2\text{O}_3$ (400°C) chi fit	25	75	-
3ML $\text{MoO}_x/\text{Fe}_2\text{O}_3$ (500°C) XANES fit	-	38	62
3ML $\text{MoO}_x/\text{Fe}_2\text{O}_3$ (600°C) XANES fit	-	40	60



Figures 28-30. (28) XANES spectra of 3ML MoO_x/Fe₂O₃ catalysts annealed to different temperatures, and linear combination fits (LCF) of 3ML MoO_x/Fe₂O₃ (400 °C) using MoO₃ and 3ML MoO_x/Fe₂O₃ (120 °C) as standards fitted in (29) χ (non-phase corrected) and (30) normalised XANES.

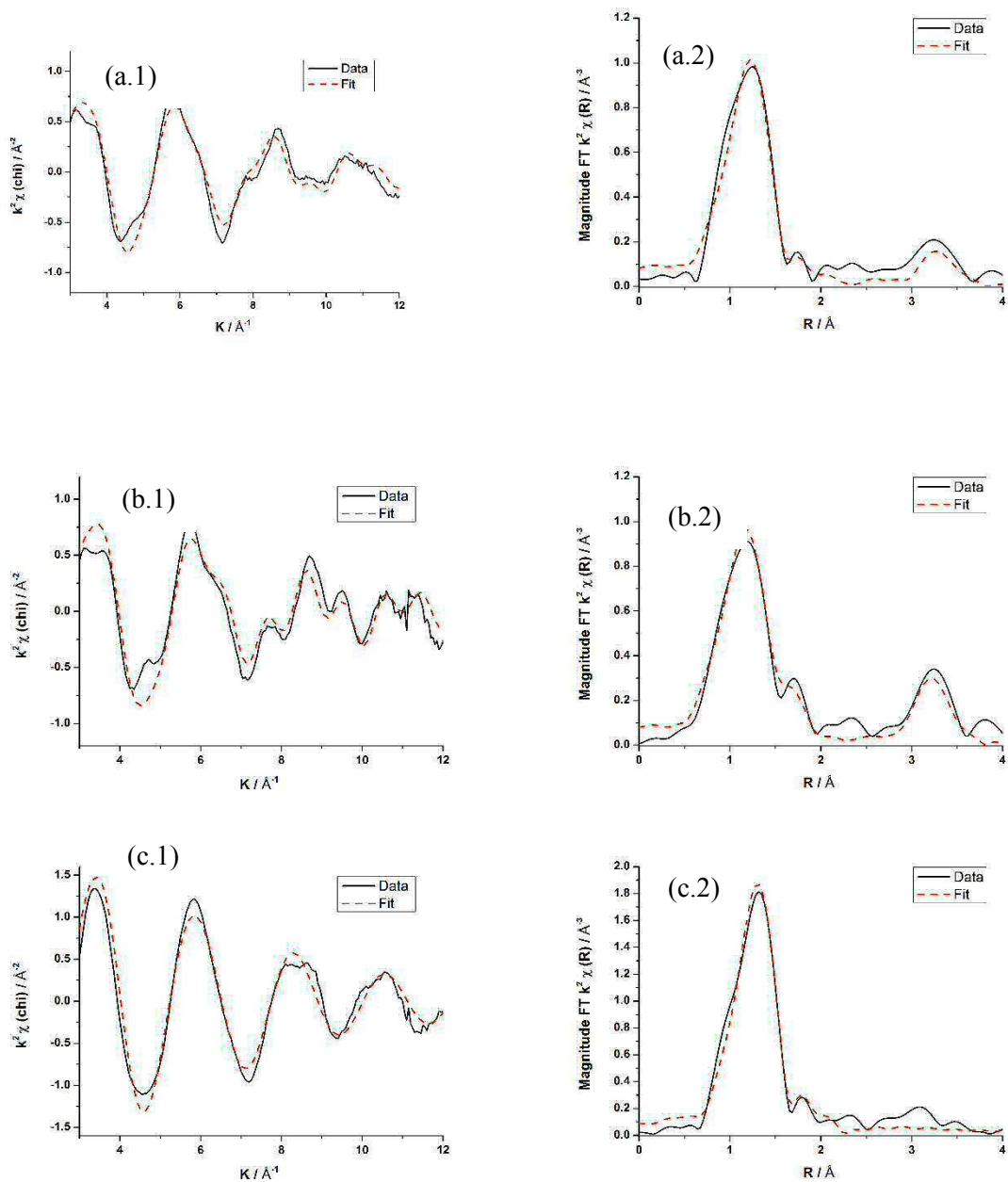
3.7.1.2. EXAFS Analysis

EXAFS data of the various calcined 3ML MoO_x/Fe₂O₃ samples has also been analysed. The k^2 weighted EXAFS data and corresponding Fourier transforms are presented in Figures 31-32. The data generated from fitting the extracted EXAFS data are in good agreement with the findings from the XANES analysis. The data for 3ML MoO_x/Fe₂O₃ catalyst calcined to 300 °C (Figure 31(a)) and the dried 3ML material are almost identical, and as in the case of the XANES, show Mo in a distorted O_h (octahedral) geometry, with limited dimensionality. To fit the data, two oxygen distances are required. The first oxygen shell occurs at 1.71 Å, which is well defined in nature. This shell shows a relatively low level of disorder, as demonstrated by the low Debye Waller factor (Table 9). The second oxygen co-ordination shell occurs at approximately 2.2 Å, however this longer shell distance has a much larger Debye Waller factor (0.03 Vs. 0.004) and therefore represents a more disordered environment. The reasoning behind this is assumed that there is a greater range of O distances comprised within this shell. Also within the model is a small Mo contribution, at a distance seen as a strong contribution in MoO₃. This again emphasises the lack of long range order on these lower calcined samples.

The fitting parameters for the 3ML MoO_x/Fe₂O₃ 400 °C (Figure 31(b)) sample are similar to those calcined at lower temperature, except in this instance there is a much larger Mo contribution, seen at 3.68 eV. This is indicative of MoO₃ formation, as discussed above. The EXAFS data for the 3ML MoO_x/Fe₂O₃ samples calcined to 500 and 600 °C (Figure 31(c) and (d)) can be modelled by one Mo–O contribution at 1.75 Å (co-ordination number ~ 4) as expected. This closely resembles the values seen for Fe₂(MoO₄)₃, so the tetrahedral resemblance to Fe₂(MoO₄)₃ can be assigned with confidence. The additional overlayer (denoted MoO_x) predicted to be present by the XANES measurement, cannot be modelled. This is due to the limited Mo-Mo interactions, hence the less significant contribution further out in R space. However, it is expected that the Mo-O d-shell would be dampened, due to the distorted nature of the octahedral structure of the overlayer (See Figure 32 for evidenced comparison of the FT (Fourier Transformed) data of this catalyst with bulk Fe₂(MoO₄)₃).

Table 9. EXAFS fitting parameters for 3ML MoO_x/Fe₂O₃ calcined at different temperatures. Fitting Parameters: $s_0^2=0.82$, Fit Range: $3 < k < 12$, $1 < R < 4$, 16 independent points ($1 < R < 3$ for the 500/600 °C calcined samples, 11 independent points). Where N= Co-ordination number, R= Bond distance/ Å of the Absorber-Scatterer, $2\sigma^2$ = Mean squared disorder term (sometimes referred to as the Debye waller factor), $E_f = E_0$, $R_{\text{factor}} = A$ statistic of the fit, which is a way of visualizing how the misfit is distributed over the fitting range.

Calcination temperature / °C	Abs. Sc.	N	R / Å	$2\sigma^2$ / Å ²	E_f / eV	R_{factor}
120 °C	Mo – O	3 (fixed)	1.71 (1)	0.005 (1)	-1 (3)	0.02
	Mo – O	3 (fixed)	2.24 (5)	0.03 (2)		
	Mo – Mo	1.6 (7)	3.68 (3)	0.006 (3)		
	Mo – O	3 (fixed)	1.71 (1)	0.005 (1)		
300 °C	Mo – O	3 (fixed)	2.23 (5)	0.03 (2)	-1(4)	0.02
	Mo – Mo	1.6 (6)	3.68 (3)	0.007 (3)		
	Mo – O	3 (fixed)	1.67 (3)	0.006 (1)		
400 °C	Mo – O	3 (fixed)	2.24 (3)	0.013 (4)	-7(3)	0.02
	Mo – Mo	3 (1)	3.66 (2)	0.006 (2)		
500 °C	Mo – O	4.5 (3)	1.75 (1)	0.004 (1)	8 (2)	0.01
600 °C	Mo – O	4.5 (3)	1.75 (1)	0.003 (1)	7 (2)	0.01



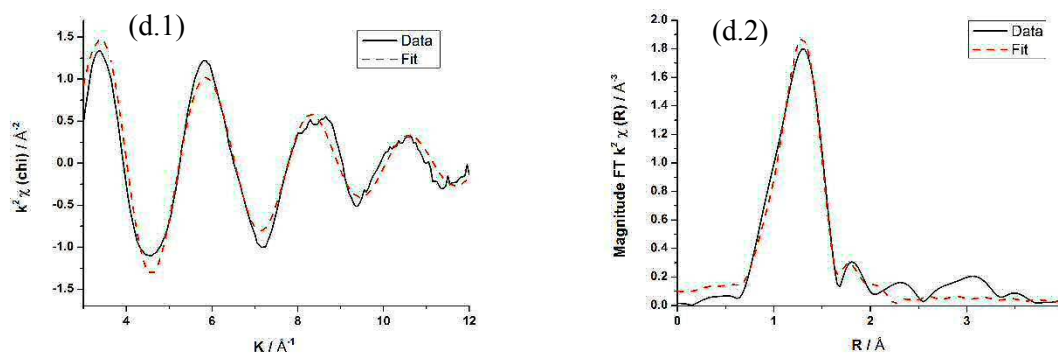


Figure 31. Experimental k^2 weighted EXAFS data (1) and corresponding Fourier transform (2) (non phase-corrected) with associated fits for 3ML $\text{MoO}_x/\text{Fe}_2\text{O}_3$ calcined to (a) 300 °C, (b) 400 °C, (c) 500 °C, and (d) 600 °C. For fitting standards see Table 8.

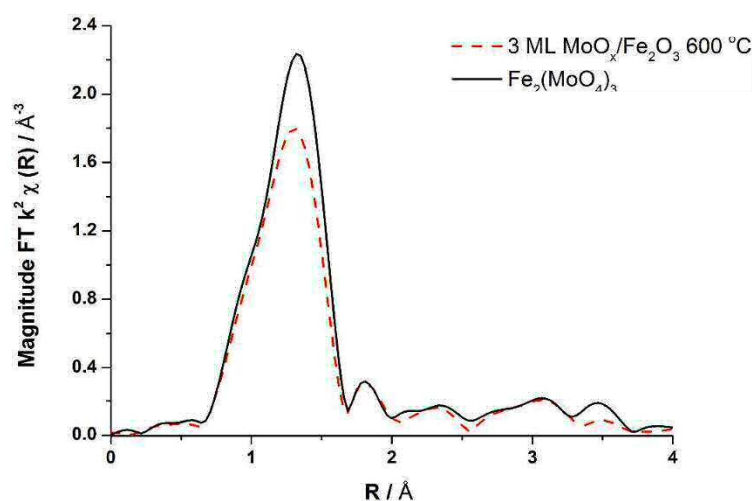


Figure 32. Fourier transform (non phase-corrected) of the EXAFS chi data of $\text{Fe}_2(\text{MoO}_4)_3$ and 3ML $\text{MoO}_x/\text{Fe}_2\text{O}_3$ calcined to 600 °C.

In conclusion of the findings so far, a series of MoO_x -modified Fe_2O_3 catalysts have been prepared in an attempt to make core-shell oxidic materials of the type $\text{MoO}_x/\text{Fe}_2\text{O}_3$. Cross referencing to the corresponding reactivity data, there are some significant findings which enable crucial information about the surface active layer in these core-shell structures. It is conclusively shown that for three monolayers of Mo dosed, the Mo stays in the surface region (as proven by TEM EDX), even after annealing to high temperature. Only once the calcination temperature exceeds 400 °C does the Mo convert to $\text{Fe}_2(\text{MoO}_4)_3$ as proven through a variety of characterisation methods, but particular through XAFS

which shows a definite change in co-ordination geometry to T_d (tetrahedral) structure (Figure 28).

It was discovered that reactivity was comparable between the various 3ML $\text{MoO}_x/\text{Fe}_2\text{O}_3$ catalysts calcined at 120-600 °C, even when characterisation by conventional techniques (Raman, XRD, IR) showed a change in the oxide phase at different temperatures. Due to the similarity in reactivity, this would suggest a resemblance in the active surface layer performing the chemistry. Only subtle differences in selectivity were evident, assumed to be due to the spread of Mo at the surface.

XAS enabled the identification of an amorphous Mo monolayer in octahedral co-ordination, common to all catalysts even after calcination to 600 °C. This surface layer appears to be present at all temperatures between 300 and 600 °C, and it is the nanoparticles of MoO_3 that are present at the lower temperature that react to form $\text{Fe}_2(\text{MoO}_4)_3$ (Figure 33).

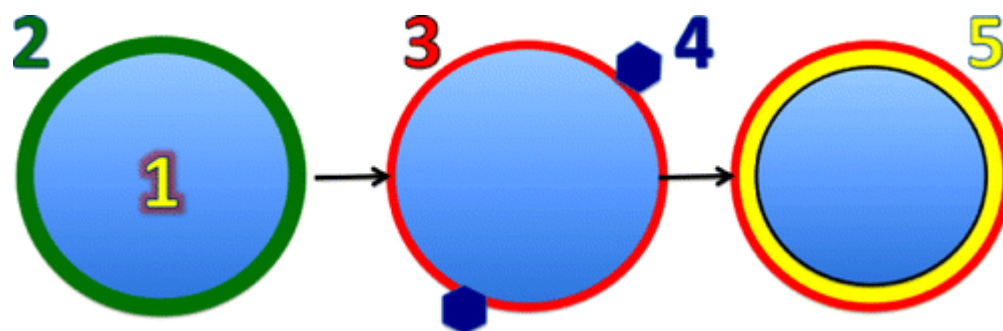


Figure 33. The evolution of the surface structure of the 3 ML catalyst as a function of annealing. On the left, the surface consists of an amorphous MoO_x layer (2), supported on the Fe_2O_3 core (1), which is the structure at low temperatures. In the middle, shown is the structure at 400 °C with both nanocrystallites of MoO_3 (4) at the surface of the catalysts and the surface of MoO_x present. Finally, in the right-hand panel, is the structure after annealing, in which the nanoparticles of MoO_3 have mostly converted to ferric molybdate (yellow layer 5), but with the active monolayer overlaying it.

It is proposed that it is the MoO_x layer on the MoO_3 or $\text{Fe}_2(\text{MoO}_4)_3$ under layer that makes the surface active and selective for formaldehyde synthesis. The Fe_2O_3 acts as a combustor for the reaction. The material is both activated and improved in selectivity due to the dominance of the methoxy species on the Mo-doped material, as opposed to formate which dominated on Fe_2O_3 .

3.7.2. XAS Analysis Mo K-edge 1, 3 and 6 ML MoO_x/Fe₂O₃: Varying the Monolayer Coverage at the Surface of Fe₂O₃

Having identified a bound terminating layer of octahedral Mo units as the active and selective phase in core-shell structures of 3ML MoO_x/Fe₂O₃, a range of monolayers were investigated to see if the same structure was apparent. Since the reactivity of these catalysts are comparable to those used industrially, it was also questioned whether only 1 monolayer of Mo on iron oxide alone is efficacious for this reaction. This section highlights how catalyst surfaces are significantly different to bulk structures, and this difference is crucial for catalyst performance.

3.7.2.1. XANES Analysis

Calcination temperature has been investigated for each of the monolayer loadings, as was carried out for the 3ML MoO_x/Fe₂O₃ catalyst (Figure 28). Tables 10-12 detail the relative compositions of the dosed Mo for each of the monolayer loadings at calcination temperatures between 120-600 °C.

For the 6ML MoO_x/Fe₂O₃ catalyst, there is a substantial amount of MoO₃ at 300 °C, at 53 %, which equates to approximately 50 % of the total Mo dosed, the remainder fitted with the original dried sample denoted MoO_x (Figure 34, Table 10). By 400 °C, the formation of MoO₃ has peaked and risen to 67 % (XANES fit), which constitutes two thirds of the total Mo dosed, the remainder as MoO_x. In comparison, it was shown that the formation of MoO₃ does not occur until 400 °C for the 3ML equivalent, at just 25 %, with the remaining 75 % as MoO_x (Figure 35, Table 11).

Both catalysts show Fe₂(MoO₄)₃ formation at the higher calcination temperature of 500 °C, with no MoO₃ remnant. Fe₂(MoO₄)₃ can be confidently assigned, with an example of the fits achieved shown in Figure 38 and Table 12. The fits at this temperature can be performed using the initial dried catalyst for each monolayer and Fe₂(MoO₄)₃, with the dried phase forming approximately one monolayer equivalent of the fit (See Figures 34-35).

Table 10. Linear combination fits (XANES and Chi) for 6ML MoO_x/Fe₂O₃ after varying calcination treatments. References used were MoO₃, Fe₂(MoO₄)₃ and dried 6ML MoO_x/Fe₂O₃.

Sample	Reference Standards (%)			
	MoO ₃	MoO _x /Fe ₂ O ₃	Fe ₂ (MoO ₄) ₃	R _{factor}
6ML MoO _x /Fe ₂ O ₃ (300 °C) XANES	53	47	-	2×10 ⁻⁵
6ML MoO _x /Fe ₂ O ₃ (300 °C) chi fit	60	40	-	1 x 10 ⁻³
6ML MoO _x /Fe ₂ O ₃ (400 °C) XANES	67	33	-	1×10 ⁻⁴
6ML MoO _x /Fe ₂ O ₃ (400 °C) chi fit	82	18	-	2×10 ⁻⁵
6ML MoO _x /Fe ₂ O ₃ (500 °C) XANES	-	12	88	1×10 ⁻³
6ML MoO _x /Fe ₂ O ₃ (500 °C) chi fit	-	8	92	4×10 ⁻⁵
6ML MoO _x /Fe ₂ O ₃ (600 °C) XANES	-	10	90	0.02
6ML MoO _x /Fe ₂ O ₃ (600 °C) chi	-	6	94	7×10 ⁻³

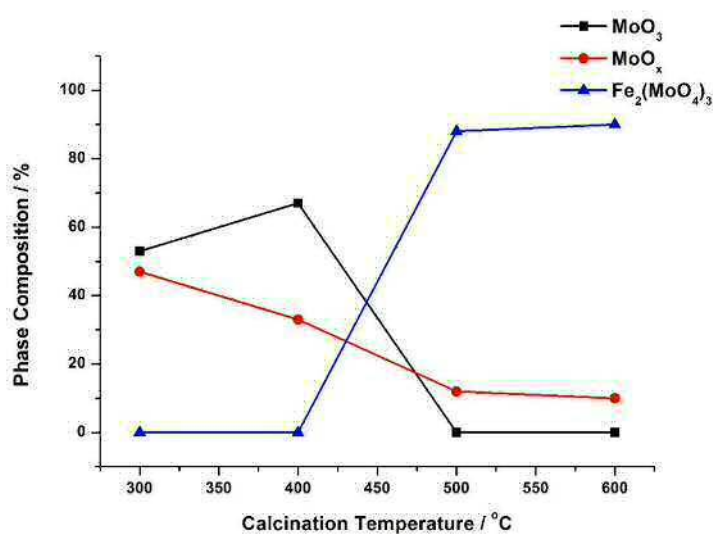


Figure 34. Results for a XANES linear combination fit analysis for 6ML MoO_x/Fe₂O₃ calcined at 300, 400, 500 and 600 °C. References used were MoO₃, Fe₂(MoO₄)₃ and dried 6ML MoO_x/Fe₂O₃. At the end of the calcination, it is shown that the catalyst is formed from 90 % Fe₂(MoO₄)₃ and 10 % Dried MoO_x/Fe₂O₃. This dried phase corresponds to approximately 1 monolayer of the total Mo dosed.

Table 11. Linear combination fits (XANES and Chi) for 3ML MoO_x/Fe₂O₃ after increasing calcination treatments. References used were MoO₃, Fe₂(MoO₄)₃ and dried 3ML MoO_x/Fe₂O₃.

Sample	Reference Standards (%)			R _{factor}
	MoO ₃	MoO _x /Fe ₂ O ₃	Fe ₂ (MoO ₄) ₃	
3ML MoO _x /Fe ₂ O ₃ (300 °C) XANES	0	100	-	0
3ML MoO _x /Fe ₂ O ₃ (400 °C) XANES	14	86	-	7×10 ⁻⁵
3ML MoO _x /Fe ₂ O ₃ (400 °C) Chi	25	75	-	0.03
3ML MoO _x /Fe ₂ O ₃ (500 °C) XANES	-	32	68	1×10 ⁻⁴
3ML MoO _x /Fe ₂ O ₃ (600 °C) XANES	-	34	66	2×10 ⁻⁵

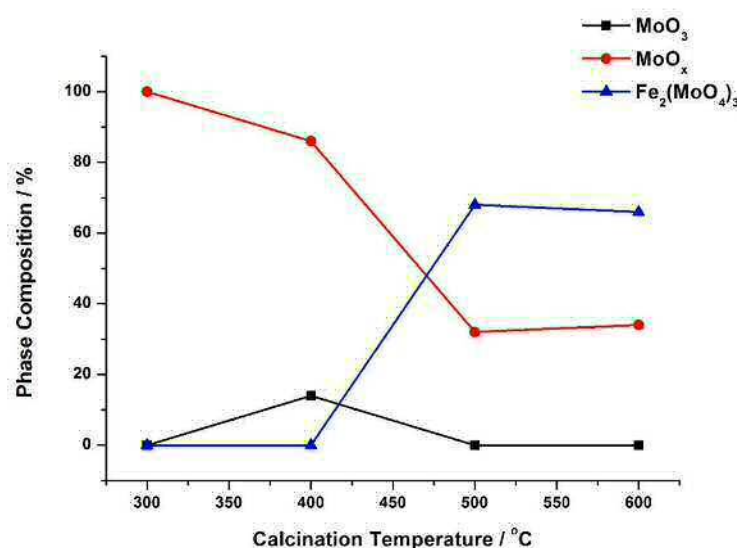


Figure 35. Results for a XANES linear combination fit analysis for 3ML MoO_x/Fe₂O₃ calcined at 300, 400, 500 and 600 °C. References used were MoO₃, Fe₂(MoO₄)₃ and dried 6ML MoO_x/Fe₂O₃. At the end of the calcination, it is shown that the catalyst is formed from 75 % Fe₂(MoO₄)₃ and 25 % Dried MoO_x/Fe₂O₃. This dried phase corresponds to approximately 1 monolayer of the total Mo dosed.

For the catalyst with just 1ML equivalent of molybdenum, the catalyst is consistent with a distorted O_h geometry throughout the calcination range. All samples are identical to the 1ML MoO_x/Fe₂O₃ catalyst dried at 120 °C (Figure 36). It is therefore established that for monolayer (or sub-monolayer) amount of a species labelled as MoO_x, the molybdenum remains segregated at the surface of the Fe₂O₃, with complete O_h geometry under all

calcination conditions (TEM EDX was performed to evidence this, and XPS proved surface Mo enrichment remains at 600 °C (Figure 13)). This segregated overlayer readily forms at low temperatures, and even generates when a physical mixture of MoO_3 and Fe_2O_3 is exposed to the same calcination regime. It is evident that this Mo surface is very stable, remaining unchanged even after extensive calcinations at high temperatures over long periods of time.

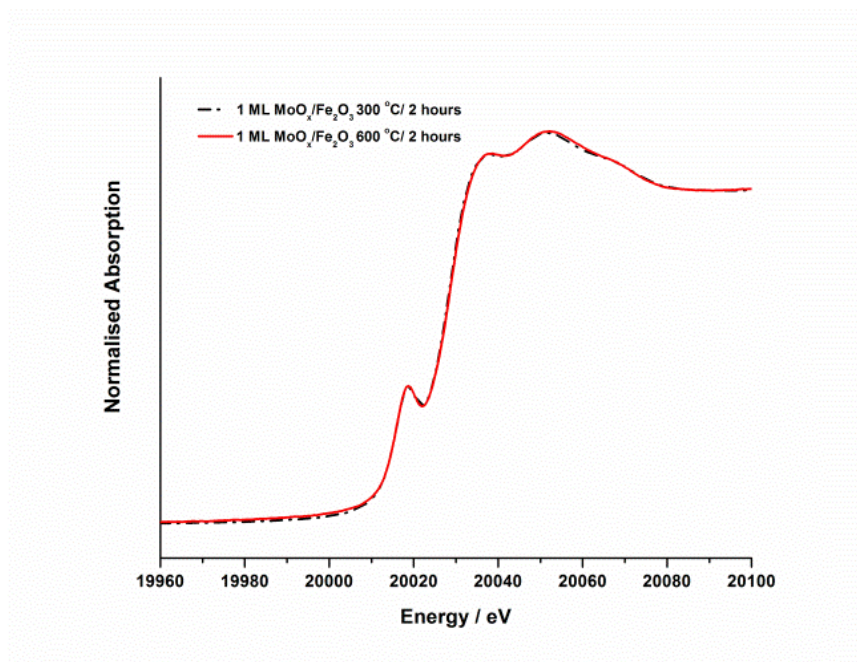
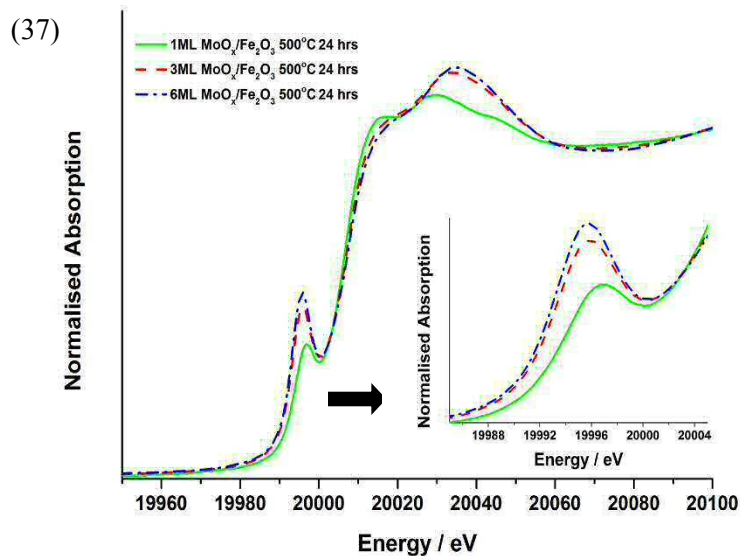


Figure 36. Normalised XANES spectra of 1ML $\text{MoO}_3/\text{Fe}_2\text{O}_3$ catalysts annealed to 300 and 600 °C. Spectra are identical across the calcination range.

Table 12. XANES linear combination fit analysis for 1, 3 and 6ML MoO_x/Fe₂O₃ calcined at 500 °C / 24 hours. R factors are given to portray the degree of correlation between the theory and experiment.

Sample	Reference Standards			R Factor
	% MoO _x	% MoO ₃	% Fe ₂ (MoO ₄) ₃	
1ML MoO_x/Fe₂O₃ 500 °C / 24 hours (XANES fit)	100	-	-	0
3ML MoO_x/Fe₂O₃ 500 °C / 24 hours (XANES fit)	27	-	73	1.8 x 10 ⁻⁴
6ML MoO_x/Fe₂O₃ 500 °C / 24 hours (XANES fit)	12	-	88	3.8 x 10 ⁻⁵

Figures 37-38 illustrate XANES spectra the 1, 3 and 6ML MoO₃/Fe₂O₃ catalysts annealed 500 °C for 24 hours, with the accompanying linear combination fits (LCF's). It is clear that with an increase in monolayer loading, the pre-edge feature at ~ 19995 eV becomes more defined in nature, signifying a higher proportion of T_d nature in the catalyst. Table 12 summarises the relative amounts of phases formed at the surface, clearly demonstrating that with an increase in monolayer coverage, the O_h to T_d ratio varies, with the 6 monolayer catalyst exhibiting the greatest T_d character. Moreover, the phase composition generated by linear combination analysis of the XANES data confirms that all samples have approximately 1 monolayer of O_h Mo units, denoted MoO_x, present at their surface. For example, for 6MLs MoO_x/Fe₂O₃, it is established that there are 5 ML equivalents of Fe₂(MoO₄)₃ present, with 1ML MoO_x as the terminating overlayer (as proven by TEM EDX). In the case of the 3ML MoO_x/Fe₂O₃ catalyst, 2ML equivalents of Fe₂(MoO₄)₃ co-exist with 1ML MoO_x. If this trend is extended, it would be expected that even a bulk (stoichiometric) Fe₂(MoO₄)₃ catalyst would have a surface terminating in O_h Mo units, and certainly enrichment of Mo in the surface region of such catalysts has been agreed [6].



*Figure
caption with
following
Figure

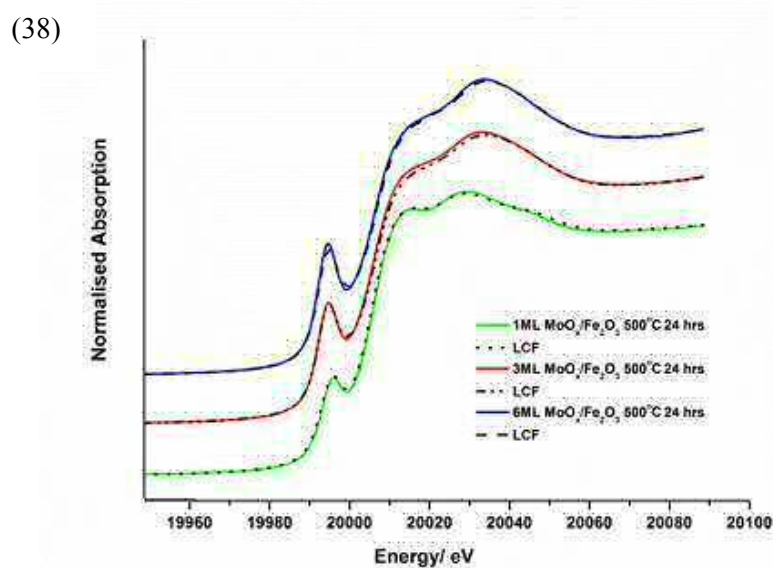


Figure 37-38. XANES spectra of 1, 3, and 6ML $\text{MoO}_3/\text{Fe}_2\text{O}_3$ catalysts annealed 500 °C / 24 hours, and accompanying linear combination fits (LCF's) using MoO_3 and $\text{MoO}_x/\text{Fe}_2\text{O}_3$ (120 °C) as standards.

3.7.2.2. EXAFS Analysis

EXAFS data has been performed for the varying monolayer samples. Figure 39 shows the non phase-corrected Fourier transform of the k^2 -weighted EXAFS data (plus imaginary components of the data and scattering paths) for the 1ML MoO_x/Fe₂O₃ sample annealed at 500 °C for 24 hrs. The XANES data confirmed the presence of O_h Mo. EXAFS can show this in more detail. Data shows the primary Mo O_h environment is comprised of oxygen neighbours, with the major contribution at low values of R in the Fourier transform associated with a short Mo–O (distance = 1.74 Å) scattering path (Table 13). There is also a longer Mo–O scattering path at 1.95 Å, albeit weaker as a consequence of the large disorder associated with it. The combination of these two scattering paths results in a good correlation between the experimental and simulated data for values of R < 2 Å.

With a lower loading of Mo, it becomes easier to probe the interaction of the Mo to the Fe₂O₃ surface, as there are fewer interactions to consider with less interference of several scattering paths. EXAFS shows that these units are bound to the Fe₂O₃ surface with a clear Mo–Fe interaction. The subsequent co-ordination environment post that for the oxygen co-ordination, is associated with the Mo–Fe scattering paths. Results indicate a site in which the Mo has three Fe neighbours at approximately 3.1 Å, and one Fe neighbour at a shorter distance of 2.82 Å. The relatively weak intensity of four Mo–Fe neighbours is a result of the out of phase behavior of the different Mo–Fe distances, as seen in the imaginary part of the Fourier transform (Figure 39).

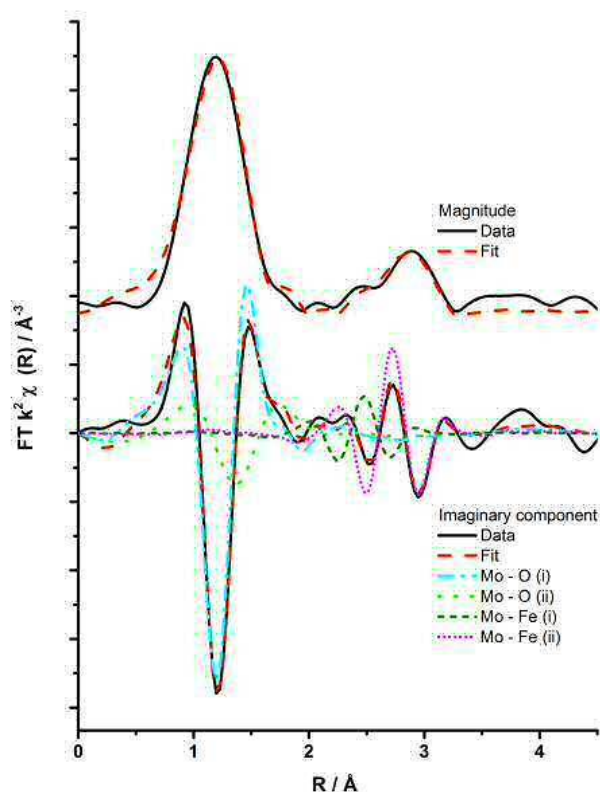


Figure 39. Magnitude and imaginary component of the k^2 -weighted Fourier transform (non phase-corrected) for the EXAFS data of the 1ML $\text{MoO}_x/\text{Fe}_2\text{O}_3$ catalyst calcined to 500°C / 24 hours. Associated scattering paths are included for the imaginary component.

Table 13. EXAFS fitting parameters for the 1ML $\text{MoO}_x/\text{Fe}_2\text{O}_3$ catalyst calcined to 500°C . Fitting parameters: $S_0^2 = 0.82$ as deduced by MoO_3 standard: Fit range $2.6 < k < 9.7$, $1 < R < 3.5$: # of independent points = 11. Where N = Co-ordination number, R = Bond distance/ \AA of the Absorber-Scatterer, $2\sigma^2$ = Mean squared disorder, $E_f = E_0$, R_{factor} = A statistic of the fit.

Abs. Sc.	N	R / \AA	$2\sigma^2$ / \AA^2	E_f / eV	R_{factor}
Mo – O	3 (fixed)	1.74 (2)	0.006 (1)	7 (3)	0.005
Mo – O	3 (fixed)	1.95 (6)	0.03 (1)		
Mo – Fe	1 (fixed)	2.85 (4)	0.009 (6)		
Mo – Fe	3 (fixed)	3.10 (3)	0.009 (3)		

3.8. Computer Modelling

Computational modelling was undertaken in collaboration with David Mora Fonz of UCL University, to determine the nature of the preferred adsorption site on Fe_2O_3 . For the purpose of the study, the most stable surface of $\alpha\text{-Fe}_2\text{O}_3$ [42] was used since the stability of this surface has been shown at a wide range of oxygen partial pressures. A neutral MoO_3 unit can

be accommodated at five topologically distinct adsorption sites with mixed oxide-iron termination as shown in Figure 40.

To conduct the study, a series of *ab initio* DFT plane-wave calculations were performed [42, 43] (see Appendix A10), using (1 x 1) and (2 x 2) surface models, with a MoO₃ neutral unit placed at each of the five sites. To describe surfaces within three-dimensional periodic boundary conditions, the slab method was employed. Under this approach, a (1 x 1) surface model was constructed as a unit cell containing 65 atoms forming an approximately 29 Å thick slab, with a vacuum gap between the slabs of approximately 20 Å. Simulations of the formation of MoO₃ overlayer on Fe₂O₃ were then performed identically on both sides of the slab to ensure that the slab dipole moment perpendicular to the surface was zero. The MoO₃ neutral units were accommodated approximately 3 Å away from the surface, which would correspond to 0.5 and 0.2 ML MoO₃ surface coverage, respectively, considering only the uppermost cationic layer. Close-range MoO₃-MoO₃ interactions have thus been avoided in agreement with EXAFS data.

Several observations were noted upon placing MoO₃ above the different sites. Whenever the Mo ion was placed just above a surface oxygen (adsorption site D), it moved off this site and preferred to stabilise above the Fe ion of the second (subsurface) layer in either configuration A or B (Figure 41). For this reason, this site is not referred to in the table presented. Above interstitial site E, the Mo ion relaxed slightly towards the surface as one of the molybdate O ions was displaced towards the first layer Fe, forming a Mo-O-Fe bridge. The adsorption site C proved to be highly unfavourable. Here, the Mo ions stayed above the uppermost Fe atom with no strong Mo relaxation. The neutral MoO₃ monolayer remained almost flat at a non-bonding distance above the surface, so the situation was deemed unrealistic.

Sites A and B showed a large Mo relaxation into the surface, and are therefore suggested to be the most favoured adsorption sites. An octahedral co-ordination is adopted in both cases. At the most stable site A, Mo has one Fe ion neighbor at 2.80 Å, and three further at 2.96 Å, whereas at site B it has three Fe neighbours at 2.94 Å and one at 3.05 Å. Adsorption site A highly agrees with the co-ordination numbers in the EXAFS analysis, and shows a good agreement with most of the bond distances (Table 14 compares the values obtained from theoretical investigation versus that obtained experimentally through EXAFS). The calculations using the (2 x 2) surface model predict the three short Mo-O bond distances to be 3.44 % greater, and the Fe-O distances 1.4 % and 3.59 % smaller. However, the calculations yield the three long Mo-O bond distances 14.87 % greater than experiment.

This discrepancy in data can be accounted for due to the structural disorder in the position of Mo ions on the surface.

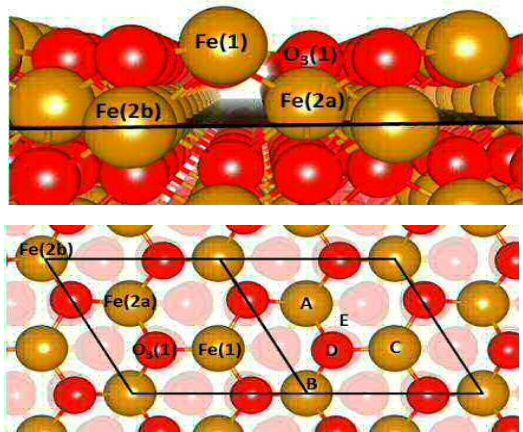


Figure 40. (Top)side view of the α -Fe₂O₃ (0001) surface. The drawn plane marks the position of the semi-transparent oxygen ions. Brown sphere= Fe, Red sphere= O, (bottom) view along the hexagonal axis of the α -Fe₂O₃ (0001) surface. Different initial adsorption sites (from A to E) for the MoO₃ unit are shown; the rhombi represent the surface unit cell.

Adsorption site	A	B	C	E
View along the hexagonal axis				
Side view				
Energies	0	29	440	81

Figure 41. The relaxed structures for the different adsorption sites. Energies based on (1x1) surface calculation. Red sphere= Fe, Brown sphere= O, Violet sphere= Mo. Energies are in kJ mol⁻¹.

It should be noted that ‘adsorption’ here does not mimic the real experimental synthetic conditions. However it can provide useful information to aid establishing the interface structure. In summary, it has been possible to identify the optimum adsorption site for the molybdenum (identified as site A), which agrees well with the XAFS data, showing good agreement with most of the bond distances. More significantly, this theoretical model agrees with the Fe exposure suggested at the surface for the 1 ML $\text{MoO}_x/\text{Fe}_2\text{O}_3$ catalyst (site A in Figure 40).

Table 14. Mo-O and Mo-Fe distances (\AA) of the relaxed $\text{MoO}_3/\text{Fe}_2\text{O}_3$ structures.

Co-ordination number is shown in parenthesis. DFT + U and EXAFS experimental data are displayed.

	(1x1) Surface			(2x2) Surface	EXAFS
	Site A	Site B	Site C	Site A	
Mo-O	1.77 (x3)	1.77 (x3)	1.74 (x3)	1.80 (x3)	1.74 (x3)
	2.24 (x3)	2.21 (x3)		2.18 (x3)	1.95 (x3)
Mo-Fe	2.80 (x1)	2.94 (x3)	2.70 (x1)	2.81 (x1)	2.85 (x1)
	2.96 (x3)	3.05 (x1)		2.99 (x3)	3.10 (x3)

4. Conclusions

The development of more efficient catalysts for the industrial chemical process of methanol to formaldehyde would bring significant economic benefits, as well as having a positive impact on the wider society. To make step-change improvements in catalytic performance however, a fundamental understanding of the active site within the used catalytic systems is crucial.

The chapter described has involved an extensive study into the active surface layer in core-shell structures of the type $\text{MoO}_x/\text{Fe}_2\text{O}_3$. Through dosing Mo strictly at the surface, it has enabled the use of techniques such as XAFS and Raman (which usually probe bulk structures), to become surface sensitive. Fe_2O_3 is inherently known as a combustor of methanol, so in dosing Mo onto this unselective support demonstrates the effect Mo has on improving catalyst performance. The relevance of studying these systems is to relate the surface terminating layer to that in bulk mixed FeMo oxides such as $\text{Fe}_2(\text{MoO}_4)_3$, where there is great debate and limited knowledge of the active site.

Initial work involved the study of 3ML’s $\text{MoO}_x/\text{Fe}_2\text{O}_3$ prepared under varying calcination temperature. It is proposed that the evolution of surface structure is as shown in Figure 33.

After calcination at 300 °C, the surface appears to contain a layer of very well dispersed amorphous Mo oxide on the surface of the iron oxide, showing broad peaks in Raman and local co-ordination. Upon ramping in temperature to 400 °C, sharper more discrete bands appear in the Raman spectra, representing MoO₃ crystallites. XAFS shows the presence of octahedral Mo, and it is likely that these exist in the form of very small MoO₃ nanoparticles. Unfortunately it was not possible to identify these nanoparticles through TEM, but this could be due to the low number of nanoparticles in an environment dominated by iron oxide particles. Upon annealing to 500 °C the production of Fe₂(MoO₄)₃ occurs, confirmed through a variety of techniques including Raman, FT-IR, XRD and XAFS.

However, although significant changes in catalyst structure, the reactivity of these catalysts does not change so much, and this is believed to be due to the presence of a third component of the surface, MoO_x, which is the dominant surface component. This component, discovered through XAFS, is present throughout the calcination range forming one monolayer equivalent of the total Mo dosed at the highest calcination temperature. The MoO₃ present at 400 °C is able to react with the Fe₂O₃ support at and above 500 °C, to form the T_d co-ordinated Fe₂(MoO₄)₃. This is present as an underlayer, to the topmost amorphous MoO_x present throughout.

The study then compared a series of different monolayer loadings of MoO_x/Fe₂O₃ catalysts, also screening an O_h overlayer of molybdenum oxide units at the surface. This layer remains at the surface as the topmost and active layer, since all catalysts showed a comparable reaction profile. Most significantly, it is shown that for catalysts with just one monolayer coverage of molybdenum (1ML MoO_x/Fe₂O₃), an O_h overlayer of molybdenum oxide units remains at the surface, and results in a highly selective catalyst for methanol oxidation to formaldehyde.

In view of this, it is proposed that the MoO_x overlayer structure identified is the fundamental, active surface for the selective oxidation of methanol to formaldehyde, since catalysts prepared at varying calcination temperatures and monolayer coverages showed both similar activity, and this structure in common.

It is believed that this active layer is also directly related to Fe₂(MoO₄)₃ catalysts used commercially. To complete the study, a series of monolayer doped MoO_x/Fe₂O₃ catalysts were compared to conventionally prepared Fe₂(MoO₄)₃ for their performance in the selective oxidation of methanol to formaldehyde. Reactor data showed that the reactivity of the two systems is comparable, however in general, the *selectivity* of the monolayer catalysts were unable to uphold the selectivity of bulk catalysts such as MoO₃ and Fe₂(MoO₄)₃. That said, the monolayer catalysts did show a significantly improved *activity* over that of the

conventional bulk oxides. This shows potential for new catalysts, provided their selectivity can be matched and their longevity improved.

5. References

- House, M.P., et al., *Effect of varying the cation ratio within iron molybdate catalysts for the selective oxidation of methanol*. The Journal of Physical Chemistry C, 2008. **112**(11): p. 4333-4341.
- Soares, A.P.V., et al., *Mechanism of deactivation of iron-molybdate catalysts prepared by coprecipitation and sol-gel techniques in methanol to formaldehyde oxidation*. Chemical Engineering Science, 2003. **58**(7): p. 1315-1322.
- Soares, A.P.V., et al., *Iron molybdate catalysts for methanol to formaldehyde oxidation: effects of Mo excess on catalytic behaviour*. Applied Catalysis A: General, 2001. **206**(2): p. 221-229.
- Glisenti, A., G. Favero, and G. Granozzi, *Reactivity of simple alcohols on Fe₂O₃ powders - An XPS and FTIR study*. Journal of the Chemical Society-Faraday Transactions, 1998. **94**(1): p. 173-182.
- Bowker, M., et al., *The selective oxidation of methanol on iron molybdate catalysts*. Topics in Catalysis, 2008. **48**(1-4): p. 158-165.
- House, M.P., M.D. Shannon, and M. Bowker, *Surface segregation in iron molybdate catalysts*. Catalysis Letters, 2008. **122**(3-4): p. 210-213.
- Soares, A.P.V., M.F. Portela, and A. Kiennemann, *Iron molybdates for selective oxidation of methanol: Mo excess effects on the deactivation behaviour*. Catalysis Communications, 2001. **2**(5): p. 159-164.
- Soderhjelm, E., et al., *On the Synergy Effect in MoO₃-Fe₂(MoO₄)(₃) Catalysts for Methanol Oxidation to Formaldehyde*. Topics in Catalysis, 2008. **50**(1-4): p. 145-155.
- Adkins, H. and W.R. Peterson, *The oxidation of methanol with air over iron, molybdenum, and iron-molybdenum oxides*. Journal of the American Chemical Society, 1931. **53**(4): p. 1512-1520.
- Okamoto, Y., et al., *Role of excess of MoO₃ in Fe₂O₃-MoO₃ methanol oxidation catalysts studied by X-ray photoelectron spectroscopy*. Journal of the Chemical Society, Chemical Communications, 1981(19): p. 1018-1019.
- Sun-Kou, M.R., et al., *Influence of the preparation method on the behaviour of Fe-Mo catalysts for the oxidation of methanol*. Journal of Materials Science, 1995. **30**(2): p. 496-503.
- Routray, K.W., I. E. , Prepr.-Am. Chem. Soc., Div. Pet. Chem. , 2007(52): p. 25-29.
- Bowker, M., et al., *The selective oxidation of methanol to formaldehyde on iron molybdate catalysts and on component oxides*. Catalysis Letters, 2002. **83**(3-4): p. 165-176.
- Bowker, M., A.F. Carley, and M. House, *Contrasting the behaviour of MoO₃ and MoO₂ for the oxidation of methanol*. Catalysis Letters, 2008. **120**(1-2): p. 34-39.
- Boreskov, G., et al., *Study of an iron-molybdenum oxide catalyst for the oxidation of methanol to formaldehyde. II. Phase composition and nature of the catalytically active component*. Kinet. Catal.(Engl. Transl.), 1965. **7**(1): p. 125.
- Bowker, M., et al., *Evolution of active catalysts for the selective oxidative dehydrogenation of methanol on Fe₂O₃ surface doped with Mo oxide*. Physical Chemistry Chemical Physics, 2013. **15**(29): p. 12056-12067.
- Busca, G., et al., *FT-IR study of the adsorption and transformation of formaldehyde on oxide surfaces*. Journal of the American Chemical Society, 1987. **109**(17): p. 5197-5202.

18. Hill, C.G. and J.H. Wilson, *Raman spectroscopy of iron molybdate catalyst systems: Part I. Preparation of unsupported catalysts*. Journal of Molecular Catalysis, 1990. **63**(1): p. 65-94.
19. Söderhjelm, E., et al., *On the Synergy Effect in $\text{MoO}_3\text{-Fe}_2(\text{MoO}_4)_3$ Catalysts for Methanol Oxidation to Formaldehyde*. Topics in Catalysis, 2008. **50**(1-4): p. 145-155.
20. Gai, P.L. and P.A. Labun, *Electron microscopy studies relating to methanol oxidation over ferric molybdate and molybdenum trioxide catalysts*. Journal of Catalysis, 1985. **94**(1): p. 79-96.
21. Radhakrishnan, R., et al., *Variability in the structure of supported MoO_3 catalysts: Studies using Raman and X-ray absorption spectroscopy with ab initio calculations*. Journal of Physical Chemistry B, 2001. **105**(36): p. 8519-8530.
22. Xu, Y., et al., *Structural and morphological characterization of Mo coatings for high gradient accelerating structures*. 15th International Conference on X-Ray Absorption Fine Structure (Xafs15), 2013. **430**.
23. Hu, H.C., I.E. Wachs, and S.R. Bare, *SURFACE-STRUCTURES OF SUPPORTED MOLYBDENUM OXIDE CATALYSTS - CHARACTERIZATION BY RAMAN AND $\text{Mo L}(3)$ -EDGE XANES*. Journal of Physical Chemistry, 1995. **99**(27): p. 10897-10910.
24. Dent, A.J., et al., *Performance of B18, the Core EXAFS Bending Magnet beamline at Diamond*. 15th International Conference on X-Ray Absorption Fine Structure (Xafs15), 2013. **430**.
25. Dent, A.J., et al., *B18: A core XAS spectroscopy beamline for Diamond*. 14th International Conference on X-Ray Absorption Fine Structure (Xafs14), Proceedings, 2009. **190**.
26. Ressler, T., et al., *Time-resolved XAS investigation of the reduction/oxidation of $\text{MoO}_3\text{-x}$* . Journal of Catalysis, 2000. **191**(1): p. 75-85.
27. Beale, A.M., et al., *An iron molybdate catalyst for methanol to formaldehyde conversion prepared by a hydrothermal method and its characterization*. Applied Catalysis a-General, 2009. **363**(1-2): p. 143-152.
28. Massa, M., et al., *Oxidation of methanol to formaldehyde on cation vacant Fe-V-Mo-oxide*. Applied Catalysis a-General, 2011. **408**(1-2): p. 63-72.
29. Routray, K., et al., *Origin of the synergistic interaction between MoO_3 and iron molybdate for the selective oxidation of methanol to formaldehyde*. Journal of Catalysis, 2010. **275**(1): p. 84-98.
30. Wilson, J.H., C.G. Hill, and J.A. Dumesic, *RAMAN-SPECTROSCOPY OF IRON MOLYBDATE CATALYST SYSTEMS .3. INSITU STUDIES OF SUPPORTED AND BULK CATALYSTS UNDER REACTION AND REDOX CONDITIONS*. Journal of Molecular Catalysis, 1990. **61**(3): p. 333-352.
31. Briand, L.E., A.M. Hirt, and I.E. Wachs, *Quantitative determination of the number of surface active sites and the turnover frequencies for methanol oxidation over metal oxide catalysts: application to bulk metal molybdates and pure metal oxide catalysts*. Journal of Catalysis, 2001. **202**(2): p. 268-278.
32. Davies, R., et al., *The oxidation of Fe(III)*. Surface Science. **605**(17-18): p. 1754-1762.
33. Tian, H.J., C.A. Roberts, and I.E. Wachs, *Molecular Structural Determination of Molybdena in Different Environments: Aqueous Solutions, Bulk Mixed Oxides, and Supported MoO_3 Catalysts*. Journal of Physical Chemistry C, 2010. **114**(33): p. 14110-14120.
34. Belhekar, A.A., S. Ayyappan, and A.V. Ramaswamy, *FT-IR Studies on the Evolution of Different Phases and their Interaction in Ferric Molybdate-Molybdenum Trioxide Catalysts*. Journal of Chemical Technology and Biotechnology, 1994. **59**: p. 395.

35. Beale, A.M., et al., *An iron molybdate catalyst for methanol to formaldehyde conversion prepared by a hydrothermal method and its characterization*. Applied Catalysis A: General, 2009. **363**(1): p. 143-152.
36. Söderhjelm, E., et al., *On the Synergy Effect in $\text{MoO}_3\text{-Fe}_2(\text{MoO}_4)_3$ Catalysts for Methanol Oxidation to Formaldehyde*. Topics in Catalysis, 2008. **50**(1-4): p. 145-155.
37. Huang, Y., et al., *The surface evolution of a catalyst jointly influenced by thermal spreading and solid-state reaction: A case study with an $\text{Fe}_2\text{O}_3\text{-MoO}_3$ system*. Journal of Molecular Catalysis A: Chemical, 2009. **302**(1): p. 48-53.
38. Soares, A.P.V., et al., *Iron molybdate catalysts for methanol to formaldehyde oxidation: effects of Mo excess on catalytic behaviour*. Appl. Cat., A., 2001. **206**(2): p. 221-229.
39. Arruano, J. and S. Wanke, *Effect of High Temperature Treatment on the Properties of Fe/Mo Oxide Catalysts*. Canad. J. Chem. Eng., 1975. **53**: p. 301.
40. Soares, A.P.V., M.F. Portela, and A. Kinnemann, *Methanol Selective Oxidation to Formaldehyde over Iron-Molybdate Catalysts*. Catal. Rev., 2004. **47**: p. 125.
41. Trifiro', F., S. Notarbartolo, and I. Pasquon, *The Nature of the Active Component in a $\text{Fe}_2\text{O}_3\text{-MoO}_3$ Catalyst. II. Study of the Variations Occurring During High Temperature Treatment*. Journal of Catalysis, 1971. **22**: p. 324.
42. Rohrbach, A., J. Hafner, and G. Kresse, *Ab initio study of the (0001) surfaces of hematite and chromia: Influence of strong electronic correlations*. Physical Review B, 2004. **70**(12): p. 125426.
43. Kresse, G. and J. Hafner, *Ab initio molecular-dynamics simulation of the liquid-metal-amorphous-semiconductor transition in germanium*. Physical Review B, 1994. **49**(20): p. 14251-14269.

Chapter 5: *In situ* studies for Understanding Surface Structural Changes

Contents

1. Introduction.....	242
2. <i>In situ</i> Calcination of Core-Shell Structures $\text{MoO}_x/\text{Fe}_2\text{O}_3$ with Combined XAFS/Raman and DRIFTS.....	242
2.1. Introduction.....	242
2.2. XAFS/Raman Experimental	244
2.3. Results and Discussion	247
2.3.1. <i>In situ</i> calcination studies under XAFS/ Raman	247
2.3.1.1. <i>In situ</i> XAFS	247
2.3.1.2. Combined <i>in situ</i> XAFS/ Raman	250
2.3.2. <i>In Situ</i> DRIFTS	252
3. <i>In Situ</i> Reduction XAFS Studies.....	253
3.1. Introduction.....	253
3.2. Experimental.....	257
3.3. Results and Discussion	258
3.3.1. Raman	258
3.3.2. XRD	260
3.3.3. BET	261
3.3.4. XAFS	261
3.3.4.1. XANES	262
3.3.4.2. EXAFS.....	263
3.3.5. Catalytic Testing.....	267
4. Continuous Isothermal Studies	270
5. Conclusions.....	272
5. References.....	272

1. Introduction

Chapter 4 highlighted the use of model $\text{MoO}_x/\text{Fe}_2\text{O}_3$ catalysts with precise structural surface motifs, to gain knowledge on the possible surface terminations in the bulk FeMo systems. Work herein exploits the use of *in situ* techniques under preparation and deactivation of the same materials, to shed light on how these fundamental processes occur in conventional iron molybdate catalysts. Specifically, the reaction mechanisms occurring with methanol will be addressed.

As the chapter will be divided into various sections, a small literature review will form the basis of each section, specific to the topic discussed. Each section will also contain the experimental set up, with results and discussion thereafter.

2. *In situ* Calcination of Core-Shell Structures $\text{MoO}_x/\text{Fe}_2\text{O}_3$ with Combined XAFS/Raman and DRIFTS

2.1. Introduction

Unravelling the nature of the active site in commercial $\text{Fe}_2(\text{MoO}_4)_3$ catalysts has always proved challenging. With the requirement that the industrial catalyst must incorporate excess Mo into the synthesis procedure, this creates a mixed phase catalyst containing both the $\text{Fe}_2(\text{MoO}_4)_3$ and MoO_3 phases [1]. Consequently, the involvement of each of these phases during the reaction is not well understood. Some identify bulk $\text{Fe}_2(\text{MoO}_4)_3$ as the active component, with the excess MoO_3 branded a spectator phase, due to its slow redox nature (See Chapter 6), and therefore inability to regenerate for maintained selectivity. However, for the counter argument, MoO_3 is defined to be an essential component of the system, demonstrating 100 % selectivity to formaldehyde under MeOH TPD [2]. MoO_3 is argued to have a direct effect on the catalyst selectivity, whilst also acting as a reservoir for lost MoO_3 through sublimation at the reactor hot spots [3].

A further hypothesis has been postulated in Chapter 4, supporting the work of Routray *et al.* [4]. To dissect the active phase in the industrial iron molybdate catalysts, model systems of the type $\text{MoO}_x/\text{Fe}_2\text{O}_3$, were designed to isolate the contribution of surface molybdena from that of the bulk. Under this approach, the surface layer in FeMo based catalysts was suggested to be composed of O_h Mo units, compared to the T_d Mo centres found in $\text{Fe}_2(\text{MoO}_4)_3$ [5, 6]. This is a key finding, as $\text{Fe}_2(\text{MoO}_4)_3$ is a catalyst of significant industrial

importance, being widely used in the selective oxidation of methanol to formaldehyde [7-12]. 1, 3 and 6ML MoO_x/Fe₂O₃ samples calcined to 120, 300, 400, 500 and 600 °C were run *ex situ*, monitoring the Mo K-edge through XAFS. At 120 °C, for the 3 and 6 ML coverages, both demonstrated an amorphous Mo phase with limited dimensionality, which did not resemble that of bulk MoO₃ or any other obtainable Mo oxide reference. This phase was denoted MoO_x. Upon calcination, linear combination fittings (LCF's) showed there was an evident phase change to O_h geometry in the form of MoO₃ at 400 °C and 300 °C, for the 3 and 6ML MoO_x/Fe₂O₃ samples respectively (Chapter 4). By 500 °C, both monolayer coverages demonstrated a proportion of tetrahedrally co-ordinated Fe₂(MoO₄)₃. All catalysts maintained an unchanged 1ML O_h MoO_x overlayer across the entire calcination range.

Although *ex situ* analysis has provided a good means of investigating the catalyst composition at various pre-defined calcination temperatures, it does have its limitations. Primarily, it is incapable of studying the catalyst in real-time, as it morphs under the various heat treatments described. *Ex situ* analysis is also restricted in that it cannot detect any transient phases formed prior to those identified at the chosen calcination treatments. By covering the whole calcination range from 120 through to 650 °C, this enables the identification of the exact point at which the formed MoO₃ is incorporated into the supporting Fe₂O₃, to produce the mixed metal oxide, Fe₂(MoO₄)₃.

In comparison, *in situ* studies provide a way of observing successive changes within the catalyst structure under variable experimental conditions. Despite this, conventional *in situ* bulk techniques on Fe₂(MoO₄)₃ are limited in the information they can reveal about the *surface* structure [13, 14]. This is because they are representative of the whole sample, and the Mo at the surface forms just a small proportion of the total Mo dosed. XAFS studies are element specific, and provide a per atom average of all environments. However, when Mo is exclusively at the surface, and the Mo edge monitored, XAFS is able to provide surface-sensitive information. Subsequently, when XAFS is applied under relevant *in situ* conditions, it can provide accurate information about the nature of the active site in MoO_x/Fe₂O₃ systems, and how it is formed with increasing calcination temperature.

In addition to this, with the continual development of synchrotron radiation sources [15], scientists are now able to study *in situ* using a collection of techniques simultaneously, to examine how catalysts change under more realistic conditions [16-21]. It is well known that vibrational spectroscopy such as Raman is fundamental in the characterisation of mixed metal oxides. The literature shows confident assignment of the various bands for iron molybdate based catalysts, and has been successfully employed in studying these catalysts *in situ*. Wilson *et al.* [22] approach the use of *in situ* Raman to study various Fe/Mo/O catalysts under reaction and redox, whilst Qian *et al.* investigate MoO₃ surface formation during the

calcination of Mo-rich catalysts [23]. Integrating Raman with the surface sensitive approach of XAFS, will develop a knowledge of the surface phase composition in these complex, multicomponent oxide catalysts. The chapter herein looks to exploit *in situ* based techniques, to gain a further understanding of the catalysts described. 3 and 6 monolayers of Mo have been dosed onto the surface of Fe_2O_3 , to develop core-shell catalysts of the type $\text{MoO}_x/\text{Fe}_2\text{O}_3$ to be studied and compared to bulk $\text{Fe}_2(\text{MoO}_4)_3$ materials.

2.2. XAFS/Raman Experimental

In situ calcinations were performed under transmission mode XAFS, using the in-house microreactor available at the beamline. The microreactor is equipped with a gas supply system, integrated heating system, and a Cirrus 100 quadrupole mass spectrometer used to monitor the outlet gas composition online under various conditions. The sample stage contains a quartz capillary (OD 6mm, wall thickness 250 μm), into which the sample is loaded (See Figures 1-4 for set up).

0.5 g of catalyst was mixed with boron nitride (the diluent) and loaded into the capillary. Quartz wool was used at either end of the catalyst bed to prevent the catalyst from moving along the quartz tube under the applied gas flow pressure. The catalyst bed was aligned with the beam, and an initial spectrum acquired to ensure a homogeneous location of the X-ray on the sample. Calcination studies used a staircase heating procedure with a ramp rate of $12^\circ\text{C min}^{-1}$ between each 20°C increments up to 650°C . The temperature was held for ten minutes at each increment point. XAFS data were recorded throughout the experiment, at a typical rate of 1 min/scan. On reaching the maximum temperature, the sample was held isothermally for 30 minutes, to ensure no further changes occurred, after which it was cooled to room temperature.

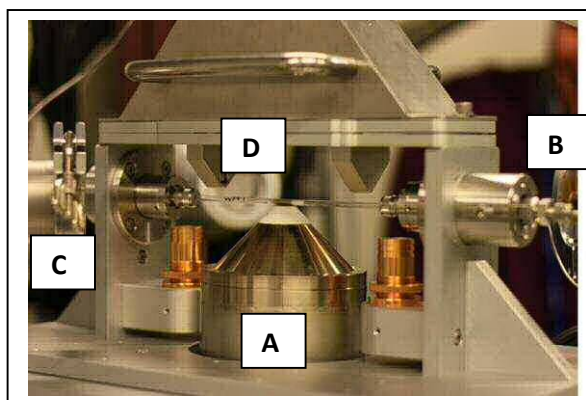


Figure 1. *In situ* quartz capillary microreactor for XAFS studies. (a) Hot air blower, (b) I_0 , (c) I_e , and (d) Fluorescence detector.

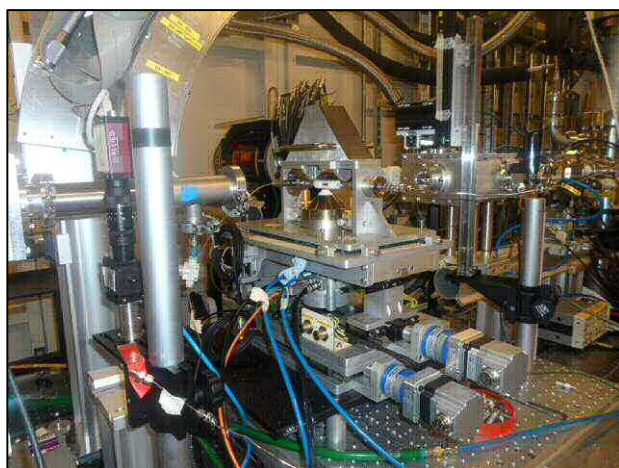


Figure 2.

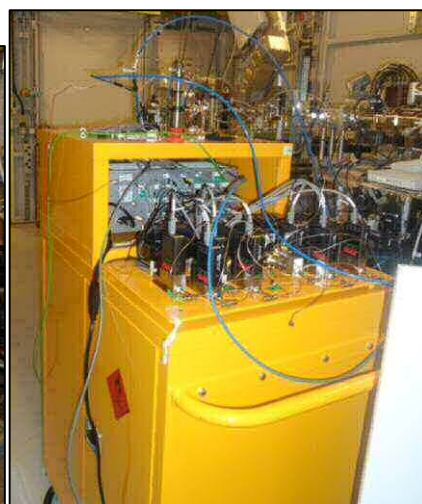


Figure 3.

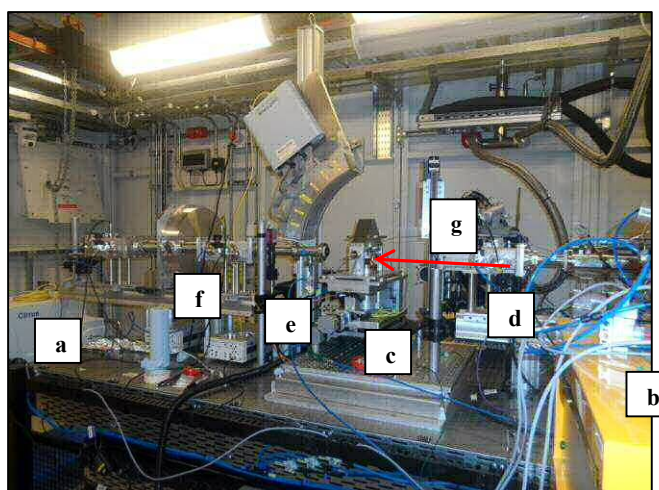


Figure 4.

Figures 2-4. (2) Photo of the general set up with the microreactor sample stage in line of the beam, (3) Mass flow controllers with gas trolley rig, and (4) Overview of the whole set up with (a) Mass Spectrometer, (b) Mass flow controllers, (c) Sample stage, (d) I_o detector, (e) I_t detector, (f) I_{ref} detector, (g) Path of beam.

Combined XAFS/Raman studies were performed using the same microreactor described, coupled with a custom-built optic fibre coupled, confocal Raman probe system (Figure 7). The system uses a Renishaw RA100 spectrometer, with a Peltier cooled CCD detector and 1200 line grating, and a 300 mW, 785 nm diode laser (Renishaw HP785NIR). Laser light from the diode source was directed into the Raman probe using a multimode fibre optic, where lenses expanded and collimated the light. A x20 magnification lens at the exit aperture of the probe focused the laser light to a $\sim 500\ \mu\text{m}$ spot at the sample. Edge filters (cut-off 100 nm above the laser line wavelength) were used to reject the laser light in the back reflected

signal into the probe, and a condensing lens was used to focus this signal into a second multimode fibre optic which directed the signal into the RA100 spectrometer. Slits were used to attenuate the laser power on the sample to ~ 15 mW, to prevent sample damage and saturation of the detector. The spectrometer was calibrated using the emission lines from a Ne lamp, and checked using the main Raman band from a silicon wafer, setting the centre of this peak to 520 cm^{-1} . Spectra were collected for 20×1 second scans using ‘static’ mode, with the grating angle fixed to illuminate the Raman spectrum across the CCD. The techniques were combined to follow the calcination study (as described previously), with the XAFS geometry adjusted to fluorescence mode. The change in acquisition mode to fluorescence allowed for undiluted materials to be used, in order to maximise Raman signal from the sample. Due to the bulky nature of the Raman probe, the sample stage had to be loaded at 45° , which also complimented the fluorescence set up (Figures 5-6).

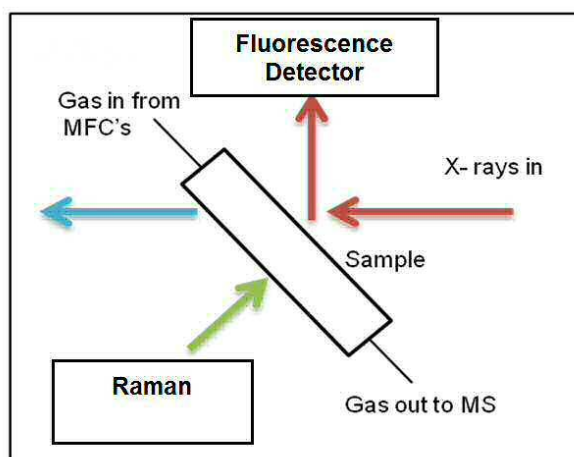


Figure 5. Schematic of the *in situ* XAFS/Raman set up performed in Fluorescence mode.

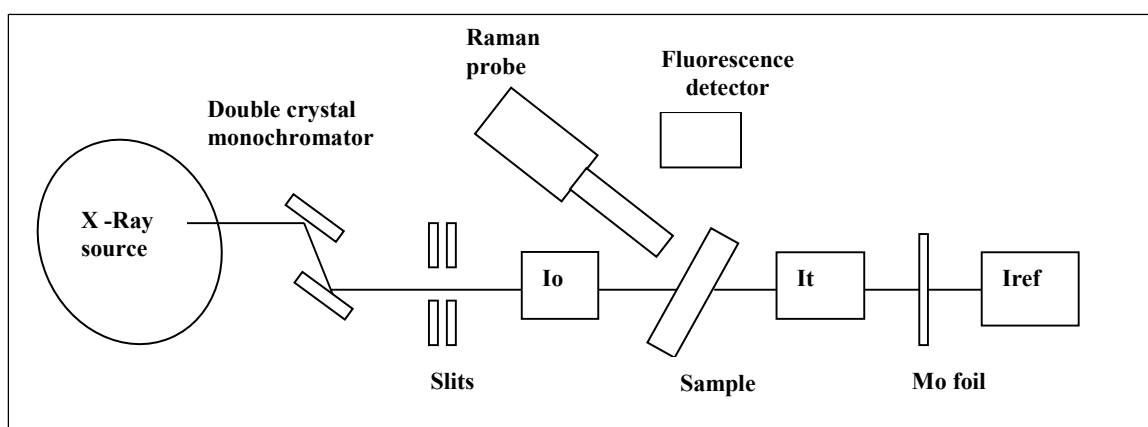


Figure 6. Schematic of the overall set up for the combined *in situ* XAFS/Raman experiment.

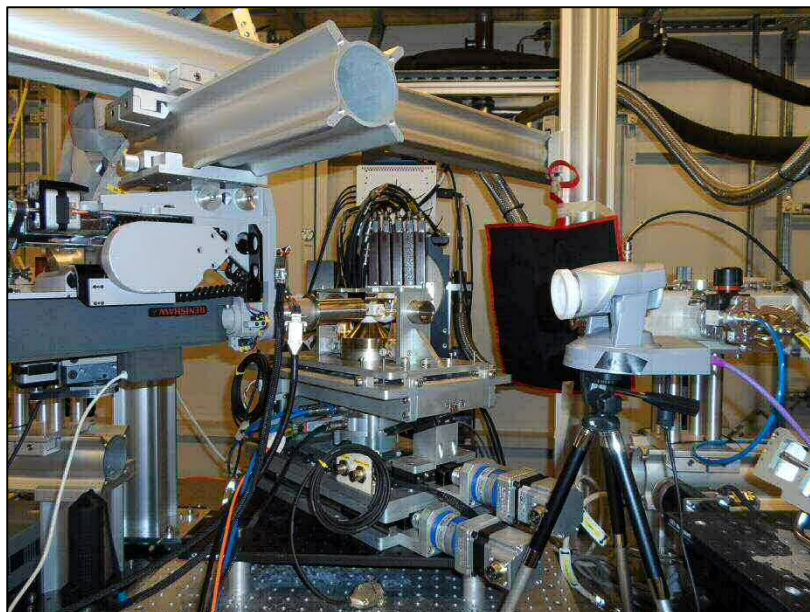


Figure 7. Photo of the *in situ* XAFS/Raman set up, performed in Fluorescence mode.

2.3. Results and Discussion

2.3.1. *In situ* calcination studies under XAFS/ Raman

Prior to any experiments performed on the beamline, all catalysts were subjected to a variety of characterization techniques *ex situ*, as detailed in Chapter 4.

2.3.1.1. *In situ* XAFS

Results for the *in situ* calcination study observed through XAFS investigations are presented in Figures 8-10. The experiments involved steadily increasing the temperature of the catalyst bed, until no further changes were observed under XANES spectroscopy. Data for the 3 and 6ML MoO_x/Fe₂O₃ catalysts are conclusive, with both screening a substantial increase of the Mo pre-edge with increasing calcination temperature. This is a clear indication of a change in geometry to tetrahedral co-ordination. The effect was most pronounced for the 6ML catalyst, as expected for the higher Mo content within the catalyst.

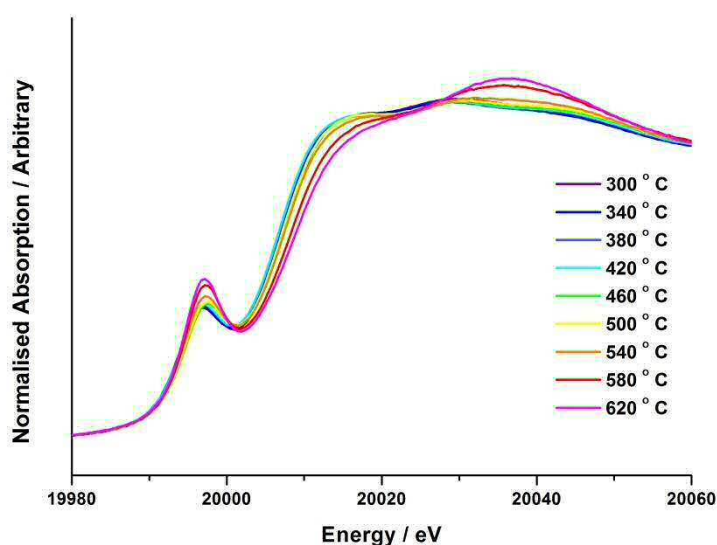
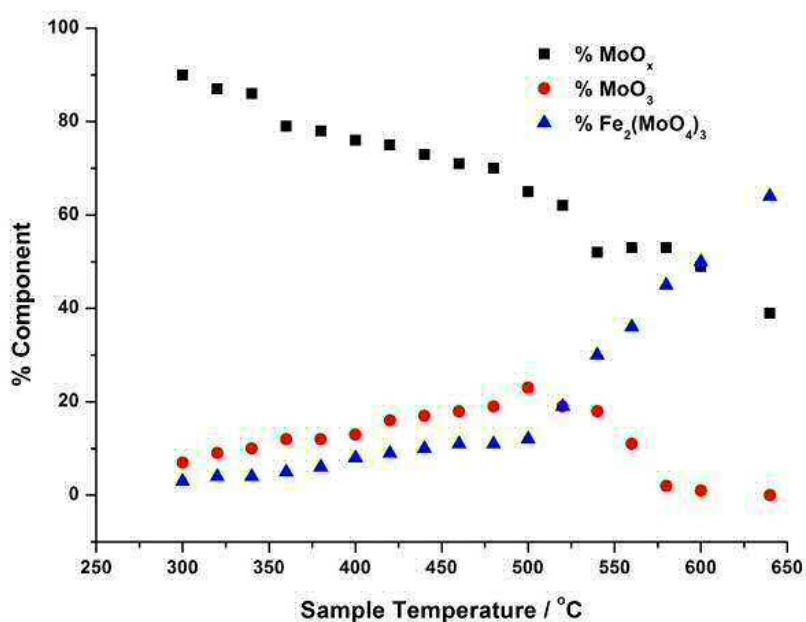


Figure 8. Normalised XANES data for 6ML $\text{MoO}_x/\text{Fe}_2\text{O}_3$ *in situ* calcination study from 300 to 640 °C. Approximately 0.5 g of the dried material for 6ML $\text{MoO}_x/\text{Fe}_2\text{O}_3$ was mixed with BN and loaded into the sample capillary. A 10 % O_2/He mixture was passed over the catalyst whilst heating to 640 °C at a constant ramp rate. No changes were seen in the XANES below 300 °C, so results are not shown.

Linear combination fits were performed to assess the amount of MoO_x , MoO_3 and $\text{Fe}_2(\text{MoO}_4)_3$ present within the sample upon varying the calcination temperature. Results are revealed in Figures 9-10. LCF's were performed at approximately 20 °C intervals. Referring to the 3ML $\text{MoO}_x/\text{Fe}_2\text{O}_3$ catalyst, upon ramping from 50 °C, there is an immediate and steady decrease in the MoO_x phase initially dosed at the surface. Parallel to this, there is also a slow but steady rise in the MoO_3 phase present. At this point, the amount of $\text{Fe}_2(\text{MoO}_4)_3$ within the fit does not rise significantly. By 520 °C however, a discernible loss of MoO_3 occurs, depreciating by 6 %. This triggers the onset of $\text{Fe}_2(\text{MoO}_4)_3$ formation, with a rise in its contribution in the LCF's. The results imply that the formation of MoO_3 and subsequent reaction with Fe_2O_3 is responsible for the creation of $\text{T}_d \text{Fe}_2(\text{MoO}_4)_3$. At the highest temperature of 650 °C, there is no evidence for MoO_3 . $\text{Fe}_2(\text{MoO}_4)_3$ dominates, with 64 % of the total Mo dosed. It is important to note that even at this temperature, LCF's demonstrate a 1 monolayer equivalent of surface MoO_x (the Mo oxide phase shown for the dried sample) still present, which fails to be incorporated into the bulk to form $\text{Fe}_2(\text{MoO}_4)_3$. The stability of this overlayer has been established in Chapter 4, and still remains after calcination at 650 °C for 24 hours.

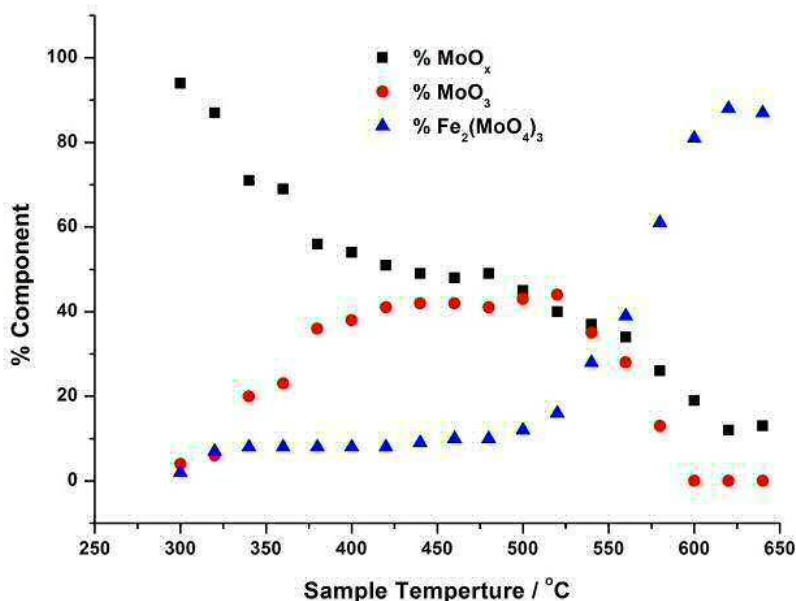
A complimentary study was performed for the 6ML $\text{MoO}_x/\text{Fe}_2\text{O}_3$ catalyst (a relative comparison could not be made to the 1ML catalyst since here we see no change in phase formation across the calcination range (Chapter 4, Figure 38)). The trends observed for the 6ML catalyst (Figure 11), are similar in nature to those discussed for 3ML $\text{MoO}_x/\text{Fe}_2\text{O}_3$, however with slight variations. MoO_3 is again shown to primarily form, but in this case it forms at a significantly increased rate, as shown by the steeper gradient of its formation from 300 °C. By 360 °C, XANES analysis demonstrates 20 % MoO_3 , with only 8 % $\text{Fe}_2(\text{MoO}_4)_3$. The occurrence of $\text{Fe}_2(\text{MoO}_4)_3$ plateaus between 300 and 500 °C, and only begins to sharply increase above 500 °C, once MoO_3 production ceases. This rise in $\text{Fe}_2(\text{MoO}_4)_3$ formation is complemented by the sudden decrease in MoO_3 as it reacts with bulk Fe_2O_3 , to establish the mixed phase oxide. As was noted for the 3ML sample, at the end of the calcination, a 1ML equivalent of MoO_x remains segregated at the surface of the Fe_2O_3 . This exists alongside approximately 90 % $\text{Fe}_2(\text{MoO}_4)_3$.

(9)



*Figure caption with following figure.

(10)



Figures 9-10. Phase composition of MoO_x, MoO₃, Fe₂(MoO₄)₃ with calcination temperature, ascertained through linear combination fitting for 3 (Previous) and 6ML (Above) MoO_x/Fe₂O₃. The calcination was performed as in Figure 8, and the phase compositions were determined using linear combination fittings using references of MoO₃ (Sigma Aldrich), Fe₂(MoO₄)₃ (produced in-house) and dried MoO_x/Fe₂O₃ (also produced in-house).

2.3.1.2. Combined *in situ* XAFS/ Raman

With a knowledge of the phase changes occurring at the catalyst surface under increasing temperature, consequent work involved combining with complimentary techniques such as Raman spectroscopy, to confirm the findings of the study. The Raman set up presented has been recently commissioned on the XAFS beamline at Diamond Light Source, and the experiment was an opportunity to test the rig as primary users. Figure 12 reveals data for the combined *in situ* XAFS/Raman experiment for 6ML's MoO_x/Fe₂O₃. The Raman signal for this higher monolayer coverage was most intense, so for this reason this coverage is discussed.

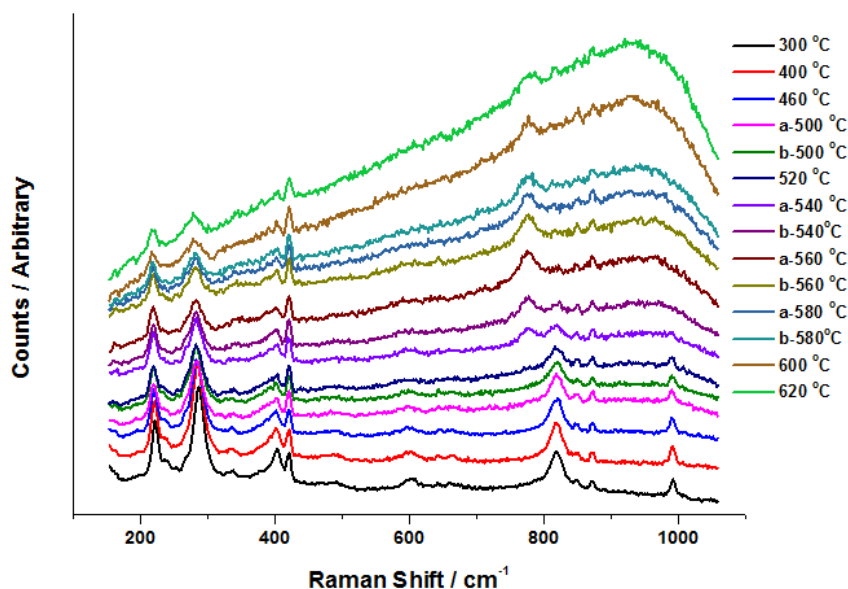


Figure 11. Raman data for 6ML $\text{MoO}_x/\text{Fe}_2\text{O}_3$ collected *in situ* with combined XAFS/Raman. The catalyst was ramped to 640°C at a rate of $12^\circ\text{C min}^{-1}$. Temperatures from 300°C to 620°C are shown a= Preliminary scan on initially reaching the stated temperature, b= Final scan after ten minutes at the stated temperature. Results reiterate the changes seen through XANES. The MoO_x overlayer was not apparent at lower calcination temperatures, however this can be expected given that Raman scattering is a weak effect, and the contribution of the MoO_x surface is small. For this reason, data is only given at and above 300°C .

At 300°C , MoO_3 related bands are clearly observed at 820 and 990 cm^{-1} , assignable to the Mo-O-Mo bridge and Mo=O terminal stretches, respectively [7]. With increasing temperature above 500°C , these bands appear to diminish, which is complementary to the XANES analysis in which a drop in the % MoO_3 phase is observed. At 540°C , a new band appears at 780 cm^{-1} , indicative of Mo-O-Mo asymmetric vibrations in $\text{Fe}_2(\text{MoO}_4)_3$ [24]. The intensity of this new band continues to increase with further rises in temperature, with the bands at 820 and 990 cm^{-1} (corresponding to MoO_3) decreasing simultaneously. This is as a result of the conversion of MoO_3 to $\text{Fe}_2(\text{MoO}_4)_3$ through reaction with the Fe_2O_3 support. Above 600°C , the relative peak intensity readily diminishes for all bands, as a result of the raised fluorescence background observed. Data becomes hard to interpret. These effects could be ascribed to the sample becoming more amorphous at higher temperatures, as the metal oxides become more mobile and the structure loses its regularity. Upon cooling these bands reappeared, with the $\text{Fe}_2(\text{MoO}_4)_3$ related bands reinstated.

In summary, the combined XAFS/Raman experiment was able to provide crucial information, superior to the information achievable through *ex situ* analysis. It was discovered that production of MoO_3 progressively forms with raising the calcination temperature. It is only once the levels of this oxide plateau and begin to decrease, that $\text{Fe}_2(\text{MoO}_4)_3$ production can prevail. This was seen in both XANES and Raman spectra for both monolayer loadings studied. It can therefore be concluded that the following process must occur: $\text{MoO}_x \rightarrow \text{MoO}_3 \rightarrow \text{Fe}_2(\text{MoO}_4)_3$. The process of forming MoO_3 occurs significantly faster in 6ML $\text{MoO}_x/\text{Fe}_2\text{O}_3$, however neither monolayer coverages (3 and 6) form any surface $\text{Fe}_2(\text{MoO}_4)_3$ until 500°C . It is believed therefore, that this is the thermal input required to drive the MoO_3 into bulk Fe_2O_3 to form the mixed phase oxide.

2.3.2. *In Situ* DRIFTS

In situ DRIFTS studies were performed in a Harrick high temperature DRIFTS cell fitted with ZnSe FTIR windows. The cell was attached to the Praying Mantis Optics and spectra were collected with an Agilent Carey 680 FTIR spectrometer taking 64 scans with a resolution of 4 cm^{-1} using the DTGS detector. Calcination studies were performed with the gas inlet and outlet of the cell open to air, using a temperature ramp of $10^\circ\text{C min}^{-1}$.

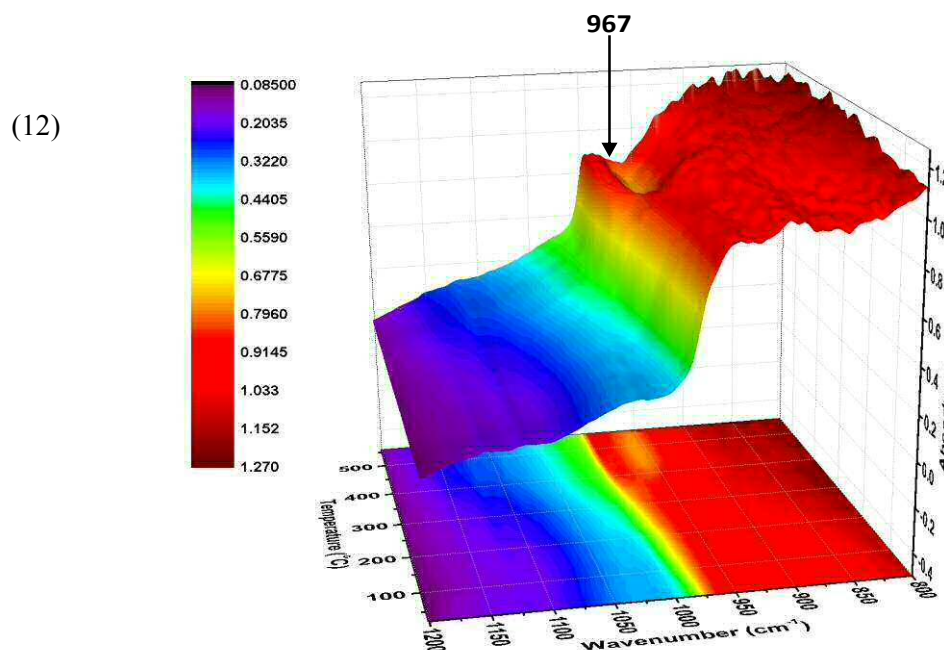
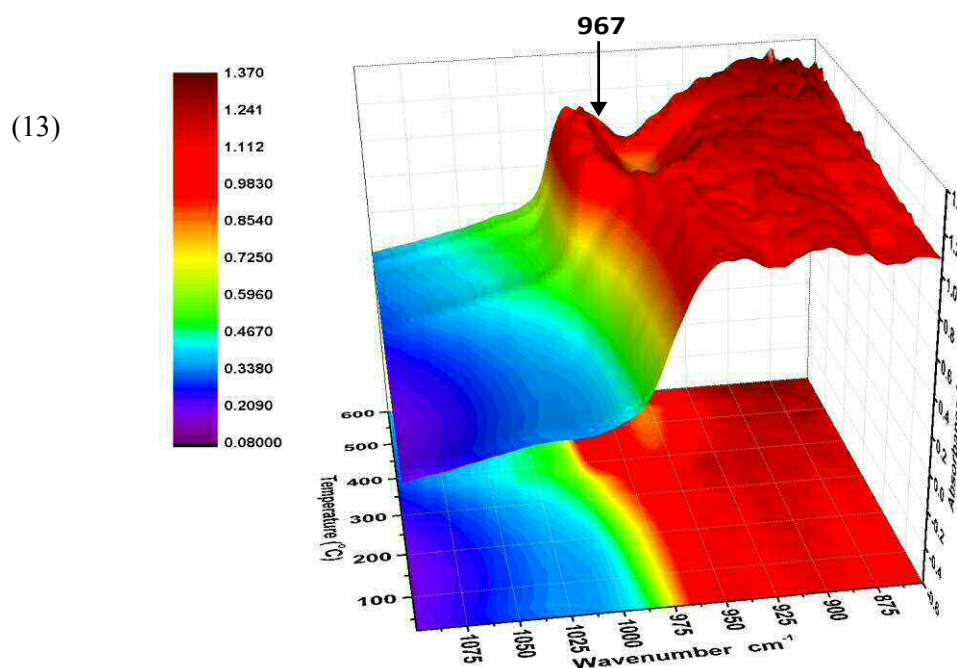


*Figure caption with following figure.



Figures 12-13. DRIFTS spectra collected *in situ* for 3 (Previous) and 6ML (Above) $\text{MoO}_x/\text{Fe}_2\text{O}_3$ during calcination. In each case, the dried material was placed in the sample cell and the calcination temperature increased at $12^\circ\text{C min}^{-1}$, until no further changes were observed.

In collaboration with Emma Gibson (UCL), FTIR spectra were collected during the calcination of the 3ML and 6ML samples using an *in situ* DRIFTS cell, as depicted in Figures 12-13 respectively. Spectra were collected every 15°C during a $10^\circ\text{C min}^{-1}$ ramp from room temperature to 600°C . At approximately 380°C on both catalysts, a band at 997 cm^{-1} appeared which can be assigned to the $\nu(\text{Mo}=\text{O})$ band of MoO_3 [25]. By 560°C , a band at 967 cm^{-1} appeared consistent with the $\nu(\text{Fe}-\text{O}-\text{Mo})$ band of $\text{Fe}_2(\text{MoO}_4)_3$ [26, 27]. These assignments are in agreement with the *in situ* Raman data (Section 2.3.1.2), which also showed the formation of MoO_3 , followed by the formation of $\text{Fe}_2(\text{MoO}_4)_3$.

3. *In Situ* Reduction XAFS Studies

3.1. Introduction

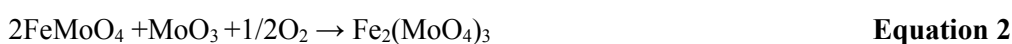
$\text{Fe}_2(\text{MoO}_4)_3$ currently stands as the world leading catalyst in methanol oxidation to formaldehyde, and has done since first reported by Adkin and co-workers in 1931 [28]. Although widely valued for its efficacy in the reaction, there is still a surprisingly low knowledge regarding the catalyst surface layer and how it reacts with methanol. This has been a topic widely studied, with many authors able to identify the phases which are formed

through reduction and regeneration of the catalyst [3, 16, 29, 30], but unable to define the mechanism behind these processes.

It is agreed that during the reaction, partial reduction of the surface occurs, which is then counteracted by a quick regeneration through gas phase oxygen. On bulk $\text{Fe}_2(\text{MoO}_4)_3$, the reduction mechanism has been reported to occur as follows, resulting in a mixed phase catalyst [16]:



Which then re-oxidises as follows:



TPR studies have been performed by Zhang *et al.* [31] on $\text{Fe}_2(\text{MoO}_4)_3$ with excess MoO_3 . They define peaks ascribed to the transformation of $\text{Fe}_2(\text{MoO}_4)_3$ to $\beta\text{-FeMoO}_4$ and Mo_4O_{11} , MoO_3 to MoO_2 and $\beta\text{-FeMoO}_4$ to $\text{Fe}_2\text{Mo}_3\text{O}_8$ and Fe_3O_4 . Beale *et al.* also detail work on this [16], studying $\text{Fe}_2(\text{MoO}_4)_3$ using *in situ* WAXS, XANES and UV-Vis. Under redox conditions, they were able to confirm the reduction to produce $\beta\text{-FeMoO}_4$ and MoO_3 , which can further reduce to MoO_2 . It is thought from previous literature studies of methanol oxidation over bulk $\text{Fe}_2(\text{MoO}_4)_3$, that the formation of reduced $\alpha\text{-FeMoO}_4$ occurs at lower temperatures, whilst $\beta\text{-FeMoO}_4$ dominates at higher temperatures above 310°C .

The mechanisms involved in the selective oxidation reaction with methanol are clearly a focal point amongst authors [32, 33]. Machiels *et al.* [34] demonstrated that methanol oxidation over $\text{Fe}_2(\text{MoO}_4)_3$ is redox in nature, as proven through isotopic oxygen reaction. House *et al.* [10, 35] also support this theory, using TPD and pulse flowed studies to investigate the mechanisms behind formaldehyde production. The reaction and reduction of iron molybdate ($\text{Mo}:\text{Fe} = 2.2:1$) with methanol feedstock was studied. Under anaerobic conditions, the first pulse of methanol demonstrated comparable conversion and selectivity to formaldehyde, as would be seen under aerobic conditions. This indicates that gas phase oxygen is not directly required in the reaction, but is merely there to re-oxidise the surface for continued use. With further reduction at low temperatures, the catalyst performance diminishes, reflecting the significant loss of oxygen from the catalyst surface. However, contrary to this, as the temperature is elevated above 250°C , the catalyst is able to reinstate its previous activity, as bulk oxygen migrates to the surface to enable the production of

formaldehyde. With loss of bulk oxygen, further oxide phases inevitably form, with XRD evidencing α -FeMoO₄, MoO₂, and Mo₄O₁₁. With prolonged reduction at further elevated temperatures (300 °C), combustion products in the form of CO₂ are detected, thus indicating the formation of Fe₂O₃, a known combustor of methanol. The study was informative not only in providing information regarding these reduced phases, but also a preliminary investigation of the mechanisms occurring at the surface. In particular, they evidence the requirement for surface oxygen in the reaction to formaldehyde as opposed to the gas phase oxygen usually inferred. The result supports a Mars-van Krevelen redox mechanism, commonly suggested in the literature [2, 36].

Since Mo has been highlighted to be segregated at the surface of Fe₂(MoO₄)₃, focus has turned to investigating the mechanisms on Mo dominated catalysts. The crystallographic planes in MoO₃ have been resolved by electron diffraction as the apical (001 + 101), side (100) and basal (010) planes. The basal (010) plane possesses the lowest free energy, lying parallel to the double layer. *Ab initio* quantum mechanical calculations [37] and TPD studies support a multistep mechanism involving reaction of methanol with dual-dioxo catalytic sites. Since these dual sites are shown to exist on the (010) face of MoO₃ (Figure 14), this face has been deemed as the reactive site [36]. However, this is not unanimously agreed, with several authors revealing that the (010) plane exhibits especially low saturation, and any methanol adsorption occurring does not contribute to formaldehyde production. Therefore the role of this face is still under investigation for selective methanol oxidation [36, 38]

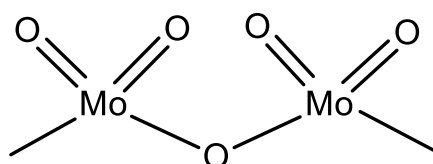


Figure 14. Proposed dual-dioxo catalytic sites on the 010 face of α -MoO₃.

It has since been proposed that methanol adsorption occurs at the edge and defects sites of α -MoO₃, since the uptake of methanol correlates accordingly with the number of active centres on these sites. Edge planes are formed by the bond cleavage perpendicular to the MoO₃ double-layers [39], exposing co-ordinatively unsaturated molybdenum onto which adsorption can occur [40]. Non (010) faces possess the required dual acid-base sites, as outlined in Figure 15. Pre-treatment of the surface with pyridine is shown to inhibit methanol oxidation due to poisoning of the MoO₃ surface. This implies Lewis acid sites, as

proposed by Tatibouet *et al.* [40]. The Lewis acid character revealed by these adsorption studies [41], facilitates substrate interactions.

.

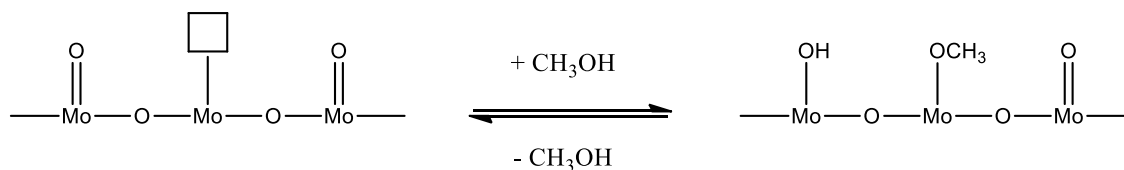


Figure 15. Dissociative chemisorption of methanol on α -MoO₃ [42]. The dual acid-base sites are formed from an unsaturated metal cation (O-Mo-O), and adjacent terminal oxygen (Mo=O) [40]. Methanol can dissociatively chemisorb at these dual sites. The unsaturated Mo atom performs as a Lewis acid centre, acting as the adsorption site for a methoxy intermediate. The basic M=O site abstracts a proton simultaneously to form a hydroxyl. Both intermediates have been evidenced through IR studies [43, 44].

The steps which follow the methoxy adsorption are dependent on the oxidation state of the Mo active centre. If Mo exists as active and selective Mo(VI), the reactions proceed via scission of the C-H bond, reckoned as the rds. The process yields formaldehyde and a proton, which reacts with lattice oxygen to form a second hydroxide, which proceeds to be lost as water under oxidative conditions [45]. If oxygen is not sufficiently supplied, the produced hydrogen will be introduced into the surface, creating a surface bronze denoted H_xMoO₃. With even further reduction, loss of H occurs with subsequent MoO₂ formation, a known reduced state of MoO₃.

In situ characterisation of the reaction mechanisms occurring in these bulk oxides is limited. With a multitude of different phases evident, the characterisation becomes somewhat complicated, and further to this, bulk techniques such as Raman are limited due a number of reasons:

- i) They are unable to solely characterise the surface layer.
- ii) Problems arise in studying many of the reduced phase catalysts, due to their dark colour and absorbing characteristics.
- iii) Previous studies *ex situ* have shown catalysts are able to partially re-oxidise back to their original state under atmospheric conditions. This is further accelerated under the heat of the Raman laser.

In this section, the reduction process in various FeMo based catalysts is examined. Specifically, core-shell $\text{MoO}_x/\text{Fe}_2\text{O}_3$ catalysts are used to enable the use of *in situ* XAFS as a surface sensitive analysis tool. In this way, the focus becomes purely concentrated on the uppermost active layer, and how it restructures under reducing conditions. Work demonstrates the formation of surface phase intermediates under redox conditions, which are believed to be analogous to those forming momentarily on reaction with methanol. Methanol itself essentially acts as a reductant, removing oxygen from the surface. Under ordinary reaction conditions, the reaction proceeds under MeOH/O_2 , and the surface is quickly able to regenerate back to its original Mo(VI) state. The changes occurring are too fast to be observed under usual experimental set up. Therefore in inducing a forced reduction of the surface under MeOH/He , the changes occurring under reaction with MeOH become permanent, and can be analysed in more detail to provide insight regarding surface reconstruction with methanol adsorption.

3.2. Experimental

In situ reduction studies were performed under transmission mode XAFS, using the microreactor as detailed in Section 2.2 of this chapter. Approximately 0.5 g of catalyst was mixed with boron nitride (the diluent), and loaded into the capillary (set up as 2.2). Reduction was carried out in a continuous flow of MeOH/He , whilst heating to 350°C at a rate of $12^\circ\text{C min}^{-1}$. A methanol bubbler was positioned prior to the catalyst bed, through which the He flow was bubbled (Figure 16). XAFS spectra were recorded throughout (~ 1 min per scan). Upon reaching 350°C , the gas flow mixture was switched to pure He , and the sample cooled to room temperature.

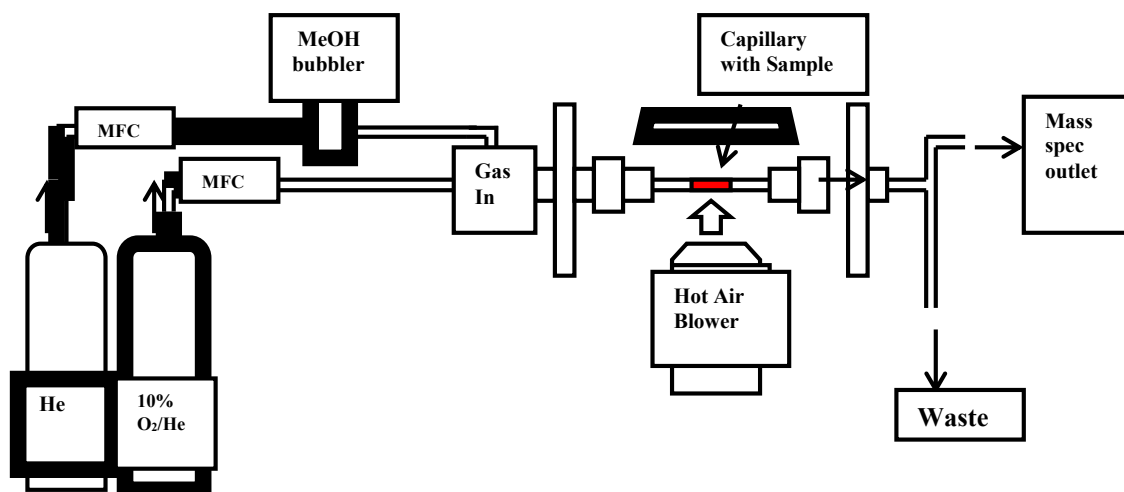


Figure 16. *In situ* microreactor set up for the outlined reduction studies. He is passed through MeOH, which subsequently flows through the catalyst bed at the sample stage. Products of the reaction are analysed through mass spectrometer analysis. The hot air blower controls the temperature of the catalyst bed.

3.3. Results and Discussion

3.3.1. Raman

Raman data has been recorded for a range of reduced samples, with data presented below in Figures 17.

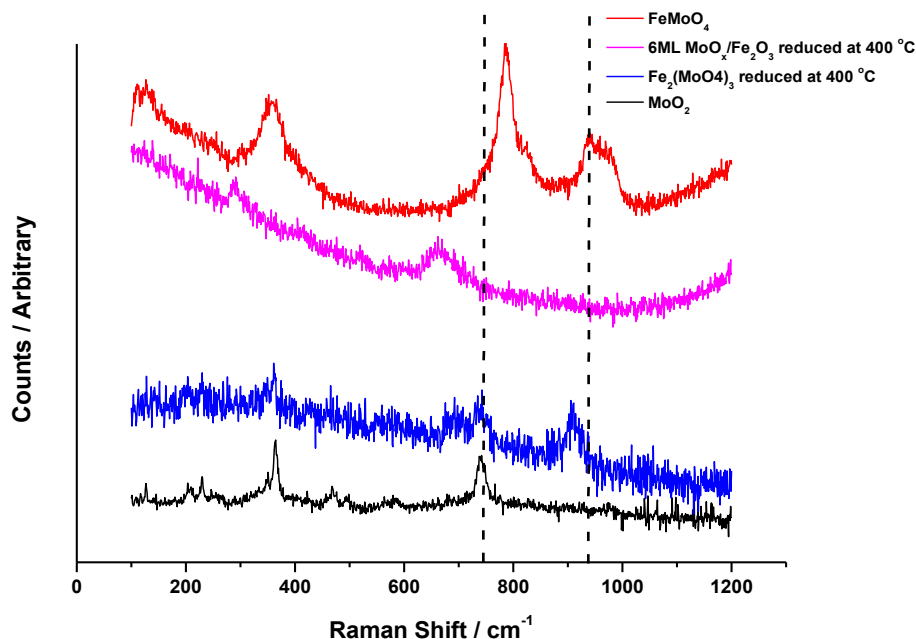


Figure 17. Reduced Raman data for bulk $\text{Fe}_2(\text{MoO}_4)_3$ with a Mo:Fe ratio 1.7:1, and 6ML $\text{MoO}_x/\text{Fe}_2\text{O}_3$ after reduction treatment under MeOH/He. It is shown that MoO_2 phase formation is unique to the bulk iron molybdate catalyst.

Raman modes are reported by L. Kumari *et al.* [46] for bulk MoO_2 at 202.9, 226.3, 346.2, 360.2, 458.2, 494.1, 567.2, 584.4, and 738.5 cm^{-1} . The slight shift in Raman modes for the MoO_2 spectra presented in Figure 17 may be attributed to the presence of strain within the sample, or growth defects, as a result of the reduced phase being produced in-house through reduction of commercial MoO_3 . Referring to Figure 17, several bands appear evident for the reduced iron molybdate catalyst with a Mo:Fe ratio of 1.7:1 (an iron molybdate catalyst containing MoO_3 and $\text{Fe}_2(\text{MoO}_4)_3$ in its chemical composition, Chapter 3). Bands at 370 cm^{-1} and 745 cm^{-1} are clearly present, indicative of MoO_2 formation, possibly from the reduction of MoO_3 . There is no evidence of FeMoO_4 , a known reduced phase of $\text{Fe}_2(\text{MoO}_4)_3$. Problems arise in the identification of this phase, due to both the reference and the sample re-oxidising under the heat of the Raman laser. A third compound was identified from the Raman band at 907 cm^{-1} , attributed to terminal Mo-O vibration in orthorhombic Mo_4O_{11} [47].

For the 6ML $\text{MoO}_x/\text{Fe}_2\text{O}_3$ catalyst, a substantial difference is viewed in the reduced spectra. There is no evidence for MoO_2 formation, with the bands at 340 and 745 cm^{-1} clearly not present. An alternative reduction process would appear to take place when Mo is dosed at the catalyst surface, as opposed to when it exists in the bulk. It has not been possible to index the band at 650 cm^{-1} , however the very broad nature is indicative of its amorphous nature, or presence as a monolayer formation.

3.3.2. XRD

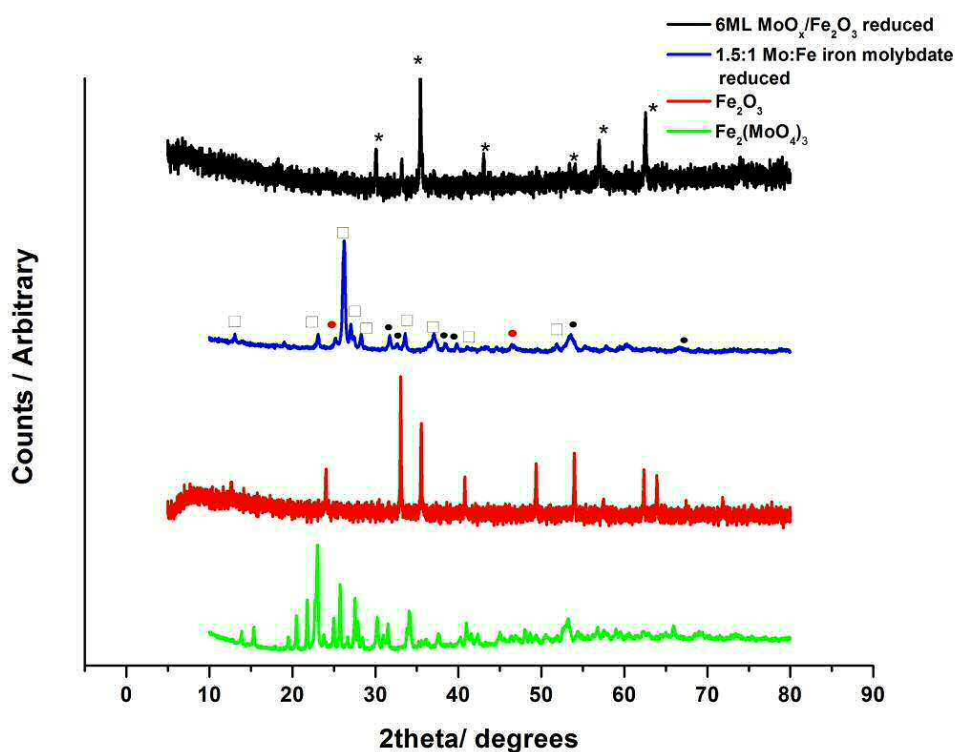


Figure 18. XRD data pre and post reduction for bulk $\text{Fe}_2(\text{MoO}_4)_3$, 6ML $\text{MoO}_x/\text{Fe}_2\text{O}_3$ and references Fe_2O_3 and $\text{Fe}_2(\text{MoO}_4)_3$. Phases indicated [29]: MoO_2 (black circles), $\beta\text{-FeMoO}_4$ (white squares), and Fe_3O_4 (asterix). The results agree with the findings of the Raman.

XRD was performed using a Panalytical X'pert pro analyser with Cu K alpha radiation across a 2θ range of $0\text{--}80^\circ$. Comparing data sets (Figure 18), it is clear that for the sample in which there is a Mo:Fe ratio of 1.7:1, the catalyst contains MoO_2 , shown through the bands at $26, 38$ and $53^\circ 2\theta$, corresponding to the (011), (020) and (022) reflections [46, 48] respectively. This corresponds well with the Raman data, which also demonstrates MoO_2 as the principal reduced phase. In addition to this, there is strong evidence for $\beta\text{-FeMoO}_4$, most easily identified through the Bragg peaks at 12.97° and $26.31^\circ 2\theta$. This extends upon the information obtained through Raman, which could not isolate this phase.

In contrast for the 6ML $\text{MoO}_x/\text{Fe}_2\text{O}_3$ catalyst, these phases were not observed, with an entirely different component forming. The phase formed could not be indexed to any of the known crystalline iron molybdate or molybdenum like phases. Referring to the literature, it is apparent that Fe_2O_3 has reduced to Fe_3O_4 [49]. Peaks at $30.08, 35.35, 43.06, 53.41, 57.09$, and $62.62^\circ 2\theta$, correspond to the (220), (311), (400), (422), (511) and (440) planes in Fe_3O_4 respectively.

3.3.3. BET

Table 1. Surface areas for catalysts pre and post reduction, as measured by BET. * Catalysts were calcined after AHM impregnation at 500 °C for 2 or 24 hours as indicated. ** Catalysts were reduced at 350 °C under a constant flow of MeOH/He under the tube furnace set up described (Chapter 2, Figure 1).

Sample calcined at 500 °C	Surface Area / m ² g ⁻¹
Commercial Fe₂O₃ (<50nm)	21
1ML MoO₃ /Fe₂O₃ / 2 Hours *	20
3ML MoO₃ /Fe₂O₃ / 2 Hours *	15
6ML MoO₃ /Fe₂O₃ / 2 Hours *	12
3ML MoO₃ /Fe₂O₃ / 24 Hours *	14
Fe₂O₃ reduced at 350 °C in MeOH/He **	21
1ML MoO₃ /Fe₂O₃ reduced at 350 °C in MeOH/He **	17
3ML MoO₃ /Fe₂O₃ reduced at 350 °C in MeOH/He **	14
6ML MoO₃ /Fe₂O₃ reduced at 350 °C in MeOH/He **	11
1ML MoO₃ /Fe₂O₃ re-oxidised at 500 °C in the muffle furnace after reduction.	17

BET was recorded pre and post reduction, to assess whether this process has any substantial effect on the surface area of the catalysts. It is shown that the surface area is comparable both pre and post reduction, for all of the monolayer coverages described. Table 1 also summarises the acquired data and after re-oxidation for the 1ML MoO_x/Fe₂O₃ catalyst. Again, the surface area is sustained despite the relatively harsh conditions employed. This shows promise for such catalysts, inferring that after re-oxidation they may be able to retain their activity and be used repeatedly as in the case for industrial Fe₂(MoO₄)₃. However, since the majority of the catalyst is formed from Fe₂O₃, it is not possible to comment on the Mo specific surface area from these results.

3.3.4. XAFS

In order to consider the structural changes occurring under reduction with methanol more thoroughly, XAFS analysis has been a fundamental tool in assessing the local structural changes occurring under such treatments. As mentioned previously, the driving force behind investigating these surface changes under reduction, is to gain insights into the catalytic mechanisms which occur at Mo rich surfaces. Methanol is essentially a reductant, with Bowker *et al.* proposing a Mo (VI)/Mo(IV) oxidation state change under reaction with this alcohol. The surface is then able to efficiently regenerate back to Mo(VI), through re-oxidation using gas phase oxygen. However, the changes in Mo oxidation state are not easy to observe under conventional *in situ* characterisation techniques, since the timescales of the

experiment are usually not fast enough to observe this. By carrying out the reaction with methanol in He however, this incurs more permanent changes to the catalyst structure, since the surface becomes deprived of gas phase oxygen to perform the regeneration. It is possible that the reduced state structure enforced, is analogous to that which forms temporarily under ordinary reaction conditions with MeOH/O₂.

3.3.4.1. XANES

1, 3 and 6ML MoO_x/Fe₂O₃ have been investigated under reduction with MeOH/He through XAFS (Set up as Figure 16). Changes in the XANES data were originally analysed. Figure 19 details the extent of reduction as a function of temperature for each of the monolayer coverages. It was not possible to source appropriate references to perform satisfactory LCF's as has been done in previous chapters. Instead, results were ascertained through observing the shift in edge position between Mo(VI) indexed from the original post reduced catalyst, to reduced Mo(IV) referenced from MoO₂. All catalysts demonstrate an edge shift of approximately 70 % towards Mo(IV), with the onset of reduction occurring more readily for the 1 and 3ML MoO_x/Fe₂O₃ catalysts, as shown by the shift in temperature to lower values for increasing Mo(IV) formation.

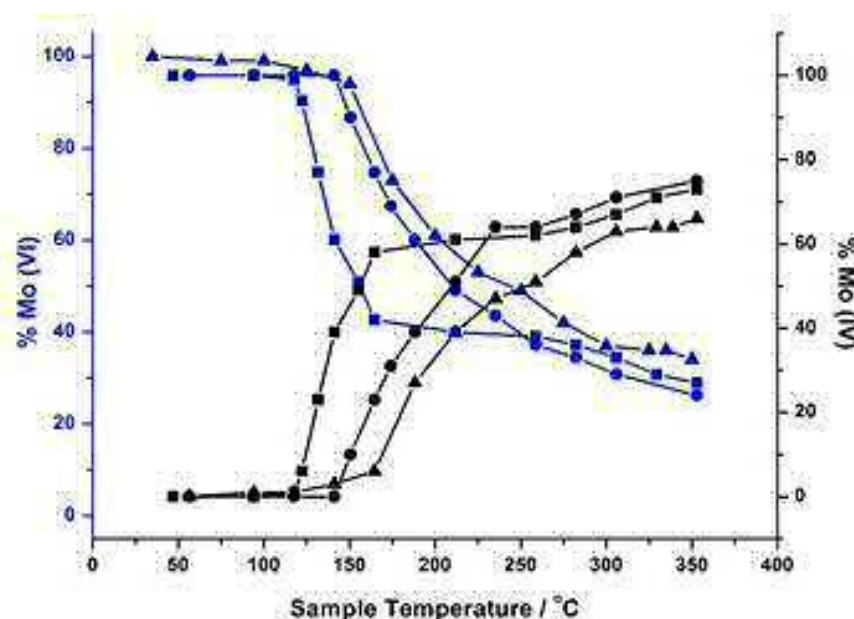


Figure 19. Oxidation state changes during the *in situ* reduction of 1, 3 and 6ML MoO_x/Fe₂O₃ ascertained through monitoring the change in absorption edge position from Mo(VI) to Mo(IV). Reduction studies were carried out in a MeOH/He flow whilst heating to 350 °C at a rate of 12 °C min⁻¹. XAFS spectra were collected throughout (~1 min per scan). 1ML= Squares, 3ML= Circles, 6ML= Triangles.

Since Mo is dosed at the surface, the results are representative of the surface situation. Studying *in situ* has allowed for successive changes to be tracked during the reduction process, without the possibility for re-oxidation on exposure to air for *ex situ* analysis. The shift in the absorption edge to lower energy was clearly evident with increasing reduction temperature for 1, 3 and 6ML $\text{MoO}_x/\text{Fe}_2\text{O}_3$ when analysing under XANES (See Figure 20 for 6ML $\text{MoO}_x/\text{Fe}_2\text{O}_3$ as example).

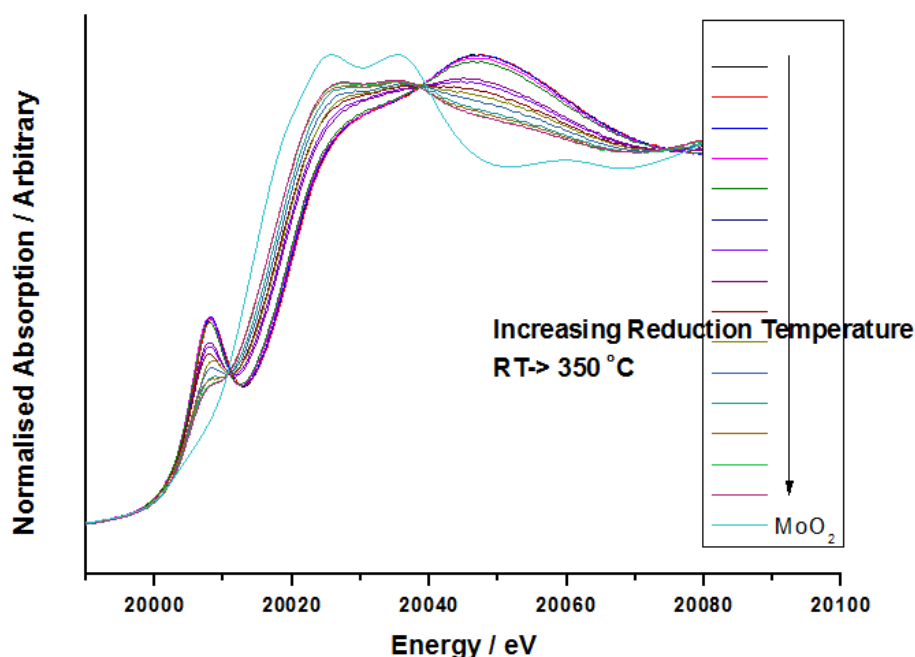


Figure 20. Reduction of 6ML $\text{MoO}_x/\text{Fe}_2\text{O}_3$ in MeOH/He from Room temperature to 350 °C, together with MoO_2 reference (pale blue). An obvious shift in the absorption edge is seen with increasing temperature, to lower energy for the highest temperatures. This is indicative of a lower oxidation state. It is not however apparent that MoO_2 is formed, since the reduced Mo oxide state maintains a small pre-edge feature even for the 350 °C reduced sample, as well as only a 70 % shift towards the structure for MoO_2 .

3.3.4.2. EXAFS

To assess this reduction process further, EXAFS analysis has been implemented. Initial data was investigated for bulk $\text{Fe}_2(\text{MoO}_4)_3$ with a Mo:Fe ratio of 1.7:1. Appendix A11 details the non-phase corrected k^2 -weighted Fourier transform data for bulk $\text{Fe}_2(\text{MoO}_4)_3$ after reduction *ex situ*. The primary Mo environment is comprised of oxygen neighbours, with major contributions at low values of R in the Fourier transform. These are associated with a shorter $\text{Mo}^{4+}\text{-O}$ distance found in MoO_2 , and a longer $\text{Mo}^{6+}\text{-O}$ distance, accredited to FeMoO_4 , a known reduced form of $\text{Fe}_2(\text{MoO}_4)_3$. Additionally, further out in R-space, there is

a significant shell at 2.5 Å, representing a Mo^{4+} - Mo^{4+} interaction [50]. This is analogous to the bonded Mo-Mo unit found within the di-nuclear units of MoO_2 . MoO_2 forms with extended structure as evidenced in Appendix 11, which compares this bulk reduced iron molybdate structure to bulk MoO_2 . There is a consistent match between the two materials. Data agrees well with that seen through Raman and XRD (Figures 17-18), verifying the production of MoO_2 in this bulk catalyst.

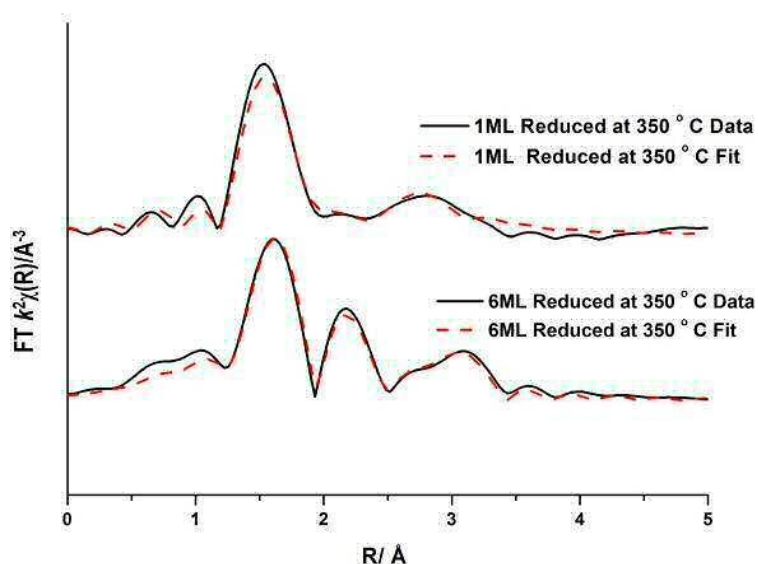


Figure 21. Magnitude component of the k^2 weighted Fourier transform for the EXAFS data of the 1 and 6ML $\text{MoO}_x/\text{Fe}_2\text{O}_3$ catalyst reduced.

EXAFS data has been analysed in more detail for the monolayer catalysts, being 1, 3 and 6ML $\text{MoO}_x/\text{Fe}_2\text{O}_3$. Plots for the k^2 -weighted Fourier transform data for the end state reduced samples of 1 and 6ML $\text{MoO}_x/\text{Fe}_2\text{O}_3$ are disclosed in Figure 21. Results for the reduced 3ML $\text{MoO}_x/\text{Fe}_2\text{O}_3$ catalyst are consistent for those with those seen for 6ML $\text{MoO}_x/\text{Fe}_2\text{O}_3$ (Also Appendix A11) and therefore will not be discussed. The obtained fits for all $\text{MoO}_x/\text{Fe}_2\text{O}_3$ catalysts are comprised of 5 scattering paths: 2 Mo-O, Mo-Mo and 2 Mo-M, where M=Fe or Mo. Two oxygen scattering paths feature at 1.78 and 2.02 Å. Since a spread of distances are seen, this implies a distorted nature of the reduced Mo octahedra, whilst also inferring that there may be variable oxidation states present. The range for the forward Fourier transform was $2.5 < k < 11.5$.

All monolayers have a significant contribution from Mo-Mo at 2.6 Å (Table 2). Literature attributes this to a bonded distance indicative of a Mo(V) dimer or Mo(IV) trimer [37]. MoO_2 also contains a Mo-Mo bonding contribution (Appendix A12 and Figure 8 Chapter 1) however at a shorter distance of 2.5 Å [51], and with a reduced co-ordination number to that

seen in these monolayer systems. This change in bond length is a significant difference between the catalysts. Previous work of Kikutani *et al.* [52] has established a 2.6 Å Mo–Mo bond in fixed dimer catalysts as the most distinctive feature for unique dimeric active sites.

Also noted during the reduction, was that the end state reduced catalysts of $\text{Fe}_2(\text{MoO}_4)_3$ and the monolayer system showed differing colours. The monolayer catalysts appeared dark brown in colour, whilst the bulk $\text{Fe}_2(\text{MoO}_4)_3$ catalyst appeared very black. The dark brown colour has been attributed to an excitation to the energy levels of the 2.6 Å Mo–Mo bonds, a result of mixing of the energy levels in the molybdenum atoms. Without this Mo–Mo interaction, simple d-electron transitions of isolated molybdenum would have a much weaker absorbance.

The Mo–M paths are difficult to assign with confidence due to their out of phase nature. If two photoelectron waves (due to two different scatterers) are at similar distance they can interfere. The waves don't sum-up linearly so hence interfere with each other. If the difference is 180 degrees, they are perfectly out of phase (destructive interference, so that the maxima of the first wave correspond to the minima of the second one) and the intensity is therefore zero so you won't see any peak in the Fourier Transform. However, in carrying out extensive analysis using the Artemis software applying various scatter path options, contributions from metal scatterers are apparent for a desired fit (Table 2, Figure 21). For the 1ML $\text{MoO}_x/\text{Fe}_2\text{O}_3$ sample, the required fit was achieved with 2 Mo–Fe contributions at 3.07 and 3.55 Å, which corresponds well with Chapter 4 which also demonstrates the interaction between Mo and Fe at this low loading [5, 53]. The 3ML $\text{MoO}_x/\text{Fe}_2\text{O}_3$ and 6ML $\text{MoO}_x/\text{Fe}_2\text{O}_3$ samples are dominated by Mo–Mo contributions, with Mo–Fe distances being difficult to establish. The relatively weak intensity of the peaks further out in R-space, is a result of the out of phase behaviour of the different Mo–M distances, as is evidenced in the imaginary part of the Fourier transform when carrying out the analysis.

Table 2. EXAFS fitting parameters for the 1 and 6ML MoO_x/Fe₂O₃ reduced under MeOH/He at 350 °C. The R_{factor} for the 1 and 6 ML reduced MoO_x/Fe₂O₃ catalysts were 0.03 and 0.01 respectively. Where N= Co-ordination number, R= Bond distance/ Å of the Absorber-Scatterer, $2\sigma^2$ = Mean squared disorder (sometimes referred to as the Debye waller factor), $E_f = E_0$, R_{Factor} = A statistic of the fit, which is a way of visualizing how the misfit is distributed over the fitting range.

<i>Sample</i>	<i>Abs. Sc.</i>	<i>N</i>	<i>R / Å</i>	<i>2σ² / Å²</i>	<i>E_f / eV</i>	<i>R_{factor}</i>
1ML MoO_x/Fe₂O₃ end state Reduced	Mo-O	2 (2)	1.76 (5)	0.012 (1)	-1 (6)	0.03
	Mo-O	4.0 (1)	2.02 (2)	0.003 (Fixed)		
	Mo-Mo	1.3 (Fixed)	2.68 (3)	0.007 (2)		
	Mo-Fe	2 (2)	3.05 (6)	0.007 (Fixed)		
	Mo-Fe	2 (1)	3.36 (2)	0.007 (Fixed)		
6ML MoO_x/Fe₂O₃ end state Reduced	Mo-O	1.5 (1)	1.78 (2)	0.007 (7)	0 (2)	0.01
	Mo-O	3.4 (3)	2.03 (1)	0.003 (Fixed)		
	Mo-Mo	1.3 (Fixed)	2.62 (2)	0.003 (1)		
	Mo-Mo	2.5 (1)	2.82 (2)	0.01 (1)		
	Mo-Mo	4.0 (2)	3.37 (2)	0.01 (1)		

Evidence obtained through EXAFS has elaborated on the information obtained through XANES. EXAFS analysis indicates the presence of a reduced cluster of Mo after reduction under MeOH/He. The reduced molybdenum species is shown to possess molybdenum units with 2.6 Å Mo–Mo bonds, but the extent of aggregation of the Mo units is not clear. The significance of these Mo clusters is that the possible dimer unit suggests a two centred Mo reaction site, which could be the reactive site that momentarily forms on reaction with methanol under oxidative reaction conditions, before its quick and efficient re-oxidation back to the original catalyst.

Current research is limited with regards to the catalytic mechanisms involved in the selective dehydrogenation reaction to methanol. The majority of authors have identified Mo=O sites as possible dehydrogenation centres for the mild oxidation [10, 30, 40, 42, 53]. Trifiro *et al.* [54] have long maintained the opinion that Mo=O double bonds are essential in oxidation catalysts, with dioxo centres at the core of the reactivity due to their ability to extract both hydrogens from methanol.

As previously mentioned, a study by Allison *et al.* [37] uses *Ab Initio* quantum mechanics to examine the reaction mechanisms of methanol on MoO₃. It was discovered that dioxo sites were essential for methanol activation, with the single site single step proposal unfavorable. In their work, it is concluded that the catalytic active site involves two adjacent

dioxo units of Mo=O. In a more recent review of Bowker *et al.* [55] the behaviour of bi-cationic oxide catalysts is assessed, with specific focus on the selective oxidation of methanol mechanism. It was found that on increasing the amount of Mo added to Fe₂O₃, the product selectivity was determined by the distribution of the dual and single sites of each species. With increased loading, the product detected transitioned from CO under single Mo sites, to formaldehyde with sufficient Mo dosed for dual site activity. This would fit well with the discovered 2.6 Å Mo-Mo distance, and would support the suggestion of a 2-site adsorption centre responsible for the dehydrogenation of methanol.

3.3.5. Catalytic Testing

Catalytic testing of the reduced samples (Figures 22-25) was performed using TPD of MeOH/He. This technique provides insights into the possible surface phase intermediates which form under reduction and reaction with methanol.

XRD has shown that the monolayer MoO_x/Fe₂O₃ samples reduce to Fe₃O₄. For comparative purposes, reduced Fe₂(MoO)₄ has also been tested under TPD with methanol. Referring to the different catalysts, all produce CO (Mass 28), H₂CO (Mass 30), H₂ (Mass 2) and CO₂ (Mass 44) during the desorption process. Two peaks also occur for water desorption. The first is coincident with methanol, and the second, at a higher desorption temperature coincident with CO₂ as a combustion product (Equation 3).



The CO by-product (Mass 28) is consistent with isolated Fe sites, where a change in binding energy at Fe-O-Mo bridging oxygen encourages dehydrogenation of the adsorbed methoxy intermediate. The 1ML MoO_x/Fe₂O₃ catalyst demonstrates the highest yield of this carbon containing product. With just one monolayer of Mo oxide present, if clusters of Mo aggregate upon reduction, this will most certainly leave a high proportion of Fe sites exposed to yield unselective by-products such as CO. This agrees with the suggested theory of Mo clustering under reaction, shown through the XAFS studies (3.3.4).

The higher temperature H₂ and simultaneous CO₂ production are indicative of methanol decomposition via formate intermediate (Equation 3). Formate is known to adsorb on the surface of Fe rich materials, specifically at two adjacent Fe sites. This therefore implies that there are an increased number of Fe sites at the surface after reduction, again agreeing with the Mo cluster theory presented. Clearly there is a higher population of these for the 1 ML catalyst compared with the 6ML sample, as shown through the increased signal for CO₂

(Mass 44) and H_2 (Mass 2). The majority of the upper layer is thought to be comprised of Fe_3O_4 , as proven through XRD (Section 3.3.2).

Disregarding the differences in the onset temperature of the various by-products, on assessment of these data there appears to be a strong correspondence between the reduced bulk and monolayer catalyst reactivity profiles. All produce H_2 and CO_2 as the major products. Since monolayer and bulk reduced catalysts perform so similarly, this would infer a similar surface termination in each of these materials.

The overall surface area of the catalysts do not change substantially after reduction (Table 1). Although aggregation of Mo to cluster formation may be assumed to evoke a decrease in surface area, it must be remembered that the Mo forms just a small proportion of the overall catalyst composition, the majority being formed from Fe_3O_4 , which possesses a high surface area.

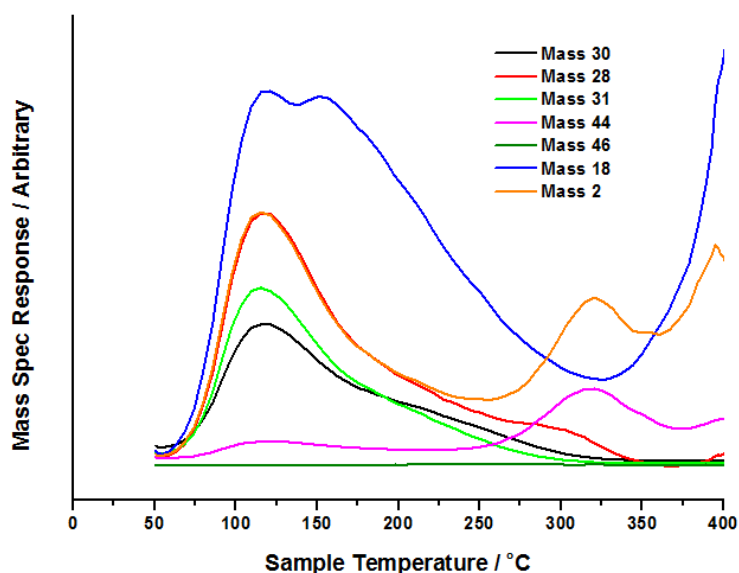


Figure 22. TPD data for reduced $\text{Fe}_2(\text{MoO}_4)_3$ of ratio Mo:Fe 1.7:1. The catalyst was reduced at 350°C *ex situ* under a continuous flow of MeOH/He, using a MeOH bubbler fitted prior to the tube furnace set up (Chapter 2, Figure 1). A reduction was carried out for 4 hours, and the catalyst was seen to turn black in colour. A TPD was then performed, saturating the catalyst surface with MeOH/He followed by ramping the catalyst to 400°C whilst monitoring the products desorbed. Mass 30= Formaldehyde, Mass 28= Carbon Monoxide, Mass 31= Methanol, Mass 44= Carbon Dioxide, Mass 46= Dimethyl Ether, Mass 18= Water, Mass 2= Hydrogen.

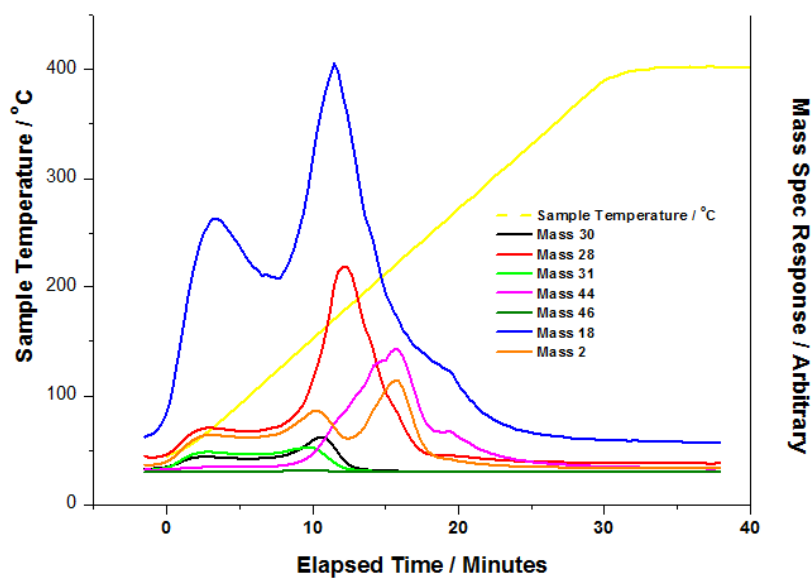


Figure 23. TPD of MeOH/He for 1ML MoO_x/Fe₂O₃ after reduction at 350 °C. Set up as Figure 22.

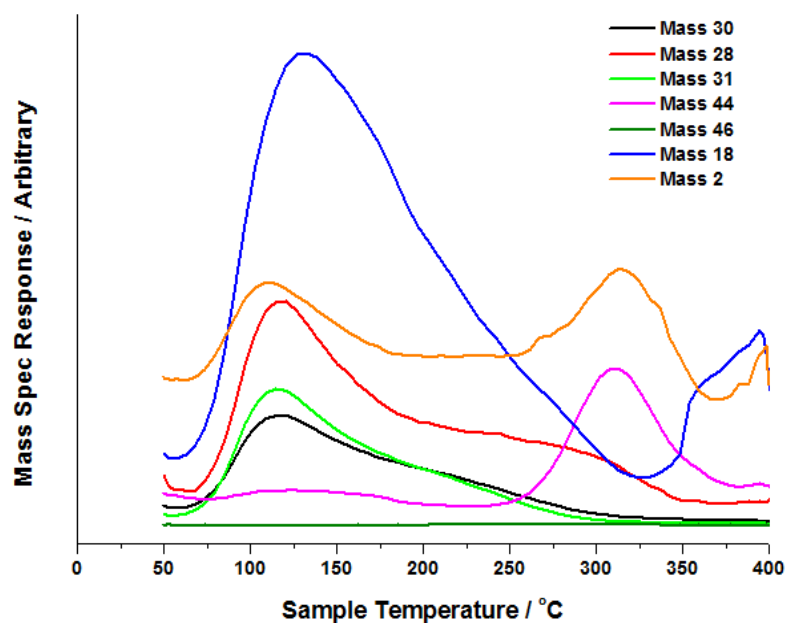


Figure 24. TPD of MeOH/He for 3ML MoO_x/Fe₂O₃ after reduction at 350 °C. Set up as Figure 22.

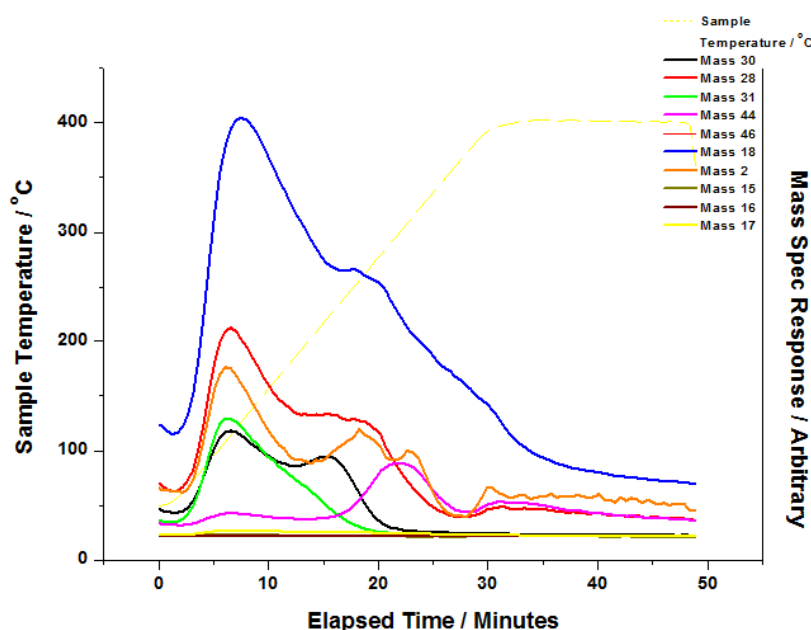


Figure 25. TPD of MeOH/He for 6ML MoO_x/Fe₂O₃ after reduction at 350 °C. Set up as Figure 22.

4. Continuous Isothermal Studies

To complete the studies discussed so far in this chapter, the nature of Mo during the *oxidative* reaction with methanol has been assessed. *In situ* isothermal reaction studies were performed under transmission mode XAFS, using the microreactor as detailed in Section 2.1 combined with mass spectrometry. A methanol bubbler was positioned prior to the catalyst bed, through which a 10 % O₂/He flow was bubbled (Chapter 2, Figure 1). XAFS spectra were recorded across a time period of 120 minutes (~1 min scan every 5 minutes), whilst maintaining the temperature isothermally at 250 °C. XAFS was carried out in the absence of the combined Raman experiment to enable the acquisition in transmission mode.

Figure 26 displays the XANES data for 6ML MoO_x/Fe₂O₃ obtained throughout a 120 minute time period of reaction with MeOH under O₂. No obvious changes were observed in the Mo speciation, with the absorption edge position remaining constant and T_d co-ordination being maintained throughout. The Mo environment was therefore preserved under reaction conditions, enabling the sustained production of formaldehyde, as shown through the mass spectrometer data collected online during the experiment (Figure 27). 90 % formaldehyde selectivity could be maintained for the course of the reaction, the other 10 % formed from a small amount of DME and CO. Previous studies have identified that surface oxygen is consumed in the reaction. It is therefore apparent that any removal of surface

oxygen through extensive reduction of Mo, is followed by rapid re-oxidation by gas phase oxygen to maintain the catalyst in its desired Mo(VI) state. However it could be that Mo(IV) exists momentarily, but is unable to be seen due to the time scale of these studies.

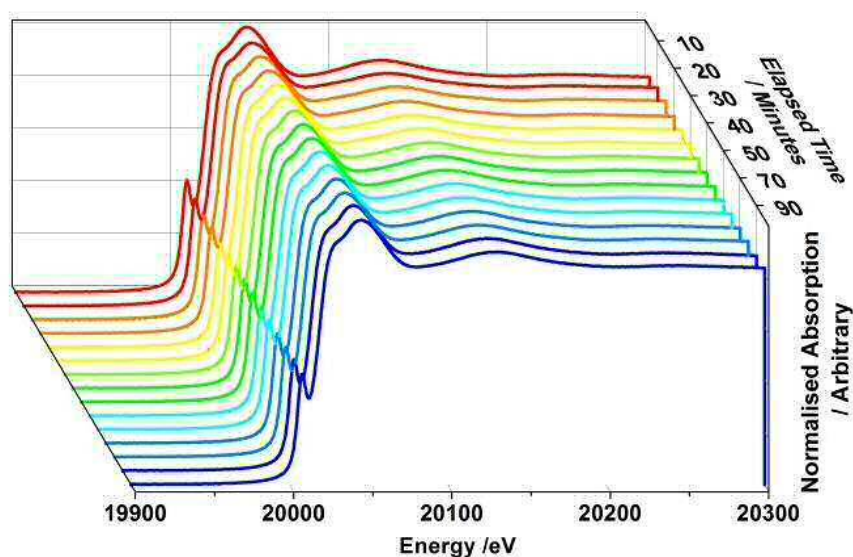


Figure 26. XANES data over a 120 minute period for 6ML MoO_x/Fe₂O₃ when reacted isothermally at 250 °C under a continuous flow of MeOH/O₂. XAFS data was collected continuously using 1 minute scans, whilst mass spectrometer data was recorded simultaneously to ensure the reaction was ongoing. No changes in the catalyst structure are evident.

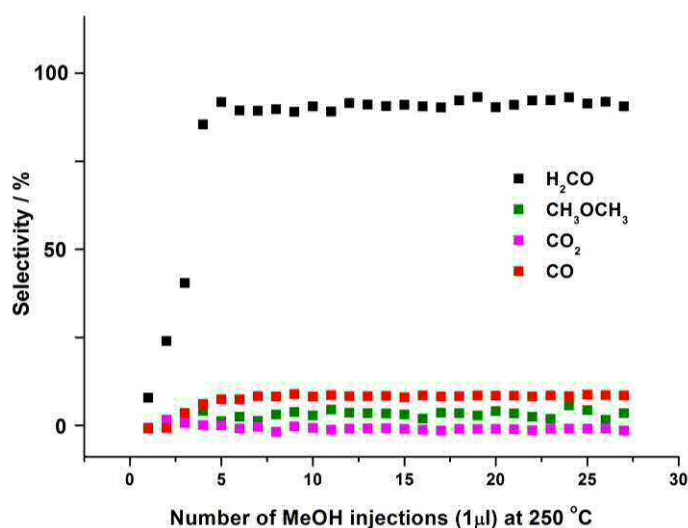


Figure 27. Online mass spectrometry data for 6ML MoO_x/Fe₂O₃, when reacted isothermally in continuous flow under MeOH/O₂ at 250 °C. Results show the reaction ensues, the majority of the selectivity towards H₂CO. 88 % MeOH conversion was achieved. This is lower than the 93 % quoted industrially. See Figure 16 for experimental details.

5. Conclusions

This chapter highlights the use of *in situ* techniques to observe changes in catalyst structure under reaction and preparation conditions. The set ups used have provided quick and accurate analysis, endorsing more confident identification of the differing molybdenum species at the surface of Fe_2O_3 under a change of sample environment. The work has yielded crucial insights into the structural properties of $\text{MoO}_x/\text{Fe}_2\text{O}_3$ catalysts and by extension to bulk $\text{Fe}_2(\text{MoO}_4)_3$.

The *in situ* XAFS/Raman investigations detailed the evolution the active phase of the catalysis during the pre-catalysis activation of calcination. Results demonstrated clear and complementary changes in both techniques, identifying a change in co-ordination geometry from O_h to T_d with increasing sample temperature. By study the calcination procedure with a steady increase in sample temperature, it has been possible to track the exact point at which changes occur in the phases forming, along with the ability to learn more about the changes across the calcination range. In summary, the activation procedure for the multi-layer systems show that the formation of the T_d $\text{Fe}_2(\text{MoO}_4)_3$ phase is preceded by the formation of MoO_3 , however, an active O_h Mo overlayer remains at all times.

Further work involved probing the catalyst under reaction with MeOH/He using *in situ* XAFS. This enforced a reduction of the surface, which could be analogous to the structural changes which occur momentarily with reaction under MeOH in aerobic conditions. Analysis isolated a Mo-Mo bond distance of 2.6 Å. It is well known from the literature that chemisorption of methoxy occurs at $\text{Mo}=\text{O}$ bonds on the surface, which can be assigned to Mo^{4+} - Mo^{4+} or Mo^{5+} - Mo^{5+} units. From this, it can be inferred that multiple Mo sites are involved in the selective oxidation of methanol to formaldehyde.

5. References

1. House, M.P., et al., *Effect of varying the cation ratio within iron molybdate catalysts for the selective oxidation of methanol*. The Journal of Physical Chemistry C, 2008. **112**(11): p. 4333-4341.
2. Bowker, M., A.F. Carley, and M. House, *Contrasting the behaviour of MoO_3 and MoO_2 for the oxidation of methanol*. Catalysis Letters, 2008. **120**(1-2): p. 34-39.
3. Soares, A.P.V., et al., *Mechanism of deactivation of iron-molybdate catalysts prepared by coprecipitation and sol-gel techniques in methanol to formaldehyde oxidation*. Chemical Engineering Science, 2003. **58**(7): p. 1315-1322.
4. Routray, K., et al., *Origin of the synergistic interaction between MoO_3 and iron molybdate for the selective oxidation of methanol to formaldehyde*. Journal of Catalysis, 2010. **275**(1): p. 84-98.
5. Brookes, C., et al., *Molybdenum Oxide on Fe_2O_3 Core-Shell Catalysts: Probing the Nature of the Structural Motifs Responsible for Methanol Oxidation Catalysis*. Acs Catalysis, 2014. **4**(1): p. 243-250.

6. Routray, K., et al., *Origin of the synergistic interaction between MoO₃ and iron molybdate for the selective oxidation of methanol to formaldehyde*. Journal of Catalysis, 2010. **275**(1): p. 84-98.
7. Uhlrich, J.J., et al., *Preparation and characterization of iron-molybdate thin films*. Surface Science, 2011. **605**(15-16): p. 1550-1555.
8. Jin, G., et al., *Fe-2(MoO₄)(3)/MoO₃ nano-structured catalysts for the oxidation of methanol to formaldehyde*. Journal of Catalysis, 2012. **296**: p. 55-64.
9. Bowker, M., et al., *Evolution of active catalysts for the selective oxidative dehydrogenation of methanol on Fe₂O₃ surface doped with Mo oxide*. Physical Chemistry Chemical Physics, 2013. **15**(29): p. 12056-12067.
10. Bowker, M., et al., *The selective oxidation of methanol on iron molybdate catalysts*. Topics in Catalysis, 2008. **48**(1-4): p. 158-165.
11. Hassan, K.H. and P.C.H. Mitchell, *Evaluation of different methods to prepare the Fe(2)O(3)/MoO(3) catalyst used for selective oxidation of methanol to formaldehyde*, in *Scientific Bases for the Preparation of Heterogeneous Catalysts: Proceedings of the 10th International Symposium*, E.M. Gaigneaux, et al., Editors. 2010. p. 475-478.
12. Ramachandra, B., et al., *Partial oxidation of methanol to formaldehyde on molybdenum based mixed oxide catalyst*. Catalysis Letters, 2005. **105**(1-2): p. 23-27.
13. Beale, A.M., et al., *An iron molybdate catalyst for methanol to formaldehyde conversion prepared by a hydrothermal method and its characterization*. Applied Catalysis A: General, 2009. **363**(1-2): p. 143-152.
14. Beale, A.M. and G. Sankar, *In situ characterization of iron phosphate and bismuth molybdate catalysts prepared by hydrothermal methods: An EDXRD and combined XRD/XAS study*. Nuclear Instruments and Methods in Physics Research Section B: Beam Interactions with Materials and Atoms, 2003. **199**(0): p. 504-508.
15. Jacques, S.D.M., et al., *Recent progress in the use of in situ X-ray methods for the study of heterogeneous catalysts in packed-bed capillary reactors*. Catalysis Today, 2009. **145**(3-4): p. 204-212.
16. O'Brien, M.G., et al., *A Combined Multi-Technique In Situ Approach Used to Probe the Stability of Iron Molybdate Catalysts During Redox Cycling*. Topics in Catalysis, 2009. **52**(10): p. 1400-1409.
17. Tinnemans, S.J., et al., *Combining operando techniques in one spectroscopic-reaction cell: New opportunities for elucidating the active site and related reaction mechanism in catalysis*. Catalysis Today, 2006. **113**(1-2): p. 3-15.
18. Stierle, A. and A.M. Molenbroek, *Novel in situ probes for nanocatalysis*. Mrs Bulletin, 2007. **32**(12): p. 1001-1005.
19. Shishido, T., et al., *Study of formation process of metal nanoparticles on metal oxides by in-situ XAFS technique*. 15th International Conference on X-Ray Absorption Fine Structure (Xafs15), 2013. **430**.
20. Mesu, J.G., et al., *Synchrotron radiation effects on catalytic systems as probed with a combined in-situ UV-Vis/XAFS spectroscopic setup*. Journal of Physical Chemistry B, 2005. **109**(9): p. 4042-4047.
21. Rodriguez, J.A., et al., *In situ/operando studies for the production of hydrogen through the water-gas shift on metal oxide catalysts*. Physical Chemistry Chemical Physics, 2013. **15**(29): p. 12004-12025.
22. Hill, C.G. and J.H. Wilson, *Raman spectroscopy of iron molybdate catalyst systems.: Part I. Preparation of unsupported catalysts*. Journal of molecular catalysis, 1990. **63**(1): p. 65-94.
23. Xu, Q., et al., *Surface phase composition of iron molybdate catalysts studied by UV Raman spectroscopy*. The Journal of Physical Chemistry C, 2008. **112**(25): p. 9387-9393.
24. Beale, A.M., et al., *An iron molybdate catalyst for methanol to formaldehyde conversion prepared by a hydrothermal method and its characterization*. Applied Catalysis a-General, 2009. **363**(1-2): p. 143-152.

25. Ramis, G., et al., *Characterization of MoO₃-P₂O₅-ZrO₂ catalysts: an oxide-supported mixed oxide*. Materials Chemistry and Physics, 1998. **55**: p. 15.
26. Belhekar, A.A., S. Ayyappan, and A.V. Ramaswamy, *FT-IR studies on the evolution of different phases and their interaction in ferric molybdate—molybdenum trioxide catalysts*. Journal of Chemical Technology and Biotechnology, 1994. **59**: p. 8.
27. Trifiro, F., V.D. Vecchi, and I. Pasquon, *Nature of the Active Component in a Fe₂O₃-MoO₃ Catalyst I. Study on the Catalyst Reduction and Oxidation*. Journal of Catalysis, 1969. **15**: p. 9.
28. Adkins, H. and W.R. Peterson, *The oxidation of methanol with air over iron, molybdenum, and iron-molybdenum oxides*. Journal of the American Chemical Society, 1931. **53**(4): p. 1512-1520.
29. Ivanov, K.I. and D.Y. Dimitrov, *Deactivation of an industrial iron-molybdate catalyst for methanol oxidation*. Catalysis Today, 2010. **154**(3): p. 250-255.
30. O'Brien, M.G., et al., *On the Active Oxygen in Bulk MoO₃ during the Anaerobic Dehydrogenation of Methanol*. Journal of Physical Chemistry C, 2009. **113**(12): p. 4890-4897.
31. Zhang, H., J. Shen, and X. Ge, *The Reduction Behavior of Fe-Mo-O Catalysts Studied by Temperature-Programmed Reduction Combined with in Situ Mössbauer Spectroscopy and X-Ray Diffraction*. Journal of Solid State Chemistry, 1995. **117**(1): p. 127-135.
32. Jacques, S., et al., *Redox Behavior of Fe Mo O Catalysts Studied by Ultrarapid In Situ Diffraction*. Angewandte Chemie, 2006. **118**(3): p. 459-462.
33. O'Brien, M.G., et al., *A combined multi-technique in situ approach used to probe the stability of iron molybdate catalysts during redox cycling*. Topics in Catalysis, 2009. **52**(10): p. 1400-1409.
34. Chowdhry, U., et al., *Mechanism and surface structural effects in methanol oxidation over molybdates*. Applications of Surface Science, 1984. **19**(1): p. 360-372.
35. House, M.P., A.F. Carley, and M. Bowker, *Selective oxidation of methanol on iron molybdate catalysts and the effects of surface reduction*. Journal of Catalysis, 2007. **252**(1): p. 88-96.
36. Farneth, W.E., et al., *Mechanism of partial oxidation of methanol over molybdenum(VI) oxide as studied by temperature-programmed desorption*. The Journal of Physical Chemistry, 1985. **89**(12): p. 2493-2497.
37. Allison, J.N. and W.A. Goddard III, *Oxidative dehydrogenation of methanol to formaldehyde*. Journal of Catalysis, 1985. **92**(1): p. 127-135.
38. Bowker, M., et al., *The selective oxidation of methanol to formaldehyde on iron molybdate catalysts and on component oxides*. Catalysis Letters, 2002. **83**(3-4): p. 165-176.
39. Farneth, W.E., et al., *A comparison of the surface chemistry of two polymorphic forms of molybdenum trioxide*. Langmuir, 1987. **3**(2): p. 217-223.
40. Tatibouet, J.M., *Methanol oxidation as a catalytic surface probe*. Applied Catalysis A: General, 1997. **148**(2): p. 213-252.
41. Tatibouet, J.M., *Acido-basicité et sensibilité à la structure de la réaction d'oxydation catalytique du méthanol sur α -MnO₃ cristallisé. I: Sites acides*. Comptes-rendus des séances de l'Académie des sciences. Série 2, Mécanique-physique, chimie, sciences de l'univers, sciences de la terre, 1983. **297**(9): p. 703-708.
42. Tatibouët, J.M. and J.E. Germain, *A structure-sensitive oxidation reaction: Methanol on molybdenum trioxide catalysts*. Journal of Catalysis, 1981. **72**(2): p. 375-378.
43. Groff, R.P., *An infrared study of methanol and ammonia adsorption on molybdenum trioxide*. Journal of Catalysis, 1984. **86**(1): p. 215-218.
44. Wadayama, T., T. Saito, and W. Suétaka, *Metastable surface species on MoO₃ observed in methanol vapor at an elevated temperature with polarization*

- modulation infrared spectroscopy*. Applications of Surface Science, 1984. **20**(1–2): p. 199-201.
45. Chung, J.S., R. Miranda, and C.O. Bennett, *Mechanism of partial oxidation of methanol over MoO₃*. Journal of Catalysis, 1988. **114**(2): p. 398-410.
 46. Kumari, L., et al., *X-ray diffraction and Raman scattering studies on large-area array and nanobranched structure of 1D MoO₂ nanorods*. Nanotechnology, 2007. **18**(11): p. 115717.
 47. Dieterle, M. and G. Mestl, *Raman spectroscopy of molybdenum oxides Part II. Resonance Raman spectroscopic characterization of the molybdenum oxides Mo₄O₁₁ and MoO₂*. Physical Chemistry Chemical Physics, 2002. **4**(5): p. 822-826.
 48. Xiang, Z., et al., *Preparation and photoelectric properties of semiconductor MoO₂ micro/nanospheres with wide bandgap*. Ceramics International, 2015. **41**(1, Part B): p. 977-981.
 49. Martín, M., et al., *Preparation of core-shell Fe₃O₄@poly (dopamine) magnetic nanoparticles for biosensor construction*. Journal of Materials Chemistry B, 2014. **2**(6): p. 739-746.
 50. Ressler, T., et al., *Bulk structural investigation of the reduction of MoO₃ with propene and the oxidation of MoO₂ with oxygen*. Journal of Catalysis, 2002. **210**(1): p. 67-83.
 51. Ressler, T., J. Wienold, and R.E. Jentoft, *Formation of bronzes during temperature-programmed reduction of MoO₃ with hydrogen—an in situ XRD and XAFS study*. Solid State Ionics, 2001. **141–142**(0): p. 243-251.
 52. Kikutani, Y., *Structures of molybdenum silica catalysts reduced by ethanol, and their relations to catalytic oxidation reactions: I. Structure changes of Mo/SiO₂ with gradual reduction by ethanol*. Journal of Molecular Catalysis A: Chemical, 1999. **142**(2): p. 247-263.
 53. Brookes, C., et al., *The Nature of the Molybdenum Surface in Iron Molybdate. The Active Phase in Selective Methanol Oxidation*. Journal of Physical Chemistry C, 2014. **118**(45): p. 26155-26161.
 54. Trifiro, F., P. Centola, and I. Pasquon, *The role of a metal-oxygen double bond in the activity of molybdates in oxidation reactions*. Journal of Catalysis, 1968. **10**(1): p. 86-88.
 55. Bowker, M., A.A., Brookes, C., Gibson, E., House, M., Wells, P., *Selectivity Determinants for Dual Function catalysts: applied to methanol selective oxidation on iron molybdate* Catalysis Structure Reactivity, 2015.

Chapter 6: Investigating the Redox Nature of FeMo Based Catalysts

Contents

1. Introduction.....	277
2. Experimental.....	279
2.1. Catalyst Reduction.....	279
2.2. Re-oxidation Studies.....	280
2.3. Preparation of MoO _x Supported Catalysts.....	280
3. Results and Discussion	280
3.1. Catalyst Sustainability	280
3.2. Anaerobic Reactivity	284
3.2.1. Fe ₂ (MoO ₄) ₃ vs. MoO ₃	284
3.2.2. 1ML MoO _x /Fe ₂ O ₃ vs. 6ML MoO _x /Fe ₂ O ₃	291
3.3. Investigating Oxygen Lattice Mobility	294
3.4. Supported Mo Catalysts.....	296
3.4.1. Raman	298
3.4.2. XRD	299
3.4.3. SEM	301
3.4.4. BET	303
3.4.5. Catalytic Testing	304
4. Conclusions and Further Work	312
5. References.....	313

1. Introduction

In industry, the catalyst typically contains excess MoO_3 , to replace the eventuality of any lost through volatilisation at reactor hot spots [1, 2]. With this surplus present, catalyst lifetimes are typically between 6 and 12 months, before the catalyst performance is compromised and replacement is required. The proportion of MoO_3 in the overall catalyst composition must be carefully considered (Equations 2-3). Too high, and the rate of its sublimation is enhanced, leading to a fast increase in the pressure drop over the reactor. Too low however, and a rapid deactivation of $\text{Fe}_2(\text{MoO}_4)_3$ occurs (Equation 3). Maintaining the $\text{Fe}_2(\text{MoO}_4)_3$ in its active form is crucial to prolonged performance.

It is known that methanol is capable of reacting through the following oxidative process [3] (Equation 1):



Re-oxidation in excess of MoO_3 :



Re-oxidation in a shortage of MoO_3 :



The mechanism of methanol oxidation to formaldehyde has been discussed (Chapter 5). The redox ability of molybdenum based catalysts is unanimously recognised [1, 4-6], with the oxidation state of the Mo a key contribution in catalyst reactivity. A paper of Bowker *et al.* [7] discusses this in detail. It is recognised that Mo segregates to the surface of iron molybdate catalysts, as proven by STEM and XPS. The active site for the reaction is accepted as Mo(VI), which cycles through Mo(IV) during the reaction. In an additional paper by the same authors, the oxidation of methanol has been measured on MoO_3 and MoO_2 [8]. The properties of the two oxides are interchangeable, depending upon the conditions employed during the reaction. MoO_3 containing Mo(VI), demonstrates high yields of formaldehyde, whilst on MoO_2 this is not the case, establishing a high selectivity to CO. However, it was also discovered that under anaerobic conditions MoO_2 can demonstrate a reactivity akin to MoO_3 at high temperatures above 300°C . Oxygen transport within the lattice becomes significant above 300°C [4, 9], so that formaldehyde production may continue.

Although surface Mo has been isolated as the active species, the majority phase of the industrial catalyst is comprised of $\text{Fe}_2(\text{MoO}_4)_3$. The presence of this iron containing phase is thought to bring multiple benefits, with many theories postulated [10-12]. Firstly it yields a catalyst with a reasonably high surface area, bringing improved overall activity in the oxidative reaction. Secondly, although it cannot compete with MoO_3 , $\text{Fe}_2(\text{MoO}_4)_3$ shows a remarkable selectivity to formaldehyde. Moreover, $\text{Fe}_2(\text{MoO}_4)_3$ is thought to have superior properties such as its bulk lattice oxygen mobility, which allows the catalyst to always ensure sufficient oxygen regeneration to the surface during reaction, maintaining catalyst selectivity. The bulk reduction process of iron molybdate based catalysts has been investigated by Mössbauer [13] measurements on pure $\text{Fe}_2(\text{MoO}_4)_3$. The reduction takes place at temperatures above 230°C ; with the catalyst reducing to $\beta\text{-FeMoO}_4$. The process is shown to be completely reversible under oxygen at temperatures above 270°C , with the catalyst efficiently reinstating its former $\text{Fe}_2(\text{MoO}_4)_3$ structure. Further investigation into the properties in $\text{Fe}_2(\text{MoO}_4)_3$ will be addressed in this chapter, in an attempt to define the role of Fe in the industrially employed catalyst.

In previous chapters it is shown that the reactivity of the catalyst is strongly influenced by the surface structure. With Mo dosed at the surface of Fe_2O_3 , catalytic activity is essentially independent of calcination temperature applied, with all catalysts after a range of thermal treatments demonstrating a common topmost layer denoted MoO_x which highly influences the production of formaldehyde. It could be possible that the Fe phase enables an optimum configuration for the active surface Mo structure.

Given that catalyst performance is strongly influenced by the surface terminating layer, it is important to address this active layer in more detail. However, since the surface layer makes up such a small proportion of the net catalyst composition, and with a limit to the number of surface-specific characterisation techniques, it has been difficult to carry out these investigations.

If the contribution of the surface could be increased through use of a higher surface area support, it may be possible to exploit bulk techniques to expose further information on surface contributions. The choice of support material needs careful consideration. *In situ* Raman studies have been conducted to investigate the function of specific oxide supports including TiO_2 , ZrO_2 , Nb_2O_5 and Al_2O_3 , with various MoO_3 loadings [14]. Whilst the surface molybdenum oxide species were selective to formaldehyde, the oxide support derived additional by-products, including DME for Al_2O_3 and Nb_2O_5 , and methyl formate for ZrO_2 . Titania was relatively inactive. The TOF for the selective oxidation of methanol

varied by a factor of 2-4 with changing Mo surface coverage, and by a factor of ten with changing oxide support. Mo surface structure varied between isolated tetrahedral at low coverages, and polymerised octahedral/tetrahedral at high coverages. The order of magnitude variation in the TOF with varying oxide support was thought to correlate to the reducibility of the support, and it was highlighted that the Mo-O-support bond plays a crucial role in controlling the TOF. Catalyst preparation of supported molybdenum oxide catalysts generally uses the impregnation method, however problems have been recorded due to the lack of reproducibility and discrepancy in Mo dispersion in synthesised catalysts [6, 15].

The final part of this chapter will consider SiC and Al₂O₃ as alternative supports for Mo, in an attempt to heighten the information obtainable from the surface layer, whilst in addition assessing whether Mo forms a similar terminating layer in these catalysts, as it does on Fe₂O₃. It has been discovered that for MoO_x/Fe₂O₃, the MoO_x overlayer demonstrates a good stability even after extensive calcinations at high temperatures (Chapter 4). The stability of these monolayer catalysts will be compared to the stability already observed for bulk catalysts such as MoO₃ and Fe₂(MoO₄)₃ [2, 16].

2. Experimental

Initial catalyst preparation has been performed as in previous chapters, including the synthesis of bulk catalysts with varying Mo:Fe ratios, and catalysts of the type MoO_x/Fe₂O₃ with varying Mo monolayer dosages. Catalyst testing has been performed through TPD and TPPFR as detailed in the experimental section of Chapter 2.

2.1. Catalyst Reduction

Catalysts have been reduced under a flow of MeOH/He, using a small tube furnace fitted with a methanol bubbler prior to the sample bed. Approximately 1 g of catalyst was packed in the quartz tube specifically adapted for the furnace. A steady and continuous flow of He was passed through the methanol bubbler and subsequently over the catalyst bed. The temperature was ramped to 350 °C at a ramp rate of 10 °C min⁻¹, where it was held isothermally for 4 hours. Catalysts showed a clear colour change to black upon reduction.

A second method was adapted to study the reactivity of the catalyst after reduction. Catalysts were reduced in the CATLAB microreactor (See CATLAB set up, Chapter 2, Figure 2), by injecting 1 µl of MeOH into a flow of He over the catalyst bed, every minute for one hour at 350 °C. The reactivity of the catalyst could then be assessed in the Hiden

reactor, without the possibility of catalyst re-oxidation, since the catalyst could remain in the reactor between treatments.

2.2. Re-oxidation Studies

Catalyst re-oxidation was carried out in one of two ways. Firstly, catalysts were re-oxidised in the muffle furnace under static air at 500°C, for 24 hours. Alternatively, 0.5 g of catalyst was re-oxidised in the CATLAB microreactor under a flow of 10% O₂/He for 1 hour at 400°C.

An investigation into the oxygen mobility in bulk catalysts has been studied through exploitation of the oxygen pulsing facility in the CATLB software. Approximately 0.05 g of reduced catalyst was loaded into the microreactor. The catalyst was pre-reduced following the procedure in section 2.1. The catalyst was then exposed to continual oxygen pulses at room temperature and 350°C, with the uptake of oxygen monitored for the individual catalysts.

2.3. Preparation of MoO_x Supported Catalysts

Various supports have been investigated for their effectiveness in the selective oxidation of methanol to formaldehyde.

MoO_x supported on SiC or Al₂O₃ was prepared using the incipient wetness technique. Commercial SiC (Sigma Aldrich) or γ -Al₂O₃ (Sigma Aldrich, <50 nm) was first calcined at 500°C for 3 hours, before dosing with the desired amount of aqueous ammonium heptamolybdate for 1, 3 or 6 MLs of MoO_x. The samples were dried at 120°C for 24 hours, before being calcined at 500°C for a further 24 hours in the muffle furnace.

3. Results and Discussion

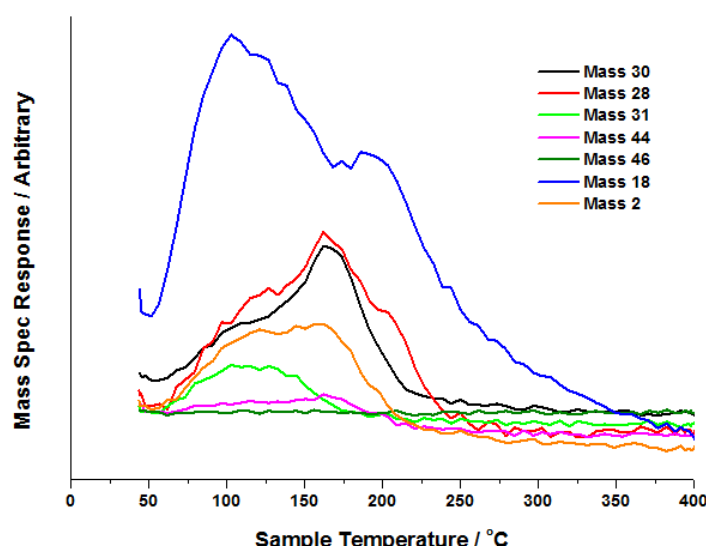
3.1. Catalyst Sustainability

In light of the fact that bulk iron molybdate is acknowledged for its redox nature and long term stability, studies have been performed using continual TPD and TPPFR to assess the catalyst performance with repeated catalytic cycling. Results are detailed in Figures 1-6 for 3ML MoO_x/Fe₂O₃ and bulk Fe₂(MoO₄)₃ respectively.

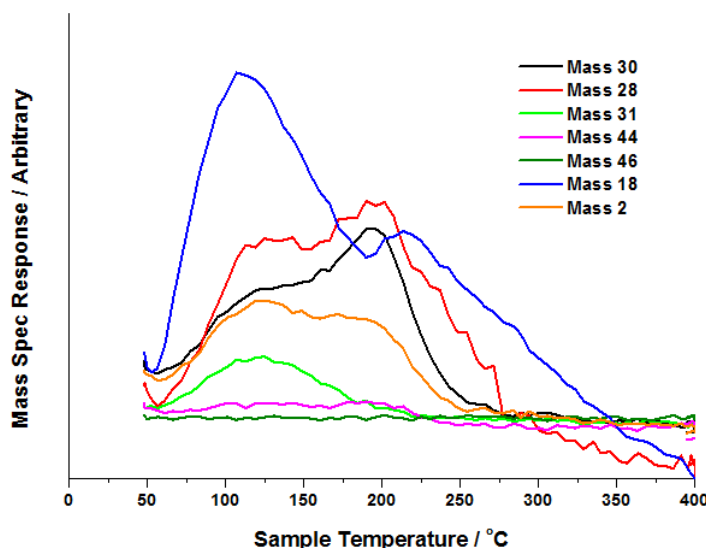
Referring to the 3ML MoO_x/Fe₂O₃ sample, the data after one TPD cycle and after five TPD cycles (Figures 1-2) are well matched in their selectivity, however the temperature of CO (Mass 28) and H₂CO (Mass 30) desorption differ between the two. For the initial TPD,

H₂CO is shown to desorb from the catalyst surface at 165 °C, whilst CO desorbs at 210 °C. In comparison, after five TPD cycles (involving repeated TPD in MeOH/He followed by re-oxidation), there is a shift in the desorption temperatures of these two carbon containing products, with an increase in temperature by approximately 50 °C for both. The catalyst performance after five reaction cycles is akin to that of bulk Fe₂(MoO₄)₃. This would suggest that the catalyst is unstable over time, incurring a chemical change at the surface. It may be that the catalyst is remaining partially reduced from reaction with methanol, and therefore less active.

(1)



(2)



Figures 1-2. After one TPD in MeOH/He (top), and five TPD in MeOH/He (bottom) for 3ML MoO_x/Fe₂O₃. After each TPD cycle the catalyst was re-oxidised via the CATLAB method reported in Section 2.2. Raw data is shown. Mass 30 is indicative of formaldehyde production, Mass 28 for CO, Mass 31 for MeOH, Mass 44 for CO₂, Mass 46 for DME, Mass 18 for water, and Mass 2 for hydrogen.

TPPFR data has been performed pre and post the same cycling process, to support the findings through TPD. Conversion data has been assessed for 3ML MoO_x/Fe₂O₃ (Figure 3). With an increase in the number of catalytic cycles, there is a significant drop in conversion, with the temperature for 50 % conversion rising from 190 °C to 270 °C. This agrees with the TPD data discussed, showing an appreciable deactivation. At the highest temperatures, 100 % conversion is obtained in both cases.

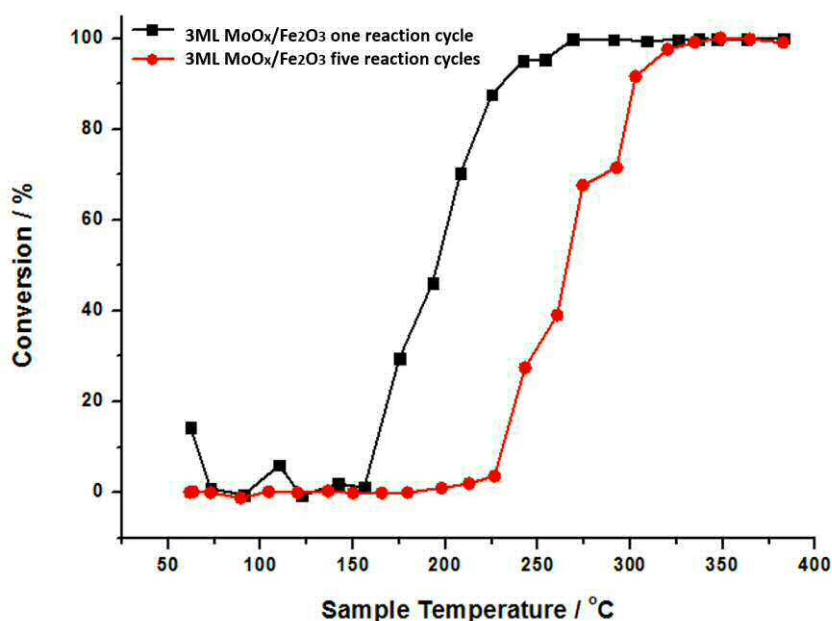
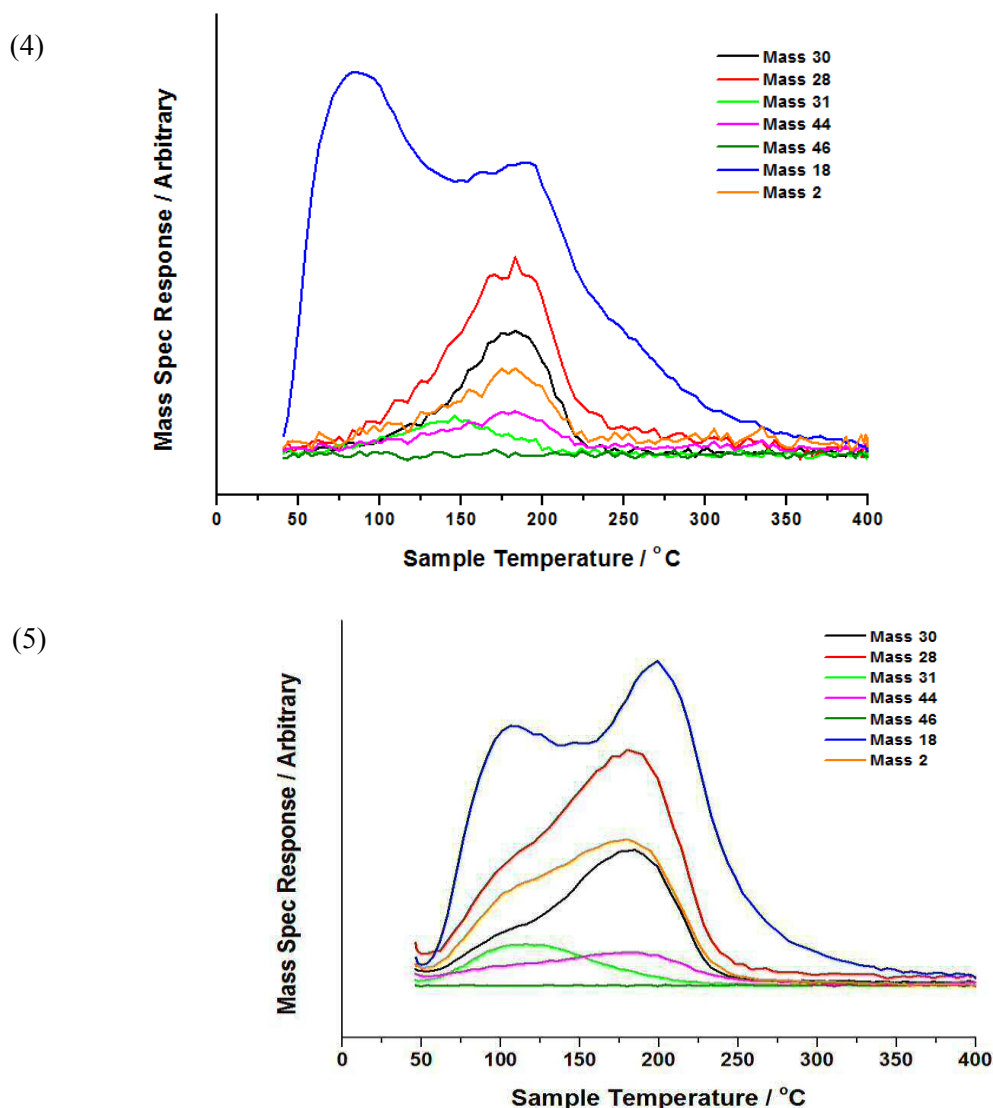


Figure 3. Conversion data for 3ML MoO_x/Fe₂O₃ after one reaction (black), and after five reaction cycles (red) with MeOH/O₂. For the reaction cycling, catalysts were reacted under MeOH, and then re-oxidised via the CATLAB method in Section 2.2.

An identical study has been performed on bulk iron molybdate, with a Mo:Fe ratio of 1.7:1. The TPD data is again consistent in terms of selectivity between the two data sets pre and post five reaction cycles, and in addition for this bulk material, the temperature of formaldehyde desorption is conserved at 190 °C. This proves the stability and consistency of the catalyst, and shows its potential for long term use.



Figures 4-5. After one TPD in MeOH/He (top), and five TPD in MeOH/He (bottom) for bulk iron molybdate Mo:Fe 1.7:1, raw data. After each TPD the catalyst was re-oxidised via the CATLAB method reported in Section 2.2.

TPPFR data was again analysed to assess the effects of repeated catalyst use on the rate of methanol conversion. Only a slight shift in conversion temperature occurs after five reaction cycles, reiterating the ability of the catalyst to maintain its catalytic performance. 50 % conversion occurs at approximately 225°C, below the temperature recorded after five reaction cycles of the 3ML (monolayer) sample. This catalytic behaviour is recognised by many others [2, 17-21]. The bulk material is able to uphold its original performance, showing a more satisfactory performance than the monolayer system after the same treatment. It is shown that $\text{Fe}_2(\text{MoO}_4)_3$ has a greater redox capability than Fe_2O_3 , with a more efficient uptake of oxygen under re-oxidation. This aids the effective and continual redox cycling of active surface Mo, through its variable oxidation states.

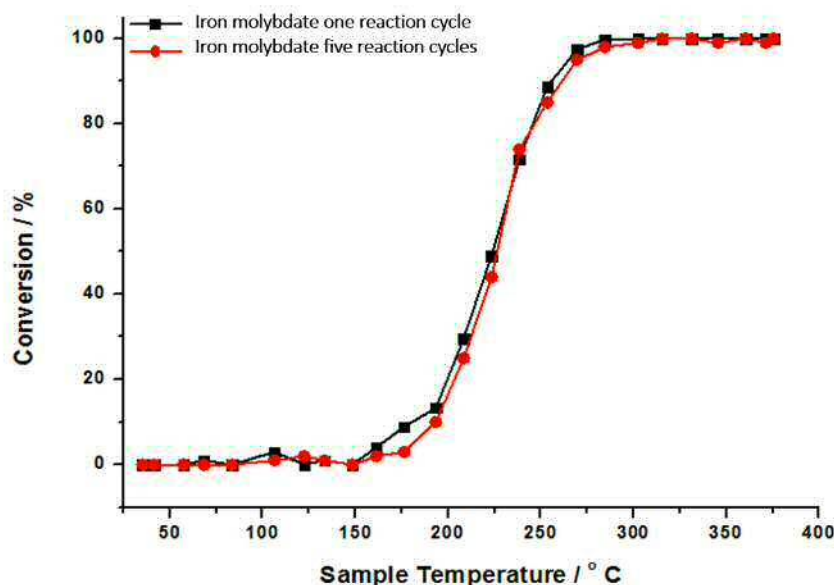


Figure 6. Conversion data for bulk $\text{Fe}_2(\text{MoO}_4)_3$ Mo:Fe 1.7:1, after one reaction cycle (black), and after five reaction cycles (red) in MeOH/ O_2 . For the reaction cycling, catalysts were reacted under MeOH under TPPFR, and then re-oxidised via the CATLAB method in Section 2.2.

3.2. Anaerobic Reactivity

3.2.1. $\text{Fe}_2(\text{MoO}_4)_3$ vs. MoO_3

To investigate the redox potential of $\text{Fe}_2(\text{MoO}_4)_3$ in more detail, MeOH pulsing studies have been executed under anaerobic conditions. Catalysts were subjected to continual MeOH dosing, whilst held isothermally at 350 °C under He. Figures 7-8 display the results of the experiment. After two MeOH pulses (Mass 31) conversion is constant (approximately 90 %), and the selectivity is biased towards formaldehyde and CO as shown through the maintained level of Mass 30 (black) and Mass 28 (red) (It should be noted that Mass 28 for CO has a contribution from Mass 30, and the data presented does not account for this subtraction). It is concluded that oxygen mobility at this temperature is enabled in $\text{Fe}_2(\text{MoO}_4)_3$, especially since the mixed oxide is able to maintain a selectivity to formaldehyde for the duration of the experiment (Figure 7). However, in comparison to aerobic conditions, also produced is a higher yield of CO and the minor product DME. The production of DME normally occurs at much lower temperature. Dehydration is therefore facilitated more easily on the reduced surface. Water occurs in connection with formaldehyde production, and other masses are present as cracking fragmentations. Towards the end of the experiment, a slight rise in the signal for Mass 15/16 is evidence of methane

production, which indicates a reduction to bulk metal. The changes in selectivity are likely caused by the loss of O at the surface, which is not replaced during the pulse duration.

The presence of H₂CO (Mass 30) is indicative of a methoxy intermediate at the surface (Chapter 3). Methoxy has been proven to be present on MoO₃, which delivers 100 % selectivity to formaldehyde. However methanol can react both aerobically and anaerobically in the following way (Equations 4-5):

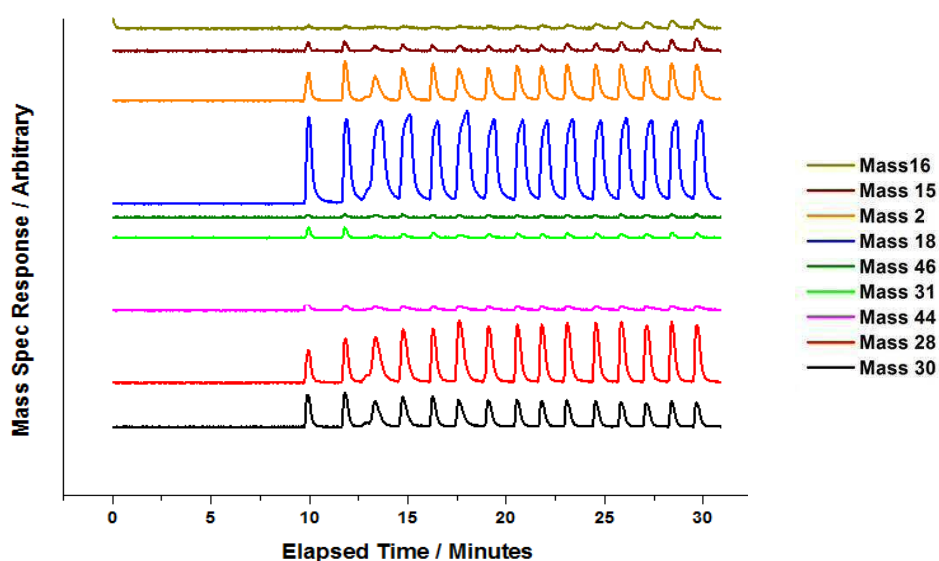


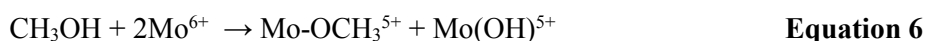
Figure 7. Pulse flow data for Fe₂(MoO₄)₃ Mo:Fe 1.5:1 under anaerobic conditions. MeOH pulsing was continually applied to the catalyst under He at 350 °C. **Order of masses (Top to bottom):** Mass 16, Mass 15, Mass 2, Mass 18, Mass 46, Mass 31, Mass 29, Mass 44, Mass 28, Mass 30, as will be consistent throughout this chapter.

An equivalent pulsing experiment was performed on MoO₃. The catalyst was unable to match the performance of Fe₂(MoO₄)₃, with the conversion of methanol (Mass 31) shown to occur much later. No significant reaction evidences until 25 minutes have elapsed, as shown through the drop in Mass 31 for methanol at this point. The delay in conversion is a result of the sluggish movement of oxygen through MoO₃. In addition, the selectivity of formaldehyde is not maintained for the duration, with a more significant decrease in its production after just 30 minutes, and a simultaneous and greater increase in CO production than for Fe₂(MoO₄)₃. This again implies that bulk oxygen diffusion is hindered for MoO₃, and methanol will react anaerobically as Equation 5. Lattice oxygen is limited, particularly in comparison to Fe₂(MoO₄)₃, suggesting that Fe₂(MoO₄)₃ has properties other than just

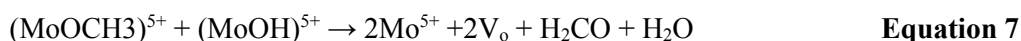
providing an improved activity of the catalyst. This corresponds well with work in the literature [19, 22, 23]. A study by Ressler *et al.* [20] investigates the reduction of MoO₃ in propene, and corresponding re-oxidation of MoO₂ by *in situ* X-ray diffraction (XRD) and X-ray absorption spectroscopy (XAS). The study revealed crucial information regarding solid-state kinetics of the processes, whilst also elucidating the structural changes occurring. It is believed that at temperatures below 600 K, the contribution of oxygen from the MoO₃ bulk is negligible, leaving MoO₂ at the catalyst surface. A paper of Bowker *et al.* contrasts the behaviour of MoO₃ and MoO₂, with the latter showing an overall worse selectivity with a significantly higher proportion of produced CO. It is not until 700 K that oxygen vacancy diffusion in the bulk is enough to allow for a slow-moving redox mechanism to occur. Partially reduced MoO₃ occurs in the process. Above 700 K it is believed that fast oxygen diffusion is permitting the participation of a considerable amount of the lattice oxygen.

It should be noted that with each methanol injection, the surface is becoming more reduced when performed anaerobically. Therefore the production of non-selective products is feasible through alternative mechanisms. TPD of MoO₂ and FeMoO₄ have shown a strong selectivity to CO, a result of reduced Mo(IV) species created [7]. In the experiments described for Fe₂(MoO₄)₃ (Figure 7), above 250 °C, bulk oxygen diffuses to the surface to become available for reaction. For this reason, the data shown in Figure 7 shows retained formaldehyde production. The CO produced may be due to a partially reduced surface containing Mo(IV) or Mo(V). It is imperative for Mo to exist in its Mo(VI) oxidation state. High oxidation states maintain a highly selective catalyst.

The dissociation of methanol requires acid-base catalysis at the acidic proton of the methanol molecule. During the reaction with methanol, the binding initially occurs by interaction of the methanol non-bonding lone pairs with the cation sites. Surface methoxy binds to the Mo site (Equation 6) [8]:



Formaldehyde is then produced through dehydrogenation in the following way (Equation 7):



The molybdenum is then ordinarily re-oxidised (Equation 8) through gas phase oxygen (MVK):



The sample therefore upholds its selective Mo (VI) state.

However, under anaerobic conditions, the surface is further reduced by methanol (Equation 9), to Mo (IV):



The surface reactivity increases, being able to abstract further hydrogen atoms from the methoxy group to yield CO (Equation 10):



Liberated hydrogen reacts with surface oxygen to produce H_2O , and consequently leaves further vacancies. It is therefore imperative that the surface is in the selective Mo(VI) state, cycling rapidly between Mo(V) and Mo(VI). Reduced Mo is ordinarily short lived, as demonstrated in Chapter 5.

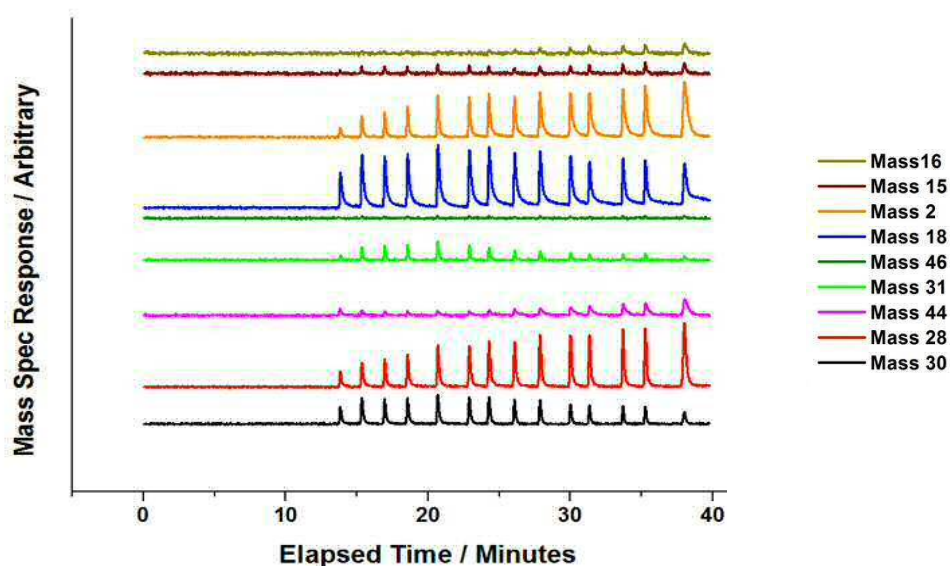


Figure 8. Pulse flow data for MoO_3 under anaerobic conditions at 350°C , experimental as Figure 7. Key to the RHS will be used also in the following figures.

Analogous studies were carried out to investigate the temperature at which bulk oxygen becomes available for reaction, specifically for $\text{Fe}_2(\text{MoO}_4)_3$. Isothermal reductions were carried out under the following temperatures regimes: 175, 200, 250, 300 and 350 °C, (Figures 9-13) pulsing MeOH/He at regular time intervals over $\text{Fe}_2(\text{MoO}_4)_3$.

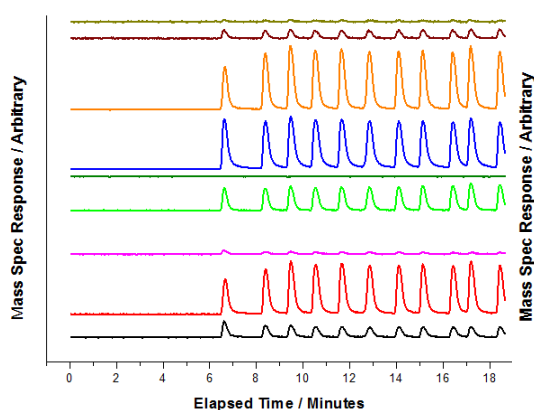


Figure 9. Isothermal reduction 175 °C.

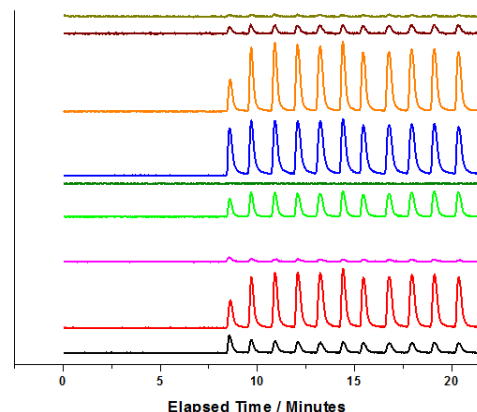


Figure 10. Isothermal reduction 200 °C.

Figures 9-13: MeOH was continually pulsed under He over the catalyst bed ($\text{Fe}_2(\text{MoO}_4)_3$), and the products of the reaction monitored under isothermal conditions using mass spectrometry. Various temperatures were trialled.

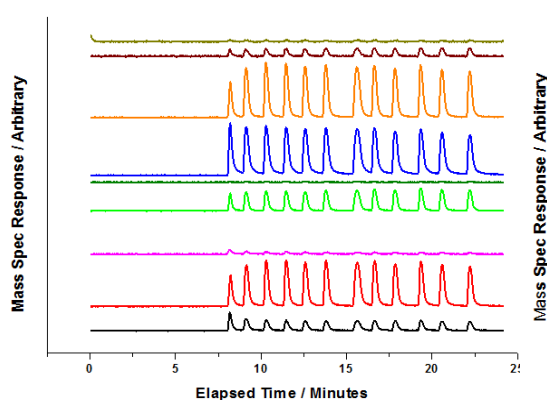


Figure 11. Isothermal reduction 250 °C.

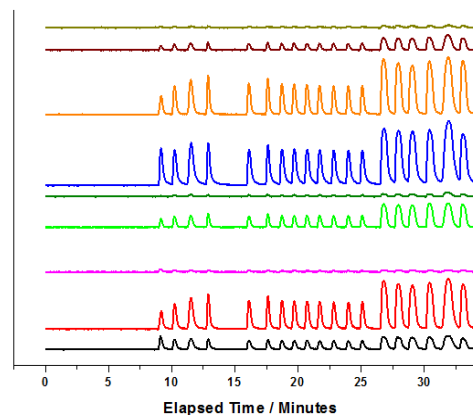


Figure 12. Isothermal reduction 300 °C.

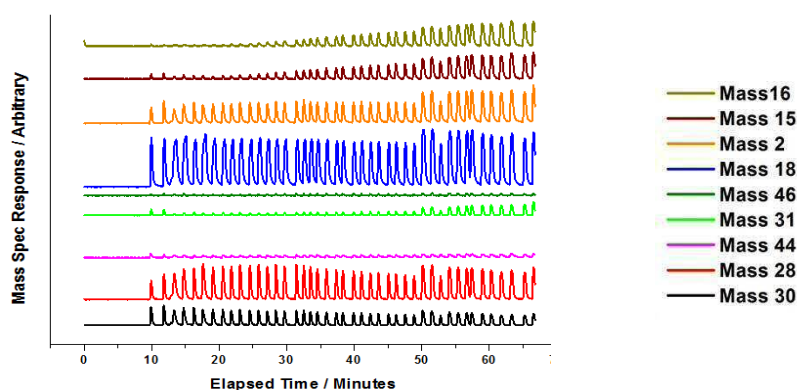


Figure 13. Isothermal reduction 350 °C. Post 50 minutes, injecting sizes were increased from 1 to 2 μl , to encourage reduction of the sample.

Inspecting the data, MeOH conversion is hindered below 300 °C, as shown through the sustained signal for Mass 31, MeOH, throughout the course of the temperatures investigated. Any formaldehyde produced is short lived, with the aldehyde evident for just one or two pulses of methanol. After this, the surface of the catalyst becomes reduced, and can no longer perform to yield selective products. The majority of selectivity is towards CO, implying the catalyst is dehydrogenating the methanol, also inferred by the increase in H_2 production. Oxygen cannot transfer through the bulk.

By 350 °C however, a vast improvement in conversion of methanol occurs, rising to 90 %. Here, bulk lattice oxygen now becomes available for the selective oxidative reaction to formaldehyde, as highlighted by the sustained production of formaldehyde (Mass 30, Black) and significant loss of methanol signal (Mass 31, Light Green) at this temperature. As the oxygen supply increases at higher temperature, the bulk lattice becomes reduced. The formaldehyde produced therefore starts to subside post 50 minutes, accompanied by a rise in CO (Mass 28) as the surface begins to reduce to Mo(IV). At this point the formation of reduced FeMoO_4 is believed to occur, as well as the possibility of Mo_4O_{11} , which may form from the matter ejected from the ferric molybdate lattice in forming ferrous molybdate. However some propose [24], that Mo_4O_{11} is only formed as an intermediate material formed by reaction between MoO_3 and MoO_2 when Mo is present in excess. Formaldehyde is purely a cracking fragmentation of methanol for the lower temperatures, whereas at 350 °C, this can no longer be the case as the methanol response is very small, whilst the response for formaldehyde (Mass 30) is substantially larger. A rise in DME selectivity is also noted above 300 °C, with also an increase in water production (Mass 18). The formation of water implies that the surface can still enable selective oxidation to formaldehyde, coming from the lattice oxygen at the surface. A gain in DME production is derived from Lewis acid sites with redox properties.

The work described agrees well with opinions Trifiro *et al.*, who highlight three different transformations in this catalyst with increasing calcination temperature. The first change in catalyst properties was not found until 350 °C, characterised by the start of bulk diffusion, accompanied by a noticeable change in the electric conductivity and higher selectivity to CO [25]. A similar pulsing study of House *et al.* calculates the oxygen loss from the catalyst from the product distribution [26]. The loss was strongly dependent on the reduction temperature employed. Below 350 °C, 21 % oxygen loss resulted, reducing to MoO₂ and FeMoO₄. However at 350 °C, a considerable increase in oxygen loss occurred rising to 49 %. Other reduced phases are presumed to occur, but the authors do not identify these, and claim them to be present in small amounts or as an amorphous state.

After the reduction process, the catalyst was inspected. An obvious colour change was noted from the original yellow to very dark brown in colour, a sign of reduction. This colour change is not observed under aerobic conditions, which implies the catalyst is changing dramatically in some form. This has been seen elsewhere [27]. XPS studies have shown the presence of Mo(IV) and Mo(V) at the surface after reduction [2], notably due to the rapid solid-state oxygen supply at elevated temperatures.

Bowker *et al.* [7] present a paper which discusses the mechanism of methanol oxidation in more detail, specifically clarifying the roles of the different types of oxygen present, including lattice, surface bridging and terminal oxygen species. When run under anaerobic conditions, Fe₂(MoO₄)₃ is shown to form lower oxidation states if the pulsing experiment is continued, significantly reducing the bulk. As the reduction process continues, selectivity is vastly compromised. Mars and Krevelen only consider the reaction in terms of the surface oxygen [28], without contemplating bulk oxygen migration to the surface. Bowker and co-workers therefore suggest an adapted mechanism, referred to as the ‘Extended Mars-van Krevelen kinetics’, prevalent under oxygen deficient environments. If the re-oxidation process from the gas phase is limited during the reaction, it is shown the catalyst is self-sufficient in restoring its original Mo(VI) oxidation state, thus enabling continued selectivity to formaldehyde. This is a remarkable feature of the mixed phase oxide, adding to its repertoire of already suggested benefits: including its increased activity, and possibility that it aids in nurturing the correct surface termination geometry of segregated Mo.

Similar isothermal investigations have also been carried out on MoO₃, produced in-house with a higher surface area of 6 m²g⁻¹. A successive reduction process was carried out as aforementioned, from 175 to 350 °C (Appendix A13).

As in the case of Fe₂(MoO₄)₃, reaction to formaldehyde only occurs from 350 °C, however the formaldehyde produced (Mass 30) is shorter lived, with a 50 % decrease in its

production within 10 minutes of beginning the pulsing regime. At this point CO production dominates (Mass 28). CO₂ (Mass 44) and CH₄ (Mass 15/16) are also produced after 10 minutes of pulsing along with the already mentioned CO production (Appendix A13). This would imply that the oxygen within bulk MoO₃ is less mobile, therefore making it less available at the surface to maintain formaldehyde production. It could be that a higher temperature is required for oxygen mobility to ensue, however at such elevated temperatures any formaldehyde produced could further react or breakdown. The movement of oxygen from bulk to surface cannot be maintained, unlike for Fe₂(MoO₄)₃ where it is becoming apparent that the combination of Fe is aiding oxygen mobility in some form. H₂O and CO₂ are still produced towards the end of the study, implying that the reduction process is still proceeding, as lattice oxygen continues to be transferred to the surface to carry out the reaction.

Isotopic exchange experiments using C¹⁸O₂ have shown the basal (010) face of MoO₃ to be a more efficient oxygen exchanger at 350 °C than samples with lateral faces (truncated (110), (120) and (130) planes) [29]. The more facile oxygen exchange at the (010) face, is due to the presence of oxygen vacancies, which cannot be filled by oxygen from the bulk. At very high temperatures (above 500 °C), continuous oxygen exchange occurs via two pathways: firstly a fast surface oxygen exchange, and secondly the migration of oxygen from the lateral towards basal faces and/or slower migration of oxygen from the bulk to the lateral faces. This latter process hinders the catalyst performance when run in anaerobic conditions.

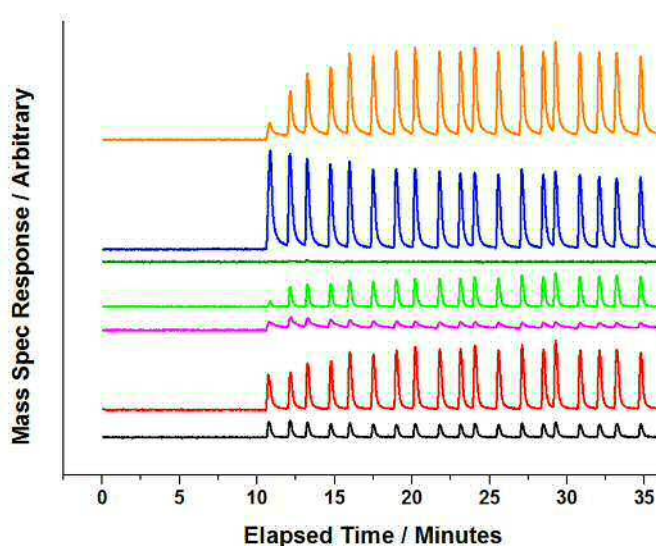
3.2.2. 1ML MoO_x/Fe₂O₃ vs. 6ML MoO_x/Fe₂O₃

Corresponding studies under anaerobic conditions were carried out on the monolayer systems: being 1 and 6ML MoO_x/Fe₂O₃. At 350 °C, it was found that the 6ML MoO_x/Fe₂O₃ catalyst was able to maintain its activity and selectivity of methanol to formaldehyde for longer than the 1ML equivalent loading (Figures 14-16). For 1ML MoO_x/Fe₂O₃, after just 1 MeOH pulse at 350 °C, MeOH (Mass 31) reaction to H₂CO (Mass 30) ceases, with the resultant Mass 30 signal a consequence of MeOH fragmentation. Figure 16 represents the data for formaldehyde production more clearly. In addition to formaldehyde loss, a decrease in MeOH conversion occurs, shown by the rise in Mass 31 signal (Figure 14). However some conversion does ensue, with a rise in CO (Mass 28) and H₂ (Mass 2) production. For the 6ML catalyst, the additional Fe₂(MoO₄)₃ below the active surface layer appears to evoke an increase in the lifetime of formaldehyde production, with methanol conversion to formaldehyde continuing for 4-5 injections. This would support the redox nature of iron molybdate already reported. For 6ML's, the catalyst has been shown through XANES

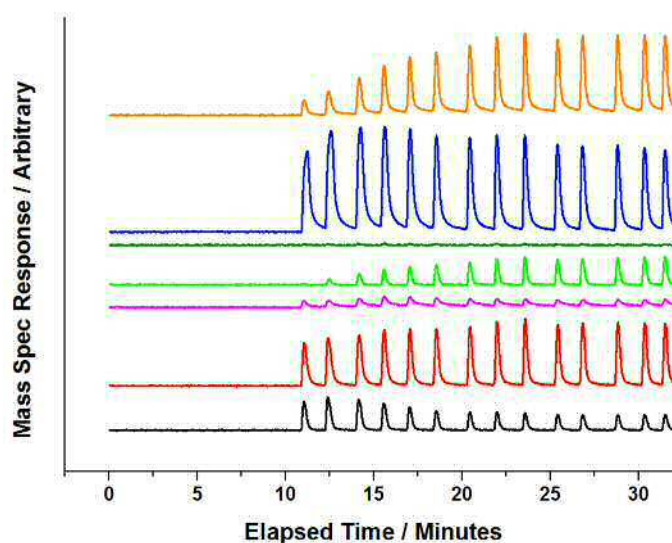
analysis to be comprised of Mo present as 1ML of amorphous MoO_x on 5ML's of $\text{Fe}_2(\text{MoO}_4)_3$ when calcined at 500°C (Chapter 4). These under layers appear to enable a prolonged performance of the catalyst. For the 1ML $\text{MoO}_x/\text{Fe}_2\text{O}_3$ catalyst, the Mo is anchored directly to Fe_2O_3 , and it would appear that this oxide is unable to provide bulk lattice oxygen in the same way under anaerobic conditions.

To summarise, the presence of $\text{Fe}_2(\text{MoO}_4)_3$ appears crucial for catalyst selectivity. It is shown that with just 5 monolayer equivalents of this mixed phase oxide at the surface, the reactivity can be substantially improved, showing the potential benefits of using this mixed oxide phase as a bulk catalyst. However, due to the low concentrations of this phase in these monolayer systems compared to bulk $\text{Fe}_2(\text{MoO}_4)_3$ materials, it is unlikely that they are able to perform in the long term.

(14)



(15)



Figures 14-15. Isothermal MeOH/He pulsing in anaerobic conditions at 350 ° C, for 1ML MoO_x/Fe₂O₃ (Previous) and 6ML MoO_x/Fe₂O₃ (Above). **Order of Masses** Orange= Mass 2, Blue= Mass 18, Dark Green= Mass 46, Light Green= Mass 31, Pink= Mass 44, Red= Mass 28, Black= Mass 30. Raw data is shown. Mass 30 is indicative of formaldehyde production, Mass 28 for CO, Mass 31 for MeOH, Mass 44 for CO₂, Mass 46 for DME, Mass 18 for water, and Mass 2 for hydrogen.

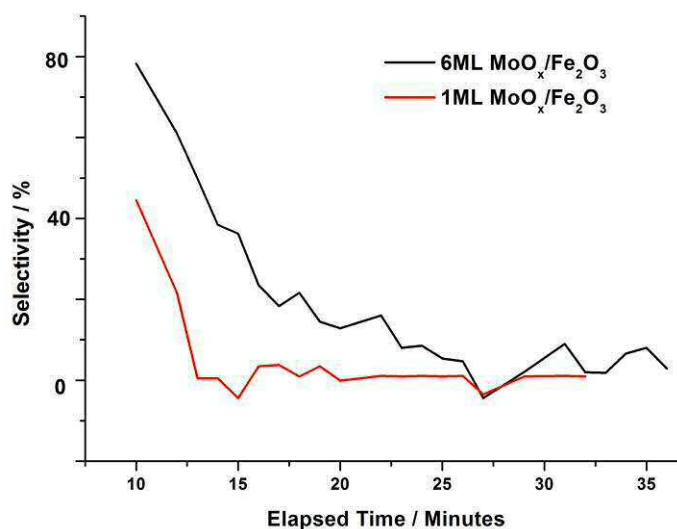


Figure 16. Selectivity to formaldehyde under isothermal MeOH pulsing in He at 350 ° C for 1 (red) and 6 (black) ML's MoO_x/Fe₂O₃. Selectivity to formaldehyde is shown to maintain for longer for the higher monolayer loading.

3.3. Investigating Oxygen Lattice Mobility

To elaborate further on this bulk to surface phenomenon, the oxygen lattice mobility has been investigated for $\text{Fe}_2(\text{MoO}_4)_3$ and MoO_3 (produced in-house, with a surface area equivalent to that of $\text{Fe}_2(\text{MoO}_4)_3$) (Figure 17-18). A relative comparison could not be made to Fe_2O_3 , due to the significantly increased surface area of this material, which would inevitably result in a greater uptake of oxygen. Following reduction in MeOH/He , catalysts were subjected to pulses of 10 % O_2/He every 2 minutes at 350°C , through use of the pulsing facility on the CATLAB software. It is shown that for $\text{Fe}_2(\text{MoO}_4)_3$ (Figure 17), it is not until approximately 60 minutes into stage one of the pulsing regime, that the Mass 32 (oxygen) signal begins to appear and rise. Saturation of oxygen is not reached until 180 minutes, as shown through the consistency in peak area after this time.

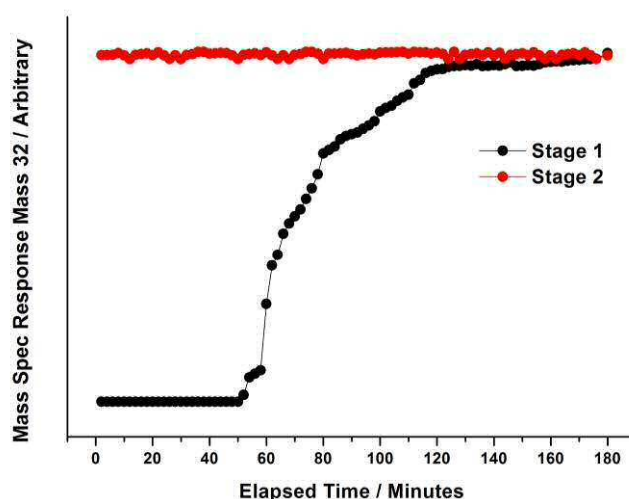
In an equivalent study on MoO_3 , (Figure 18), a response for Mass 32 is seen after just 20 minutes into stage one of the pulsing regime, with a sharp rise from 40 minutes. The catalyst becomes fully saturated with oxygen after just 120 minutes, with no further uptake from this point.

From these pulsing studies, it is revealed that $\text{Fe}_2(\text{MoO}_4)_3$ takes up more oxygen than MoO_3 , implying that the catalyst was more reduced under the same reduction regime. This therefore infers a better redox active catalyst. The study compliments well, the reactivity data for the two catalysts. Under TPPFR with MeOH/O_2 , it is shown (Chapter 3), that surface oxygen is more readily removed from $\text{Fe}_2(\text{MoO}_4)_3$, demonstrated through the lowered temperature of conversion and formaldehyde production for this oxide. The catalyst is able to give up its surface oxygen more easily due to its more reducible nature. Previous work within this chapter has also demonstrated that for the mixed phase oxide, bulk lattice becomes readily available at 350°C , when the reaction in methanol is performed anaerobically. Methanol is able to convert to formaldehyde (Mass 30) for a sustained period of time, with only a slight drop in selectivity post 50 minutes (Figure 7). For MoO_3 , reaction to formaldehyde also does not occur until 350°C anaerobically, however, the formaldehyde produced (Mass 30) is much shorter lived with a 50 % decrease in its production within 10 minutes of beginning the pulsing (Figure 8). The oxygen within the bulk is far less mobile in this catalyst, enforcing the idea that the catalyst cannot perform with the same redox nature as shown for $\text{Fe}_2(\text{MoO}_4)_3$. The ease of reducibility has been shown by others to be in the order $\text{Fe}_2\text{O}_3 > \text{Fe}_2(\text{MoO}_4)_3 > \text{MoO}_3$ [16], suggesting that the mobility of the oxygen ions within the oxides follows the same order with the highest mobility in Fe_2O_3 and lowest in MoO_3 .

In summary of the work highlighted, it has been possible to gain insights into the process of oxygen removal and reduction in $\text{Fe}_2(\text{MoO}_4)_3$. The catalyst used industrially is commonly

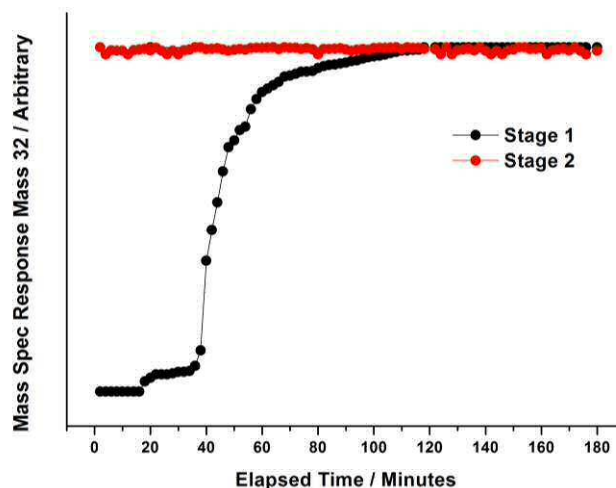
described as a composition of bulk $\text{Fe}_2(\text{MoO}_4)_3$ with an excess of MoO_3 [10, 30]. Mo is shown frequently to be dominating the surface region, and the question challenged is: what is the exact role of $\text{Fe}_2(\text{MoO}_4)_3$?

A clear role is in providing an improvement in the overall surface area of the catalyst, as already seen in Chapter 3 and elsewhere. A further property of the mixed oxide is proven here to be its high redox ability. Large amounts of oxygen are readily removed from the catalyst sample when reacted anaerobically with methanol above 250°C , as lattice oxygen becomes readily available for reaction (with reduction at low temperatures (under 250°C), conversion of the catalyst is low due to the loss surface oxygen which cannot be replaced with oxygen from the bulk). Results enforce the opinion that oxygen levels must be maintained along the length of the catalyst bed, especially in industry, to preserve formaldehyde production. Studies imply that in comparison to MoO_3 , the combination of Mo and Fe in the catalyst appears to enable an efficient diffusion of oxygen from the lattice to the surface. Diffusion is only sluggishly followed in MoO_3 [31]. That stated, it should be noted that although the diffusion of bulk oxygen can maintain catalyst activity, the selectivity will readily diminish, due to a partial reduction of the surface. This enforces the importance of high oxidation states at the surface. The oxidation state of an oxide catalyst is a crucial factor in the oxidation reaction of methanol. With a low oxidation state (Mo(IV)), this leaves a catalyst with less terminal oxygen, driving unselective reactions. Terminal methoxy groups on the surface are more reactive and responsible for terminal methoxy conversion to formaldehyde.



Figures 17. Oxygen pulsing study on reduced $\text{Fe}_2(\text{MoO}_4)_3$ at 350°C , Stages 1-2.

Catalysts were subjected to a 10 % O_2/He pulses with a known sample loop volume every two minutes. The uptake of oxygen can be monitored through the change in peak integral of Mass 32.



Figures 18. Oxygen pulsing study on reduced MoO_3 at 350°C , Stages 1-2 (Studies as for $\text{Fe}_2(\text{MoO}_4)_3$ Figure 17).

3.4. Supported Mo Catalysts

It has been highlighted that Fe_2O_3 has frequently been used as a support, due to its high surface area and therefore ability to bring improvement in the activity of supported molybdenum [12, 23, 32, 33]. However, the support itself is deemed detrimental to catalyst performance, leading to combustion products of methanol. It has been shown in Chapters 4 and 5, that when dosing Mo at the surface of Fe_2O_3 , it is imperative that there are no Fe sites left exposed to incoming methanol adsorbents, since the consequence of this will be an increased selectivity to CO and CO_2 by-product formation. Lower surface area $\text{Fe}_2(\text{MoO}_4)_3$ however, demonstrates a good selectivity, whilst also possessing superior properties such as its efficient lattice oxygen mobility, therefore making it an obvious choice for a catalyst with long term stability.

If it were possible to combine these two properties, that is incorporating a high surface area with sustained selectivity, it may be possible to create a catalyst with optimum performance. Two supports have been investigated; SiC and $\gamma\text{-Al}_2\text{O}_3$.

Al_2O_3 is commonly exploited in the literature due to its significantly high surface area, being widely used as a catalyst support for many industrial applications [34-37]. Its largest scale application is in the Claus process, which converts hydrogen sulfide waste gases into elemental sulphur [38]. Another primary use is in the dehydration of alcohols to alkenes. Also referred to as alumina, the most common existing polymorph exists as $\alpha\text{-Al}_2\text{O}_3$.

α - Al_2O_3 and α - Fe_2O_3 share the corundum crystal structure, which could result in a similar binding to Mo when dosing ammonium heptamolybdate onto these surfaces.

SiC is appreciated for its inert nature, which could prove useful in acting as a neutral support for Mo. SiC exists in many crystalline forms with slight variations, or polytypes. α -SiC is the most common polymorph, presenting a hexagonal crystal structure, and is the one available to use in the laboratory. There are several advantages associated with the use of SiC; it has a high resistance to oxidation, as well a high surface area, especially when synthesising the β -SiC form. For this reason it is popularly used as a heterogeneous support for the oxidation of hydrocarbons.

The section herein will investigate the use of these two supports as a foundation for Mo doping, including characterisation and testing. An interesting observation has been made by Briand *et al.* [39] when comparing the performance of bulk versus monolayer catalysts, based on methanol TOF's. Using methanol chemisorption enables the quantification of surface active sites and the calculation of the activity per surface active site. Specifically, the performance of 18 w/t % $\text{MoO}_3/\text{Al}_2\text{O}_3$ has been compared to $\text{Al}_2(\text{MoO}_4)_3$, with a surprising similarity between the TOF of the bulk and supported Mo oxide catalysts. This infers a similar surface composition between the two materials, however the structure of the surface was not identified itself. If a lower w/t % of Mo could be dosed onto the support and perform in the same way, it would enable the production of more economically viable materials, since the costs of Mo are very high.

3.4.1. Raman

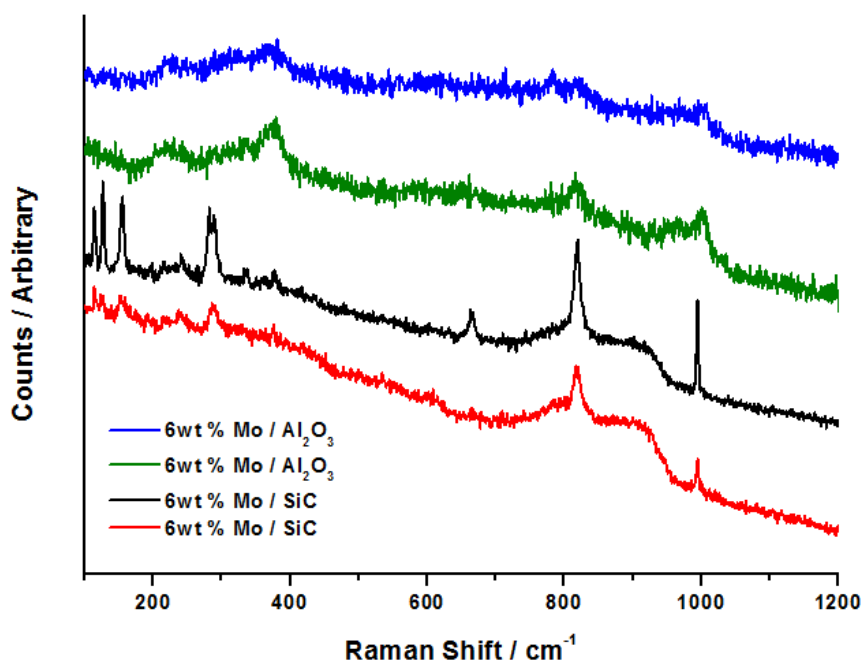


Figure 19. Raman spectra for 6 w/t % of Mo dosed onto Al_2O_3 and SiC, prepared through incipient wetness impregnation of AHM (ammonium heptamolybdate) and calcination at 500°C . Mapping was performed to assess the homogeneity of the sample. Two spectra are shown for each Mo dosed surface.

Initial characterisation involved Raman spectroscopy. To exploit the use of Raman to its full potential, 6 w/t % Mo was investigated for each support, since this would maximise the Raman signal obtained from the sample.

With 6 w/t % of Mo dosed, the SiC catalyst clearly shows a set of strong and sharp bands at 996 , 820 and 667 cm^{-1} (Figure 19, Black Line), indicative of crystalline MoO_3 [40]. Due to their sharp nature, this infers that a significant amount of Mo is not well dispersed on the support, and instead is present as segregated clusters of MoO_3 with bulk crystalline properties. Results were not conclusive across a range of different areas however, demonstrating an inhomogeneous nature within the material. The broad band centred at approximately 900 cm^{-1} is typical for surface polymolybdates [41], so may indicate the presence of monolayer species on the support, in addition to segregates of MoO_3 .

The Raman spectra for supported $\text{Mo}/\text{Al}_2\text{O}_3$ ($\gamma\text{-Al}_2\text{O}_3$) are also shown in Figure 19. Raman mapping evidenced that in the majority of cases the spectrum was as in the blue spectrum, featuring broad bands centred around 800 and 1000 cm^{-1} . The band at approximately 1000 cm^{-1} is characteristic of a $\text{Mo}=\text{O}_t$ stretching mode in dehydrated

polymolybdate phases. However, bands for MoO_3 also featured (green line) at 820 and 990 cm^{-1} in a few cases [42]. The broad nature of the majority of the bands imply that the Mo is far more dispersed across this oxide support, compared to SiC which unanimously showed the presence of MoO_3 crystallites. With the presence of MoO_3 occasionally present, it could be that MoO_3 is initially formed, but then converts into smaller Mo clusters or dispersed Mo species across the surface of the alumina support. Raman spectroscopy indicates that the interaction of Mo species are higher on $\gamma\text{-Al}_2\text{O}_3$ than SiC, shown by the more dispersed nature on Al_2O_3 . This can be attributed to the very different surface properties of the two support materials. Bergwerff and co-workers [43] have applied time resolved Raman spectroscopy to study the preparation of shaped $\text{Mo}/\text{Al}_2\text{O}_3$ catalysts. After impregnation of AHM, a strong interaction between $\text{Mo}_7\text{O}_{24}^{6-}$ and Al_2O_3 results in a slow transport of the Mo complex through the support to form $\text{Al}(\text{OH})_6\text{Mo}_6\text{O}_{18}^{3-}$ at the outer surface. It has not been possible to identify this phase through Raman spectroscopy.

3.4.2. XRD

It has been shown elsewhere (Chapter 4, Section 3.4) that it is possible to detect Mo oxide present at just 6 w/t % on the surface of Fe_2O_3 through XRD. For 6 ML $\text{MoO}_x/\text{Fe}_2\text{O}_3$, this co-incidentally corresponds to approximately 6 w/t % total Mo dosing, as proven through initial calculations (Appendix A14). A calcination process between $120\text{-}600^\circ\text{C}$ brings significant changes in the Mo structure, forming MoO_3 at 300°C , which converts to $\text{Fe}_2(\text{MoO}_4)_3$ when exposed at the higher calcination treatments.

XRD has been executed for 6 w/t % MoO_x on the surfaces of both Al_2O_3 and SiC with the result displayed in Figure 20.

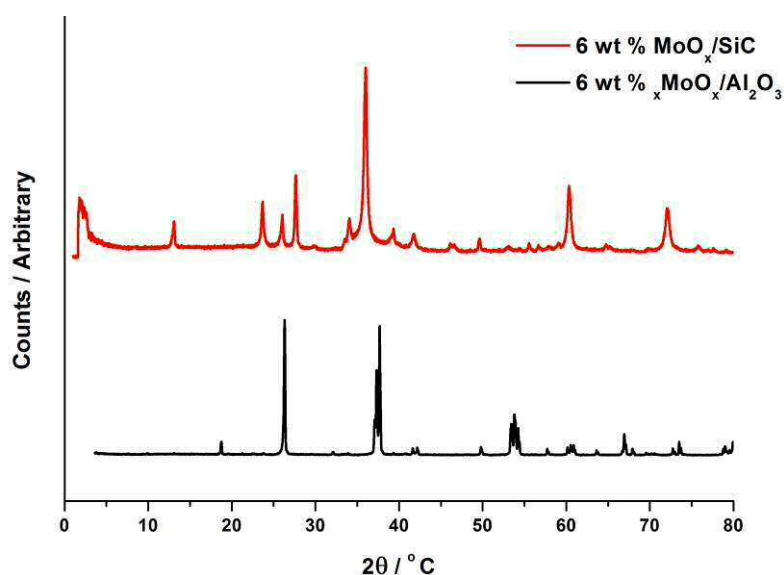


Figure 20. XRD for 6 w/t % of Mo dosed onto SiC (Red) $\gamma\text{-Al}_2\text{O}_3$ (Black), prepared through incipient wetness impregnation of AHM (ammonium heptamolybdate) and calcination to 500°C .

For the 6 w/t % $\text{MoO}_x/\text{Al}_2\text{O}_3$ catalyst calcined at 500°C , the pattern shows several well-defined peaks located at 18° , 27° , 37° , 38° , 54° , and $67^\circ 2\theta$. Of these, the peaks at 18° , 37° , 39° and $67^\circ 2\theta$ can be indexed to the (111), (311), (222) and (440) planes in $\gamma\text{-Al}_2\text{O}_3$ respectively [44, 45]. Other peaks are also present for $\alpha\text{-Al}_2\text{O}_3$, specifically the peaks at 26° , 42° and $54^\circ 2\theta$ corresponding to the (012), (113) and (024) planes respectively [46]. This would imply that the sample in-house is not pure, and contains a mixture of the two oxide phases. It is not possible that alumina phase transformations have occurred, since a temperature of over 1000°C is required to induce a phase change from γ to $\alpha\text{-Al}_2\text{O}_3$ [47]. Prior to performing XRD, the sample was calcined at 500°C . This rules out the possibility of alumina hydrate formation, $\text{AlO}(\text{OH})$, caused by trapped water or surface OH groups.

There are no peaks related to either MoO_3 or $\text{Al}_2(\text{MoO}_4)_3$, implying that surface Mo has formed and that the bulk support does not form the mixed metal molybdate at high temperatures ($500\text{--}600^\circ\text{C}$), as it does for $\text{MoO}_x/\text{Fe}_2\text{O}_3$. This observation is in agreement with the opinions of McMillan *et al.* [48], who show $\text{Al}_2(\text{MoO}_4)_3$ is only formed at high MoO_3 loadings and calcination temperatures above 600°C . However, the results are contrary to the opinions of Rajagopal *et al.* [49], who report the formation of $\text{Al}_2(\text{MoO}_4)_3$ at relatively low loading of Mo on silica-aluminas, when calcined at only 500°C . It has been reported that the preparation of supported MO's on Al_2O_3 is crucial, with Okamoto [50] demonstrating a sensitivity towards surface area of alumina, volume of the impregnation solution, drying process, pH of the impregnation solution, and calcination conditions. This could explain the discrepancy in these findings. The Mo present cannot be

deduced, however for Al_2O_3 (surface area $>90 \text{ m}^2\text{g}^{-1}$), 6 w/t % of Mo corresponds to approximately 1.5 monolayers of Mo dosed at the surface, as deciphered through theoretical calculations. This Mo may be well dispersed or existing as an amorphous overlayer, unable to be detected through this diffraction technique which relies heavily on long range order. It is observed through SEM mapping (Figures 21-25 following section), that molybdenum disperses homogeneously on alumina, and therefore the formation of an amorphous overlayer appears likely. If the Mo is well dispersed across the surface, it is anticipated that the catalyst may be able to perform well in the selective oxidation of methanol, due to the high surface area of the support yielding a very active catalyst. Since Al_2O_3 is such an acidic support, it must be adequately covered with Mo in order to prevent poor selectivity.

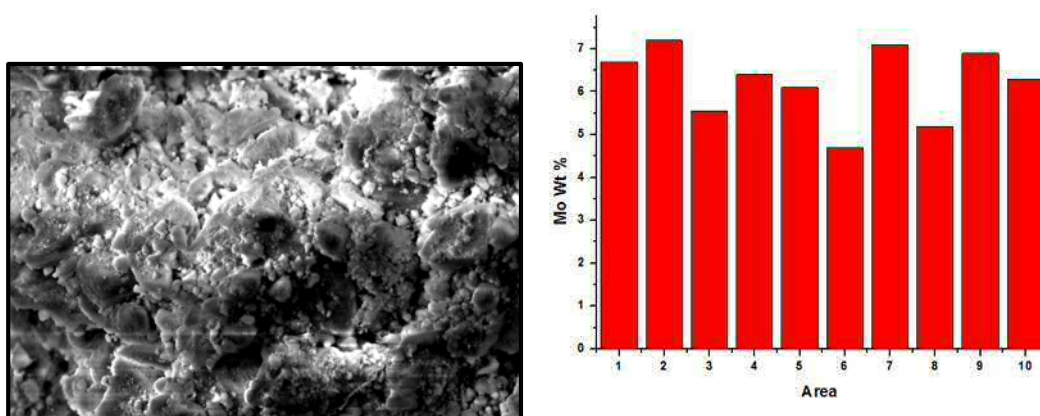
For SiC doped Mo, the calcined catalyst shows a set of strong peaks suggestive of MoO_3 formation at $12.7, 23.3, 25.5, 27.3, 33.7$ and $49.2^\circ 2\theta$, agreeing with Raman spectroscopy showing that the MoO_3 is not well dispersed on the support, and instead present as clusters of MoO_3 . This might be expected due to the inert nature of the support, and has been commonly observed elsewhere [51, 52]. In addition to peaks indexed to MoO_3 , there is also a significant peak for SiC, present at $36^\circ 2\theta$, which dominates the spectrum. The general broad nature of the peaks could be a result of a reduction in the crystallite size as well as the microstrain induced in powder particles [53]. It must be remembered that the area of the SiC is significantly lower than that of alumina, so therefore for the same w/t % of Mo, this will correspond to a greater monolayer coverage of Mo at the surface.

Unfortunately, with the likeliness that the majority of Mo is present as clusters on the surface, (albeit also the presence of polymeric species seen through Raman spectroscopy), this would bring no specific surface area increase in the Mo at the surface, as might be hoped. There are however other benefits that SiC can bring. Nano-silicon carbide has been applied as a novel catalyst support in proton exchange membrane (PEM) fuel cells to improve catalyst stability, as a result of its excellent resistance to electrochemical oxidation. Further exploitations of SiC include as a nickel supported catalyst, successfully used in the partial oxidation of methane into synthesis gas. The high thermal conductivity of the SiC support prevents the formation of hot spots on the catalyst surface at the start of the reaction, in contrast to what is observed on the same catalyst with Al_2O_3 [54, 55]. Also, with its inert nature, the chemistry can only occur at the Mo active sites, preventing any unwanted side reactions which many supports including Al_2O_3 and Fe_2O_3 , often bring.

3.4.3. SEM

The SEM micrographs and EDX elementary analysis of both MoO_x/SiC and $\text{MoO}_x/\text{Al}_2\text{O}_3$ are presented in Figures 21-25. It is shown that the morphology of the $\text{Mo}/\text{Al}_2\text{O}_3$ is uniform,

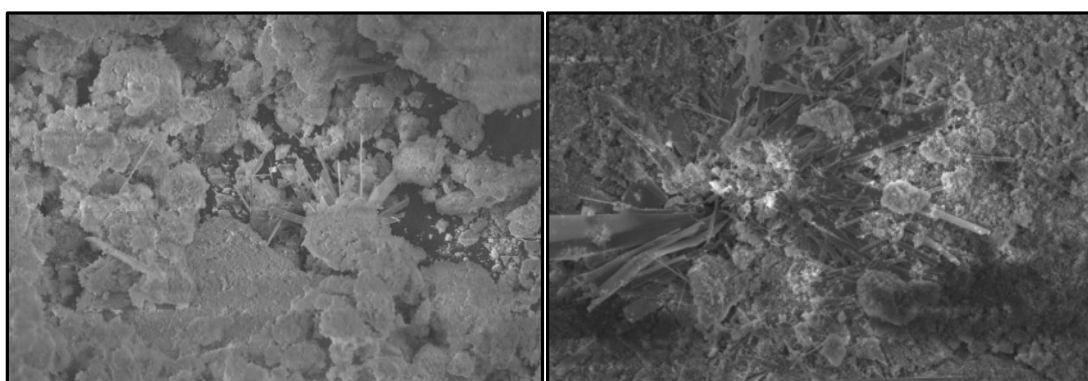
with no evidence for aggregates of Mo clusters. Elemental mapping confirmed this, as shown through Figure 22, plotting mapping point versus Mo w/t %. Comparing with Mo/Fe₂O₃ catalyst (Chapter 3), the composition is similar, showing a comparable uniformity.

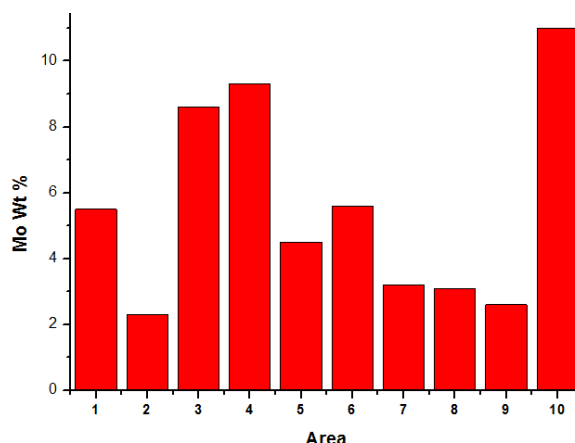


Figures 21-22. SEM image and corresponding EDX mapping (respectively) across a section of 6 w/t % Mo/Al₂O₃.

A corresponding investigation on 6 w/t % Mo/SiC is shown through Figures 23-25. A striking contrast was found for this sample, which presents very large MoO₃ particles, evidenced as spike like features in the micrograph. Point and ID analysis on these features identified Mo.

Moreover, the EDX line scan analysis of this catalyst showed a heterogeneous distribution of Mo (Figure 25), ranging from 2- 11 w/t % of the total weight.





Figures 23-25. SEM images (Above and previous page) and corresponding EDX mapping (respectively) across a section of 6 w/t % Mo/SiC. Results from mapping show a heterogeneous distribution of Mo across the catalyst.

3.4.4. BET

Table 1. BET surface area measurements of various supports and when loaded through incipient wetness with AHM, to form the Mo supported material.

Catalyst	Surface Area / m^2g^{-1}
Fe_2O_3	21
$\gamma\text{-Al}_2\text{O}_3$	90
SiC	31
6 w/t % $\text{MoO}_x/\text{Fe}_2\text{O}_3$	14
6 w/t % $\text{MoO}_x/\text{Al}_2\text{O}_3$	54
6 w/t % MoO_x/SiC	24

BET data have been recorded for each of the Mo supported catalysts with results presented in Table 1. It is shown that there is huge potential for the Al_2O_3 supported catalyst, demonstrating a surface area approximately four times that of the Fe_2O_3 supported catalyst. TPD data for $\text{Fe}_2(\text{MoO}_4)_3$ vs. 6ML $\text{MoO}_x/\text{Fe}_2\text{O}_3$ (Chapters 3-4) evidenced a shift in formaldehyde desorption from 190 to 165 °C respectively, as a result of the increase in surface area for the monolayer dosed catalyst. With further increases in surface area, it is anticipated that the alumina supported catalyst will demonstrate an even lower temperature of formaldehyde desorption, with an overall raised performance in terms of conversion rates. That said however, the specific surface area of the Mo cannot be measured, and is the key contributing factor in the activity of methanol oxidation.

For 6 w/t % MoO_x/SiC , the catalyst shows a reasonable surface area of 24 m^2g^{-1} . However, Raman and XRD are conclusive in showing a large proportion of Mo to be present as MoO_3 aggregates, as opposed to all Mo being present as a well dispersed layer at the

surface as in the case of Fe_2O_3 . Therefore the increased surface area will mainly be a result of the SiC support itself, and not due to an improvement in the Mo surface area.

3.4.5. Catalytic Testing

Catalytic testing has been performed for various w/t %'s of Mo on Al_2O_3 and SiC. Both TPD and TPPFR have been used as invaluable analysis tools.

The nature of the surface active sites highly influences catalyst selectivity. Redox sites characteristically yield H_2CO , acidic sites CH_3OCH_3 and basic sites CO_2 . Redox sites are able to liberate oxygen and yield H_2CO , whilst surface acidic sites are not able to liberate this oxygen, contain either H^+ or oxygen vacancies, therefore producing CH_3OCH_3 (DME) through a bimolecular dehydration reaction [56, 57]. Surface acidity including type and strength of the acid sites in the catalyst can be characterized by the adsorption of probe molecules [58]. Typically, the use of CO as a probe molecule makes it possible to estimate the strength and number of Lewis acid sites at the surface. For instance, CO can adsorb onto Al_2O_3 in three ways, with FTIR able to identify these and assign them to basic or acidic sites [59]. Common alternative probe molecules include NH_3 , CH_3CN , NO and pyridine. The oxidation of methanol is well adapted for spectroscopic studies, enabling the detection of the distribution of reaction products on the catalyst surface. In general, oxidative–reductive processes lead to oxidized products such as formaldehyde, formic acid, and carbon oxides, whereas acid–base interaction mainly leads to the dehydration product (DME). Consecutive dehydrations of oxidation products can lead to dimethoxymethane or methyl formate formation.

Figure 26 represents the TPD data for methanol dosing on pure $\gamma\text{-Al}_2\text{O}_3$. As might be expected, the catalyst performs poorly, with the spectra showing a significant proportion of DME (Mass 46) in the mass spectrometer response. This has not been seen in the TPD data for previous FeMo containing catalysts, and is unique to Al_2O_3 [60–62]. This is due to the presence of strongly acidic sites driving the dehydration reaction between two adsorbed methoxy molecules. A lack of formaldehyde production (Mass 30) indicates a low stability of the methoxy. As the concentration of the methoxy diminishes, the mechanisms revert to a decomposition pathway, producing CO (Mass 28), hydrogen (Mass 2) and methane (Mass 15, however the signal is very small). The mechanism of the catalytic methanol oxidation has been extensively investigated on unsupported MoO_3 [63–65], and is also detailed in previous chapters. In summary, the first reaction step involves the formation of methoxy groups by dissociative adsorption of methanol at dual acid–base sites. The subsequent steps are highly dependent on the acid strength of the adsorption site, and the nature of the active

centres in close proximity. The rate determining step, which is defined as the cleavage of the C-H bond, will depend on the basic or nucleophilic character of oxygen species close to the methoxy group. In addition, desorption of the reaction products will be highly favoured by weak rather than strong acid sites. To selectively produce formaldehyde, both a weak acid and basic site is required to limit the H abstraction and prevent a too strong a bond to formaldehyde. If the acid sites present at the surface are too strong, the residence time of formaldehyde species is too long, forming a dioxymethylene species (Busca *et al.* [66]). This intermediate species can react with neighbouring methoxy groups or adsorbed methanol to form methylal. If both acid and basic sites are stronger than those needed for methylal formation, the dioxymethylene species are oxidized into formate species which quickly react with methanol to form methyl formate, or alternatively are further oxidized to carbon oxides. If strong acid sites and very weak basic centres are present, only dimethyl ether is formed. When dehydration reactions to DME become favourable, the overall selectivity to formaldehyde is compromise

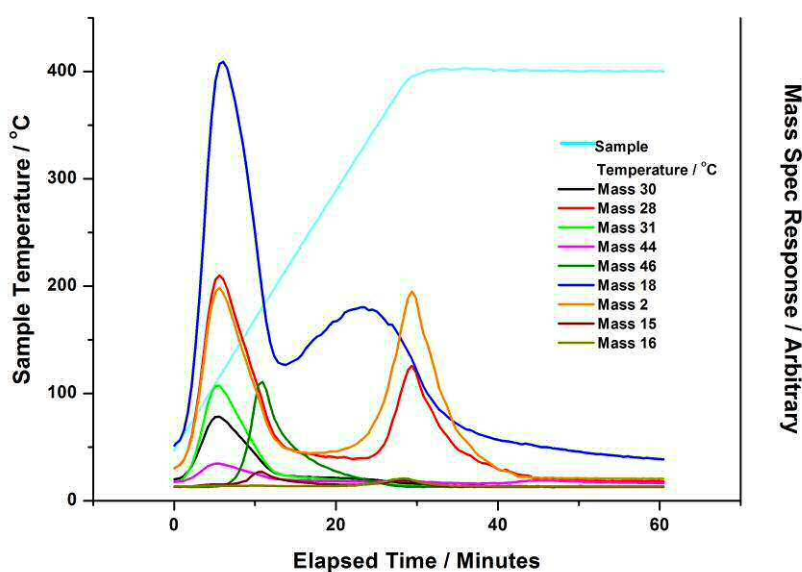


Figure 26. TPD of MeOH/He on γ -Al₂O₃. The catalyst surface was saturated with MeOH/He, and the temperature of the catalyst bed raised to 400 °C monitoring the products of desorption through mass spectrometry. Raw data.

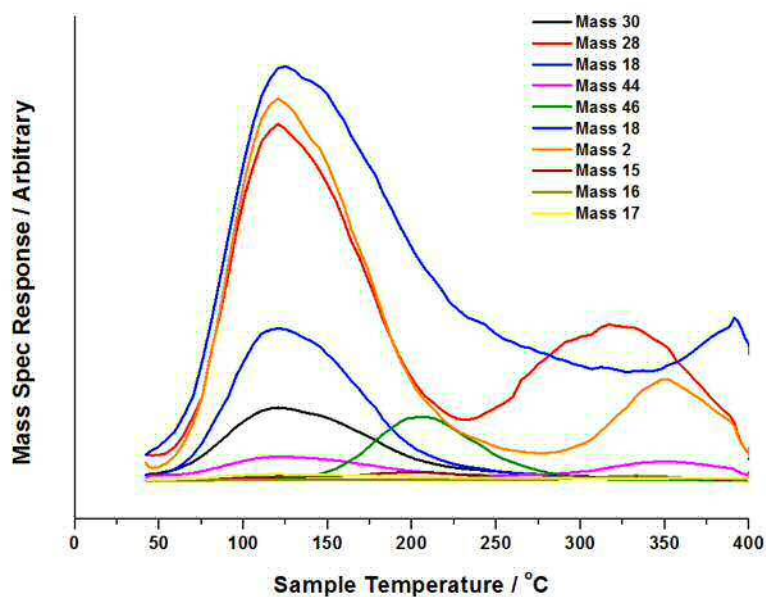


Figure 27. TPD of MeOH/He on 1 w/t % Mo on γ -Al₂O₃. The catalyst surface was saturated with MeOH/He, and the temperature of the catalyst bed raised to 400 °C monitoring the products of desorption through mass spectrometry. Raw data.

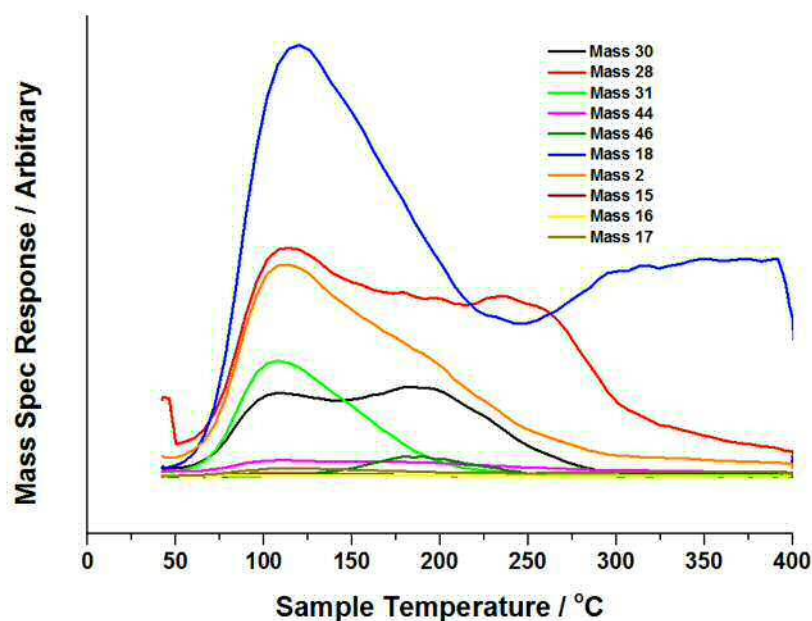


Figure 28. TPD of MeOH/He on 3 w/t % Mo on γ -Al₂O₃. The catalyst surface was saturated with MeOH/He, and the temperature of the catalyst bed raised to 400 °C monitoring the products of desorption through mass spectrometry. Raw data.

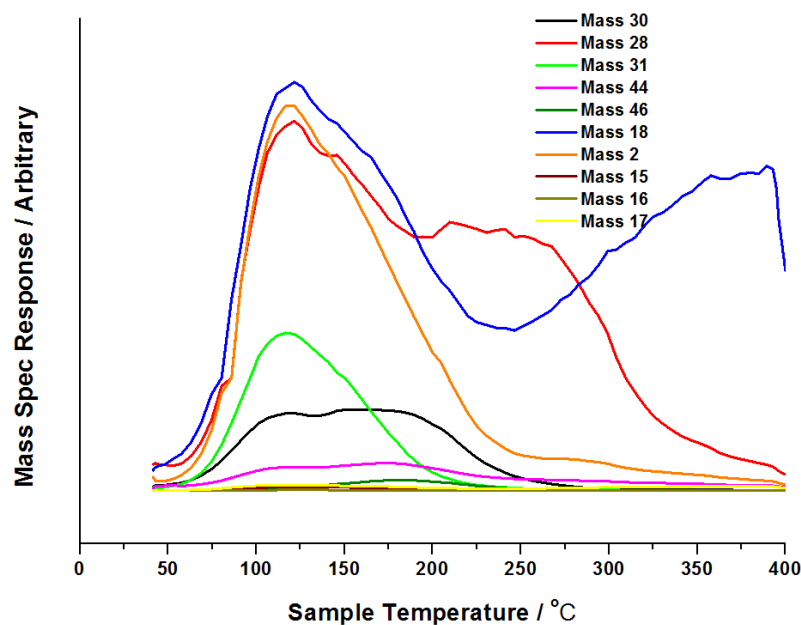


Figure 29. TPD of MeOH/He on 6 w/t % Mo on γ -Al₂O₃. The catalyst surface was saturated with MeOH/He, and the temperature of the catalyst bed raised to 400 °C monitoring the products of desorption through mass spectrometry. Raw data.

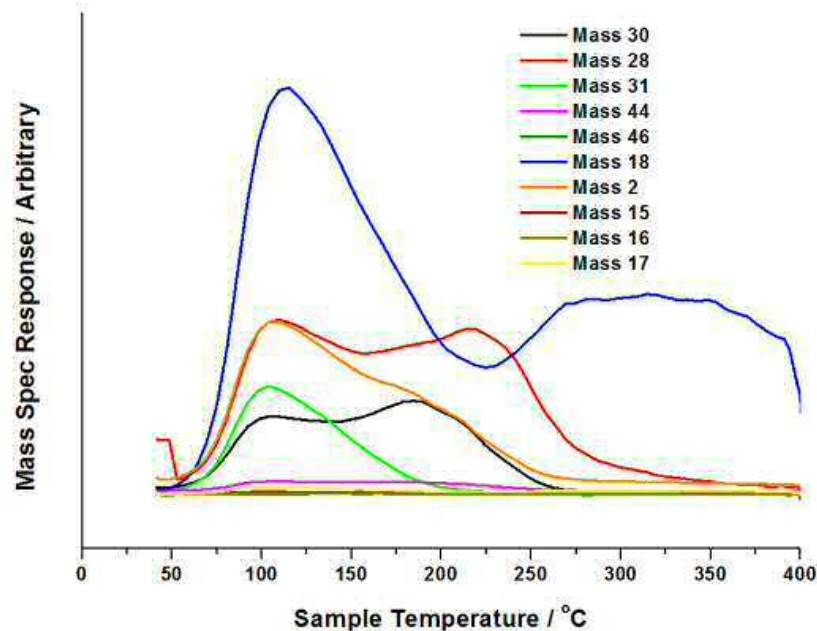


Figure 30. TPD of MeOH/He on 10 w/t % Mo on γ -Al₂O₃. The catalyst surface was saturated with MeOH/He, and the temperature of the catalyst bed raised to 400 °C monitoring the products of desorption through mass spectrometry. Raw data.

1, 3, 6 and 10 w/t % of Mo has been dosed onto the surface of Al_2O_3 (Figures 27-30). For 1, 3 and 6 w/t % Mo / Al_2O_3 , it is shown that the TPD profiles are dominated by the unselective products of DME (Mass 46) [41] and CO (Mass 28). While supported catalysts have proved useful for research purposes, they are usually not considered for commercial purpose, since support interaction with formaldehyde results in its further oxidation to CO (Mass 28) and CO_2 (Mass 44). A small amount of CO_2 is seen for 1 w/t % Mo/ Al_2O_3 , where complete combustion of methanol occurs to yield CO_2 (Mass 44) and water (Mass 18). Also for this w/t % loading, there is no evidence for formaldehyde production (Mass 30), implying that either the Mo at the surface is too isolated, denying close enough proximity of 2 Mo adsorption centres for selective methanol adsorption, or that the dominance of the surface by Al_2O_3 leads to further oxidation products as already mentioned. The strong signal for DME (Mass 46) would imply that for 1 w/t % loading, the surface of Al_2O_3 is significantly exposed, with the DME signal comparable to that for pure Al_2O_3 (Figure 26). It would also imply a high coverage of methoxy species on the catalyst surface.

For 3 w/t % Mo dosed on Al_2O_3 , formaldehyde production becomes evident (Mass 30): indicating that two Mo(VI) species are now in close enough proximity to follow a dual site mechanism selective to formaldehyde. The formation of DME occurs at 200 °C, since at higher temperatures desorption of methanol prevents a dehydration reaction from occurring.

With further increases in the w/t % of Mo dosed, the selectivity to DME diminishes, as the exposure of Al_2O_3 at the surface reduces. It is shown that at least 10 w/t % is required for a desirable selectivity profile (Figure 30) [67]. For this weight loading, DME is no longer in existence, attributed to the complete coverage of the Al_2O_3 surface. In fact, the catalyst begins to show a comparable selectivity to that of bulk $\text{Fe}_2(\text{MoO}_4)_3$, and due to the high surface area nature of the support, a slight improvement in the temperature of H_2CO desorption is seen (at 175 °C as opposed to 190 °C for $\text{Fe}_2(\text{MoO}_4)_3$). This demonstrates the ability of the catalyst in lowering of the activation energy of the reaction. The increase in desired selectivity agrees well with theoretical calculations, which demonstrate that approximately 8 w/t % of Mo is required to saturate the surface of Al_2O_3 . Also present in the TPD profile are large methanol (Mass 31), water (Mass 18) and CO (Mass 28) desorptions, centred at 100, 130 and 220-320 °C respectively.

With an increase in Mo dosage, it is noted that the temperature of CO production shifts to lower temperature. Previous studies of methanol TPD on $\gamma\text{-Al}_2\text{O}_3$ have shown DME at 300 °C, with coincident CO and H_2 production at 430 °C [68]. CO_2 was only observed from the methanol TPD on the 1 w/t % Mo/ Al_2O_3 catalyst. It has been shown from BET data (Section 2.3.4), that the surface area of these materials increases with decreasing Mo weight

loading. It is assumed that this increase will yield higher conversion, hence favouring the consecutive reactions, leading to the predominant formation of carbon oxides which are the more thermodynamically favoured products.

Referring to the literature, at low surface coverages of Mo/Al₂O₃, MoO_x are reported to be isolated and tetrahedrally co-ordinated (Wachs *et al.* [69]). At higher coverages, a mixture of octahedrally and tetrahedrally co-ordinated species exist. It should be considered that the change in activity could be attributed to such changes. The molecular structure of the molybdena is reported to have a slight influence over TOF [69]. The TOF is controlled by the reducibility of the support, suggesting a strong influence of the Mo-O-support bond.

TPPFR analysis has also been fundamental in assessing the effectiveness of supported Mo oxides. Figure 31 demonstrates the TPPFR for pure γ -Al₂O₃ after a calcination at 500 °C.

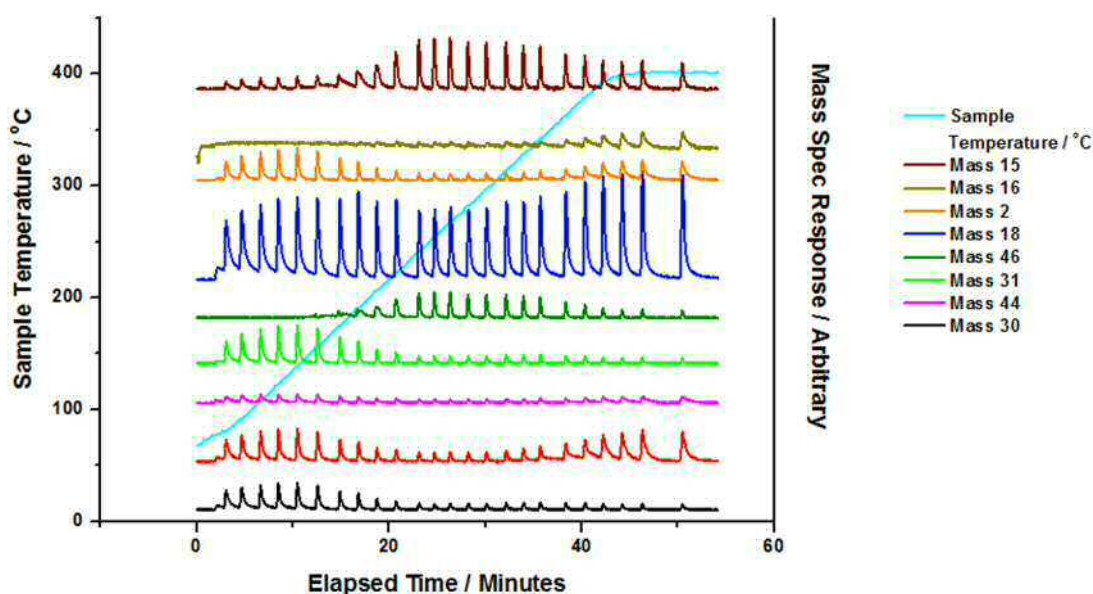


Figure 31. TPPFR data of MeOH/O₂ on γ -Al₂O₃. 1 μ L of MeOH was pulsed over the catalyst bed approximately every 2 minutes, whilst ramping the temperature of the sample to 400 °C. Raw data.

Referring to Figure 31, as the conversion of methanol reaches approximately 50 % (Mass 31), dehydration begins, shown by an increase in the selectivity to DME (Mass 46). High selectivities to DME are observed from 220 °C, with 86 % MeOH conversion (Mass 31) in total achieved. The dehydration reaction which occurs, is due to the high surface coverage and retention time of methoxy species at lower temperatures on Al₂O₃. On increasing the temperature further, DME selectivity decreases, with co-incident CO (Mass 28) and CO₂ (Mass 44) production from 340 °C. The production of methane (Mass 15) is also well

established as the reaction continues, in line with DME decomposition. This also explains the increase in CO production (Mass 28).

Under the same study, the catalyst of 10 w/t % Mo/Al₂O₃ (Figure 32) reveals an activity superior to that of bulk Fe₂(MoO₄)₃, with 50 % methanol conversion reached at approximately 190 °C, as opposed to the former 225 °C seen for Fe₂(MoO₄)₃. The catalyst shows reasonable formaldehyde selectivity at low conversions (approximately 60 % selectivity is maintained until reaching 100 % conversion of methanol). On increasing the temperature above 275 °C however, the selectivity drops rapidly, as CO production begins to prevail, reaching 80 % selectivity by 400 °C. A small amount of methane production was also detected. There is no evidence for CO₂ production. DME selectivity is high, much higher than has been seen for any other catalysts throughout this thesis. Selectivity to DME is particularly high at low temperatures and conversion, peaking at 37 % at 325 °C and 60 % conversion. In all, although the catalyst demonstrates a superior activity, the selectivity of the catalyst is compromised, and cannot compete with the above >90 % selectivity to formaldehyde demonstrated by Fe₂(MoO₄)₃.

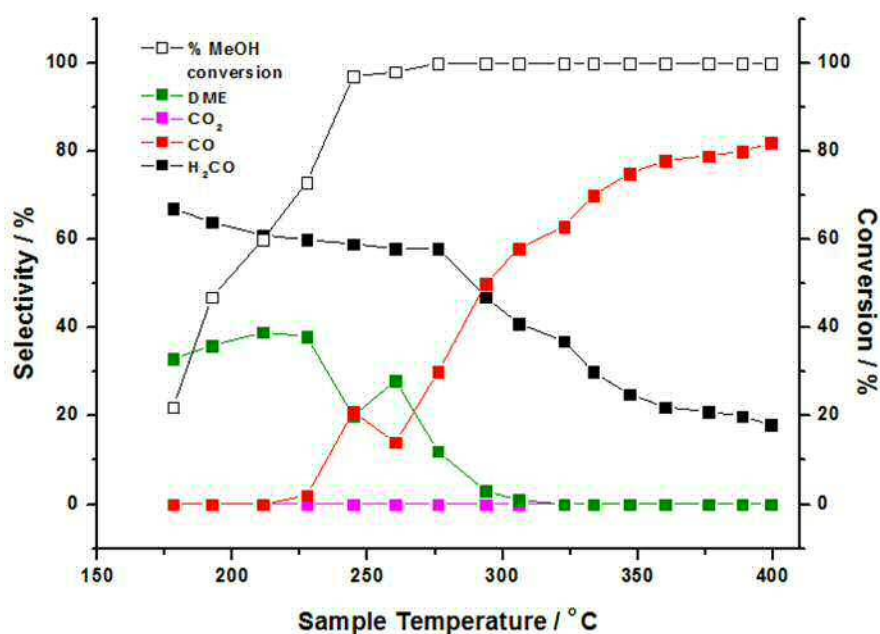


Figure 32. TPPFR data of MeOH/O₂ on 10 w/t % Mo/Al₂O₃. 1 μL of MeOH was pulsed over the catalyst bed approximately every 2 minutes, whilst ramping the temperature of the sample to 400 °C.

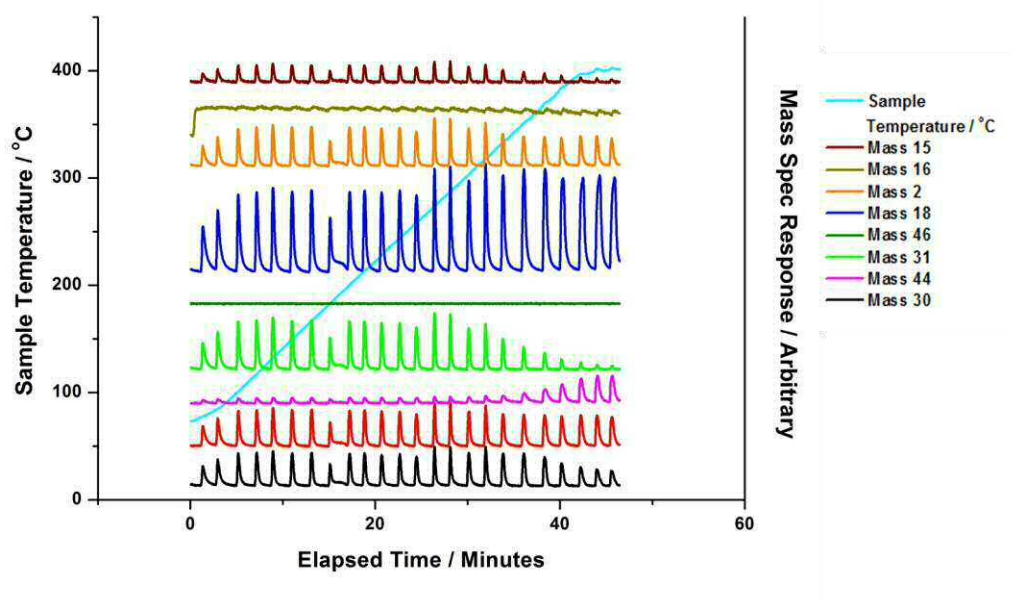


Figure 33. TPPFR data of MeOH/O₂ on commercial SiC. 1 μ L of MeOH was pulsed over the catalyst bed approximately every 2 minutes, whilst ramping the temperature of the sample to 400°C. Raw data.

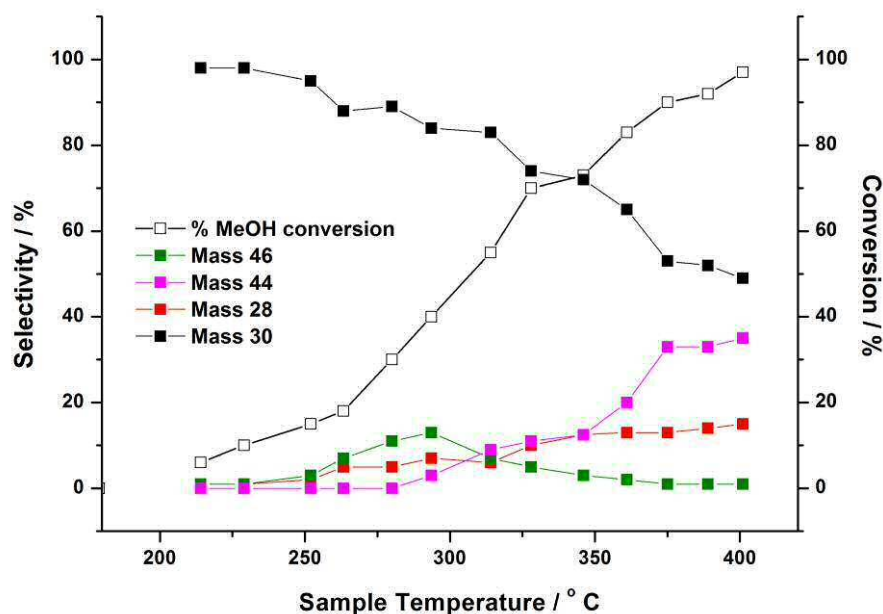


Figure 34. TPPFR data of MeOH/O₂ on 10 w/t % Mo/SiC. 1 μ L of MeOH was pulsed over the catalyst bed approximately every 2 minutes, whilst ramping the temperature of the sample to 400°C.

The TPPFR profile for 10 w/t % Mo/SiC is presented in Figure 34, showing a clear contrast to that seen for the same weight loading on Al₂O₃ (Figure 32). The catalyst performs poorly in terms of its activity, with a slow and delayed progression towards 100 %

conversion at 400 °C. 50 % conversion is not achieved until 320 °C, which is also a far stretch from bulk $\text{Fe}_2(\text{MoO}_4)_3$ which demonstrates 50 % conversion below 250 °C. It has been shown that Mo doses onto the surface as clusters of MoO_3 on this carbide material, as evidenced through SEM, XRD and Raman mapping. This will therefore bring no increase to the active Mo specific surface area. In addition to this, SiC demonstrates a very low reactivity towards methanol (Figure 33), so any exposed SiC will have a limited effect on catalyst performance. On pure SiC alone (Figure 33), conversion does not begin until above 300 °C, with formaldehyde production short lived as the selectivity turns to CO (Mass 28) and CO_2 (Mass 44) at the highest temperatures. Many authors have turned to new methods to create highly porous, mesostructured SiC with unique thermophysical characteristics, which will have a greater activity due to a dramatic increase in surface area [70]. If it were possible to bind Mo as a homogeneous overlayer onto the support, it could create a catalyst with huge potential.

Conversion aside, the catalyst does show a reasonable performance in terms of its selectivity, demonstrating a 100 % selectivity to formaldehyde at the lowest temperatures and conversions, albeit <10 % conversion. This selectivity is short lived however, dropping to 49 % by 400 °C. CO and CO_2 emerge and rise to 15 and 35 % respectively at the highest temperatures. Under the high temperatures of formaldehyde production, it is likely that further oxidation is readily occurring to these carbon containing products. Since the reaction is performed under O_2 , SiC is under threat of combusting to CO_2 . DME production is negligible when compared to Al_2O_3 , reinforcing the inert nature of the support. A weak interaction with formaldehyde results in its short lived retention time, and therefore inability to react with a further methoxy/incoming methanol, to induce a bimolecular dehydration reaction to DME [56, 57].

4. Conclusions and Further Work

The chapter described has demonstrated insights into the redox potential of iron molybdate based catalysts, demonstrating that $\text{Fe}_2(\text{MoO}_4)_3$ has many properties which place it as the forerunner in the selective oxidation of methanol to formaldehyde. Above 250 °C, oxygen mobility within the bulk lattice enables a movement towards the surface, permitting the catalyst to perform under anaerobic conditions via the Extended Mars-van Krevelen mechanism [7]. Such properties ensure maintained catalyst performance ensues, in the outcome that the uptake of gas phase oxygen is not efficient. Eventually the catalyst will reduce to form MoO_2 and FeMoO_4 , as significant amounts of lattice oxygen are removed, inducing a reduction in formaldehyde production. The importance of $\text{Fe}_2(\text{MoO}_4)_3$ present

within the catalyst composition has been highlighted when comparing different monolayer dosages of Mo at the surface of Fe_2O_3 . With 1 ML Mo dosed at the surface of Fe_2O_3 , the catalyst performs poorly under anaerobic conditions, unable to achieve formaldehyde production after just one pulse of MeOH/He over the catalyst at 300°C . However, for 6 ML $\text{MoO}_x/\text{Fe}_2\text{O}_3$ where the Mo overlayer is existing on 5 monolayer equivalents of $\text{Fe}_2(\text{MoO}_4)_3$, formaldehyde production can be maintained for 4-5 pulses, due to the facile movement of oxygen in this mixed phase oxide.

Finally, work in previous chapters has highlighted a surface terminating layer in FeMo based catalysts, (defined MoO_x), existing as an amorphous active overlayer in both ML $\text{MoO}_x/\text{Fe}_2\text{O}_3$ and bulk catalysts. Since Fe_2O_3 is known for its poor performance in methanol oxidation, other supports have been trialled and tested for their effectiveness in the same reaction. It was discovered that Mo/SiC , although selective, is not active for the reaction, whilst in a reverse situation $\text{Mo}/\text{Al}_2\text{O}_3$ is active but not as selective. However, if a sufficient coverage of Mo (10 w/t %) is achieved, the selectivity could be vastly improved, and due to the very high activity which is superior to $\text{Fe}_2(\text{MoO}_4)_3$, this catalyst could be a potential competitor for the oxidative reaction. Characterisation through XRD, SEM and Raman showed a uniform spread of Mo at the surface of Al_2O_3 , however a molybdate phase, $\text{Al}_2(\text{MoO}_4)_3$, did not form as it does as $\text{Fe}_2(\text{MoO}_4)_3$ on $\text{MoO}_x/\text{Fe}_2\text{O}_3$. Further studies are required to assess the active overlayer in these catalysts, particularly XAFS studies, which could help define the surface terminating structure. The stability of supported $\text{Mo}/\text{Fe}_2\text{O}_3$ is shown at the beginning of this chapter to be short lived, since the conversion decreases after just 5 catalytic cycles due to sintering of the catalyst. Similar studies and characterisation are required to consider $\text{Mo}/\text{Al}_2\text{O}_3$ as potential catalysts.

5. References

1. House, M.P., et al., *Effect of varying the cation ratio within iron molybdate catalysts for the selective oxidation of methanol*. The Journal of Physical Chemistry C, 2008. **112**(11): p. 4333-4341.
2. Soares, A.P.V., et al., *Mechanism of deactivation of iron-molybdate catalysts prepared by coprecipitation and sol-gel techniques in methanol to formaldehyde oxidation*. Chemical Engineering Science, 2003. **58**(7): p. 1315-1322.
3. Bowker, M., et al., *The selective oxidation of methanol to formaldehyde on iron molybdate catalysts and on component oxides*. Catalysis Letters, 2002. **83**(3-4): p. 165-176.
4. O'Brien, M.G., et al., *On the active oxygen in bulk MoO_3 during the anaerobic dehydrogenation of methanol*. The Journal of Physical Chemistry C, 2009. **113**(12): p. 4890-4897.
5. Jacques, S.D.M., et al., *Redox Behavior of Fe-Mo-O Catalysts Studied by Ultrarapid In Situ Diffraction*. Angewandte Chemie, 2006. **118**(3): p. 459-462.

6. Carbucicchio, M. and F. Trifiro, *Redox processes at the surfaces of Fe₂O₃/MoO₃/SiO₂ catalysts*. Journal of Catalysis, 1980. **62**(1): p. 13-18.
7. Bowker, M., et al., *The selective oxidation of methanol on iron molybdate catalysts*. Topics in Catalysis, 2008. **48**(1-4): p. 158-165.
8. Bowker, M., A.F. Carley, and M. House, *Contrasting the behaviour of MoO₃ and MoO₂ for the oxidation of methanol*. Catalysis Letters, 2008. **120**(1-2): p. 34-39.
9. Kuang, W., Y. Fan, and Y. Chen, *State and reactivity of lattice oxygen ions in mixed Fe-Mo oxides*. Langmuir, 2000. **16**(3): p. 1440-1443.
10. Soares, A.V., et al., *Iron molybdate catalysts for methanol to formaldehyde oxidation: effects of Mo excess on catalytic behaviour*. Applied Catalysis A: General, 2001. **206**(2): p. 221-229.
11. Pernicone, N., *MoO₃/Fe₂(MoO₄)₃ catalysts for methanol oxidation*. Journal of the Less Common Metals, 1974. **36**(1): p. 289-297.
12. Kim, T.H., et al., *Selective oxidation of methanol to formaldehyde using modified iron-molybdate catalysts*. Catalysis Letters, 2004. **98**(2-3): p. 161-165.
13. Carbucicchio, M. and F. Trifirò, *Surface and bulk redox processes in iron-molybdate-based catalysts*. Journal of Catalysis, 1976. **45**(1): p. 77-85.
14. Hu, H. and I.E. Wachs, *Catalytic properties of supported molybdenum oxide catalysts: in situ Raman and methanol oxidation studies*. The Journal of Physical Chemistry, 1995. **99**(27): p. 10911-10922.
15. Matsuoka, Y., M. Niwa, and Y. Murakami, *Morphology of molybdena supported on various oxides and its activity for methanol oxidation*. Journal of Physical Chemistry, 1990. **94**(4): p. 1477-1482.
16. Kuang, W., Y. Fan, and Y. Chen, *Structure and reactivity of ultrafine Fe-Mo oxide particles prepared by the sol-gel method*. Langmuir, 2000. **16**(11): p. 5205-5208.
17. Soares, A.V., M.F. Portela, and A. Kiennemann, *Iron molybdates for selective oxidation of methanol: Mo excess effects on the deactivation behaviour*. Catalysis Communications, 2001. **2**(5): p. 159-164.
18. Chowdhry, U., et al., *Mechanism and surface structural effects in methanol oxidation over molybdates*. Applications of Surface Science, 1984. **19**(1): p. 360-372.
19. Jacques, S., et al., *Redox Behavior of Fe/Mo/O Catalysts Studied by Ultrarapid In Situ Diffraction*. Angewandte Chemie, 2006. **118**(3): p. 459-462.
20. Ressler, T., et al., *Bulk Structural Investigation of the Reduction of MoO₃ with Propene and the Oxidation of MoO₂ with Oxygen*. Journal of Catalysis, 2002. **210**(1): p. 67-83.
21. Burriesci, N., A. Gennaro, and M. Petrera, *On the reduced phase of Fe/Mo oxide catalysts*. Reaction Kinetics and Catalysis Letters, 1980. **15**(2): p. 171-177.
22. Routray, K., et al., *Origin of the synergistic interaction between MoO₃ and iron molybdate for the selective oxidation of methanol to formaldehyde*. Journal of Catalysis, 2010. **275**(1): p. 84-98.
23. Soares, A.P.V., M.F. Portela, and A. Kiennemann, *Methanol Selective Oxidation to Formaldehyde over Iron Molybdate Catalysts*. Catalysis Reviews, 2005. **47**(1): p. 125-174.
24. Ressler, T., et al., *Bulk structural investigation of the reduction of MoO₃ with propene and the oxidation of MoO₂ with oxygen*. Journal of Catalysis, 2002. **210**(1): p. 67-83.
25. Pasquon, I., F. Trifiro, and G. Caputo, *NATURE OF ACTIVE COMPONENTS IN FE₂O₃-MOO₃ CATALYST. 2. BEHAVIOR OF BETA-FEMOO₄, FE₂O₃-MOO₃, FE₂O₃-MOO₃-TEO₂ IN OXIDATION OF 1-BUTENE*. CHIMICA & L INDUSTRIA, 1973. **55**(2): p. 168-175.
26. House, M.P., A.F. Carley, and M. Bowker, *Selective oxidation of methanol on iron molybdate catalysts and the effects of surface reduction*. Journal of Catalysis, 2007. **252**(1): p. 88-96.

27. Andersson, A., M. Hernelind, and O. Augustsson, *A study of the ageing and deactivation phenomena occurring during operation of an iron molybdate catalyst in formaldehyde production*. Catalysis Today, 2006. **112**(1–4): p. 40–44.
28. Mars, P. and D.W. Van Krevelen, *Oxidations carried out by means of vanadium oxide catalysts*. Chemical Engineering Science, 1954. **3**: p. 41–59.
29. Guerrero-Ruiz, A., et al., *Description of active sites on molybdenum oxide as detected by isotope exchange between C 18 O 2 and Mo 16 O 3*. Catalysis Today, 1996. **32**(1): p. 223–227.
30. Ivanov, K.I. and D.Y. Dimitrov, *Deactivation of an industrial iron-molybdate catalyst for methanol oxidation*. Catalysis Today, 2010. **154**(3): p. 250–255.
31. Routray, K., et al., *Origin of the synergistic interaction between MoO₃ and iron molybdate for the selective oxidation of methanol to formaldehyde*. Journal of Catalysis, 2010. **275**(1): p. 84–98.
32. Forzatti, P. and G. Buzzi-Ferraris, *Reaction-deactivation kinetics of methanol oxidation over a silica-supported iron oxide-molybdenum oxide (Fe₂O₃-MoO₃) catalyst*. Industrial & Engineering Chemistry Process Design and Development, 1982. **21**(1): p. 67–73.
33. House, M.P., M.D. Shannon, and M. Bowker, *Surface segregation in iron molybdate catalysts*. Catalysis Letters, 2008. **122**(3–4): p. 210–213.
34. Okumura, M., et al., *Chemical vapor deposition of gold on Al₂O₃, SiO₂, and TiO₂ for the oxidation of CO and of H₂*. Catalysis Letters, 1998. **51**(1–2): p. 53–58.
35. Smirniotis, P.G., et al., *Manganese oxide catalysts supported on TiO₂, Al₂O₃, and SiO₂: A comparison for low-temperature SCR of NO with NH₃*. Industrial & engineering chemistry research, 2006. **45**(19): p. 6436–6443.
36. Olsson, L., et al., *A kinetic study of oxygen adsorption/desorption and NO oxidation over Pt/Al₂O₃ catalysts*. The Journal of Physical Chemistry B, 1999. **103**(47): p. 10433–10439.
37. Galli, A., et al., *The effect of potassium on the selective oxidation of n-butane and ethane over Al₂O₃-supported vanadia catalysts*. Catalysis Letters, 1995. **34**(1–2): p. 51–58.
38. Smirnov, M.Y., et al., *Interaction of Al₂O₃ and CeO₂ Surfaces with SO₂ and SO₂ + O₂ Studied by X-ray Photoelectron Spectroscopy*. The Journal of Physical Chemistry B, 2005. **109**(23): p. 11712–11719.
39. Burcham, L.J., L.E. Briand, and I.E. Wachs, *Quantification of active sites for the determination of methanol oxidation turn-over frequencies using methanol chemisorption and in situ infrared techniques. 2. Bulk metal oxide catalysts*. Langmuir, 2001. **17**(20): p. 6175–6184.
40. Rinaldi, N., T. Kubota, and Y. Okamoto, *Effect of citric acid addition on the hydrodesulfurization activity of MoO₃/Al₂O₃ catalysts*. Applied Catalysis A: General, 2010. **374**(1–2): p. 228–236.
41. Brandhorst, M., et al., *Catalytic oxidation of methanol on Mo/Al₂O₃ catalyst: An EPR and Raman/infrared operando spectroscopies study*. Catalysis Today, 2006. **113**(1–2): p. 34–39.
42. Py, M., P.E. Schmid, and J. Vallin, *Raman scattering and structural properties of MoO₃*. Il Nuovo Cimento B Series 11, 1977. **38**(2): p. 271–279.
43. Bergwerff, J.A., et al., *Envisaging the physicochemical processes during the preparation of supported catalysts: Raman microscopy on the impregnation of Mo onto Al₂O₃ extrudates*. Journal of the American Chemical Society, 2004. **126**(44): p. 14548–14556.
44. Mallakpour, S. and F. Sirous, *Surface coating of α -Al₂O₃ nanoparticles with poly(vinyl alcohol) as biocompatible coupling agent for improving properties of bio-active poly(amide-imide) based nanocomposites having l-phenylalanine linkages*. Progress in Organic Coatings, 2015. **85**(0): p. 138–145.
45. Billik, P., et al., *Mechanochemical-molten salt synthesis of α -Al₂O₃ platelets*. Ceramics International, (0).

46. Bourbia, A., et al., *Phase transformation in rapidly solidified Al–Al₂O₃ alloys by high-frequency melting*. Physica Scripta, 2012. **85**(5): p. 055601.
47. Yalamaç, E., A. Trapani, and S. Akkurt, *Sintering and microstructural investigation of gamma–alpha alumina powders*. Engineering Science and Technology, an International Journal, 2014. **17**(1): p. 2-7.
48. Kouachi, K., et al., *Mo/γ-Al₂O₃ catalysts for the Biginelli reaction. Effect of Mo loading*. Journal of Molecular Catalysis A: Chemical, 2014. **395**(0): p. 210-216.
49. Rajagopal, S., et al., *Silica-Alumina-Supported Acidic Molybdenum Catalysts - TPR and XRD Characterization*. Journal of Catalysis, 1994. **147**(2): p. 417-428.
50. Okamoto, Y., et al., *A study on the preparation of supported metal oxide catalysts using JRC-reference catalysts. I. Preparation of a molybdena - Alumina catalyst. Part I. Surface area of alumina*. Applied Catalysis A: General, 1998. **170**(2): p. 315-328.
51. Wang, X.-h., L. Weng, and W.-g. Zhang, *A SiC/Mo(Si_{1-x}Al_x)₂ oxidation-resistant coating for carbon/carbon composites*. New Carbon Materials, 2014. **29**(2): p. 126-131.
52. Wei, W.-C. and J.S. Lee, *Formation and reaction kinetics of Mo and Mo silicides in the preparation of MoSi₂/SiC composites*. Journal of the European Ceramic Society, 1998. **18**(5): p. 509-520.
53. Williamson, G. and W. Hall, *X-ray line broadening from fcc aluminium and wolfram*. Acta metallurgica, 1953. **1**(1): p. 22-31.
54. Keller, N., et al., *New catalysts based on silicon carbide support for improvements in the sulfur recovery. Silicon carbide as support for the selective H₂S oxidation*. Journal of the Brazilian Chemical Society, 2005. **16**(2): p. 202-209.
55. Kim, S.K. and H.J. Yoo, *Formation of bilayer Ni–SiC composite coatings by electrodeposition*. Surface and coatings Technology, 1998. **108**: p. 564-569.
56. Tatibouet, J.M., *Methanol oxidation as a catalytic surface probe*. Applied Catalysis A: General, 1997. **148**(2): p. 213-252.
57. Alessandrini, G., et al., *Chemical, structural and catalytic modifications of pure and doped iron(III) molybdate*. Journal of the Less Common Metals, 1977. **54**(2): p. 373-386.
58. Zeng, D., et al., *Effect of Surface Acid Properties of Modified VO_x/Al₂O₃ Catalysts on Methanol Selective Oxidation*. Catalysis Letters, 2013. **143**(6): p. 624-629.
59. Wu, W., et al., *In situ FT-IR spectroscopic studies of CO adsorption on fresh Mo₂C/Al₂O₃ catalyst*. The Journal of Physical Chemistry B, 2003. **107**(29): p. 7088-7094.
60. Deo, G. and I.E. Wachs, *Reactivity of supported vanadium oxide catalysts: the partial oxidation of methanol*. Journal of Catalysis, 1994. **146**(2): p. 323-334.
61. Matsuoka, Y., M. Niwa, and Y. Murakami, *Morphology of molybdena supported on various oxides and its activity for methanol oxidation*. The Journal of Physical Chemistry, 1990. **94**(4): p. 1477-1482.
62. Matyshak, V., et al., *Surface species in the methyl formate-methanol-dimethyl ether-γ-Al₂O₃ system studied by in situ IR spectroscopy*. Kinetics and catalysis, 1999. **40**(2): p. 269-274.
63. Niwa, M., et al., *Mechanism of methanol oxidation over oxide catalysts containing MoO₃*. Journal of Catalysis, 1981. **70**(1): p. 14-23.
64. Holstein, W. and C. Machiels, *Inhibition of methanol oxidation by water vapor—effect on measured kinetics and relevance to the mechanism*. Journal of Catalysis, 1996. **162**(1): p. 118-124.
65. Chung, J.S., R. Miranda, and C.O. Bennett, *Mechanism of partial oxidation of methanol over MoO₃*. Journal of Catalysis, 1988. **114**(2): p. 398-410.
66. Busca, G., A.S. Elmi, and P. Forzatti, *Mechanism of selective methanol oxidation over vanadium oxide-titanium oxide catalysts: a FT-IR and flow reactor study*. Journal of Physical Chemistry, 1987. **91**(20): p. 5263-5269.

-
67. Zhao, C. and I.E. Wachs, *Selective oxidation of propylene over model supported V 2 O 5 catalysts: Influence of surface vanadia coverage and oxide support*. Journal of Catalysis, 2008. **257**(1): p. 181-189.
 68. Larsen, G., et al., *Tungsta supported on zirconia and alumina catalysts: temperature-programmed desorption/reaction of methanol and pyridine DRIFTS studies*. Catalysis Letters, 1996. **37**(1,2): p. 57-62.
 69. Hu, H., I.E. Wachs, and S.R. Bare, *Surface structures of supported molybdenum oxide catalysts: characterization by Raman and Mo L3-edge XANES*. The Journal of Physical Chemistry, 1995. **99**(27): p. 10897-10910.
 70. Xu, J., et al., *A hybrid sol-gel synthesis of mesostructured SiC with tunable porosity and its application as a support for propane oxidative dehydrogenation*. Physical Chemistry Chemical Physics, 2011. **13**(21): p. 10111-10118.

Chapter 7: Conclusions and Future Work

Contents

7.1. Conclusions.....	318
7.2. Future work.....	322
7.3. References.....	323

7.1. Conclusions

The aims of this thesis were to investigate the structure and reactivity of iron molybdate based catalysts, in particular the roles of the various phases present for the selective oxidation of methanol. The existence of Mo(VI) has been frequently documented to be vital to the catalyst performance, with many authors highlighting its existence as surface segregated MoO₃ in industrial catalysts [1-5]. That said, the majority of the catalyst is formed from bulk Fe₂(MoO₄)₃, and the purpose of this mixed phase oxide is often questioned. Catalysis is one of the most important technologies in our modern economy. The surface structure of iron molybdate is of great significance, since this is the industrial catalyst for the direct selective oxidation of methanol to formaldehyde. There is dispute concerning whether Fe₂(MoO₄)₃ acts as a benign support for segregated MoO₃, or if there is an fundamental property of the surface structure which facilitates the catalytic process [1, 6].

In Chapter 3, the importance of the surface structure is highlighted through investigation of catalytic testing coupled with multiple characterisation techniques. Various bulk catalysts, including commercial MoO₃ and Fe₂O₃, and synthesised Fe₂(MoO₄)₃ with changing Mo:Fe ratios were studied. If the surface is Fe₂O₃ dominated, it was discovered that the catalyst performs poorly, acting as a combustor of methanol to yield CO₂ and H₂. For catalysts in which the overall composition is Mo deficient (Mo:Fe < 1.5:1), CO dominates in the reactivity profile. Isolated Mo sites are deemed the primary cause of this, leading to a high energy direct pathway to CO. As the ratio of Mo:Fe increases, the selectivity to formaldehyde improves, with the surface becoming dominated by Mo. Formaldehyde prevails, with the formation of CO only occurring as a secondary oxidation product [2, 7].

The surface of $\text{Fe}_2(\text{MoO}_4)_3$ must be sufficiently covered with Mo to provide a catalyst with optimised selectivity and industrial potential. DRIFTS analysis was fundamental in assessing the surface intermediates responsible for product formation. It was concluded that Mo has a marked effect on catalyst selectivity, with even small loadings of Mo showing a substantial improvement in catalyst performance. By example, hematite itself is a very poor catalyst, with high selectivity to combustion products. When only 0.25 monolayers of Mo are deposited onto the surface, formaldehyde and CO selectivities are greatly enhanced, to the detriment of CO_2 . The chapter emphasized the importance of Mo at the surface, which paved the way for further chapters.

The composition and structure of the surface, as well as the surface area, is important for the efficiency of any reaction. The surface region is one of high energy, with the free bonding states at the surface acting as the driving force for catalysis. With a higher availability of bonding sites on the surface, this favours the catalytic process. It is important to learn as much as possible about the surface, in order to make adaptations and successfully improve catalyst performance. Chapter 4 adopted a novel approach to investigate the active surface region in more detail. A series of MoO_x modified Fe_2O_3 catalysts were prepared as core-shell materials to exclusively isolate Mo for surface sensitive characterisation. This design approach allowed bulk characterization techniques such as X-ray Absorption Fine Structure (XAFS) and Raman, to provide surface sensitive information. It is conclusively shown that for 3 monolayers of Mo oxide dosed, the Mo stays at the surface region and it remains here even after prolonged heat treatments at high temperatures above 500 °C. TEM EDX studies have proven this surface enrichment. Several phase changes occur with increasing anneal temperature. Below 300 °C, the Mo is present as octahedral amorphous Mo, denoted MoO_x for the purpose of this study. At 400 °C, MoO_3 forms at the surface. It is not until 500 °C however, that the Mo can undergo reaction with the Fe_2O_3 support to form mixed phase $\text{Td Fe}_2(\text{MoO}_4)_3$, as proven through XANES fittings. However, a 1 monolayer equivalent of Mo remains in its original octahedral MoO_x form as a significant overlayer for all anneal temperatures. It is the nanoparticles of MoO_3 present at 400 °C, which react to form ferric molybdate. The MoO_x overlayer makes the surface active and selective for formaldehyde synthesis, with all catalysts for the varying anneal temperatures showing similar activity due to their common surface termination. The materials proved both active and selective due to the dominance of the methoxy species on the Mo-doped material, as opposed to the much more stable formate, shown to form on Fe_2O_3 . To extend upon this theory further varying monolayers of Mo have been dosed at the surface of Fe_2O_3 . The stability of the MoO_x overlayer was further proven when assessing the catalyst structure for 1ML $\text{MoO}_x/\text{Fe}_2\text{O}_3$ at several anneal temperatures. The Mo remained at the surface under all

calcination regimes whilst exhibiting high selectivity and activity. The work highlights how catalyst surfaces are significantly different from bulk structures and this difference is crucial for catalyst performance.

In Chapter 5, *in situ* Raman/XAFS and catalytic testing have been exploited to provide insights during the crucial processes of calcination, formaldehyde production and reduction. *In situ* experiments are vital for advanced scientific research. The use of vibrational spectroscopy, particularly Raman [8], is widely valued in the characterisation of mixed metal oxides, and has commonly been adopted in studying iron molybdate catalysts [9-12]. Through integrating Raman spectroscopy with the surface sensitive approach of XAFS for the aforementioned core-shell materials, it was possible to study the surface phase composition of these complex, multicomponent oxide catalysts in more depth. The calcination studies were initially followed by a combination of XAFS and Raman, and demonstrated that amorphous multi-layers of MoO_x are first converted to MoO_3 before formation of $\text{Fe}_2(\text{MoO}_4)_3$. The production of MoO_3 progressively forms with rising calcination temperature. This was seen simultaneously in both XANES and Raman, for each of the catalysts investigated. It is only once all MoO_3 production has been accomplished, and the levels of MoO_3 plateau, that $\text{Fe}_2(\text{MoO}_4)_3$ production can commence. It was inferred that MoO_3 is a prerequisite to $\text{Fe}_2(\text{MoO}_4)_3$ synthesis. The set up detailed provided quick and accurate analysis, allowing the identification of different species of dosed molybdenum at the surface of Fe_2O_3 under increasing calcination temperature.

XAFS has also been used to assess the nature of Mo species during the isothermal oxidation of methanol. No obvious changes were observed in the absorption edge position, whilst the Mo overlayer remained in O_h co-ordination as Mo(VI) over the course of the reaction. The catalyst structure was hence preserved under reaction, enabling the sustained production of formaldehyde, shown through mass spectrometer analysis. It could be that Mo(IV) exists momentarily as a transient phase, but is unable to be seen due to the time scale of the study. Gas phase oxygen is present to ensure a quick and efficient regeneration to Mo(VI) in the eventuality of any Mo(VI) forming during the reaction. A reduction study therefore enabled further information about the redox cycling of the Mo species. Previous characterisation performed *ex situ* has revealed that catalysts re-oxidise when left under atmospheric conditions. XPS of the reduced samples show a mixed $\text{Mo(V)}/\text{Mo(VI)}$ oxidation state, an indication that the catalyst has partially re-oxidised back to its original Mo(VI) state. This is further accelerated under the heat of the focussed Raman laser, therefore making such techniques impractical for the study of oxide states. XAFS was employed to investigate the mechanisms occurring at the surface of FeMo based catalysts under reaction

with MeOH/He, inducing a reduction of the surface, which could be analogous to the reduction which occurs under redox mechanisms with methanol.

Initial *ex situ* studies probed the reduction process in bulk $\text{Fe}_2(\text{MoO}_4)_3$, revealing an obvious reduction to MoO_2 ascertained through XAFS, Raman and XRD. With the objectives to probe the surface layer and the mechanisms which occur with methanol, XAFS studies under *in situ* reduction were fundamental. In analysing core-shell $\text{MoO}_x/\text{Fe}_2\text{O}_3$ materials, the topmost layer was exclusively analysed without the presence of secondary phases such as FeMoO_4 and MoO_2 which arise in bulk materials.

EXAFS analysis revealed that for these surface Mo structures, the formation of reduced Mo-Mo clusters with a bonding distance of 2.6 Å were present. Literature defines this as a bonded distance indicating a Mo(V) dimer or Mo(IV) trimer [13]. This varies from bulk MoO_2 , which demonstrates a Mo-Mo bonding contribution at a shorter distance of 2.5 Å, with reduced co-ordination number. Previous work of Kikutani *et al.* [14] has established a 2.6 Å Mo–Mo bond in fixed dimer catalysts, as the most distinctive feature for unique dimeric active sites.

The significance of these Mo clusters, is that the possible Mo-Mo dimer unit suggests a two centered Mo reaction site, which momentarily forms on reaction with methanol. It was concluded that the catalytic active site offers two adjacent dioxo units of $\text{Mo}=\text{O}$. Initial chemisorption of methoxy occurs at one of the $\text{Mo}=\text{O}$ units. This in turn, places a C-H bond in close enough proximity to one of the oxo bonds of the second dioxo unit. C-H bond cleavage occurs at the second Mo unit, yielding a hydroxyl, which will likely bridge to an adjacent Mo centre. Finally, formaldehyde with simultaneous H_2O is released. The mechanism has been debated in the literature, however the proposed reaction mechanism agrees well with the work of Allison *et al.* [15] Methanol adsorption occurs readily at these bi-functional sites. The use of *in situ* XAFS to study the surface of FeMo based catalysts during reaction has not been previously reported in the literature, and brought with it significant findings.

The final chapter addressed the relevance of $\text{Fe}_2(\text{MoO}_4)_3$ in the catalyst, demonstrating the high redox capability of the mixed oxide due to its superior lattice oxygen mobility. Above 250 °C, oxygen mobility within the bulk lattice allows a movement towards the surface, enabling the catalyst to perform under anaerobic conditions via the Extended Mars-van Krevelen mechanism [7]. Such properties ensure maintained catalyst performance even with low oxygen levels in the gas phase. Work in previous chapters highlighted a surface terminating layer on Fe_2O_3 catalysts, denoted amorphous MoO_x . Fe_2O_3 is inherently

recognised for its poor reactivity in methanol oxidation, so it is imperative that the whole surface is covered by Mo to prevent unwanted side reactions.

Other supports have been trialled for their effectiveness in the same reaction. In changing the support, this can cause an increase/decrease in activity/selectivity, depending on the dispersion and charge transfer available. The support can be used as a way to tailor the performance of a catalyst, since the nature and dispersion of the metal alters the interaction with the support. Supports considered included SiC and Al_2O_3 : SiC for its inert nature and Al_2O_3 for its high surface area. It was discovered that Mo/SiC, although selective, was not active for the reaction, whilst in a reverse situation Mo/ Al_2O_3 was active but not as selective. Further work, predominantly XAFS, is required to investigate the Mo surface layer in these catalysts, as has been executed for Fe_2O_3 , to gain insights into the surface structure and how Mo binds to the support. Mo segregation to the surface is a fundamental property of iron molybdates which gives rise to the prolonged selectivity to formaldehyde. The stability of supported Mo/ Fe_2O_3 is shown at the beginning of this Chapter 6 to be short lived, since the conversion decreases after just 5 catalytic cycles due to sintering of the catalyst. Similar studies and characterisation are required to consider Mo/ Al_2O_3 as a potential catalyst.

7.2. Future work

Currently, the structure of the active phase in iron molybdates is still ambiguous, and continuous efforts are ongoing to enable its identification. However, XAS analysis throughout this work unveiled an amorphous surface overlayer of MoO_x dispersed over a well ordered $\text{Fe}_2(\text{MoO}_4)_3$ phase for multilayer Mo doping. This situation closely mimics that reported for VPO catalysts, applied to the selective oxidation of *n*-butane to produce maleic anhydride [16]. Although possible to identify this MoO_x amorphous layer and information regarding its co-ordination through EXAFS and theoretical models, it has not been possible to formally identify the exact geometric structure in the 2-D surface layer. Supplementary techniques to uncover further information have not been possible, due to the low overall weight loading of just one surface overlayer. In addition, many techniques are often limited to the probing of bulk materials, so are therefore unable to exclusively analyse the active surface region. To disclose further information, a stable, higher surface area oxide support is required to increase the proportion of the Mo phase at the surface. Initial work has involved a collaboration with UCL, successfully synthesising high surface area Fe_2O_3 by introduction of 5 w/t % aluminium dopant. STEM and XPS analyses favoured a homogeneous distribution of Al and Fe in the haematite framework. Work was carried out by Stephanie Chapman, an MChem student placed at Harwell for a 6 month period. Lattice strain induced by isomorphous substitution of Fe(III) for the smaller Al(III) cations, induced a constraint in

unit cell growth, resulting in a reduction in the overall particle size versus that of the commercial Fe_2O_3 (as evidenced through line broadening in XRD). Further analysis is required to expose the findings, especially using Raman spectroscopy.

It has been mentioned that Mo(VI) acts as the primary active site for selective methanol oxidation. Several theories are postulated to explain the significance of Mo, with many arguing its high oxidation state as a key contributing factor. With this in mind, it may be possible to trial other transition metal oxides to assess their effectiveness in the same reaction. Of particular interest is Re, which is able to demonstrate a high +7 oxidation state. Such studies also enable a theoretical understanding of why Mo works so well. Characterisation of V-, Nb-, W- and Re-doped haematite is still in its preliminary stages. It is hoped that an understanding of surface-support interactions for a range of surface oxides may disclose the reason for Mo oxide surface segregation.

Finally, it has been suggested that $\text{Fe}_2(\text{MoO}_4)_3$ has several purposes in the catalyst, including its ability to maintain catalyst selectivity under O_2 lean conditions, whilst also aiding the Mo structure at the catalyst surface. Work may be extended to further systems, replacing the Fe within the network with other cations to form isostructural molybdates. These could include $\text{Al}_2(\text{MoO}_4)_3$ or $\text{Bi}_2(\text{MoO}_4)_3$. It is possible that the Mo may form an alternative structure at the surface, demonstrating different redox mechanisms. Catalyst testing would be key. The Mo=O bond strength plays a crucial role in catalyst performance. With a change in the Mo=O bond strength, this will induce an alteration in the selectivity of the catalyst.

7.3. References

1. Kim, T.H., et al., *Selective oxidation of methanol to formaldehyde using modified iron-molybdate catalysts*. Catalysis Letters, 2004. **98**(2-3): p. 161-165.
2. Bowker, M., et al., *The selective oxidation of methanol to formaldehyde on iron molybdate catalysts and on component oxides*. Catalysis Letters, 2002. **83**(3-4): p. 165-176.
3. Routray, K., et al., *Origin of the synergistic interaction between MoO₃ and iron molybdate for the selective oxidation of methanol to formaldehyde*. Journal of Catalysis, 2010. **275**(1): p. 84-98.
4. Routray K, W.I.E., *Surface Segregation in Iron Molybdate catalysts*, 2006 Prep Paper, Am Chem Soc. Div Pet.
5. Soderhjelm, E., et al., *On the Synergy Effect in MoO₃-Fe₂(MoO₄))₃ Catalysts for Methanol Oxidation to Formaldehyde*. Topics in Catalysis, 2008. **50**(1-4): p. 145-155.
6. Pernicone, N., *MoO₃-Fe₂(MoO₄))₃ catalysts for methanol oxidation*. Journal of the Less Common Metals, 1974. **36**(1-2): p. 289-297.
7. Bowker, M., et al., *The selective oxidation of methanol on iron molybdate catalysts*. Topics in Catalysis, 2008. **48**(1-4): p. 158-165.

8. Xu, Q., et al., *Surface phase composition of iron molybdate catalysts studied by UV Raman spectroscopy*. Journal of Physical Chemistry C, 2008. **112**(25): p. 9387-9393.
9. Routray, K., et al., *Origin of the synergistic interaction between MoO₃ and iron molybdate for the selective oxidation of methanol to formaldehyde*. Journal of Catalysis, 2010. **275**(1): p. 84-98.
10. Uhlrich, J.J., et al., *Preparation and characterization of iron-molybdate thin films*. Surface Science, 2011. **605**(15-16): p. 1550-1555.
11. Cheng, W.H., *Methanol and formaldehyde oxidation study over molybdenum oxide*. Journal of Catalysis, 1996. **158**(2): p. 477-485.
12. Hill, C.G. and J.H. Wilson, *RAMAN-SPECTROSCOPY OF IRON MOLYBDATE CATALYST SYSTEMS .2. PREPARATION OF SUPPORTED CATALYSTS*. Journal of Molecular Catalysis, 1991. **67**(1): p. 57-77.
13. Allison, J.N. and W.A. Goddard Iii, *Oxidative dehydrogenation of methanol to formaldehyde*. Journal of Catalysis, 1985. **92**(1): p. 127-135.
14. Kikutani, Y., *Structures of molybdenum silica catalysts reduced by ethanol, and their relations to catalytic oxidation reactions: I. Structure changes of Mo/SiO₂ with gradual reduction by ethanol*. Journal of Molecular Catalysis A: Chemical, 1999. **142**(2): p. 247-263.
15. Allison, J.N. and W.A. Goddard Iii, *Oxidative dehydrogenation of methanol to formaldehyde*. J. Catal., 1985. **92**(1): p. 127-135.
16. Ballarini, N., et al., *VPO catalyst for n-butane oxidation to maleic anhydride: A goal achieved, or a still open challenge?* Topics in Catalysis, 2006. **38**(1-3): p. 147-156.